Manoj K. Shukla
Veera M. Boddu
Jeffery A. Steevens
Reddy Damavarapu
Jerzy Leszczynski   *Editors*

Energetic Materials

From Cradle to Grave

Springer

Challenges and Advances in Computational Chemistry and Physics

Volume 25

Series editor

Jerzy Leszczynski
Department of Chemistry and Biochemistry
Jackson State University, Jackson, MS, USA

This book series provides reviews on the most recent developments in computational chemistry and physics. It covers both the method developments and their applications. Each volume consists of chapters devoted to the one research area. The series highlights the most notable advances in applications of the computational methods. The volumes include nanotechnology, material sciences, molecular biology, structures and bonding in molecular complexes, and atmospheric chemistry. The authors are recruited from among the most prominent researchers in their research areas. As computational chemistry and physics is one of the most rapidly advancing scientific areas such timely overviews are desired by chemists, physicists, molecular biologists and material scientists. The books are intended for graduate students and researchers.

More information about this series at http://www.springer.com/series/6918

Manoj K. Shukla · Veera M. Boddu
Jeffery A. Steevens · Reddy Damavarapu
Jerzy Leszczynski
Editors

Energetic Materials

From Cradle to Grave

Editors
Manoj K. Shukla
US Army Engineer Research and
    Development Center
Vicksburg, MS
USA

Veera M. Boddu
US Department of Agriculture
Agricultural Research Service
Peoria, IL
USA

Jeffery A. Steevens
US Army Engineer Research and
    Development Center
Vicksburg, MS
USA

Reddy Damavarapu
US Army Armament Research,
    Development and Engineering Center
Picatinny, NJ
USA

Jerzy Leszczynski
Jackson State University
Jackson, MS
USA

Printed on acid-free paper

Preface

With a great pleasure, we take this opportunity to bring the current volume "Energetic Materials: From Cradle to Grave" under the series "Challenges and Advances in Computational Chemistry and Physics". This volume brings experimentalists and theoreticians on a common platform integrating recent advances in the "Cradle to Grave" of munition compounds through scholarly contributions. The 13 contributed chapters included in this volume cover wide area ranging from design and development of munitions, nanomaterials in munitions application, fate and transport, and munition-induced toxicity.

Chapter "High Performance, Low Sensitivity: The Impossible (or Possible) Dream?" contributed by Politzer and Murray discusses the design and development of high-performance and low-sensitivity munitions (insensitive munitions), their characteristics, and how and if such dream can be materialized. Chapter "Recent Advances in Gun Propellant Development: From Molecules to Materials" by Rozumov provides an overview of recent advances in the development of gun propellants including making the gun propellant formulations less sensitive to shock and thermal stimuli. The utilization of quantitative structure–property relationships (QSPR) models in the design and development of munition compounds including prediction of various properties has been the focus of the next chapter by Fayet and Rotureau. The use of energetic polymers is expected to be beneficial since they contribute several advantageous characteristics such as temperature and pressure stabilities, produce less smoke, and so on. The recent advances in the synthesis and applications of energy polymers have been reviewed by Paraskos in Chapter "Energetic Polymers: Synthesis and Applications". The large surface area and enhanced reactivity of nanoscale metallic powder can be utilized as an efficient pyrophoric materials. In Chapter "Pyrophoric Nanomaterials", Haines et al. present an overview of recent progress in pyrophoric nanomaterials including pyrophoric foams and various safety consideration.

In the rocket motor design, the information about the burning rate of propellant plays an important role. Isert and Son have reviewed the relationship between flame structure and burning rate for ammonium perchlorate composite propellants in Chapter "The Relationship Between Flame Structure and Burning Rate for Ammonium

Perchlorate Composite Propellants". Picatinny Arsenal FRAGmentation (PAFRAG) is used to evaluate explosive fragmentation ammunition lethality and safe separation distance without costly arena fragmentation tests. The fundamentals of this methodology and applications have been reviewed in the next chapter by Gold. In Chapter "Grain-Scale Simulation of Shock Initiation in Composite High Explosives", Austin et al. have detailed the application of single- and multi-crystal simulation to understand response and detailed chemical and physical processes for energetic material safety. In the next chapter, Mukherjee and Davari have reviewed the development of various computational models to investigate fate, transport, and evolution of energetic nano-materials. In Chapter "Physical Properties of Select Explosive Components for Assessing Their Fate and Transport in the Environment", Boddu et al. have reviewed the physical properties for assessing the fate and transport of select munition compounds in the environment. In Chapter "High Explosives and Propellants Energetics: Their Dissolution and Fate in Soils", Dontsova and Taylor have reviewed the dissolution and fate of high explosives and propellants in soils while in the following chapter, Taylor et al. have reviewed the fate and dissolution of insensitive munitions formulations in the soils. The last chapter by Lotufo provides a comprehensive overview of toxicity and bioaccumulation of energetic compounds in the aquatic and soil organisms and in terrestrial plants.

We take this opportunity to thank all contributors for devoting their time and hard work to make this project a success. We would like to thank Dr. Elizabeth A. Ferguson, Senior Science Technical Manager and Lead Technical Director for Environmental Quality and Installations, US Army Engineer Research and Development Center, Vicksburg, Mississippi, USA, for continuous support and encouragement to publish this book. Of course, many thanks go to our family members and friends. Without their support, the development and completion of the book would not have been possible.

Vicksburg, MS, USA   Manoj K. Shukla
Peoria, IL, USA   Veera M. Boddu
Vicksburg, MS, USA   Jeffery A. Steevens
Picatinny, NJ, USA   Reddy Damavarapu
Jackson, MS, USA   Jerzy Leszczynski

Contents

High Performance, Low Sensitivity: The Impossible (or Possible) Dream?

Peter Politzer and Jane S. Murray

Abstract After mentioning methods for quantifying detonation performance and sensitivity, we proceed to discuss some factors that govern these properties. To enhance the likelihood of an explosive having high performance in conjunction with low or moderate sensitivity, it *should have* (a) a high density, and (b) a large number of moles of gaseous detonation products per gram of explosive, and *should avoid having* (c) a strongly positive electrostatic potential in the central portion of its molecular surface, (d) a large amount of free space per molecule in its crystal lattice, and (e) a large maximum heat of detonation. In particular, we demonstrate that a large heat of detonation is unnecessary from the standpoint of performance and undesirable from the standpoint of sensitivity. We summarize some specific molecular features that may help to satisfy the guidelines listed above.

Keywords Explosives · Detonation performance · Sensitivity · Detonation heat release · Electrostatic potential · Free space in crystal lattice

1 The Problem

High detonation performance tends to be accompanied by high sensitivity. The most powerful explosives tend to be overly vulnerable to unintended detonation caused by accidental stimuli such as shock or impact. This observation, perhaps not surprising, is based upon experience but it is also supported by systematic studies [1, 2]. The basic problem is that factors promoting one of the desired objectives—high performance or low sensitivity—frequently conflict with the other. Hence efforts to design improved explosives often become, as recently described, "a quest for balance" [3].

P. Politzer (✉) · J.S. Murray
Department of Chemistry, University of New Orleans, New Orleans, LA 70148, USA
e-mail: ppolitze@uno.edu

P. Politzer · J.S. Murray
CleveTheoComp, 1951 W. 26th Street, Suite 409, Cleveland, OH 44113, USA

Nevertheless, even the two studies mentioned above [1, 2], which confirmed that high performance was likely to be accompanied by high sensitivity, held out hope for what Licht called the "ideal explosive candidate," that approaches high performance and low sensitivity [1]. We intend to explore this hope. However we must first be explicit about how detonation performance and sensitivity are to be characterized.

2 Detonation Performance

2.1 *Measurement*

There are a number of quantitative measures of detonation performance [1, 2, 4–10]; a partial list includes:

(a) Detonation velocity, D: the stable velocity of the shock front that characterizes detonation.
(b) Detonation pressure, P: the stable pressure developed behind the shock front.
(c) Brisance, B: the capacity of the detonation products for doing work, i.e. their shattering effect.
(d) Gurney velocity, $\sqrt{2E_G}$: the velocity of the metal fragments.

While each of these quantities has a definite significance, they are not completely independent of each other. For example, the detonation pressure is an indicator of brisance [4, 5], and there is a rough relationship between detonation velocity and Gurney velocity (Fig. 1) [1, 10, 11]. In fact, Urtiew and Hayes have shown that a variety of key detonation properties can be estimated for many explosives from their detonation velocities [12].

Fig. 1 Relationship of experimental detonation velocities and Gurney velocities. Data are taken from Ref. [1]
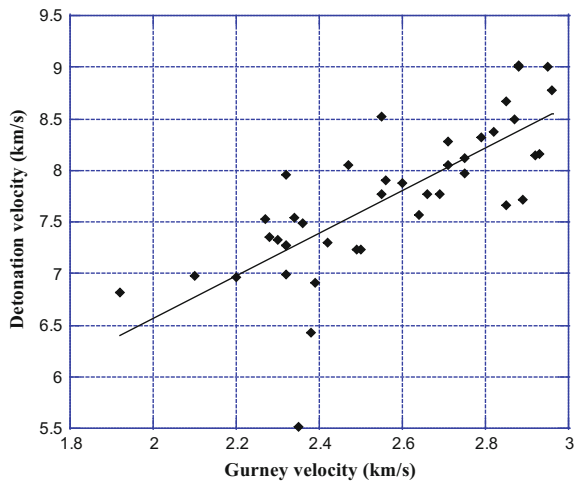
In view of such relationships, it seems reasonable to use the detonation velocity D and detonation pressure P as overall measures of detonation performance. These properties are indeed very widely invoked for this purpose. Large values of D and P characterize high performance.

Detonation velocity and detonation pressure can be determined experimentally by various methods [1, 2, 5, 7] or predicted by means of computer codes, e.g. BKW [13], EXPLO5 [14] and CHEETAH [15]. For gaining insight into what governs these properties, however, particularly useful are empirical equations for D and P that were developed by Kamlet and Jacobs for C, H, N, O-containing explosives [16].

2.2 Some Governing Factors

Kamlet and Jacobs showed that D and P can be expressed quite well in terms of four quantities [16]:

(1) The number of moles N of gaseous detonation products per gram of explosive.
(2) The average molecular mass M_{ave} of the gaseous detonation products, in g/mol.
(3) The magnitude Q of the total heat release of the detonation reaction, in calories per gram of explosive.
(4) The loading density ρ, in g/cm^3. For a single explosive compound, in the absence of other information, this is typically taken to be its known or estimated crystal density.

The Kamlet-Jacobs equations are [16]:

$$D(\text{km/s}) = 1.01 \left[N^{0.5} M_{ave}^{0.25} Q^{0.25} (1 + 1.30\rho) \right] \tag{1}$$

$$P(\text{kbar}) = 15.58 \left[N M_{ave}^{0.5} Q^{0.5} \rho^2 \right] \tag{2}$$

The effectiveness of Eqs. (1) and (2) has been confirmed through many comparisons with experimental D and P [16–21].

Using Eqs. (1) and (2) requires knowing or assuming the composition of the final detonation products of the explosive in question, which is needed in order to evaluate N, M_{ave} and Q. This could be a problem, since the detonation process involves a series of reactions and equilibria, producing a variety of gaseous intermediates [13, 22]. Fortunately, the final products for a C, H, N, O explosive are usually composed almost entirely of just $N_2(g)$, $CO(g)$, $CO_2(g)$, $H_2O(g)$, $H_2(g)$ and solid carbon [13, 16, 20, 23, 24]. However the proportions of these are still an issue; they are affected by the loading density of the explosive, the temperature and other physical conditions [16, 22, 23].

Several sets of rules have been proposed for predicting the proportions of the final products; they are summarized elsewhere [25–27]. Particularly widely used are the rules of Kamlet and Jacobs [16], which prescribe the products $N_2(g)$, $H_2O(g)$, $CO_2(g)$ and $C(s)$, with oxygens going to H_2O before CO_2. No CO is predicted. In contrast, the other sets of rules envision more CO than CO_2 and often some H_2 as well, but less $C(s)$.

Rather remarkably, it has been found that different assumed product compositions, for a given explosive and loading density, lead to similar values for its detonation velocity and detonation pressure, as obtained by Eqs. (1) and (2) [23, 27]. To understand this, we first rewrite Eqs. (1) and (2) as,

$$D(\text{km/s}) = 1.01\, \varphi(1 + 1.30\rho) \tag{3}$$

$$P(\text{kbar}) = 15.58\, \varphi^2\rho^2 \tag{4}$$

where $\varphi = N^{0.5}M_{ave}^{0.25}Q^{0.25}$. For D and P to be similar for a particular density, it is necessary that φ be relatively independent of the product composition for that explosive. Why would this be the case?

N and M_{ave} are easily calculated for any set of products. Q is commonly taken to be the negative of the enthalpy change in the overall detonation reaction (although in practive Q also depends upon physical factors, e.g. the loading density and the extent of expansion of the gaseous products [7, 9, 22, 23]). Thus, for an explosive X,

$$Q = -\frac{1}{M_X}\left[\sum_i n_i\Delta H_{f,i} - \Delta H_{f,X}\right] \tag{5}$$

in which M_X is the mass of X in g/mol, n_i is the number of moles of final product i, having molar heat of formation $\Delta H_{f,i}$, and $\Delta H_{f,X}$ is the molar heat of formation of X. When the products contain more moles of the diatomic gases CO and H_2 and correspondingly fewer of the triatomic CO_2 and H_2O, the effect is to increase N and decrease M_{ave}. Q is also diminished because the heats of formation of CO(g) and $H_2(g)$ are much less negative than those of $CO_2(g)$ and $H_2O(g)$ [28]. However since N appears in φ to a higher power than do M_{ave} and Q, the changes in these three quantities approximately cancel and φ is roughly constant [23, 27].

Accordingly the different sets of rules for predicting detonation products generally yield quite similar D and P for a particular explosive and loading density [23, 27], although the D and P resulting from the Kamlet-Jacobs rules are closest to the experimental values for loading densities near the crystal density [13, 27]. From Eqs. (3) and (4) and the observation that $\varphi \sim$ constant also follow the long-known relationshps, for a given explosive, $D \sim \rho$ and $P \sim \rho^2$ [13, 19, 25, 29, 30].

It should be noted, however, that while φ—and therefore D and P—vary relatively little with assumed product composition, this is not generally true of N, M_{ave}

and Q individually. They can be quite significantly affected [27]. This should be kept in mind if it is specifically the volume of gases produced or the heat released that is of interest.

3 Sensitivity

3.1 Measurement

Sensitivity refers to the ease with which unintended detonation initiation can occur. A variety of accidental stimuli can cause this: impact, shock, friction, heat, electric sparks, etc. A particular explosive is not, in general, similarly sensitive to all of these stimuli [3], although Storm et al. [31] have found correlations between sensitivities to (a) shock and impact, and (b) shock and heat. The most extensively reported type of sensitivity is that due to impact, and this shall be our focus in the discussion to follow.

Impact sensitivity is commonly measured by dropping a given mass m upon a sample of the explosive and determining the height from which 50% of the drops cause reaction [31–34]. The magnitude of this height, which is labeled h_{50}, depends of course upon the mass being dropped. It is therefore necessary to specify this, which unfortunately is not always done. An alternative that avoids this problem is to report the corresponding impact energy, mgh_{50}, where g is the gravitational acceleration. For a typical mass of 2.5 kg, an h_{50} of 100 cm is equivalent to an impact energy of 24.5 J (24.5 Nm).

The smaller is the drop height h_{50}, the less is accordingly the impact energy mgh_{50} that is required to initiate reaction, and the more sensitive is the explosive. For most C, H, N, O explosives, the h_{50} values range from about 10 cm (impact energy = 2.5 J), which indicates high sensitivity, to about 300 cm (impact energy = 74 J), very low sensitivity.

A notorious problem with measuring impact sensitivity is that the result depends not only upon the chemical nature of the explosive but also upon physical factors: the sizes, shapes and hardness of the crystals, their purity and surface roughness, lattice defects, the polymorphic form of the crystals, the temperature and humidity, etc. [34–39]. For meaningful results, it is essential that the mode of preparation of the sample—crystallization, purification, grinding, etc.—and the testing procedure and environment be kept as uniform as possible. The h_{50} values obtained in different laboratories for the same explosives may disagree considerably. However the trends will be similar if the laboratories consistently follow their respective preparation and testing procedures [40].

3.2   Some Governing Factors

Unfortunately, there is no equivalent of the Kamlet-Jacobs equations that would, for different classes of explosives, provide insight into what determines their sensitivities toward various stimuli and also allow satisfactory quantitative estimates of these sensitivities. This is not for lack of effort. There have been reported numerous correlations between (usually) impact sensitivity and a remarkable array of molecular and crystalline properties, as summarized in several overviews [3, 32, 41–44]. Such correlations can sometimes be quite useful, but they are typically limited to explosives of a particular chemical type, e.g. nitroaromatics.

The fact that more than a dozen molecular and crystalline properties have thus been "linked" to sensitivity suggests, however, that some (perhaps many) of these relationships are symptomatic, i.e. they *reflect* some more general factor(s). We and others have identified three such factors. (There may be yet additional ones.) The three are:

(1) The characteristic strongly positive electrostatic potentials on the central portions of the molecular surfaces of explosives (and above and below their $C–NO_2$ and $N–NO_2$ bonds) [3, 33, 41, 43, 45, 46]. This feature is not found on most organic molecules; compare Figs. 2 (phenol) and 3 (the explosive picric acid).

Fig. 2 Computed electrostatic potential on the molecular surface of phenol, as defined by the 0.001 au contour of its electronic density. Hydroxyl group is at the top. Positions of nuclei are within the surface and are shown as gray spheres. Color ranges, in kcal/mole, are: *red* greater than 20; *yellow* between 20 and 0; *green* between 0 and −10; *blue* more negative than −10. The central portion of the surface is completely negative; the strongest positive potential (*red*) is associated with the hydroxyl hydrogen
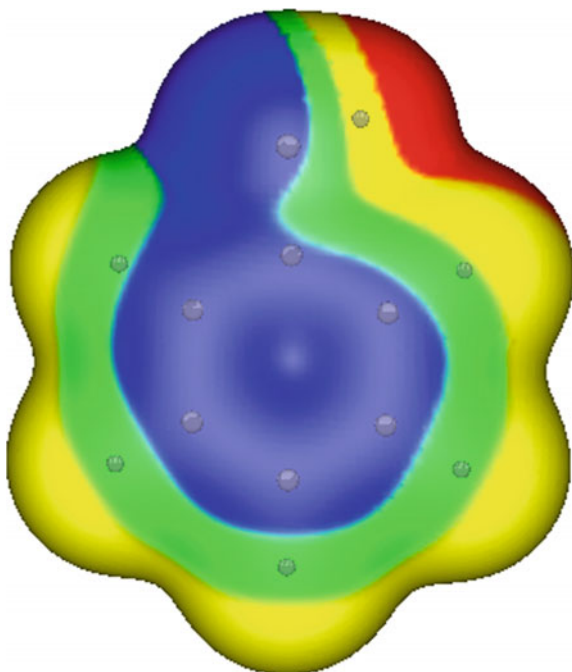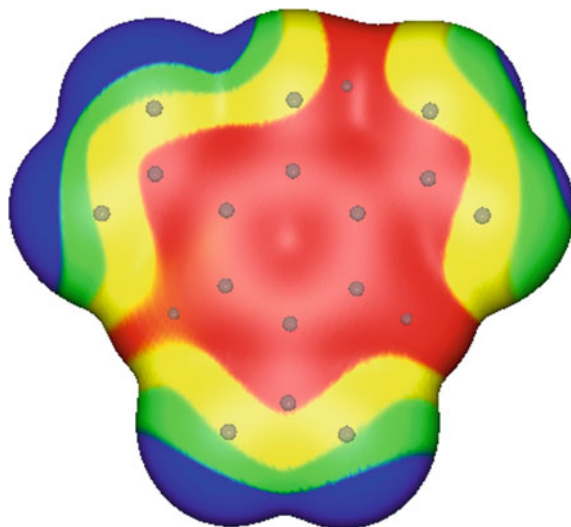
Fig. 3 Computed electrostatic potential on the molecular surface of picric acid (2,4,6-trinitrophenol), as defined by the 0.001 au contour of its electronic density. Hydroxyl group is at the *top*. Positions of nuclei are within the surface and are shown as *gray spheres*. Color ranges, in kcal/mole, are: *red* greater than 20; *yellow* between 20 and 0; *green* between 0 and −10; *blue* more negative than −10. There are strong positive potentials (*red*) above and below the ring and the C–NO$_2$ bonds. The peripheral negative potentials are associated with the oxygens

(2) The amounts of free space per molecule in the crystal lattices of explosives [3, 40, 47].

(3) The maximum available detonation heat releases, either per unit mass [33, 48] or per unit volume [40, 49, 50].

In general, larger or more positive values of these properties tend to be associated with greater impact sensitivities. These are *not* correlations, but rather overall trends.

In order to have some understanding of why these three factors promote sensitivity, consider some of the key events that are involved in the initiation of detonation [6, 10, 40, 49, 51–60]. When a crystalline explosive is subjected to impact or shock, it undergoes compression; the rate and degree of this depend upon the nature of the explosive and the strength of the external stimulus. This compression results in structural effects within the crystal lattice of the explosive: shear/slip (lattice planes shifting past each other), disorder, collapse of voids and vacancies and other changes in lattice defects, etc. The resistance to these structural effects produces local buildups of thermal energy ("hot spots") in small regions within the lattice. The transfer of some of this hot-spot energy to molecular vibrational modes leads to bond breaking and molecular rearrangements, followed by self-sustaining exothermal chemical decomposition that releases energy and gaseous products. This results in a high pressure, supersonic shock wave

propagating through the system (detonation). Factors that favor these and related events increase the sensitivity of the explosive.

How is sensitivity associated with the strongly positive electrostatic potentials in the central regions of the molecular surfaces of explosives? First we want to point out that the electrostatic potential is a real physical property that rigorously reflects the overall distribution of charge—nuclear and electronic—in a system [61, 62]. It should not be confused with atomic charges, which have no physical basis and are arbitrarily defined by one of more than 30 proposed methods. The electrostatic potential can be determined both experimentally and computationally.

The role of the strong positive potentials on explosive molecular surfaces in promoting sensitivity is believed to be both causative and symptomatic [3, 40]. The repulsion between the positive regions on neighboring molecules increases the resistance to the shear/slip that results from the compression following impact or shock. This increased resistance enhances the hot spot formation that is an intregral part of detonation initiation. The positive potentials are also symptomatic of the withdrawal of electronic charge by NO_2 groups, aza nitrogens, etc., that weakens $C-NO_2$ and $N-NO_2$ bonds and facilitates their ruptures [41, 63]; these ruptures may sometimes be initiating steps in the chemical decompositions. The strengths and extents of these positive regions have indeed been correlated with impact sensitivity, both quantitatively [45, 46, 63] and qualitatively [33, 64–67], for compounds with similar molecular frameworks. In the present discussion, however, we focus upon the overall tendency (not a correlation) of the impact sensitivities of diverse explosive compounds to be related to the strongly-positive electrostatic potentials in the central portions of their molecular surfaces.

The effect upon sensitivity of free space in the lattice is two-fold [40]. It facilitates the compression that follows impact or shock, and thus the conversion of the mechanical energy of the external stimulus into thermal energy, particularly hot spots. In addition, $C-NO_2$ and $N-NO_2$ bonds have been shown to be weaker and more easily broken when the molecules are on the surfaces of lattice voids (free space) than when they are in the bulk lattice [68, 69].

The free space per molecule in the unit cell, designated ΔV, is given by,

$$\Delta V = V_{eff} - V_{int} \tag{6}$$

where V_{eff} is the hypothetical "effective" volume per molecule that would correspond to the unit cell being completely filled (no free space) and V_{int} is the "intrinsic" volume of the molecule. V_{eff} is equal to M/ρ, M being the molecular mass and ρ the crystal density. We take V_{int} to be the volume enclosed by the 0.003 au contour of the molecule's electronic density [40, 47, 70]. This choice of V_{int} produces packing coefficients (V_{int}/V_{eff}) that agree well with the range and average value of those determined by Eckhardt and Gavezzotti for explosives [71]. (The packing coefficient is the fraction of the unit cell that is completely filled).

In Table 1 are some experimentally-determined properties of a series of explosives: impact sensitivities, heats of formation, molecular masses and densities. In Table 2 are calculated properties for the same explosives, including V_{int} and ΔV.

Table 1 Experimental properties: impact sensitivities h_{50}, solid phase heats of formation ΔH_f, molecular masses M and densities ρ

Compound	h_{50} (cm)[a]	$\Delta H_f(s)$ (kcal/mol)[b]	M (g/mol)	ρ^k (g/cm^3)
Bis(trinitroethyl)nitramine	5	−6.69	388.1	1.953
Tetraazidoazo-1,3,5-triazine	6[n]	518.9[n]	352.2	1.72[n]
PETN (pentaerythritol tetranitrate)	12	−128.8[c]	316.1	1.76[c]
β-CL-20 (hexanitrohexaazaisowurtzitane)	14[d]	103.0[d]	438.2	1.985[d]
Tetraazidohydrazo-1,3,5-triazine	18[n]	419.0[n]	354.2	1.65[n]
Trinitropyridine N-oxide	20	24.40[e]	230.1	1.875[l]
LLM-119 (diaminodinitropyrazolopyrazole)	24[f]	114[f]	228.1	1.845[f]
RDX (trinitrotriazacyclohexane)	26	18.9	222.1	1.806
TNAZ (1,3,3-trinitroazetidine)	29[g]	8.70[c]	192.1	1.84[m]
HMX (tetranitrotetraazacyclooctane)	29	24.5	296.2	1.894
Tetryl (2,4,6-trinitro-N-methyl-N-nitroaniline)	32	9.8	287.1	1.731
N,N′-Dinitro-1,2-diaminoethane	34	−24.81[c]	150.1	1.709
2,3,4,6-Tetranitroaniline	41	−11.74	273.1	1.861
2,4,6-Trinitroresorcinol	43	−111.7	245.1	1.83[c]
Benzotrifuroxan	50	144.9	252.1	1.901
2,4,5-Trinitroimidazole	68	15.5[h]	203.1	1.88[h]
FOX-7 (1,1-diamino-2,2-dinitroethylene)	72[f]	−32[f]	148.1	1.885[f]
Picric acid (2,4,6-trinitrophenol)	87	−52.07	229.1	1.767[c]
TNB (1,3,5-trinitrobenzene)	100	−8.9	213.1	1.76[c]
2,4-Dinitroimidazole	105	5.6[h]	158.1	1.770
2,4,6-Trinitrobenzoic acid	109	−97.91	257.1	1.786
LLM-105 (2,6-diamino-3,5-dinitropyrazine 1-oxide)	117[i]	−3.10[j]	216.1	1.919[i]
TNT (2,4,6-trinitrotoluene)	160	−15.1	227.1	1.654[c]
LLM-116 (4-amino-3,5-dinitropyrazole)	165[f]	17.3[o]	173.1	1.90[f]
Picramide (2,4,6-trinitroaniline)	177	−17.4	228.1	1.773
NTO (3-nitro-1,2,4-triazole-5-one)	291	−24.09[c]	130.1	1.918

[a]Reference [31] unless otherwise indicated
[b]Reference [72] unless otherwise indicated
[c]Reference [7]. [d]Ref. [73]. [e]Ref. [28]. [f]Ref. [74]. [g]Ref. [75]
[h]Reference [76]. [i]Ref. [77]. [j]Ref. [66]. [k]Ref. [78] unless otherwise indicated
[l]Reference [79]. [m]Ref. [80]. [n]Ref. [81]. [o]Ref. [82]

We have demonstrated earlier that the h_{50} values of explosives of different types tend in general to decrease (increasing sensitivity) as ΔV becomes larger [40, 47, 70]. This is seen again in Fig. 4 for the explosives in Tables 1 and 2. Figure 4 does

Table 2 Calculated properties: Intrinsic molecular volume V_{int}, free space per molecule in crystal lattice ΔV, detonation heat release Q_{max}, number of moles N of gaseous detonation products per gram of explosive, average molecular mass M_{ave} of gaseous detonation products, detonation velocity D and detonation pressure P

Compound	V_{int} (Å³)	ΔV (Å³)	Q_{max} (kcal/g)[a]	N (mol/g)[a]	M_{ave} (g/mol)[a]	D (km/s)[b]	P (kbar)[b]
Bis(trinitroethyl)nitramine	257.4	73	1.25	0.03092	32.34	8.91	369
Tetraazidoazo-1,3,5-triazine	255.5	85	1.47	0.02839	28.01	7.85	266
PETN (pentaerythritol tetranitrate)	225.2	73	1.51	0.03164	30.41	8.65	327
β-CL-20 (hexanitrohexaazaisowurtzitane)	281.0	86	1.60	0.03081	31.13	9.48	422
Tetraazidohydrazo-1,3,5-triazine	259.2	97	1.18	0.03106	25.65	7.39	229
Trinitropyridine N-oxide	157.2	47	1.58	0.02608	34.35	8.56	333
LLM-119 (diaminodinitropyrazolopyrazole)	162.2	43	1.42	0.03069	27.44	8.45	321
RDX (trinitrotriazacyclohexane)	158.6	46	1.50	0.03377	27.21	8.83	347
TNAZ (1,3,3-trinitroazetidine)	136.6	37	1.63	0.03123	30.02	9.00	364
HMX (tetranitrotetraazacyclooctane)	210.5	49	1.50	0.03376	27.22	9.13	381
Tetryl (2,4,6-trinitro-N-methyl-N-nitroaniline)	205.9	70	1.44	0.02699	30.46	7.80	264
N,N′-Dinitro-1,2-diaminoethane	117.2	29	1.30	0.03664	24.02	8.28	295
2,3,4,6-Tetranitroaniline	187.2	57	1.39	0.02655	33.12	8.24	307
2,4,6-Trinitroresorcinol	166.6	56	1.15	0.02550	33.94	7.66	263
Benzotrifuroxan	165.4	55	1.69	0.02380	36.02	8.50	331
2,4,5-Trinitroimidazole	135.5	44	1.49	0.02831	34.80	8.83	355
FOX-7 (1,1-diamino-2,2-dinitroethylene)	107.4	23	1.20	0.03376	27.22	8.61	338
Picric acid (2,4,6-trinitrophenol)	160.2	55	1.28	0.02510	33.06	7.57	251
TNB (1,3,5-trinitrobenzene)	153.4	48	1.36	0.02464	32.02	7.53	248
2,4-Dinitroimidazole	111.3	37	1.29	0.02846	31.13	7.96	278
2,4,6-Trinitrobenzoic acid	177.9	61	1.15	0.02431	33.94	7.35	239

(continued)

Table 2 (continued)

Compound	V_{int} (Å^3)	ΔV (Å^3)	Q_{max} (kcal/g)[a]	N (mol/g)[a]	M_{ave} (g/mol)[a]	D (km/s)[b]	P (kbar)[b]
LLM-105 (2,6-diamino-3,5-dinitropyrazine 1-oxide)	152.0	35	1.17	0.03008	28.63	8.28	316
TNT (2,4,6-trinitrotoluene)	169.9	58	1.29	0.02532	28.52	7.01	207
LLM-116 (4-amino-3,5-dinitropyrazole)	122.8	29	1.28	0.03033	28.97	8.47	328
Picramide (2,4,6-trinitroaniline)	163.5	50	1.26	0.02630	30.02	7.55	251
NTO (3-nitro-1,2,4-triazole-5-one)	91.5	21	0.982	0.03075	29.53	8.07	300

[a]Q_{max}, N and M_{ave} were calculated assuming detonation products as given by Kamlet-Jacobs rules [16]

[b]Calculated using Eqs. (1) and (2), with ρ from Table 1 and Q_{max}, N and M_{ave} from this table. For calculating D and P, Q_{max} must be in cal/g

Fig. 4 Relationship between measured impact sensitivity h_{50} and calculated free space per molecule in the crystal lattice ΔV for the 26 compounds in Tables 1 and 2
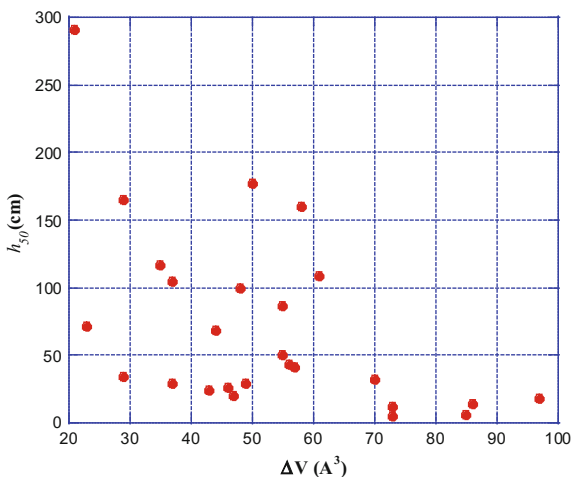
not represent a correlation, but rather an overall trend for explosives to be more sensitive as there is more free space in the crystal lattice. There are some distinct outliers, which will be discussed later.

Proceeding now to the detonation heat release (the third of the factors thus far identified as affecting sensitivity), it is what allows the chemical decomposition to become self-sustaining, producing the high pressure, supersonic shock wave of detonation. The magnitude Q of this heat release depends of course upon the actual composition of the detonation products. Given that the major products for C, H, N, O explosives are usually some combination of $N_2(g)$, $CO(g)$, $CO_2(g)$, $H_2O(g)$, $H_2(g)$ and $C(s)$ [13, 16, 20, 23, 24], the maximum value of Q, by Eq. (5), is if all of the oxygen is converted to $CO_2(g)$ and $H_2O(g)$ [27, 50], since these have the most negative heats of formation [28]: $CO_2(g)$: −94.05 kcal/mol; $H_2O(g)$: −57.80 kcal/mol; $CO(g)$: −26.42 kcal/mol; $N_2(g)$, $H_2(g)$ and $C(s)$: zero. This maximum Q, labeled Q_{max}, corresponds to using the Kamlet-Jacobs rules for predicting the detonation products.

Pepekin et al. [50] pointed out that Q_{max} can be viewed as an intrinsic property of each explosive, representing its "limiting capability" to convert chemical energy into thermal energy. It has now been shown on several occasions that sensitivity is linked roughly to Q_{max}, the latter being either per unit mass (i.e. Q_{max} itself) [33, 48] or per unit volume (i.e. ρQ_{max}) [40, 49, 50]. This is demonstrated once more in Fig. 5, using the h_{50} in Table 1 and the Q_{max} in Table 2. Again, this should not be regarded as a correlation, but simply as an overall trend: There is a general tendency for explosives to be more sensitive to impact (h_{50} lower) as their maximum heats of detonation are greater (Q_{max} larger). This conclusion pertains specifically to the *maximum* heat of detonation (an intrinsic property of the explosive) regardless of what the actual heat of detonation may be under any particular circumstances.

It is now more understandable why, for C, H, N, O explosives of the same chemical type, impact sensitivity correlates approximately with "oxygen balance"

Fig. 5 Relationship between measured impact sensitivity h_{50} and calculated maximum heat of detonation Q_{max} for the 26 compounds in Tables 1 and 2
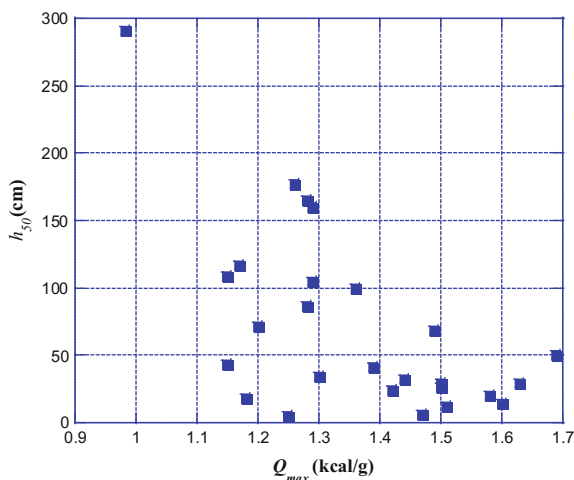
[35, 36, 83]. This term refers to the degree to which there is sufficient oxygen in the molecule to oxidize all carbons to CO_2 and all hydrogens to H_2O. As the proportion of oxygen in the molecule (and hence the oxygen balance) increases, more CO_2 and H_2O can in principle be formed. Since these have the most negative heats of formation of the probable final detonation products, a higher oxygen balance will correspond to a larger maximum heat of detonation, by Eq. (5), and therefore—by Fig. 5—is likely to be accompanied by greater impact sensitivity.

We have discussed three factors that appear to be related to sensitivity: (1) The strongly-positive electrostatic potential in the central region of the molecular surface, (2) the amount of free space per molecule in the crystal lattice, and (3) the maximum available heat of detonation. Since these factors pertain to different phases of the detonation initiation process, sensitivity should not be expected to correlate closely with any one of them (nor in general with any single molecular or crystal property). Such a correlation would require that the effects of the other factors be essentially constant, which should not be anticipated except under special circumstances, e.g. a group of explosives of the same chemical type.

It is accordingly entirely predictable that there will be some significant outliers in Figs. 4 and 5; many of these can be explained by the need to take all three factors (and perhaps others) into consideration. In Fig. 4, the primary outliers are FOX-7 ($h_{50} = 72$ cm, $\Delta V = 23$ Å^3),   N,N′-dinitro-1,2-diaminoethane   ($h_{50} = 34$ cm, $\Delta V = 29$ Å^3) and TNAZ ($h_{50} = 29$ cm, $\Delta V = 37$ Å^3). In each case the compound is actually more sensitive (lower h_{50}) than would be expected from its ΔV and the overall trend in Fig. 4. However the respective Q_{max} (1.20, 1.30 and 1.63 kcal/g) are large enough so that these compounds fit reasonably well the trend in Fig. 5, consistent with the measured h_{50}.

In Fig. 5, the major outliers are tetra(azido)hydrazo-1,3,5-triazine ($h_{50} = 18$ cm, $Q_{max} = 1.18$ kcal/g), bis(trinitroethyl)nitramine ($h_{50} = 5$ cm, $Q_{max} = 1.25$ kcal/g)

and 2,4,6-trinitroresorcinol (h_{50} = 43 cm, Q_{max} = 1.15 kcal/g). Again, the actual sensitivities are greater than the Q_{max} and the trend in Fig. 5 would predict. However the respective ΔV (97, 73 and 56 Å^3) in conjunction with Fig. 4 are fully in agreement with the measured h_{50}. (Of course any discussion of outliers should also recognize the well-known uncertainties in the experimental values of h_{50} [3, 31, 33, 35] and ΔH_f [24, 84]).

These examples show that the general factors upon which we have focused may indicate quite different sensitivities in some instances. Unfortunately it appears that the factor indicating the greatest sensitivity is likely to be the determining one.

4   An Apparent Dilemma

In pursuing the impossible dream—high performance, low sensitivity—we confront an apparent dilemma. It is nearly axiomatic in the area of explosives that a large heat of detonation is needed for a high level of detonation performance. This is one of the reasons for the considerable interest, some years ago, in strained or cage-like molecules [85] (e.g. octanitrocubane and CL-20), and more recently in high-nitrogen heterocyclic molecules [74, 81] (e.g. tetraazidoazo- and tetraazidohydrazo-1,3,5-triazine and LLM-119). Explosive compounds involving strained or cage-like molecules, or high-nitrogen heterocycles, tend to have heats of formation ΔH_f that are positive and often quite large, in contrast to the negative ΔH_f of many other explosives; see Table 1. By Eq. (5), a positive ΔH_f for an explosive increases the heat of detonation, which is historically viewed as very desirable.

The dilemma arises because Fig. 5 shows that a large Q_{max} is generally accompanied by high impact sensitivity. As discussed earlier, Q_{max} is a well-defined intrinsic property that characterizes an explosive; thus the trend in Fig. 5 is independent of whatever may be the actual heat of detonation in a given case. It follows from Fig. 5 that the magnitude of Q_{max} needs to be kept within some reasonable bounds (e.g. <1.4 kcal/g) if a high sensitivity is to be avoided. This should be viewed as a necessary but not sufficient condition because sensitivity also depends upon other factors, such as the free space in the lattice and the molecular surface electrostatic potential.

The idea of intentionally limiting the magnitude of Q_{max} in designing new explosives may provoke skepticism, as being incompatible with the objective of a high level of detonation performance. But this is not necessarily the case.

According to Eqs. (1) and (2), detonation velocity D and detonation pressure P increase as the quantities N, M_{ave}, Q and ρ become larger. However M_{ave} and N vary roughly inversely [27], as is shown in Fig. 6. Thus M_{ave} partially cancels N, but N appears in Eqs. (1) and (2) to a higher power than does M_{ave}. These equations can therefore be approximated as,

Fig. 6 Relationship between the number of moles N of gaseous detonation products per gram of explosive and their average molecular mass M_{ave} for the 26 compounds in Tables 1 and 2. There are only 24 points visible because RDX, HMX and FOX-7 have the same N and M_{ave}
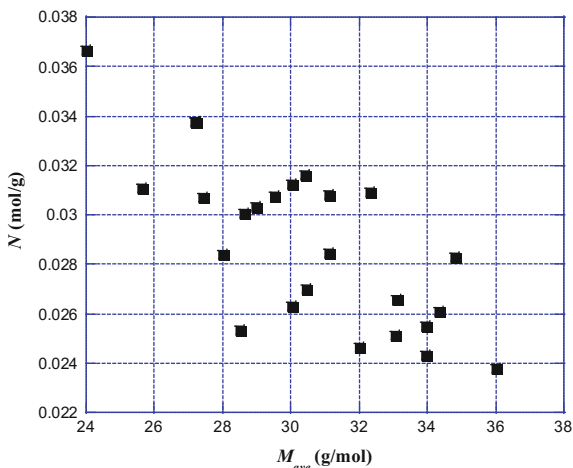
$$D(\text{km/s}) \sim N^{0.25}Q^{0.25}(1+1.30\rho) \qquad (7)$$

$$P(\text{kbar}) \sim N^{0.5}Q^{0.5}\rho^2 \qquad (8)$$

In Eqs. (7) and (8), the density ρ is to a power four times as great as are N and Q. It is therefore quite understandable that a large density is viewed as a very desirable attribute of an explosive. However Eqs. (7) and (8) are somewhat deceptive in this respect. The densities of C, H, N, O explosives tend to be greater than those of organic solids in general [71] but they vary over a relatively small range. For example, the largest density in Table 1 is only 20% greater than the smallest, whereas the largest N and Q_{max} in Table 2 are respectively 54 and 72% greater than the smallest. Thus, as pointed out earlier [20], the role of the density in determining the relative magnitudes of the detonation velocities D and the detonation pressures P of different explosives is not as dominant as Eqs. (7) and (8) may suggest.

This is illustrated by the case of RDX. It has only an intermediate density relative to the other compounds in Table 1, but it is in the top tier of D and P values due to its high N and Q_{max} (Table 2). On the other hand, the density of benzotrifuroxan is essentially the same as that of HMX and it has the highest Q_{max} in Table 2, exceeding both HMX and β-CL-20, but its D and P are considerably less than those of HMX and are not in the top tier of values. The reason is the very low N of benzotrifuroxan, the lowest in Table 2.

Perusal of Tables 1 and 2 suggests that a high level of detonation performance requires that at least two of the three quantities N, Q_{max} and ρ have large magnitudes and that the third be no worse than moderate. Of course the best performance would be if all three were large (as is the case for HMX and β-CL-20) but Fig. 5

tells us that a large Q_{max} is not acceptable from the standpoint of sensitivity. So to pursue the impossible dream—high performance, low sensitivity—we should focus upon large N and ρ and moderate Q_{max}.

Tables 1 and 2 offer us considerable encouragement, by showing that a moderate Q_{max} does not preclude high detonation performance. For example, FOX-7 has a Q_{max} that is 20% lower than that of RDX, but their D and P are within 2.6% of each other. The Q_{max} of bis(trinitroethyl)nitramine is 23% less than that of TNAZ, but its D and P are comparable to those of TNAZ and are among the top ones in Table 2. [The high sensitivity of bis(trinitroethyl) nitramine, despite its moderate Q_{max}, can be attributed to its large ΔV, as discussed in Sect. 3.2.] Further putting the role of Q_{max} into perspective is the fact that NTO has by far the lowest Q_{max} in Table 2 but its D and P exceed those of ten of the other explosives.

Another way of demonstrating the feasibility of limiting the magnitude of Q_{max} is by estimating the effects of diminishing the Q_{max} of β-CL-20 from its present 1.60 kcal/g to a more moderate but still relatively high 1.40 kcal/g, while leaving N, M_{ave} and ρ unchanged. Figure 5 indicates that this should significantly lower its sensitivity, from $h_{50} = 14$ cm to h_{50} in the range 50–80 cm. However the calculated D would decrease only from 9.48 to 9.17 km/s, and the P from 422 to 395 kbar— still the best detonation performance in Table 2! Similar analyses were made earlier for HMX and for TNT [48].

While Q_{max} needs to be kept within reasonable bounds, it also should not be too low. For example, 3,3'-azo-bis(6-amino-1,2,4,5-tetrazine) (**1**, DAAT) has a density of 1.78 g/cm^3, nearly the same as RDX (Table 1), and a much greater heat of formation, 206 kcal/mol [81]. Its N value is also higher than that of RDX, 0.03633 versus 0.03377 mol/g. However **1** has a low Q_{max} of only 0.936 kcal/g, and so its D and P, 7.60 km/s and 254 kbar, are greatly inferior to the 8.83 km/s and 347 kbar of RDX (Table 2).
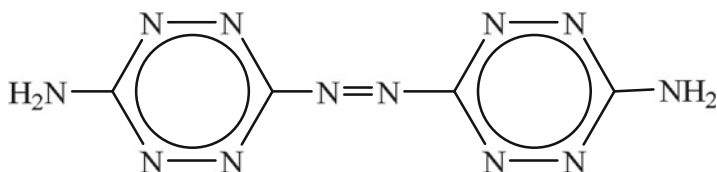
1

To summarize this discussion, the "dilemma" of needing to avoid high heats of detonation is more apparent than real. It simply means that the focus should be upon achieving high N, high ρ and moderate Q_{max}.

5   In Quest of the Impossible Dream

The preceding sections have proposed several general guidelines for pursuing the dream of high performance and low (or moderate) sensitivity. To be sought are a high density ρ and a large number of moles of gaseous detonation products per gram of explosive, N. To be avoided are a strongly positive electrostatic potential in the central portion of the molecular surface, a large amount of free space per molecule in the crystal lattice, ΔV, and a large maximum heat of detonation, Q_{max}. What specific molecular features should an explosive have to help it satisfy these guidelines?

5.1   Molecular Dimensions

Generalizing cautiously, explosive compounds composed of planar or near-planar molecules are somewhat more likely to have high densities [86, 87]. However there are certainly numerous deviations from this generalization. The two highest densities in Table 1 are for compounds having non-planar molecules [β-CL-20 and bis (trinitroethyl)nitramine]. At the other extreme are 4-nitro-1,2,3-triazole and 3,5-dihydrazino-1,2,4,5-tetrazine (neither is in Table 1), the molecules of which are planar but the densities are low: 1.689 g/cm^3 [78] and 1.61 g/cm^3 [74], respectively.

More clearcut, but perhaps unexpected, is the relationship for explosive compounds between molecular size and the free space per molecule in the crystal lattice, ΔV. As the intrinsic molecular volume V_{int} increases, ΔV becomes larger [87]. An opposite conclusion was reached by Dunitz et al. [88] for aromatic hydrocarbons. For explosives, Fig. 4 shows that a large ΔV is undesirable in terms of sensitivity.

A further advantage of molecular planarity, in addition to possibly increasing the density, is that it enhances the chances of the crystal lattice consisting of parallel or near-parallel planar layers, i.e. being graphitic. Such lattices may offer less resistance to the shear/slip that follows impact or shock, and thus be less vulnerable to subsequent hot spot formation and detonation initiation [3, 55, 56, 58, 89, 90].

It is interesting to compare FOX-7 and TATB (2,4,6-triamino-1,3, 5-trinitrobenzene). Both have planar molecules and layered lattice structures [56, 89]. However the layers in TATB are planar while those in FOX-7 are zigzag, and will accordingly offer more resistance to shear/slip. This may help to account for the greater sensitivity of FOX-7 (h_{50} = 72 cm [74]) compared to TATB (h_{50} > 320 cm [31]). For additional examples, see Veauthier et al. [90].

5.2   Molecular Framework

Rather than an all-carbon framework (as in TNT, picric acid, TNB, TATB, etc.), it is beneficial for the framework to include some nitrogens. Those often increase the compound's density, because a nitrogen atom has a larger mass and smaller volume than the C–H unit that it typically replaces [91]. Nitrogens also increase the heat of formation of the compound, making it more positive; this is because the hypothetical formation reaction requires breaking the very strong N≡N bond in N_2 and creating the much weaker C–N, C=N, N–N and/or N=N bonds [48]. Increasing ΔH_f, and therefore Q_{max} [by Eq. (5)], can be desirable as long as Q_{max} does not become too large, resulting in high sensitivity (Fig. 5). Accordingly the framework nitrogen/carbon ratio should be limited.

5.3   Molecular Stoichiometry

A large value of N, the number of moles of gaseous detonation products per gram of explosive, is promoted by having an appropriate number of hydrogens and oxygens in the molecule, since these can form the lightest of the likely gaseous products, $H_2O(g)$ and $H_2(g)$. The problem that can result from a total absence of hydrogens is illustrated by benzotrifuroxan, as discussed earlier: because of its very low N, its detonation properties (Table 2) are well below what would be anticipated from its high density and very high Q_{max}.

Another benefit of producing $H_2O(g)$ is that its heat of formation is sufficiently negative (−57.80 kcal/mol [28]) to help achieve a moderate Q_{max} but not as negative as that of another of the likely products, $CO_2(g)$ (−94.05 kcal/mol [28]), which forms after $H_2O(g)$ [16]; too much $CO_2(g)$ will lead to a large Q_{max}. $CO_2(g)$ is also the heaviest of the primary products, which diminishes N.

A desirable number of oxygens would therefore be such as to convert all of the hydrogens to $H_2O(g)$ but only a limited number of the carbons to $CO_2(g)$. A reasonable approach to restricting the number of oxygens is to introduce N-oxides, to some extent, instead of NO_2 groups. An attractive feature of N-oxides is that they partially counteract the destabilizing effects of nitrogen catenation (several linked nitrogens) [92–94].

5.4   Amino Substituents

It is well known that the introduction of NH_2 groups tends to diminish sensitivity. A famous example is the progressive decrease in impact sensitivity in going from 1,3,5-trinitrobenzene (TNB) to its mono-, di- and triamino derivatives [31].

NH$_2$ groups are donors of electronic charge through conjugation. Accordingly their presence tends to weaken the characteristic strongly-positive electrostatic potentials on the central portions of the molecular surfaces of explosives; see, for instance, Rice and Hare [33]. One consequence may be less intermolecular repulsion and resistance to the shear/slip that follows impact or shock, and therefore diminished hot spot formation (Sect. 3.2). The charge donation from NH$_2$ groups should also strengthen C–NO$_2$, N–NO$_2$ and other bonds [95], the rupture of which might be involved in detonation initiation.

A second important role of NH$_2$ groups is in inter- and intramolecular hydrogen bonding with NO$_2$, ONO$_2$ or N → O oxygens or with azine nitrogens. This has a stabilizing effect that decreases the heat of formation and often Q_{max}; compare, for example, the ΔH_f and Q_{max} of TNB and picramide in Tables 1 and 2. The ΔH_f and Q_{max} of the triamino member of the series, TATB, are yet lower at −33.40 kcal/mol and 1.09 kcal/g [40]. Intermolecular hydrogen bonding should also promote the formation of a graphitic crystal lattice [56, 89] (as in TATB), thereby lessening the resistance to shear/slip. It has further been suggested that intermolecular hydrogen bonding may increase thermal conductivity, thereby promoting the diffusion and dissipation of hot spot energy [52]. The insensitive TATB, which participates in extensive hydrogen bonding, has "the highest thermal conductivity of the common organic explosive molecules" [53].

Any or all of the above factors may help to explain the desensitizing effects of NH$_2$ groups. However a benefit that they cannot consistently provide, perhaps surprisingly, is increased density. Analysis of numerous crystal structures by Dunitz et al. [86] failed to find a relationship between hydrogen bonding and density. While such a relationship might intuitively have been expected, Dunitz et al. point to the case of ice: strong directional hydrogen bonding creates an open structure with low density. (It should be noted, however, that their analysis did not focus specifically upon energetic compounds, which—as has been noted [3, 41, 46, 71]— sometimes differ significantly from other organic compounds.

5.5   *Molecular Structural Modifications*

We have already pointed out that replacing some C–H units by nitrogen atoms in the molecular framework frequently increases the density as well as the heat of formation (Sect. 5.2). Another approach to achieving a higher density that might prove interesting was proposed by Mondal et al. [96]. It involves inserting an atom or atoms into a space within a molecule, forming a bridge between two atoms of the original framework. For example, force field calculations showed that replacing two hydrogens of RDX by an oxygen linking the respective carbons had essentially no effect upon the volume but of course increased the mass and therefore the density.

6   Final Remarks

We conclude by reemphasizing the key concept that *a large heat of detonation Q_{max} is not necessary for a high level of detonation performance and is certainly undesirable from the standpoint of sensitivity.* Recognition of this clearly has implications for the design and synthesis of new explosives.

It suggests that the impossible dream be pursued by accepting a moderate Q_{max} and focusing upon achieving large N and ρ, a small ΔV, and a less strongly-positive molecular surface electrostatic potential. Specifically:

(1) The molecules should be relatively small, to diminish ΔV, and planar or near-planar, to promote the possibility of a graphitic crystal lattice with less resistance to shear/slip.
(2) The molecular framework should contain some nitrogens, to increase the density, but not so many as to result in a large heat of formation and large Q_{max}.
(3) The molecule should contain hydrogens and oxygens in order to produce H_2O (g) and increase N, but the number of oxygens should reflect the need to limit the amount of $CO_2(g)$ that is formed (since it increases Q_{max} and decreases N).
(4) Using N-oxides rather than NO_2 groups as a source of oxygens helps to restrict their number and also somewhat stabilizes nitrogen catenation.
(5) The molecule should contain NH_2 groups, to moderate the strongly-positive electrostatic potential and to allow hydrogen bonding that (a) helps to limit Q_{max} through its stabilizing effect, (b) promotes a graphitic lattice, and (c) may increase thermal conductivity and the dissipation of hot spots.

Will all this help to realize the impossible dream? That remains to be seen.

References

1. Licht H-H (2000) Propell Explos Pyrotech 25:126
2. Džingalašević V, Antić G, Mlađenović D (2004) Sci Tech Rev 54:72
3. Politzer P, Murray JS (2014) Adv Quantum Chem 69:1
4. Eremenko LT, Nesterenko DA (1989) Propell Explos Pyrotech 14:181
5. Hornberg H, Volk F (1989) Propell Explos Pyrotech 14:199
6. Dlott DD (2003) In: Politzer P, Murray JS (eds) Energetic materials, part 2. Detonation, combustion. Elsevier, Amsterdam, p 125
7. Meyer R, Köhler J, Homburg A (2007) Explosives, 6th edn. Wiley-VCH, Weinheim, Germany
8. Pepekin VI, Gubin SA (2007) Combust Explos Shock Waves 43:84
9. Pepekin VI, Gubin SA (2007) Combust Explos Shock Waves 43:212
10. Klapötke TM (2011) Chemistry of high-energy materials. de Gruyter, Berlin
11. Danel J-F, Kazandjian L (2004) Propell Explos Pyrotech 29:314
12. Urtiew PA, Hayes B (1991) J Energ Mater 9:297
13. Mader CL (1998) Numerical modeling of explosives and propellants, 2nd edn. CRC Press, Boca Raton, FL
14. Sučeska M (2004) Mater Sci Forum 465–466:325

15. Bastea S, Fried LE, Glaesemann KR, Howard WM, Sovers PC, Vitello PA (2006) CHEETAH 5.0, User's manual, Lawrence Livermore National Laboratory, Livermore, CA
16. Kamlet MJ, Jacobs SJ (1968) J Chem Phys 48:23
17. Kamlet MJ, Hurwitz H (1968) J Chem Phys 48:3685
18. Kamlet MJ, Dickinson C (1968) J Chem Phys 48:43
19. Urbánski T (1984) Chemistry and technology of explosives, vol 4. Pergamon Press, Oxford, UK
20. Politzer P, Murray JS (2011) Cent Eur J Energ Mater 8:209
21. Shekhar H (2012) Cent Eur J Energ Mater 9:39
22. Ornellas DL (1968) J Phys Chem 72:2390
23. Kamlet MJ, Ablard JE (1968) J Chem Phys 48:36
24. Rice BM, Hare J (2002) Thermochim Acta 384:377
25. Akhavan J (2004) The chemistry of explosives, 2nd edn. Royal Society of Chemistry, Cambridge, UK
26. Muthurajan H, How Ghee A (2008) Cent Eur J Energ Mater 5(3–4):19
27. Politzer P, Murray JS (2014) Cent Eur J Energ Mater 11:459
28. Linstrom PJ, Mallard WG (eds) NIST chemistry WebBook, NIST Standard Reference Database No. 69, National Institute of Standards and Technology, Gaithersburg, MD, http://www.nist.gov
29. Gibbs TR, Popolato A (eds) (1980) LASL explosive property data. University of California Press, Berkeley, CA
30. Zhang Q, Chang Y (2012) Cent Eur J Energ Mater 9:77
31. Storm CB, Stine JR, Kramer JF (1990) In: Bulusu SN (ed) Chemistry and physics of energetic materials. Kluwer, Dordrecht, p 605
32. Zeman S (2007) Struct Bond 125:195
33. Rice BM, Hare JJ (2002) J Phys Chem A 106:1770
34. Doherty RM, Watt DS (2008) Propell Explos Pyrotech 33:4
35. Kamlet MJ (1976) Proceedings of the sixth symposium (international) on detonation, Report No. ACR 221, Office of Naval Research, Arlington, VA, p 312
36. Kamlet MJ, Adolph HG (1979) Propell Explos 4:30
37. Armstrong RW, Coffey CS, DeVost VF, Elban WL (1990) J Appl Phys 68:979
38. Armstrong RW, Elban WL (2006) Mater Sci Tech 22:381
39. Wang Y, Jiang W, Song X, Deng G, Li F (2013) Cent Eur J Energ Mater 10:277
40. Politzer P, Murray JS (2015) J Mol Model 21:25
41. Politzer P, Murray JS (2014) In: Brinck T (ed) Green energetic materials. Wiley, Chichester, p 45
42. Brill TB, James KJ (1993) Chem Rev 93:2667
43. Politzer P, Murray JS (2003) In: Politzer P, Murray JS (eds) Energetic materials. Part 2. Detonation, combustion. Elsevier, Amsterdam, p 5
44. Anders G, Borges I Jr (2011) J Phys Chem A 115:9055
45. Murray JS, Lane P, Politzer P (1995) Mol Phys 85:1
46. Murray JS, Lane P, Politzer P (1998) Mol Phys 93:187
47. Politzer P, Murray JS (2014) J Mol Model 20:2223
48. Politzer P, Murray JS (2015) J Mol Model 21:262
49. Fried LE, Manaa MR, Pagoria PF, Simpson RL (2001) Annu Rev Mater Res 31:291
50. Pepekin VI, Korsunskii BL, Denisaev AA (2008) Combust Explos Shock Waves 44:586
51. Tsai DH, Armstrong RW (1994) J Phys Chem 98:10997
52. Tarver CM, Chidester SK, Nichols AL III (1996) J Phys Chem 100:5794
53. Tarver CM, Urtiew PA, Tran TD (2005) J Energ Mater 23:183
54. Nomura K, Kalia RK, Nakano A, Vashishta P (2007) Appl Phys Lett 91:183109
55. Zhang C (2007) J Phys Chem B 111:14295
56. Zhang C, Wang X, Huang H (2008) J Am Chem Soc 130:8359
57. Kuklja MM, Rashkeev SN (2009) J Phys Chem C 113:17
58. Kuklja MM, Rashkeev SN (2010) J Energ Mater 28:66

59. An Q, Liu Y, Zybin SV, Kim H, Goddard WA III (2012) J Phys Chem C 116:10198
60. Zhou T, Zybin SV, Liu Y, Huang F, Goddard WA III (2012) J Appl Phys 111:124904
61. Politzer P, Murray JS (2002) Theor Chem Accts 108:134
62. Murray JS, Politzer P (2011) WIREs Comput Mol Sci 1:153
63. Murray JS, Concha MC, Politzer P (2009) Mol Phys 107:89
64. Hammerl A, Klapötke TM, Nöth H, Warchhold M (2003) Propell Explos Pyrotech 28:165
65. Hammerl A, Klapötke TM, Mayer P, Weigand JJ (2005) Propell Explos Pyrotech 30:17
66. Gökçinar E, Klapötke TM, Bellamy AJ (2010) J Mol Struct (Theochem) 953:18
67. Klapötke TM, Nordheiter A, Stierstorfer J (2012) New J Chem 36:1463
68. Zhang C (2013) J Mol Model 19:477
69. Sharia O, Kuklja MM (2012) J Phys Chem C 116:11077
70. Pospíšil M, Vávra P, Concha MC, Murray JS, Politzer P (2011) J Mol Model 17:2569
71. Eckhardt CJ, Gavezzotti A (2007) J Phys Chem B 111:3430
72. Byrd EFC, Rice BM (2006) J Phys Chem A 110:1005
73. Simpson RL, Urtiew PA, Ornellas DL, Moody GL, Scribner KJ, Hoffman DM (1997) Propell Explos Pyrotech 22:249
74. Pagoria PF, Lee GS, Mitchell AR, Schmidt RD (2002) Thermochim Acta 384:187
75. Watt DS, Cliff MD (1998) DSTO-TR-0702, Defense Science and Technology Organization, Melbourne, Australia, Sect. 4.1, p 13
76. Calculated value, ref. 40
77. Gilardi RD, Butcher RJ (2001) Acta Cryst E 57:657
78. Rice BM, Byrd EFC (2013) J Comput Chem 34:2146
79. Li J-R, Zhao J-M, Dong H-S (2005) J Chem Cryst 35:943
80. Archibald TG, Gilardi R, Baum K, George C (1990) J Org Chem 55:2920
81. Huynh M-HV, Hiskey MA, Hartline EL, Montoya DP, Gilardi R (2004) Angew Chem Int Ed 43:4924
82. Calculated value, present work
83. Kamlet MJ, Adolph HG (1981) Proceedings of the seventh symposium (international) on detonation, Report No. NSWCMP-82-334, Naval Surface Warfare Center, Silver Springs, MD, p 60
84. Rice BM, Pal SV, Hare J (1999) Combust Flame 118:445
85. Alster J, Iyer S, Sandus O (1990) In: Bulusu SN (ed) Chemistry and physics of energetic materials. Kluwer, Dordrecht, p 641
86. Dunitz JD, Filippini G, Gavezzotti A (2000) Tetrahedron 56:6595
87. Politzer P, Murray JS (2016) Struct Chem 27:401
88. Dunitz JD, Gavezzotti A (1999) Acc Chem Res 32:677
89. Kuklja MM, Rashkeev SN (2007) Appl Phys Lett 90:151913
90. Veauthier JM, Chavez DE, Tappan BC, Parrish DA (2010) J Energ Mater 28:229
91. Stine JR (1993) Mater Res Soc Symp Proc 296:3
92. Wilson KJ, Perera SA, Bartlett RJ, Watts JD (2001) J Phys Chem A 105:7693
93. Churakov AM, Tartakovsky VA (2004) Chem Rev 104:2601
94. Politzer P, Lane P, Murray JS (2013) Struct Chem 24:1965
95. Politzer P, Concha MC, Grice ME, Murray JS, Lane P (1998) J Mol Struct (Theochem) 452:75
96. Mondal T, Saritha B, Ghanta S, Roy TK, Mahapatra S, Durga Prasad M (2009) J Mol Struct (Theochem) 897:42

Recent Advances in Gun Propellant Development: From Molecules to Materials

Eugene Rozumov

Abstract The development of gun propellants from 2010 to 2016 has been a broad endeavor. Researchers worldwide have examined every facet of energetic materials involved with gun propulsion in efforts to improve both safety and performance. They have looked at individual molecules to maximize energy content, as well as revisiting past molecules and improving upon their original properties. A great deal of effort has gone towards understanding and producing energetic nano-materials. Co-crystallization of energetic materials has also emerged as a promising new methodology to prepare energetics. Processing modifications to the propellant material have shown improvements in burn rate modification. Charge consolidation has seen a resurgence and novel gun concepts have both lead to significant improvements in muzzle velocity at the prototype level. Virtually every aspect of a gun propellant has been examined and improved upon.

Keywords Gun propellant · Energetics · Energetic nano-materials · Energetic co-crystals · Ignition

1 Gun Propellant Ballistics in a Nutshell

The role of gun propellants is to push a projectile out of a tube. The propellant occupies the space in a gun chamber immediately behind the projectile that it is supposed to expel as shown in Fig. 1. It is usually a solid energetic material that upon the application of a proper energy stimulus rapidly decomposes into small gaseous molecules. The subsequent rapid volumetric expansion of the gasses propels the projectile down the bore of the gun. Guns can be characterized by whether their target is hit via a line of sight (small caliber guns, medium caliber guns, tank guns) or non-line of sight (grenade launchers, mortars, artillery)

E. Rozumov (✉)
U.S. Army—Armaments Research Development and Engineering Center (ARDEC), Picatinny Arsenal, USA
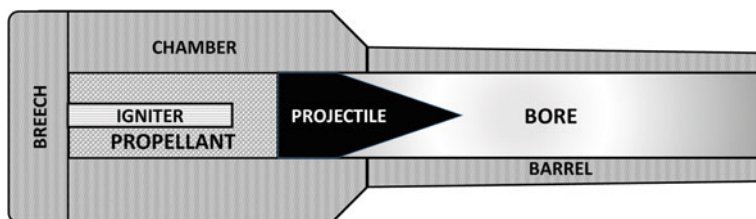e-mail: eugene.rozumov.civ@mail.mil

Fig. 1 Basic diagram of a gun

trajectory. Each of these systems has its own set of requirements for maximum chamber pressure, blast over pressure, muzzle velocity, gun barrel erosion, composition of the combustion gasses, and flame temperature. Furthermore, the propellant must be entirely consumed by the time the projectile exits the gun barrel and capable of being safely stored for several decades. Let us also not forget that these gun propellants are also required to ballistically perform the same way in an operating temperature range from −60 to +70 °C.

As an example, mortars have a much thinner chamber wall than any other large caliber gun, and thus have strict requirements for low chamber pressures. The blast overpressure and flame temperature must also be low since the warfighter is standing in close proximity to the muzzle. Gun barrel erosion is not a significant concern owing to the low cost of a mortar gun tube. Once a gun system and the requirements of the propellant are identified, propellant development can begin. As you can see, even though their primary function is quite simple, the requirements that gun propellants must fulfill are quite vast and often competing.

Historically, gun propellants are categorized into three groups. Single base propellants are composed primarily of nitrocellulose, an energetic polymeric binder. The addition of nitroglycerine, a highly energetic and sensitive plasticizer, to nitrocellulose, created a very energetic and hot propellant dubbed a double base propellant. To reduce the flame temperature of a double base propellant, which was necessary to utilize them in large caliber gun applications to extend barrel life, nitroguanidine was added to double base propellant formulations. These propellants consisting of nitrocellulose, nitroglycerine, and nitroguanidine were termed triple base propellants. They are intermediate in energy and flame temperature between single and double base propellants.

A propellant functions by first being ignited at the base of the cartridge or breech of the chamber by an igniter as shown in Fig. 1. Traditional chemical igniters include black powder, boron potassium nitrate ($BKNO_3$), Benite, or clean burning igniter (CBI), which is about 98% nitrocellulose (NC). These materials ignite the propellant bed via a combination of convective heat transfer from the fast moving hot gasses they generate and from conductive heat transfer of hot particles embedding themselves into the propellant grains. The exothermic energy they release is due to the myriad of oxidative combustion reactions that occur during deflagration. Recently, nano-Boron particles were incorporated into a $BKNO_3$

igniter. It was demonstrated that heat output and pressurization rates increased due to the smaller particle sizes, but the maximum pressure generated was not altered by the use of nanoparticles [1].

Once ignited, the propellant undergoes its own combustion reactions laterally from the surface of the grains, filling the gun chamber with more gaseous molecules that push against the projectile base until it exits the gun barrel. Behind the projectile, hot fuel rich gasses are also expelled forming a concentrated plume that is re-ignited upon exposure to atmospheric oxygen owing to its high temperature to produce muzzle flash, which must also be mitigated so as not to give away the position of the gun system [2]. Everything that has been described up until now has to occur in a gun within a few tens of milliseconds.

The pressure versus time trace inside the gun is provided in Fig. 2. The pressure rises and the projectile is pushed into the gun barrel. The projectile begins to move just prior to the chamber pressure reaching a maximum. The pressure inside the chamber rapidly dissipates and while the projectile is moving down the bore and out of the muzzle it is decelerating. To boost gun performance in terms of range, or projectile time of flight, one needs to boost the projectiles muzzle velocity which is directly related to pressure inside the chamber during the ballistic cycle. However, since most fielded guns are already operating at near their maximum pressures, it is not feasible to simply boost the energy of the propellant without modifying the chamber. The optimal way to achieve this would be to widen the pressure time trace without increasing the maximum pressure. This would increase the amount of work performed on the projectile by the propellant gasses thus leading to higher muzzle velocities. To date, a variety of methods involving charge design have been attempted to widen the pressure time curve, but the substantial increase in muzzle velocity has remained elusive.

An alternative approach is to utilize two propellants with significantly different burn rates which would attain maximum pressure at different times, thus in effect increasing the overall pressure experienced by the projectile without surpassing the maximum allowable pressure. One recent approach has been to use a two stage gun design. In this case, the gun chamber contains two propellants, and two igniters,

Fig. 2 Pressure and projectile velocity profile during the ballistic cycle
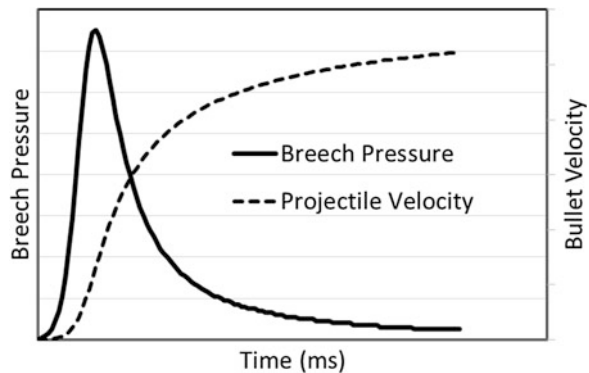
separated by a piston. The propellant adjacent to the projectile is ignited first, which pushes the projectile. Then, a short delay igniter initiated the second propelling charge. The second propelling charge pushes on the piston which then begins to move towards the projectile already moving down the barrel. This compresses the gasses behind the projectile and increases the pressure behind the projectile. This produced a double hump in the pressure time trace, which increased the muzzle velocity by about 30% [3]. Although the increased muzzle velocity was achieved, this gun setup required that the two igniters were part of the breech and barrel. This type of setup requires the development of an entirely new gun system to be practical.

2 Ignition of Propellants

For a gun propellant to function properly and efficiently, its deflagration needs to be initiated. Ideally, the entire propellant bed should be ignited instantaneously, however in practice this is rarely achievable. Besides the chemical ignition methodology described previously, other forms of ignition being examined for gun systems include electrothermal-chemical (ETC) [4], and laser ignition [5]. Both laser and ETC ignition are much more consistent in their delay times than conventional chemical ignition, and offer improved ballistics, but their implementation has been hampered by a variety of reasons.

In ETC ignition, the igniter produces a plasma that imparts its energy directly onto the propellant bed. The benefit of this type of plasma ignition is that ignition delays become very consistent, higher charge loading densities can be efficiently ignited, the entire propellant bed is ignited virtually instantaneously, and the energy input can be compensated to better control ignition during temperature extremes. It has been demonstrated that in a propellant employing plasma igniters, the ignition delay is shortened by about 90%. Furthermore, the plasma achieves similar results to a standard igniter, with less overall energy required. Using a deterred NC strand as an igniter, it was calculated that the NC igniter imparts 2.6 kJ of energy to the propellant based on the calculated heat of explosion under constant volume conditions. The plasma deposited energy was calculated to be 1.05 kJ from the experimental currents and voltages [6].

A variant of ETC known as electrothermal ignition (ETI), incorporates an empty space between the propellant and the formed plasma. This space permits the plasma to become a working fluid before it interacts with the propellant. In a recent study, ETI was employed as an ignition source for a CAB based low vulnerability (LOVA) propellant in a 45 mm laboratory gun at two loading densities (0.5 and 0.7 g/cc) and two temperatures (21 and −40 °C). Gun propellants are known to lose some muzzle energy at extreme cold temperatures leading to reductions in muzzle velocity and subsequent range. It was demonstrated in this effort that ignition delays

were indeed reduced, and very consistent. At the lower charge density, the velocity of the projectile at cold temperature was effectively compensated for by the addition of more plasma energy. However, when this technique was employed with the larger loading density, large negative differential pressures (NDP) were observed between the breech of the gun and the projectile base. These were mitigated by lowering the plasma energy at the expense of increasing ignition delays from about 1.5 ms to 3 ms [7].

The occurrence of NDPs is in many cases due to ignition. Because chemical ignition occurs at the base of the chamber and spreads towards the projectile, the bulk propellant is not ignited simultaneously. This in turn leads to pressure waves forming inside the gun chamber. Once the pressure wave travels from the ignition source towards the projectile, it can get reflected back by the base of the projectile. This reflected wave begins raising the pressure significantly behind the projectile and is traveling towards the breech of the gun, thus forming an NDP [8]. This spike in pressure will also force the remaining unburnt propellant to burn even faster, as discussed later, and further exacerbates the situation in the gun chamber. If the NDP is great enough, catastrophic gun failure results. This can be traditionally mitigated by careful propellant formulation, grain, and charge design.

Nakamura and co-workers examined the effects of igniter tube length, igniter tube perforation area, and igniter mass for their ability to generate NDPs from a triple base propellant in a closed vessel fitted with a burst disk and several pressure transducers. They demonstrated that with a Benite igniter (a mixture of black powder and nitrocellulose), longer igniter tubes were able to significantly reduce the NDP magnitude because a larger fraction of the propellant bed was ignited early in the ballistic cycle [9]. Thusly, long center core igniters can help mitigate NDP formation in larger caliber guns.

Thermite compositions consisting of a metal fuel and oxidizer have also been demonstrated to be effective igniters for propellants. Howard demonstrated that a variety of thermite oxidizer and fuel combinations can effectively ignite a disc composed of JA2, a high energy propellant. Furthermore, different combinations of oxidizer and fuel were able to ignite the JA2 in different ways. Some lead to a rapid rise in pressure within the chamber from the JA2 disc while others produced a softer more delayed pressurization [10]. This clearly demonstrated how ignition can control propellant ballistic performance.

Baschung and coworkers compared the nanothermite composition WO_3/Al as an igniter against black powder and plasma ignition in a 60 mm gun with a LOVA propellant. As the prefix implies, nanothermites are composed of nanometer scaled particles of oxidizer (WO_3) and fuel (Al). In conventional thermites, upon activation, the oxidizer and fuel undergo redox reactions that generate tremendous heat. In nanothermites, the increased surface area drastically increases the rate of reaction, thereby releasing tremendous amounts of heat very rapidly. Since no gasses are generated in a thermite reaction, convective heating of the propellant bed is not possible. Convective heating, however, is necessary for efficient ignition of the

propellant bed. To alleviate this, the $WO_3/2Al$ nanothermite also had azodicar-bonamide added at 10% by weight as a gas generator. They demonstrated that the ignition delays of the nanothermite significantly increased relative to the black powder while the velocity of the projectile and maximum pressure in the chamber remained unchanged. They also demonstrated that the plasma ignition was significantly more consistent with regards to ignition delay, and by once again adjusting the plasma energy, they were able to compensate for poor low temperature performance of the LOVA propellant [11].

Recently two nanothermites were examined for their ability to ignite JA2. Both nanothermite igniters were sandwiched between a JA2 disk and a nanoporous silicon wafer filled with potassium perchlorate. The potassium perchlorate would ignite the thermite, which in turn would ignite the JA2 propellant disc. It was demonstrated that a Bi_2O_3 nanothermite was incapable of igniting the JA2 because it generated high velocity gasses which prevented the hot particles from having sufficient contact with the propellant for heat/energy transfer to occur. A copper oxide thermite on the other hand was successful in igniting the JA2 disk [12].

Su and co-workers utilized a supercritical CO_2 fluid technology to generate a foamed NC igniter with titanium particles (5–15%) embedded in it. The titanium particles would increase the effects of conductive heating, thus igniting the propellant bed in a more efficient manner. In comparison to Benite, they clearly demonstrated that their NC-Ti foamed propellant had a higher burning rate, calculated energy, and a significantly higher maximum pressure. Interestingly, the sample with 10% titanium particles had the highest values for burn rate and pressure, demonstrating that there is an optimal amount of titanium that is beneficial for ballistic performance, while below or above that point the material quickly worsens in performance [13].

3   Combustion of Propellants

In combustion, a material is oxidized to the maximal extent of available oxygen. Combustion is a series of complex redox reactions in which a large molecule is broken apart, atom by atom, to form low molecular weight gasses such as water, nitrogen, carbon monoxide, and carbon dioxide, among others. As an example, the combustion of nitroglycerin (NG) is presented in Eq. 1.

$$2C_3H_5N_3O_9 \rightarrow 6CO_2 + 5H_2O + 3N_2 + 1/2\,O_2 \qquad (1)$$
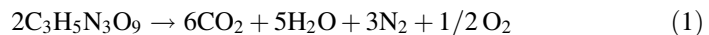
As can be seen, NG is oxygen rich. In this idealized case of combustion, all carbons are converted to CO_2, hydrogens are converted to water, and nitrogens were converted to N_2. However, most gun propellant ingredients have an insufficient amount of oxygen, and the reaction described above cannot go to completion. Therefore, the combustion reactions of gun propellants become more complex.
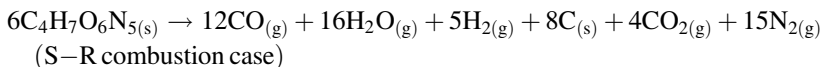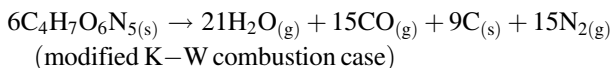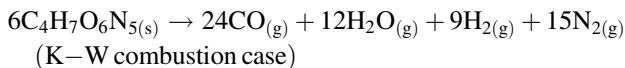
A quantitative measure of a molecule or material's ability to undergo combustion to form CO_2 is its oxygen balance (OB_{CO_2}). The OB_{CO_2} of an energetic material, provides essential information regarding whether enough oxidizer is present in a molecule or material for it to effectively deflagrate. The formula for oxygen balance follows:

$$\%OB_{CO_2} = -\frac{1600}{Mol.Wt.}\left(2x + \frac{y}{2} + M - z\right) \tag{2}$$

wherein x is the number of carbon atoms, y is the number of hydrogen atoms, M is the number of metal atoms, and z is the number of oxygen atoms. This value reflects the ability of the material to undergo sustained oxidative combustion to form carbon dioxide. An oxygen balance of zero implies that the material has equal parts oxidizer and fuel. A positive oxygen balance implies that the material is rich in oxidizer and should burn to completion. If a material has a negative oxygen balance, it is fuel rich and will probably not burn to completion. One thing to note is the absence of nitrogen in the equation, since nitrogen preferentially forms N_2, thus not requiring the oxygen for it to undergo oxidative combustion. The more oxygen balanced the molecule/material, the more likely deflagration can be sustained.

Since most energetic materials are slightly oxygen deficient, the prediction of gaseous combustion products based on the idealized case of NG in Eq. 1 are insufficient. The Kistiakowsky-Wilson (K-W) rules treat the formation of CO_2 in a step-wise manner and are applicable towards propellants and materials with an OB greater than −40%. In these cases, carbon is first oxidized to carbon monoxide. Then the remaining oxygen is utilized to convert hydrogen to water. Finally any available oxygen converts the carbon monoxide to carbon dioxide. Once again (and in all subsequent methodologies), all nitrogens are converted to N_2. For propellants with an oxygen balance lower than −40%, modified K-W rules should apply. In this case the primary step is the conversion of hydrogen to water, followed by the step-wise conversion of carbon to carbon monoxide, and carbon dioxide respectively. In all of the described methodologies, any unoxidized carbon and hydrogen is converted to carbon residue, and hydrogen gas. Another methodology that attempts to account for inconsistencies observed during actual gun firings are the Springall-Roberts (S-R) rules. Just like the K-W rules, carbon is first converted to carbon monoxide. Hydrogen is converted to water, and then the carbon monoxide is converted to carbon dioxide. Two other caveats are also present. Firstly, one third of the carbon monoxide formed, is converted to carbon residue and carbon dioxide. Then, one sixth of the original carbon monoxide is converted to more carbon residue and water (assuming that not all of the hydrogens were converted to water) [14]. All of the above described methodologies are shown below for an idealized molecule $C_4H_7O_6N_5$ with an OB of −40% and as can be seen, each one produces different amounts of combustion products for the same molecule. Since gun

propellants are essentially gas generators, an accurate prediction of the amounts of gasses formed during deflagration is essential.

$$6C_4H_7O_6N_{5(s)} \rightarrow 18CO_{2(g)} + 6C_{(s)} + 21H_{2(g)} + 15N_{2(g)} \quad \text{(ideal combustion case)}$$

$$6C_4H_7O_6N_{5(s)} \rightarrow 24CO_{(g)} + 12H_2O_{(g)} + 9H_{2(g)} + 15N_{2(g)}$$
$$\text{(K−W combustion case)}$$

$$6C_4H_7O_6N_{5(s)} \rightarrow 21H_2O_{(g)} + 15CO_{(g)} + 9C_{(s)} + 15N_{2(g)}$$
$$\text{(modified K−W combustion case)}$$

$$6C_4H_7O_6N_{5(s)} \rightarrow 12CO_{(g)} + 16H_2O_{(g)} + 5H_{2(g)} + 8C_{(s)} + 4CO_{2(g)} + 15N_{2(g)}$$
$$\text{(S−R combustion case)}$$

As discussed above, combustion of propellants may not proceed completely to the formation of carbon dioxide due to insufficient oxygen being present in the molecule or material. An oxygen balance can also be calculated based on the formation of carbon monoxide instead of carbon dioxide as in Eq. 3 and may be more indicative of combustion efficiency. Unfortunately, none of these rules are absolute in predicting the actual combustion products, since in actual gun firings, trace gasses have been reported consisting of various nitrogen oxides and hydrogen cyanide. Thusly, not all of the materials nitrogen's are exclusively converted to nitrogen gas.

$$\%OB_{CO} = -\frac{1600}{Mol.Wt.}\left(x + \frac{y}{2} + M - z\right) \tag{3}$$

Some common energetic propellant ingredients that will be discussed shortly are presented in Table 1 with their respective oxygen balances, densities and heats of formation. As can be seen, as the nitration level of NC increases, its oxygen balance rises, as does its heat of formation (ΔH_f). In energetic formulations, large positive heats of formation are desirable owing to their high potential energy contributions. Nitroglycerin (NG) is a molecule that has an excess of oxygen. The cyclic nitramines RDX and HMX both have OB_{CO}'s of zero and positive ΔH_f's demonstrating their utility in energetic formulations. It has been shown that OB correlates to the brisance of an energetic molecule, but a similar trend has not been observed in multi-component materials, such as propellant formulations. One other noteworthy trend in the table is that for all molecules except for NQ, the OB_{CO} is positive indicating that there is sufficient oxygen present for those materials to undergo combustion and form CO and water. This would indicate that perhaps OB_{CO} is a more realistic indicator of an energetic materials performance than OB_{CO_2}. It also becomes apparent that neither OB_{CO_2} nor OB_{CO} correlate well with ΔH_f.

Recently, a group demonstrated through modeling and experiment, that below a certain threshold value for oxygen balance of a gun propellant, residue appears

Table 1 Properties of some common propellant energetic ingredients

Energetic	Mol. wt. (g/mol)	Formula	OB_{CO_2} (%)	OB_{CO} (%)	Density (g/cc)	ΔH_f (kJ/mol)
NG	227.09	$C_3H_5N_3O_9$	3.52	24.66	1.59	−371
PETN	316.14	$C_5H_8N_4O_{12}$	−10.12	15.18	1.78	−539
RDX	222.12	$C_3H_6N_6O_6$	−21.61	0.00	1.82	70
HMX	296.16	$C_4H_8N_8O_8$	−21.61	0.00	1.91	75
NQ	104.07	$C_1H_4N_4O_2$	−30.75	−15.37	1.76	−92
NC (12.6% N)	272.38	$C_6H_{7.55}N_{2.45}O_{9.9}$	−34.51	0.73	1.66	−708
NC (13.15% N)	279.66	$C_6H_{7.37}N_{2.64}O_{10.2}$	−31.38	2.95	1.66	−688
NC (13.45% N)	284.15	$C_6H_{7.26}N_{2.74}O_{10.4}$	−29.45	4.34	1.66	−678
NC (14.14% N)	297.13	$C_6H_7N_3O_{11}$	−24.23	8.07	1.66	−653

owing to the incomplete combustion of the propellant. They altered the oxygen balance between −29 and −103% by altering the amount of dibutyl phthalate (an inert material with few oxygens) present. They also demonstrated a strong correlation between nitroglycerin content of the propellant and the pressure inside the vessel during combustion. Higher NG content, oxygen balance, and pressures lead to less residue formation [15].

Once properly ignited, gun propellants burn laterally from their surface. The top of the grain exposed to the hot gasses and particles of the igniter begins to form a condensed reaction phase zone within which oxidative chemical decompositions begin forming lower molecular weight gasses which are expelled laterally away from the propellant. This gaseous efflux gives the condensed phase layer a foamy appearance. This reactive zone also increases the temperature of the propellant grain below it, thus lowering the required activation energy for the material beneath it to undergo a combustion reaction. Immediately above this condensed reaction phase zone, there exists the flame front. Between the flame front and the reaction zone is a dark zone, whose height is determined by the velocity of the gasses coming off of the propellant grain and the pressure experienced within the combustion vessel [16].

Since propellant grains burn laterally from exposed surfaces, their burn rate would need to be determined to effectively harness their energy release. A closed vessel (CV) test is usually performed to achieve this. Just as the name implies, it is a completely closed vessel built to withstand enormous pressures. Strand burner tests can also be utilized but are more suited for the lower chamber pressures associated with rocket propellants. From this CV test, in which a fixed amount of propellant grains of known geometry are ignited, and allowed to deflagrate, the burn rate of the propellant can be determined at varying pressures. Furthermore, the coefficients of Vielle's law (Eq. 4) for burn rate can be determined.

$$r = \beta P^{\alpha} \tag{4}$$

For gun propellants, a pressure exponent $(\alpha) > 1$ implies that the propellant's burn rate is very sensitive towards pressure. Thus, as a propellant with $(\alpha) > 1$

deflagrates inside the test chamber, the burn rate increases faster than the pressurization. This may be indicative that the material can undergo a deflagration to detonation transition in some cases. Energetic materials that have an $(\alpha) < 1$ are fairly irresponsive towards pressure changes and are desirable. Black powder falls into this latter category, which is what makes it a very useful igniter. It allows the black powder to be utilized effectively in igniters in virtually any configuration such as bag charges since they do not need pressurization to effectively form flames and hot particles.

It has been demonstrated that CV analysis is quite sensitive towards the testing conditions. An increase in the amount of igniter material employed, changes in the propellant loading density, how the igniter and propellant are packaged, and the dimensions of the CV all play a critical role in determining the burn rate parameters of the propellant. Furthermore, when the burn rate data from the various firing configurations was used to compute the ballistic profile of a 7.62 mm round, none of the closed vessel predicted burn rates permitted an accurate match to the experimental gun firings, thereby indicating that the CV test does not mimic the intended system sufficiently well, and requires further fitting factors to be employed [17]. It is imperative that when comparing burn rates from the literature, the entire procedure for propellant sample preparation is provided.

Variants of the closed vessel test exist, and also provide meaningful information. Interrupted burning of propellants can be achieved by placing burst discs in the CV apparatus which burst and depressurize the chamber after it reaches a critical pressure. The rapid depressurization quenches the deflagration leaving partially burnt propellant. Thus, partially burned grains can be examined. In this manner, multi-perforated propellant grains were demonstrated to exhibit wave-like deflagration inside the perforations instead of uniform lateral deflagration [18].

Based on all of the above information, grains can be designed in which the pressurization rate can be tailored to meet the specific gun requirements. Since deflagration occurs at the surface of a grain, it is directly related to the available surface area. As a spherical or cylindrical grain burns, the available surface area diminishes as shown in Fig. 3. Since there is less available surface area as the deflagration proceeds, the burn rate and pressurization slows down. This is termed regressive burning. Neutral burning can be achieved by adding a single perforation down the middle of a cylindrical grain. Thus, as deflagration proceeds, the outside layer of the grain diminishes in surface area, while the perforation grows in diameter, thus compensating for the lost surface area from the outside of the grain. Multiple Perforations can also be employed to make a propellant exhibit progressive burning, in which the surface area increases as deflagration proceeds. By utilizing multi-perforated cylindrical grains, the increased surface area inside the multiple perforations over compensates for the reduced surface area of the outer grain leading to rapid pressurization until the grain falls apart into slivers, at which point it undergoes regressive burning.

Fig. 3 Effects of grain geometry on available surface area during propellant combustion
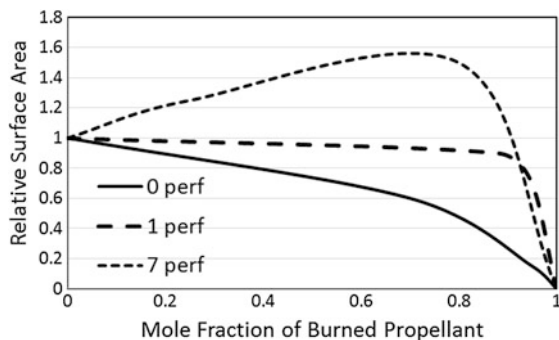
4 Propellant Ingredients

4.1 Energetic Molecules

What makes a material, and a molecule energetic? By definition, an energetic material is one that contains a large amount of stored chemical energy. When exposed to a sufficient shock, thermal, or impact stimulus, which can overcome the initial activation energy of these materials, they rapidly release this stored energy in an exothermic process. This exothermicity provides the energy for subsequent energetic molecules to overcome their activation energy barriers and the cascade of energy release continues. Therefore, a useful thermodynamic parameter to gauge the strength of an energetic material is its heat of formation (ΔH_f). The higher the value of ΔH_f, the more energy is available to be released.

Energetic materials can be composed of an oxidizer and a fuel source. Once the proper stimulus is applied, the oxidizer and fuel will mix and deflagrate as in a rocket propulsion system. In gun systems it is very challenging to design this two component system to achieve deflagration. Instead, both the oxidizer and fuel are present in the same material and even the same molecules.

Traditionally, to make a molecule energetic, nitroester, nitro, nitramines, and azido groups are added to it as shown in Fig. 2. Besides each group containing at least one nitrogen atom, these groups also share another commonality: they all have a weak heteroatom bond that can be cleaved to initiate the cascade of reactions leading to energy release. The nitroester O–N bond is quite labile and can undergo rapid homolytic degradation to form oxide and NO_2 radicals. The azido groups undergo decomposition during combustion to form nitrogen gas, hydrogen gas, and a cyanide functional group while releasing 685 kJ/mol [19]. Azides are especially attractive because they have very high heats of formation (~ 350 kJ/mol) [20].

Incorporating multiple nitrogen atoms into aromatic rings is another method of making energetic materials as in the case of tetrazoles and tetrazines.

nitroester **nitro** **nitramine** **azido** **tetrazole**
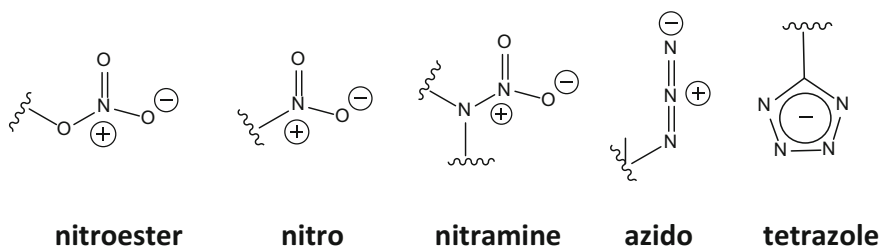
The typical gun propellant is comprised of a combination of energetic materials to achieve its desired function. Energetics for gun propellants are in essence controlled gas generators and should deflagrate, not detonate. Ideal gun propellants burn to completion, leaving no residue, and generate small molecular weight gases such as N_2, CO_2, CO, and H_2O. These gases, through their motion, bombard the projectile and generate the pressure that propels the projectile out of the gun barrel.

4.2 Energetic Binders
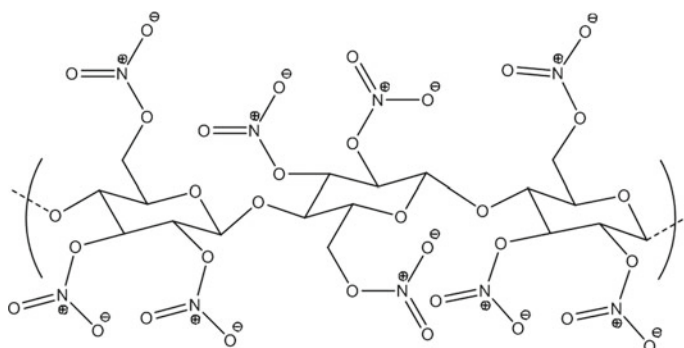
Nitrocellulose

Traditionally, a gun propellant consisting solely of the energetic binder nitrocellulose has been called a single base propellant. The polymeric nature of this binder allows the material to be extruded into any desirable configuration and maintain its shape. The predominant binder in single base and all gun propellants is nitrocellulose (NC). Currently fielded single base propellants include AFP-001, and M1.

NC is a nitrated form of cellulose. There are three hydroxyl groups available for nitration, and depending on the reaction conditions various positions get nitrated. Generally, nitration is performed in a mixture of nitric (HNO_3) and sulfuric acids (H_2SO_4). At HNO_3 concentrations less than 75% and greater than 82% by weight it has been demonstrated that the nitrocellulose product is perfectly soluble in the reaction medium and this is termed homogeneous nitration [21]. The mechanism of homogeneous nitration proceeds in a stepwise manner as shown in scheme 1. In this case, the relative equilibrium constant for the nitration (K_n) is indicated for each free hydroxyl group. The hydroxyl of cellulose at position six has the highest K_n of 30 and is most likely to undergo the first nitration reaction, while the hydroxyl at position 3 has the lowest K_n. The mono-nitrated cellulose will then undergo subsequent nitration to the di-nitrated and finally tri-nitrated NC polymer. Sparse
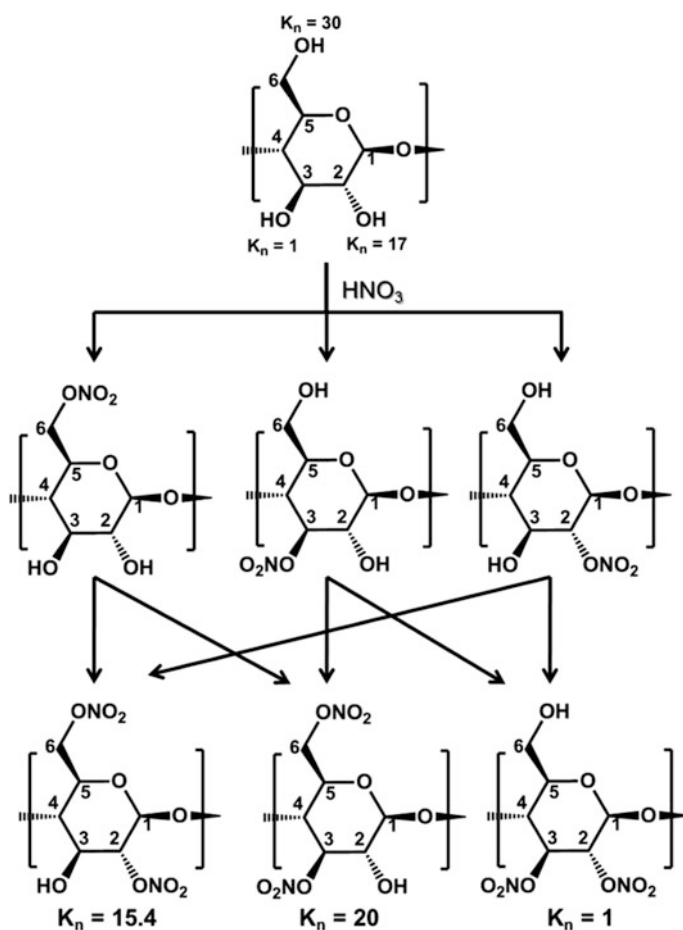
Scheme 1 Formation of nitration products of cellulose

amounts of the 2, 3 dinitrated products are formed [22]. Homogeneous nitration is not employed to make military grade NC, owing to the fact that the presence of water in the reaction mixture severely hampers nitration.

Heterogeneous nitration is performed at HNO_3 concentrations between 75 and 82% by weight. In this case, the NC is an undissolved solid in solution. This may at first appear counterintuitive as to why higher nitration levels are achieved in a molecule that is not fully dissolved, but it has been demonstrated that water diffuses less into the solid NC than does the HNO_3. Therefore, the free hydroxyl groups have higher local concentrations of acid in the heterogeneous process [23]. It was demonstrated via [13] C-nuclear magnetic resonance analyses that in heterogeneous nitration, the free hydroxyl at position 6 of cellulose is exclusively nitrated in the initial step [24]. Only subsequent nitrations occur at the 2 and 3 positions of the polymer.

Other important aspects of the properties of NC are determined by the source of cellulose. Cellulose can be obtained from wood pulp or cotton linters. The source greatly affects the mechanical properties of NC, which in turn effects its ballistic performance. Recently, a group examined NC made from bacterial cellulose. Bacterial cellulose is composed of ribbon-like microfibrils that are two orders of magnitude smaller than plant cellulose. They demonstrated that thermally it behaves the same as conventional NC, but owing to its differing physical properties, it may exhibit altered performance ballistically [25].

A variant of NC, cellulose acetate nitrate (CAN), was also recently examined in gun propellants. In this case, any free hydroxyl groups on NC were acetylated. This was performed in efforts to reduce the sensitivity of the material, however the addition of the non-energetic acetate groups also leads to a reduction in available energy. It was demonstrated in a 105 mm howitzer that although a CAN based propellant formulation was able to perform similar ballistically to the standard M67 propellant, the CAN propellant fared worse in a fragment impact test. It was proposed that the more severe response to fragment impact was due to the higher burn rate of the CAN propellant causing over-pressurization before the deflagrating propellant could vent through the holes caused by the fragment [26].

Recently, the functionalization of cellulose with energetic groups other than nitrate esters was performed in various efforts to produce an energetic polymer with material properties similar to those of NC, yet with more long term stability. It was demonstrated via variable heating rate differential scanning calorimetry (DSC) experiments that the thermal stability of the azidodeoxy cellulose (AZDC) was greater than CAN, which was greater than azidodeoxy cellulose nitrate (AZDCN) [27]. Nitramine functionalized variations of cellulose have also been synthesized. Butylnitraminocellulose (BNAC) and methylnitraminocellulose (MNAC) were synthesized and mixed with aminodinitramide (ADN). BNAC and

MNAC propellants were found to outperform NC at binder concentrations below 50% by weight [28].

AZDC   AZDCN   BNAC   MNAC
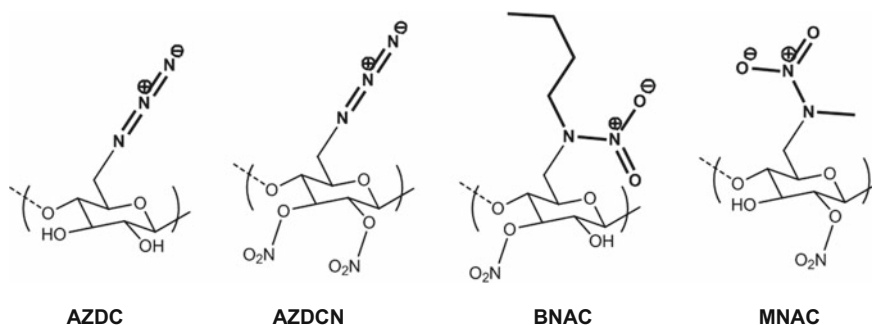
4.3   Energetic Plasticizers

Another common component of propellant formulations are energetic plasticizers that make the material easier to form into various shapes and allow for some mobility of materials within a propellant grain. Plasticizers function by intercalating themselves between the polymer chains and disrupting the weak van der Waals and hydrogen bonding interactions that hold the polymer chains tightly together. This intercalation is caused by the plasticizer in essence solvating the polymer and swelling the material, thusly also increasing the void volumes between polymer chains. Since plasticizers are usually small molecules, once intercalated, they permit the polymer chains to twist and glide, thus acting as a lubricant. All of these interactions between the energetic polymers and plasticizers are aimed at lowering the glass transition temperature (T_g) of the material. The glass transition temperature is the temperature below which the components of an amorphous material such as a gun propellant have no motility causing the material to become very brittle. Brittleness is detrimental towards proper ballistic performance, since a brittle propellant breaks up into many fragments during the ballistic cycle thus increasing the available surface area for combustion. As can be inferred, the plasticizer's melting point correlates to how low the T_g of the resultant material will be.

Plasticizers improve the mechanical properties of propellants. One test to evaluate these mechanical properties is via uniaxial compression. This test simulates the types of compressive forces that the propellant grains would experience during the ballistic cycle by being thrown into other grains and the chamber walls. A typical uniaxial compression result is presented in Fig. 4. In Fig. 4a, a viscoelastic propellant is examined. Initially it undergoes an elastic compression up until the yield point and the slope of that line is the Compressive Modulus (Young's Modulus). The material then work hardens (deforms) up to the failure point, after which the
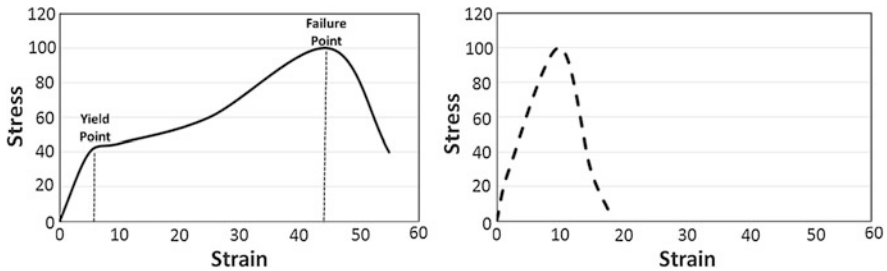
Fig. 4 Typical stress-strain profiles for a (**a**) viscoelastic material and (**b**) Brittle material

material loses all integrity. In a brittle material as presented in Fig. 4b, there is no yield point or work hardening. The material quickly reaches a failure point and loses all integrity.
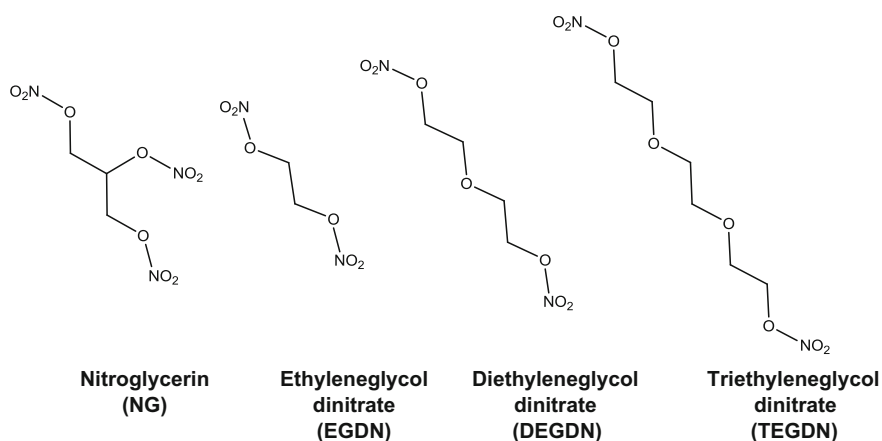
Propellants consisting of an energetic binder and energetic plasticizer are dubbed double base propellants. Historically, double base propellants consist of nitrocellulose as the binder and nitroglycerin as the energetic plasticizer [29]. The energetic plasticizer is critical to keep the propellant grains from fracturing during the ballistic cycle by improving the Young's modulus for the grains and its ability to work harden and resist fracture due to stress and strain. If the grains fracture, there is a sudden increase in available surface area for deflagration which causes a sudden jump in pressure inside the gun. This could be detrimental ballistically and lead to catastrophic failure of the gun [30]. Currently fielded double base propellants include M9 and JA2.

Recently, JA2, a viscoelastic highly energetic propellant, was examined and its Young's modulus, stress at failure, and strain at failure were determined at 10° intervals from −50 to +80 °C. It was demonstrated that at temperatures below 60 °C, elastic behavior was followed by work hardening prior to material failure. Above 60 °C no elastic region was identifiable. SEM analysis of samples just below the failure strain demonstrated that above 20 °C, the flow in the orthogonal direction relative to the compression was evident due to decreasing microvoid formation. Below 20 °C, microvoid formation and crack tip propagation were the primary failure modes [31].

A variation on uniaxial compression was recently developed by Zhang et al. [32]. In a traditional uniaxial compression test, right cylindrical grains are compressed along their lengths. The grains experience forces only on their circular faces and the sides of the grain are free to expand in the direction perpendicular to the compressive force. In Zhang's apparatus, a large double base propellant grain was pressurized from all sides via the addition of pressurized hydraulic oil inside the chamber, and then underwent uniaxial compression, at various oil pressures. As the oil pressure surrounding the grain increased so did the yield point. Grain fracturing was not observed at higher confining pressures. Also, failure of the grain was shown to occur beyond the limits of the apparatus. Basically, the grain was forced to maintain its shape due to the oil. This may be a better representative test of what

is occurring inside a gun chamber during rapid pressurization. The pressure may not be allowing the grains to deform as much as they do in a standard uniaxial compression tester.

The most common energetic plasticizer is nitroglycerin (NG). It is simply the nitrated form of glycerol. This material is highly energetic and extremely sensitive towards any type of stimuli. However, when this material is mixed with NC, there is a synergistic effect in terms of sensitivity. The resulting double base propellant becomes significantly less sensitive than either of the neat materials. A significant concern with double base propellants having a high NG concentration is that the NG migrates over time owing to its small size and structural similarity to NC [33]. It has been known to even seep out of the grain and condense on the surface. In such cases, it makes the propellant very sensitive. Recently, isothermal thermogravimetric analysis (TGA) revealed how readily NG evaporates from the propellant grain at elevated temperatures. Furthermore, like all nitrate esters, NG undergoes catalytic decomposition, which requires the addition of stabilizers to quench these reactions [34]. Many of these properties may be attributed to the NG existing as fine droplets instead of well dispersed molecules in the NC matrix [35]. Below are some nitrate ester plasticizers that have historically been employed as energetic plasticizers which owing to their similarity to NG share the same benefits and drawbacks to varying degrees. Recently, a propellant consisting of 60% NC, 28% NG, and 9.5% TEGDN prepared by a solventless extrusion technique was analyzed for its safety and thermal stability. It was shown that this well plasticized propellant's thermal characteristics were mainly governed by NC's thermodynamic behavior [36].

Nitroglycerin (NG)   **Ethyleneglycol dinitrate (EGDN)**   **Diethyleneglycol dinitrate (DEGDN)**   **Triethyleneglycol dinitrate (TEGDN)**

More recent plasticizers for gun propellants include bis-dinitro-propyl acetal/formyl (BDNPA/F), and a variety of nitrooxyethyl nitramines (NENA). BDNPA/F is a eutectic mixture of BDNPA and BDNPF. BDNPF is a solid which is soluble in BDNPA, a liquid. Together they successfully lower the glass transition temperature of the propellant and are quite energetic yet stable owing to the geminal

Table 2 Properties of various NENA derivatives

Properties	Me-NENA	Et-NENA	Pr-NENA	Bu-NENA
Density (g/cm^3)	1.53	1.32	1.26	1.21
m.p. (°C)	38–40	1–5	−2	−27 to −28
DSC exotherm (°C)	218	210	210	210
ΔH_f (kJ/mol)	1113	784	503	259

dinitro groups present. The NENAs utilize both nitramines and nitroesters as sources of their energy. They have been demonstrated to enable propellants to exhibit high burn rates yet retain low flame temperatures. They all have highly positive ΔH_f's. One disadvantage of NENAs with R groups shorter than a butyl functionality, is their melting temperatures are above −2 °C and increase as the alkyl chain shortens (as shown in Table 2), which in turn would raise the T_g of the propellant formulation. Sadly, the ΔH_f follows the opposite trend with butyl-NENA having the lowest value (259 kJ/mol), yet they are all positive [37]. Thusly, butyl-NENA has been shown to improve the energy content, insensitivity, and mechanical properties in single, double, and triple base propellant formulations [38].

BDNPF   BDNPA   NENA
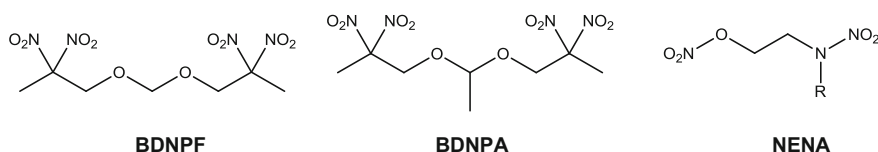
Recently, Yan's group examined 10 nitrate ester plasticizers as shown in Fig. 5, to determine their thermal stabilities and correlate them to structural motifs [39]. They determined that each nitrate ester undergoes the same decomposition mechanism beginning with homolytic cleavage of the O–NO$_2$ nitroester bond with a bond dissociation energy on the order of 150 kJ/mol. Three exceptions to this trend were NG, TMPTN, and TMETN which exhibited significantly lower decomposition activation energies of 100 kJ/mol owing to their tendency to evaporate. They also demonstrated that in these nitrate esters a general trend towards improved thermal stability was the placement of nitromethyl groups (–CH$_2$–ONO$_2$) at tertiary carbons, followed by nitro groups (–NO$_2$), and lastly methyl groups (–CH$_3$).

Another plasticizer that has garnered some interest over the past few years is Dinitro-diaza-alkane (DNDA 57). This is a mixture of three linear nitramines, 2,4-dinitro-2,4-diazapentane (DNDA-5), 2,4-dinitro-2,4-diazahexane (DNDA-6), and 3,5-dinitro-3,5-diazaheptane (DNDA-7). Propellants that utilize it have exhibited the ability to have flat temperature profiles [40]. Traditionally, propellants exhibit lower muzzle energies at colder temperatures. Thusly, at cold temperatures, muzzle velocity and range in gun systems is reduced. A good deal of effort has been placed in improving cold temperature performance especially via plasticizers.
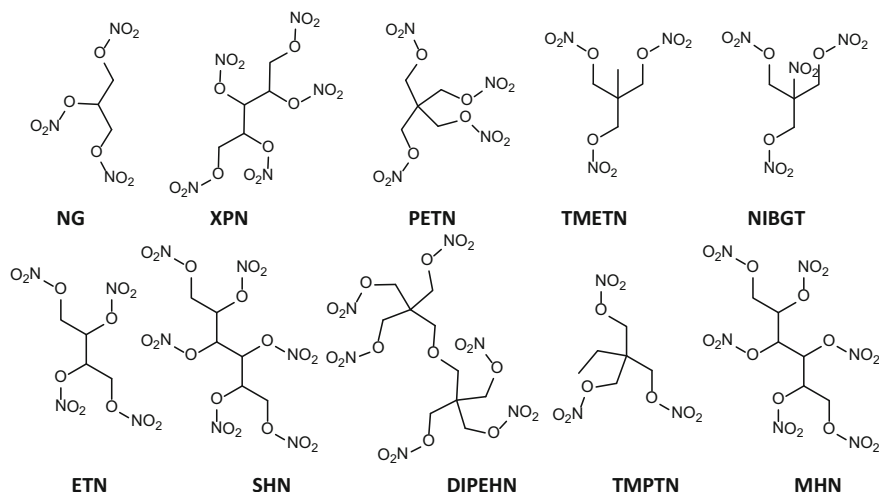
Fig. 5 Series of Nitroesters examined by Yan for thermal stability/structural relationships

The three components of DNDA 57 were individually synthesized and their fragmentation patterns determined by gas chromatography coupled with mass spectrometry in both electron impact and chemical ionization modes. They were shown to all fragment in the same pattern with the first fragment forming via cleavage between the two nitramine groups. The DNDA mixture was demonstrated to have excellent small scale sensitivity properties with an impact sensitivity of 170 cm (RDX is 42 cm), and a frictional sensitivity of 36 kg (RDX is 16 kg). Furthermore, through analysis of viscosity, it was demonstrated that for the energetic binder poly glycidyl nitrate, DNDA 57 is a significantly better plasticizer than BDNPA/F [41]. BDNPA/F as discussed previously is a good plasticizer but is very difficult to produce at large scales. DNDA 57 is much easier to produce at large scales.
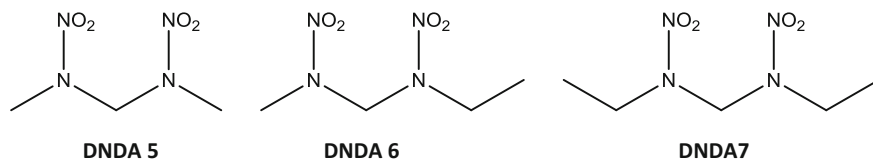
Recently, energetic plasticizers containing azide functional groups have been synthesized and examined. Propellants containing bis[2-azido-1-(azidomethyl) ethyl]malonate (AMEM) and bis[2-azido-1-(azidomethyl)ethyl]glutarate (AMEG)

plasticizers were produced and exhibited good ballistic properties [42]. Another azido plasticizer, 1,3-diazido-2-ethyl-2-nitropropane (AENP), was synthesized in three steps from nitropropane. This plasticizer had an energy output of around 2000 J/g, a low glass transition temperature of −96.8° C, and significantly lowered the viscosities of the formulations during processing with azido binders such as GAP, BAMMO, and polyNIMMO thereby producing homogeneous mixtures [43].

AMEM   **AMEG**   **AENP**
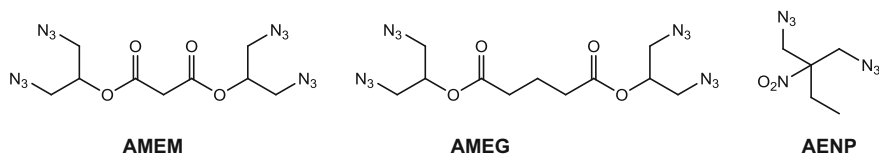
Two other promising azido plasticizers, 1,3-Bis (azido acetoxy)-2-azido acetoxy methyl-2-ethyl propane (TAAMP) and 1,3-Bis (azido acetoxy)-2,2-bis(azido methyl) propane (BABAMP), were thoroughly evaluated in small quantities [44]. Both of these plasticizers were demonstrated to be quite insensitive towards impact and friction stimuli, yet were quite energetic. However, when these plasticizers were incorporated into a propellant at small percentages (1–2%), there was a slight worsening of the overall propellants response towards impact and friction stimuli. This was not surprising, since these energetic plasticizers were used to replace an inert plasticizer, dibutyl phthalate, thus making the overall formulation more energetic. The ΔH_f of TAAMP and BABAMP were −157.5 kJ/mol and 605.6 kJ/mol, respectively. The very high and positive ΔH_f of BABAMP makes it an attractive plasticizer for high energy propellant formulations and warrants further examination of their effects on mechanical properties and cold temperature performance.

TAAMP   **BABAMP**
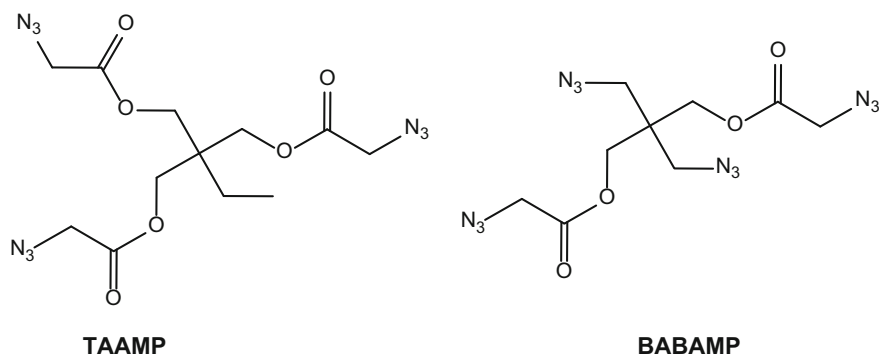
4.4 Energetic Fillers

Another common procedure when formulating propellants is to add a solid energetic filler to double base propellants. Thusly, propellants containing a binder (traditionally NC), plasticizer (traditionally NG), and an energetic filler (traditionally nitroguanidine) are called triple base propellants. Nitroguanidine is an energetic molecule that acts as a flame temperature reducer. Flame temperature reduction is necessary for large caliber applications in order to reduce barrel erosion, since higher flame temperatures have been demonstrated to be one of the primary contributors to gun barrel erosion. Thusly, most triple base propellants are for large caliber applications and are currently in use in the modular artillery charge system.

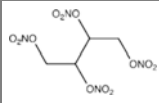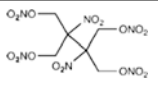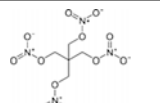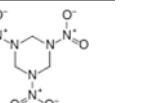Solid fillers have also been incorporated into double base propellants in order to boost the ballistic energy of propellant formulations. High energy nitramines such as hexahydro-1,3,5-trinitro-1,3,5-triazine (RDX) and octahydro-1,3,5,7-tetranitro-1,3,5,7-tetrazocine (HMX) have been added to propellants as fillers in order to eliminate dependence on NG for the energy boost owing to NGs stability and migratory issues. In comparison to other fillers examined, such as nitro and azido derivatives, the nitramines possess a higher density, better thermal stability, and positive heats of formation. In the case of HMX as a filler, it has been demonstrated that below 10 MPa, the burning rate of the propellant is controlled by the binder or by binder-nitramine interactions, rather than by the burning rates of HMX itself, but its cost makes it prohibitive to use in gun propellants [45]. RDX has been employed extensively in developmental gun propellants, but its toxicity is an issue [46].

Since these energetic materials are solids, and their incorporation into propellant formulations generally involves the use of solvents in which they are insoluble, their morphology is critical for processability and sensitivity. It has been demonstrated that spherical particles fare better than their non-spherical variants by orders of magnitude in sensitivity tests such as impact and friction. In the case of HMX, it was recently demonstrated that smaller particle sizes lead to improved thermal conductivity, reducing the likelihood hot spot formation, and the resultant sensitivity towards mechanical stimuli such as impact and friction [47]. Attaining the proper morphology of these energetic fillers is critical. Recently, spherical 3-nitro-1,2,4-triazol-5-one (NTO) was produced via crystallization in a variety of particle sizes. It was demonstrated that the particle size was controllable via modification of the cooling and stir rates of the solution (water: N-methyl-2-pyrolidone) [48].

Recently, two nitrate ester solid fillers, erythritol tetranitrate (ETN) and 1,4-dinitrato-2,3-dinitro-2,3bis(nitratomethylene) butane (DNTN), were synthesized and analyzed as shown in Table 3 [49]. It was demonstrated that in comparison to PETN the materials have a more positive oxygen balance and higher heats of formation. However, the heats of formation are less than that of RDX. One other barrier to their use as gun propellant ingredients are the low melting point temperatures of ETN and DNTN. It would appear that based on their oxygen balances and heats of formation, ETN and DNTN are better solid energetic fillers than PETN, but not RDX.

Table 3 Comparison of nitrate ester fillers to RDX

Structure				
Name	ETN	DNTN	PETN	RDX
Molecular Formula	$C_4H_6N_4O_{12}$	$C_6H_8N_6O_{16}$	$C_5H_8N_4O_{12}$	$C_3H_6N_6O_6$
ΔH_f (KJ/mol)	−474.8	−371	−538.48	−70
m.p. (°C)	61	85–86	143	204
MW	302.11	420.16	316.14	222.11
OB_{CO_2}	5.29	0	−10.12	−21.61
OB_{CO}	26.48	22.85	15.18	0

4.4.1 High Nitrogen Content (HNC) Energetic Materials and Polynitrogen

High nitrogen content (HNC) materials were designed to contain many nitrogen atoms bonded to one another via single and double bonds. The bond energy of a N–N single bond is 38 kcal/mol, N-N double bond is 100 kcal/mol, and the N–N triple bond is 226 kcal/mol. Therefore, during combustion, nitrogen wants to form triply bonded nitrogen. Because of this drastic increase in bond energy, HNCs release a lot of energy during combustion owing to their large positive ΔH_f.

One of the first HNC compounds was 3-nitro-1,2,4-triazole-5-one (NTO). It was synthesized in 1905, but its demonstration as an energetic material came 80 years later [50]. This molecule had only two carbons. It was demonstrated that NTO had very low shock sensitivity, but good explosive properties. Later HNCs would utilize nitrogen rich heterocycles as their building blocks in order to reduce the amount of hydrogen present. Tetrazoles, such as triaminoguanidinium azotetrazolate (TAGzT), are materials with a lot of energy, and few carbon atoms [51]. TAGzT has been demonstrated to increase the burning rates of a variety of gun propellants especially those containing RDX over a wide pressure range [52]. This was achieved due to the exothermic decomposition of the azotetrazolate in the foam layer, and from fast gas-phase reactions between triaminoguanidine decomposition products, such as hydrazine, interacting with the decomposition products of the RDX [53].

Tetrazole was utilized extensively because of how easy it was to synthesize via click chemistry. In these reactions organic azides are readily reacted with organic cyanides in the presence of a copper catalyst to generate tetrazoles in excellent yields and at low temperatures [54]. Tetrazines have also been coupled to tetrazoles as in the case of 3,6-bis(1H-1,2,3,4-tetrazol-5-amino)-s-tetrazine (BTATz). It has been demonstrated that in the case of hydroxylammonium 3-dinitromethanide-1,2,4-triazolone, which is the salt readily prepared from 3-dinitromethyl-1,2,4-triazolone as
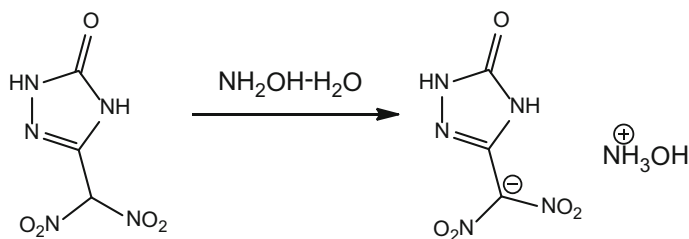
Scheme 2 Synthesis of hydroxylammonium 3-dinitromethanide-1,2,4-triazolone

in scheme 2, π-stacking and extensive hydrogen bonding leads to reduced friction and impact sensitivities even in relation to the uncharged starting material [55].
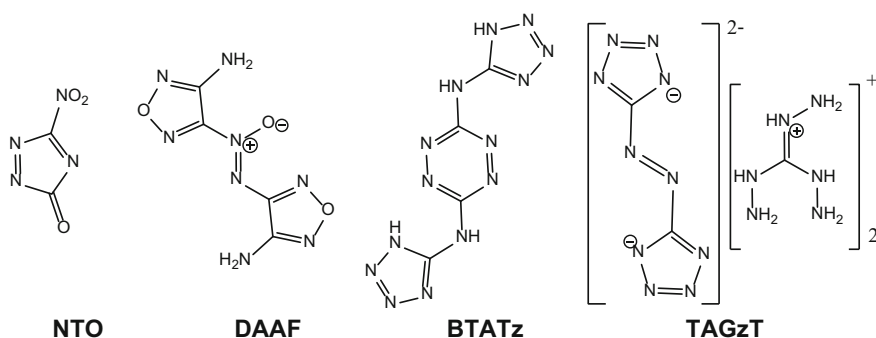
Recent work on the mechanism of combustion involving triaminoguanidinium (TAG) nitrate has demonstrated that TAG acts as an additional heat source for the rest of the propellant owing to its lower thermal stability in comparison to other propellant fillers that are usually present such as ammonium nitrate, and RDX. Kinetic data also demonstrated that the heat generation of TAG combustion is kinetically faster than the heat generation from the combustion of AN or RDX [56]. Basically, TAG compounds burn faster and release more heat which in turn allows other materials such as AN and RDX to combust.

Recently, the effects of the aminoguanidinium counter-cation were examined for their effects on burn rate. Three tetranitrobiimidazolate salts were prepared containing monoamino (aTNBA), diamino (dTNBA), and triamino (tTNBA) guanidinium counter cations [57]. They demonstrated in a strand burner at pressures from 0.2 to 8.6 MPa, that as the guanidinium becomes more functionalized with amino groups, the burn rate increases while the pressure exponent decreases, allowing propellant designers to tailor their burn rates by simply choosing which aminoguanidine to incorporate. This occurs because the density of the material remains relatively unchanged, but the energy of the molecules increase as the degree of amino substitutions increase. Thus the molecules became more energetic

per unit density and are able to produce more gas. Recently, two tetranitrobiimi-dazolate salts containining diammonium and bishydrazinium counter cations were synthesized. They exhibited high densities, positive heats of formation, and were fairly insensitive towards impact and friction [58].

aTNBA   **dTNBA**   **tTNBA**
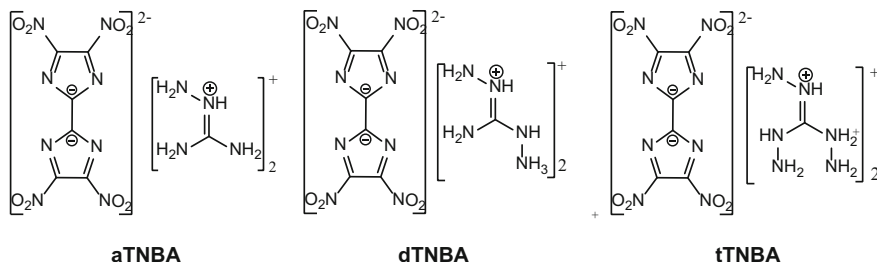
Other counter cations recently examined include 5-aminotetrazolium (ATZ) and 2,4,6-triamino-s-triazinium (TATZ). Both compounds are significantly less sensitive than RDX and neither is capable of detonating due to shock. However, TAGzT has been detonated under similar conditions. The only drawback is that the TATZ does exhibit some electrical sensitivity [59].

ATZ   **TATZ**
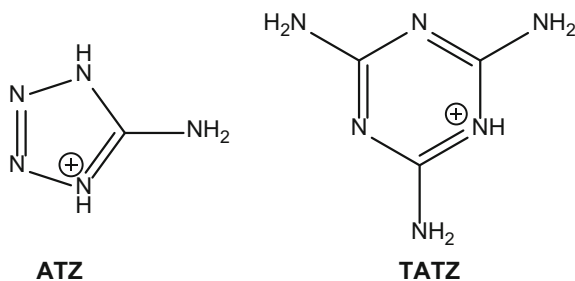
Similarly, the energetic salts of 5-oxotetrazole (OTz), were examined for their properties with various counter cations [60]. Traditionally, oxotetrazole derivatives have provided significant energy content, but their sensitivities are very high. As shown in Table 4, a series of guanidine salts and short amines were examined. There is a trend in the first group consisting of guanidinium-5-oxotetrazolate (gOTz), aminoguanidinium-5-oxotetrazolate (agOTz), diaminoguanidinium-5-oxotetrazolate (dgOTz), and triaminoguanidinium-5-oxotetrazolate (tgOTz), that as the counter-cation increases in size by the addition of amine groups the OB becomes less negative, the heat of formation becomes significantly more positive, and the melting point of the materials increase. All of the salts in this group are insensitive towards impact, friction, electrostatic discharge (ESD), with the exception of tgOTz. This data contradicts the general trend in terms of melting point and sensitivities of energetic molecules, which may be due to the addition of another amine moiety to the cation not contributing to an increase in hydrogen bonding with the OTz as evidenced by the crystal structures of the salts. The second group consisting of short amine

Table 4 Properties of OTz salts

Name	OTz	gOTz	agOTz	dgOTz	tgOTz	aOTz	hOTz	haOTz
Mol. formula	CH_2N_4O	$C_2H_7N_7O$	$C_2H_8N_8O$	$C_2H_9N_9O$	$C_2H_{10}N_{10}O$	CH_5N_5O	CH_6N_6O	$CH_8N_6O_3$
MW	86.05	145.12	160.13	175.15	190.16	103.08	118.09	152.11
OB_{CO_2}	−37.18	−71.66	−69.93	−68.51	−67.30	−54.32	−54.19	−31.55
OB_{CO}	−18.59	−49.61	−49.95	−50.24	−50.48	−38.80	−40.64	−21.03
%N	65.10	67.56	69.97	71.97	73.65	67.93	71.16	55.24
ΔH_f (kJ/mol)	5	0	116	224	340	16	173	167
Density (g/cm^3)	1.699	1.612	1.587	1.654	1.625	1.618	1.594	1.634
m.p. (°C)	–	132	156	175	171	199	164	–
D.Temp (°C)	239	189	179	190	174	205	195	138
Impact (J)	>40	>40	>40	>40	15	>40	>40	>40
Friction (N)	360	>360	>360	>360	240	>360	>252	>360
ESD (J)	0.6	1	1	0.65	1	1.5	1.5	0.4

Scheme 3 Revised synthesis of FOX-12

counter-cations included ammonium-5-oxotetrazolate (aOTz), hydrazinium-5-oxotetrazolate (hOTz), and hydroxylammonium-5-oxotetrazolate·NH$_3$O (haOTz) also exhibited a similar trend regarding the addition of amine moieties to the counter-cation. An identical study examining the guanidinium, aminoguanidinium, and hydroxylammonium salts of 2-nitrimino-5,6-dinitrobenzimidazole was performed and demonstrated similar trends and magnitudes of heats of formation [61].

Guanylurea dinitramide (GUDN or FOX-12) has been known for several years to be an excellent energetic filler for gun propellants owing to its low impact sensitivity, low frictional sensitivity, high thermal stability, and low flame temperature [62]. A hindrance to its utilization in gun propellants has been its high cost. To alleviate this, the yield of the final step in the synthesis of FOX-12 was recently optimized to 50% by lowering the reaction temperature to −40 °C and utilizing a nitrating mixture consisting of concentrated H$_2$SO$_4$/HNO$_3$ at a 1:3 ratio as shown in Scheme 3 [63].

4.4.2 Nanomaterials

By controlling the size and morphology of energetic materials, the sensitivity and burn rates of formulations can be significantly enhanced. Nanomaterials promise to do this. Since nanoparticles have a much larger surface area available for deflagration than do their micron sized counterparts, it is evident that they provide a substantial increase in propellant burn rate. Sensitivity in micron sized materials is due in large part to defects in the crystalline structures that lead to hot spot formation during stress. Nanoparticles have fewer of these defects and are thus less sensitive [64]. However, the validity of certain energetic sensitivity tests such as the BAM friction test has been called into question owing to the experimental setup utilizing sandpaper with micron sized grooves into which the nanometer sized particles can be pushed into during friction tests, thus avoiding the full effect of the frictional forces being applied, and under estimating their true frictional sensitivity [65]. Nano RDX and ammonium nitrate powders pressed pellets were shown to burn faster at elevated pressures than samples made of micrometer-sized particles [66]. It has been shown that thermodynamic properties are dependent upon particle

size. As the surface area-to-volume ratio of a particle increases, the particle melting temperature, heat capacity and thermal stability can decrease [67].

RDX, HMX, and CL-20 particles have been produced at the nanometer scales by various methods, including ball milling [68], the rapid expansion of supercritical solutions (RESS) [69], the sol-gel method [70], and solvent-nonsolvent recrystallization [71]. Each of these technique produces nanoparticles, but of varying sizes, thus making comparisons difficult between them since it has been demonstrated that a 200 nm particle is significantly more susceptible to impact threats, than the larger 500 nm particle when both were prepared by the RESS method [72]. The type of methodology employed to make the nanoparticles is also important towards their sensitivity. When nanoRDX was prepared via milling it had an impact sensitivity height of 54 cm, while RESS prepared nanoRDX had an impact height of 75 cm. Raw micron sized RDX had an impact height of 23 cm [73].

Many nanomaterials that are formed, are quite susceptible to agglomeration owing to their increased surface area. One methodology to prevent agglomeration, similar to passivation of metallic nano-particles, is to coat or embed the nano-particles. One group used RESS produced nano-particles and coated them with several polymers. These polymers prevented the agglomeration of the nanoparticles immediately after their formation, and for a year afterwards. This produced very small RDX particles with an average size of 30 nm [74]. Similarly, spray drying produced micron sized particles with nanoRDX dispersed in a polymeric matrix [75].

One recent effort utilized solvent-nonslovent recrystallization with the ionic liquid 1-hexyl-3-methyl-imidazolium bromide as the solvent for nanoHMX formation. They were able to produce spherical and polyhedral particles ranging from 40 to 140 nm in diameter. X-ray diffraction demonstrated that the HMX is in the beta form just like micron sized HMX. The impact sensitivity of the nanoHMX was dramatically increased from an average of 21 to 47 cm drop height. Differential scanning calorimetry (DSC) at heating rates of 5, 10 and 20 °C/min permitted the calculation of the activation energy (E_a) for thermal decomposition of the HMX. This demonstrated that the nanoHMX had a 50 kJ/mol lower E_a than the micron sized HMX [76], indicating that the nanoHMX is more susceptible to thermal threats than micron sized HMX. This is readily explained by nanoparticles having a significantly higher surface area and smaller size than micron sized particle, permitting the nano-particles to absorb heat more rapidly and disperse it throughout their bulk.

NC was also produced as nano-sized spheres by dissolving the NC in a dimethyl formamide solvent at a concentration below 30 mg/mL. Evaporating the solvent at 5 °C produced spheres of NC that ranged from 200 to 900 nm. These particles exhibited a 350% increase in burn rate and a more complete combustion than micron sized particles prepared in a similar manner [77].

Current efforts are also focused on scaling up the production of these nano-materials. Spray drying of RDX has been quite effective at this. RDX nanoparticles are produced inside a polymeric matrix [78]. It has been demonstrated

that for RDX, as the particle size distribution decreases, so does its sensitivity to impact stresses [79]. Spray drying has also been employed to form nanocomposite materials from HMX and estane, a polyurethane binder. It was demonstrated that the activation energy of the material improved by 40 kJ/mol, and the average drop height sensitivity was raised by 57 cm in an ERL type 12 apparatus in comparison to raw HMX [80].

4.4.3 Co-crystalization

Co crystallization is a new approach to producing energetic materials. This technology also allows the manipulation of the materials density, thermal stability, and mechanical properties. In this case, a known energetic molecule is crystallized with another energetic or inert molecule. Crystal packing is achieved through non-covalent interactions between the two molecules. This is governed by H-bonding, π–π interactions of aromatic rings, and electrostatic interactions. Hydrogen bonding in energetic materials occurs primarily through the nitro groups as shown in Fig. 6. It has also been demonstrated that nitro groups can rotate out of plane and interact with the delocalized electron cloud of an aromatic ring to form a nitro–π interaction, which have a stabilizing energy between 10 and 52 kJ/mol [81]. This stabilization energy had a direct relationship to the molecules impact sensitivity [82]. The lack of variety in nitro containing energetic molecules to form intermolecular interactions provides some difficulty for engineering energetic co-crystals. Co-crystals should exhibit properties, such as density, energy content, and sensitivity that are quite different than if the two molecules were just blended together in a mixer.

One of the first directed co-crystallization efforts involved the co-crystallization of 2,4,6-trinitrotoluene (TNT) with various inert ingredients. In this case, density and thermal stability of several of the co-crystals were improved, but the use of inert materials did substantially lower the energy content over neat TNT [83]. Furthermore, co-crystallization in these cases involved π-stacking as the primary synthon, which would not be applicable to some of the more conventional high energy materials commonly used in propellants which are not aromatic. Similarly, 2,4,6,8,10,12-hexanitro-2,4,6,8,10,12-hexaazaisowurtzitane (CL-20) was co-crystallized with inert materials but suffered the

Fig. 6 Hydrogen Bonding and nitro–π bonding of Nitro Groups
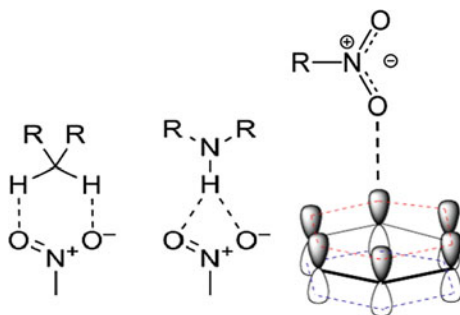
same drawbacks as the TNT effort described above [84]. CL-20 is a known powerful explosive, but has shown some promise as a triple base propellant ingredient. One of its main drawbacks, has been its very high frictional sensitivity [85]. If its sensitivity can be controlled through co-crystallization without a significant sacrifice in energy content, this material could significantly boost propellant output. Recently, porphyrins were co-crystallized with PETN, another explosive compound, from acetone. This was done in order to reduce the sublimation of PETN and improve its stability [86]. HMX was co-crystallized with N-methyl-2-pyrrolidone via a solution evaporation methodology, but other than structural and computational data, no direct information regarding performance or sensitivity was provided [87].

TNT   **CL-20**
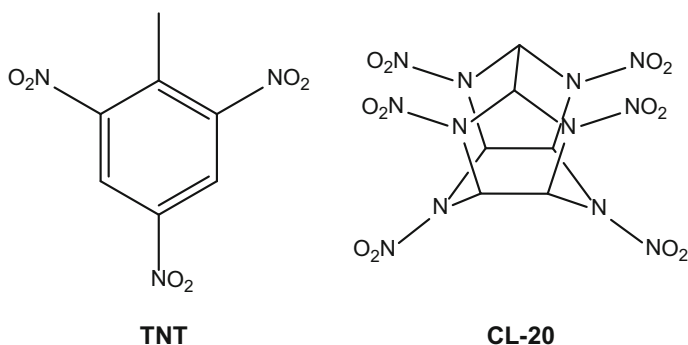
The co-crystallization of two energetic materials has also been achieved. TNT has been crystallized with (CL-20) at a 1:1 molar ratio. It was believed that through co-crystallization with another energetic material, the sensitivity properties of CL-20 could be improved without a significant drop in the materials energy content as seen in the cases where CL-20 was co-crystallized with other inert ingredients. Co-crystallization in this case occurred through hydrogen bonding of the nitro groups and aliphatic hydrogens on both molecules. One interesting result was the interaction of several CL-20 nitro groups with the electron deficient ring of TNT, mimicking the nitro–π-interactions observed in other crystals. This CL-20/TNT co-crystal exhibited a density just below that of pure CL-20, but significantly higher than that of TNT. The impact sensitivity based on drop height of an almost 3 kg weight for the CL-20/TNT co-crystal was double that of pure εCL-20. It was demonstrated that upon heating of the co-crystal to above 136 °C, the two components separate and upon cooling do not co-crystallize again [88].

A co-crystal consisting of 2CL-20 moieties and 1 HMX moiety was produced and found to be substantially less sensitive to impact than CL-20 but significantly more brisant than HMX [89]. In a follow on study using the same crystals but prepared via resonant acoustic mixing, it was demonstrated that these crystals were actually more sensitive in an ERL impact test than εCL-20 and just as sensitive in a BAM friction test [90].

A co-crystal of HMX (80%) and TNT (20%) was produced via spray drying. It was demonstrated to be different from the raw materials via scanning electron microscopy, by which the co-crystal had a completely different morphology from either of the individual crystals. X-ray Diffraction demonstrated that it was a unique crystal structure containing both HMX and TNT. Raman spectroscopy demonstrated that the intermolecular interaction is a hydrogen bond between the nitro group of HMX and the hydrogen from the methyl moiety of TNT. DSC confirmed that the co-crystal was different from both a spray dried HMX, raw HMX, raw TNT, and an intimate mixture of HMX and TNT. Impact sensitivity of the co-crystal was shown to be 62.1 cm, while the intimate mixture of the two ingredients was at 31.3 cm, thus indicating that co-crystallization could indeed improve the sensitivity of these materials [91].

A variation of co-crystallization was utilized by Jung in which they employed HMX as a seed for crystallization of NTO. They demonstrated that they were able to generate core-shell particles in which the highly energetic HMX was surrounded by the less sensitive energetic NTO [92]. Similarly, CL-20 was coated with 1,3,5-triamino-2,4,6-trinitrobenzene (TATB) using 2% by weight of an estane polymer as a glue, and the entire CL-20 surface was covered with TATB. The shell thickness varied from 3 to 10 μm, and the material exhibited significantly improved sensitivities towards friction and impact stimuli over the pure and mixed materials [93].

In a surprising turn of events, Qui et al. [94] were able to synthesize nanoparticles of a CL-20/HMX co-crystal. They employed an aqueous bead milling technique on stoichiometric amounts of CL-20 and HMX crystals. After about 1 h, all of the individual crystals of HMX and CL-20 had become co-crystals as confirmed by x-ray diffraction with particles sizes less than 200 nm as confirmed by scanning electron microscopy. Unfortunately, no sensitivity or performance data on these co-crystals have been presented as of yet.

5 Low Weight Percentage Additives

Organic and inorganic ingredients can be added to propellants in small quantities (<4%) for various desired effects. These additives include stabilizers, flash suppressants, opacifiers, burn rate modifiers (e.g. deterrents), and lubricants. In fielded propellant formulations, there may be several additives. For instance, various potassium salts may be present to mitigate flash, and dibutyl phthalate may also be present as a deterrent to control the propellant's burn rate. These low weight percentage additives can be present as either solids or liquids.

If a propellant contains an energetic material with a nitroester bond, then some kind of stabilizers will need to be present. Nitroester bonds, as discussed previously, are very labile with a dissociation energy of the N–O bond being only 150 kcal/mol. Because of this, they undergo spontaneous homolytic cleavage during long term storage. The resulting radicals further damage the remaining

energetic materials via auto-catalytic degradation which in turn causes self-heating and can eventually lead to detonation. Stabilizers such as ethyl centralite, diphenylamine, and akardite II react with the various nitro radicals that are produced during long term storage of nitroester containing energetics thus prolonging the propellant's shelf-life. A recent study demonstrated that the relative humidity plays a critical role in stabilizer depletion due to aging, with higher humidities causing less depletion of the stabilizers N-methyl-4-nitroaniline and 2-Nitro-diphenylamine [95]. By employing DSC to calculate the activation energies of decomposition of NC films containing varying amounts of diphenylamine stabilizer, the optimal amount of stabilizer can be determined [96]. Recently, researchers combined computational modeling with experimental evidence to demonstrate that for a series of structurally similar malonanilides as the HOMO-LUMO gap decreases, the stability effect increases [97]. Further study is needed to compare this trend to non-similar structures to determine if it could be a stabilizer design tool.

Recently, the zeolite Clinoptilolite was demonstrated to exhibit stabilizing properties in double base propellants (59% NC:31% NG). According to the Bergmann—Junk test and bomb calorimetry, a sample containing 4.0% by weight of the nano-Clinoptilolite (prepared by mechanical grinding of the micron sized sample) exhibited significantly better performance as a stabilizer than did the centralite present at 3.0% by weight. This stabilization effect is presumed to occur by the attraction of the NO_x to the cationic surface groups on the zeolite. Furthermore, atomic force microscopy of the propellant grain surfaces revealed that the nano-Clinoptilolite containing grains were more homogeneous on their surface [98].

A unique study was recently published wherein three identical propellants were analyzed by DSC to determine their service life. Each double base propellant was identical and utilized methylcentralite (MC) as a stabilizer and dibutylphthalate (DBP) as a surface burn rate modifier (deterrent). The only difference between the propellants was that one was recently produced, one had been in storage for 15 years, and one had been in storage for 25 years. After an exhaustive DSC analysis of the various thermodynamic properties of each propellant it was demonstrated that the unaged propellant after undergoing simulated aging at 65.6 °C for 60 days was identical thermodynamically to the 25 year naturally aged propellant [99]. When they examined the compositions of these propellants they demonstrated that the stabilizer does decrease from 3 to 2.4% during natural aging, but drops to 2.2% during accelerated aging, further indicating that in terms of stabilizer content, accelerated aging is a valid technique for estimating safe shelf-life of a propellant. They also demonstrated that during natural aging, the DBP concentration can drop from 4.9 to 4.0% over 25 years, while accelerated aging for 120 days further decreased the DBP concentration to 3.1%. Similarly, during natural aging, the NG content decreased minimally (around 1%), but under accelerated aging, the NG content diminished by roughly 6%. This loss of plasticizers during natural aging will worsen the mechanical properties, which would be further exacerbated by accelerated aging. This was confirmed by dynamic mechanical analysis (DMA), which demonstrated that the T_g increased from −27 to

−18 °C during natural aging. Accelerated aging produced the opposite trend. Surprisingly, accelerated aging of the fresh propellant first raised the T_g of the propellant, owing to the evaporation of the plasticizers from the propellant, but after 30 days it began to decrease, most probably due to NC chain scission [100].

Carbonaceous materials are extensively used in propellants as opacifiers and flame suppressants. Graphite is used as a surface glaze which reduces the frictional coefficient of propellant grains thus allowing the grains to pack more efficiently in a cartridge and have a higher loading density. But other forms of carbon have other unique effects and properties. When [60] fullerene, a soccer ball-like structure composed of benzene and pentacene substructures, was mixed with HMX at just 1% by weight, the impact sensitivity was improved by 40%, while the friction sensitivity was improved by 30% [101]. This may be due to fullerenes ability to rotate even in the solid state, thus acting like ball bearings in the material and allowing the HMX to slide as if it was lubricated [102]. Carbon nanotubes have also demonstrated their ability to desensitize HMX [103]. More recently, graphene and HMX were shown through molecular modeling to be more stable as a composite material [104].

One of the more unique procedures has been the attempts to encapsulate energetic materials inside of carbon nanotubes. Density Functional Theorem (DFT) modelling by Abou-Rachid's group demonstrated for a variety of energetic materials, that there is a significant stabilizing effect experienced by the energetics within the interior cavity of the nanotube [104]. One group, successfully filled carbon nanotubes with potassium nitrate, as evidenced by DSC, and TEM, via wet chemistry methods, and employed them as a nanoinitiator [105]. One important aspect to consider when employing carbon encapsulation as a means of energy partitioning is that you are severely lowering the oxygen balance of your energetic material since you are adding a lot of carbons to the material.

An interesting variant of graphene, is graphene oxide (GrOx). GrOx is prepared under harsh oxidizing conditions using potassium permanganate and sulfuric acid [106]. GrOx is thermally unstable and undergoes a strong exothermic degradation reaction upon heating [107]. It was recently demonstrated via non-isothermal DSC that that when GrOx was coated onto the surface of HMX crystals at 2% by weight, the activation energy for the decomposition reaction increased by 23.5 kJ/mol. Furthermore, the impact and friction sensitivities were improved by 90 and 70% respectively [108]. It is apparent that the HMX and GrOx synergistically assist one another similar to the way NC and NG mixtures become less sensitive but more energetic.

6 Propellant Formulation Modeling and Design

Before proceeding to the laboratory and starting propellant formulation development, with all of the ingredients discussed so far, some modeling is first required. There are various proprietary thermodynamic codes (TIGER [109], BLAKE [110],

CHEETAH [111], EXPLO5, [112] ZNWNI [113], THERMO [114]) currently in use that in essence provide the same information. They utilize the properties of molecules such as heat of formation, molecular formula, and density to provide the propellant developer with some useful initial information on the potential performance of the proposed propellant formulation. Most of these codes provide the impetus, which is the energy of the propellant also known as the propellant force, and the adiabatic flame temperature (T_v) of the propellant at constant volume. In these ideal cases, the impetus is the ability of the propellant to do work on a projectile [115]. Table 5 provides the BLAKE output of an M1 propellant consisting of 83.11% nitrocellulose, 9.77% dinitrotoluene, 4.89% dibutylphthalate, 0.98% diphenylamine, 0.5% water, and 0.75% ethanol [116]. In this case the loading density was varied from 0.2 to 0.3 g/cc. As the loading density increased the T_v increased slightly, while the pressure almost doubled. However, the impetus and the molecular weights of the gasses remained relatively unchanged. These predictions allow for the propellant developer to optimize a formulation before initial processing.

These thermodynamic codes also provide the concentrations of a variety of the combustion products as shown in Table 6. From the combustion products one can immediately approximate how erosive the propellant will be based on the ratios of N_2, H_2, and CO gasses coupled with the flame temperature. Certain gasses such as N_2 will form a protective coating of iron nitride with the gun barrel steel, while others such as H_2 and CO are known to react with the metals present, thus hastening the erosion by forming iron carbide [117]. There is a low activation energy for the

Table 5 Blake Output of M1 propellant

Loading density (g/cc)	T_v (K)	Pressure (MPa)	Impetus (J/g)	Mol. Wt. gas (g/mol)	Co-vol (cc/g)
0.20	2447	236.0	919.2	22.138	1.105
0.25	2454	314.5	919.7	22.188	1.077
0.30	2462	402.4	919.9	22.254	1.048

Table 6 Gaseous output of M1 propellant

Loading density (g/cc)	0.2	0.25	0.3
$CO_{(g)}$	22.94	22.88	22.79
$H_{2(g)}$	9.25	9.11	8.93
$H_2O_{(g)}$	6.09	6.13	6.17
$N_{2(g)}$	4.43	4.41	4.4
$CO_{2(g)}$	2.32	2.33	2.35
$NH_{3(g)}$	0.045	0.062	0.081
$HCN_{(g)}$	0.029	0.042	0.058
$CH_{4(g)}$	0.041	0.073	0.12

All values are in moles of gas per kilogram of propellant

dissociation of carbon monoxide on gun steel. Then hydrogen gas present in the propellants combustion products reacts with the oxygen to form water while the carbon diffuses into the gun steel, resulting in surface carburization and a lowering of the melting temperature by several hundred degrees [118]. The presence of a lot of nitrogen gas, especially when using HNC propellant ingredients nitrides the gun steel. This nitride coating prevents the carbon monoxide from reacting with the gun steel, thus reducing erosion [119]. Therefore, a propellant with low amounts of hydrogen and a high N_2:CO ratio is desirable [120].

A recent study determined that these codes tend to under-predict the concentrations of certain toxic gasses such as HCN and NH_3 [121]. In a series of 9MM firings with different propellants it was demonstrated that the concentrations of HCN and NH_3 were found to be orders of magnitude higher than predicted by EXPLO5, when compared to gas analysis performed on the actual gun firings. It was proposed that this increase may be due to more benign propellants having a lower flame temperature which leads to more production of NH_3 and CH_4. These two gasses can then react in the presence of oxygen to form HCN [122]. Reactive force field molecular dynamics (ReaxFF-MD) simulations of the individual components of the formulation, namely, NC, NG, EC, and DPA demonstrated that the major sources for these toxic gasses are the aromatic compounds EC and DPA, not from the nitro groups of NC and NG [123]. As such, these codes may be employed as a design tool to minimize the production of toxic gasses.

Two triple base formulations containing small amounts of TAAMP or BABAMP were likewise analyzed using THERMO. The software was able to predict within 15 J/g the impetus of 5 formulations with varying amounts of energetic plasticizer as validated by closed vessel testing, thus confirming the utility of thermodynamic codes in assisting propellant developers to more efficiently develop propellants [43].

Recently, Son's group demonstrated through Cheetah 6.0 and experimentally that 1,4-dinitrato-2,3-dinitro-2,3bis(nitratomethylene) butane (SMX) mixed with varying amounts of NC can, in terms of impetus, outperform JA2, a benchmark high performance and insensitive gun propellant [124]. Cheetah demonstrated that in a binary formulation consisting solely of NC and SMX, at concentrations of SMX between 35% and 70%, the impetus of the experimental formulation exceeded that of JA2. This implied the potential for SMX to be used as an NG replacement. Surprisingly the addition of 20%DEGDN to the NC/SMX formulation boosted the impetus by over 20 J/g. Normally, the addition of DEGDN to a high energy formulation at the expense of a high energy ingredient such as NG, RDX, or HMX, lowers the impetus, but in this case, the opposite occurred.

7 Processing Effects

Instead of mixing all of the ingredients together in a batch mixer, for safety reasons, there has been a recent push towards infusing the propellant after they have been formed into grains. Single base propellant has been infused with NG after it has been formed into grains and prior to deterring with a polyester. Determination of the concentration profile demonstrated that infusion with NG produced a gradient inside the grain with the lowest concentrations of NG being near the surface and centers of the grain. Their results indicate that the even though the NG was successfully infused into the grain, it also easily moved out of the grain near the surface. This is a common issue with double base propellants containing NG owing to its high mobility through the NC matrix. They demonstrated that after the deterring and infusing the propellant grain exhibited progressive burning while the unaltered base grain was undergoing neutral burning. They also demonstrated that the infused propellant was of higher energy, and produced less erosion by about 16% at a similar chamber pressure [125].

Infusion of NC was also performed with SMX. It was mixed with NC up to a concentration of 40% by weight. Crystals were observed to form on the surfaces of the NC fiber. Subsequent heating above SMX's melting point (~ 85 °C) caused the SMX to liquefy and penetrate uniformly into the grains. Using this processing methodology a propellant was made consisting of 60%NC and 40%SMX which exhibits impact sensitivity similar to JA2 with a slightly higher friction sensitivity [124]. The increase in friction sensitivity is understandable because while JA2 contains virtually no solid energetic fillers, in this case the researchers added 40% by weight of solids to the formulation.

Consolidated propelling charges are prepared by forming a large charge from smaller propellant grains. In essence, consolidated charges are small propellant grains glued together to form a larger charge. An example of this would be to form a cylinder from small ball powder grains. The benefits of a consolidated charge are the significant increase in the loading density and an inherent progressivity when the consolidated charges break apart into smaller grains, in a process termed deconsolidation. Both of these processes lead to improved ballistic performance [126].

Consolidated charges have been prepared in a variety of ways. In one method, the propellant grains are compressed inside the cartridge case [127]. Another process involves the addition of a solvent, such as acetone, to the propellant grains. Acetone partially solvates the NC causing the grains to swell. These wetted grains are then compacted into the desired charge shape. One drawback to this methodology is that the individual grains do get deformed in the process, altering the ballistics [128]. Yet another methodology employs the coating of propellant grains with a thermally curable binder. These grains were then thermally consolidated into the desired propelling charge shape [129].

Oblate spherical double base propellants plasticized with TEGDN have been consolidated by a combination of techniques. A gelled NC in acetone was utilized

as the binder to thermally consolidate the grains. Furthermore, the charge forming tool was coated with an NC/TiO_2 mixture, causing the outermost layer of this consolidated charge to have a deterrent. This combination technique demonstrated significantly improved mechanical properties in terms of uniaxial compression. Both stress and strain increased more than twofold before failing. Closed vessel analysis revealed that the consolidated charge exhibited a two stage combustion event. First the outer NC/TiO_2 coating layer burned away followed by deconsolidation of the charge which lead to a drastic jump in dynamic vivacity [130].

Recently, a combination of processing techniques were employed to improve upon consolidated gun propellants. Researchers prepared seven perforated grains using foaming and compression molding technologies. Through a series of quenched combustion tests, they were able to demonstrate a marked improvement [131] over previous consolidated propellants examined [132]. This was achieved by ensuring that deconsolidation of the propellant grains occurs later in the ballistic cycle which was a major drawback for previous efforts involving consolidated gun propellants.

Foaming of propellants increases the porosity of propellants, thusly increasing the surface area available for combustion which in turn increases the burn rate [133]. One drawback to this is the reduced density of the propellant. For this reason, foamed energetic materials have been primarily examined for combustible cartridge case and case-less ammunition applications. Recently, foaming of a poly-methylmethacrylate (PMMA)—RDX composite was examined. Foaming was achieved via saturation of the propellant in a supercritical CO_2 ($scCO_2$) fluid under high pressure. The CO_2 penetrates into the propellant and once the pressure is quickly removed the CO_2 evacuates the propellant leaving a porous material. The investigators varied both the RDX content and expansion ratio, which corresponds to porosity via a supercritical CO_2 foaming methodology. They demonstrated that at 55% RDX content the foamed material was equivalent to the existing felted fiber case technology in terms of force constants at 450 J/g. The force constants are the energy content of the material. At higher RDX concentrations (75%) they were able to achieve a force constant of 858 J/g which is getting close to the impetus of certain gun propellants. This is impressive because they employed an inert binder. If they were able to utilize an energetic binder the impetus would dramatically improve. They also demonstrated that as porosity or RDX content increased so did the progressivity of the burning in closed vessel tests. One surprising result was that foaming temperature played virtually no role in the performance of the materials [134].

Then, Yang and co-workers altered their foaming procedure, by adding a timed desorption step to their super-critical CO_2 process. In this case the supercritical CO_2 fluid is allowed to escape from the material for a specified amount of time. This leaves the surface of the propellant with less CO_2 than the core of the propellant. Once it is quenched, the CO_2 gradient that was established forms a material that is porous on the inside and has a significantly less porous skin on the exterior of the grain [135].

Foaming of NC has presented a challenge until a recent process was developed, using supercritical foaming technology which consists of dissolution of gas, cell

nucleation, cell growth, followed by stabilization of foam structures [136]. The challenges for NC foaming derive from its high crystallinity. The crystalline regions of NC prevent penetration of the inert gasses commonly employed such as CO_2, thus preventing pore formation [137].

Another recent study examined foamed NC double base propellant containing NG or TEGDN as a plasticizer [138]. These researchers were able to control porosity of the propellant grains and demonstrated via closed vessel testing that as porosity increased, so did gas generation. Furthermore they demonstrated that the presence of plasticizers, NG and TEGDN, improved $scCO_2$ uptake, and subsequent porosity increased. Without plasticizers no differences between foamed and unfoamed propellants were visible during closed vessel testing. Foaming increased the burn rates significantly. The desorption of CO_2 from foamed propellants was fastest for the NG based propellant. TEGDN demonstrated itself to be a better plasticizer for these foamed propellants. Furthermore, they also prepared samples with an outer skin and demonstrated via interrupted combustion testing in a closed vessel that the inner porous cores burn out before the outer skin does [139].

Other studies employed potassium nitrate to generate porosity in single base ball powder grains. They incorporated the potassium nitrate (KNO_3) into the formulation and after formation of the ball powders, they washed the propellant with water. The water dissolved and removed the KNO_3, but left the rest of the propellant untouched thus generating porous ball powder. The porous ball powders were then shaped with acetone or ethyl acetate which eliminated the porosity on the surface of the grains, while leaving the internal porosity intact. This produced ball powders with a fast burning core. Finally the grains were deterred with the standard dibutyl phthalate (DBP) or poly(ethylene glycol dimethacrylate) (PEGDMA) [140]. They demonstrated that the amount of KNO_3 added, and the conditions of the shaping greatly affected the combustion characteristics of the ball powders in closed vessel tests. Furthermore, the PEGDMA was polymerized inside the grain to allow the monomers to disperse into the grain and form a deterrent gradient and produce more progressive combustion than the DBP deterred grains.

Another technique that generated porosity in NC utilized titanium nanoparticles as nucleation sites. Cylindrical propellant grains were made by standard mixing, and extrusion of NC (11.8–12.4% nitrogen) with titanium nanoparticles (20–40 nm diameter). The nano-titanium ranged from 5 to 15% by weight. The cylindrical grains then underwent foaming via immersion in $scCO_2$, and the use of ethyl acetate to partially dissolve/soften the NC and allow the CO_2 to better diffuse into the grain. The titanium acted as nucleation sites for the $scCO_2$ generating NC grains that have some pores filled with nano-titanium. As the concentration of the nano-titanium increased, agglomeration became more pronounced. Also, standard mixing techniques were shown to inadequately mix the nano-titanium, causing some areas of the grain to have significantly higher local concentrations of titanium. These materials were then tested in a closed vessel and their impetus was demonstrated to decrease with increasing titanium content. However, closed vessel testing also demonstrated that the foamed propellant with 10% nano-titanium had the highest burn rate, contradicting the impetus trend observed [13].

8 Summary

Although the traditional role of gun propellants has remained essentially the same, the often competing requirements of advanced weapon systems have necessitated a tremendous amount of effort over past five years, from 2010 to 2015, to develop new binders, plasticizers, and fillers, into high energy insensitive formulations. The majority of the binder work has focused on functionalizing cellulose with non-nitrate ester groups to produce a more stable form of energetic cellulose. A wide variety of novel plasticizers have been examined that exhibit promise in making gun propellant formulations less sensitive to shock and thermal stimuli. The fillers are the broadest category of propellant ingredients, and have had the largest amount of materials examined. Nano-particles, alternate forms of carbon, and energetic co-crystals have been tested as gun propellant ingredients that can boost performance and stability while reducing sensitivity, hygroscopicity, and combustion residue generation. At the propelling charge level, novel techniques such as foaming and consolidating propellant grains promise to improve gas generation behind the projectile later in the ballistic cycle, leading to increases in muzzle energy.

While traditional propellant ingredients consist of a relatively few available and proven materials, recent discovery and manipulations of new molecules are allowing the gun propulsion developer to extend the state of the art in propellant formulations, providing the warfighter with improved capabilities on the battlefield. In the next five years, continued technical advancements in these new ingredients and formulations may lead to a paradigm shift in the development of gun propellants.

References

1. Koc S, Ulas A, Yilmaz NE (2015) Propellants, Explos, Pyrotech 40:735
2. (A) Klingenberg G (1989) Propellants Explos Pyrotech 14:57. (B) Klingenberg G, Heimerl JM (1987) Combust Flame 68:167. (C) Carfagno SP (1961) Handbook on gun flash, report DTIC AD327051. The Franklin Institute, Philadelphia, PA, USA. (D) Yousefian V, May IW, Heimerl JM (1980) 17th JANNAF combustion meeting, Hampton, 22–26 Sept 1980, vol 2, p 124. (E) Heimerl JM, Keller GE, Klingenberg G (1988). In: Stiefel L (ed) Gun propulsion technology. AIAA, Washington D.C., p. 261
3. Bougaev AV, Gerasimov S, Erofeyev VI, Kolchev SV, Mikhailova1 YA (2014) 28th international symposium on Ballistics Atlanta, GA, 22–26 Sept 2014
4. Birk A, Guercio MD, Kinkennon A, Kooker DE, Kaste P (2000) Army research laboratory technical report ARL-TR-2371
5. (A) Hamlin SJ, Beyer RA, Burke GC, Hirlinger JM, Martin J, DL Rhonehouse (2005) Proceedings of SPIE-the international society for optical engineering, p 5871(Optical Technologies for Arming, Safing, Fuzing, and Firing), 587102/1-587102/9. (B) Beyer RA, Hirlinger JM (1999) Army research laboratory technical report ARL-TR-1864. (C) Beyer RA, Boyd JK, Howard SL, Reeves GP (1999) Army research laboratory technical report ARL-TR-1993

6. Xiao Z, Ying S, Xu F (2015) Propellants, Explos, Pyrotech 40:484
7. Sättler A, Åberg D, Rakus D, Heiser R (2014) 128th International symposium on Ballistics, Atlanta, GA, 22–26 Sept 2014
8. Bieles JK (1986) 9th International symposium on Ballistics, Shrivenham, UK, April 29–May 1 1986
9. Nakamura Y, Ishida T, Miura H, Matsuo A (2007) 23rd international symposium on Ballistics, Tarragona, Spain, 16–20 Apr 2007
10. Howard SL (2011) Army research laboratory technical report ARL-TR-5658
11. Baschung B, Bouchama A, Comet M, Boulnois C (2014) 28th international symposium on Ballistics, Atlanta, GA, 22–26 Sept 2014
12. Howard SL, Churaman WA, Currano L (2014) Army research laboratory technical report ARL-TR-6950
13. Su J, Ying S, Xiao Z, Xu F (2013) Propellants, Explos, Pyrotech 38:533
14. Muthurajan H, Ghee AH (2008) Central Eur J Energ Mat 5(3–4):19
15. Zheng W, Chen H, Li Q, Pan R, Lin X (2014) Int J Energ Mat Chem Propul 13:421
16. Harrland A, Johnston IA (2012) Defence science and technology organisation technical report DSTO-TR-2735
17. Leciejewski ZK, Surma Z (2011) Combustion. Explosion, Shock Waves 47:209
18. Pauly G, Scheibel R (2008) 43rd Annual armament systems: gun and missile systems conference & exhibition, New Orleans, LA, USA, 21–25 Apr 2008
19. (A) Kubota N (1988) Propellants Explos Pyrotech 13:172. (B) Kubota N, Sonobe T, Yamamoto A, Shimizu H (1990) J Prop Power 6:686
20. Pant CS, Wagh RM, Nair JK, Gore GM, Venugopalan S (2006) Propellants, Explos, Pyrotech 31:477
21. Miles FD (1955) Cellulose nitrate. Oliver and Boyd, London
22. Rafeev VA, Rubtsov YI, Sorokina TV, Chukanov NV (1999) Russ Chem Bull 48:66
23. Rafeev VA, Rubtsov YI, Sorokina TV (1879) Russ Chem Bull 1996:45
24. (A) Wu TK (1980) Macromolecules 13:74. (B) Chicherov AA, Kuznetsov AV, Kargin YM, Klochkov VV, Marchenko GN, Garifzyanov GG (1990) Polym Sci USSR, Set. A 32:502
25. Sun D-P, Ma B, Zhu C-L, Liu C-S, Yang J-Z (2010) J Energ Mater 28(2):85
26. Manning TG, Wyckoff J, Adam CP, Rozumov E, Klingaman K, Panchal V, Laquidara J, Fair M, Bolognini J, Luhmann K, Velarde S, Knott C, Piraino SM, Boyd K (2014) Defence Technol 10:92
27. Shamsipur M, Pourmortazavi SM, Hajimirsadeghi SS, Atifeh SM (2012) Fuel 95:394
28. Betzler FM, Klapötke TM, Sproll S (2011) Central Eur J Energ Mat 8(3):157–171
29. Nobel A, Armengaud CE (1876) Improvement in gelatinated explosive compounds, US Patent 175, vol 735
30. (A) Ang HG, Pisharath S (2012) Energetic polymers: binders and plasticizers for enhancing performance. Wiley-VCH, Germany. (B) Kumari D, Balakshe R, Banerjee S, Singh H (2012) Rev J Chem 2:240–262
31. Howard SL, Leadore MG, Newberry JE (2015) Army research laboratory technical report ARL-MR-0894
32. Zhang J, Ju Y, Zhou C (2013) Propellants, Explos, Pyrotech 38:351
33. Agrawal JP, Singh H (1993) Propellants, Explos, Pyrotech 18:106
34. Suceska M, Musanic SM, Houra IF (2010) Thermochim Acta 510:9
35. Taylor S, Dontsova K, Bigl S, Richardson C, Lever J, Pitt J, Bradley JP, Walsh M, Šimůnek J (2012) US army engineer research and development center technical report, ERDC/CRREL TR-12-9
36. Yi JH, Zhao FQ, Hu RZ, Xue L, Xu SY (2010) J Energ Mater 28(4):285
37. Simmons RL (1994) NIMIC-S-275-94. NATO, Brussels, Belgium
38. Chakraborthy TK, Raha KC, Omprakash B, Singh A (2004) J Energ Mater 22(1):41
39. Yana QL, Künzela M, Zemana S, Svobodab R, Bartoskovác M (2013) Thermochim Acta 566:137

40. Mueller D (2008) 43rd annual armament systems: gun and missile systems conference & exhibition, New Orleans, LA, USA, 21–25 Apr 2008

41. Vijayalakshmi R, Naik NH, Gore GM, Sikder AK (2015) J Energ Mater 33:1

42. Kumari D, Yamajala KDB, Singh H, Sanghavi RR, Asthana SN, Raju K, Banerjee S (2013) Propellants, Explos, Pyrotech 38:805

43. Ghosh K, Athar J, Pawar S, Polke BG, Sikder AK (2012) J Energ Mater 30(2):107

44. Ghosh K, Pant CS, Sanghavi R, Adhav S, Singh A (2008) J Energ Mater 27:40

45. (A) Zimmer-Galler R (1968) AIAA J 6:2107. (B) Kubota N (1982) 19th Symposium (International) on combustion. The Combustion Institute, USA, Haifa, Israel, 8–13 Aug 1982

46. Parker GA, Reddy G, Major MA (2006) Int J Toxicol 25:373

47. Wang Y, Song X, Song D, Jiang W, Liu H, Li F (2011) Propellants, Explos Pyrotech 36:505

48. Vijayalakshmi R, Radhakrishnan S, Rajendra PS, Girish GM, Arun SK (2012) Part Syst Charact 28:57

49. Oxley JC, Smith JL, Brady JE, Brown AC (2012) Propellants, Explos, Pyrotech 37:24

50. Lee K-Y, Chapman LB, Cobura MD (1987) J Energ Mater 5:27

51. Tremblay M (1965) Can J Chem 43:1230

52. (A) Walsh C, Knott C (2004) 32nd JANNAF propellant explosives development and characterization subcommittee meeting, Seattle, Washington. (B) Mason B, Llyod J, Son S, Tappan B (2009) Int J Energ Mater Chem Propul 8:31. (C) Conner C, Anderson W (2007) 34th JANNAF propellant & explosives development and characterization subcommittee, Reno, Nevada, 13–17 Aug 2007

53. Kumbhakarna N, Thynell S, Chowdhury A, Lin P (2011) Combust Theor Model 15:933

54. (A) Kolb HC, Finn MG, Sharpless KB (2004) Angewandte Chemie international edition 2001 40. (B) Demko ZP, Sharpless KB (2002) Angewandte Chemie International Edition 41:2113

55. Zhang J, Zhang Q, Vo TT, Parrish DA, Shreeve JM (2015) J Am Chem Soc 137:1697

56. Serushkin VV, Sinditskii VP, Egorshev VY, Filatov SA (2013) Propellants, Explos, Pyrotech 38:345

57. Tappan BC, Chavez DE (2015) Propellants, Explos, Pyrotech 40:13

58. Paraskos AJ, Cooke ED, Caflin KC (2015) Propellants, Explos, Pyrotech 40:46

59. Warner KF, Granholm RH (2011) J Energ Mater 29:1

60. Fischer D, Klapotke TM, Stierstorfer J (2012) Propellants, Explos, Pyrotech 37:156

61. Klapotke TM, Preimesser A, Stierstorfer J (2015) Propellants, Explos, Pyrotech 40:60

62. (A) Bottaro JC (1996) Chem Ind 10:249. (B) Bottaro JC, Schmitt RJ, Penwell P, Ross S (1993) Dinitramide salts and method of making same, U.S. Patent 5254324, SRI International, Stanford, CA, USA

63. Badgujar DM, Wagh RM, Pawar SJ, Sikder AK (2014) Propellants, Explos, Pyrotech 39:658

64. Armstrong RW, Ammon HL, Elban WL, Tsai DH (2002) Thermochim Acta 384:303

65. Radacsi N, Bouma RHB, Krabbendam-la Haye ELM, ter Horst JH, Stankiewicz AI, van der Heijden AEDM (2013) Propellants, Explos, Pyrotech 38:761

66. Pivkina A, Ulyanova P, Frolov Y, Zavyalov S, Schoonman J (2004) Propellants, Explos, Pyrotech 29:39

67. (A) Siegel RW (1999) WTEC Panel report on nanostructure science and technology: R&D status and trends in nanoparticles, nanostructured materials, and nanodevices, International Technology Research Institute, p 49. (B) Zohari N, Keshavarz MH, Seyedsadjadi SA (2013) Central Eur J Energ Mat 10(1):135

68. (A) Patel R (2007) Insensitive munitions and energetic materials technology symposium, Miami, Florida. (B) Liu J, Jiang W, Li F, Wang L, Zeng J, Li Q, Wang Y, Yang Q (2014) Propellants Explos Pyrotech 39:30

69. (A) Stepanov V, Krasnoperov L, Elkina I, Zhang X (2005) Propellants Explos Pyrotech 30:178. (B) He B, Stepanov V, Qiu H, Krasnoperov LN (2015) Propellants Explos Pyrotech 40:659

70. Tappan BC, Brill TB (2003) Propellants, Explos, Pyrotech 28:223
71. Zhang Y, Liu D, Lv C (2005) Propellants, Explos, Pyrotech 30:438
72. Stepanov V, Anglade V, Hummers WAB, Bezmelnitsyn AV, Krasnoperov LN (2011) Propellants, Explos, Pyrotech 36:240
73. Redner P, Kapoor D, Patel R, Chung M, Martin D (2006) Production and characterization of nano-RDX. U.S. Army, RDECOM-ARDEC, Picatinny, NJ 07806-5000
74. Essel JT, Cortopassi AC, Kuo KK, Leh CG, Adair JH (2012) Propellants, Explos, Pyrotech 37:699
75. (A) Qiu H, Stepanov V, Chou T, Surapaneni A, Di Stasio AR, Lee WY (2012) Powder Technol 226:235. (B) Shi X, Wang J, Li X, An C, Central European Journal of Energetic Materials, 2014, 11(3), 433
76. An C, Li H, Guo W, Geng X, Wang J (2014) Propellants, Explos, Pyrotech 39:701
77. Zhang X, Weeks BL (2014) J Hazard Mater 268:224
78. Qiu H, Stepanov V, Di Stasio AR, Chou TM, Lee WY (2011) J Hazard Mater 185:489
79. (A) Armstrong RW, Coffey CS, DeVost VF, Elban WL (1990) J Appl Phys 68:979. (B) Wawiernia TM, Cortopassi AC, Essel JT, Ferrara PJ, Kuo KK (2009) 8th international symposium on special topics of chemical propulsion, Cape Town, South Africa, 2–6 Nov 2009
80. Shi X, Wang J, Li X, An C (2014) Central Eur J Energ Mat 11(3):433
81. Parrish DA, Deschamps JR, Gilardi RD, Butcher RJ (2008) Cryst Growth Des 8:57
82. Deschamps JR, Parrish DA (2015) Propellants, Explos, Pyrotech 40:506
83. Landenberger KB, Matzger AJ (2010) Cryst Growth Des 10:5341
84. Millar DIA, Maynard-Casely HE, Allan DR, Cumming AS, Lennie AR, Mackay AJ, Oswald IDH, Tang CC, Pulham CR (2012) Cryst Eng Comm 14(10):3742
85. Divekar CN, Sanghavi RR, Nair UR, Chakraborthy TK, Sikder AK, Singh A (2010) J Propul Power 26(1):120
86. Hikal WM, Bhattacharia SK, Weeks BL (2012) Propellants, Explos, Pyrotech 37:718
87. Lin H, Zhu S-G, Zhang L, Peng X-H, Li H-Z (2013) J Energ Mater 31(4):261
88. Bolton O, Matzger AJ (2011) Angew Chem 123:9122
89. Bolton O, Simke L, Pagoria P, Matzger A (2012) Cryst Growth Des 12:4311
90. Anderson SR, Ende DJ, Salan JS, Samuels P (2014) Propellants, Explos, Pyrotech 39:637
91. Li H, An C, Guo W, Geng X, Wang J, Xu W (2015) Propellants, Explos, Pyrotech 40:652
92. Jung JW, Kim KJ (2011) Ind Eng Chem Res 50(6):3475
93. Yang Z, Li J, Huang B, Liu S, Huang Z, Nie F (2014) Propellants, Explos, Pyrotech 39:51
94. Qiu H, Patel RB, Damavarapu RS, Stepanov V (2015) CrystEngComm 17:4080
95. McDonald BA (2011) Propellants, Explos, Pyrotech 36:576
96. Lin C-P, Chang Y-M, Gupta JP, Shu C-M (2010) Process Saf Environ Prot 88:413
97. Zayed MA, Hassan MA (2010) Propellants, Explos, Pyrotech 35:468
98. Zayed MA, El-Begawy SEM, Hassan HES (2013) Arab J Chem. doi:10.1016/j.arabjc.2013.08.021
99. Trache D, Khimeche K (2013) Fire Mater 37:328
100. Trache D, Khimeche K (2013) J Therm Anal Calorim 111:305
101. Jin B, Peng RF, Chu SJ, Huang YM, Wang R (2008) Propellants, Explos, Pyrotech 33:454
102. Pekker S, Kovats E, Oszlanyi G, Benyei G, Klupp G, Bortel G, Jalsovszky I, Jakab E, Borondics F, Kamaras K, Bokor M, Kriza G, Tompa K, Faigel G (2005) Nat Mater 4:764
103. Chi Y, Huang H, Li JS (2005) International autumn seminar on propellants, explosives and pyrotechnics (2005IASPEP), Beijing, China, 25–28 Oct 2005
104. Smeu M, Zahid F, Ji W, Guo H, Jaidann M, Abou-Rachid H (2011) J Phys Chem C 115:10985
105. Guo R, Hu Y, Shen R, Ye Y (2014) J Appl Phys 115:174901
106. (A) Hummers WS, Offeman RE (1958) J Am Chem Soc 80:1339. (B) Marcano DC, Kosynkin DV, Berlin JM, Sinitskii A, Sun ZZ, Slesarev A, Alemany LB, Lu W, Tour JM (2010) ACS NANO 4:4806

107. (A) Krishnan D, Kim F, Luo JY, Cruz-Silva R, Cote LJ, Jang HD, Huang JX (2012) Nano Today 7:137. (B) Kim F, Luo JY, Cruz-Silva R, Cote LJ, Sohn K, Huang JX (2010) Adv Funct Mater 20:2867
108. Li R, Wang J, Shen JP, Hua C, Yang GC (2013) Propellants, Explos, Pyrotech 38:798
109. Cowperthwaite M, Zwisler WH (1973) Tiger computer program documentation, Stanford Research Institute, Publication No. Z106
110. Freedman E (1988) Blake-A thermodynamics code based on TIGER: Users' Guide to the Revised Program, ARL-CR-422
111. Fried LE (1996) CHEETAH 1.39 User's manual, Lawrence Livermore National Laboratory, manuscript UCRL-MA-117541 Rev. 3
112. Sućeska M (1991) Propellants, Explos, Pyrotech 16:197–202
113. Grys S, Trzciński WA (2010) Central Eur J Energ Mat 7(2):97
114. Karir JS (2001) 28th International pyrotechnics seminar. 4–9 Nov 2001, Adelaide, South Australia
115. Xu F-M (2013) Defence Technol 9:127
116. Anderson RD, Rice BM (2000) Army research laboratory technical report ARL-TR-2326
117. (A) Klapötke TM, Stierstorfer J (2005) Proceedings of the 26th army science conference, Orlando, Florida, 1–4 Dec 2008. (B) Johnston IA (2005) Understanding and predicting gun barrel erosion, DSTO.TR.1757, Weapons Systems Division, Defence Science and Technology Organisation, Australia
118. Conroy PJ, Weinacht P, Nusca MJ (2001) Army research laboratory technical report, ARL-TR-2393
119. Conroy PJ, Leveritt CS, Hirvonen JK, Demaree JD (2006) Army research laboratory technical report, ARL-TR-3795
120. Doherty RM (2003) 9th IWCP on novel energetic materials and applications, Lerici (Pisa), Italy, 14–18 Sept 2003
121. Moxnes JF, Jensen TL, Smestad E, Unneberg E, Dullum O (2013) Propellants, Explos, Pyrotech 38:255
122. Rotariu T, Petre R, Zecheru T, Suceska M, Petrea N, Esanu S (2015) Propellants, Explos, Pyrotech 40:931
123. Jensen TL, Moxnes JF, Unneberg E, Dullum O (2014) Propellants, Explos, Pyrotech 39:830
124. Reese DA, Groven LJ, Son SF (2014) Propellants, Explos, Pyrotech 39:205
125. Liu B, Chen B, Yao Y-J, Wang Q-L, Yu H-F, Liu S-W (2015) Energy Procedia 66:121
126. Yao Y-J, Liu B, Wang Q-L, Liu S-W, Wei L, Zhang Y-B (2015) Energy Procedia 66:125
127. Martin R, Gonzalez A (1993) Proceedings of the JANNAF propulsion meeting. Monterey, California, 15–19 Nov 1993
128. Doali JO, Juhasz AA, Bowman RE, Aungst WP (1988) U.S. army ballistic research laboratory technical report, BRL-TR-2944
129. Cloutier T, Sadowski L (2005) Armament research, developments and engineering center, armaments engineering and technology center (Benet) technical report, ARAEW-TR-05006
130. Xiao Z-G, Ying S-J, Xu F-M (2014) Defence Technol 10:101
131. Li Y, Yang W, Ying S (2015) Propellants, Explos, Pyrotech 40:33
132. (A) Doali JO, Juhasz AA, Bowman RE, Aungst WP (1988) U.S. army ballistic research laboratory technical report, BRL-TR-2944. (B) Juhasz AA, May IW, Aungst WP, Doali JO, Bowman RE (1979) 16th JANNAF combustion meeting, Monterey, CA, USA, 10–14 Sept 1979. (C) May IW, Juhasz AA (1981) U.S. army ballistic research laboratory technical report, ARBRL-MR-03108. (D) Martin R, Gonzalez A (1993) JANNAF propulsion meeting, Monterey, CA, USA, 15–19 Nov 1993. (E) Cloutier T, Sadowski L (2005) Armament research, developments and engineering center, armaments engineering and technology center technical report, ARAEW-TR-05006. (F) Bonnet C, Pieta PD, Reynaud C (2001) 19th International symposium of ballistics, Interlaken, Switzerland, 7–11 May 2001

133. (A) Frolov YV, Korostelev V (1989) Propellants Explos Pyrotech 14:140. (B) Bçhnlein-Mauß J, Eberhardt A, Fischer TS (2002) Propellants Explos Pyrotech 27:156. (C) Bçhnlein-Mauß J, Krçber H (2009) Propellants Explos Pyrotech 34:239. (D) Kuo KK, Vichnevetsky R, Summerfield M (1973) AIAA J 11:444. (E) Kooker D, Anderson R (1981) 18th JANNAF combustion meeting, Pasadena, CA, USA, 19–23 Oct 1981. (F) James TB, Edward BF (1995) Army research laboratory technical report, ARL-CR-242
134. Yang W, Li Y, Ying S (2015) Propellants, Explos, Pyrotech 40:27
135. Yang W, Li Y, Ying S (2015) J Energ Mater 33:91–101
136. Su J, Ying S, Xiao Z, Xu F (2013) Propellants, Explos, Pyrotech 38(4):533
137. Jiang X-L, Liu T, Xu Z-M, Zhao L, Hu G-H, Yuan W-K (2009) J. Supercrit. Fluid 48:167
138. (A) Li Y, Yang W, Ying S (2014) Propellants Explos Pyrotech 39:677. (B) Li Y, Yang W, Ying S (2014) Propellants Explos Pyrotech 39:852
139. Li Y, Yang W, Ying S, Peng J (2015) J Energ Mater 33:167
140. Xiao Z, Ying S, Xu F (2010) Propellants, Explos, Pyrotech 35:1

How to Use QSPR Models to Help the Design and the Safety of Energetic Materials

Guillaume Fayet and Patricia Rotureau

Abstract With the increase of performances of computers, predictive methods were developed from years to access the properties of materials. Among these methods, quantitative structure-property relationships (QSPR) allow predictions from the only knowledge of molecular structure of compounds. Of common practice for biological activities under the denomination of QSAR, these models are used notably in drug design as screening tools in the development and selection of new compounds. They gained also interest for regulatory purpose in the context of REACH since they were proposed as alternative methods to reduce experimental testings. Now, the fields of application of these models are extended to a large variety of compounds and notably to energetic materials. The present contribution describes the QSPR approach from the development of the models, following strong validation principles, to their correct use to access reliable predictions. In particular, an overview of existing QSPR models from literature dedicated to energetic materials is proposed and possible uses to help the design and the safety of energetic materials are discussed.

Keywords QSPR model · REACH regulation · Safety · In silico design · Molecular descriptor

1 Introduction

Energetic materials are used in large sets of military and civil applications like in the car industry in airbags or in the space industry in propellants. Many properties are needed to ensure the best choice and use of these materials for target applications and for safety purpose [1, 2].

As a complement to experiments, computational approaches were developed from years to predict targeted properties of energetic materials taking advantage of

G. Fayet (✉) · P. Rotureau
Accidental Risk Division, Institut National de l'Environnement Industriel et des Risques (INERIS), Parc Technologique Alata, 60550 Verneuil-En-Halatte, France
e-mail: guillaume.fayet@ineris.fr

increasing computer capabilities. From many years, examinations of molecular structures were used to evidence the properties of energetic materials by identifying the presence of "explosophore" groups like $-NO_2$ or $-N_3$ groups. Some software like CHEETAH [3] were also developed based on empirical formula and/or group contribution approaches [2, 4]. Toghiani et al. [5] notably used group contribution models and the COSMO-RS method to calculate physico-chemical properties of energetic materials.

Among available predictive methods, Quantitative Structure-Property Relationships represent an increasingly popular approach to access the properties of chemicals from the only knowledge of their molecular structure, at least in screening process. Indeed, they have already been successfully used for biological [6], toxicological [7, 8] but also physico-chemical applications [9, 10].

The use of such methods may entail great advantages by reducing experimental testing and, as a consequence, costs, time and risks for operators, in particular in the case of energetic materials. In consequence, QSPR models are listed among the relevant alternative methods to experimental testing in the REACH regulation [11].

The present contribution aims to introduce the QSPR approach and the methods used to develop and validate such predictive models. A short review of existing models dedicated to physico-chemical properties of energetic materials is proposed. A focus addresses selected case studies of nitro compounds to show how quantum chemical calculations can help to the derivation of QSPR models and how a first simple model was implemented into the QSAR Toolbox [12], a prediction platform proposed by ECHA and OECD. Finally, different uses of QSPR models will be discussed: for regulatory purpose and as a tool for the design of new energetic materials.

2 Quantitative Structure-Property Relationships

2.1 Principle

The QSPR approach relies on a similarity principle that estimates that compounds with similar molecular structures present similar properties. So, it consists in correlating target experimental, i.e. macroscopic, properties to the molecular scale structure of substances, characterized through molecular descriptors, as illustrated in Fig. 1.
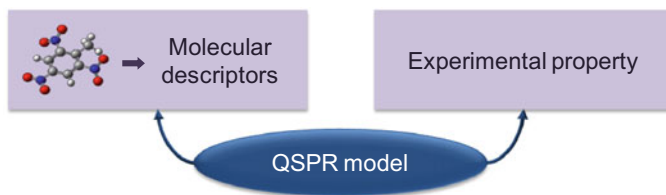
Fig. 1 Principle of the QSPR method

Molecular descriptors are numerical indicators or properties encoding the molecular composition and properties of chemicals. They are very numerous [13, 14] and can be classified into four classes (as illustrated in Fig. 2 on 2,4,6-trinitroluene (TNT)):

- *constitutional descriptors* that are related to the occurrence or count of (specific) atoms, groups of atoms or bonds in molecules;
- *topological descriptors* based on a connectivity table of atoms, that relate to the size, shape and ramification rate of molecules;
- *geometric descriptors* that characterize the 3D structure of molecules by distances, angles, molecular volumes or areas;
- *quantum chemical descriptors* issued from the information, obtained by quantum chemical calculations, on reactivity (e.g. bond dissociation energies) or electrostatic properties (e.g. atomic charges).

If the first two classes of descriptors (constitutional and topological) only need knowledge of simple 2D structures of molecules, the last two ones (geometric and quantum chemical) require preliminary quantum chemical calculations but give access to descriptors allowing in some cases a better chemical interpretation in the final proposed QSPR models.

QSPR models are interpolation models. So, an experimental dataset, that must be as large and reliable as possible, is required to develop a new model. Indeed, fitting procedures are based on statistical principles more likely adapted to large number of

Fig. 2 Different types of molecular descriptors used in QSPR models
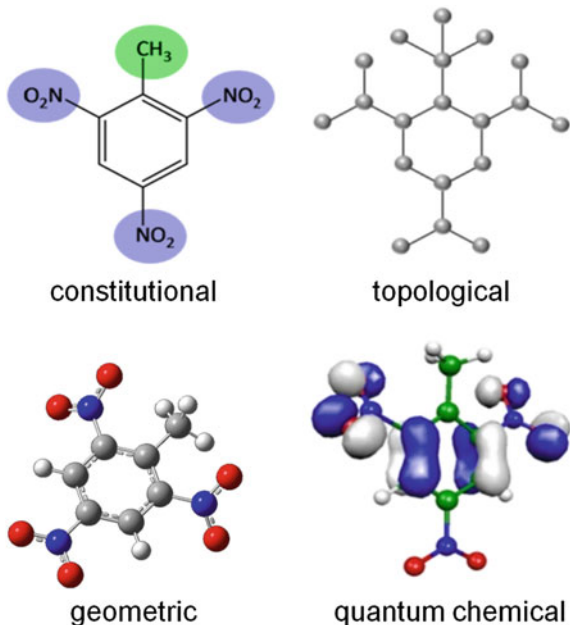
data. Moreover, large datasets allow their splitting to have a training set to fit the model and to save a validation set to estimate the predictive power of models. Concerning the reliability of data, uncertainties introduced in the measured data may be at best lowered since it propagates into the model within its fitting. Furthermore, experimental protocols must be analyzed to limit biases introduced by non homogeneous data. It is particularly important for regulatory uses since regulations impose particular testing standards. So, in such cases, the experimental values in the data set must be in agreement with these standards.

Finally, QSPR models are developed using data mining strategies to find the best models relating the experimental property to molecular descriptors. To achieve it, numerous data mining methods can be used. Among them, the most common one is the multi-linear regression (MLR) that establishes a linear equation between the property and a series of descriptors:

$$Y = a_0 + \sum a_i x_i \tag{1}$$

where Y is the target property, x_i are the molecular descriptors and a_i are the regression constants.

Other quantitative methods can be used like artificial neural networks (ANN) that can give good predictive powers by favoring the introduction of non linear trends but are, in general, less interpretable. Qualitative methods like principal component analysis (PCA) or decision trees can also be used when qualitative properties are targeted or when experimental uncertainties are particularly large [15].

An important issue in the development of QSPR model is the selection of the descriptors introduced in the models. As explained before, a large number of descriptors exist to characterize at best all molecular features that define a specific molecule and its properties. Currently, hundreds or thousands of descriptors can be calculated by a series of commercial software like Codessa [16] or Dragon [17]. So, to avoid any over-parameterization of the model, it is necessary to reduce the number of descriptors in the model. Various kinds of selection methods can help to achieve it [18], e.g. stepwise methods or genetic algorithms.

2.2 Validation of QSPR Models

Once a model has been developed, it has to be validated. This step is particularly critical in view of regulatory perspective. For this reason, five principles of validation of QSAR/QSPR models for regulatory use were proposed by OECD (Organisation for Economic Co-operation and Development) [19]:

Principle 1. A defined endpoint, including considered experimental protocols,

Principle 2. An unambiguous algorithm, with full definition of the descriptor calculation protocols, to ensure correct application,

Principle 3. A defined applicability domain, to determine when predictions can be considered as reliable,

Principle 4. Appropriate measures of the correlation, robustness and predictive power of the model,

Principle 5. An interpretation of subjacent mechanisms through the descriptors and the structure of the model.

To evaluate the performances of the model (principle 4), different validation methods are used. At first, the goodness-of-fit is estimated by the quality of fitting between the calculated and experimental values in the training set with the coefficient of determination (R^2) and errors (mean absolute errors, MAE, and root mean square errors, RMSE).

Additional internal validations are performed to check the robustness of the model (by cross-validation) and to avoid any chance correlation (by Y-randomization). Cross validation consists in excluding one or several compound(s) from the training set, refitting the model to predict the property for the excluded molecule(s) and repeating it for all compounds in the training set. A model can be estimated as robust if the correlation between the experimental values and the predicted ones with the new models is not significantly decreased from the goodness-of-fit of the actual model. Y-randomization [20] consists in randomizing experimental values a large number of times to check that models obtained from erroneous (i.e. randomized) data do not give the same level of performances than the actual model. Figure 3 represents the result of a satisfactory Y-randomizaton test. Indeed, the final model presents a good correlation whereas the ones issued from randomized data lead to low correlations R^2_{rand} that can be summarized by a low average R^2, noted R^2_{YS}, or by a low intercept of the plot of R^2 versus R^2_{rand}.

Finally, the predictive power is evaluated on an external validation set. This set must be large enough to make the statistical performances shown by the external validation reliable and it must be representative of the applicability domain of the model in terms of chemical diversity and in terms of domain of property values.

Fig. 3 Example of an acceptable result issued from a Y-randomization test
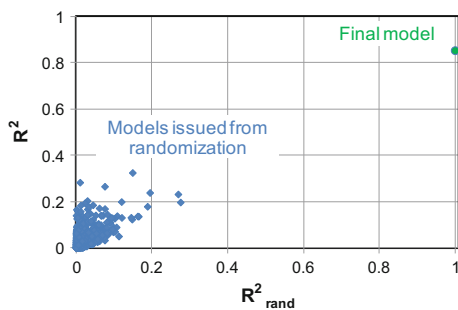
In addition to the R^2, MAE and RMSE coefficients, additional validation coefficients have been proposed in the last years: Q_{F1}^2 [19, 21], Q_{F2}^2 [22], Q_{F3}^2 [23], CCC [24] or r_m^2 and Δr_m^2 [25].

2.3 Robust Use of QSPR Models

Once a model is validated, it can be used for prediction. But to ensure a correct and relevant application of the model, some precautions must be taken. As explained before, a model is only applicable in a defined applicability domain in terms of chemical diversity (within identified families and within a defined domain in the chemical space limited by the values of descriptors in the training set) and in terms of property domain (by the range of property values in the training set). The endpoint for which it has been developed must be also relevant towards the final use of the predicted data (in particular in regulatory context). To ensure it, the following questions may be answered:

Question 1. Is the model dedicated to the family of molecules of the target compound?
Question 2. Is the endpoint of the model relevant regarding the application targeted for the predicted value?
Question 3. Is the compound in the applicability domain of the model based on the value of the molecular descriptors?
Question 4. Is the final calculated property in the applicability domain of the model?

Moreover, the model must be applied following the exact procedure defined by the developers of the model. In particular, in the case of quantum chemical descriptors, computational details, like the basis set and the method (e.g. functional), must be followed.

3 Short Overview of QSPR Models for Energetic Materials

Several reviews were published on the prediction of physico-chemical properties by QSPR models [9, 10, 26–28]. Most of the models highlighted in these reviews were not dedicated to energetic materials even if some can be applicable to them. Here are presented some QSPR models dedicated specifically to physico-chemical properties of energetic materials among those presented Fig. 4.

These models were developed for various kinds of properties of energetic materials concerning their performances for their specific applications (e.g. detonation properties), for their processability (e.g. melting point) and for their safety
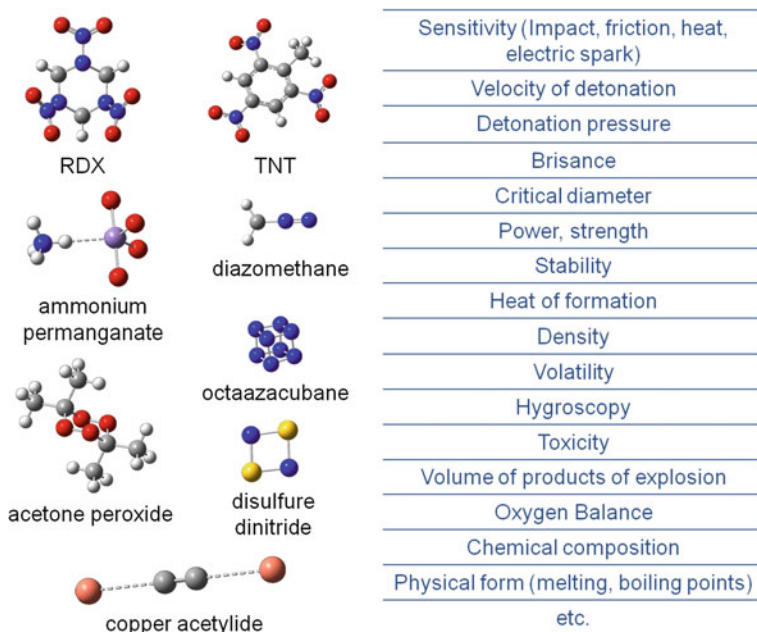
Fig. 4 Examples of energetic materials and associated properties

for humans or environment (e.g. thermal stability). In general, apart from the most recent ones, they were not developed according to the OECD principles of validation.

This overview focuses on physico-chemical properties. Nevertheless, it has to be noted that, concerning the environmental concerns, the EPI Suite [29] was developed by the EPA's Office of Pollution Prevention Toxics and Syracuse Research Corporation (SRC) to provide predictions of the relevant properties to assess the environmental fate of organic compounds. Chakka et al. [30] demonstrated that this tool that includes QSAR modules revealed relevant for a series of energetic materials, provided that they keep close to the training sets of the models (i.e. they remain in the applicability domain of the models).

3.1 Detonation Properties

Several models were developed to predict detonation performances of energetic materials. In particular, Keshavarz proposed a series of simple models mainly based on the stoichiometric composition of compounds and specific structural parameters. To predict detonation velocities D, he notably developed a model (Eq. 2) with a RMSE of 2.2% for CHNOAl compounds [31].

$$D = D_{core} - 0.620\, n'_{Al} - 1.41\, n'_{NO_3\, salt} \qquad (2)$$

with $\quad D_{core} = 1.64 + 3.65\rho_0 - 0.135a + 0.117c + 0.0391d - 0.295n_{-NRR'}$

where ρ_0 is the density, a, c, d and $n_{-NRR'}$ are the numbers of carbon, oxygen, nitrogen and –NRR′ groups in explosives; n'_{Al} and $n'_{NO_3\, salt}$ are two functions of the numbers of Al and nitrate salts, respectively.

For the detonation pressure P, he proposed a six-parameter linear equation with a maximum error of 16.9% obtained on a series of 22 explosives for which experimental values where available [32].

$$P = 221.53 - 20.437\, a - 2.2538\, b + 17.216\, c + 16.140\, d - 79.067\, C_{SSP} \\ - 66.335 n_N \qquad (3)$$

where CSSP is a specific structural parameter equal to 1 for explosives containing at least –N=N–, –O–NO$_2$, NH$_4$+ or N$_3$, and n_N is equal to $n_{NO_2}/2 + 1.5$ (in which n_{NO_2} is the number of nitro groups attached to carbon in compounds presenting $a = 1$).

More recently, Wang et al. [33] developed new models to predict detonation velocities of 54 nitrogen rich compounds based on quantum chemical descriptors with RMSE of 0.223 and 0.167 km s^{-1} for MLR and SVM (Support Vector Machine) models, respectively.

3.2 Brisance

In a recent work, Keshavarz et al. [34] proposed a first QSPR model to predict the brisance parameter which evaluates the effectiveness of explosives in military applications. It predicts the relative brisance with respect to TNT ($Bris_{relTNT}$) by the following equations with a RMSE of 10 and 11% for CHNO (Eq. 4) and CHNOAl explosives (Eq. 5), respectively.

$$Bris_{relTNT} = 85.5 + Bris_{core} - 35.96\, Bris^- + 19.69\, Bris^+ \qquad (4)$$

with $Bris_{core} = 4.812c + 2.556(d - a - b/2)$

$$Bris_{relTNT} = -42.87(d - a - b/2) + 146.71e \qquad (5)$$

where $Bris_{core}$ is the core brisance, calculated from the stoichiometric compositions in carbon, a, hydrogen, b, nitrogen, c, oxygen, d, and aluminum, e, and $Bris^+$ and $Bris^-$ are correcting factors: $Bris^+ = 1.0$ if energetic compound contains (CH$_2$ONO$_2$)$_n$ or C(CH$_2$ONO$_2$)$_n$ or (CH$_2$–NNO$_2$)$_n$ or (–HN–NO$_2$)$_n$ where n $\leq$ 4 and aromatic–N(NO$_2$)– and $Bris^- = 1.0$ for C(C=O)N, 2.0 for ONO$_2$ along with –COO–, 1.5 for more than one –COC– and 1.0 for a nitramine group.

3.3 Density

Only few QSPR models were developed for the prediction of density [35, 36] and energetic materials revealed to be the main fields of development of these models. Indeed, density is a key parameter influencing the detonation performances of explosives [37]. Early developments were proposed by Tarver in 1979 [38] based on group contributions for a database of 188 explosives and related compounds with an average error of 0.0191 g/cm^3 (i.e. 1.5%). More recently, Keshavarz et al. proposed a series of models for different families of energetic materials. The most recent one [39] is applicable to diverse nitro compounds including polynitroarenes, polynitroheteroarenes, nitroaliphatics, nitrate esters and nitramines (with a RMSE of of 2.2% on a database of 177 compounds).

$$\rho = 1.753 - 10.238\, n'_H + 9.908\, n'_H + 0.0992\, IMP - 0.0845\, DMP \tag{6}$$

where ρ is the crystal density, n'_H and n'_N are the number of hydrogen and nitrogen atoms of an energetic compound divided by its molecular weight and IMP and DMP are respectively increasing and decreasing correcting factors that depend on intermolecular interactions.

3.4 Heat of Formation

Even if heat of formation ΔH_f^0 is a property that can be accessed more directly through quantum chemical calculations [40–42], few QSPR models were proposed to predict it. In 1994, Sukhachev and Pivina [43] proposed two models based on a dataset of 59 non-aromatic nitro compounds with errors of 4.8 and 6.9 kcal/mol for Eqs. 7 and 8, respectively.

$$\Delta H_f^0 = -98.86 + 1.14\, SBE + 49.77\, ^4\kappa_r/N_{at} - 437.78\, C_{mid} + 61.76\, V_{mid}^2/N_{at}$$
$$+ 71.39\, Fr_1 - 195.44\, Fr_2 - 2933.25\, \ln(Fr_3)/N_{at} \tag{7}$$

$$\Delta H_f^0 = -22.24 - 11.73\, \ln S + 1.19\, SBE + 5.13\, ^6\kappa_r - 1.16\, E_q \tag{8}$$

where SBE is a calculated enthalpy of the hypothetic molecule without steric hindrance, $^4\kappa_r$ and $^6\kappa_r$ are the Randic indices of order 4 and 6, C_{mid} and V_{mid} are topological indices calculated from the weighed connectivity matrix, N_{at} is the number of atoms, Fr_1 is the sum of the minimum charges on the atoms in –C–C–NO$_2$ type fragments, Fr_2 is the minimum of all the minimum charges on atoms in of the X–X–N=O type fragments, where X is any atom, Fr_3 is the sum of maximum charges on atoms in all 5-atom linear chains with single bonds in the structure, S is the Van-der-Waals surface area of the atoms in the molecule and E_q is an electrotopologic index calculated from atomic charges in the molecules.

Keshavarz also studied heats of formation. In particular, he proposed a model to predict the condensed heat of formation $\Delta H_f(c)$ of nitramines, nitrate esters and nitroaliphatic energetic compounds [44], in Eq. 9, for a dataset of 79 compounds with RMSE of 29 kJ/mol.

$$\Delta H_f(c) = 9.344\,a - 9.055\,b + 23.12\,c - 15.79\,d + 51.49 \sum n_{DE}DE$$
$$- 52.00 \sum n_{IE}IE \tag{9}$$

where a, b, c and d are the stoichiometric composition in C, H, N and O, n_{DE} is the number of fragment that decreases $\Delta H_f(c)$ by a decreasing factor DE and n_{IE} is the number of fragment that decreases $\Delta H_f(c)$ by a decreasing factor IE.

3.5 Melting Point

Melting point T_m is a fundamental physical property of energetic materials involved in their chemical identification and purification and for the calculation of other physico-chemical properties like vapor pressures and solubilities. Once again, Keshavarz proposed a series of QSPR models within the last decade to predict the melting point of energetic materials [45–48]. The most recent one was developed on a dataset of 149 $C_xH_yN_vO_w$ compounds [45] with an average deviation of 5.9%.

$$T_m = 326.9 + 5.524\,T_{add} + 101.2\,T_{non-add} \tag{10}$$

with $\quad T_{add} = x - 0.5049\,y + 2.643\,v - 0.3838\,w \quad$ and $\quad T_{non\text{-}add} = T_{PC} - 0.6728T_{NC}$ where T_{PC} and T_{NC} are contributions related to some specific polar groups and molecular fragments, respectively.

More recently, Wang et al. [49] proposed new models focused on 60 carbocyclic nitroaromatic compounds. From a set of 1664 diverse molecular descriptors calculated from Dragon software [17], two models were obtained based on multilinear regression and artificial neural network. The MLR model consisted in a six-parameter equation (Eq. 11) and presented 3.98% in average error, evaluated in external validation.

$$T_m = -2.934\,D/Dr09 + 96.596\,EEig02\,x - 81.239\,or13\,u - 309.272\,Mor29v$$
$$+ 181.589\,Mor32\,v + 87.320\,C - 040 + 13.495$$

$$\tag{11}$$

where $D/Dr09$ is the distance/detour ring index of order 9, $EEig02x$ is the Eigenvalue 02 from the edge adjacency matrix weighted by edge degrees, $Mor13u$ is the 3D-MoRSE—signal 13/unweighted, $Mor29v$ is the 3D-MoRSE—signal

Table 1 Validation of the models of Wang et al. [49]

	MLR	ANN
R^2	0.781	0.853
R^2_{adj}	0.776	–
S (°C)	23.80	19.74
AARD (training set) (%)	5.31	4.42
F	37.87	–
Q^2_{LOO}	0.768	0.843
Q^2_{LMO}	0.759	0.843
R^2_{rand} intercept	−0.028	–
AARD (test set) (%)	3.98	3.82

R^2_{adj} adjusted R^2; s standard error; *AARD* average absolute relative error; *F* fisher coefficient; Q^2_{LOO} and Q^2_{LMO} coefficients issued from leave-one-out and leave-many-out cross-validation

29/weighted by atomic van der Waals volumes, *Mor32v* is the 3D-MoRSE—signal 32/weighted by atomic van der Waals volumes and *C-040* is the atom-centered fragments R–C(=X)–X/R–C#X/X=C=X groups in the molecule.

The ANN model was computed based on the same six descriptors and achieved slightly better predictivity with an average error of 3.82% in external validation.

It has to be noticed that these models are fully validated with application of internal and external validation methods, as summarized in Table 1, and with the determination of their applicability domain from William's plots [50].

3.6 Sensitivity

Sensitivity is a critical property to ensure the safe handling of energetic materials. Various experimental protocols have been proposed from years to evaluate the sensitivity under various stimuli: impact, heat, friction or electric discharge.

Among them, the most widely considered for the development of predictive methods is impact sensitivity since it is a standard test performed within regulatory frameworks like the Transport of Dangerous Goods [51]. Over the years, numerous models were proposed, as reviewed in Ref. [27]. Among them, INERIS developed a series of models for nitrocompounds that will be detailed later.

Keshavarz et al. also developed various simple predictive models [52–58], mostly based on stoichiometric composition with correcting factors related to specific molecular fragments. For instance, the model for nitroheteroarenes (that presented a RMSE on $h_{50\%}$ of 24 cm) is presented in Eq. 12.

$$\log h_{50\%} = \left(52.13\,a + 31.80\,b + 117.6 \sum SSP_i\right)/MW \qquad (12)$$

where $h_{50\%}$ is the impact sensitivity, a and b are the carbon and hydrogen compositions, SSP_i are structural correcting factors and MW is the molecular weight.

More complex models were also proposed like the ones of Xu et al. [59] based on 3-dimensional descriptors for a set of 156 nitro compounds (127 in the training set and 29 in the validation set) with errors of 0.177 and 0.130 (log) in standard deviation for their MLR and ANN models, respectively.

Few models were also developed for other stimuli but with lower success. Bénazet et al. [60] proposed, to our knowledge, the only QSPR model calculating the friction sensitivity index (FSI).

$$FSI = 125.721 + 220.69\,(MEP > 0)^2 + 1.18402(intermol\_NN - 5)^2 \\ + 725805(12.5 - intermolO/gpNRJ)^2 \tag{13}$$

where $MEP > 0$ is the positive medium electrostatic potential, intermol_NN is the number of intermolecular interactions in the neighborhood of the atom bearing the energetic group and intermolO/gpNRJ is the average number of intermolecular interactions in the neighborhood of the energetic group's terminal atoms.

Concerning electric spark sensitivity (E_{ES}), several models can be cited even if further research could keep encouraged to access better performances based notably on larger datasets. Indeed, based on a dataset of 26 nitro compounds, Fayet et al. [61] developed a four parameter MLR model with a correlation coefficient R^2 of 0.90 but the data set was not large enough to perform any external validation.

$$E_{ES} = 26.9\,n_{single} + 63.3\,N_{C,max} + 168.4\,Q_{C,min} - 27.8\,V_{C,min} + 99.4 \tag{14}$$

where n_{single} is the relative number of single bonds and $N_{C,max}$, $Q_{C,min}$ and $V_{C,min}$ are the maximum nucleophilic reactivity index, the minimum partial charge and the minimum valence for a C atom, respectively.

Keshavarz [62] also proposed a model only based on constitutional descriptors with a correlation coefficient $R^2 = 0.77$ (for a training set of 17 nitroaromatic compounds) and with a maximum error of 4.58 J observed over a test set of 14 other compounds.

$$E_{ES} = 4.60 - 0.7333\,n_C + 0.724\,n_O + 9.16\,R_{nH/nO} - 5.14\,C_{R,OR} \tag{15}$$

where n_C and n_O are the number of carbon and oxygen respectively, $R_{nH/nO}$ is the ratio of hydrogen atoms to oxygen ones and $C_{R,OR}$ characterizes the presence of alkyl (–R) or alkoxy (–OR) groups attached to an aromatic ring.

More recently, Wang et al. [63] proposed a SVM model with very high exhibited performances ($R^2 = 0.999$ and RMSE = 0.299 J in prediction), even if the performances of this model need to be confirmed on a larger set, since it has been developed on only 18 molecules and validated on only 11 compounds.

3.7 Thermal Stability

Decomposition temperatures and heats are pre-selection criteria for the classification of explosive compounds within regulatory framework. In particular, full characterization of explosive properties is not performed if the exothermic decomposition energy ($-\Delta H_{dec}$) is less than 500 J/g or if the onset of exothermic decomposition (T_o) is 500 °C or above. For these properties, first QSPR type models were proposed in 2003 by Saraf [64] based on a small data set of 22 nitroaromatic compounds without any possible external validation. Then, several models [15, 65–69] were developed for these properties, as reviewed in [27]. For instance, the best model obtained by Fayet et al. [67] to predict the heat of decomposition (in kcal/mol) consisted in a MLR model (Eq. 16) constituted of four descriptors calculated by Codessa software [16] with a predictive power R^2_{ext} of 0.84 validated on an external validation set.

$$-\Delta H_{dec} = 0.8\,G - 3.8\,WPSA1 - 4255.1\,Q_{max} + 26.8\,RPCS - 251.2 \qquad (16)$$

where G is the gravitational index, $WPSA1$ is the weighted positive surface area, Q_{max} is the maximal partial charge and $RPCS$ is the relative positively charged surface area.

This model is specifically focused on non-ortho-substituted nitrobenzene derivatives taking into account the fact that ortho-substituted ones can decompose following particular decomposition mechanisms (as illustrated in Fig. 5) as evidenced in a previous DFT study [70].
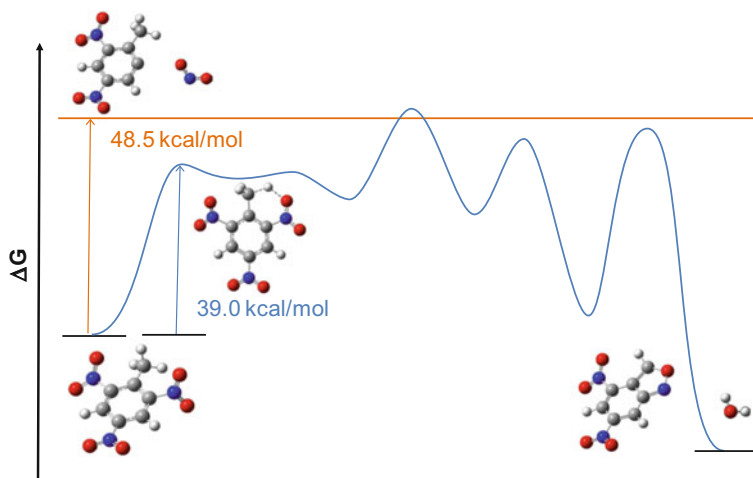
Fig. 5 Main decomposition mechanisms of TNT calculated at PBE0/6−31+G(d,p) level

4 Case Study: QSPR Models to Predict the Impact Sensitivity of Nitro Compounds

In the last decade, we developed several QSPR models for the explosive properties of nitro compounds including their impact sensitivities. In 2012, we investigated, in particular, a data set of 161 nitrocompounds (nitroaromatics, nitroaliphatics and nitramines) [71]. Within this work, if no highly predictive models were obtained for this whole applicability domain, two good local models were accessed when focusing on nitroaliphatics and nitramines, respectively.

The model for nitroaliphatics was developed on a training set of 34 molecules. More than 300 molecular descriptors (constitutional, topological, geometric and quantum chemical) were calculated by Codessa [16] based on structures optimized from DFT calculations at PBE0/6−31+G(d,p) level with Gaussian03 software [72]. From the Best Multi Linear Regression approach of Codessa, a stepwise method for the selection of descriptors in MLR models, the four-parameter equation (in Eq. 17) was selected to be the best model.

$$\log h_{50\%} = -0.438 - 0.018\,OB + 4.07\,P + 28.5\,Q^2_{NO_2,max} + 4.79\,N_{O,max} \qquad (17)$$

where $h_{50\%}$ is the impact sensitivity in cm, OB is the oxygen balance as defined in the TDG regulation [51], P is the polarity parameter defined as the difference between the maximum and minimum atomic charges, $Q_{NO_2,max}$ is the maximum charge for a NO_2 group and $N_{O,max}$ is the maximum nucleophilic reactivity index for a O atom.

This model was well correlated ($R^2 = 0.93$) and validated internally by cross validation (with a good Q^2_{LOO} of 0.90) and Y-randomization (with a low R^2_{YS} of 0.12). It was also externally validated using a validation set of 16 molecules with $R^2_{in} = 0.88$ in its applicability domain, as shown in Fig. 6.

Fig. 6 Predictive capabilities of Eq. 17 to predict the impact sensitivity of nitroaliphatics
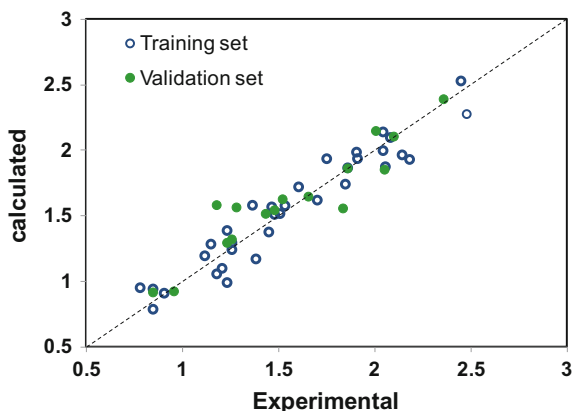
The model obtained for nitramines, in Eq. 18, was also a four-parameter equation (from a training set of 40 compounds).

$$\log h_{50\%} = -0.42 - 0.017\,OB + 0.06\,T_1^E + 50.1\,N_{O,avg} + 27.6\,N_{N,avg} \qquad (18)$$

where T_1^E is the topological electronic index, $N_{O,avg}$ and $N_{N,avg}$ is the average nucleophilic reactivity indices for a O and a N atom, respectively.

This model was also well correlated ($R^2 = 0.92$) and validated internally by cross validation (with a good Q_{LOO}^2 of 0.89) and Y-randomization (with a low R_{YS}^2 of 0.10). It was also externally validated using a validation set of 20 molecules with $R_{in}^2 = 0.85$ in its applicability domain.

As these models required quantum chemical calculations, we also looked at simpler models based on constitutional descriptors that can be derived from the only knowledge of the 2D structure of molecules. From the same databases, the two following models were obtained: Eq. 19 for nitroaliphatics [73] and Eq. 20 for nitramines [74].

$$\log h_{50\%} = 0.94 + 86.3\,\frac{n_{C=O}}{MW} - 0.017\,OB + 0.14\,n_{C-O-C} - 0.21\,n_{C=O} \qquad (19)$$

where $n_{C=O}$ and n_{C-O-C} is the numbers of C=O of C–O–C fragments and MW is the molecular weight.

$$\log h_{50\%} = 1.94 - 2.53\,n_{N,rel} + 0.07\,n_{single} + 50.1\,n_{NO_2} \qquad (20)$$

where $n_{N,rel}$ is the relative number of N atoms, n_{single} is the number of single bonds and n_{NO2} is the number of nitro groups.

If these models reached slightly lower performances than the ones using quantum chemical descriptors (as presented in Table 2), they presented the advantage to be easier and quicker to use.

Table 2 Performances of QSPR models to predict the impact sensitivity of nitroaliphatics and nitramines

		R^2	Q_{LOO}^2	R_{YS}^2	R_{in}^2
Nitroaliphatics					
QC	(Eq. 17)	0.93	0.90	0.12	0.88
Simple	(Eq. 19)	0.88	0.85	0.09	0.78
Nitramines					
QC	(Eq. 18)	0.92	0.89	0.10	0.85
Simple	(Eq. 20)	0.88	0.83	0.10	0.88

5 How to Use of QSPR Models for Energetic Materials

QSPR models allow estimating of properties of substances from the only knowledge of their molecular structure. So, they nowadays find different potential applications for energetic materials. Indeed, predictions can be useful for several reasons. At first, they can be cheaper and faster than experiment considering the need of purchasing, transport and handling hazardous substances. Moreover, they can reduce testing for toxic compounds that are hazardous for operators during the tests. In this last section, two modes of utilizations of QSPR are detailed as they can be particularly interesting in the context of energetic materials.

5.1 Use of QSPR Models in Regulatory Context

Regulatory compliance is a key problem in the framework of energetic materials since they represent by nature hazardous substances. Different regulations can be involved upon their applications (e.g. military, automotive, and aerospace). One can cite the Transport of Dangerous Goods (TDG) [51], the Globally Harmonised System of Classification and Labelling of Chemicals (GHS) [75] or the European regulation related to Registration, Evaluation, Authorisation and Restriction of Chemicals (REACH) [76].

So, a possible use of QSPR models is the prediction of properties of a target chemical for regulatory purpose. Indeed, quantitative structure-property relationships are identified as relevant alternative method to experimental testing in the REACH regulation. In particular, Annex XI states that "*Results obtained from valid qualitative or quantitative structure-activity relationship models ((Q) SARs) may indicate the presence or absence of a certain dangerous property*". This statement has been taken into account in the guidance document related to the use of grouping and QSARs in REACH [77] that details their opportunities of uses:

– providing information in priority setting procedures;
– guiding experimental testing strategies;
– improving the evaluation of existing test data;
– providing mechanistic insights, for example, to support grouping;
– filling data gaps for hazard and risk assessment, for classification and labelling or for PBT or vPvB assessment.

Up to now the use of QSPR models (or QSAR models for toxicological hazards) remain marginally used for regulatory purpose. Nevertheless, some tools were proposed to favor them by demonstrating the relevance of data obtained from QSPR models. The most recent models are nowadays more likely validated following OECD principles than the early ones.

To allow application for regulatory purpose, the model and its conditions of use may be checked. At first, the model has to fit with the five OECD validation

Table 3 (Q)SAR model reporting format

1. (Q)SAR identifier
(Q)SAR identifier (title); other related models; software coding the model
2. General information
Date of QMRF; author(s) and contact details; update(s); model developer(s) and contact details; date of model development and/or publication; reference(s) to main scientific papers and/or software package; availability of information about the model; availability of another QMRF for exactly the same model
3. Defining the endpoint (OECD principle 1)
Category definition and justification; data matrix; endpoint units; dependent variable; experimental protocol; endpoint data quality and variability
4. Defining the algorithm (OECD principle 2)
Type of model; explicit algorithm; descriptors in the model; descriptor selection; algorithm and software name and version for descriptor generation; descriptors/chemicals ratio
5. Defining the applicability domain (OECD principle 3)
Description of the applicability domain of the model; method used to assess the applicability domain; software name and version for applicability domain assessment; limits of applicability
6. Defining goodness-of-fit and robustness (OECD principle 4)
Availability and available information for the training set; pre-processing of data before modelling; statistics for goodness-of-fit; robustness—statistics obtained by leave-one-out cross-validation, by leave-many-out cross-validation, by Y-scrambling, by bootstrap and/or by other methods
7. Defining predictivity (OECD principle 4)
Availability and available information for the test set; Experimental design of test set; predictivity—statistics obtained by external validation; Predictivity - assessment of the test set; comments on the external validation of the model
8. Providing a mechanistic interpretation (OECD principle 5)
Mechanistic basis of the model; a priori or a posteriori mechanistic interpretation; other information about the mechanistic interpretation
9. Miscellaneous information
Comments; bibliography; supporting information

principles [19] presented in Sect. 2. To demonstrate the validation of models, QSAR Model Reporting Format files (QMRF) were set up. These QMRF files contain all information needed to demonstrate that the QSPR model fulfill all requirements, as shown in Table 3. These files are in particular used by committee experts to evaluate the quality of models. By this way, sort of validated models and their associated QMRF files are registered after expert evaluation in the online QSAR database of the Joint Research Center [78]. The OECD/ECHA QSAR Toolbox [12], a free prediction platform available online in which QSAR and

Table 4 Performances of QSPR model to predict the impact sensitivity of nitroaliphatics

Training set		Cross validation			Y-randomization	
R^2	RMSE	Q^2_{LOO}	Q^2_{10CV}	Q^2_{5CV}	R^2_{YS}	SD_{YS}
0.88	0.17	0.85	0.84	0.85	0.09	0.07
Validation set						
R^2_{EXT}	$RMSE_{EXT}$	Q^2_{F1}	Q^2_{F2}	Q^2_{F3}	CCC	
0.81	0.22	0.81	0.81	0.83	0.93	

QSPR models are implemented after acceptance by an expert comity on the scientific validity of the model and the technical feasibility of its implementation in the platform.

In particular, the QSAR Toolbox contains now one model dedicated to the impact sensitivity of nitroaliphatic compounds [73]. This model, presented earlier in Eq. 19, complies with the five OECD principles. Indeed, it is dedicated to the impact sensitivity which is required among explosive properties to classify substances among explosive compounds (principle 1). It consists in an unambiguous three-parameter model based on constitutional descriptors presented in Eq. 19 (principle 2). Its applicability domain was defined as limited to nitroaliphatic compounds presenting impact sensitivity between 6 and 300 cm, a relative number of nitrogen between 0.118 and 0.250, between 11 and 44 single bonds and between 2 and 12 nitro groups (Principle 3). Its performances were assessed by a series of internal and external validation methods as summarized in Table 4 (principle 4).

At last, in this model, the occurrence of NO_2 relates to the primary cleavage of the $C–NO_2$ bond which is known to be the main mechanism of decomposition of nitroaliphatic compounds [79] (principle 5).

As this model was simple enough to be easily implemented, it was accepted by the expert committee and implemented into version 3.3 of the QSAR Toolbox [12] in December 2014.

In addition to the validation of the model, the correct and relevant use of the QSPR model has also to be demonstrated by the final user. To this aim, a QSAR prediction reporting format (QPRF) file was proposed as a complement to the QMRF file. This file summarizes all information needed to demonstrate that the prediction has been performed properly, i.e. that the model has been well chosen and used, as shown in Table 5.

5.2 Use of QSPR Models for the Design of New Energetic Materials

The development of energetic materials can be costly and time-expensive. In particular, this class of materials present particular constraints related to their energetic

Table 5 (Q)SAR Prediction Reporting Formal

1. Substance
CAS and/or EC number; chemical name; structural formula; structural codes (e.g. SMILES, InChI)
2. General information
Date of QPRF; author(s) and contact details
3. Prediction
3.1. Endpoint (OECD Principle 1)
Endpoint; dependant variable
3.2. Algorithm (OECD Principle 2)
Model or submodel name; version; reference to QMRF; predicted value (model result and comments); input for prediction; descriptors values
3.3. Applicability domain (OECD Principle 3)
Domains (in descriptors, structural fragments, mechanism); structural analogues
3.4. Uncertainty of the prediction (OECD Principle 4)
If possible, comment on the uncertainty of the prediction for this chemical, taking into account relevant information (e.g. variability of the experimental results)
3.5. Chemical and biological mechanisms according to the model underpinning the predicted result (OECD Principle 5)
Discuss the mechanistic interpretation of the model prediction for this specific chemical
4. Adequacy (Optional)
Regulatory purpose; approach for regulatory interpretation of the model result; outcome; conclusion

potential. Indeed, they required particular attention during handling and testings. Moreover, to perform some tests (including regulatory tests for safety issues), they have to be transported, requiring specific procedures according to strict practical and regulatory constraints. So, the access of first estimation of properties could be of great benefit during the development of energetic materials to investigate larger ranges of possible compounds and to reduce time to market by eliminating at the earliest steps of development irrelevant candidates.

Figure 7 illustrates how QSPR models can be used to guide the design of energetic materials taking into account safety issues in the earliest steps of the decision making process, even when substances are not already available, purchased or even before their synthesis. In that context, predictions can help to select a reduced set of candidates that will be further studied by performing synthesis and experimental characterizations.

Such approach is a common computer aided molecular design (CAMD) procedure used in pharmaceutical research to discover new drugs [80]. A dataset of possible chemical structures can be gathered from supplier catalogues or from internal databases of compounds. For instance, commercial and open-source databases of drug like structures have been also widely developed [81]. Similar
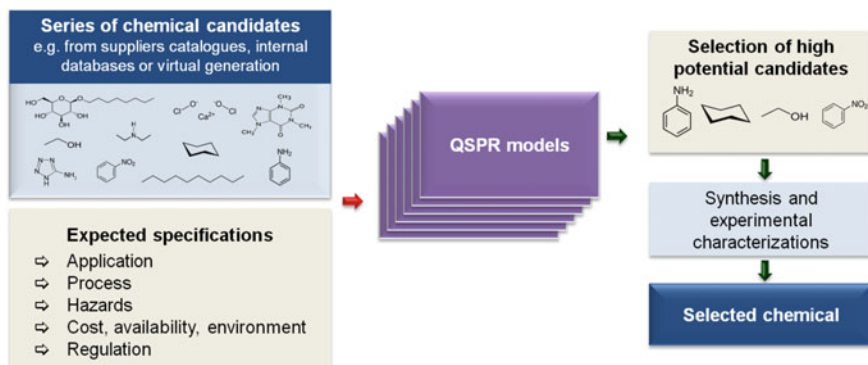
Fig. 7 Use of QSPR models as screening tools

strategies of data collection could be considered for energetic materials in the future.

Such dataset of molecular structures can also be obtained virtually by automatic computer tools. Such approach allows accessing to new innovative molecular structures that have not been already investigated. The virtual library of chemical structures is generated within a defined chemical space using different possible methods. A first one is based on the definition and combination of possible structural units and constraints. Such approach was notably proposed by Gani et al. [82], by using the group contributions involved in the group contribution methods to predict various kinds of properties (e.g. octanol/water partition coefficient, boiling point, surface tension) as the structural units used for the structure generation. Similarly, Weis et al. [83] used signature molecular descriptors both as building blocks to generate molecular structures and as molecular descriptors in the QSPR models for the prediction of properties in the solvent selection step. Another way to generate a virtual library consists in generating chemical structures by virtual reactions from selected initial molecules of interest. For instance, Moity et al. [84] used a tool called GRASS that associates bio-building blocks with co-reactants to generate new bio-based molecules. Once again such approaches could be adapted to energetic materials.

The obtained library of (existing or virtual) molecular structures is then screened for a series of expected specifications that can be related to:

- applications, like detonation properties;
- process constraints, like boiling point or melting point in agreement with specific conditions of process;
- hazards, like toxicity, flammability and explosivity;
- economic and environmental costs;
- regulations (e.g. TDG or REACH).

If all specifications are not related to the chemical structures of products, like economic costs, QSPR models can help to obtain at least a first estimation for a

large part of application, process and hazardous properties to screen the generated chemical structures and identify the best candidates for the target application.

Within screening processes, QSPR models with different levels of predictive powers can be used depending on the considered property and the expected level of screening. A first screening step can, for example, be very fast from the less predictive model to eliminate the largest part of non relevant alternatives before further analysis on the most promising candidates based on more time-consuming and/or less automated models. Of course, complementary approaches can be introduced to estimate properties like quantum chemical calculations (e.g. for ΔH_f) or equations of state or molecular modeling (e.g. for fluid properties).

6 Conclusions and Challenges

Energetic materials represent a field of applications in which predictive methods can efficiently help the development of innovative solutions. In particular, numerous quantitative structure-property relationships were developed in recent years and can now be used for energetic materials to estimate a large set of properties (detonation, brisance…) only based on their molecular structures. Such predictions can be useful when experimental values are not available for risk assessments of products and processes, for regulatory purposes, for substitution purposes but also to anticipate their properties in early steps of their design even before synthesis.

QSPR models are complementary to other computational approaches like density functional theory used not only to calculate molecular descriptors related to the geometric and electronic structure of energetic materials but also to clarify the reaction mechanisms involved in their decomposition.

If numerous models were developed for various properties of energetic materials, challenges remain.

- Existing models dedicated to energetic materials mainly focus on the most classical nitro compounds (like nitroaromatics or nitramines). But research on energetic materials investigates a larger diversity of compounds, including for instance high nitrogen content energetic materials [85].
- Among new energetic materials, energetic salts [86] represent a particular family of compounds for which specific models are needed due to their specific structure, constituted by an anion and a cation, as in ionic liquids for which QSPR models have been already developed [87–89].
- In final applications, energetic materials are in general constituted of several compounds. If first models were proposed in the literature [90] for the flash point of binary mixtures [91], QSPR models may be also developed for the properties of mixtures in the energetic material compositions.
- Models remain to be developed for some of the properties required in applications of energetic materials such as the burning rate.

- At last, even for existing models, further improvements can be done by considering larger and more robust datasets since most of the models were developed on only small datasets. Some properties present also some difficulties to overcome, notably for solid state properties.

Finally, to reach more diverse, predictive and relevant models, complementarity with experiments remains requested to compile accurate and large enough databases for the development and validation of the QSPR models and for the better understanding of underpinning mechanisms.

References

1. Urbanski T (1984) Chemistry and technology of explosives, vol 4. Pergamon Press
2. Sikder AK, Maddala G, Agrawal JP, Singh H (2001) J Hazard Mater 84:1
3. Shanley ES, Melhem GA (2000) J Loss Prevent Proc Ind 13:67
4. Benson SW (1976) Thermochemical kinetics, 2nd edn. Wiley, New York
5. Toghiani RK, Toghiani H, Maloney SW, Boddu VM (2008) Fluid Phase Equil 264:86
6. Roncaglioni A, Benfenati E (2008) Chem Soc Rev 37:441
7. Kavlock RJ, Ankley G, Blancato J, Breen M, Conolly R, Dix D, Houck K, Hubal E, Judson R, Rabinowitz J, Richard A, Setzer RW, Shah I, Villeneuve D, Weber E (2008) Toxicol Sci 103:14
8. Netzeva TI, Pavan M, Worth AP (2008) QSAR Comb Sci 27:77
9. Dearden JC, Rotureau P, Fayet G (2013) SAR QSAR Environ Res 24:545
10. Katritzky AR, Kuanar M, Slavov S, Hall CD, Karelson M, Kahn I, Dobchev DA (2010) Chem Rev 110:5714
11. Commission Regulation (EC) N° 761/2009 of 23 July 2009 amending, for the purpose of its adaptation to technical progress, Regulation (EC) N° 440/2008 laying down test methods pursuant to Regulation (EC) N° 1907/2006 of the European Parliament and of the Council on the Registration, Evaluation, Authorisation and Restriction of Chemicals (REACH)
12. OECD/ECHA (2015) QSAR Toolbox, version 3.3.5. http://www.qsartoolbox.org/. Accessed 24 Oct 2015
13. Todeschini R, Consonni V (2000) Handbook of molecular descriptors. Wiley, Weinheim
14. Karelson M (2000) Molecular descriptors in QSAR/QSPR. Wiley, New York
15. Fayet G, Del Rio A, Rotureau P, Joubert L, Adamo C (2011) Mol Inform 30:623
16. CodessaPro (2002) University of Florida
17. Dragon 6 (2013) http://www.talete.mi.it/products/dragon_description.htm. Accessed 30 Oct 2015
18. Shahlaei M (2013) Chem Rev 113:8093
19. OECD (2007) Guidance document on the validation of (quantitative) structure-activity relationships [(Q)SAR] models. Organisation for Economic Co-operation and Development (OECD)
20. Rücker C, Rücker G, Meringer M (2007) J Chem Inf Model 47:2345
21. Tropsha A, Gramatica P, Gombar KV (2003) QSAR Comb Sci 22:69
22. Schüürmann G, Ebert RU, Chen J, Wang B, Kühne R (2008) J Chem Inf Model 48:2140
23. Consonni V, Ballabio D, Todeschini R (2009) J Chem Inf Model 49:1669
24. Chirico N, Gramatica P (2011) J Chem Inf Model 51:2320
25. Roy K, Mitra I, Kar S, Ojha PK, Das RN, Kabir H (2012) J Chem Inf Model 52:396
26. Le T, Epa VC, Burden FR, Winkler DA (2012) Chem Rev 112:2889

27. Nieto-Draghi C, Fayet G, Creton B, Rozanska X, Rotureau P, De Hemptinne J-C, Ungerer P, Rousseau B, Adamo C (2015) Chem Rev 115:13093
28. Quintero FA, Patel SJ, Munoz F, Mannan MS (2012) Ind Eng Chem Res 51:16101
29. EPA (2012) Estimation programs interface suite. United States Environmental Protection Agency, Washington (USA)
30. Chakka S, Boddu VM, Maloney SW, Damavarapu R (2010) Prediction of physicochemical properties of energetic materials via EPI suite. In: Boddu V, Redner P (eds) Energetic materials—thermophysical properties, predictions, and experimental measurements. CRC Press, Boca Raton, pp 77–92
31. Keshavarz MH (2009) J Hazard Mater 166:762
32. Keshavarz MH (2007) Indian J Eng Mater Sci 14:77
33. Wang D, He G, Chen H (2014) Russ J Phys Chem A 88:2363
34. Keshavarz MH, Seif F, Soury H (2014) Propel Explos Pyrotech 39:284
35. Lyman WJ, Reehl WF, Rosenblatt DH (eds) (1990) Handbook of chemical property estimation methods. American Chemical Society, Washington
36. Reinhard M, Drefahl A (1999) Estimating physicochemical properties of organic compounds. Wiley, New York
37. Sil'vestrov VV (2006) Combust Explos Shock Waves 42:472
38. Tarver CM (1979) J Chem Eng Data 24:136
39. Keshavarz M, Soury H, Motamedoshariati H, Dashtizadeh A (2015) Struct Chem 26:455
40. Mathieu D, Simonetti P (2002) Thermochim Acta 384:369
41. Stevanović V, Lany S, Zhang X, Zunger A (2012) Phys Rev B 85:115104
42. Jaidann M, Roy S, Abou-Rachid H, Lussier L-S (2010) J Hazard Mater 176:165
43. Sukhachev DV, Pivina TS, Volk FS (1994) Propel Explos Pyrotech 19:159
44. Keshavarz MH, Sadeghi H (2009) J Hazard Mater 171:140
45. Keshavarz MH, Gharagheizi F, Pouretedal HR (2011) Fluid Phase Equil 308:114
46. Alamdari RF, Keshavarz MH (2010) Fluid Phase Equil 292:1
47. Keshavarz MH (2009) J Hazard Mater 171:786
48. Keshavarz MH (2006) J Hazard Mater 138:448
49. Wang D, Yuan Y, Duan S, Liu R, Gu S, Zhao S, Liu L, Xu J (2015) Chemometr Intell Lab 143:7
50. Atkinson AC (1985) Plots, transformations and regression—an introduction to graphical methods of diagnostic regression analysis. Oxford Science Publications
51. UN (2011) Recommandations on the transport of dangerous goods: manual of tests and criteria, 5th edn.
52. Keshavarz MH (2010) Propel Explos Pyrotech 35:181
53. Lai WP, Lian P, Wang BZ, Ge ZX (2010) J Energ Mater 28:45
54. Keshavarz MH, Zali A, Shokrolahi A (2009) J Hazard Mater 166:1115
55. Keshavarz MH, Pouretedal HR, Semnani A (2007) J Hazard Mater 141:803
56. Keshavarz MH (2007) J Hazard Mater 148:648
57. Keshavarz MH, Jaafari M (2006) Propel Explos Pyrotech 31:216
58. Keshavarz MH, Pouretedal HR (2005) J Hazard Mater 124:27
59. Xu J, Zhu L, Fang D, Wang L, Xiao S, Liu L, Xu W (2012) J Mol Graph Model 36:10
60. Bénazet S, Jacob G, Pèpe G (2009) Propel Explos Pyrotech 34:120
61. Fayet G, Rotureau P, Joubert L, Adamo C (2010) Process Saf Prog 29:359
62. Keshavarz MH (2008) J Hazard Mater 153
63. Wang R, Sun L, Kang Q, Li Z (2013) J Loss Prevent Proc Ind 26:1193
64. Saraf SR, Rogers WJ, Mannan MS (2003) J Hazard Mater 98:15
65. Theerlynck E, Mathieu D, Simonetti P (2005) Thermochim Acta 426:123
66. Prana V, Rotureau P, Fayet G, André D, Hub S, Vicot P, Rao L, Adamo C (2014) J Hazard Mater 276:216
67. Fayet G, Rotureau P, Joubert L, Adamo C (2011) J Mol Model 17:2443
68. Fayet G, Rotureau P, Adamo C (2013) J Loss Prevent Proc Ind 26:1100
69. Li J, Liu H, Huo X, Gramatica P (2013) Mol Inform 32:193

70. Fayet G, Joubert L, Rotureau P, Adamo C (2009) J Phys Chem A 113:13621
71. Fayet G, Rotureau P, Prana V, Adamo C (2012) Process Saf Prog 31:291
72. Frisch MJ, Trucks GW, Schlegel HB, Scuseria GE, Robb MA, Cheeseman JR, Montgomery JA Jr, Vreven T, Kudin KN, Burant JC, Millam JM, Iyengar SS, Tomasi J, Barone V, Mennucci B, Cossi M, Scalmani G, Rega N, Petersson GA, Nakatsuji H, Hada M, Ehara M, Toyota K, Fukuda R, Hasegawa J, Ishida M, Nakajima T, Honda Y, Kitao O, Nakai H, Klene M, Li X, Knox JE, Hratchian HP, Cross JB, Bakken V, Adamo C, Jaramillo J, Gomperts R, Stratmann RE, Yazyev O, Austin AJ, Cammi R, Pomelli C, Ochterski JW, Ayala PY, Morokuma K, Voth GA, Salvador P, Dannenberg JJ, Zakrzewski VG, Dapprich S, Daniels AD, Strain MC, Farkas O, Malick DK, Rabuck AD, Raghavachari K, Foresman JB, Ortiz JV, Cui Q, Baboul AG, Clifford S, Cioslowski J, Stefanov BB, Liu G, Liashenko A, Piskorz P, Komaromi I, Martin RL, Fox DJ, Keith T, Al-Laham MA, Peng CY, Nanayakkara A, Challacombe M, Gill PMW, Johnson B, Chen W, Wong MW, Gonzalez C, Pople JA (2004) Gaussian03. Gaussian Inc., Wallington CT
73. Prana V, Fayet G, Rotureau P, Adamo C (2012) J Hazard Mater 235–236:169
74. Fayet G, Rotureau P (2014) J Loss Prevent Proc Ind 30:1
75. UN (2009) Globally harmonized system of classification and labelling of chemicals (GHS), 3rd edn. ST/SG/AC.A10/30/Rev.3
76. Regulation (EC) N° 1907/2006 of the European Parliament and of the Council of 18 December 2006 concerning the Registration, Evaluation, Authorisation and Restriction of Chemicals (REACH)
77. ECHA (2008) Guidance Document on information requirements and chemical safety assessment, Chapter R.6: QSARs and grouping of chemicals. European Chemicals Agency (ECHA)
78. JRC (2015) (Q)SAR Model Reporting Format (QMRF) Inventory. http://qsardb.jrc.ec.europa.eu/qmrf/. Accessed 22 Oct 2015
79. Nazin GM, Manelis GB (1994) Russ Chem Rev 63:313
80. Gasteiger J, Engel T (2003) Chemoinformatics—a textbook. Wiley, Weinheim
81. Oprea TI, Tropsha A (2006) Drug Discov Today Tech 3:357
82. Harper PM, Gani R, Kolar P, Ishikawa T (1999) Fluid Phase Equil 158–160:337
83. Weis DC, Visco DP (2010) Comput Chem Eng 34:1018
84. Moity L, Molinier V, Benazzouz A, Barone R, Marion P, Aubry J-M (2014) Green Chem 16:146
85. Klapötke TM (2007) High energy density materials. Springer
86. Gao H, Shreeve JNM (2011) Chem Rev 111:7377
87. Diallo AO, Fayet G, Len C, Marlair G (2012) Ind Eng Chem Res 51:3149
88. Katritzky AR, Jain R, Lomaka A, Petrukhin R, Karelson M, Visser AE, Rogers RD (2002) J Chem Inf Comput Sci 42:225
89. Billard I, Marcou G, Ouadi A, Varnek A (2011) J Phys Chem B 115:93
90. Muratov EN, Varlamova EV, Artemenko AG, Polishchuk PG, Kuz'min VE (2012) Mol Inform 31:202
91. Gaudin T, Rotureau P, Fayet G (2015) Ind Eng Chem Res 54:6596

Energetic Polymers: Synthesis and Applications

Alexander J. Paraskos

Abstract Energetic polymeric materials typically consist of both a hydrocarbon-based fuel component as well as one or more oxidizing "explosophore" components. The use of energetic rather than fuel-rich polymers is theoretically advantageous in explosive and propellant applications as they contribute high temperature and pressure characteristics to the resulting formulations, produce less smoke (soot) and do not require the incorporation of large amounts of solid oxidizers such as ammonium perchlorate (AP), ammonium nitrate (AN) or ammonium dinitramide (ADN) in order to achieve effective combustion. The most commonly used energetic polymer, nitrocellulose (NC), is also one of the first known energetic polymers; it has been successfully utilized for decades in both rocket and gun-propellant applications. The chemistry and uses of NC have been reviewed extensively in the past. Therefore, this chapter will focus on more recent investigations and the development of modern energetic polymers, including oxirane-derived and oxetane-derived materials, energetic thermoplastic elastomers (ETPE's) as well as several other new classes of energetic polymers.

Keywords Energetic polymers · Energetic thermoplastic elastomers (ETPE's)

1 Introduction

Binders are necessary components of most commonly-used solid-phase (i.e. non-meltable) military explosives, smokeless powders, rocket propellants, and gun propellants, providing both structural integrity and moisture resistance to the resulting formulations. Inert polymeric binders assume many different forms, from simple natural waxes in the case of polymer-bonded explosive formulations [1] to more complex polymeric materials such as chemically cross-linked urethane and

A.J. Paraskos (✉)
US Army Armament Research Development and Engineering Center,
Picatinny Arsenal, NJ 07806, USA
e-mail: alexander.j.paraskos.civ@mail.mil

epoxy-cured binders based on synthetic polymers such as hydroxyl-terminated polybutadiene (HTPB), which has been used in both in cast-cure explosive [2] and rocket-propellant [3] applications. Historically, these materials consisted of under-oxidized polymers which acted essentially as fuels during combustion, necessitating that significant amounts of oxidizer such as AP be added to the overall formulation to realize efficient combustion. Energetic polymers have played an integral role in the development of propellants and explosives ever since the discovery of nitrocellulose (NC) in the mid 1800s. The propellants used for many advanced applications have steadily become increasingly complex, moving from single-base and double-base propellants (both NC-based) to composite propellants, which contain solid additives such as oxidizers (e.g. AP, AN) and nitramines (e.g. HMX, RDX). As propellants with ever higher performance characteristics are desired, the number of energetic binders that have been synthesized and explored has quickly grown as a logical extension of this development effort. Many of the binder technologies which were initially developed for propellant applications have subsequently been utilized in explosive formulations as well.

2 Non-crosslinkable Energetic Binders

2.1 Nitrocellulose

Nitrocellulose (NC), a polymeric nitrate ester derived from cellulose, has dominated in various forms as the primary energetic polymer in use since the late 1800s [4]. Cellulose is a nearly ubiquitous material in the vegetable kingdom; wood fiber, cell walls and the structural material in plants are largely comprised of cellulose. Cotton fiber consists of nearly pure cellulose. Cellulose has 3 hydroxyl groups per monomeric unit and so the trinitrated monomeric unit represents the theoretical maximum degree of nitration (14.14% N). In reality complete nitration is not practical, with the upper limit being 13.75% N for commercial product. The solubility of NC is drastically affected by the degree of nitration, with the higher nitrated products being essentially insoluble in organic solvents. In addition to NC, many other carbohydrates, starches, lignin and the like have been subjected to nitration, but none have proven as practical as nitrocellulose. The quantity of available literature on the production, treatment, and practical uses of NC is vast and as such only a brief overview of NC is provided in this chapter (Fig. 1).

Fig. 1 The chemical structure of fully nitrated nitrocellulose
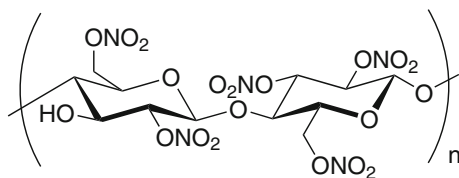
Nitrocellulose (NC) was discovered independently by Schönbein and Böttger when they nitrated cotton fibers; subsequent efforts demonstrated that wood cellulose could also be utilized successfully. They quickly began to collaborate to incorporate the material into artillery. At nearly the same time Sobrero prepared the energetic plasticizer nitroglycerin (NG), which has been used in conjunction with NC as the dominant energetic binder/plasticizer system for propellants ever since. The initial 1846 patent for the production of NC described the nitration in mixed acids (1 part HNO_3 to 3 parts H_2SO_4) for 1 h at 50–60 °C followed by extensive washes with water and dilute potassium carbonate. The material as isolated proved unstable, however, and an 1847 explosion at the Faversham factory resulted in the loss of 20 lives. Two large guncotton explosions in Vincennes and Le Bouchet stopped the production of NC in England and France for approximately 16 years. Countless other variations for the production of NC were subsequently developed; it was ultimately shown that first pulping the NC fibers, followed by extensive washing to remove residual acids, is critical to the stability of the final product. The primary use of NC has been as a binder in propellants starting with the invention of smokeless powder in 1882.

Single-based powder and propellants are comprised of essentially pure NC. Bulk powders, used in shotgun shells, contain some oxidizing (nitrate) salt added to enhance combustion and are a smokeless equivalent of black powder. Colloided powder of satisfactory quality for use in rifled guns (Poudre B) was invented in 1884 and manufactured by swelling both soluble and insoluble NC in ether-alcohol to make a gel which was kneaded, rolled into sheets and cut into squares or extruded through a die to make strips which were then cut to length and dried. Double-based propellants contain mixtures of NC and NG, which vastly improves the oxygen balance of the material such that the NC can be completely oxidized during combustion; they are used in small arms, cannons, mortars, and rockets. Ballistite is a smokeless powder invented by Alfred Nobel in 1888; production involves mixing NC with NG (various ratios have been used) in the presence of a solvent which is removed after processing is complete. Cordite, invented by Abel and Dewar, consists of acetone-swollen NC and NG combined with mineral jelly which can be extruded or rolled and cut prior to drying. Triple-based propellants, containing NC, NG and nitroguanidine (NQ) (which provides a cooling effect to reduce barrel erosion) are used in large cannons.

Castable double-base rocket propellants were developed nearly a century later, in which solid propellant is formed by heating the semi-plasticized grains in the presence of additional liquid plasticizer which is gradually incorporated into the NC forming a single monolithic grain [5]. Conducting this process in a mold of the desired shape allows for the production of star-perforated and multi-perforated grains to alter the burning rate as the propellant is consumed (progressive or regressive). The NC powder (slightly plasticized) is added and then is backfilled with additional plasticizer which further swells the NC during curing thereby forming the final grain. Significant measures must be taken to ensure acceptable

Fig. 2 Synthesis of PVN
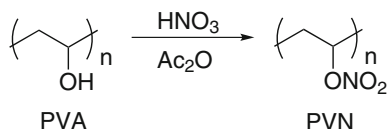
density of the powder during loading. Plastisol NC propellants differ in that a fine-particle, colloided, spherical NC is used such that it can be slurried with the full amount of plasticizer and poured into the mold with uniform results and without the use of volatile solvents [6].

2.2 Poly(vinyl nitrate)

Polyvinyl(nitrate) (PVN) has been investigated since the 1930s with the hopes that it might eventually augment or replace NC [7]. PVN is synthesized (Fig. 2) by the nitration of poly(vinyl alcohol) (PVA), a widely available synthetic product. Various nitration conditions have been utilized including addition of PVA pellets to mixed acids, to 98% nitric acid or by using a slurry method employing acetyl nitrate. Oxidation of the PVA occurs during nitration, and care must be taken such that the material does not ignite in the reaction vessel by reaction of the solid with gaseous nitrogen oxides (NO_x) in the headspace above the liquid. PVN can theoretically consist at levels of nitration up to 15.73% N, but the stability of the material decreases with increasing % N while the sensitivity to impact increases [8]. Calculations suggest that PVN can in fact out-perform NC in propellant applications. Ultimately, the use of PVN has met with limited success despite the high calculated performance characteristics due to thermal stability issues combined with the tackiness of the atactic polymer, which results in a tendency for the material to stick during extrusion or molding of propellant grains. It has been suggested that the introduction of stereo-regularity into the PVN chain may help solve at least some of these problems.

2.3 Energetic Polyesters, Polyamides and Polyurethanes

A number of energetic polyesters, polyamides and polyurethanes were investigated at Aerojet in the 1950s [9]. Common building blocks were used in combinations to make a library of polymeric materials which were synthesized by condensation polymerization; they are too numerous to cover extensively in this chapter and a brief summary list is shown in Fig. 3. The polyureas and polyurethanes were also subjected to further post-polymerization nitrations (introduction of nitro group at urea or urethane
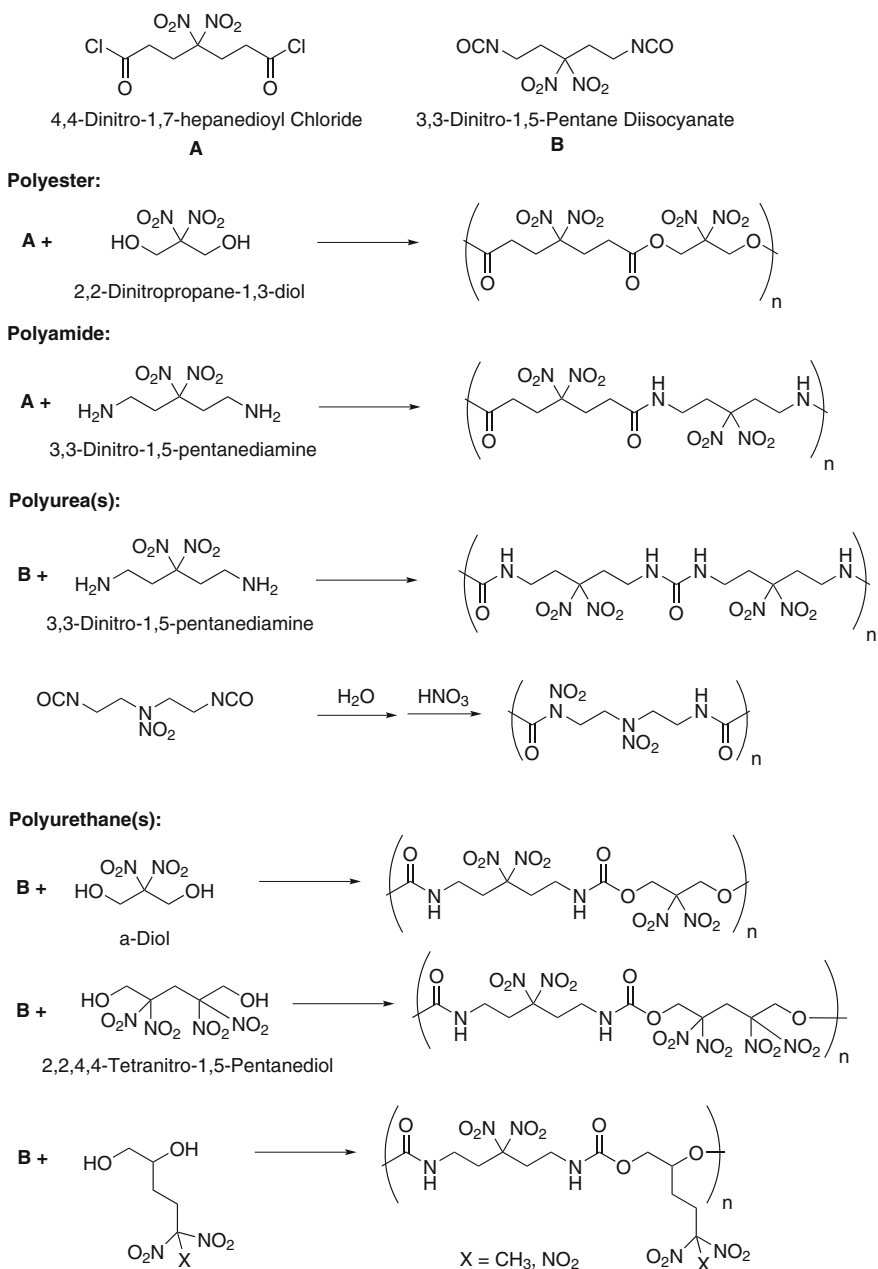
Fig. 3 Some of the many energetic polyesters, polyamides, polyureas and polyurethanes that have been investigated for propellant applications

nitrogens) making polymers of even higher energy content. These polymers are all solid, relatively low molecular weight, non-crosslinkable materials and ultimately have not found widespread use in propellant or explosive formulations.

2.4 Energetic Polyacrylates

Energetic acrylates have been investigated in some detail beginning with nitroethylacrylate and nitroethylmethacrylate in the 1950s. Since, poly(dinitropropyl acrylate) (p-DNPA) as well as the copolymer of DNPA with 2,3-bis (difluoraminopropyl) acrylate (NFPA) have been prepared using peroxide-based initiators [10] (Fig. 4). The application of these polymers as binders in extrudable high-energy plastic-bonded explosives with HMX and aluminum has been described with solids loadings up to 92% by weight. The binder has been used in explosive compositions such as LX-09-0 (93% HMX, 4.6% p-DNPA, 2.4% plasticizer). Energetic co-monomers such as 2,3-bis(difluoroamine propyl) acrylate (NFPA) were polymerized in conjunction with DNPA and energetic plasticizers such as bis(2,2-dinitro-2-fluoroethyl)formal (FEFO) and methyl-4,4-dinitropentanoate were also incorporated to tailor properties. The use of multi-modal solids consisting of precise amounts of varied discrete particle sizes was recognized as being crucial to realizing extrudable materials at high solids loadings.

2.5 Polynitrophenylene (PNP)

Polynitrophenylene is an amorphous (non-crystalline), heat-resistant polymer that can be easily formed into films [11]. It is synthesized by the oxidative cross-linking (Ullman reaction) of 1,3-dichloro-2,4,6-trinitrobenzene (styphnyl chloride) at 150–155 °C in a high-boiling solvent (nitrobenzene) in the presence of copper powder (Fig. 5). The resulting green, yellow-brown powder is readily soluble in organic solvents such as acetone and ethyl acetate which makes it easy to process into films and shapes. The properties of PNP are shown in Table 1. The material is heat resistant but extremely sensitive to impact (BAM impact = 4 J). PNP has found utility in caseless ammunition as well as high ignition temperature propellants.

2.6 Nitramine Polymers

Several nitramine-containing polymers including polyesters and polyethers have been demonstrated as illustrated in Fig. 6. Polyesters such as poly(diethylene
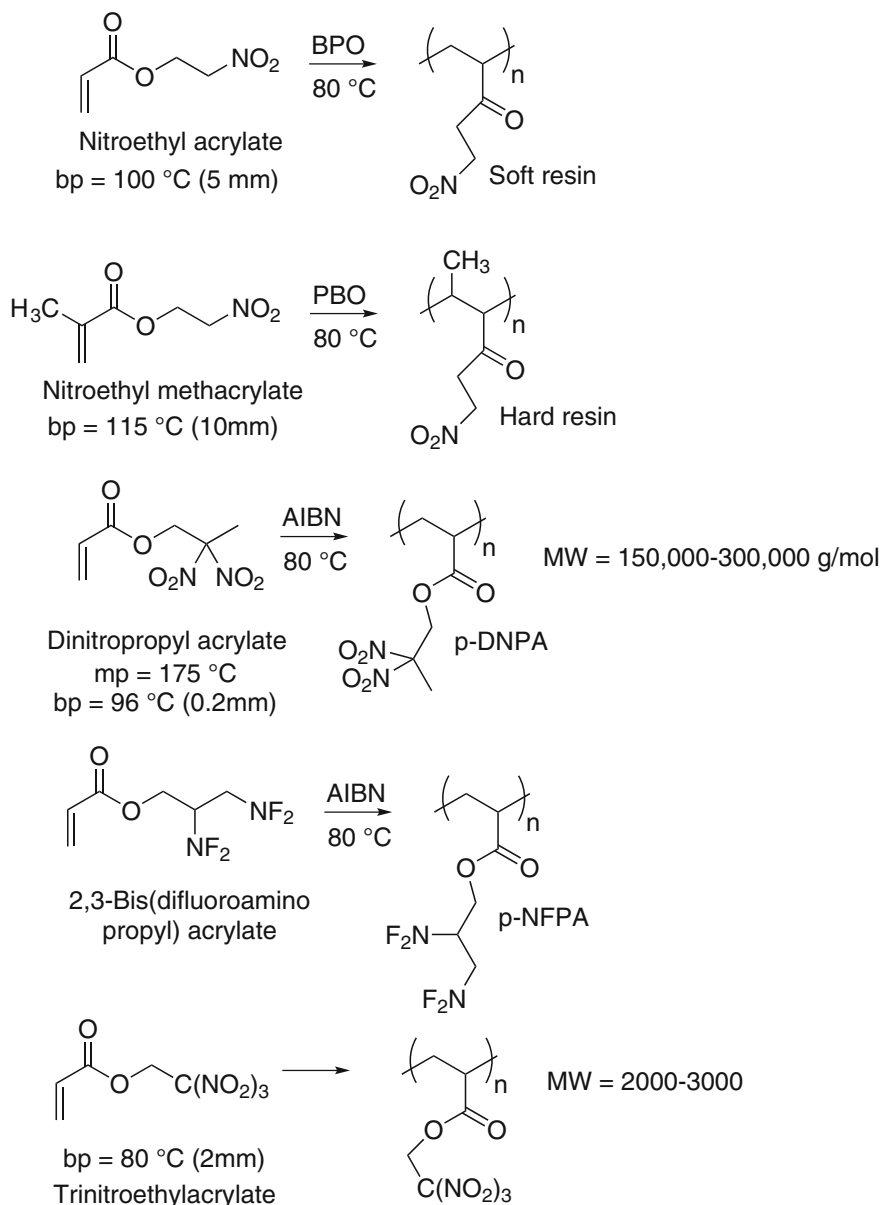
Fig. 4 Synthesis of energetic polyacrylates including p-DNPA and p-NFPA

glycol-4,7-nitrazadecanedioate) (P-DEND) and diethyleneglycol-triethyleneglycol-nitraminodiacetic acid terpolymer (DT-NIDA) are formed by the acid-catalyzed condensation of any one of a variety of dicarboxylic acid terminated nitramine containing monomers with a variety of diols, particularly poly(ethylene glycol)s
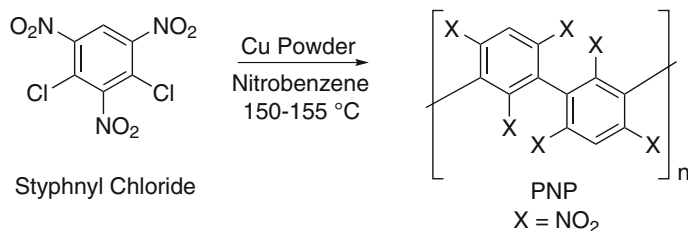
Fig. 5 Polymerization of styphnyl chloride to PNP via Ullman coupling in nitrobenzene

Table 1 Properties of PNP polymer

Density (g/cc)	1.8–2.2
GPC molecular weight (g/mol)	~ 2000
DTA/TGA exotherm onset (°C)	250
BAM impact sensitivity (J)	4
BAM friction sensitivity (N)	240 (no go)

[12]. The molecular properties can be widely tailored by the varying both the length and nitramine content of the dicarboxylic acids as well as the length and combination of the ethylene glycol-based diols utilized. A number of analogous polyethers have been formed as well by reaction of the corresponding nitramine-containing bischloromethyl (rather than dicarboxylic acid) monomers with ethylene-glycol based diols [13]. One such example is the reaction of 1,6-dichloro-2,5-dinitrazahexane (DCDNH) with ethylene glycol (EG) to form alpha-hydro-w-hydroxy poly(oxymethylenenitramine) (EDNAP), which can be further crosslinked with hexadiisocyanate to form a rubbery gumstock and was tested in an aluminized nitramine-containing rocket propellant. In an effort increase the polymer molecular weight while simultaneously lowering both the glass transition temperature as well as the viscosity of the material, polynitramine/ethers comprised of DCDNH with various ratios of ethylene glycol, diethylene glycol and 1,3-propanediol were prepared. The materials exhibited glass transition temperatures as low as −18 °C with molecular weights (M_w) ranging from 1565 to 3565 g/mol [14].

2.7 Poly(phosphazene)s

The synthesis and characterization of a variety of linear poly(phosphazene)s (PPZ's) bearing energetic side groups such as alkyl nitrate esters and alkyl azides have been explored in the United Kingdom beginning in the 1990s. Earlier research on non-energetic PPZ's typically involved synthesis of poly(dichlorophosphazene) followed by substitution with various alkoxy and alkylamine substituents in the presence of triethylamine (Fig. 7). The resulting materials were explored for
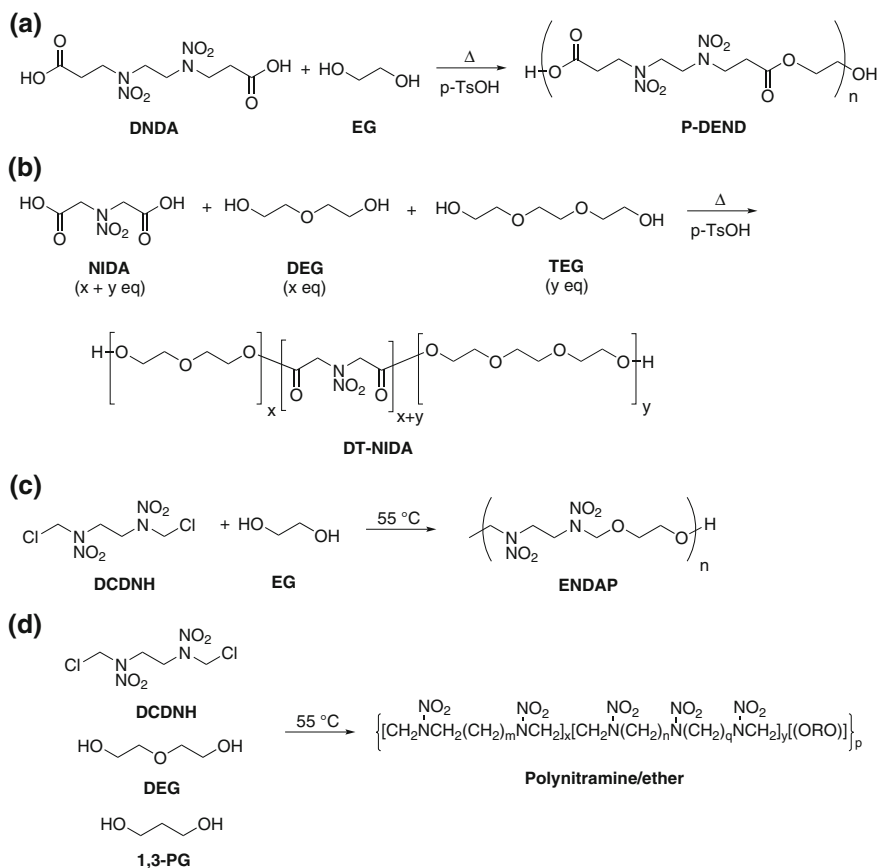
Fig. 6 Synthesis of polynitramines
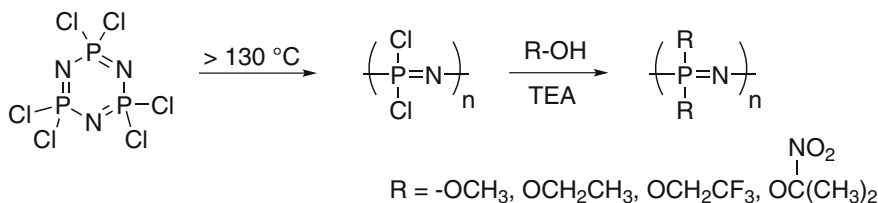
Fig. 7 Synthesis of non-energetic poly(phosphazene)s

potential use as films, moldings, coatings, fire-retardants and even rocket case insulation [15]. Energetic poly(phosphazenes) were subsequently synthesized by analogous reaction of the polydichloro precursor polymer with various nitro, nitrato and azido containing alkoxy substituents in the presence of triethylamine [16]. The

precursor polymer is synthesized by thermal polymerization of the dichlorophosphazene cyclic trimer, or alternatively by polymerization of tris(chloro)-*N*-(trimethylsilyl)phosphoranimine in the presence of catalytic phosphorous pentachloride (PCl$_5$) in dichloromethane at ambient temperature. However, the poly (dichlorophosphazene) precursor is reactive to moisture and oxygen, making handling and storage somewhat difficult; alternatively tris(1,1,1-trifluoroethoxy)-*N*-(trimethylsilyl)phosphoranimine can be directly polymerized to the polymeric product in the presence of catalytic 1-methylimidazole; direct substitution of a of the trifluoroethoxy groups with the sodium or lithium salts of a wide variety protected alcohol precursors is then possible (Fig. 8) [17]. The degree of substitution can be controlled by altering the reaction conditions. Nitrolysis with 95% nitric acid yields polynitrato-substituted polymers; several different protecting groups are available and the degree of substitution is variable as well, which permits tailoring of the relative degree of nitration and thereby the viscosity, oxygen balance and the
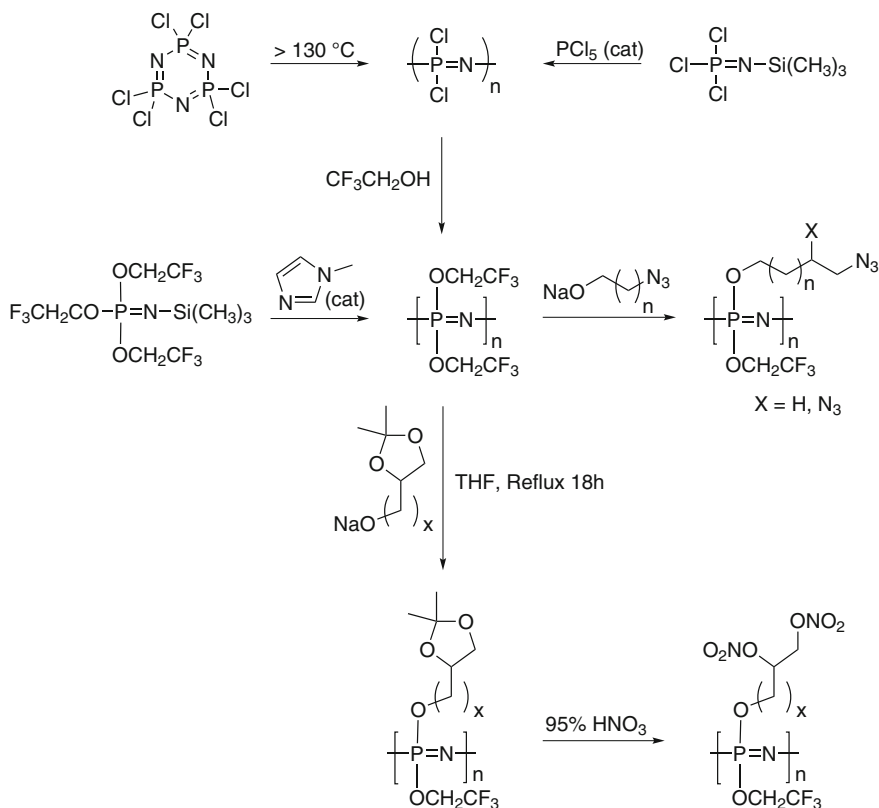
Fig. 8 Synthesis of protected a poly(phosphazene) precursor by several methods and transformation to energetic PPZ's

glass transition temperature of the resulting polymers to a very large degree. PPZ's with glass transition temperatures as low as −99.5 °C and energy densities as high as 4750 J/cm^3 have been reported.

3 Crosslinkable Non-energetic Binder Systems for Propellant Formulations

The use of cross-linkable binders in rocket propellant systems allows for the mixing of the propellant ingredients as a liquid slurry which is cast into the case of the motor, where it then is allowed to cure into a tough rubbery (elastomeric) solid material. These "cast-cure" propellant formulations consist of grains of solid oxidizers (e.g. AP) and metallic fuels such as aluminum in addition to several other potential ingredients, including plasticizers, solid nitramines, burn-rate modifiers, bonding agents among others which are all incorporated into the elastomeric binder matrix.

3.1 Polysulfides

Classic composite propellants consist of a crosslinked binder (typically organic polymers) containing solid oxidizers such as ammonium perchlorate (AP) or ammonium nitrate (AN) as well as other materials including fuels (e.g. aluminum). The first composite propellants were produced by mixing potassium perchlorate (75%) with molten asphalt binder followed by casting and cooling. However, the asphalt had very little chemical crosslinking and the materials were not true elastomers resulting in poor mechanical properties at higher solid loadings. Polysulfides were the first chemically crosslinkable binders to be used in propellants. They are formed by condensing dichloroethyl formal with sodium polysulfide, the product of which is then partially hydrolyzed to lower molecular weight liquid polymers. Researchers in 1946 at the Jet Propulsion Laboratory (JPL) mixed AP into Thiokol LP-3 polysulfide liquid polymer in the presence of the oxidative curative *p*-quinone dioxime, which causes the crosslinking reaction forming multiple disulfide bonds, as shown in Fig. 9 [18]. The polymer has an average MW of 1000 g/mol, viscosity of 7.0–12.0 poise and specific gravity of 1.27 g/cc. The end-groups A of the cured polymer are residual hydroxyl groups from the manufacture and other groups formed by side reactions.
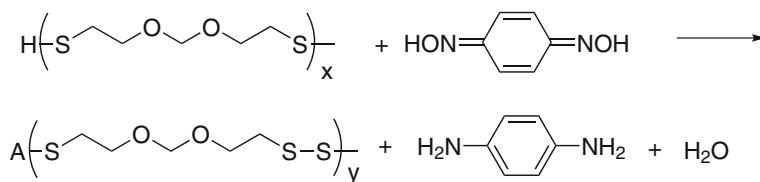
Fig. 9 The oxidative crosslinking of Thiokol LP-3 polysulfide binder

3.2 Polybutadienes with Carboxyl Functional Groups

Poly(butadienes) with carboxyl functional groups are widely used for rocket propellant applications. The most commonly used materials are the copolymer of butadiene and acrylic acid (PBAA), the terpolymer of butadiene, acrylic acid and acrylonitrile (PBAN), and carboxyl-terminated polybutadiene (CTPB) as illustrated in Fig. 10. Advantages of these materials over previous binder systems include better mechanical properties over a larger temperature range as well as higher specific impulse over other AP-based propellants. The increased performance is the result of higher maximum solids loading due to the lower viscosity prepolymers (and better mechanical properties in the resulting cured systems) as well as the greater fuel value of the butadiene binder [19].

PBAA consists of a poly(butadiene) backbone with an average of 2 randomly distributed carboxylic acids (from acrylic acid monomer) per polymer chain to provide sites for crosslinking. The prepolymer liquid with a molecular weight of 2000–3000 g/mol has a viscosity of 200–300 poise at room temperature. During propellant processing the carboxyl groups then react with one of a variety of reactive epoxide or aziridine based crosslinkers (Fig. 11). PBAN incorporates an average of 6% by weight of cyano groups through the addition of acrylonitrile monomer during the synthesis; a resulting improvement in the distance between

Fig. 10 Structures of PBAA, PBAN and CTPB. Structures are simplified for clarity
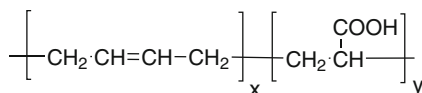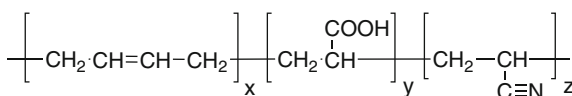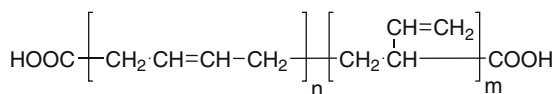
Fig. 11 Some aziridine and epoxide-based curatives used with PBAA, PBAN and CTPB

MAPO

DER-332

ERLA-0510

BITA
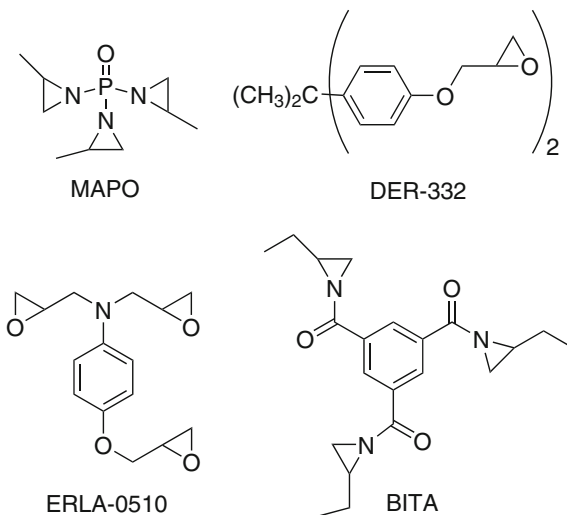
carboxyl groups is thought to be responsible for the resulting improvement in cure reproducibility and mechanical properties of PBAN propellants over those based on PBAA. PBAN binder has been employed extremely successfully for several large rocket systems, including the Titan 3, Minuteman as well as the Solid Rocket Boosters for the Space Shuttle [20].

While PBAA and PBAN are both synthesized by free radical emulsion polymerization, CTPB is produced by a more tightly controlled organolithium initiated (anionic) polymerization. Polymerization is followed by quenching with CO_2 to produce carboxy-terminated polymer chains. As a result of this chemistry, the functionality, molecular weight, distribution of cis- versus trans- double bonds, and degree of branching are all more tightly controlled in CTPB, resulting in improved properties over PBAA and PBAN. In particular, positioning of the functional groups exclusively and reliably at the termini of the CTPB polymer results in improved mechanical properties.

3.3 Polyurethanes and Hydroxy-Terminated Polybutadiene (HTPB)

Polyurethane propellants are formed by the reaction of a multifunctional hydroxyl-terminated polymer with a multifunctional isocyanate. The isocyanate curatives used for polyurethane propellants include 2,4-toluene diisocyanate (TDI), hexamethylenediisocyanate (HDI), isophorone diisocyanate (IPDI), polymethylenepolyphenyl isocyanate (PAPI), and Demodur N-100, which is a multifunctional isocyanate formed by the controlled reaction of hexamethylene diisocyanate with water. The reaction rate of the reaction between polymer and

isocyanate crosslinker can be adjusted by the use of several metal-based catalyst systems. Many different diol/triol polymers have been used as the binder pre-polymer component including polyesters such as poly(neopentylglycol azelate) (NPGA) and polyethers such as poly(propylene glycol)s (PPGs) and poly(butylene glycol) [21].

Hydroxy-terminated polybutadiene (HTPB) was then developed in the 1960s and ultimately delivered higher specific impulse for rocket propellants as well as better mechanical properties. The glass transition temperature of HTPB can be varied by changing the catalyst used during the polymerization of butadiene, which alters the amount of vinyl content (higher vinyl content leads to lower T_g). A triblock copolymer of polycaprolactone (PCL) with HTPB was formed by using the HTPB as the initiator from which to grow the PCL chains by ring-opening polymerization. While PCL contains a lower energy content than HTPB, it incorporates high-energy nitrate-ester plasticizers more readily than HTPB and so the copolymer found use in cast-cure propellant formulations [22].

3.4 Nitrated HTPB

The nitration of HTPB by various methods has been investigated as the incorporation of nitro groups to the polymer backbone should increase the performance characteristics of the polymer. Early attempts utilized a nitromercuration/demercuration route but numerous side reactions resulted in degradation of the backbone and crosslinking of the polymer into insoluble products [23]. HTPB can be directly nitrated across the double bonds N_2O_5 yielding a mixture of C-nitro and O-nitro (nitrato) bonds, however, the material is an insoluble rubber with low thermal stability at even low degrees of nitration. Eventually a more stable product NHTPB was formed by first reacting a percentage of the HTPB double bonds to epoxide groups, which were subsequently opened with N_2O_5 yielding the *vicinal* dinitrate ester as shown in Fig. 12 [24]. The degree of nitration was 10–20% and the viscocity of the polymer increased with increasing levels of nitration. NHTPB has an advantage over HTPB in that it is miscible with energetic nitrate ester plasticizers such as DEGDN, TEGDN and NG. DSC analysis showed the T_g of 10% NHTPB to be −58 °C with an exotherm onset of 156 °C with exotherm maximum at 209 °C (scan rate = 10 °C/min). The T_g of the 20% nitrated NHTPB was −22 °C. The best crosslinked urethane rubbers were formed with the 10% nitrated NHTPB with various isocyanate curatives.

3.5 Cyclodextrin Nitrate (CDN)

Several nitrated variants of cyclodextrin polymers have been described. Cyclodextrins are cyclic oligosaccharides bound in a ring structure synthesized

Fig. 12 Synthesis of *vicinal* nitrato-HTPB by epoxidation followed by nitration with N_2O_5

$$HO \!-\!\!\left[CH_2 \cdot CH\!=\!CH\!-\!CH_2 \right]_n\!\!-\! OH$$

HTPB

$CH_3\overset{O}{\overset{\|}{C}}OOH$

CH_2Cl_2

$$HO\!-\!\!\left[CH_2 \cdot CH\!=\!CH\!-\!CH_2 \right]_m\!\!\left[CH_2 \cdot \overset{O}{\overset{\diagup\diagdown}{CH\!-\!CH}}\!-\!CH \right]_{n-m}\!\!-\! OH$$

N_2O_5

CH_2Cl_2

$$HO\!-\!\!\left[CH_2 \cdot CH\!=\!CH\!-\!CH_2 \right]_m\!\!\left[CH_2 \cdot \overset{ONO_2}{\underset{ONO_2}{CH\!-\!CH}}\!-\!CH \right]_{n-m}\!\!-\! OH$$

NHTPB
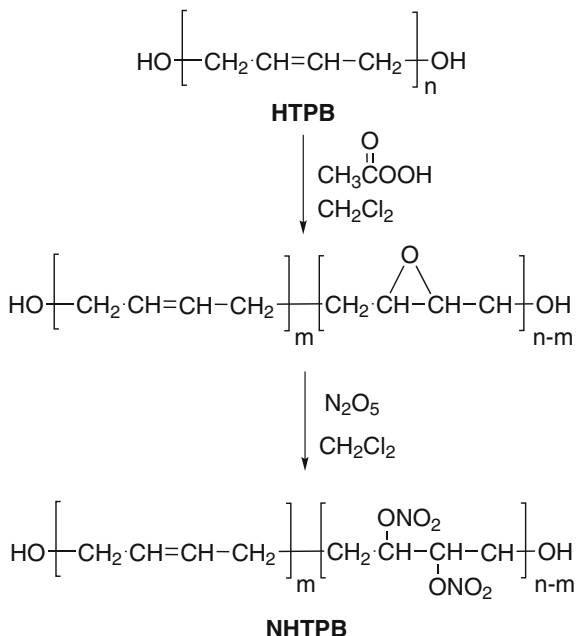
from the decomposition of starch by a bacterial enzyme. The rings form a toroidal-type structure with a somewhat hydrophobic interior and hydrophilic exterior and are capable of solubilizing small molecules forming host-guest complexes. It was postulated that perhaps a cyclodextrin nitrate (CDN) might encapsulate other "sensitive" energetic materials such as NG or RDX resulting in a reduced overall sensitivity. The nitrate ester of β-cyclodextrin (β-CDN, 7-membered ring) was synthesized by nitration with 90% HNO_3, 90% HNO_3/ oleum, as well as with mixed acids (HNO_3/H_2SO_4) on up to the 50 lb batch scale and >13% nitrogen by weight; the materials are dry ESD-sensitive powders as synthesized but were plasticized with nitrate esters such as TMETN and BTTN to form waxy materials [25]. Nitration levels of 2.6 to 3.0 nitrate ester groups per D-glucose unit were achieved. Card-gap testing of the plasticizer CDN complex in a 2/1 ratio indicated a dramatic reduction in the sensitivity (zero cards with #8 blasting cap) which was attributed to complexation of the plasticizer inside the CDN. The nitrate ester of γ-cyclodextrin (γ-CDN, 8-membered ring) was investigated with reported density of 1.654 g/cm^3 and heat of formation of 50.40 kcal/mol. Cross-linked nitrated cyclodextrins (poly-CDNs) were also investigated in an effort to increase the viscosity of the nitrate ester complexes and encapsulation of RDX in the poly-CDNs also reportedly resulted in reduced impact sensitivities [26].

4   Development of Binder Systems in Explosive Formulations

Polymer-bonded explosive (PBX) (also known as plastic-bonded explosive) formulations consist of a solid explosive crystalline material such as a nitramine (RDX, HMX, CL-20, etc.) contained within a reasonably continuous polymeric matrix which separate the explosive particles. Simple PBX's can be formed using non-curable hard polymers or waxes which are typically deposited on the surface of the explosive crystals by slurry coating; evaporation of a suitable solvent (in which the polymer has been dissolved) in the presence of a suitable non-solvent (precipitates the polymer onto the explosive as the solvent evaporates). The resulting molding powder is then pressed under high pressure (>10,000 psi) into hard solid billets consisting of crystalline explosive material contained within a polymeric matrix. These billets can retain their precise shape even under stress. The advantage of this approach is in the simplicity of the manufacture; no melting or controlled temperature environments are required.

An abbreviated list of PBX's is shown in Table 2. Early PBX's were based on solid nitramines such as RDX contained within a matrix of polystyrene [27]. Subsequently developed formulations utilize nitramines or other common explosive solids such as TATB and PETN and utilize many other plastics as binders, including hydrocarbons like polyethylene, poly(vinyl) alcohol (PVA), Nylon, and Latex. Metallized PBX's incorporate metals such as aluminum and often utilize fluorinated polymers such as Teflon, Viton, and Kel-F. The exothermic reaction of these fluorinated polymers with aluminum during detonation contributes to the explosive output of the overall formulation.

Many of the polymer systems developed for propellant formulation were quickly adapted for use in explosive formulations as well. PBX formulations were developed based on rubbery, non-energetic cross-linkable polymers and contain many of the same ingredients as are found in the propellant formulations as described in the previous section (Sect. 2). PBX's formed using thermoplastic elastomers such as Kraton and Estane can help to adsorb energy and thereby decrease the sensitivity of explosives to shock initiation. PBX-9501, consisting of 95% HMX, 2.5% Estane, and 2.5% Plasticizer (BDNPA/F) is an example of a high-energy pressable formulation which provides improved thermal stability as well as sensitivity characteristics compared to earlier comparable NC-based formulations [28]. Achieving extremely high solids loadings in cast-cure explosive systems can prove more challenging as the viscosity of the pre-cured mix increases at higher solid contents and must still be pourable into the fixture. PBXN-110 is an example of high-energy cast-cure PBX consisting of 88% HMX, 5.4% HTPB, 0.5% PAPI, 5.4% IDP and 0.7% lecithin.

Table 2 Common Polymer-bonded explosive (PBX) formulations

Formulation	Density (g/cc)	Explosive (%)	Metal (%)	Plasticizer (%)	Binder (%)
HMX/Laminac-Styrene	–	HMX (83)	–	–	Polyester resin-Styrene (17)
CB49-3	1.61	RDX (60)	Al (23)	–	Polyester resin (17)
Nylon bonded RDX-1	–	RDX (90)	–	–	Nylon (10)
PBX-1	1.83	RDX (65)	Al (26)	–	Nylon (9)
LX-04-1	1.865	HMX (85)	–	–	Viton (15)
LX-14	1.833	HMX (95.5)	–	–	Estane (4.5)
PBX-9010	1.789	HMX (90)	–	–	Kel-F (10)
PBX-9011	1.770	HMX (90)	–	–	Estane (10)
PBX-9205	1.68	RDX (92)	–	Diethylphthalate (2)	Polystyrene (6)
PBX-9501	1.843	HMX (95)	–	BDNPA/F (2.5)	Estane (2.5)
PBX-9502	–	TATB (95)	–	–	Kel-F (5)
PBXN-110	–	HMX (88)	–	IDP (5.4) Lecithin (0.7)	HTPB (5.4) PAPI (0.5)
PBXW-14	–	HMX (50) TATB (45)	–	–	Viton (5)
PAX-2A	–	HMX (85)	–	BDNPA/F (10)	CAB (5)
PAX-3	–	HMX (65)	Al (25)	BDNPA/F (6)	CAB (4)
PAX-11	–	CL-20 (94)	–	BDNPA/F (3.6)	CAB (2.4)

5 Oxirane-Based Crosslinkable Energetic Polymers

Oxirane polymers are those that are derived from the ring-opening polymerization of 3-atom cyclic ethers (epoxides). Oxirane monomers are generally the most reactive of the cyclic ethers due to the large amount of ring-strain cause by the severity of the bond angles. Epichlorohydrin (epoxide with one chloromethylene substituent) and glycidol (epoxide with one hydroxymethylene substituent) are two common oxiranes that can be utilized, however, oxiranes can also be created by the oxidation of olefins with organic peroxides [29] or by ring-closure of suitable precursors, which will be seen in the sections which follow. Oxiranes are typically polymerized by any number of cationic ring-opening polymerization catalysts in the presence of an alcohol-based initiator. Under the correct conditions, the functionality of the resultant polymer can be dictated by the functionality of the initiator (alcohol, vs. diol, vs. triol).

5.1 Poly(glycidyl nitrate) (PGN)

Poly(glycidyl nitrate) (PGN) was first investigated and its theoretical potential as an energetic binder component reported by the US Navy and at the Jet Propulsion Laboratory (JPL) in the 1950's [30–32]. These efforts resulted in a general procedure for production of PGN via cationic ring-opening polymerization of nitratomethyloxirane (glycidyl nitrate, a.k.a.—glyn). A solution of the monomer in methylene chloride was added to a Lewis-acidic catalyst such as boron trifluoride diethyletherate ($BF_3 \cdot Et_2O$) in the presence of a multi-functional initiator such as 1,4-butanediol (BDO) as shown in Fig. 13.

The PGN produced using these methods possessed several disadvantages including difficulties with monomer synthesis and purification, lower than ideal molecular weight (MW = 1500 g/mol) and low functionality (<2) in the resulting polymer, which adversely affected the properties of the resulting (cured) polyurethane binder. However, the potential promise of PGN as an energetic pre-polymer based on its properties (Table 3) [33] ultimately resulted in a renewed interest in the material beginning in the 1980s at Thiokol Corp (Elkton, USA) and the Defence Research Agency (United Kingdom). During this time and the decades to come several methods were developed for both the production of the glyn monomer and for its polymerization to PGN which vastly improved the quality of the final product.

Willer et al. at Thiokol patented several improvements for the polymerization of glyn, which they synthesized two steps from epichlorohydrin [34]. Treatment of epichlorohydrin with nitric acid yields the nitrated species; ring-closure with aqueous base then affords glyn with epichlorohydrin as a byproduct. The monomer is purified by spinning band distillation prior to polymerization. Several advances in the polymerization conditions used to produce PGN were introduced; firstly, it was noted that if $BF_3 \cdot Et_2O$ were to be used as a catalyst, the ether must be removed by vacuum after complexation with the BDO initiator, failure to do so results in some

Fig. 13 Synthesis of poly (glycidyl nitrate)
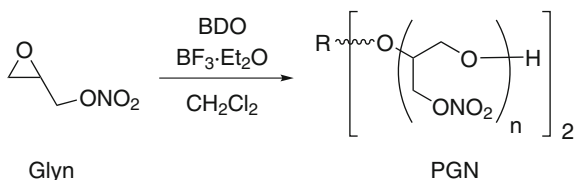
Table 3 Properties of PGN	Density	1.45
	Tg (°C)	−35
	Heat of formation (kcal/mol)	−68
	Functionality	2 or 3
	Oxygen balance	−60.5
	Ignition temperature (°C)	170

percentage of ethyoxy-terminated PGN polymer (i.e. f < 2) due to ether-intiated polymerization followed by loss of one ethyl group during quenching of the reaction. Another very important process improvement consisted of keeping the concentration of monomer in the reaction medium to a minimum by achieving a monomer addition rate essentially equal to the rate of monomer consumption due to polymerization. This strategy for the controlled cationic ring-opening polymerization of cyclic ethers helps to minimize the formation of cyclic oligo-mers by reducing the amount of polymeric back-biting caused by polymerization via the active chain end (ACE) mechanism, in which the chain-ends are "active" oxonium species prone to reaction with alcohols including or even other ethers (see Fig. 14). The more desired idealized reaction mechanism is the activated monomer (AM1) mechanism, in which the activated monomeric units are added to the terminal hydroxyl groups of the growing polymer chains [35–37]. More recent studies have suggested that a combination of the two mechanisms is most likely at work in the polymerization of glyn to PGN [38]. The conditions described yielded products with functionality of 2 and with average hydroxyl equivalent weights of 1200–1600 g/mol (M_n = 2400–3200 g/mol). A related patent to the Elkton
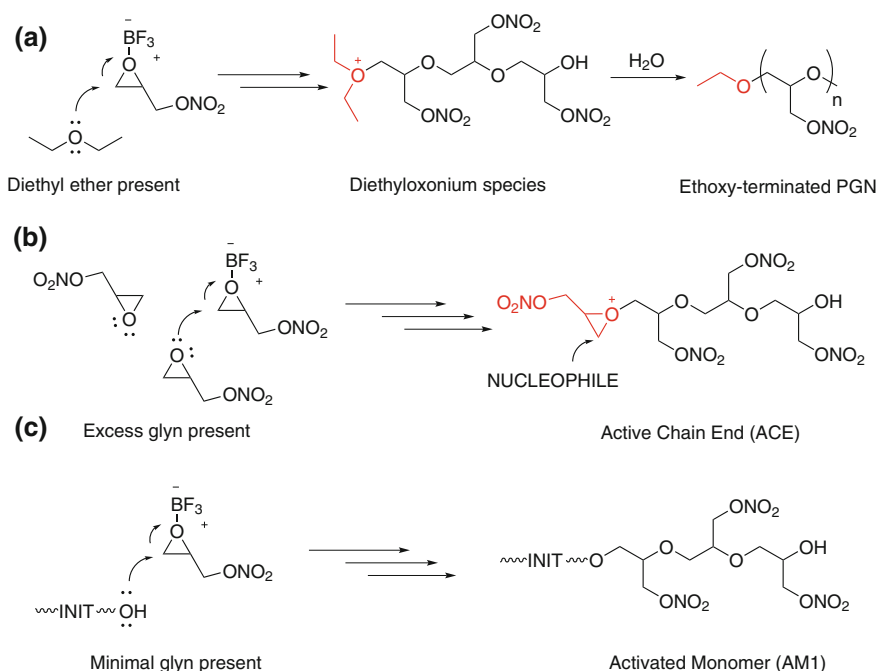
Fig. 14 Polymerization of glycidyl nitrate **a** in the presence of Et$_2$O resulting in ethyoxy-terminated PGN, **b** with build-up of unreacted glyn resulting in polymerization by the active chain-end (ACE) mechanism, which leaves the active chain end open to ring-opening by any nucleophile leading to back-biting, chain-extension and other undesired reactions, **c** by the desired activated monomer (AM1) mechanism

researchers describes the use of fully nitrated oligomeric PGN species as energetic plasticizers [39]. And in further related research, the team successfully synthesized isotactic PGN by polymerizing chiral (R or S) glycidyl nitrate monomer, formed by treating the chiral glycidyl tosylate(s) with nitrate acid followed by sodium hydroxide [40]. The isotactic PGN is interesting in that due to the increased molecular order, the polymer is crystalline in form (mp = +47.2 °C) as opposed to the usual atactic PGN which is a liquid at room temperature (Tg = −35 °C).

During this same period of time, researchers in the UK [Defence Research Agency (England) and ICI Explosives (Scotland)] were involved making their own improvements to PGN as a research material. One notable difference in the UK method was in their production of the glyn monomer by the action of dinitrogen pentoxide (N_2O_5) on glycidol; this method was used to form several cyclic nitrate ester materials at the time, including glyn and 3-nitratomethyl-3-methyl oxetane (NIMMO) [41–43]. This process is advantageous in that the nitration conditions are quite gentle and a clean product is obtained in good yield without the need for purification prior to polymerization. The methods used for polymerization were quite similar to those used in the United States at that time, with the main difference that the catalyst commonly used seemed to be HBF_4 rather than BF_3Et_2O [44] (presumably to avoid formation of ethoxy-terminated PGN as described previously), though many catalysts were tried by researchers through the years. Using these methods PGN was reportedly made in up to 3 kg batches with number average molecular weights of 3000–4500 g/mol reported for difunctional material. Trifunctional polymer was also made with Mn = 1900–3400 g/mol as well as fully nitrated oligomeric PGN for use as plasticizer. Properties including heat of explosion were calculated as well [45].

Researchers at Alliant Techsystems in the United States then began exploring a potential low-cost method for the synthesis of glyn and for PGN. The research was based on a method of preparing otherwise hazardous nitrate esters by nitration of the corresponding polyol within an inert solvent such as dichloromethane; this provides a heat sink to help prevent runaway exothermic reactions, removes the nitrate ester from the acidic medium as it is formed to help reduce side reactions including decomposition, and decreases the impact sensitivity of the nitrate ester through dilution [46]. Highsmith et al. subsequently showed that high purity PGN could be produced using glyn that had been synthesized from glycerin [47]. The glycerin was nitrated in methylene chloride with HNO_3 to form a mixture of mono-, di- and tri-nitroglycerin species (the relative ratios of each are determined by a combination of nitric acid concentration, reaction time and temperature). Ring-closure with sodium hydroxide solution affords glyn as the main product, with smaller amounts of mononitroglycerin (MNG) and trinitroglycerin (NG). It was found that the undesired MNG was washed away in the aqueous phase and that the NG can be carried through the polymerization step to be later washed away during post-polymerization treatments. The potential advantages of such a method include the low cost of the starting materials (glycerin, nitric acid and sodium
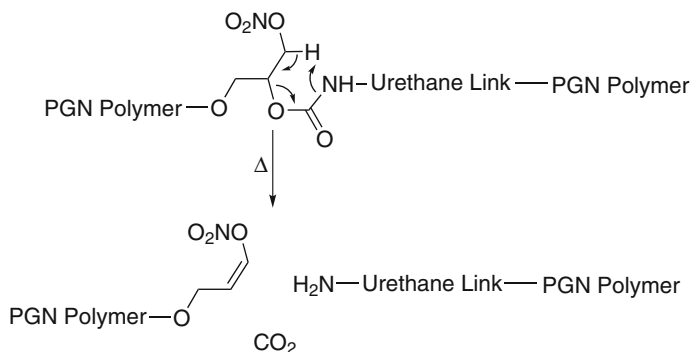
Fig. 15 Chain scission mechanism implicated in the softening of PGN-based polyurethanes over time

hydroxide) compared to the other known alternatives [48], and a pilot-scale continuous process was eventually developed for the production of glyn from glycerin on the multi-kilogram scale [49].

Though several methods had been developed for the synthesis of PGN, it quickly became apparent that there were inherent problems with PGN as a binder ingredient. While it was observed that PGN formed a relatively tough rubbery solid product when cured with a suitable poly(isocyanate) such hexamethylene diisocyanate (HDI) or common oligomeric isocyanates like Desmodur N100 and Desmodur N3400, these rubbery products would in fact soften, even to the point of liquefaction, during accelerated aging testing at elevated temperatures. The postulated decomposition method involves chain scission caused by the acidity of the hydrogen beta to the nitrate ester combined with the proximity and somewhat basic nature of the urethane nitrogen as shown in Fig. 15 [50].

There are two methods that have been developed to solve the decuring problem encountered when using PGN with common aliphatic isocyanates. The first simply involves changing the isocyanate system; Sanderson et al. demonstrated that by using polyaromatic polyisocyanate curatives such as PAPI (poly-methylenepolyphenylisocyanate, MDI) that the Shore A hardness of the resulting formulations did not appreciably change after 40 days at 62.8 °C (145 °F) [51]. It is postulated that the decrease in reactivity may be a result of the lower basicity of nitrogen atom when connected to a phenyl ring (aromatic) then when connected to an aliphatic chain (due to inductive effect of phenyl ring).

5.2 *End-Group Modification of Poly(glycidyl nitrate)*

While the use of polyaromatic isocyanates does appear to be a viable solution to the problem of PGN "decure" reactions during aging, it is desirable to have a product

that is tolerant enough to enable researchers to access the wide variety of aliphatic polyisocyanate curatives commonly in use without fear of product degradation. The preferred solution to date is to chemically modify the PGN such that the terminal nitrate esters are transformed to primary hydroxyl groups [52]. Researchers dubbed this "end-capping" or "end-group modification". Initial efforts focused on simple base hydrolysis of the nitrate ester groups, which was not successful; however, it was quickly realized that under the correct conditions with the addition of minimal base an elimination reaction occurs specifically at the termini of the polymer with the formation of oxirane groups (epoxide rings). Subsequent acid-catalyzed ring-opening of the epoxide end-groups yields chloride-terminated polymer in the presence of weak hydrochloric acid (HCl); the action of weak sulfuric acid on the epoxide terminated polymer yields the hydroxyl-terminated PGN (Fig. 16). Use of a lyophilic solvent system such as THF is necessary to insure complete conversion. This end modified PGN was shown to yield polyurethane products with satisfactory stability properties (no decrease in Shore A Hardness) over extended periods of time at elevated temperature of 60 °C [53] particularly if the material was properly washed to remove residual acids during the work-up procedure. A subsequent advance was made with the introduction of a one-pot, one-solvent procedure for the production of end-modified PGN, which reduces the amount of solvent and manipulation required during the process [54].
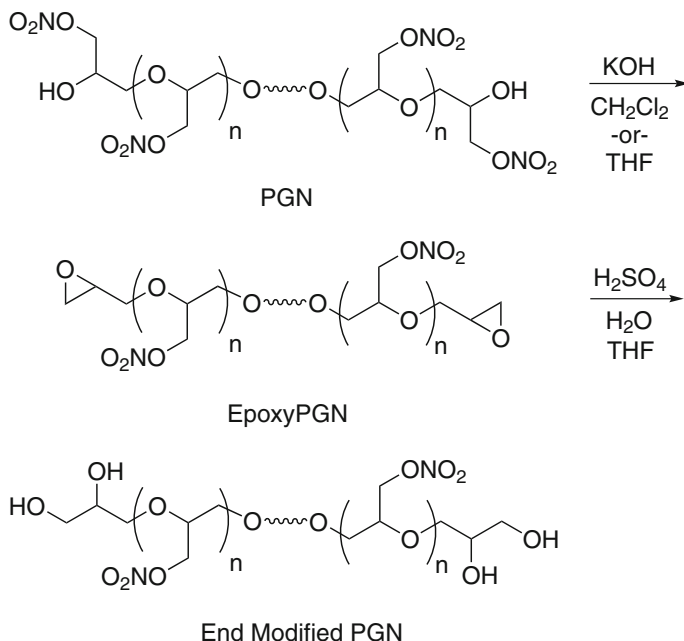
Fig. 16 End modified PGN produced via the epoxy-PGN intermediate

5.3 Glycidyl Azide Polymer (GAP)

Glycidyl azide polymer is structurally related to PGN in that it consists of a poly (ethylene oxide) backbone with azidomethyl groups in place of the nitratomethyl groups. Early attempts at Rocketdyne to synthesize GAP by the ring-opening polymerization of glycidyl azide were unsuccessful as the ring proved unreactive using standard conditions. The synthesis of glycidyl azide polymer (GAP) was first described in 1972 by Vandenberg et al. of Hercules, Inc. by azidation of very high molecular weight (6×10^6 g/mol) poly(epichlorohydrin) (PECH) [55]. However, due to the high molecular weight the material was a rubber. The first GAP material that was suitable for investigation as a cast-cure propellant binder was prepared at Rocketdyne in 1976 by preparation of low MW epichlorohydrin (1500–2600 g/mol) which was then reacted with sodium azide in DMSO (Fig. 17) [56]. This method is convenient in that it utilizes commercially available PECH as the starting material (3M Dynamar), but somewhat problematic in that it requires the use of dimethylsulfoxide as the solvent which is difficult to remove completely from the final product due to its high boiling point. Subsequent methods included azidation of PECH in dimethylformamide (DMF) as a solvent. Difunctional polymer with molecular weight of approximately 2500 g/mol was produced in 73% yield; however, purification of this material was nearly as difficult as in the case of DMSO [57]. This difficulty was significantly reduced by Frankel et al. with an aqueous process for the production of GAP by azidation of PECH in the presence of a phase-transfer catalyst [58]. GAP of increased purity and stability was ultimately produced by the azidation of PECH in relatively non-polar reaction mediums based on low molecular weight poly(ethylene oxide), which proved easier to remove from the product with repeated aqueous washes than the relatively polar solvents such as DMSO and DMF [59].

Some of the basic properties of GAP are shown in Table 4 [60]. GAP possesses lower density in comparison to PGN, but a higher positive heat of formation due to

Fig. 17 Synthesis of GAP from poly(epichlorohydrin)
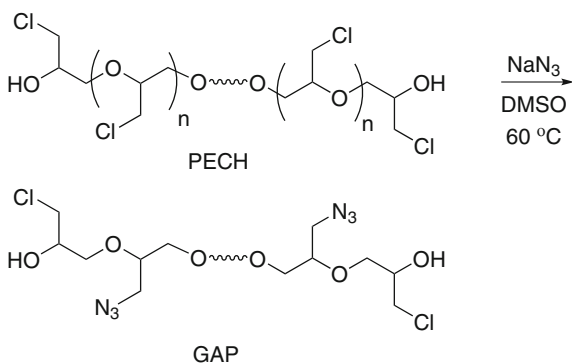
Table 4 Properties of GAP diol and GAP triol

Product	GAP diol	GAP triol
Density	1.29	1.29
Tg (°C)	−45	−45
Heat of formation (kcal/mol)	+117	+117
Functionality	2.0	2.5–3.0
Molecular weight (Mn) (g/mol)	1700 ± 300	≥ 900

Table 5 Constituents of GAP-containing nitramine-based castable explosive formulations

Ingredient	Weight %
HMX Class A (or RDX)	60.00 ± 10.00%
HMX Class E (or RDX)	20.00 ± 5.00%
GAP	8.00 ± 2.00%
N-100, HDMI or IPDI	1.00 ± 0.50%
TMETN	2.00 ± 0.50%
TEGDN (or BDNPA/F)	0.3 ± 0.50%
TPB or octanoic acid	0.10 ± 0.2%

Table 6 Sensitivity data for GAP-containing nitramine-based castable explosive formulations

Ingredient	Weight %
Density (g/cc)	1.74
Impact sensitivity (50% pt, 2.5 kg) (cm)	17–19
Friction sensitivity (no go @ 1000 lb)	20/20
Electrostatic sensitivity (no go @ 0.25 J)	20/20
Glass transition temperature (Tg)	−55 °C
GAP test (NOL) (cards)	170
Vacuum thermal stability (48 h @100 °C) (ml)	0.28
Self-heating (critical temp) (°C)	165
Detonation velocity (km/s) (calc'd)	8.4
Detonation pressure (GPa) (calc'd)	30.9

the influence of the multiple pendant azide groups, each of which contributes approximately 85 kcal/mol to the material. As a result, GAP polymer burns quite readily as a neat material. The combination of its relative ease of synthesis (one step from PECH) and excellent binder properties has made it one of the most available (commercially available from 3M as 5527 polyol) and widely utilized experimental high-energy binders [61].

An example of a simple nitramine containing GAP-based castable explosive formulation is shown in Table 5 and the sensitivity data is shown in Table 6 [62].

5.4   Variants of Glycidyl Azide Polymer (GAP)

Ampleman demonstrated that by forming epoxy-terminated PECH through the reaction with base (in a manner directly analogous to the formation of epoxy-terminated PGN) followed by acid-catalyzed ring-opening in the presence of water or short chain polyols such as tris-1,1,1-hydroxymethyl ethane or pentaery-thrytol one can form PECH with double, triple or quadruple the functionality of the starting material. This increased functionality PECH can then be transformed into higher functionality GAP through azidation in the standard fashion [63]. The example of "quadrupled functionality" GAP is illustrated in Fig. 18. GAP polymers of increasing structural complexity have been examined, such as branched chain azido polymers formed from the linking of PECH with poly (epichlorohydrin/alkylene oxide) copolymer (PEEC) followed by azidation [64]. It is proposed that in this way one can reduce reliance on multifunctional isocyanates and polyol additives in the subsequent formulations. Indeed, methodologies are emerging in which some proportion of the pendant azides of GAP are replaced by other groups such as dinitrobenzyl groups [65].
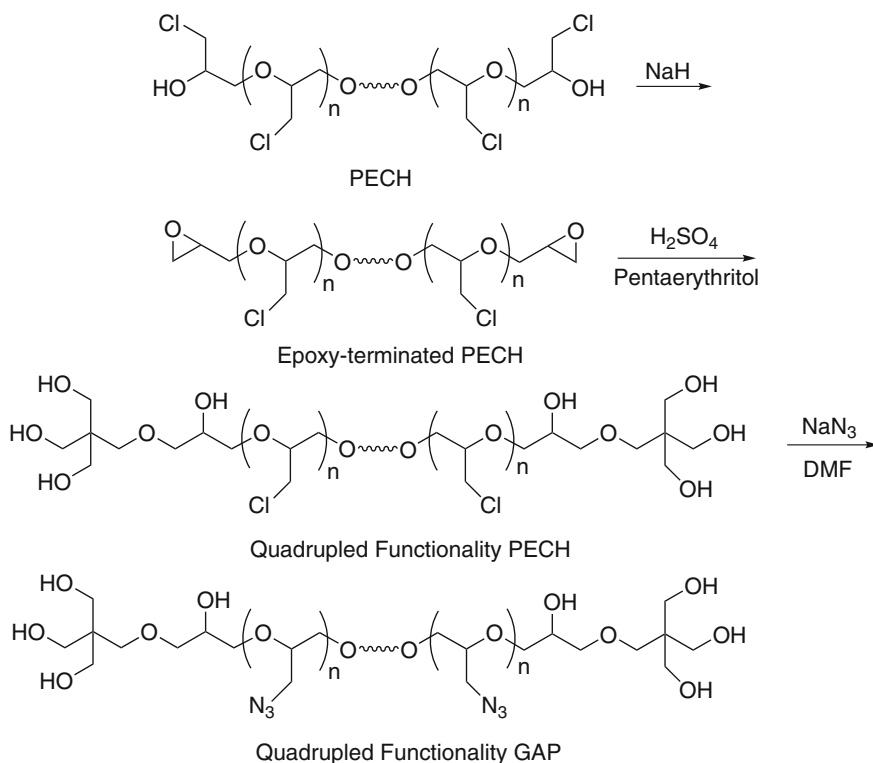
Fig. 18 Synthesis of GAP of increased functionality from poly(epichlorohydrin) per Ampleman

5.5   Other Oxirane-Based Energetic Polymers

While GAP and PGN are the most extensively explored of energetic oxirane-based polymers, other materials have also been investigated. Kim et al. describe the preparation of poly(2-nitratoethyl oxirane) ("M-PGN"), which can be considered as PGN with an added pendent methylene ($-CH_2-$) group [66]. The monomer is produced in a method analogous to that used by Highsmith for the synthesis of glyn [42, 43]. Nitric acid is added to a mixture of 1,2,4-butanetriol in methylene chloride in an ratio such that predominantly 1,4-dinitrato-2-butanol is formed. Polymerization of the monomer with 1,4-BDO and BF_3 yield the desired polymer as shown in Fig. 19. Alternately, the monomer can be produced by nitration of 3-butene-1-ol with acetyl nitrate followed by epoxide formation with m-chloroperoxybenzoic acid [67]. This material was investigated as a proposed solution to the problem of the PGN "decure" reaction in propellants formed with aliphatic polyisocyanates. The added methylene groups serve to reduce the acidity of the hydrogen atoms beta to the terminal nitrato moiety as well as to reduce their spatial proximity to the nearest urethane nitrogen atom. The material was made with a molecular weight of 1800–2400 g/mol, the T_g is −43.0 °C and the material appears to be stable in urethane-based formulations. The additional methylene group should theoretically diminish the performance relative to PGN, although many of the properties such as density and heat of formation are not known at this time.

Kim et al. have described several other glycidol-based monomers and their corresponding polymers, including dinitropropyl glycidyl carbonate [68] and glycidyl dinitropropyl formal [69, 70]. The syntheses and polymerizations are conducted as shown in Fig. 20. The researchers at Agency for Defense Development in South Korea have additionally investigated glycidol-based monomers with pendant dinitroazetidine groups [71]. The properties of the polymer of not yet been described.

Kurt Baum of Fluorochem in Azusa, CA described the synthesis of polymers of significantly higher energy content by directly alkylating dinitropropanol and
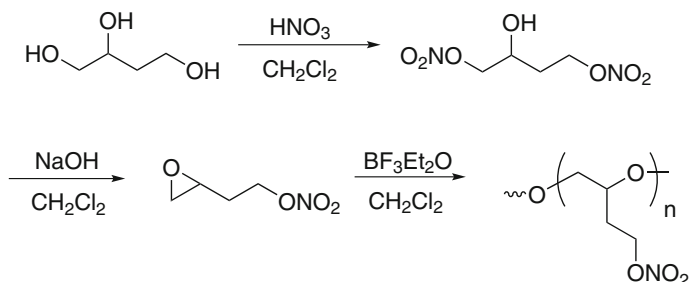
Fig. 19   Synthesis and polymerization of 2-nitratoethyl oxirane to "M-PGN"
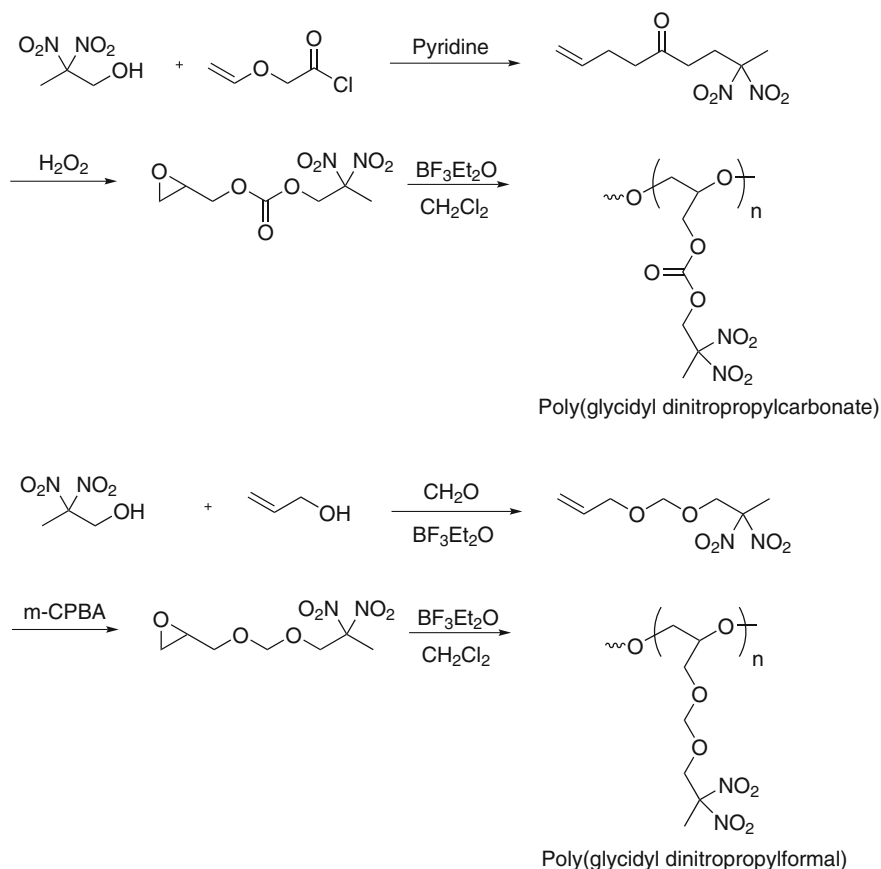
Fig. 20 Synthesis and polymerization of poly(glycidyl dinitropropylcarbonate) and poly(glycidyl dinitropropylformal)

trinitroethanol with allyl triflate and then converting it to the corresponding oxirane for polymerization as shown in Fig. 21 [72]. Conversion of the allyl alcohol to the triflate permits alkylation under neutral conditions, which helps to avoid deformylation of the 2,2-dinitropropanol/2,2,2-trinitropropanol during the reaction. Polymerization of the materials with various di- and tri-functional initiators has resulted in materials with theoretical MW's of up to 12,000 g/mol. The properties of the polymers are shown in Table 7. These polymers have been subjected to only preliminary gumstock testing with polyisocyanates and will require more investigation before their utilities as energetic binders are truly known.
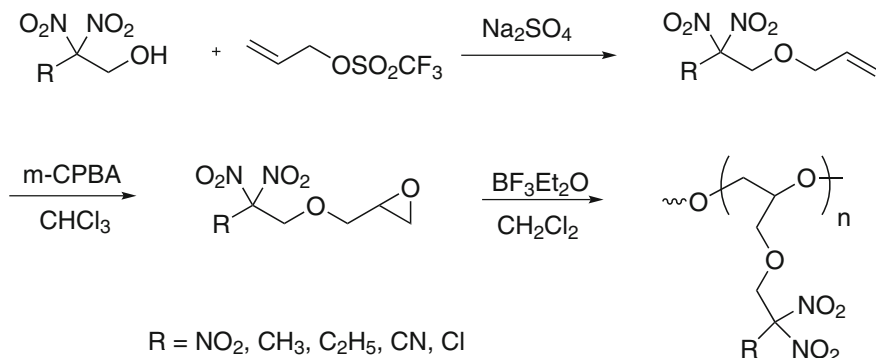
Fig. 21 Synthesis of new high-energy oxirane-based polymers based on dinitropropanol (PGDNP) and trinitroethanol (PGTNE) among others

Table 7 Properties of PGTNE versus RDX standard

Product	PGTNE	RDX
Impact (kg-cm)	140	49
Friction (psi @ drop angle °, threshold)	>100@90°	1200@90°
ESD (J @ 5 kV (threshold)	>1.0	0.38
Tg (°C)	−19	n/a
DSC exotherm onset (°C)	156	n/a

6 Oxetane-Based Energetic Polymers

Oxetane polymers are those that are derived from the ring-opening polymerization of 4-atom cyclic ethers (1,3-propylene oxides). Oxetane monomers are generally significantly less reactive than oxiranes due to the lower amount of ring-strain contained in the four-membered ring. Oxetane polymers are produced from their monomeric units by the same cationic ring-opening polymerization methods as are used for oxirane polymers, and many of the considerations are identical. As with the oxirane systems, the activated monomer (AM1) method is still desired for controlled growth of the polymer chains into materials with low polydispersity and reproducible molecular weights.

6.1 Ring-Substituted Oxetanes

Some of the earliest work on energetic oxetanes involved monomers with energic moieties attached directly to the ring structure. Several of these structures are shown in Fig. 22. 3-Difluoramino-fluoroaminooxetane was prepared in 1967 by treatment of 3-methylene oxetane with tetrafluorohydrazine in Freon-113 [73].
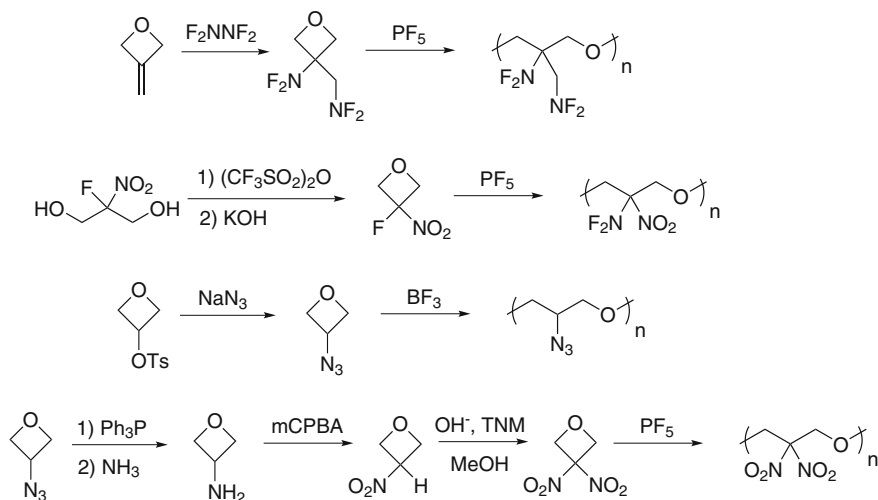
Fig. 22 Oxetanes containing explosophores directly attached to the 3-position of the ring-structure

Polymerization was achieved using phosphorous pentafluoride (PF$_5$) yielding nearly difunctional polymers with molecular weights up to 9783 g/mol, which were reported as strong elastic materials. Chain-extension of the polymer in methylene chloride with toluene diisocyante (TDI) and ferric acetylacetonate (Fe(acac)$_3$) was also described. Baum described synthesis and polymerization of 3-fluoro-3-nitrooxetane with PF$_5$ as the catalyst (BF$_3$ was not sufficiently activating to cause polymerization) with a density of 1.59 g/cc, MW $\sim$ 2500 g/mol and a melting point of 234 °C [74]. The synthesis of 3-hydroxyoxetane was described by various methods [75] and then was used to make several energetic monomers and polymers [76]. 3-Azidooxetane was synthesized by displacement of 3-oxetyl tosylate with sodium azide in a polar organic solvent, and its polymerization with BF$_3$ to MW $\sim$ 3000–3100 g/mol and subsequent reaction with TDI resulted in rubbery polymers [77].

Much more recently a particularly interesting poly(oxetane) was described by Willer et al. with the synthesis of poly(3-nitratooxetane) (PNO) [78]. Addition of 3-hydroxyoxetane to a mixture of acetic anhydride and100% HNO$_3$ (acetyl nitrate) in methylene chloride affords nitration conditions that are gentle enough that the ring is not opened during the reaction. Polymerization proceeds using standard conditions as shown in Fig. 23.

PNO is attractive in that it is extremely energy dense; it is in fact a structural isomer of PGN and can be synthesized to give a polymer with almost identical properties (Table 8). While PNO contains primary terminal hydroxyl groups (vs. secondary in PGN) it contains secondary nitrate esters (vs. primary in PGN). The potential promise of PNO over PGN is that it is not likely to suffer the issue of polyurethane "de-cure" and so no further chemical modification need be

Fig. 23 Synthesis and
polymerization of
3-nitratooxetane to PNO
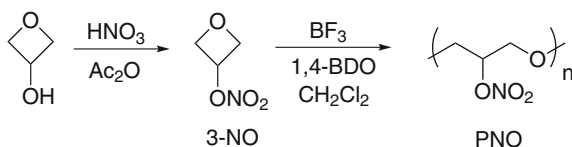
Table 8 Properties of PNO
polymer compared to PGN
polymer

	PNO	PGN
ΔHf (kcal/mol)	−58 to −72	−68
Density (g/cc)	1.44	1.45
DSC peak exotherm (°C)	210	215
Molecular weight	25,000	3000

made to the polymer prior to curing with polyfunctional isocyanates [79]. It is
not clear at this time whether the benefits of PNO will ultimately result in its
replacement of PGN as an energetic binder for use in high energy cast-cure
formulations.

6.2   Methyl-Substituted Oxetanes

A variety of energetic polymers derived from methyl-substituted oxirane monomers
were developed by G.E. Manser in the early 1980s. The first polymers were syn-
thesized from oxetanes functionalized in the 3-position with azidomethyl groups, as
in 3,3-bis(asidomethyl)oxetane (BAMO) and 3-azidomethyl-3-methyl oxetane
(AMMO) (Fig. 24) [80]. Other substituted oxetanes quickly followed, including
3,3-bis(methylnitraminomethyl)oxetane   (BMNAMO)   and   3-methyl-3-
nitraminomethyl oxetane (MNAMMO) [81], nitratoalkyl oxetanes such as 3,3-bis
(nitratomethyl) oxetane (BNMO) and 3-nitratomethyl-3-methyl oxetane (NMMO),
[82] difluoroaminomethyl oxetanes 3,3-bis(difluoroaminomethyl) oxetane
(BIS-NF$_2$-oxetane) and 3-difluoroaminomethyl-3-methyl oxetane (MONO-NF$_2$-
oxetane). Even oxetanes of mixed functionalities were explored as in the case of
3-azidomethyl-3-nitratomethyl oxetane [83]. The synthesis of the monomers
BAMO, AMMO, BMNAMO, and MNAMMO involve substitution of halide or
tosylate groups from the desired pendant methyl position(s) of the oxetane by a
nucleophilic salt of the explosophore. In the case of BAMO and AMMO, the
reaction with sodium azide often necessitated the use of polar aprotic solvents such
DMF or DMSO which are difficult to remove from the final polymer. Alternatively,
it was found that the azidation could be conducted with a solution of sodium azide
in water with the aid of a phase-transfer catalyst [84]. The nitrate-ester monomers
BNMO and NMMO were synthesized from the hydroxymethyl-substituted oxe-
tanes by nitration with acetyl nitrate in methylene chloride. The difluoramino
monomers were produced by fluorination of the ethyl carbamates of the
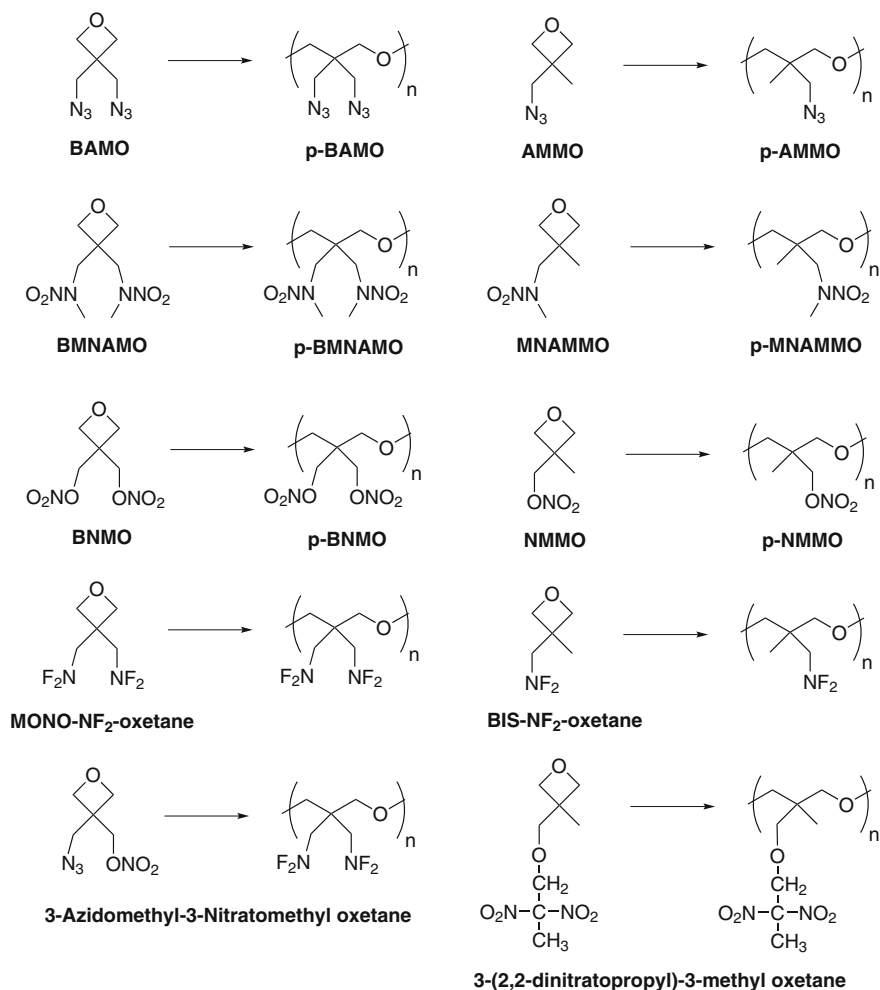
Fig. 24 Methyl-substituted oxetanes and their corresponding polymers

corresponding aminomethyl oxetanes with 10% fluorine gas in nitrogen. Generally, the cationic polymerizations were conducted in the presence of catalytic boron trifluoride and an initiator such as 1,4-butanediol in methylene chloride. It was discovered that in some cases the use of catalytic boron trifluoride tetrahydrofuranate ($BF_3 \cdot THF$) produced polymers with improved functionalities and lower polydispersities. Properties of some of the more commonly used oxetane polymers are listed in Table 9 [85]. In all cases the symmetrically substituted monomers are crystalline as are their polymers, while the unsymmetric monomers and polymers tend to be either liquids or waxes. This led to their extensive use as hard and soft blocks in energetic thermoplastic elastomers (ETPE's).

Table 9 Properties of common oxetane polymers

Material	Density	ΔH_f (kcal/mol)	Formula
AMMO	1.17	34.04	$C_5H_9N_3O_1$
BAMO	1.30	103.6	$C_5H_8N_6O_1$
BNMO	1.4	−89.82	$C_5H_8N_2O_7$
NMMO	1.31	−79.99	$C_5H_9N_1O_4$

6.3 Energetic Thermoplastic Elastomers (ETPE's)

Elastomers are polymeric materials which respond to an applied force with an immediate, linear and reversible response up to high strain [86]. Typical elastomers consist of relatively high molecular weight polymeric chains which are capable of uncoiling chain segments into more linear conformations when force is applied; chemical cross-linking prevents viscous flow at high extensions and maintains the shape of the material upon removal of the applied force. Thermoplastic elastomers (TPE's) are a subset of elastomers in which the chemical cross-links present in classic elastomers are replaced by physical cross-links in the form of crystalline segments ("hard blocks") within the elastomeric polymer chain. Thus polymers which are TPE's are "block copolymers" consisting of repeating segments of crystalline polymer ("hard block") alternating with repeating segments of elastomeric polymer ("soft block") (Fig. 25). The crystalline segments provide the physical crosslink of chains to maintain the shape of the polymer; when the polymer is heated above the melting point or glass transition (T_m or T_g) of the hard block this physical cross-link disappears and the material can then flow and change shape.
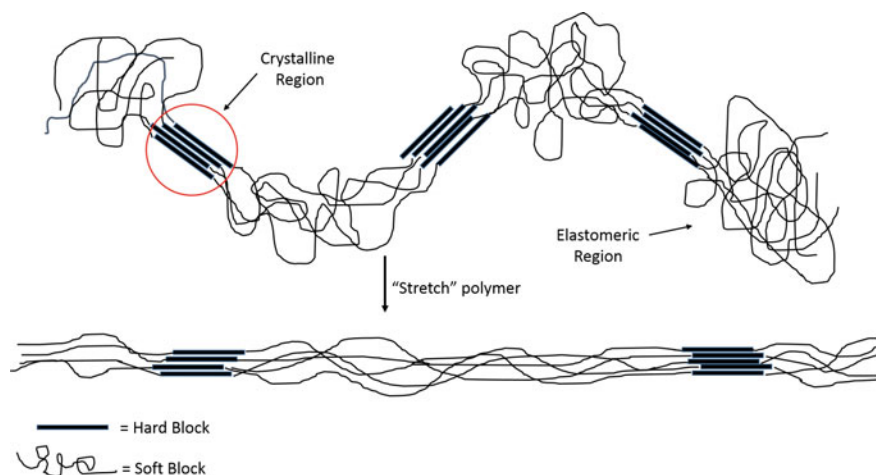
Fig. 25 A much simplified representation of thermoplastic elastomers with crystalline regions formed by hard blocks and elastomeric regions formed by soft blocks. Upon stretching the elastomeric regions uncoil until the physical cross-links of the crystalline regions prevent further extension. Heating above the melting point of the hard blocks causes the crystalline regions to melt and the material to flow and change shape

This makes TPE's amenable to several industrial processing techniques such as extrusion, injection molding, compression molding, blow molding, and thermo-forming. Their properties can be adjusted by the addition of plasticizers and other agents. Propellant and explosive formulations using TPE's such as Kraton (polysterene-polybutadiene-polystyrene), Estane (polyurethane-based TPU), and polylactone-polybutadiene-polylactone were proposed and investigated as binders in composite rocket propellants as well as explosives [87]. The potential advantages of TPE's over the more conventional cast-cure chemical crosslinking method of making propellants and explosives formulations are numerous; for example, chemically cross-linked elastomers must be cast within a relatively short period of time after the addition of the curative (or catalyst); this period of time is known as the "pot-life" of the formulation. Exceeding the pot-life before casting will result in curing within the mixing bowl. Also, cross-linked elastomers cannot be easily removed from an end-item, making disposal difficult. TPE's on the other hand can be pre-made and then processed on demand and in theory can be removed from end-items with simple application of heat to melt the polymer.

Energetic thermoplastic elastomers (ETPE's) are simply a subset of TPE's in which the hard block, the soft block or both blocks are comprised of energetic polymers such that they can be utilized in and contribute to the performance of energetic formulations as ingredients in gun propellants, explosives, gas generants, combustible cartridge cases, etc. Desirable properties of an ETPE include: melting point above 60 °C (to allow for extended storage at elevated temperatures) and below 120 °C (practical and safe limit for processing of many propellant formulation ingredients), thermal stability well above 120 °C, good mechanical properties at high solids loadings (90% w/w), and glass transition temperature below −40 °C.

The properties of energetic oxetanes provided an excellent source of building blocks for the synthesis of ETPE's. The thermoplastic properties of a TPE (such as melting point) are dominated by the glassy "hard block" domains. Poly(BAMO) was a natural choice as an energetic hard block segment as it has a melting point of approximately 83 °C, while most of the unsymmetrical oxiranes and oxetanes such as GAP, PGN, p-AMMO and p-NMMO are elastomeric providing suitable energetic "soft block" segments.

Manser first described the co-polymerization of energetic oxetanes with tetrahydrofuran (THF) thereby forming random elastomeric copolymers such as BAMO/THF and AMMO/THF in an effort to reduce viscosity during formulation and reduce the crystallinity of the polymers [88]. The realization of energetic thermoplastic elastomers necessitated greater control of the polymerization conditions resulting in the controlled formation of functional blocks within the polymer chain. Many of the approaches focused on the creation of A-B-A block co-polymers, in which A represents a "hard block" segment and B represents a "soft block" segment.

Two initial main strategies for the formation of A-B-A type ETPE's were pursued. The first involves the formation of blocks during polymerization by the
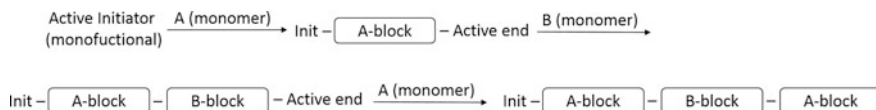
Fig. 26 Formation of A-B-A block copolymers by sequential addition of monomers

sequential addition of monomers to the reaction flask in a "living polymerization" approach. For example, the A monomer may be reacted with an initiator in the presence of catalyst to form an A block by cationic polymerization and allowed to continue until the concentration of unreacted A monomer is substantially low. Then B monomer is then added to the flask, being initiated from the active end of the polymeric A block. When monomer B is consumed, additional monomer A is added to polymerize from the active end of the B block. Alternatively a difunctional initiator is utilized in the polymerization of monomer B to form a difunctional B block, from which block of A could then be grown from each end at one time (Fig. 26). Through careful selection of reaction conditions, scientists at Thiokol corporation did demonstrate excellent control over both molecular weight and functionality of ETPE's formed in this manner, and vast improvements over previous attempts using this methodology were realized [89]. Even more complex AnB star polymers were synthesized using these methods [90]. Ultimately, however, researchers quickly found that a block linking approach afforded materials with much improved mechanical properties.

The block linking approach to A-B-A ETPE's involves prior polymerization of each monomer separately to a predetermined molecular weight followed by isolation of the discrete difunctional A and B polymers (Fig. 27). These polymers are then subsequently linked together with a difunctional isocyanate such as toluene diisocyanate (TDI). TDI is a preferred linker material as the isocyanate moiety in the 4-position is significantly more reactive (approximately 26 times more reactive) than the isocyanate moiety in the 2-position, which is somewhat sterically hindered by the presence of the ortho-situated methyl group. This allows encapping of the polymer without substantial undesired chain extention reactions occurring. Both the A and B blocks are capped in this manner with TDI and then block formation is achieved by adding the A-capped and B-capped polymers together with a short reactive linker such as 1,4-butanediol [91]. Alternatively, just a monofunctional A block can be prepared and capped with TDI; subsequent addition of the difunctional B block results in A-B-A polymers of excellent quality [92].

Many different energetic ETPE's have been made and studied over the years by many different methods. For example, a study of the theoretical performance of several BAMO-based ETPE's as binders in both gun propellant as well as explosive formulations was conducted [93]. The explosive performance calculations were performed with 85% solids loading of HMX; the polymers consisted of
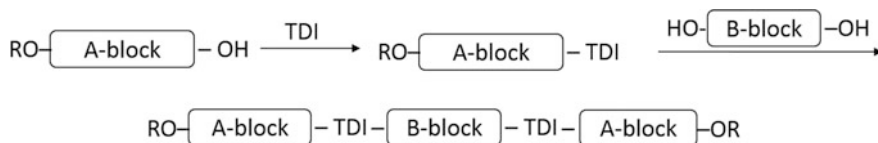
Fig. 27 Block linking approach to A-B-A polymers

Table 10 Explosive calculated performance for various ETPE-based formulations at 85% HMX loading

Composition	Solids (%)	Density (g/cc)	P_{cj} (GPa)	V_{cj} (km/s)	ΔE @ V/V_o = 6.5 (KJ/cc)
PAX-2A	85	1.780	31.71	8.428	7.87
BAMO-AMMO/HMX	85	1.751	29.71	8.308	7.74
BAMO-GAP/HMX	85	1.779	31.81	8.539	8.15
CE-BAMO/HMX	85	1.779	32.02	8.549	8.22
BAMO-NMMO/HMX	85	1.783	31.46	8.488	8.09
BAMO-PGN/HMX	85	1.813	33.36	8.704	8.44

25% BAMO and 75% various soft blocks, as well as BAMO polymer which has been chain-extended by reaction with TDI (CE-BAMO). The results are shown in Table 10. Each of the ETPE-based formulations outperforms PAX-2A with the BAMO-PGN\HMX formulation having the highest calculated performance.

Similar calculations were conducted to evaluate gun propellants containing the same ETPE's. RDX was used as the energetic fill at 75% solids loadings. The propellants were processed first in a mixer, then were RAM extruded and roll milled. The results are shown in Table 11. The propellants with CE-BAMO and BAMO-GAP have some of the highest impetus values while maintaining relatively cool flame temperatures due to their high nitrogen content. The BAMO-PGN exhibits high impetus but higher flame temperatures due to the additional oxygen content in this polymer.

Table 11 Gun propellant calculated performance for various ETPE-based formulations with 85% RDX

Composition	Solids (%)	Density (g/cc)	I (J/g)	T_f (K)	Gamma
JA2	0	1.57	1151	3423	1.227
BAMO-AMMO/RDX	75	1.604	1167	2776	1.275
BAMO-GAP/RDX	75	1.644	1289	3229	1.264
CE-BAMO/RDX	75	1.643	1320	3287	1.266
BAMO-NMMO/RDX	75	1.649	1258	3180	1.259
BAMO-PGN/RDX	75	1.692	1307	3538	1.245

Significant work has been conducted in the formulation of layered gun propellants utilizing BAMO/NMMO copolymer (BN7) which is prepared by sequential addition of BAMO and NMMO to give a triblock copolymer of ABA architecture [94]. In the layered configuration, the inner layer is designed to burn quickly and the outer layer slowly for a more even pressure profile over time. The propellant was processed, extruded and then roll milled. The measured performance was considerably improved over JA2 propellant.

Another approach to ETPE's was adopted by the Defence Research Establishment of Valcartier (DREV). The ETPE's were formed by chain extending glycidyl azide polymer (GAP) with 4,4′-methylenebis-phenyl isocyanate (MDI) [95]. In this case the isocyanate linker itself functions as the hard block in the ETPE. This approach was somewhat problematic. Because the MDI has a very high melting point ($\sim$200 °C) which is within a few degrees of the onset temperature of the GAP polymer, the resulting "ETPE" could not actually be melted safely. In addition, the relatively low molecular weight of the MDI hard block severely limited the molecular weight of the GAP that could be used. In practice, use of GAP with MW = 2000 g/mol (10% hard block) did not result in adequate hardness and mechanical properties suffered, while GAP of 500 g/mol (40% hard block) was better with regard to mechanical properties, but the energy levels were lower than desired. In a compromise of energy versus mechanical properties, a GAP of MW = 1000 g/mol was used. Because the polymer could not be melted, it was dissolved in ethyl acetate and formulated with plasticizer and other HELOVA gun propellant ingredients in a sigma-blade mixer.

The GAP/MDI ETPE's were also used in explosive formulations [96]. Because these particular ETPE's cannot be safely melted, they were dissolved into TNT-based melt-pourable formulations. The rubbery polymer imparted some elasticity to the melt-pour mixtures. While the mix viscosities were increased significantly (up to 5X at 20% loading) the mechanical properties of the cast final products were also significantly improved. Detonation velocities of the final formulations were between 94–99% Comp-B, while the detonation pressures were lower at 81–95% Comp-B. The shock sensitivity (as measured by GAP Test results) in Octol formulations was improved significantly at up to 20% loading of ETPE (increase in peak pressure from 8.06GPa for Octol to 11.12GPa for 20% ETPE containing Octol). Some reduction in bullet impact reaction was observed as well, suggesting lower vulnerability of the ETPE-containing formulations. More recent efforts have focused on the addition of nitramines to increase the performance of the melt-case materials. Performance results (from plate dent tests), shock sensitivity (by card GAP testing) and bullet impact test results are shown in Table 12.

DREV developed a series poly(α-azidomethyl-α-methyl-β-propiolactone) (PAMMPL) polyester based ETPE's [97]. PAMMPL is an energetic polyester hard block. Hydroxyterminated GAP (MW = 2000 g/mol) was activated by reaction with n-butyl lithium and used to initiate the polymerization of a halogenated monomer (precursor to PAMMPL) forming the halogenated block copolymer. This block copolymer was then dissolved in DMF and reacted with sodium azide to give the final PAMMPL-GAP-PAMMPL (Fig. 28). The polymer was not quite elastic

Table 12 Performance, shock sensitivity and bullet impact test results for ETPE-containing melt pours

	Nitramine content (%)	ρ Exp (g/cc)	VoD (m/s)	Dent (cm)	Relative performance (% Comp B)	# Cards	Bullet impact test results (mock 105 mm shells)		
							Sample 1	Sample 2	Sample 3
XV-XRT 1	75	1.70	8107	0.820	104.9	204	Type II–III	No reaction	No reaction
XV-XRT 1	70	1.76	8160	0.841	107.5	172	No reaction	No reaction	Type II–III
XV-XRT 1	69.5	1.73	8064	0.826	105.6	167	Burn	Burn	Burn
Comp-B	60	1.69	7885	0.782	100	216	Type 1–II	Type I–II	Type I–II
XRT 10%	54	1.64	7689	0.714	91.3	167	No reaction	No reaction	Burn
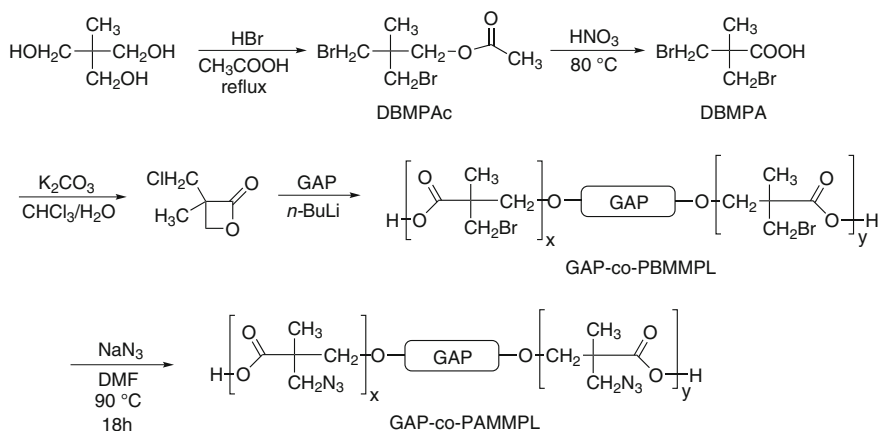
Fig. 28 Synthesis of GAP-co-PAMMPL polymer

enough however; efforts to use higher molecular weight GAP (50,000–70000 g/mol) resulted in polymers which were rubbery, but exceedingly viscous [98]. Further tailoring of the molecular weight of the GAP block is necessary to find the balance between mechanical properties and mix viscosity.

Triazole-Cure Polymers

Triazole polymers are synthesized by 1,3-dipolar cycloaddition of azides with terminal alkynes via "Click Chemistry", so called owing to the extremely high yield and efficiency of the reaction between an organic azide group and a properly chosen terminal organic alkyne [99]. This type of crosslinking reaction has been suggested as a possible replacement for the more standard poly(urethane) cure systems more commonly used in cast-cure explosive and propellant formulations in an effort to increase the energy content (burn rate) as well as avoid the use of toxic isocyanates during formulation. Randomly crosslinked 1,2,3-triazole-polymers formed by the reaction of azide containing polymers and ETPE's such as BAMO/AMMO, BAMO/NMMO, and GAP with short multifunctional alkynes were first studied as binder systems for explosive formulations [100]. This random crosslinking approach is not suitable for use in rocket propellants, where the mechanical properties requirements are much higher, necessitating more control over the crosslink density and chain length between triazole groups. Significant efforts have been conducted under the guidance of Office of Naval Research (ONR) to create many different combinations of alkyne-terminated as well as azide-terminated small molecules, oligomers, and polymers in order to study the formation of well-defined 1,2,3-triazole binder systems (Fig. 29) [101]. The degree of cross-linking can be controlled by the use of polyfunctional acetylenes and/or azides. This is a promising technology that will likely be explored further in the future as environmental and toxicity issues are given more consideration in the development of new propellant and explosive formulations.
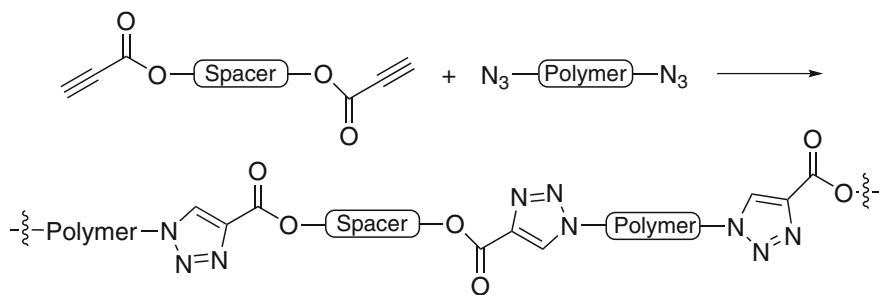
Fig. 29 Generalized scheme for the formation of triazole-cured polymeric binders from terminal acetylenes and terminal azides

Conclusions and Future Outlook

The field of energetic binders has undergone significant changes in the past 50+ years. New and innovative approaches to and uses for these materials have emerged. Energetic binders offer improved performance, reduced shock sensitivity, improved opportunities for reclamation and recycling through the lifecycle of a material, as well as a potentially more environmentally sustainable footprint over traditional binder materials. As research continues one of the main challenges will be to reduce the cost of energetic binders such that they are more competitive with traditional workhorse materials such as nitrocellulose while still delivering their added advantages.

References

1. Meyer R, Kohler J, Homburg A (2007) Explosives: sixth, Completely revised edn. Wiley-VCH, Weinheim
2. Agrawal JP (2010) High energy materials: propellants, explosives and pyrotechnics. Wiley-VCH, Weinheim
3. Arendale WF (1969) Chemistry of propellants based on chemically crosslinked binders. In: Boyars C, Klager K (eds) Chapter 1 in propellants manufacture, hazards, and testing. Advances in chemistry, American Chemical Society, Washington, D.C
4. (a) Davis TL (1943) The chemistry of powder and explosives. Angriff Press, Las Vegas, NV (b) Urbanski T (1964) Chemistry and technology of explosives, vol 4. Pergamon Press, Chapter 12, pp 339–353
5. Steinberger R, Drechsel PD (1969) Manufacture of cast double-base propellant. In: Boyars C et al (eds) Chapter 1 in propellants manufacture, hazards and testing. Advances in chemistry, American Chemical Society, Washington, DC, 1969
6. Steinberger R, Drechsel PD (1969) Nitrocellulose plastisol propellants. In: Boyars C et al (eds) Chapter 2 in propellants manufacture, hazards and testing. Advances in chemistry, American Chemical Society, Washington, DC
7. (a) Burrows LA, Filbert W (1938) Process for preparing polyvinyl nitrate, US Patent #2,118,487. (b) Urbanski T (1964) Chemistry and technology of explosives, vol 4. Pergamon Press, Chapter 12, pp 413–419. (c) Evans RR, Mayer AG, Scott J (1948)

Polyvinyl nitrate—experimental manufacture and evaluation as a propellant ingredient. U.S. Naval Powder Factory, Indian Head, MD Technical Report No. 22

8. (a) Durgapal UC, Dutta PK, Mishra SC, Pant J (1995) "Investigations on polyvinyl nitrate as a high energetic material", vol 20. pp 64–69. (b) Deans SAV, Nicholls RVV (1949) Polyvinyl nitrate. Can J Res 27(Section B):705–715. (c) Kaye SM (1978) Encyclopedia of explosives and related items, PATR 2700, vol 8. US Army Armament Research and Development Command, Dover, NJ, pp 356–358

9. Kaye SM (1978) Encyclopedia of explosives and related items, PATR 2700, vol 8. US Army Armament Research and Development Command, Dover, NJ, pp N140–N157

10. (a) Finger M, Haryward EJ, Archibald P (1969) Multiphase extrudable explosives containing cyclotrimethylenetrinitramine or cyclotetramethylenetetranitramine. US Patent #3,480,490. (b) Stott BA (1967) Castable explosive compositions based on dinitropropylacrylate and HMX. U.S. Naval Ordnance Test Station (NOTS) Technical Publication 4387. (c) Stott BA, Koch LE (1992) High Energy cast explosives based on dinitropropylacrylate. US Patent #5,092,944

11. (a) Hagel R, Redecker K (1981) Polymers obtained from polynitroaromatic compounds. US Patent #4,250,294. (b) Redecker KH, Hagel R (1987) Polynitropolyphenylene, a high-temperature resistant, non-crystalline explosive. Propellants Explos Pyrotech 12:196–201

12. Day RW, Hani R (1991) Process for the preparation of nitramine-containing homopolymers and co-polymers. US Patent #5,008,443

13. Legare TF, Rosher, R (1974) Alpha-hydro-gamma-hydroxy poly(oxy-methylenenitroamino) polymer comfort. US Patent #3,808,276

14. Day RW, Hani R (1994) Nitramine-containing polyether polymers and a process for the preparation thereof. US Patent #5,319,068

15. (a) Allcock HR (1975) Preparation of Phosphazene polymers. US Patent #3,888,800. (b) Hergenrother WL, Halasa AF (1980) Polyphosphazene copolymers containing nitroalkyl substituents. US Patent #4,182,835 (c) Hergenrother WL, Halasa AF (1980) Polyphosphazene copolymers containing substituents derived from substituted 2-nitroethanols. US Patent #4,221,900. (d) Hartwell JA, Hutchens DE, Junior KE, Byrd JD (1998) Method of internally insulating a propellant combustion chamber. US Patent #5,762,746

16. Allcock HR, Maher AE, Ambler CM (2003) Side group exchange in poly(organophosphazenes) with fluoroalkoxy substituents. Macromolecules 3:5566–5572

17. (a) Golding P, Trussell SJ (2004) Energetic polyphosphazenes—a new category of binders for energetic formulations. 2004 insensitive munitions and energetic materials technology symposium, San Francisco, CA, 14–17 Nov, NDIA. (b) Golding P, Trussell J, Colclough E, Hamid J (2012) Energetic polyphosphazenes. US Patent #8,268,959 B2

18. Arendale WF (1969) Chemistry of propellants based on chemically crosslinked binders. In: Boyars C et al (eds) Chapter 4 in propellants manufacture, hazards and testing. Advances in chemistry, American Chemical Society, Washington, DC

19. Mastrolia EJ, Klager K (1969) Solid propellants based on polybutadiene binders. In: Boyars C et al (eds) Chapter 6 in propellants manufacture, hazards and testing. Advances in chemistry, American Chemical Society, Washington, DC

20. (a) Hunley JD (1999) The history of solid-propellant rocketry: what we do and do not know. In: Proceedings of the AIAA, ASME, SAE, ASEE Joint propulsion conference and exhibit, Los Angeles, CA, 20–24 June. (b) Cohen MS (1966) Advanced binders for solid propellants—a review. In: Advanced propellant chemistry, Advances in chemistry series 54, American Chemical Society, Washington DC

21. Oberth AE, Bruenner RS (1969) Polyurethane-based propellants. In: Boyars C et al (eds) Chapter 5 in propellants manufacture, hazards and testing. Advances in chemistry, American Chemical Society, Washington, DC

22. Bennett SJ, Barnes MW, Kolonko KJ (1989) Propellant binder prepared from a PCP/HTPB block copolymer. US Patent #4,853,051

23. Chien JWC, Kohara T, Lillya CP, Sarubbi T, Su B-H, Miller RS (1980) J Polym Sci Part A Polym Chem 18:2723

24. Colclough ME, Paul MC (1996) Nitrated hydroxy-terminated polybutadiene: synthesis and properties. In: Chapter 10 in nitration: ACS symposium series, American Chemical Society, Washington, DC, pp 97–103

25. (a) Consaga JP, Collignon SL (1992) Energetic composites of cyclodextrin nitrate esters and nitrate ester plasticizers. US Patent #5,114,506. (b) Consaga JP, Gill RC (1998) Synthesis and use of cyclodextrin nitrate. In Proceedings of the 29th annual conference of ICT, 5-1 to 5-6

26. Ruebner A, Statton G, Robitelle D, Meyers C, Kosowski B (2000) Cyclodextrin polymer nitrate. 31st annual conference of ICT, 12-1 to 12-10

27. Kaye SM (1978) Encyclopedia of explosives and related items, PATR 2700, vol 8. US Army Armament Research and Development Command, Dover, NJ, pp 61–77

28. Benziger TM (1973) High-energy plastic-bonded explosive. US Patent #3,778,319

29. Indictor N, Brill WF (1965) J Org Chem 30(6):2074

30. Murbach WJ, Fish WR, Van Dolah RW (1953) Polyglycidyl nitrate: part 1, preparation and characterization of glycidyl nitrate. NAVORD Report 2028, Part 1 (NOTS 685), May 6, 1953

31. Metitner JG, Thelen CJ, Murbach WJ, Van Dolah RW (1953) Polyglycidyl nitrate: part 1, preperation and characterization of polyglycidyl nitrate. NAVORD Report 2028, Part 2 (NOTS 686), May 7, 1953

32. Ingham JD, Nichols PL Jr (1957) High performance PGN-polyurethane propellants. Jet Propulsion Laboratory Publication No. 93

33. Cumming A (1995) New directions in energetic materials. J Def Sci 1(3):319

34. Willer RL, Day RS, Stern AG (1992) Process for producing improved poly(glycidyl nitrate). US Patent #5,120,827

35. Penczek S, Kubisa P, Szymanski R (1986) Makromol Chem Macrom Symp 3:203–220

36. Mojtania M, Kubisa P, Penczek S (1986) Makromol Chem Macrom Symp 6:201–206

37. Kubisa P (2002) Hyperbranched polyethers by ring-opening polymerization: contribution of activated monomer mechanism. J Polym Sci Part A 41:457–468

38. Paraskos AJ, Sanderson AJ, Cannizzo LF (2004) Polymerization of glycidyl nitrate *via* catalysis with bf3thf: compatibility with the activated monomer (AM) mechanism. In: Insensitive munitions and energetic materials technology symposium, San Francisco, CA, 14–17 Nov, 2004, NDIA

39. Willer RL, Stern AG, Day RS (1995) PolyGlycidyl nitrate plasticizers. US Patent #5,120,827

40. Willer RL, Stern AG, Day RS (1993) Isotactic poly(glycidyl nitrate) and synthesis thereof. US Patent #5,264,596

41. Millar RS, Paul NC, Golding P (1992) Preparation of epoxy nitrates. US Patent #5,136,062

42. Paul NC, Millar RW, Golding P (1992) Preparation of nitratoalkyl-substituted cyclic esters. US Patent #5,145,974

43. Bagg G, Desai H, Leeming WBH, Paul NC, Paterson DH, Swinton PF (1992) Scale-up of polyglycidylnitrate manufacture process development and assessment. In: Proceedings of the American Defense Preparedness Association's joint international symposium on energetic materials technology, 5–7 Oct 1992, Louisiana, USA

44. Stewart MJ (1994) Polymerization of cyclic ethers. US Patent #5,313,000

45. Desai HJ, Cunliffe AV, Lewis T, Millar RW, Paul NC, Stewart MJ (1996) Synthesis of narrow molecular weight α,ω-hydroxy telechelic poly(glycidyl nitrate) and estimation of theoretical heat of explosion. Polymer 37(15):3471–3476

46. Marken CD, Kristofferson CE, Roland MM, Manzara AP, Barnes MW (1977) A low hazard procedure for the laboratory preparation of polynitrate esters. Synthesis 1977:484–485

47. Highsmith TK, Sanderson AJ, Cannizzo LF, Hajik RM (2002) Polymerization of poly(glycidyl nitrate) from high purity glycidyl nitrate synthesized from glycerol. US Patent #6,362,311 B1

48. Cannizzo LF, Hajik RM, Highsmith TK, Sanderson AJ, Martins LJ, Wardle RB (2000) A new low-cost synthesis of PGN. In: Proceeds of the 31st annual conference of ICT, 36-1 to 36-9

49. Highsmith TK, Johnston HE (2005) Continuous process for the production of glycidyl nitrate from glycerin, nitric acid and caustic and conversion of glycidyl nitrate to poly (glycidyl nitrate). US Patent #6,870,061 B2

50. Paul NC, Desai H, Cunliffe AV (1995) An improved polyglyn binder through end group modifications. In: Proceedings of the American Defense Preparedness Association's international symposium on energetic materials technology, 24–27 Sept 1995, Phoenix, AZ, pp 52–60

51. Sanderson AJ, Martins LJ, Dewey MA (2005) Process for making stable cured poly (glycidyl) nitrate and energetic compositions comprising same. US #6,861,501 B1

52. Bunyan PF, Cunliffe AV, Leeming WBH, Marshall EJ, Paul NC (1995) Stability of cured polyglyn and end modified polyglyn. In: Proceedings of the American Defense Preparedness Association's joint international symposium on energetic materials technology, 4–27 Sept 1995, Phoenix, AZ, pp 271–280

53. Bunyan PF, Clements BW, Cunliffe AV, Torry SA, Bull H (1997) Stability studies on end-modified PolyGLYN. In: Insensitive munitions and energetic materials technology symposium, Orlando, FL, 6–9 Oct, NDIA, pp 1–6

54. Paraskos AJ, Dewey MA, Edwards W (2010) One pot procedure for poly(glycidyl nitrate) end modification. US Patent #7,714,078 B2

55. Vandenberg EJ, Woods W (1972) Polyethers containing azidomethyl side chains. US Patent #3,645,917

56. Frankel MB, Grant LR, Flanagan JE (1992) Historical development of glycidyl azide polymer. J Propul Power 8(3):560–563

57. Frankel MB, Flanagan JE (1981) Energetic hydroxy-terminated azido polymer. US Patent #4,268,450

58. Frankel MB, Witucki EF, Woolery DO (1983) Aqueous process for the quantitative conversion of polyepichlorohydrin to glycidyl azide polymer. US Patent #4,379,894

59. Earl RA (1984) Use of polymeric ethylene oxides in the preparation of glycidyl azide polymer. US Patent #4,486,351

60. Provotas A (2000) Energetic polymers and plasticizers for explosive formulations—a review of recent advances. DSTO-TR-0966

61. Ang HG, Pisharath S (2012) Energetic polymers: binders and plasticizers for enhancing performance, 1st edn. Wiley-VCH GmbH & Co, KGaA, Weinheim

62. Chan ML, Roy EM, Turner A (1994) Energetic binder explosive. US Patent #5,316,600

63. Ampleman G (1993) Glycidyl azide polymer. US Patent #5,256,804

64. Ahad E (1994) Improved branched energetic azido polymers. European Patent #0 646,614 A1

65. Tong TH, Nickerson DM (2011) Energetic poly(azidoaminoethers). US Patent #8,008,409

66. Kim JS, Cho JR, Lee KD, Kim JK (2007) 2-nitroethyl oxirane, poly(2-nitratro oxirane) and preparation method thereof. US Patent #7,288,681 B2

67. Kim J, Kim J, Cho R, Kim J (2004) A new energetic polymer: structurally stable PGN prepolymer. In: Insensitive munitions and energetic materials technology symposium, San Francisco, CA, 14–17 Nov, NDIA

68. Kim JS, Cho JR, Lee KD, Park BS (2004) Glycidyl dinitropropyl carbonate and poly (glycidyl dinitropropyl carbonate) and preparation method thereof. US Patent #6,706,849 B2

69. Kim JS, Cho JR, Lee KD, Kim JK (2007) Glycidyl dinitropropyl formal poly(glycidyl dinitropropyl formal) and preparation method thereof. US Patent #7,208,637 B2

70. Kim JS, Cho JR, Lee KD, Kim JK (2008) Glycidyl dinitropropyl formal poly(glycidyl dinitropropyl formal) and preparation method thereof. US Patent #7,427,687 B2

71. Kown Y-H, Kim J-S, Kim H-S (2009) US 2009/0299079 A1 "1-Glycidyl-3,3-dinitroazetidine containing explosive moiety and preparation thereof". US Patent Application

72. Baum K, Lin W-H (2012) Synthesis and polymerization of glycidyl ethers. US Patent #8,318,959 B1
73. Stogryn EL (1967) 3-difluoroaminomethyl-3-difluoroaminooxetane and polymers thereof. US Patent #3,347,801
74. Baum K, Berkowitz PT (1980) 3-fluoro-3-nitrooxetane. US Patent #4,226,777
75. Baum K, Vytautas G, Berkowitz PT (1983) Synthesis of 3-hydroxyoxetane. US Patent #4,395,561
76. Baum K, Berkowitz PT, Grakauskas V, Archibald TG (1983) Synthesis of electron-deficient oxetanes. 3-azidooxetane, 3-nitrooxetane, and 3,3-dinitrooxetane. J Org Chem 48(18):2953–2956
77. Berkowitz PT, Baum K, Grakauskas V (1983) Synthesis and polymerization of 3-azidooxetane. US Patent #4,414,384
78. Willer RL, Baum K, Lin W-H (2011) Synthesis of poly-(3-nitratooxetane. US Patent #8,030,440 B1
79. Willer RL (2009) Calculation of the density and detonation properties of C, H, N, O and F compounds: use in the design and synthesis of new energetic materials. J Mex Chem Soc 53 (3):108–119
80. (a) Manser GE (1983) Cationic polymerization. US Patent #4,393,199. (b) Manser GE (1984) Energetic copolymers and method of making same. US Patent #4,483,978
81. Manser GE, Fletcher RW (1987) Nitramine oxetanes and polyethers formed therefrom. US Patent #4,707,540
82. Manser GE, Hajik RM (1993) Method of synthesizing nitrato alkyl oxetanes. US Patent #5,214,166
83. Manser GE, Malik AA, Archibald TG (1996) 3-azidomethyl-3-nitratomethyloxetane. US Patent #5,489,700
84. Malik AA, Manser GE, Carson RP, Archibald TG (1996) Solvent-free process for the synthesis of energetic oxetane monomers. US Patent #5,523,424
85. Schmidt RD, Manser GE (2001) Heats of formation of energetic oxetane monomers and polymers. In Proceedings of the 32st annual conference of ICT, 140-1 to 140-8
86. Shanks R, Kong I (2012) Thermoplastic elastomers. Adel El-Songbati (ed) InTech Europe
87. (a) Allen HC (1982) Thermoplastic composite rocket propellant. US Patent #4,361,526. (b) Johnson NC, Gill RC, Leahy JF, Gotzmer C, Fillman HT (1990) Melt cast thermoplastic elastomeric plastic bonded explosive. US Patent #4,978,482. (c) Wardle RB, Hinshaw JC (2002) Poly(butadiene)poly(lactone) thermoplastic block polymers, methods of making, and uncured high energy compositions containing same as binders. US Patent #6,350,330
88. Manser GE (1984) Energetic copolymers and method of making same. US Patent #4,483,978
89. Wardle RB, Cannizzo LF, Hamilton SH, Hinshaw JC (1994) Energetic oxetane thermo-plastic elastomer binders. Thiokol Corp., Final Report to the Office of Naval Research Mechanics Division, Contract #N00014-90-C-0264
90. Wardle RB, Edwards WW (1990) Synthesis of ABA triblock polymers and AnB star polymers from cyclic ethers. US Patent #4,952,644
91. Wardle RB (1989) Method of producing thermoplastic elastomers having alternate crystalline structure for use as binders in high-energy compositions. US Patent #4,806,613
92. Wardle RB, Edwards WW, Hinshaw JC (1996) Method of producing thermoplastic elastomers having alternate crystalline structure such as polyoxetane ABA or star block copolymers by a block linking process. US Patent #5,516,854
93. (a) Wallace IA, Braithwaite P, Haaland AC, Rose MR, Wardle RB (1998) Evaluation of a homologous series of high energy oxetane thermoplastic elastomer gun propellants. In: Proceedings of the 29st annual conference of ICT, 87-1 to 87-7. (b) Braithwaite P, Edwards W, Sanderson AJ, Wardle RB (2001) The synthesis and combustion of high energy thermoplastic elastomer binders. In: Proceedings of the 32st annual conference of ICT, 9-1 to 9-7

94. Manning TG, Park D, Chiu D, Klingaman K, Lieb R, Leadore M, Homan B, Liu E, Baughn J, Luoma JA (2006) Development and performance of high energy high performance co-layered gun propellant for future large caliber system. In: NDIA insensitive munitions and energetic materials technology symposium, Bristol, UK, 24–28 April, pp 1–6

95. Ampleman G, Marois A, Desilets S, Beaupre F, Manzara T (1998) Synthesis and production of energetic copolyurethane thermoplastic elastomers based on glycidyl azide polymer. In: Proceedings of the 29th annual conference of ICT, 6-1 to 6-16

96. (a) Brousseau P, Ampleman G, Thiboutot S (2001) New melt-cast explosives based on energetic thermoplastic elastomers. In: Proceedings of the 32st annual conference of ICT, 89-1 to 89-14. (b) Ampleman G, Marois A, Desilets S (2002) Energetic copolyurethane thermoplastic elastomers. US Patent #6,479,614 B1

97. (a) Brousseau P, Ampleman G, hiboutot S, Diaz E, Trudel S (2006) High performance melt-cast plastic-bonded explosives. In: Proceedings of the 37th Annual conference of ICT, 2-1 to 2-15. (b) Beaupre F, Ampleman G, Nicole C, Belancon J-G (2003) Insensitive propellant formulations containing energetic thermoplastic elastomers. US Patent #6,508,894 B1. (c) Ampleman G, Brousseau P, Thiboutot S, Dubois C, Diaz E (2003) Insensitive melt cast explosive compositions containing energetic thermoplastic elastomers. US Patent #6,562,159 B2. (d) Ampleman G, Marois A, Brousseau P, Thiboutot S, Trudel S, Beland P (2012) Preparation of energetic thermoplastic elastomers and their incorporation into greener insensitive melt cast explosives. In: Proceedings of the 43rd annual conference of ICT, 7-1 to 7-15

98. (a) Ampleman G, Brochu S, Desjardins M (2002) Synthesis of energetic polyester thermoplastic elastomers. In: Proceedings of the 33rd annual conference of ICT. (b) Ampleman G, Brochu S, Desjardins M (2001) Synthesis of energetic polyester thermoplastic homopolymers and energetic thermoplastic elastomers formed therefrom. Defence Research Establishment Valcartier, Technical Report, DREV TR 2001–175. (c) Ampleman G, Brochu S (2003) Synthesis of energetic polyester thermoplastic homopolymers and energetic thermoplastic elastomers formed therefrom. US Patent Application #US 2003/0027938 A1

99. (a) Kolb HC, Finn MG, Sharpless KB, Lutz J-F (2001) Click chemistry: diverse chemical function from a few good reactions. Angew Chem Int Ed 40(11):2004–2021. (b) Binder WH, Sachsenhofer R (2008) Polymersome/silica capsules by 'click'-chemistry. Macromol Rapid Comm 29(12–13):1097–1103. (c) Lutz J-F (2007) 1,3-dipolar cycload-ditions of azides and alkynes: a universal ligation tool in polymer and materials science. Angew Chem Int Ed 46(7):1018–1025

100. (a) Manzara AP (1997) Azido polymers having improved burn rate. US Patent #5,681,904. (b) Reed R (2000) Triazole cross-linked polymers. US Patent #6,103,029

101. (a) Wang L, Song Y, Gyanda R, Sakhuja R, Meher NK, Hanci S, Gyanda K, Mathai S, Sabri F, Ciaramitaro DA, Bedford CD, Katritsky AR, Duran RS (2010) Preparation and mechanical properties of crosslinked 1,2,3-triazole polymers as potential propellant binders. J Appl Polym Sci 117:2612–2621. (b) Katritsky AR, Sakhuja R, Huang L, Gyanda R, Wang L, Jackson DC, Ciaramitaro DA, Bedford CD, Duran RS (2010) Effect of filler loading on the mechanical properties of crosslinked 1,2,3-triazole polymers. J Appl Polym Sci 118(1):121–127

Pyrophoric Nanomaterials

Chris Haines, Lauren Morris, Zhaohua Luan and Zac Doorenbos

Abstract Nanomaterials are a relatively untapped resource for energetic materials research and development. This is partly due to the new-fangled nature of nanotechnology, but more so due to a lack of mature processing science for their incorporation into conventional materials. The high surface area of nanomaterials provides the opportunity to realize enhanced reactivity, superior burn rates, and enhanced detonation properties. In addition, particle size effects may also offer an ability to achieve tunable energetic materials. Nanoscale metallic powders are known to be highly pyrophoric, with noble metals being the exception. In addition, we will discuss how mechanically milled metal powders can be made pyrophoric with a minimal amount of processing time. Nanoporous thin films and coatings exhibiting pyrophoricity are also presented. Work is currently ongoing in exploiting the high surface area of three-dimensional foam materials. All of these materials require special handling and storage considerations, which will be discussed briefly.

Keywords Nanomaterials · Pyrophoric · Pyrophoricity · Nanopowder · Mechanical milling · Foams

1 Introduction

Nanotechnology, which involves all of the science and engineering of materials at the molecular level, is a pervasive technology across a wide range of applications including batteries, pharmaceuticals, cosmetics, automotive, sporting goods, and even clothing. So it should be no surprise that these materials have made their way into energetics. The rationale for exploring nanomaterials for energetic applications

C. Haines (✉) · L. Morris · Z. Luan
US Army Armament Research Development and Engineering Center,
Picatinny Arsenal, NJ 07806, USA
e-mail: christopher.d.haines2.civ@mail.mil

Z. Doorenbos
Innovative Materials and Processes, LLC, Rapid City 57702, SD, USA

is pretty straightforward: materials at this length scale can be highly reactive, as well as tunable. The enhanced reactivity is due to their tremendously high surface area, either as discrete particles or as the high volume percent of grain boundaries or void space in bulk materials. The tunability aspect arises from the fact that a material's properties are highly dependent on particle size, or grain size in a bulk material. In addition, there is an added benefit of being able to manipulate the degree of mixing at the nanoscale. By utilizing building blocks that are on the order of tens of nanometers, you can synthesize materials where the length scale of mixing is also on the nanoscale. This minimizes the diffusion distance in multi-component systems, thereby increasing the reactivity. In some cases, materials may become so reactive that they demonstrate pyrophoric behavior.

This chapter will focus on discussing the pyrophoric aspects of nanomaterials, including one dimensional (1-D) (Nanopowders—Sect. 2 and Milled Powders—Sect. 3), two dimensional (2-D) (Coatings/Thin Films—Sect. 4), and three dimensional (3-D) (Foams—Sect. 5) materials. The word pyrophoric originates from the Greek language for "fire-bearing." Webster defines a pyrophoric materials as one that (1) ignites spontaneously (2) emits sparks when scratched or struck especially by steel [1]. Further, OSHA defines a pyrophoric chemical as "a chemical that will ignite spontaneously in air at a temperature of 130 °F (54.4 °C) or below" [2]. There are only a limited number of conventional materials which meet these definitions, namely certain finely divided metallic powders (e.g., lithium, magnesium) or organometallic compounds (such as lithium hydride, diethyl zinc and arsine) [2]. However, as will be presented in the following sections, nanotechnology opens up a new class of pyrophoric materials. This chapter will discuss the synthesis and processing of these materials, as well as some associated applications. Special considerations for safety, storage, handling, and will also be discussed (Safety—Sect. 6); however, a more detailed, systematic guidance on nanomaterial safety considerations is given by Collier [3].

2 Nanoscale Powders

2.1 Introduction

Nanoscale powders (i.e. powders with a primary particle between 1 and 100 nm) have elicited a tremendous amount of research in the past few decades due to their extremely high surface area, which lead to vastly different properties than their macroscale counterparts. This has led to the realization of unique optical, physical, chemical, magnetic, and mechanical properties; to name a few. There seems to be a "sweet spot" in material science for materials with at least one dimension in the nanoscale, a phenomenon where scientists have merely begun to scratch the surface. Nanoscale metal powders have an additional level of interest in the energetics community due to their inherent pyrophoricity [4]; with the exception of noble

metals (e.g., Ag, Au, Pt). At this size scale, the ratio of surface atoms to bulk atoms is very high [5] and leads to enhanced reactivity with oxygen, even at room temperature. It is interesting to note that even tungsten, with the highest melting point (3422 °C) of all the elements on the periodic table, becomes pyrophoric when the particle size is less than 50 nm [4]. This inherent property in nanoscale metals make them an attractive candidate for use in metallized propellants [6], metallized explosives [7], and even infrared countermeasures [8].

Due to the pyrophoric nature of these powders, extreme care has to be taken in handling and storage after synthesis. A common practice is to expose the powders to a small amount of oxygen in a controlled manner either during synthesis, or post-synthesis, such that a nascent oxide shell can be formed as a passivation mechanism. However, if the end use of a particular powder is going to be for combustion, it is important to minimize the percent oxide content as this becomes "dead weight". As the size of a nanoparticle decreases, the volume percent of oxide rises very rapidly, especially as the size approaches 20–30 nm. The reason for this lies in the fact that the nascent oxide shell thickness tends to be constant for each material (i.e. material dependent, not particle size dependent). Therefore, as the volume of the unreacted metal decreases, the volume of the oxide shell is essentially constant. Figure 1 shows how this leads to a very rapid rise in the oxide content as the particle size decreases. The thickness of the oxide shell was set to 4 nm for the purpose of these calculations.

As mentioned previously, most non-noble metals exhibit pyrophoricity at the nanoscale; however, the actual threshold particle size for pyrophoricity varies for each metal and is nearly impossible to measure precisely since most powders have a Gaussian particle size distribution. In general, the higher a metal's affinity for oxygen, the larger the threshold particle size is. Metals with high affinities for oxygen (e.g., Mg, Zr, Al, Ti) start to become pyrophoric well above 100 nm (Mg well above 1 μm), while metals with a lower affinity (e.g., W, Mo, Cu) only exhibit pyrophoricity below 100 nm. In addition, the minimum ignition energy (MIE) for powders at this size scale is highly dependent on particle size. As an example, Bouillard showed that the MIE for a 200 nm aluminum particle is 7 mJ, while the MIE for a 100 nm aluminum particle is 1 mJ [9]. It is assumed that both of these powders contained a nascent oxide shell since they were not inherently pyrophoric.

Fig. 1 Volume percent oxide as a function of particle size assuming 4 nm thick oxide shell
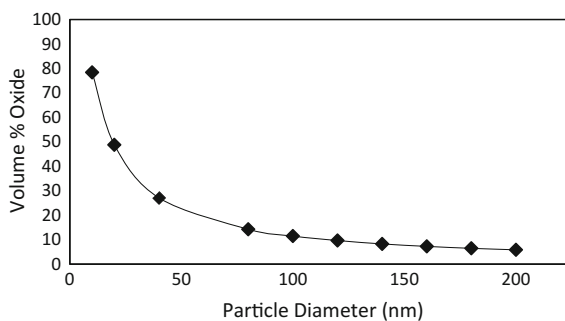
2.2 Aluminum Nanopowder

Nanoscale aluminum has attracted a considerable amount of attention due to its high combustion enthalpy, making it an excellent candidate for usage in propellants, explosives, and pyrotechnics [6–8]. A number of different techniques for production of aluminum nanopowders have been reported including aluminum exploding wire (ALEX) [10], plasma [11, 12], and wet chemistry [13]. ALEX and plasma synthesis have been the two most promising methods due to the associated production rates in comparison with wet chemistry, which has primarily remained at the lab scale. The ALEX process, as the name implies, involves discharging a capacitor across a fine aluminum wire which results in an explosion from the vaporization of the wire. The vapor then condenses into a very fine powder, with the particle size dictated by the processing parameters. This discharge takes place inside of an inert environment reaction chamber as to avoid oxidation of the highly pyrophoric nanopowder. The powders are then transferred to a passivation chamber to slowly introduce oxygen and build up a protective nascent oxide shell. One of the advantages of this process is that nearly all of the electrical energy is directly utilized to explode the wire, thereby resulting in a highly efficient process. This approach can also easily be scaled by using multiple wire feeds and/or increasing wire feed rates. One of the drawbacks is that there is no easy way of doing a controlled in situ passivation procedure. Figure 2 shows a scanning electron microscopy (SEM) image of some aluminum powder made via ALEX.

Inert gas, inductively coupled plasma synthesis (IG-ICP) has been one of the most utilized techniques for nanopowder production due to its capability for high throughput and high purity materials. In this process, a radio frequency (RF) induction plasma torch is used as a heat source. Liquid or powder feedstock is axially injected, with a carrier gas, into the center of the plasma discharge via a water cooled injection probe. A cold quench gas is then used to condense the nanoparticles out of the vapor stream. A schematic of the process is seen in Fig. 3.

Fig. 2 SEM image of aluminum nanopowder made via the ALEX process
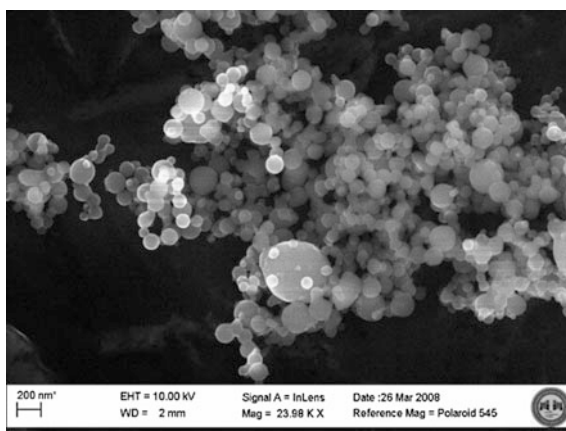
Fig. 3 Schematic of IG-ICP process
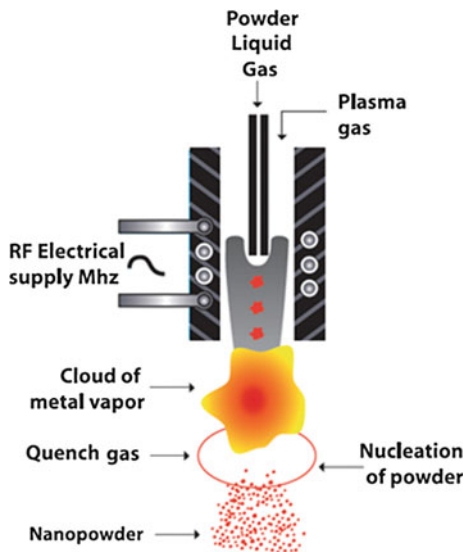
These systems often utilize cyclone separators to separate any coarse powders from the ultrafine nanopowders. The ultrafine particles then deposit on the outside of porous filters (typically metallic or ceramic) and are periodically blown off and collected. This method is highly versatile, and allows for the introduction of reactive gases at multiple stages in the process. This provides the ability to do in situ passivation either with oxygen or alternative passivation coatings.

The powders made via IG-ICP exhibit a fairly broad particle size distribution, which can be seen in the SEM images in Fig. 4. This has been attributed to the highly chaotic nature of the fluid dynamics in and around the plasma flame. The path of any one particle is never the same, hence the thermal history can vary immensely. The ideal case of an incoming feed particle coming directly down the center of the plasma, being vaporized, and the resulting vapor constituents continuing directly to the quench gas and condensing is not likely. It is known from modeling that there are re-circulatory flows in and around the plasma which can allow particles to grow in size or even acquire smaller satellite particles on its surface.

The passivation of metallic nanopowders has been an active area of research in the energetics community for quite some time. Researchers have investigated novel passivation approaches such as self-assembled monolayers (SAM) [13], transition metals [14], and even other high enthalpy metals like silicon [15]. The impetus for exploring novel passivation techniques is to eliminate the need for a nascent oxide shell which significantly diminishes the combustion performance of these powders. As was seen in Fig. 1, with a 4 nm thick oxide shell, an 80 nm aluminum nanoparticle is already down to $\sim$85% unreacted aluminum. A 15 vol.% Al_2O_3 shell significantly impacts the combustion performance, therefore it is desired to
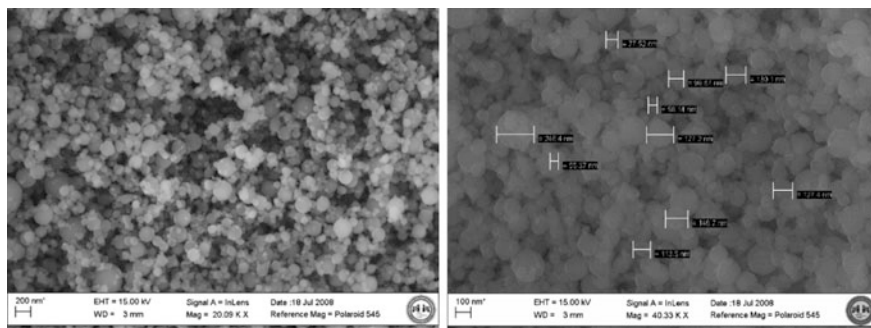
Fig. 4 SEM images of aluminum nanopowders synthesized via the IG-ICP process

develop technologies which yield aluminum nanoparticles with higher percent unreacted aluminum. Crouse was able to increase the unreacted aluminum content to greater than 90% by coating unpassivated aluminum nanopowders with silicon, and allowing the thinner SiO_2 nascent oxide serve as the passivation mechanism. Jouet investigated SAM as a passivation mechanism, and was successful in synthesizing oxygen free nanoparticles of very small size. Unfortunately the SAM-passivated aluminum nanoparticles ended up yielding only ∼15% unreacted aluminum due to their very small size in comparison with the SAM coating.

2.3 Iron Nanopowder

Iron nanopowders have seen a significant amount of research as well, however the focus has been primarily for applications in magnetic materials, catalysis, and environmental remediation. Huber has conducted a detailed review of this research [16]. The pyrophoric nature of iron has been known for centuries [17]. Simple reduction of iron oxides or sesquioxides can lead to pyrophoric material. However, the degree of pyrophoricity of these material is often dictated by how finely divided they are. Nanoscale and nanostructured iron (latter sections of this chapter) have a much more predictable, and tailorable, pyrophoric response. Nanoscale iron powders have been synthesized via a variety of wet chemistry approaches [16, 18, 19], reduction of nanoscale oxides [20], and IG-ICP [4]. Figure 5 shows an SEM image of iron nanopowders made via IG-ICP. The powders synthesized via this process tend to be much larger in size than those via wet chemistry.

While aluminum has been the material of choice for metallized propellants and explosives due to its high combustion enthalpy, iron has been the preferred material for pyrotechnic applications due to its infrared (IR) signature. Baldi [21] has exploited this inherent property of nanoporous iron foils for use in infrared countermeasure decoys. Nanoscale iron powders exhibit nearly identical burn

Fig. 5 **Fig. 5** SEM image of iron
nanopowder synthesized via
IG-ICP
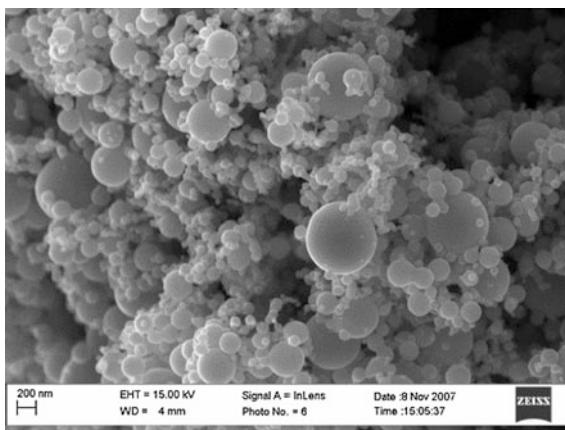
characteristics and have been evaluated as a more environmentally benign alternative to the nanoporous foils which require caustic leach baths to fabricate. However, one of the biggest challenges has been how to incorporate the loose nanopowders into a form factor which can be deployed in a similar fashion to the foils. This will be discussed in more detail in Sect. 4.

3 Milled Powders

3.1 Introduction

Section 2.1 discussed using plasma synthesis as a non-equilibrium processing method to make nanoscale pyrophoric aluminum. Another well-documented non-equilibrium processing technique that can be employed to make both nanoscale and nanostructured pyrophoric materials is mechanical milling (MM) or the grinding of metal powders. Mechanical milling can be optimized to produce the precisely tuned metastable structures required for pyrophoricity; however, unlike other non-equilibrium techniques MM is simple, fast and takes place at room temperature. Typical MM involves the grinding of elemental, intermetallic, or pre-alloyed powders to reduce particle size or to change the morphology of the powder particles [22]. True alloying of the starting powders does not take place during MM and is typically not required to produce pyrophoric nanostructures.

Several types of high surface area pyrophoric materials can be synthesized by milling. Hard, brittle materials, such as silicon, can be pulverized to nanoscale particle sizes less than 100 nm. More ductile metals like aluminum, and magnesium can be milled under inert atmospheres into two dimensional flakes that are so thin they appear transparent. Finally, multiple metals can also be milled into pyrophoric micron-sized nanocomposite aggregates. Figure 6 shows SEM images of various pyrophoric materials synthesized by MM [23]. The following section describes the
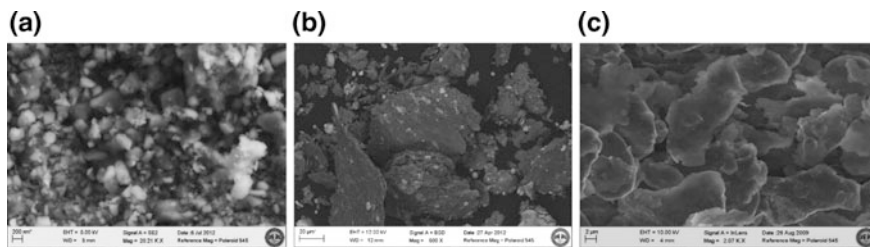
Fig. 6 Scanning electron micrographs of milled pyrophoric materials **a** nanoscale silicon **b** Al, Mg, Fe, Ti nanocomposite **c** aluminum flakes [23]

mechanism of milling, and the selection of various milling parameters (types of mills, raw materials, and process variables) involved in producing pyrophoric materials. Methods of characterizing the tuning the material properties of milled pyrophoric materials is also presented.

3.2 Mechanism

Conventional mechanical milling involves mixing commercially available powders with a grinding medium (typically steel balls) and agitating (tumbling, shaking, or stirring) the system. During agitation the steel balls collide, plastically deforming powder particles between them. The powder particles repeatedly deform, fracture, cold weld, and work harden until size reduction and/or morphological changes are accomplished. The type of material being milled and its physical properties will dictate how the imparted energy is distributed. Fracture occurs more readily in hard, brittle materials, while cold-welding and plastic deformation are the predominant phenomena seen ductile materials. Figure 7 shows the morphological changes induced in entrapped powder particles when grinding media collide during milling. Each time a powder particle is deformed or fractured a fresh surface of that particle is exposed to the milling atmosphere and/or combined with another particle surface. Under inert and reducing milling atmospheres the newly exposed particle surfaces and intermetallic interfaces (if any) are kept clean and are virtually free from oxidation. The increased surface area and reactivity of the milled particles are responsible for the pyrophoric signature produced when the highly reactive, and clean surfaces and interfaces react with oxygen.

Mechanical milling is carried out for a desired period of time until the morphology, particles size, and intermixedness are conducive for pyrophoricity. The energy required for size reduction, E, is given by the Eq. 1

$$E = \gamma \cdot \Delta S, \tag{1}$$
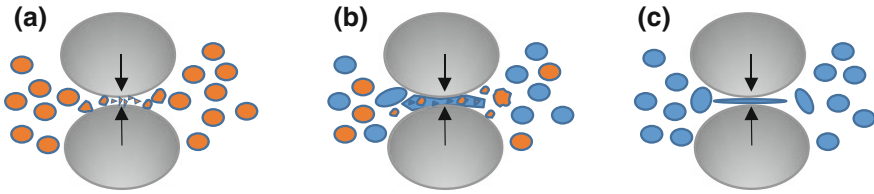
Fig. 7 Schematic of particle entrapment during high energy mechanical milling of **a** single brittle particles **b** a ductile and brittle particle blend **c** single ductile particles [23]

where γ is the specific surface energy and ΔS is the increase in specific surface area. The mechanism of milling is generally described in three phases: early, intermediate, and steady-state In the early stages of milling particles are soft and tend to weld together very easily, often leading to increases in particle size/decreases in surface area. This phenomenon is especially evident when milling very ductile metals like aluminum. In very early stages, particles tend to exist as large high aspect ratio flakes or layered composites thereof. Metals with a high affinity for oxygen (e.g., aluminum and magnesium) exhibit pyrophoric behavior with this large, flaky morphology. As milling goes on, the powders begin to get work hardened and the particles develop a higher tendency for fracturing than for cold-welding. This intermediate phase of milling is where the particle size reduction is accomplished. Large flakes formed in the early stages are fractured into smaller flakes, and the length scale of composite mixing is decreased. The grain size, d, of the powder during early milling stages is given by Eq. 2

$$d = Kt^{-2/3}, \tag{2}$$

where t is milling time and K is a constant [24]. In general, the rate of particle size reduction is logarithmic with processing time [22]. Eventually, a steady-state is reached, where the tendency for particle size to increase by cold welding equals the tendency for particle size decrease by fracturing. At steady-state, size reduction is no longer thermodynamically favored, and the particle size hits a lower limit, d_{min}, but further structural deformations (e.g., alloying) are possible. The length of milling time required for a given system is function of the materials themselves and of the specific operating parameters. It is typical when producing pyrophoric materials to stop milling in the early or intermediate phases (<2 h in a high energy ball mill) where flake formation and particle size reduction mechanisms dominate.

3.3 Process Control

3.3.1 Types of Mills

There are dozens of commercially available mills that differ from one another in grinding medium, intensity, capacity, and versatility. Since a detailed review of mechanical alloying is given by Suryanarayana [25] the following discussion is brief. Most mills are divided into three separate categories: dry, wet, and cryogenic. Wet mills use a liquid grinding medium (aqueous or organic solvents) to help lower the surface energy of the particles and to prevent cold-welding. However, to date, no wet-synthesis methods have been demonstrated for large-scale production of pyrophoric nanopowders [26]. The use of organic solvents, complexity of solvent recovery, and low stability of the synthesized pyrophoric materials remains problematic in wet milling. Recently the ability to increase the specific surface area of Al from 0.5 to 26.1 m^2/g within 4–5 h of wet milling was demonstrated, creating ultra-thin nanostructured flakes [26]. However, the wet-milled flakes were not pyrophoric and contained a nascent aluminum oxide shell, and aluminum carbide contamination, an artifact from drying the organic solvent. Cryogenic milling suffers from many of the same disadvantages as wet milling. Cryogenic milling takes place either directly in cryogenic bath or in a cryogenically jacketed vessel. Liquid nitrogen or liquid argon is used to embrittle the powders to minimize flake formation and maximize size reduction. Despite being able to attain smaller particle sizes in wet and cryogenic milling as compared to dry milling, contamination of powder surfaces remains a hurdle to making pyrophoric materials.

Dry, high energy attritor milling equipment is best for production of pyrophoric materials. Attritor mills are horizontal or vertical drums with an impeller that rotates at very high speeds to agitate and energize the grinding media and powder. These high energy attritors are capable of imparting the extreme amounts of energy required to produce pyrophoric morphologies. Several brands of attritor mills are commercially available for high energy grinding; however, to make pyrophoric materials several precautions must be taken to avoid premature oxidation or ageing of the materials. Specifically, the Zoz Maschinenbau GmbH (Germany) Simoloyer (Fig. 8) has several functions that make it a great high energy attritor mill for pyrophoric material synthesis. Firstly, the atmosphere in the Zoz Simoloyer mill can be tightly controlled (air, argon, nitrogen, hydrogen) [27]. In addition, all powders can be charged into and discharged from the milling vessel in hermetically sealed containers for easy transport in and out of a glovebox.

The impeller rotates horizontally at very high speeds (up to 1800 RPM, 11 m/s linear tip speed) with kinetic energy (KE) of the grinding media during collision given by following equation:

$$KE = \frac{1}{2}mv^2, \tag{3}$$

Fig. 8 Zoz Simoloyer CM01
high energy ball milled used
to synthesize pyrophoric
materials
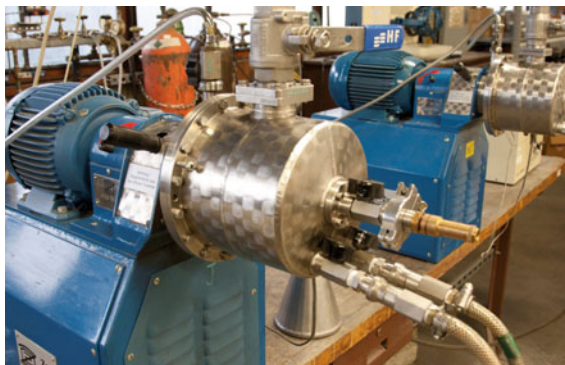
where m is the mass of a grinding ball, and v is the velocity of the media at the time of a collision. To maximize the amount of energy transferred to the powder, you must maximize the frequency of collisions (i.e. use many smaller balls) and the velocity of the media during agitation.

3.3.2 Selection of Raw Materials

Careful selection of the raw materials is critical for successful synthesis of a pyrophoric material. Commercially available pure metal, pre-alloyed, and intermetallic powders are typically used for MM of pyrophoric materials. The starting powder particle size is not critical and generally ranges from 1 to 200 μm. Starting materials can be spherical, flaky, or irregular in shape. While size and morphology are not critical, the quality of the powders is. It is important to minimize the amount of oxygen in the starting materials to minimize the amount in the final product. It is also worth noting that many chemical suppliers normally quote purity of metal powders on a metals basis, meaning they do not disclose other impurities such as oxygen or oxygen containing ceramics.

Some elements that are known to produce pyrophoric signatures after milling under inert conditions are aluminum, magnesium, iron, titanium, zirconium, zinc, tin, boron, silicon, and hafnium. The pyrophoric signature (color, speed of combustion, etc.) of each of these elements is slightly different; milling various stoichiometric ratios of these and many other elements produces pyrophoric materials with tunable signatures. These pyrophoric nanocomposites typically have a ductile metal (Al or Mg) flaky matrix with harder, more brittle materials embedded in the matrix. When making pyrophoric nanocomposites, materials can be milled in one step or in a series of steps to precisely tailor particle size and length scale of mixing.

3.3.3   Time and Intensity

Milling time for pyrophoric materials is generally short. The process should allow just enough time that fresh surfaces are exposed and size reduction and morphological changes are generally uniform (typically <2 h). The intensity of the milling should be sufficient such that no dead zones are created in the milling chamber and the energy imparted in the system is high enough to form non-equilibrium phases. Cyclical milling (adjusting the intensity up and down with time) is a useful technique to ensure no dead zones are created. For example, rather than milling for 10 min at 1600 RPM, one might instead run two 5 min cycles where the RPM is maintained at 1600 RPM for 4 min and then dropped to 1400 RPM for 1 min. Repeated changes in the agitator speed help to adjust the particle flow inside the chamber.

3.3.4   Process Control Agents

Lubricants and surfactants are often added to the milling system to minimize the effects of cold welding and agglomeration. These materials are called process control agents (PCAs) and are instrumental in the formation of pyrophoric materials by MM. When ductile metal particles are plastically deformed they have a tendency to stick together and coat surfaces of the grinding media and the milling chamber. PCAs mitigate this problem by absorbing on the surface of the powders lowering surface energy of the solid material and driving an increases in surface area (Eq. 1). PCAs can be gas, liquid, or solid and are typically used in 1–5 wt% of the total powder charge [22]. PCAs do contribute to contamination of the powders and are integrated into folds and inclusions in the powder during milling. Therefore, the PCA should be chosen carefully so as not to interfere with the desired pyrophoric signature.

   The most popular PCAs are organic waxes, like stearic acid. These waxes have relatively low decomposition temperatures and can be degassed if necessary. Because PCAs are used in such low amounts that they do not form continuous coatings on the milled metal particles, they do not usually hinder the pyrophoric response. The amount of and type of PCA used depends on the ductility of the metal, the desired morphology, the chemical and thermal stability of the PCA, and the purity requirement. Oxygen and hydrogen containing milling environments also act as PCAs by creating a hard oxide and hydride layer on the powder surface and embrittling the powder for fracture [22, 28].

3.3.5   Media

The type, size and amount of grinding media used during milling should be optimized for the given system. Stainless steel and yttria stabilized zirconia (YSZ) are ideal materials for milling media because they are hard and dense. YSZ should be

used over stainless steel when purity is paramount. The size of the balls should be small enough that the frequency of collisions is still high, but large enough that they still have a substantial mass (Eq. 3). Typically, 5 mm is a safe starting diameter. Smaller media ultimately leads to smaller particle sizes. The ball to powder ratio (BPR) is normally maintained at 10:1 or 20:1 and influences the time required for milling. A higher ratio means shorter milling times. The filling or charge ratio of the milling chamber is also an important variable. The chamber should be full enough that collisions are high frequency, but empty enough that balls are still able to accelerate to high velocities before colliding. Forty volume percent of the vessel is a standard chamber charge.

3.3.6 Atmosphere

It is critical to maintain an atmosphere in the mill conducive for making pyrophoric materials, i.e. one free of oxygen and other surface contaminating impurities. The best way to ensure no oxygen is in the system is to purge the milling and collection vessels with an inert gas. Argon gas is the best blanketing gas because of its high relative density and resistance to react with the powder, even at high temperatures. Helium and nitrogen can also be used. In cases when hydrogen or oxygen gas is being used as a PCA, careful mass control flow is required. All powders should be transferred and stored under inert conditions as well to preserve purity.

3.3.7 Contamination

The atmosphere is the biggest contributor of contaminants with oxygen being the worst offender for pyrophoric materials. Oxygen can be picked up during milling, transfer, and storage of these materials. Pyrophoric materials are known to age (even in a glovebox environment) and lose their pyrophoric signature if enough of an oxide shell builds up on the surfaces of particles. The grinding chamber, attritor blades, and grinding media also all contribute to contamination of the powder. Most mills are lined with ultra-wear-resistant materials to minimize contamination; however, some level of contamination will always be present. Typical materials for grinding chambers and media are, in order of increasing contamination, zirconia, tungsten carbide, and hardened steel. For pyrophoric materials milled for short periods of time, the amount of impurities in the products is typically not more than 1–2% by weight. Contamination levels increase with increased milling times, and since contamination can never be totally avoided, one should choose a grinding chamber and media that is compatible with the product. Depending on the application of the pyrophoric material, such contaminants may or may not pose a problem.

3.4 Tunability

The structural, physical, and chemical properties (Sect. 3.3) of a pyrophoric material influence the thermal and visible signature that material displays upon reaction. Combustion and intermetallic chemical reactions contribute to the amount of and type of radiation that is emitted. Therefore, any property which influences the reaction kinetics and thermodynamic equilibrium of these reactions will in turn influence the signature. The chemical, physical, and structural properties of nanomaterials can be fully characterized. A thorough review of nanomaterial characterization is given elsewhere [29], and a brief description of special considerations is given later in this chapter (Table 1).

The composition of a pyrophoric material will dictate the radiant emission spectra and thus the thermal and visible pyrophoric signature. Visibility and color of the signature depends on the wavelength and energies of emitted photons, each color being associated with a discrete wavelength. Metal salts have been used for decades in the smart design of pyrotechnic ammunition, and their properties are well known. Pyrophoric materials should be smartly designed for their individual application with respect to the emission of infrared, visible, and ultra-violet radiation.

Composition, particle size, surface area, morphology, and degree of mixedness also influence the intensity and duration of the pyrophoric response. Pyrophoric metals with high affinities for oxygen (e.g., Mg, Zr, Al, Ti) react faster and more violently than their lower affinity counterparts. With respect to primary particle size, smaller particles combust more rapidly than large ones. Sieving is a useful and easy way to classify milled powders by size, and to tune the burn rate. While sieving pyrophoric powders must take place under a protected atmosphere it is a cheap and useful way to adjust the burn time.

In milled nanocomposite systems, intermetallic reactions also contribute to the overall signature. Changing the length scale of mixing of the metals within the composite is analogous to changing the particle sizes and will influence the reaction kinetics. A small scale of mixing (on the order of nanometers) is favored for elements involved in intermetallic reactions because it ensures good contact between the reacting elements. Figure 9 shows a compositional map of a quaternary milled pyrophoric nanocomposite. The more ductile elements (aluminum and magnesium) form a well-mixed flaky matrix in which the harder elements (titanium and iron) are dispersed. In general, longer milling times lead to shorter length scales of mixing. For nanocomposite systems comprised of ductile and brittle materials, size reduction of the brittle material is usually not accomplished during co-milling because the ductile material tends to absorb more of the energy. Oftentimes it is necessary to mill the brittle component alone to accomplish size reduction prior to co-milling the entire composite system.

Table 1 Characterization techniques and tips for analyzing pyrophoric materials

	Technique	Properties	Equipment	Special considerations for analysis of pyrophoric powders (PPs)
Structural properties	Sieve analysis	Particle size distribution	Sieves of varying mesh sizes	Sieving must be done in a glovebox
	Gas adsorption	Surface area	Surface area and pore size analyzer	Sample cells should be loaded for analysis with PPs in a glovebox
				Powder frits should be used to seal off sample cell from atmosphere until it is loaded in the instrument for analysis
	Electron microscopy	Size, morphology	Scanning or transmission electron microscope (SEM/TEM)	PP should be kept wet with organic solvent when preparing sample stubs for measurement
	Dynamic light scattering	Particle size distribution	Particle size analyzer	PPs should be kept wet in organic solvent prior to measurements
				Liquid medium must be compatible with PP (many pyrophoric metals will react violently with water to produce H_2 gas)
	X-ray diffraction	Phase, crystallite size, lattice strain	X-ray diffractometer	PP powder should be mixed in the glovebox with petroleum jelly or another protective medium to prevent reaction prior to analysis
				Protective medium should be accounted for in the background measurement
Chemical properties	Oxygen analysis	Oxygen content (percent by weight)	Light element analyzer	Sample crucibles should be loaded for analysis with PPs in a glovebox
	Energy dispersive X-ray spectroscopy (EDS)	Phase, length scale of mixing	SEM/EDS	PP should be kept wet with organic solvent when preparing sample stubs for measurement
	Burn test	Visible signature (burn time, color, etc.)	Burn chamber	PP can be kept in a glass vial that is shattered to expose PP to air

Table 1 (continued)

	Technique	Properties	Equipment	Special considerations for analysis of pyrophoric powders (PPs)
Physical properties	Thermal analysis	Mass change	Thermogravi-metric analyzer (TGA)	PP should be kept wet with organic solvent when preparing crucible for measurement
		Phase transitions, heat flow	Differential scanning calorimeter (DSC)	Solvent should be removed at very low temperatures prior to measuring pyrophoric response
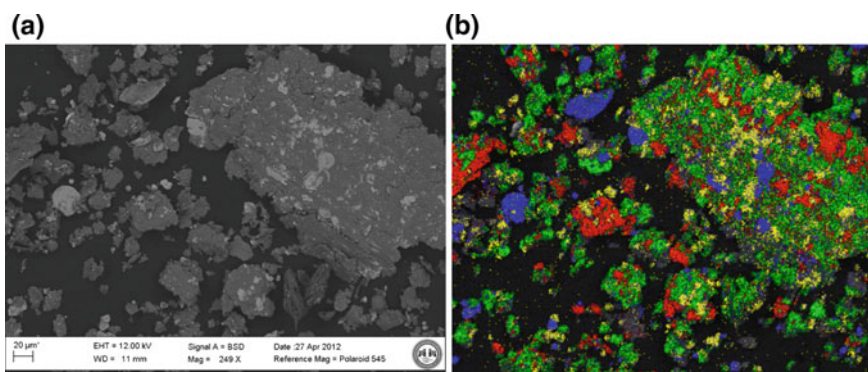
Fig. 9 **a** Scanning electron micrograph, in backscatter mode, of a quaternary milled pyrophoric nanocomposite **b** compositional EDS map of aluminum (*green*), magnesium (*yellow*), iron (*red*) and titanium (*blue*) [23]

4 Coating/Substrates

4.1 Introduction

This chapter has discussed different processing methods for the production of pyrophoric and passivated nanoscale powders. This section will present an overview of selected techniques currently in use or being developed for the formation of pyrophoric substrates or structures, with a main focus on pyrophoric alpha iron (α-Fe) nanoscale composites. Iron is a preferred pyrophoric material for many applications due to its natural abundance in both pure and oxide form and the benign nature of the oxidation products. In addition to their use as pyrophoric materials, reactive iron materials have been utilized for decades in many different applications (i.e. catalysts). Alpha iron nanopowders are highly reactive when exposed to oxygen with the reaction kinetics being dependent on particles

size/specific surface area [30]. One application of pyrophoric iron foils is for the generation of infrared signals. When used for this application the material is referred to as a solid-state combustion emitter.

Different precursor materials and methods have been demonstrated for the production of iron based pyrophoric substrates and structures. This section will discuss not only production techniques but the pyrophoric response data, when available, for the pyrophoric substrates and structures. In addition to the methods presented for the production of pyrophoric iron materials, a technique that requires the use of chemical leaching with a warm caustic solution for the formation of high specific surface area iron will be discussed.

4.2 Substrate/Structure Production Techniques

4.2.1 Chemical Leaching

For over half a century, high specific surface area nickel catalysts have been produced using a chemical leaching technique for the formation of materials referred to as Raney materials [31]. Applying this processing method to the production of other material, specifically iron, became prevalent in the 1980s. Patents for Raney iron materials date back to the mid-1980s but are based on the technique developed several decades earlier [32]. The method for synthesizing Raney iron is a multi-step process that requires the use of high temperatures and caustic solution. It starts by the diffusion of aluminum or zinc into an iron foil through the application of heat and an oxygen free environment for the formation of an alloyed foil material [32]. The produced alloy is then exposed to a warm caustic solution (sodium or potassium hydroxide) to leach the aluminum or zinc from the alloy for the generation of a high specific surface area thin foil. A SEM image of the porous iron foil produced using this method is presented in Fig. 10. The inventor claims that boron or other fuels can be added to the alloy, at low concentrations, to modify the pyrophoric response of the foils after leaching.

In depth studies of the pyrophoric oxidation reaction of the porous iron foils have been conducted by Wilharm [33] and a mathematical model derived and tested. In the paper, Wilharm claims that the only governing reaction of the pure porous iron foils is the reaction between iron and oxygen. This is backed up by the inventors [32]. The mathematical model, generates predicted temperature profiles that match experimental results for the combustion of the porous iron foils. However, Koch [34] in his publication indicates that there is some residual aluminum within the substrates that has an effect on the pyrophoric response. Additional techniques have been developed for the production of the porous iron foils but the information that has been published on this new technique is extremely limited.
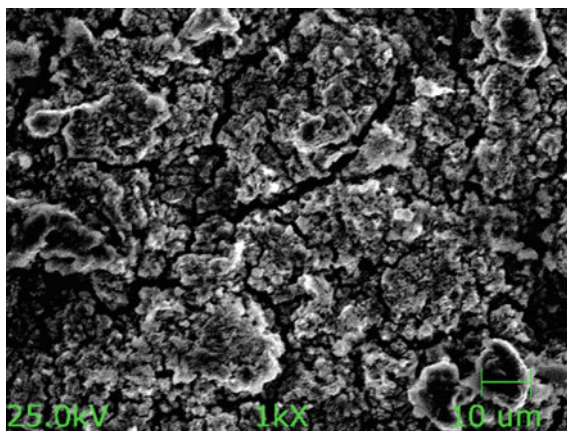
4.2.2   Sol-Gel Techniques

Sol-gel processing is a traditional technique in the area of materials science that has been used for over a century for the production of solid particles and porous structures [35]. This chapter has previously discussed various techniques for the production of pyrophoric nanomaterials. Therefore, this section will provide only a brief overview of the use of sol-gel process and the techniques used for the formation of pyrophoric substrates. Applying the work of Gash [36, 37] and traditional sol-gel formation recipes the group of Shende [38–41] generated FeOOH gels that coated porous and non-porous substrates. After coating, the FeOOH gels were calcined to form Fe_2O_3 nanoparticles on the surface of the substrates. The sol-gel processing steps are summarized in Fig. 11. The sol-gel processing was used for coating non-porous steel substrates through spin-coating techniques or dip-coating of porous alumina substrates prior to gelation. SEM micrographs of the porous and non-porous substrates coated with iron oxide nanoparticles using the sol-gel technique are shown in Fig. 12.

Once coating and calcination were complete, hydrogen activation of the substrates was conducted to generate pyrophoric iron nanoparticles on the surface [38–41]. The porous substrates generated a pyrophoric response after hydrogen activation, but there was reported problems of adhesion of the particles to the substrates. On the other hand, the spin-coated, non-porous substrates did not generate a significant pyrophoric response after hydrogen activation. It is believed that this lack of response is due to the amount of material coated on the surface of the steel substrate and the high heat transfer coefficients of the steel substrate causing the quenching of the oxidation reaction from heat loss.
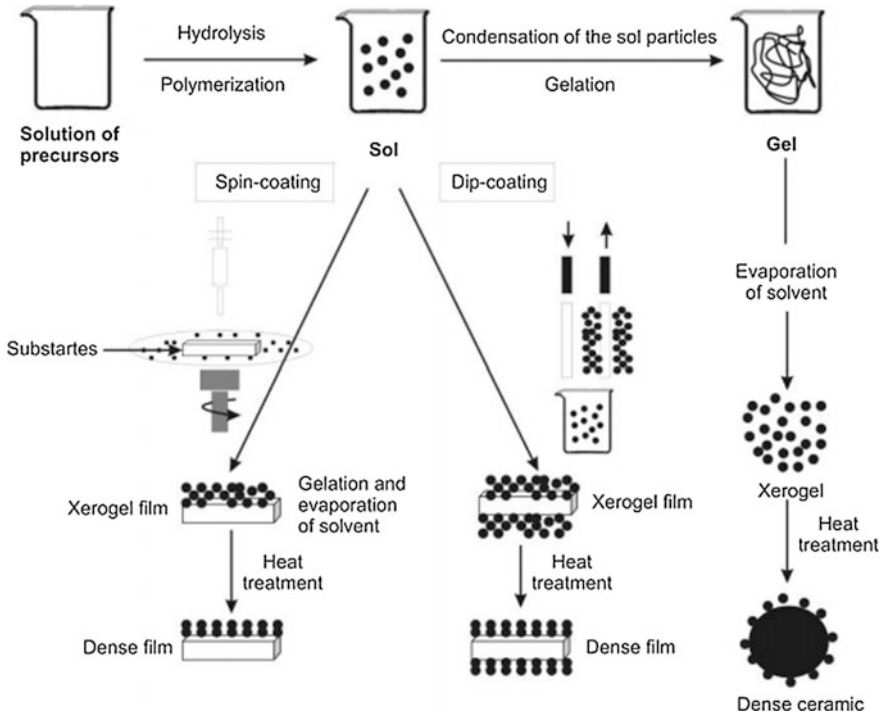
Fig. 11 Two example sol-gel processing techniques [74]
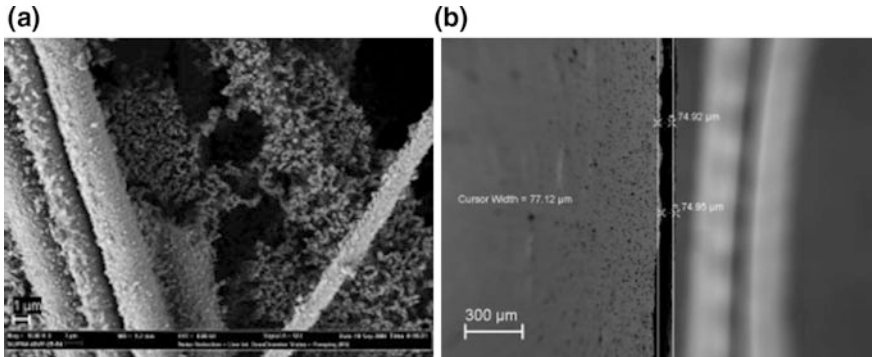
Fig. 12 SEM micrographs of **a** porous and **b** non-porous substrates using the sol-gel processing techniques [44]

4.2.3 Filtration

Filtration is a widely used mechanical process technique for the separation of a solid from a liquid. While this technique is not normally used for the formation of substrates, it can be applied to make substrates using a suspended slurry of the desired substrates material. The filtration technique was applied for the formation of two types of porous self-supporting carbon-based substrates. The technique applies the concept of Bucky paper™ for the formation of the self-supporting carbon matrix using multi-walled carbon nanotubes and/or carbon fibers with the addition of nanoparticles trapped within the matrix. Details of the production methods are presented by Doorenbos [42] and Groven [43]. The use of filtration allows for a bottom-up formation approach where iron oxide nanoparticles are suspended in a solvent (i.e. water) with multi-walled carbon nanotubes and/or carbon fibers prior to filtration. To ensure the formation of uniform substrates that are free of defects, de-bundling of the carbon tubes and fibers along with good dispersion of the nanopowder within the solvent is required. An ultrasonic wand has proved to be one of the best techniques for this application. The suspension of the materials with the solvent must be stable as the filtration process can take up to several hours to complete. The suspension remains stable through the addition of a dispersant.

The bottom-up production method was used for the formation of two types of self-supporting carbon-based substrates. The first substrate type is referred to as a non-layered substrate and requires three processing steps: (1) preparation and pressure filtration of the composite slurry of the iron oxide nanoparticles and multi-walled carbon nanotube/carbon fiber dispersed in water, (2) drying and cutting of the substrate into sample coupons, and (3) hydrogen activation. The second substrate type is referred to as a layered substrate and requires five processing steps and consists of three separate layers: (1) preparation and filtration of a multi-walled carbon nanotube/carbon fiber slurry in water, (2) preparation and filtration of a composite iron oxide nanoparticles and multi-walled carbon nanotube/carbon fiber composite slurry in water, (3) preparation and filtration of a multi-walled carbon nanotube/carbon fiber slurry in water, (4) drying and cutting of the substrate into sample coupons, and (5) hydrogen activation. A visual representation of the two substrate types is present in Fig. 13.

The bottom-up formation approach provides a method that allows for the combustion properties of the carbon-based substrates to be tuned based on composition by adjusting the amount of iron or the addition of a fuel (i.e. aluminum, boron, magnesium, etc.) to the slurry prior to filtration. The substrates produced using this method have limited structural integrity and must be handled with care.

The oxidation reaction kinetics for the iron nanoparticles has been determined and reported elsewhere [44]. The reaction kinetics of the prepared porous carbon-based substrates can be affected by the filtration pressure used during production. A typical pressure used for the production of the nano-layered substrates was 20 psig. If the filtration pressure is greater than 50 psig, the porosity of the substrate is reduced thereby reducing the diffusion of air into the substrate.
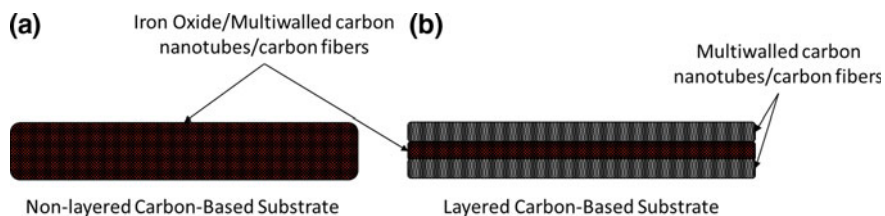
Fig. 13 Visual representation of **a** non-layered and **b** layered porous carbon-based composite substrates

Fig. 14 SEM image of iron oxide nanoparticles within the multi-walled carbon nanotube matrix of a non-layered substrate form by pressure filtration [44]. *Source* Zac Doorenbos's doctoral thesis
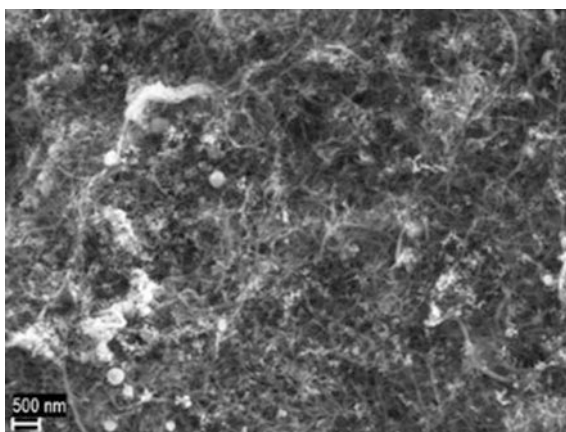
The reduction of air diffusion into the substrates can reduce or eliminate the pyrophoric response of the substrates (Fig. 14).

4.2.4 Tape Casting

The technique of tape casting, otherwise known as doctor blading or knife casting, is a traditional ceramic and metal processing technique that is used extensively in industry for the formation of large, thin, flat ceramic or metallic parts. The green density of the substrates formed using tape casting is dependent on gravity and the shrinkage of the binder during the drying process. Production using tape casting requires the effective dispersion of the composite constituents and is extremely important. Depending on the system, different dispersion techniques such as ball milling or ultrasonic dispersion may be used. A newer mixing technique, referred to as acoustic mixing, was developed by the Resodyn Corporation. The Resodyn acoustic mixer is a unique form of mixing that provides a uniform shear field within the mixing vessel [45]. This unique mixing technology provides dispersion of the components on the microscale even in high viscosity slurries [45].

Pyrophoric substrates with increased structural strength and environmentally acceptable processing techniques are of great interest. The application of the acoustic mixing technology allowed for the uniform dispersion of an iron oxide nanopowder and a ceramic additive within a high viscosity binder solution (>15,000 cps); the solution was then tape casted and dried, resulting in substrates with thicknesses between 0.014 and 0.026 in., or larger. The ceramic additive was used in the formation of the substrates to provide strength after the removal of the organic binder. To provide that strength, heat treatment or sintering of the substrates prior to activation is required. Sintering is used a great deal in the processing of ceramic materials to consolidate powders into a dense part which provides increased strength. Composite substrates were made using the following ceramic additives at concentrations ranging from 5 to 50 wt%: feldspar, boehmite, bentonite, talc (magnesium silicate monohydrate), montmorillonite, sodium silicate, lithium silicate, and aluminum silicate. After an initial set of sintering experiments, it was determined to merely use the different silicates for the formation of composite substrates based on strength, easy of processing, and pyrophoric response.

4.2.5   Cold Isostatic Pressing

Another common technique used in powder metallurgy and ceramic processing was applied to the production of composite structures. Cold isostatic pressing (CIP) is an attractive technique for the production of bulk materials as it allows for the consolidation of powders into basically any shape via isostatic (omnidirectional) pressure. Another advantage of this technique is the total consolidation time for each sample can be short (<1 min at maximum pressure). CIP was used in the formation of iron oxide/ceramic composite structures with a $1'' \times 1'' \times 9''$ soft rubber mold. CIP consolidation pressures for the composite structures ranged from 10,000 to 45,000 psi. For these materials, higher consolidation pressures reduced the porosity of the structures, thereby limiting the pyrophoric response. After consolidation end items with a cross-sectional dimension of $\sim 0.74'' \times \sim 0.77''$ that were several inches in length were generated. As previously discussed, sintering of these structures was required prior to activation to ensure that the structural integrity was maintained during the activation process.

4.3   Dynamic Combustion Characteristics

4.3.1   Carbon-Based Substrates

Application of the two bottom-up formation techniques produced porous pyrophoric substrates. Of the two techniques, the non-layered approach was the most successful for the formation of substrates. A sample pyrophoric response of a carbon-based non-layered substrate is presented in Fig. 15.
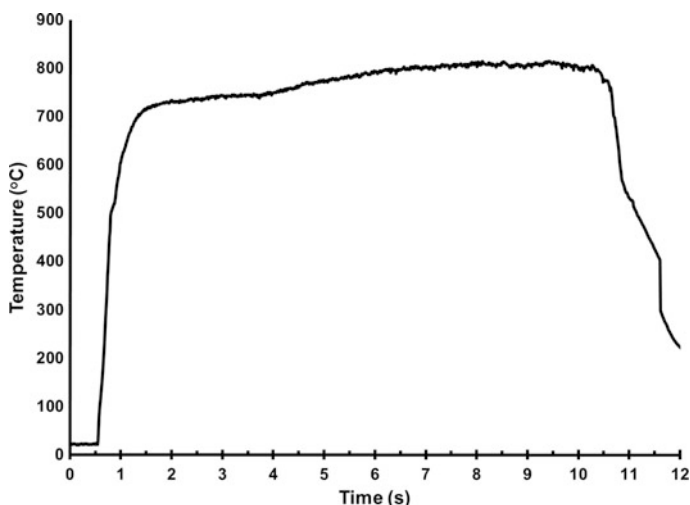
Fig. 15 Dynamic pyrophoric response of a carbon-based non-layered substrate

4.3.2 Iron/Ceramic Composite Substrates

The iron/ceramic composite substrates were characterized through dynamic analysis of the pyrophoric response in a flow air atmosphere using infrared pyrometers. Sintering temperature and time have a significant effect on the pyrophoric response of the substrates. As previously discussed, the iron oxidation reaction kinetics are highly dependent on the particle size/specific surface area of the materials. If the sintering process is too long, grain growth and particle size reduction can reduce or eliminate the pyrophoric response of the substrate even with the subsequent hydrogen activation step. In general, the shorter the sintering time at maximum temperature, the better this pyrophoric response (<60 min). Total sintering time can range from 2 to up to 20 h depending on the heating and cooling rates. A low heating rate (<1 °C per minute) is required to ensure the substrates do not crack during the binder removal and sintering processes. Of all the ceramic additives tested, the substrates made with the silicate ceramics had the best characteristics, with aluminum silicate having the best strength and ease of processing. The dynamic pyrophoric response of five iron/ceramic composite substrates is presented in Fig. 16.

4.3.3 Iron/Ceramic Composite Structures

The dynamic combustion characteristics of activated iron/ceramic composite structures was measured using a two-color infrared pyrometer and selected data is presented Fig. 17. A sample block provided a maximum combustion temperature of
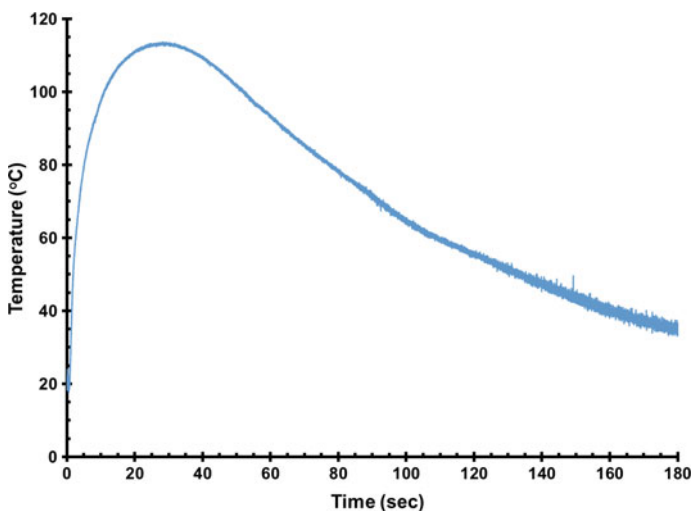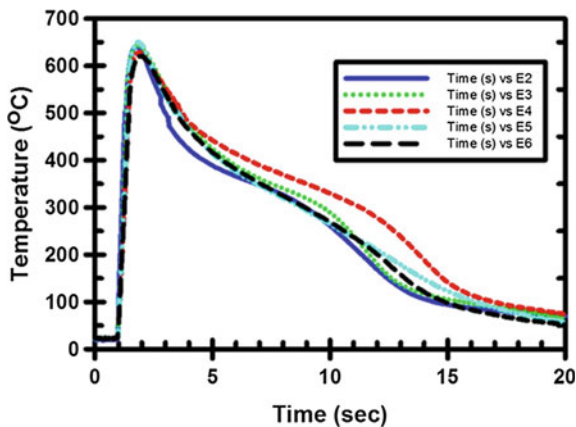
Fig. 17 Dynamic combustion profile for an iron/ceramic composite block pressed at 15,000 psi
and reduced under flowing hydrogen for 5 h

113 °C when exposed to oxygen. Further investigation into techniques for
increasing the porosity of the structures while maintaining the structural integrity
is required prior to the development of an application for these composite
structures.
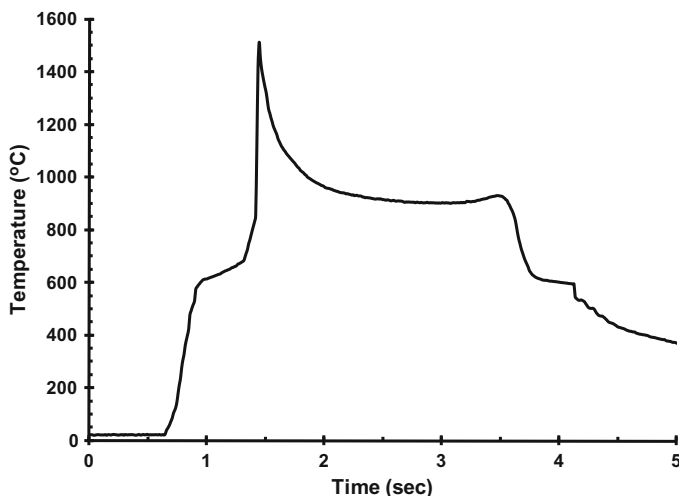
Fig. 18 Dynamic combustion temperature profile for a non-layered carbon-based substrate with aluminum

4.4 Tunability Through Addition of Tertiary Reactives

The application of traditional thermite reactions for the further tuning of the combustion characteristics of the carbon-based substrates can be conducted. The maximum combustion temperature of the substrates made with just iron is limited to less than 1000 °C. The addition of a fuel such as aluminum, silicon, or boron to the substrate allows for a secondary thermite reaction to occur after the oxidation of the iron. In this case, flake aluminum produced using a milling technique, and with a specific surface area of ca. 17 m^2/g and a reactive aluminum content of 84% was added to the carbon based substrates along with a pH buffer to allow for processing in water. Figure 18 presents a dynamic combustion profile for a non-layered carbon-based substrate with aluminum added.

5 Pyrophoric Foams

5.1 Introduction

As discussed in the previous sections of this chapter, the energetic properties of the powdered metal particles are largely defined by their particle size and the associated surface area. For instance, iron powder has been shown to be extremely pyrophoric upon direct contact with the air if the particle size is in the range of 18–20 nm [46], corresponding to a surface area larger than 6 m^2/g [47, 48]. Obviously, the particle

size and surface area of any given metal powder are two important parameters in determining its energetic properties, but they are not necessarily independent variables. The surface area is a function of the particle size, but there are other means to achieve high surface area materials besides decreasing the particle size. Many other types of nanostructures have been shown with extremely high surface areas and somewhat energetic characteristics, including metal nanoparticles as objects small in all physical dimensions (i.e. zero dimension or 0-D), 1-D nanowires and nanorods [49, 50], 2-D flakes or thin films [51–54], and highly porous foams with interconnected framework structures (3-D), such as metallic foams [55] and activated carbons [56]. However, much of the development work in the areas of the metallic materials for energetic application has so far been limited to the metallic nanopowders; the latter morphologies of metallic materials are very much overlooked, with few literature reports about their energetic application.

5.2 Metallic Foams

Metallic foams, especially aluminum foams, with interconnected framework structures are well known [55, 57, 58], and the commercial products with varying porosity, surface area, wall thickness, and structural morphology have become readily available. These metallic foam materials are known to have many interesting physical and mechanical properties which dense materials do not exhibit. The density of this class of materials, for example, is only a fraction of that of a solid structure but with high specific strength and stiffness. They make excellent candidates for damping, capable of high absorption of impact energy, vibration and sound. These properties make metallic foam materials attractive for a wide range of industrial applications, particularly in automotive and construction fields. There are many conventional metallurgical processes for fabricating metallic foams depending on the physical state of the starting metals (solid or liquid). Melted metal liquids can be foamed directly by injecting gas, gas-releasing foaming agents or by producing supersaturated metal and gas solutions [55]. Metal powders can also be used as starting materials for metallic foams by forming compacted mixtures with foaming agents that can be foamed in a controlled heating process [57]. In a well-documented process to fabricate the aluminum foam via this powder metallurgy route [55], aluminum powder is blended uniformly with titanium hydride powder, TiH_2, which functions as a foaming agent, decomposing at a temperature near the melting point of aluminum, releasing hydrogen gas. The precursor mix is then compacted and heated to slightly above its melting point, resulting in melting, gas evolution, subsequent expansion of the liquefied, highly viscous, metal slurry, and the eventual formation of an aluminum foam structure with high porosity. Various fabrication parameters such as mix composition, compaction pressure, and foaming temperature, are found to be critical to the structural properties of the aluminum foams. The fabrication of metallic foams has also been shown to be feasible via a so-called self-propagating high-temperature synthesis (SHS) [58, 59], where the synthesis is initiated by

Fig. 19 Concept of
synthesizing porous Al–Ni
intermetallics by the
self-propagating foaming
process [59]
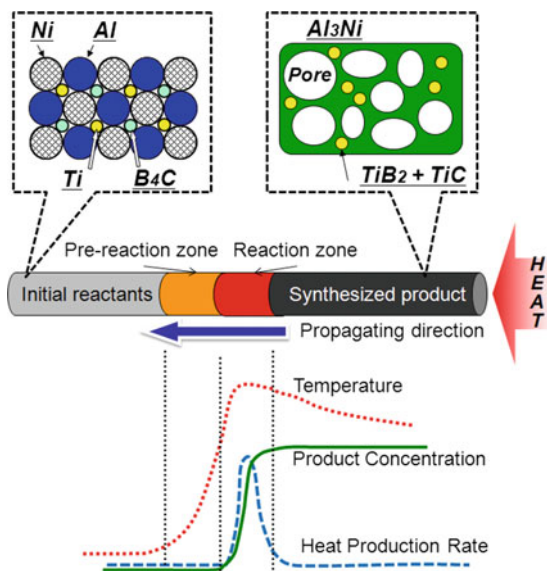
point-heating of a pyrotechnic formulation column containing precursor chemicals
to form targeted foam products, and sustained with a wave of exothermic reactions
with constant stoichiometry passing steadily through consecutive sections of the
column. As an example, Kobashi recently showed the feasibility of a
self-propagating foaming process to produce aluminum-nickel alloy foams by
combining a highly exothermic reaction of titanium and boron carbide (761 kJ/mole
boron carbide) as reactive agents [59], as illustrated in Fig. 19. It was pointed out
that the microstructure of the materials could be controlled by tailoring the reactant
composition and distribution, and the porosity of the material is dependent on the
percentage of reactive agents present in the synthesis matrix which contain mainly
hydrogen absorbed in elemental powders.

Despite this progress, most of those metallic foam materials produced so far are
for applications where the overall structural properties, such as specific strength and
stiffness are paramount. There are very limited references, to the best of our
knowledge, for using metallic foam materials for energetic applications.

For energetic applications, most of those known metallic foam materials lack
hierarchical micro/nano-scale structures with defined wall thickness. As a result, it
would be difficult to expect any level of uniformity for an energetic formulation in
which a metallic foam material were employed. Some opportunities for developing
such metallic foams with hierarchical micro/nano-scale structures into energetic
materials have been discussed before [60], however, a method disclosed by Gash
represents a significant attempt to produce highly energetic porous metallic mate-
rials at ambient condition [53]. It was demonstrated that a highly porous and
pyrophoric iron material with relatively high surface area could be produced via a
sol-gel synthesis route. First, a nanostructured metal oxide-based gel was produced
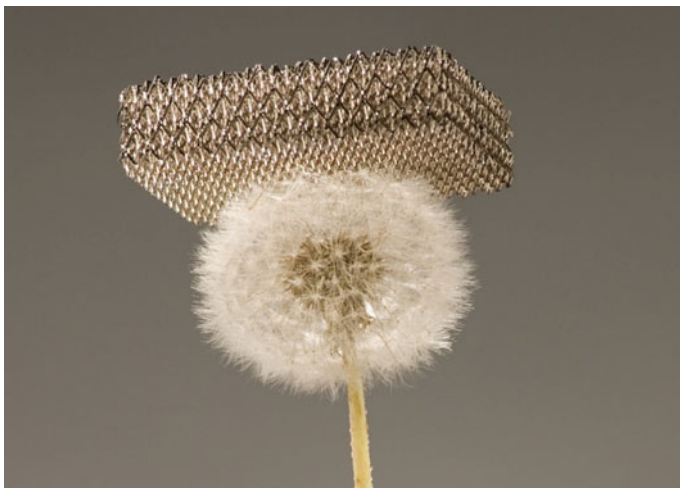
Fig. 20 The metallic "microlattice" structure of interconnected hollow tubes being supported by a dandelion seed head [61]. Photo by Dan Little © HRL Laboratories, LLC

in aqueous solution, followed by drying to produce a xerogel, or aerogel by atmospheric evaporation or CO_2 supercritical solvent extraction, respectively. Further thermal treatment of the xerogel (or aerogel) in a reducing atmosphere led to the formation of a porous iron material which possessed relatively high surface area and was ignitable with the application of a thermal source such as a flame. It was pointed out that the sol-gel synthesis route was very attractive because it offered a low temperature alternative to synthesize homogeneous materials with variable compositions, morphologies, and densities.

Most recently, Schaedler reported the synthesis of a so-called metallic microlattice, shown in Fig. 20, an ultralight metallic foam material with a density as low as 0.9 kg/m^3 and close to 99.99% air filled by volume [61]. The material was regarded as one of the lightest structural materials known to science.

To produce the metallic microlattice, a large free-standing 3-D polymer lattice template was first prepared, then coated with a thin layer of metal by electroless metal plating. The template was subsequently etched away, leaving behind a free-standing, porous metallic foam structure. The initial metallic microlattice samples were reported made of a nickel-phosphorus alloy, composed of a network of interconnecting hollow struts of about 100 micrometers in diameter and wall thickness of close to 100 nm. These metallic microlattices were observed with superb elasticity similar to an elastomer with their shape completely recovered after significant compression, giving them a significant advantage over other known ultralight nonmetallic materials, such as silica aerogels and aerographite [62] which are brittle in nature. The potential application for these metallic microlattices has been suggested to be in the areas of thermal and vibration insulators, such as shock

absorbers, spring-like energy storage devices, and battery electrodes as well as catalyst supports. As a potential energetic material, it would certainly be interesting to see its burning characteristics being examined.

5.3 Metallic Composite Foams

Carbon, though not generally considered metallic, is an interesting element in terms of its energetic properties, which are actually comparable to many metallic materials, giving it the potential to facilitate construction of various metallic structures. Among known carbon allotropes, including amorphous carbon, graphite, diamond, and the newly discovered fullerenes like buckyballs, carbon nanotubes, carbon nanobuds and nanofibers [63], the amorphous carbon is the most common form present as the main constituent of substances in charcoal, lampblack (soot) and activated carbon. Carbon in certain forms is known to be highly flammable, and somewhat pyrophoric at certain conditions, and its use as fuel in energetic formations, such as black powder, a unique blend of potassium nitrate (saltpeter), charcoal and sulfur, has been known for over a thousand years [64]. In addition to those known carbon materials which typically possess very small micro porosity of less than 1 nm and extremely high surface area, a new class of carbon foam materials with much larger and defined pore structures have also been developed in the past decades [65]. These carbon foams were typically made by the pyrolysis of thermosetting polymer, mesophase pitches, or other alternative precursors with a "blowing" technique prior to final carbonization and graphitization steps [66, 67]. More recently, a process that does not require the traditional blowing and stabilization steps was also developed at Oak Ridge National Laboratory (ORNL) [67]. As demonstrated in Fig. 21, the foam obtained with this process was of graphitic nature with open cell structures comprised of large cavities and channels which would be important to mass transportation. The measured density of these foams were between 0.2 and 0.6 g/cc.

Due to its light weight, high thermal conductivity and low thermal expansion, ORNL's carbon foams have been evaluated for many aerospace and industrial applications, including thermal insulation, impact absorption, catalyst support, and metal and gas filtration. It would be very interesting to further evaluate those carbon foam materials for their potential application as energetic materials, either as fuels or energetic hosts for metallic fuels, oxidizers and other energetic ingredients.

Incorporation of metallic elements into highly porous carbon foams has long been known as an effective way to produce composite materials with much enhanced energetic properties. Gash recently described a process for fabricating highly pyrophoric metallic carbon foam [68], in which a carbon monolith was first produced and thermally activated in carbon dioxide gas or steam to create a foam structure with a bimodal pore structure of micropores and macropores. The metal ions of iron, platinum, titanium, nickel, tin, and/or zirconium were then loaded into the pores of the carbon foams via liquid impregnation of an aqueous or
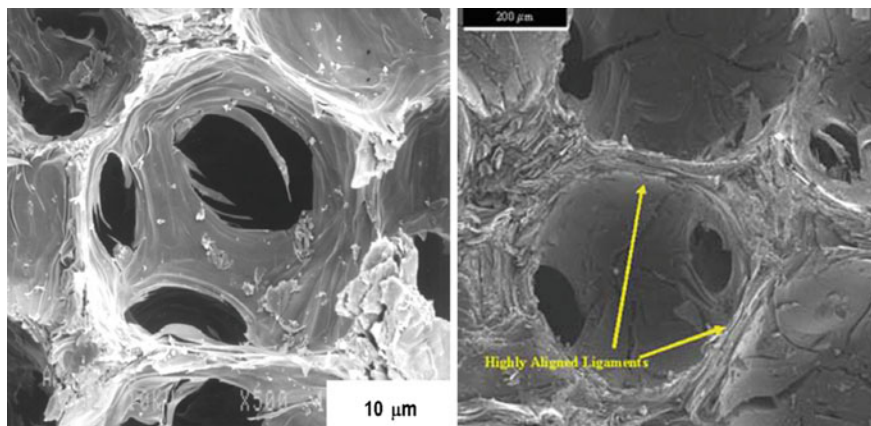
Fig. 21 Carbon foams produced by the conventional "blowing" process (*left*) and mesophase pitch-based carbon foam (*right*) [67]
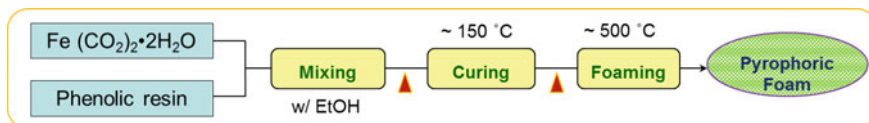
Fig. 22 Schematic of the process to produce highly pyrophoric foam materials

non-aqueous metal salt solution, followed by further thermal treatment in the presence of a chemically reducing agent, such as hydrogen gas or carbon monoxide in an inert carrier gas, to reduce the metal ions to metal particles. The resulting metal-carbon composite foams were reported pyrophoric and burned spontaneously upon exposure to air. It was pointed out that the loading percentage of metals was a defining parameter for the energetic properties of metal-carbon composite foams. In the case of metal iron, the metal-carbon composite foams only become pyrophoric if the iron loading was higher than 3% by weight. However, the loading level of metal ions in such a carbon foam is presumably dictated by its porosity, which is predominately microporous with less than 1.0 nm channels typical for activated carbons. Therefore, the transportation of the precursor iron ingredients into the existing narrow channels of activated carbons is severely hindered, as is its inter-action with oxygen in air for use as a pyrophoric material. This class of materials is reported in the past mostly as catalysts rather than pyrophoric materials.

A novel one-pot synthesis process to produce extremely pyrophoric foam materials was recently revealed, in which pyrophoric metal particles and a flam-mable carbon matrix were formed concurrently [69]. As illustrated in Fig. 22, the precursor metal molecules, such as iron oxalate dehydrate, were first well dispersed and locked into a polymeric matrix, such as a thermoset polymer, followed by thermal treatment to produce pyrophoric iron particles in tailor-built cavities and channels formed by the simultaneous carbonization of the polymeric matrix.

Since the decomposition of the precursor iron metal molecules or clusters and the carbonization of the polymeric matrix both occur simultaneously, the synergy between these chemical reactions are fully exploited. The gaseous products from the decomposition serve as the foaming and activation agents for the carbonization of the polymeric matrix, while the evolving carbon matrix is being continuously carved to accommodate the newly formed pyrophoric iron particles. Upon exposure to air, these foam materials burn intensely; both the pyrophoric iron particles and the carbon matrix are highly flammable and contribute to the total heat output.

As a final note, the temperature and radiated energy of the pyrophoric foam materials could be well predicted as a function of the physical characteristics of the materials, such as porosity, pore size, specific surface area. It would be providing a great service to the energetic communities if further studies are conducted on the diffusive mass transport, heat transport, and chemical reactions of the pyrophoric foams, which might lead to the development of a mathematic model for the combustion.

6 Safety Considerations

6.1 Safety, Handling, and Characterization

The first 10–20 years of research in nanotechnology brought about a plethora of breakthroughs in the areas of materials science, physics, chemistry, and beyond. The manipulation of materials at the nanoscale has led to the realization that there indeed is, "plenty of room at the bottom" [70]. The excitement in nanotechnology quickly led to investment of billions of dollars in research funding, with the United States currently investing over $1B per year, and over $20B in total since 2001 when the National Nanotechnology Initiative (NNI) was established [71]. Unfortunately, the environmental, health, and safety (EHS) considerations of these materials were, for the most part, an afterthought. Only recently has there been an increase in the amount of research dollars allocated for investigating the EHS considerations of nanomaterials. The bulk of this research has centered on the potential health effects of exposure to nanomaterials via inhalation, dermal contact, or ingestion. The environmental, safety, and occupational hazards (ESOH) of nanomaterials has been investigated thoroughly by Center for Disease Control and Prevention (CDC) and National Institute for Occupational Safety and Health (NIOSH), with a guide to best practices given here [72]. Nanomaterials are a complex class of materials to assess due to the incorporation of a large set of materials into one category, with the only qualifier being on feature size in an arbitrary size scale (i.e. 1–100 nm). This can include discreet 0-D nanoparticles (e.g., quantum dots), 1-D rods/fibers (e.g., carbon nanotubes), 2-D sheets (e.g., graphene), and 3-D (e.g., buckyballs). Such a complicated class of materials requires a systematic approach for proper assessment. A framework for doing so is given by Collier [3].

The subset of *pyrophoric* nanomaterials is a much smaller class of materials, and as such, much more manageable from a safety perspective. In general, this chapter has discussed a large majority of these materials. The primary safety consideration to consider with this class of nanomaterials is flammability. For unpassivated metallic nanopowders, this is a given. However, even well passivated materials must be treated with the same precautions. We must remind ourselves that these particles are typically only protected from further oxidation by a shell that is often only a few nanometers in thickness. It is not unlikely that this passivation layer could open up, or even be non-uniform across a particle. There are even some elements, like zirconium, whose nascent oxide shell is highly porous making it a very unpredictable barrier to ignition. Agglomeration of powders during synthesis is very common, and this can also give rise to interconnected regions where no passivation is present. Should these regions fracture, the highly pyrophoric metal surface would be exposed and increase the likelihood of ignition. As with all flammable materials, even one small spark can lead to a chain reaction where the entire sample will burn.

Some general guidelines for handling/storing pyrophoric nanomaterials are given below:

1. When at all possible, handle and/or store pyrophoric materials in an inert atmosphere glovebox.
2. Keep the quantities of powder stored in each canister as small as logistically possible such that any incident will be kept to a minimal amount of material.
3. Try to always use glass or metal canisters for storage, minimizing the likelihood that a fire spread beyond one canister.
4. If it becomes absolutely necessary to expose a pyrophoric material to air, slowly introduce air into the canister. This can be done in a manner such as slightly unscrewing the cap, then resealing the cap a number of times, as to allow oxygen to slowly enter the canister and passivate any reactive surface.
5. Always have either a Class D fire extinguisher, or some sort of dry powder extinguishing agent. Sand can even be used if nothing else is available. *Never* use water to extinguish a fire involving metal powders as this will accelerate the reaction and lead to hydrogen gas generation.

It is important to note that nanoscale powders require the same personal protection equipment (PPE) that would be utilized for non-pyrophoric powders due to the possibility of inhalation and dermal contact.

Due to the flammability hazards associated, characterization of pyrophoric energetic materials requires special considerations as well. Pyrophoric materials can be characterized for a variety of chemical and physical properties, including reactivity, size, surface area, morphology, phase, and oxygen content. Details of conventional nanomaterial characterization techniques can be found elsewhere [29] and the theory of such techniques will not be discussed here. However, the following section will discuss how conventional techniques may be adapted to handle

pyrophoric materials. Whenever possible, all materials should be stored, transferred, and handled under inert atmospheres, i.e. a glovebox. If exposure to air is necessary, the pyrophoric materials must be wetted with an organic or other compatible solvent to prevent combustion. Table 1 summarizes a few key characterization techniques and tips for pyrophoric materials.

The tendency of a metal powder to ignite spontaneously in air depends largely on the surface to volume ratio and particle size. Measuring surface area and particle size can be accomplished through a variety of techniques including gas adsorption, dynamic light scattering, and electron microscopy. It should be noted that because milled particles (and others) are generally not spherical, it can be hard to calculate particle size directly from specific surface area [29]. The aspect ratio of a particle should be taken into account when analyzing data from gas adsorption and light scattering. Scanning electron microscopy is a great tool for analyzing particle morphology. When combined with EDS, SEM analysis also gives information on phase content and the length scale of mixing.

X-ray diffraction, thermal analysis, and oxygen analysis are all other key techniques for analyzing the material properties of a pyrophoric material before and after reaction. The mechanism of reaction (elemental combustion versus intermetallic reaction) can be determined by analyzing the products formed after exposure to oxygen. Oxygen analysis is also particularly useful in evaluating the quality and ageing characteristics of a pyrophoric material. No single technique can give all the properties of interest for a given material. Therefore, it is important that each of these techniques be viewed as one tool in a large tool bag. Results from one test may help give insight into interpreting results from another. It is best practice to run all of the analysis techniques at your disposal and to synthesize results to build a robust property pedigree for your material. The better we can understand how a pyrophoric material's properties dictate its energetic response, the more smartly we can manipulate these materials in the nanoscale for a desired application.

As pyrophoric nanomaterials have started to make their way towards applications, research has begun on understanding the nature of these materials post-combustion. This is a very important endeavor in understanding the total life cycle of pyrophoric materials from cradle (synthesis) to the grave (post-combustion). There is additional safety considerations with nanomaterials since there is a possibility, albeit small, that the post-combustion material could also contain nanomaterials. However, at least in one case of pyrophoric nanomaterials being utilized in nanothermite primer application, Poda [73] was able to show that the resultant materials after combustion were comprised solely of micron-scale powders. This type of research must continue for each specific application, whether it be in propellants, explosives, or pyrotechnics. Many of these application involve scenarios where a Soldier or civilian could be exposed to the spent material, so we need to know the nature of this material in all instances.

7 Conclusions

This chapter has reviewed the relatively new class of energetics materials we refer to as pyrophoric nanomaterials. These materials exploit the unique properties inherent with materials possessing at least one dimension on the nanoscale (1–100 nm), namely high surface area and hence reactivity. These materials can be synthesized via bottom-up (e.g., nanoscale powders, foams) as well as top-down (e.g., mechanical milling, chemical leaching) approaches. Once synthesized, these materials are inherently pyrophoric, therefore proper safety considerations have been given for both handling and storage. We also discussed methods for both temporary and semi-permanent passivation. Lastly, a thorough list of relevant characterization techniques for pyrophoric materials is given.

References

1. www.merriam-webster.com
2. www.osha.gov/dsg/hazcom/ghd053107.html
3. Collier ZA, Kennedy AJ, Poda AR, Cuddy MF, Moser RD, MacCuspie RI, Harmon A, Plourde K, Haines CD, Steevens JA (2015) J Nanopart Res 17:1
4. Haines CD (2006) US Army ARDEC Laboratory notebooks. Unpublished work
5. Klabunde KJ, Stark J, Koper O (1996) J Phys Chem 100:12142
6. De Luca LT, Galfetti L, Severini F, Meda L, Marra G, Vorozhtsov AB, Sedoi VS, Babuk VA (2005) Combust Explos Shock Waves 41:680
7. Brousseau P, Dorsett HE, Cliff MD, Anderson CJ (2002) In: Proceedings 12th international detonation symposium 11
8. Shende R, Doorenbos Z, Vats A, Puszynski J, Kapoor D, Martin D, Haines C (2008) In: Proceedings 26th Army science conference
9. Bouillard J, Vignes A, Dufaud O, Perrin L, Thomas D (2010) J Hazard Mat 181:873
10. Ivanov GV, Tepper F (1997) In: Kuo KK (ed) Challenges in propellants and combustion: 100 years after nobel. Begell House, New York, p 636
11. Pivkina A, Ivanov D, Frolov Y, Mudretsova S, Nickolskaya A, Schoonman J (2006) J Therm Anal Calorimetry 86:733
12. Haines CD, Martin DG, Kapoor D, Paras JP, Carpenter RC (2011) Technical report ARMET-TR-10020. www.dtic.mil/cgi-bin/GetTRDoc?AD=ADA584507
13. Jouet RJ, Warren AD, Rosenberg DM, Bellitto VJ, Park K, Zachariah MR (2005) Chem Mater 17:2987
14. Foley TJ, Johnson CE, Higa KT (2005) Chem Mater 17:4086
15. Crouse C (2012) UES, Inc. on Army SBIR A112-089, Innovative passivation technologies for aluminum nanoparticles. Unpublished work
16. Huber DL (2005) Small 1:482
17. Troost ML, Hautefeuille (1875) Phil Mag 49:413
18. Guo L, Huang Q, Li X, Yang S (2001) Phys Chem Chem Phys 3:1661
19. Farrell D, Majetich SA, Wilcoxon JP (2003) J Phys Chem B 107:11022
20. Shende R, Vats A, Doorenbos Z, Kapoor D, Haines C, Martin D (2008) Proc NSTI-Nanotech 1:692
21. Baldi A (1984) US Patent 4,435,481
22. Suryanarayana C (2001) Progress Mat Sci 46:1
23. Davis RM, McDermott B, Koch CC (1998) Metall Trans A 19:2867

24. Li S, Wang K, Sun L, Wang Z (1992) Scripta Metall Mater 27:437
25. Suryanarayana C (1998) ASPM Handbook 7:80
26. Puszynski JA, Groven LJ (2010) In: Altavilla C, Ciliberto E (eds) Inorganic nanoparticles: synthesis, applications, and perspectives. CRC Press, Boca Raton, vol 133
27. http://www.zoz-gmbh.de/_ENGLISCH/content/view/36/49/lang,en/
28. André B, Coulet MV, Esposito PH, Rufino B, Denoyel R (2013) Mater Lett 110:108
29. Cao G (2004) Nanostructures and nanomaterials: synthesis, properties, and applications. Imperial College Press, London
30. Schmitt C (1996) Pyrophoric materials handbook. Towson State University
31. Adkins H, Billica HR (1948) J Am Chem Soc 70:695
32. Baldi A (1990) US Patent 4,895,609
33. Wilharm GK (2003) Propellants, explosives. Pyrotechnics 28:296
34. Koch EC (2006) Propellants Explos Pyrotech 31:3
35. Hench LL, West JK (1990) West Chem Rev 90:33
36. Simpson RL, Gash AE, Hubble W, Stevenson B, Satcher JH, Metcalf P (2003) Safe and Environmentally Acceptable Sol-Gel-Derived Pyrophoric Pyrotechnics(SERDP Final Report) Livermore, CA: Lawrence Livermore National Laboratory, pp 1276
37. Gash AE, Satcher JR JH, Simpson RL (2006) US Patent Application 11/165,734
38. Shende R, Vats A, Kapoor D, Puszynski J (2007) In: Proceedings AIChE annual conference, Salt Lake City, UT
39. Shende R, Vats A, Doorenbos Z, Kapoor D, Haines C, Martin D, Puszynski J (2008) NSTI-Nanotech 1:692
40. Shende R, Doorenbos Z, Vats A, Puszynski J, Kapoor D, Martin D, Haines C (2008) In: Proceedings 26th Annual Army Science Conference
41. Carles V, Alphonse P, Tailhades P, Rousset A (1999) Thermochim Acta 334:107
42. Doorenbos Z, Groven L, Haines C, Kapoor D, Puszynski JA (2010) AIChE annual meeting. Salt Lake City, UT
43. Groven L, Doorenbos Z, Puszynski J, Haines C, Kapoor D (2010) 27th Army science conference. Orlando, FL
44. Doorenbos ZD (2010) Size classification, processing & reactivity of nanoenergetic materials. Doctoral Dissertation, South Dakota School Mines & Tech
45. http://www.resodynmixers.com/technologies/
46. Folmanis GE, Ivanova VS (2002) Metallurgist. New York, NY, United States (translation of Metallurg. Moscow, Russian Federation) vol 46, p 244
47. Evans JP, Borland W, Mardon PG (1976) Powder Metallurg 19:17
48. Watt GW, Jenkins WA (1951) J Am Chem Soc 73:3275
49. Hu L, Wu H, Cui Y (2011) MRS Bull 36:760
50. Miao L, Bhethanabotla VR, Joseph B (2005) Phys Rev 72:134109
51. Umbrajkar S, Trunov MA, Schoenitz M, Dreizin EL, Broad R (2007) Propellants, Explos, Pyrotech 32:32
52. Rose JE, Elstrodt D, Puszynski JA (2003) US Patent 6,663,731
53. Gash AE, Satcher JH, Simpson RL (2006) US Patent Application US 2006/0042417 A1
54. Callaway JD, Towning JN, Cook R, Smith P, McCartney DG, Horlock AJ (2009) PCT Int Appl WO 2009127813 A1 20091022
55. Hunt EM, Pantoya ML, Jouet RJ (2006) Intermetallics 14:620
56. Ahmadpour A, Do DD (1997) Carbon 35:1723
57. Orru R, Cao G, Munir ZA (1999) Metall Mat Trans A: Phys Metallurg Mat Sci 30:1101
58. Turnbull T (2008) Self-propagating high-temperature synthesis of aluminum-titanium metallic foams. Senior Thesis, Texas Tech University
59. Kobashi M, Kanetake N (2009) Materials 2:2360
60. DTIC report, (submitted), Citation Number 228425
61. Schaedler TA, Jacobsen AJ, Torrents A, Sorensen AE, Lian J, Greer JR, Valdevit L, Carter WB (2011) Science 334:962

62. Mecklenburg M, Schuchardt A, Mishra YK, Kaps S, Adelung R, Lotnyk A, Kienle L, Schulte K (2012) Adv Mater 24:3486
63. Geckeler KE, Samal S (1999) Polym Int 48:743
64. Conkling J, Mocella C (2010) Chemistry of pyrotechnics: basic principles and theory, 2nd edn. CRC Press, Boca Raton, pp 1–7
65. Ford W (1964) US Patent 3,121,050
66. Stiller AH, Stansberry PG, Zondlo JW, US Patent 5,888,469
67. Klett J (2000) US Patent 6,033,506
68. Gash AE, Satcher JH, Simpson RL, Baumann TF, Worsley, M US Patent 8,172,964
69. Luan Z, Mills KC, Morris LA, Haines CD (2017) US patent application 2017/0137340
70. Feynman R (1960) Caltech Eng Sci 23:22
71. www.nano.gov (2017)
72. Approaches to Safe Nanotechnology, DHHS (NIOSH) Publication No. 2009–125. Available at www.cdc.gov/niosh
73. Poda AR, Moser RD, Cuddy MF, Doorenbos Z, Lafferty BJ (2013) J Nanomater Mol Nanotechnol 2:1
74. Kołodziejczak-Radzimska A, Jesionowski T (2014) Materials 7:2833

The Relationship Between Flame Structure and Burning Rate for Ammonium Perchlorate Composite Propellants

Sarah Isert and Steven F. Son

Abstract The burning rate of a propellant is one of the most desired pieces of information for rocket motor design. Propellant burning rate is known to be linked to the microscale flame structures located just above the propellant surface. Flame structure and burning rate for an ammonium perchlorate composite propellant depend in large part on three factors: ammonium perchlorate particle size, propellant formulation, and pressure. Propellant burning rates are in general higher with decreasing AP particle size and increasing pressure. When the microscale flame structures sit higher, on average, above the propellant surface, the propellant will have slower burning rates due (in part) to decreased heat feedback to the propellant surface. The addition of burning rate modifiers to the propellant will also change the flame structure, and therefore the burning rate. Currently, propellants are developed using iterations of mixing and testing to obtain burning rates and physical parameters for computer models. However, this method is not optimal due to the large amount of time and cost involved with this highly empirical approach. Ideally, modelers would be able to make a priori predictions of formulation burning rates, but we are far from that currently. Modelers do desire to create high-fidelity computer models to simulate burning rocket propellants, and much progress has been made in recent years; however, relatively little is known about the actual flame structure in composite propellants which has had limited advances. Knowledge of the variation of flame structure with pressure and propellant formulation will not only assist in the validation of these high-fidelity computer models but will also provide insight to propellant formulators as they seek to use alternate ingredients and methods. This chapter seeks to describe the current data we have on the flame structures in ammonium perchlorate composite propellants and how microscale flame structure affects global burning rate. We review the status of current

S. Isert
School of Aero/Astronautical Engineering,
Purdue University, West Lafayette, IN, USA

S.F. Son (✉)
School of Mechanical Engineering,
Purdue University, West Lafayette, IN, USA
e-mail: sson@purdue.edu

modeling, diagnostics that have been applied, simplified configurations that have been considered, and recent in situ measurements that are now available for at least the final diffusion flame. Although much remains to be done, significant advancement has been made to reach the ultimate goal of truly predictive propellant simulation and design.

Keywords Solid rocket propellant · Planar laser-induced fluorescence · Ammonium perchlorate · Burning rate · Flame structure

Abbreviations

AP   Ammonium perchlorate
APCP   Ammonium perchlorate composite propellant
BDP   Beckstead-Derr-Price model
CTPB   Carboxy-terminated polybutadiene
DCPD   Dicyclopentadiene
HTPB   Hydroxyl-terminated polybutadiene
ICCD   Intensified charge-coupled device
LPDL   Low pressure deflagration limit
PBAA   Polybutadiene acrylic acid
PBAN   Polybutadiene acrylonitrile
PLIF   Planar laser-induced fluorescence
PS   Polystyrene
PU   Polyurethene
SEM   Scanning electron microscope

1   Introduction and Background

Since the early days of using composite solid rocket propellants, researchers have sought to model the combustion to enable predictions of burning rate. It was recognized early on that knowledge of the microscale flame structure would be key in allowing these predictions to be made [1–3]. Solid rocket propellants are used in a variety of settings due to their simplicity, reliability, and high thrust-to-weight ratio. Though solid propellants have been used for hundreds of years, modern solid propellants made significant advancements in the 1950s when composite propellants began to replace some the double-base propellants already in use [4]. Though modeling double-base propellants is not an easy task, due in part to chemistry involved with the dark zone and various energetic additives that might be present, moving from a double-base to a heterogeneous propellant adds a layer of complexity due to the presence of microscale diffusion flames that may be present between the oxidizer crystals and binder. As these microscale flame structures are small both spatially and temporally, modeling and experimental observation are very challenging.

Heterogeneous propellants, also known as composite propellants, consist of fuels, oxidizers, and burning rate modifiers that are mixed physically and encased in a rubbery binder [5]. Typically the fuel, oxidizer, and burning rate modifiers are solid and have particle sizes on the order of 10s to 100s of micrometers (μm), though some very fine AP or burning rate catalysts can be nanoscale [6, 7]. The most commonly used oxidizer in solid rocket propellants is ammonium perchlorate (AP). A clear crystalline material that appears as a white powder, AP has a high oxygen balance (+34%), good safety and stability characteristics, and is readily available [8]. Though it will decompose when heated at low pressures, pure AP will not self-deflagrate at pressures below the low pressure deflagration limit (LPDL) of about 2.0 MPa [9]. Though AP has many desirable characteristics, it produces significant amounts of hydrogen chloride (HCl) during combustion—each of the space shuttle solid rocket boosters, for example, produced over 100 tons of HCl per launch [10]. Simplified configurations, such as sandwich configurations, have been used to better understand the flame structure of composite propellants.

Flame structure has been investigated using a variety of methods from visual imaging to thermocouples, each with their attendant pros and cons. Planar laser-induced fluorescence has been used to measure the NH, OH, and CN species profiles for a series of sandwich propellants that used different oxidizers as a way to determine where in the flame structure these species, and associated diffusion flames, occur. In these experiments, AP exhibited strong diffusion flames close to the surface that persisted at elevated pressures. Compared with other materials such as cyclotrimethylene-trinitramine (RDX), cyclotetramethylene-tetranitramine (HMX), 1,3,3-trinitroazetidine (TNAZ), ammonium dinitramide (ADN), and hydrazinium nitroformate (HNF) only AP showed strong diffusion flames that allow burn-rate control. The nitramines exhibited no diffusion flames, as might be expected for fuel-rich materials, and the other materials showed weak diffusion flames that were too far from the surface to affect the burning rate [11]. Though research is ongoing to find alternative oxidizers, AP is still the most commonly used oxidizer and will be the main focus of this chapter.

In order to produce a propellant with the highest possible performance, multiple AP particle sizes are typically used in a propellant to yield a high solids loading. Multimodal propellants typically consist of 2–3 average particle sizes; these may be small (tens of μm), medium (100–200 μm), and/or large (maximum 400 μm) particles. Using multimodal AP distributions allow for the highest oxidizer packing, as the smaller particles will fill the interstitial voids between the larger AP particles [12, 13]. Bimodal propellants (two oxidizer sizes) are commonly used. The maximum possible packing for spherical particles in a bimodal propellant occurs at about 30% fine, 70% coarse oxidizer [13]. Packing fraction increases when the sizes of the coarse and fine AP are very different, as seen in Fig. 1. Experimental packing data differ somewhat from calculated data, mostly because real AP particles are not perfectly spherical.

Adding metal fuels to a composite propellant increases the flame temperature, heat of combustion, and propellant density [15]. The increased flame temperature from burning the metal fuel will increase the specific impulse of the propellant,
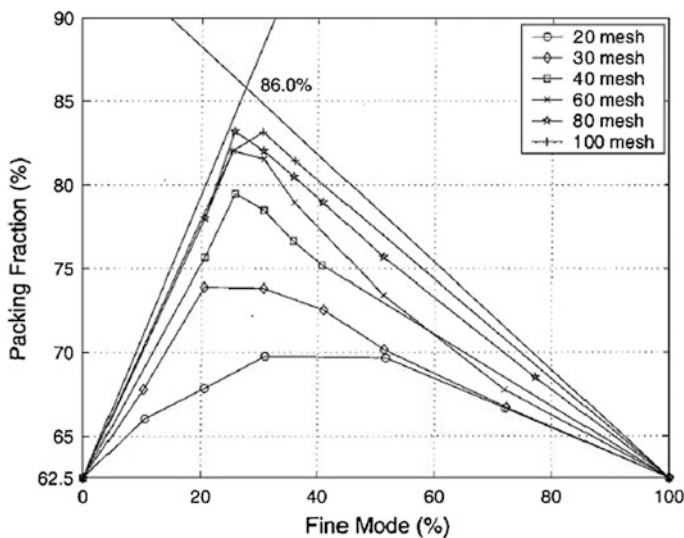
Fig. 1 Binary mechanical packing of coarse steel shot with some other sizes. Figure from Ref. [14]. Used with permission. Coarse mode is 7 mesh (3149.6 μm) and fine mode ranges from 20 (914.4 μm) to 100 mesh (165.1 μm), or a C/F particle diameter ratio from 3.4 to 19.1. McGeary plots the packing volume v for a fixed particle volume of 6.25, on a linear scale, and the packing fraction is 62.5/v × 100%, plotted on a nonlinear scale. The packing fraction is shown here on a linear scale [13]

though two-phase flow losses due to slag production in the motor can be significant compared to theoretical performance [16]. Fuels can be used to help decrease combustion instabilities [17]. The most typically used metal fuel added to APCP is aluminum.

Burning rate modifiers are added to propellants to tailor the burning rate of a formulation. Catalysts are added to increase the propellant burning rate. Catalysts such as iron oxide (Fe_2O_3), copper oxide (CuO), manganese dioxide (MnO_2), copper chromate ($CuCr_2O_4$) and other transition metal oxides are often used [6, 18], though other, more exotic catalysts such as decorated graphene have also been investigated [19–24]. Iron oxide, in particular, is commonly used as it is relatively nontoxic, easy to manufacture, and is a good modifier at rocket pressures; in addition to this, the burning rates it produces are highly reproducible and well-characterized [6, 25–36]. Catalysts can either be mixed into the binder directly or encapsulated into the fine AP [37, 38], and can be micron- or nano-sized, with the nano-sized catalysts appearing to have a greater effect on increasing propellant burning rates [6, 25].

Binders used in composite propellants are most often viscoelastic polymers. The binder starts out as a liquid but cures to a solid. As the binder provides the structural support for the granular components of the propellant grain there must be sufficient binder to hold everything together; however, a high binder percentage decreases

propellant performance as the binder is also a fuel in propellant combustion. Often, even with the minimum amount of binder, the propellant is fuel-rich. Binders in use include hydroxyl-terminated polybutadiene (HTPB), carboxyl-terminated polybutadiene (CTPB), polybutadiene acrylonitrile acrylic acid (PBAN), and polybutadiene acrylic acid (PBAA) [15].

Processes that occur during the combustion of APCP propellant include condensed-phase heating, decomposition of the AP and binder, melting, pyrolysis, and gas phase reactions. Propellant combustion depends on propellant microstructure, 3D heat transfer, ingredient melt and decomposition behavior, 3D microscale flame behavior, and the interaction of all of the above [39], which are in turn functions of factors like propellant composition, AP particle size, initial and ambient conditions, and propellant surface morphology [40]. The burning rate of a composite solid propellant grain depends in large part on propellant formulation. Propellants with a finer average AP particle size will burn faster than those with a coarser average particle size. It is generally believed that the particle size burning rate dependence is in large part due to the microscale flame structure above the solid propellant [41].

2 Flame Structure Models

Modeling the APCP flame structure began shortly after composite propellants were introduced. One of the earliest models described the flame structure as a quasi-steady gaseous flame adjacent to the surface where the mixing of the oxidizer and fuel only occurred in the gas phase. This model, known as the 'granular diffusion flame' (GDF) model, postulated that the oxidizer and fuel are released in adjacent pockets. The pockets are gradually consumed at a rate controlled by the diffusion of the fuel and oxidizer into one another and by the kinetics at the burning pressure [3]. More complicated models were developed that took into account fuel and oxidizer decomposition, heterogeneous chemical reactions between the fuel and decomposed oxidizer near the AP particles, and the gas phase combustion of the final diffusion products. The new models sought to explain important aspects of APCP combustion that were not captured by earlier models, such as the dependence of the burning rate on pressure and the oxidizer particle size distribution [2].

The most commonly accepted model of the flame structure above an ammonium perchlorate composite propellant first appeared in 1970. The Beckstead-Derr-Price (BDP) model describes the flame structure above a coarse AP crystal embedded in binder as having three flame zones: a primary diffusion flame between the binder and AP decomposition products, a monopropellant flame above the coarse AP crystal, and a final diffusion flame from the products of the other two flames [42]. The premise of the BDP model is that, as a composite propellant burns, the binder and oxidizer undergo decomposition processes and the resulting gaseous products

Fig. 2 Modified BDP flame
structure. Here (*1*) represents
the monopropellant flame, (*2*)
indicates the fine AP/binder
matrix pseudo-premixed
flame, (*3*) is the final diffusion
flame, and (*4*) are the
leading-edge flames
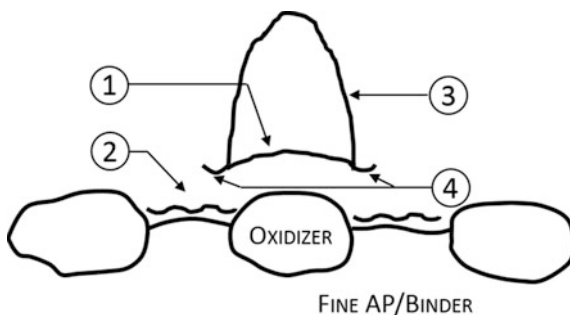
mix and react at some point above the propellant surface. The kinetics of these reactions increase with pressure. At low pressures one might expect mixing to occur completely before reaction, while at high pressures the mixing step may be the limiting process, resulting in diffusion flames.

The flame structure of the modified BDP model is shown in Fig. 2. At high enough pressures or with sufficient heat feedback, coarse AP particles will burn essentially as a monopropellant. This flame is highly dependent on pressure and produces excess oxygen [43]. The flame above the fine AP and binder is often considered to be premixed, especially for computational efforts. The fine AP decomposes very rapidly and the decomposition products have time to mix well with the decomposition products of the binder before ignition [44–47]. This pseudo-premixed flame will typically be fuel rich. A significant feature of the original BDP model was the inclusion of a primary diffusion flame located at the edge of the AP particle that occurs between the binder and AP decomposition products. This primary diffusion flame, also known as the leading-edge flame [41, 48], is hot and sits close to the propellant surface. The primary diffusion flame is often considered to be a premixed, or partially premixed, rather than a diffusion flame [46].

The secondary or final diffusion flame forms between the binder matrix products and the AP decomposition/monopropellant flame products. As the flame forms by diffusion and the diffusion distances are comparatively long, the final diffusion flame will form farther above the propellant surface than the other three flames. The hot final diffusion flame will have a greater or lesser effect on propellant burning rate depending on pressure, becoming more dominant at higher pressures as it is pushed closer to the propellant surface [42].

The BDP model has been slightly altered over the years but continues to be the basis for nearly all the models proposed for APCP combustion, and remains a useful conceptual model. Most of these alternate models merely extend the BDP model into three dimensions and multimodal oxidizer sizes. Other models predict flames similar to the BDP 3-flame model [49] or use columnar diffusion flames and AP monopropellant flames instead of the 3-flame model [50].

3   Research Methods

Characterizing flame structure of solid propellants is difficult due to the small length scales (largest are ∼100s of micrometers) and short time scales (longest are ∼100s of milliseconds) involved, multiple flames and an active propellant surface. Several methods have been developed in an attempt to characterize the flame structure. A brief description of common experimental techniques will be given below.

3.1   Linear Burning Rate Measurements

The linear burning rate as a function of pressure is one of the most important and common metrics of a propellant. Burning rate is strongly coupled to microscale flame structure. Linear burning rate is typically obtained as a function of pressure and initial temperature in a (typically) windowed Crawford-type strand burner. Burning rate is tracked by break wires and/or optically as a propellant strand burns. Generally, propellants are inhibited on the lateral sides to avoid flame spread. Break wires are fuse wires tied to a timing circuit and placed down the length of the propellant. As the wires break, a signal is sent to the timing circuit. As the distance between the break wires is known, the burning rate can be calculated by dividing the distance between the wires by the time between the received electrical signals.

To calculate linear burning rate optically, a windowed bomb is required. A framing camera is placed in front of the window so the propellant is visible. As the propellant burns video is taken. The location of the burning surface is tracked and plotted against time. The slope of the position-time curve is the linear burning rate. Whether the burning rate is determined via break wires or optically, several burning rate measurements are performed at several pressures. The burning rates are then plotted against pressure on a log-log scale and fitted to the St.-Robert (or Vieille) burning rate law:

$$r_b = ap^n \tag{1}$$

Here r_b is the linear burning rate, a is a pre-exponential factor, p is pressure, and n is the burning rate exponent. For a good solid propellant n is typically in the range of 0.3–0.5 and typically must not be greater than 1 for stability considerations.

If the strand burner is optically accessible, bulk flame structure can be determined [51]. A typical optically accessible strand burner can be seen in Fig. 3a and a sample image from a burning propellant at 1000 psig can be seen in Fig. 3b. Other information about the microscale flame structure can be determined in the combustion vessel environment. For example, Summerfield et al. seeded the propellant with NaCl, focused a spectrometer on the burning propellant, and by using the yellow D lines of sodium were able to see the point above the surface where the NaCl had reached its boiling temperature of 1700 K [3]. Researchers have also
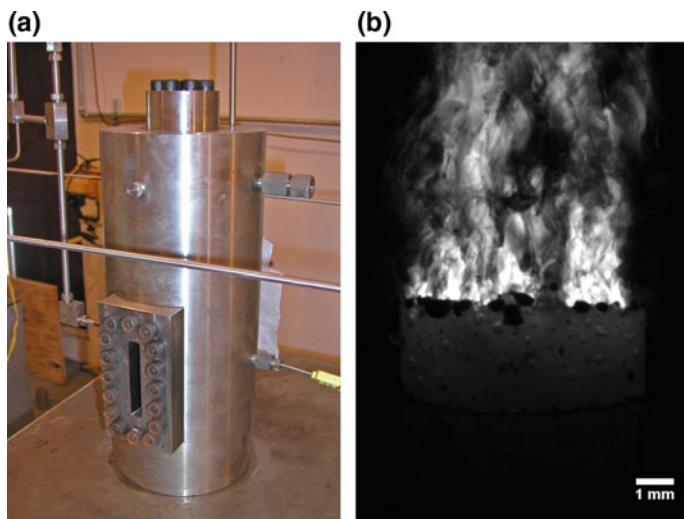
Fig. 3 Shown is **a** a Crawford-type strand burner at Purdue University and **b** a sample image of a burning AP/HTPB propellant at 1000 psig

made thermocouple measurements to determine the flame and subsurface temperatures in neat materials and solid propellants [1, 52].

As solid propellant flame structure occurs on a very small dimensional scale, minimally intrusive probes are required so as to not perturb the flame structure [53]. Additionally, transience is the natural state of an AP/HTPB propellant and experimental methods require fast time responses to capture even the timescale of the larger crystals (on the order of 100 ms). The environment is harsh with high pressures and temperatures; and the flame is generally dirty, making probing the flame a difficult problem. Ideal experimental techniques are minimally intrusive, temporally and spatially resolved, species-, temperature-, or velocity-specific, often multichanneled, and robust [53].

3.2 Optical Emission and Transmission

Ultraviolet and infrared optical emission and transmission have been used to image flame structure and surface profile. In optical emission, light emitted by the flame passed through notch filters at wavelengths associated with known species such as OH* in the UV and HCl rovibrational excitation in the IR [54–56]. The filtered light is imaged by an intensified charge-coupled device (ICCD). The ICCD captures both an emission image and a transmission image; the transmission image, which is backlit by a lamp, is used to obtain the surface profile. Optical emission and

transmission tests can be performed at pressures above 1 atm. These techniques are particularly useful in relating flame structure to varying binder configurations and have been used to help determine properties of the primary diffusion flame.

3.3 Laser Induced Fluorescence

Laser-induced fluorescence (LIF) occurs when atoms or molecules absorb laser photons and the atoms or molecules are raised to an excited electronic state. The electrons must de-excite to return to the stable ground state. One of the ways electronic de-excitation can occur is by re-emission of the photons as fluorescence. Both the absorption and emission are wavelength selective; therefore, LIF diagnostics can be very species selective depending on the choice of excitation and detection wavelengths. Laser-induced fluorescence methods monitor the ground electronic state of flame species; chemiluminescence comes from excited electron states [11]. Background flame emission can interfere with the LIF signal, but pulsed lasers and gated detection methods help discriminate between the LIF signal and chemiluminescence or particle incandescence. Fluorescence can be widely separated in wavelength from the exciting laser, allowing for diagnostics to occur in dirty flames.

The LIF measurement is captured by focusing the fluorescence on a slit perpendicular to the beam and detecting the fluorescence with a filtered photomultiplier [57]. This method allows for detection of a qualitative concentration profile in a steady flame. While early measurements were made at 10–40 Hz, high-speed lasers and photomultipliers or photodetectors can increase the temporal resolution. Though LIF is useful in determining temperatures and species concentrations, there are only a small number of species of interest in propellant combustion accessible to current laser systems, and most of these are simple diatomic molecules. Some of the accessible species, however, are quite relevant to combustion. Certain species have overlapping transitions, which can make determining what species is fluorescing somewhat difficult. On the other hand, one can pump overlapping transitions and detect multiple species simultaneously.

Broadband emission from soot particles can be difficult to discriminate against, or can severely attenuate the signal [58]. Collisional quenching, radiation trapping, and laser beam absorption can all decrease observed signal [53, 59]. Despite these difficulties, however, LIF began to appear in the propellant literature in the late 1980s and has slowly been growing in use. It has been joined by its two-dimensional analogue, planar laser-induced fluorescence (PLIF) . Instead of passing the point laser beam through the flame, the PLIF technique expands the beam via a series of optics to a diagnostic sheet, resulting in two-dimensional images of the flame structure [57]. A sample PLIF setup is shown in Fig. 4. Species that have been investigated with PLIF in propellants include OH [11, 27, 60–69], NH [11, 66–69], CN [11, 66–69], and NO [66, 68, 69]. Both qualitative and quantitative measurements have been taken. Measurements have typically been at
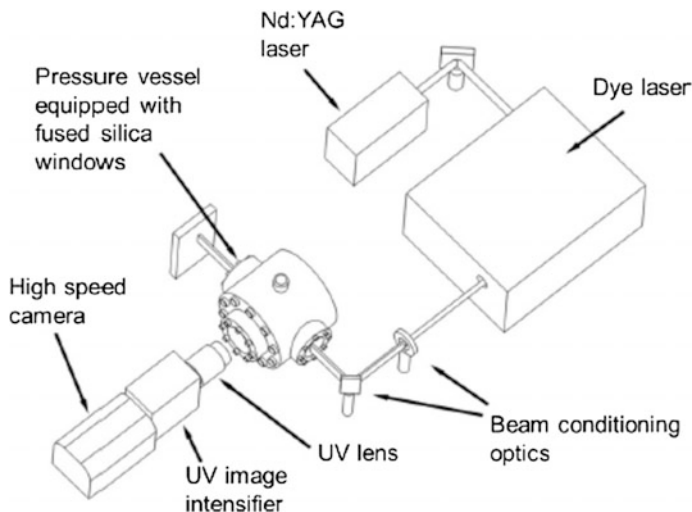
Fig. 4 A PLIF setup. A 532 nm beam from a pump laser is passed through a dye laser, producing a UV beam. The UV beam is expanded into a diagnostic sheet and passed into a pressure vessel. Molecules in the flame are excited by the UV beam, and the resulting emission is collected by a high-speed image intensified camera. Figure is from Ref. [64]. Used with permission

1 atm and 10 Hz [11, 65–69]. Recently, however, PLIF measurements at 5 kHz and both atmospheric and elevated pressures have appeared in the literature [27, 60–64]. Scanned PLIF has been recently used in solid propellants to create pseudo-3D images of the burning surfaces of the solid propellants [70]. These images are formed as the laser sheet is rapidly scanned across the flow field using a rotating mirror.

Other methods including Raman scattering [59, 66, 68], schlieren imaging [71], emission spectroscopy [72], thermocouple measurements [3, 43, 73], and infrared surface temperature measurements [73] have been used to investigate propellant flame structure.

4 Formulation Effect on Flame Structure

The formulation of the solid propellant will have an effect on flame structure. To try and understand formulation effects on a basic level, experiments have been designed to examine solid propellants in simplified configurations. Insights into flame structure will be described ranging from very simplified 1-D configurations ranging to flames in propellant environments. A brief description of the general experiment will be followed by descriptions of the flame structure.

4.1 Counterflow Diffusion Flames

Counterflow or opposed flow burners consist of a fuel and oxidizer, axially aligned, that flow opposing each other so that a stagnation plane forms between the jets and a diffusion flame is established [74]. A diagram of an opposed flow burner is shown in Fig. 5. The simple, 1-dimensional geometry allows for control of many of the variables present in the experiment, such as chemistry, thermal properties (e.g., via dilution of the fuel), and strain rate [68], and extends the diffusion flame to allow probing of the flame structure for information to be used in kinetic modeling [66].

In AP counterflow studies, the fuel is gaseous while the oxidizer is a pressed AP pellet. Several types of fuel have been used to approximate HTPB decomposition products, including ethylene [68, 75, 76], methane [69, 75], and a combination of C_2H_2, N_2, and C_2H_4 [66]. The fuel gas flow rate is often varied to investigate the effect on AP regression rate. Often, the diffusion flame is strained by flowing an inert gas parallel to the fuel flow. Changing the strain rate can help measure how the strength of different flames affects the overall AP pellet regression [75, 77]. Depending on what data is wanted, counterflow experiments can be performed at either atmospheric or elevated pressures. A number of diagnostic techniques can be used to probe the resulting flame structure, including thermocouples, visual imaging, PLIF of various species, adsorption measurements, laser-induced incandescence to measure soot particle concentrations, and Raman spectroscopy.

The basic flame structure observed was an AP monopropellant flame above the AP surface with a diffusion flame formed from the fuel and AP monopropellant flame products closer to the stagnation plane [68, 75]. The flame structures lie on the AP side of the stagnation plane [66, 68, 69]. Four distinct regions of the flame were seen: an orange region with a very short standoff distance from the AP surface, a light blue zone, a reddish-purple zone, and a bright yellow flame. These zones are

Fig. 5 Schematic diagram for the counterflow diffusion flame experiments. Figure is adapted from Ref. [66]
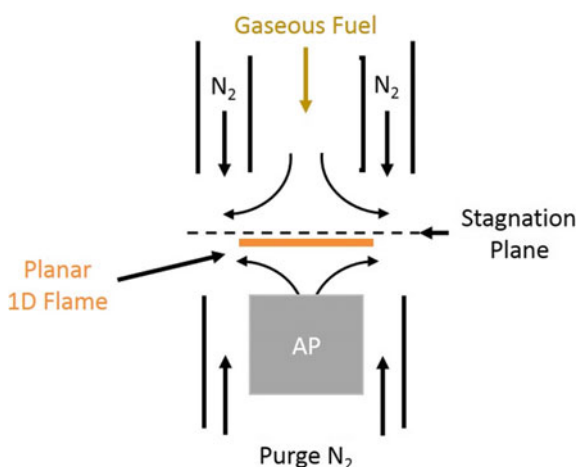
thought to correspond to the AP self-deflagration flame, the appearance of OH radicals, the primary diffusion flame, and a soot flame [68]. Flame structure and regression rate were found to be sensitive to impurities in the AP [69].

Temperatures were seen to rise rapidly moving away from the AP pellet surface with a slower temperature decrease approaching the fuel jet [68]. The rapid rise in temperature near the AP surface is due to the monopropellant flame and the heat release associated with the chlorine chemistry, with the chlorine concentration dropping off rapidly as distance from the AP surface increases [69]. The hydrogen concentration also decreases with distance from the AP surface, indicating the formation of HCl. Though the peak temperature occurred in the region of the diffusion flame, peak heat release occurred close to the AP surface due to the highly exothermic chlorine chemistry [69]. The NO peak occurred within about 0.5 mm of the AP surface, the OH maximum corresponded with the peak temperature, and the CN peak was approximately co-located with the stagnation plane [66].

It is commonly known that pure AP will not burn below 2 MPa. However, experiments with the counterflow diffusion flame have shown that an AP pellet will burn below the self-deflagration pressure limit if there is heat feedback from another source; for example, from the diffusion flame between the AP and fuel [75]. At low pressures the diffusion flame is more coupled to the monopropellant flame and provides heat feedback to help sustain AP decomposition [75]. As pressure increases the monopropellant flame kinetics become faster, shifting the monopropellant flame closer to the surface and increasing the AP regression rate without significantly changing the location of the AP/fuel diffusion flame. The increased kinetics allow the monopropellant flame to propagate without needing heat feedback from another flame at pressures above the LPDL. The presence of the monopropellant diffusion flame below the low-pressure deflagration limit of AP is an important observation from counterflow diffusion flames.

4.2   Ported Pellets

To move from one-dimensional to a relatively simple, steady two-dimensional configuration, ported pellets have been fabricated where small holes have been drilled in a pressed AP pellet and used as fuel flow ports [67] or filled with HTPB [77]. The ported pellet configuration is useful as length scales can be controlled and the interfacial region locations are fixed, making it easier to measure species and temperature profiles. The size and number of the ports can be varied for different fuel/oxidizer ratios and to simulate AP propellants with very large particle sizes [77]. Examples of ported pellets are shown in Fig. 6.

The flames above ported pellets have been investigated visually and using PLIF imaging. The port geometry was found to partially premix the fuel species with AP monopropellant flame products, adding a layer of complexity not seen in the counterflow diffusion flames. Flame heights were found to be proportional to the square of the port diameter when the fuel was gaseous, as expected from laminar
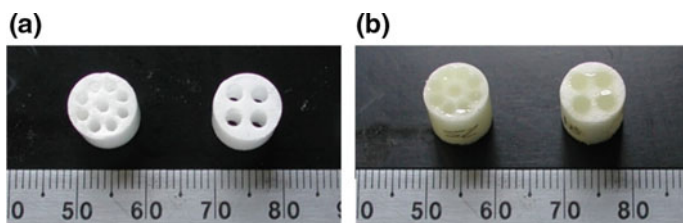
Fig. 6 Manufactured 9 and 4 port AP pellets **a** pre- and **b** post-filling with HTPB. Figure from Ref. [77]. Used with permission

flow theory [67]. This would indicate that flame height will vary in the propellant environment with as the thickness of the binder matrix between coarse AP particles changes. A short ignition delay was seen prior to the formation of a two-stage flame [67]. Diffusion is thought to play a part in the ignition delay, as the gaseous fuel will need to mix with the AP decomposition products. The delay is also caused in part by the inhibiting action of HCl on the CO oxidation reaction; this inhibiting effect allows O_2 to diffuse into the centerline of the flame, resulting in a partially premixed fuel/oxidizer flame that stabilizes above the fuel decomposition flame [67].

When the ports were filled with HTPB, the flames were cylindrical overventilated jet-like structures [77]. The AP/binder interface regressed into the propellant surface, producing dome-shaped fuel surfaces. One of the reasons to use ported AP pellets was to permit the formation of the leading-edge, final, and monopropellant flames, and to compare that to the opposed flow experiments which only have the monopropellant and final diffusion flames. Additionally, by using counterflowing nitrogen to strain the flame, Johansson et al. found that when the counterflow velocity was increased past a certain point the final diffusion flame was extinguished and pellet regression stopped, indicating that the heat feedback from the secondary diffusion flame is needed to support the monopropellant and leading edge flames at 1 atm [77]. This observation supports the idea that the AP monopropellant flame is present at 1 atm under certain circumstances due to support from the final diffusion flame. The ported pellet experiments also allowed the premixed leading-edge flames to be investigated, and revealed that they vary with binder width and oxidizer size, and that they are indeed probably premixed in nature.

4.3 Sandwich/Lamina

Flame structure measurements in the composite propellant environments are difficult to make because of the highly three-dimensional nature of the propellant. To investigate flame structure, sandwich or laminar propellants are used to model AP composite propellants in a simpler geometry while still retaining some heterogeneous structure [26, 48]. In a sandwich propellant, a laminate of binder is sandwiched between lamina of AP or vice versa, as can be seen in Fig. 7. By using the

Fig. 7 Sandwich mechanics. Not to scale
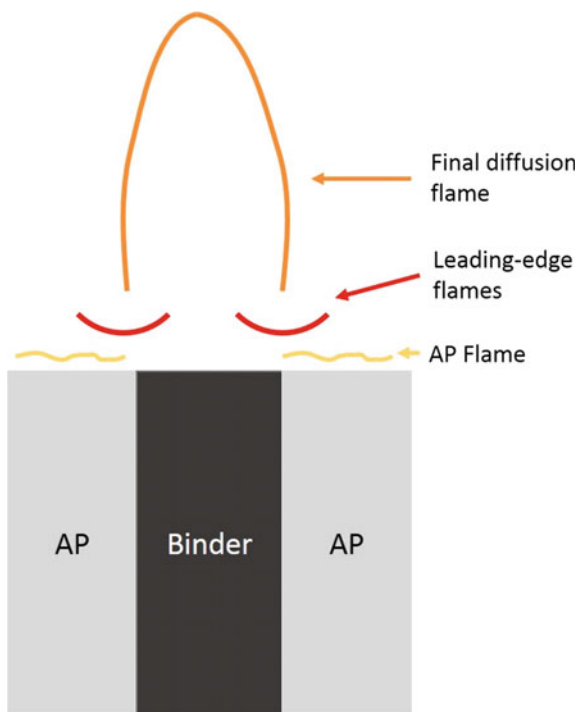
sandwich structure the surface geometry, flame structure, burning rate, binder width, and overall propellant formulation can be varied. Sandwiches are not directly analogous to composite propellants; for example, they are often fuel-lean rather than fuel-rich. However, the sandwich geometry remains useful for screening propellants and providing basic information on the flame structure above AP/binder interfaces.

Binders used in sandwich propellant experiments include PBAA, HTPB, PBAN, CTPB, polyurethane (PU), and polystyrene (PS) [71, 78]. The type and thickness of binder plays a part in what the flame structure looks like. Pure AP does not burn below 2 MPa, but sandwich propellants will burn at atmospheric pressure unless the binder is too thin [48]. If the binder pyrolysis/decomposition products are relatively small molecules the LEF will sit closer to the surface. If binder decomposition products are relatively large and must decompose further prior to combustion, the LEF will have a larger flame standoff. In early work single crystals of AP were used for the AP lamina, but later work found that pressed polycrystalline AP produced very similar results to the single crystal data [78].

The sandwich (or laminate) propellant flame structure is similar to a modified BDP propellant with the AP monopropellant flame above the AP lamina, leading-edge flames (LEF) located on the boundary between the AP and binder laminate, and a final diffusion flame above them all [79]. Emission and transmission

imaging shows that the heat release above sandwich propellants is concentrated in the LEF [80]. The LEF form from the AP and binder combustion products almost directly over the AP/binder interface and sit closer to the propellant surface than the final diffusion flame. Unlike the final diffusion flame, LEF are strongly dependent on kinetics since they stand in a partially premixed flow [48, 79]. Though LEF have not been directly observed in solid rocket propellants, they have been observed in gaseous fuel flames and theoretical considerations suggest they likely exist in solid propellants [41, 48].

Leading edge flames take on a few different forms that change with binder laminate thickness and pressure. The flame structures are typically described as combined or split (see Fig. 8) [56]. Combined LEF often occur when the binder laminate is thin. With thin binder lamina, the flames merge over the binder, resulting in higher temperatures, reduced standoff distances, and consequently higher sandwich burning rates than for split flames [9]. However, if the binder becomes very thin the LEF will detach from the binder as they become fuel deficient [81]. Combined LEF are predicted to be unstable or quench when AP laminate thickness is small, pressure is low, and mixture ratio is fuel rich. Under these conditions the LEF will move away from the surface to find a stable heat loss/heat release condition, decreasing flame heat feedback to the propellant [81].

If the binder is very thick or protrudes into the gas phase, the LEF will split and a distinct flame will form at each AP/binder interface due to an increase in the diffusion length scale across the binder laminate [9]. As the flames move closer and begin to interact (but do not combine) they begin to augment the binder laminate burning rate. When the LEF are split they primarily affect the AP regression rate and the binder tends to protrude above the average surface [81].

Combined or split, leading-edge flame standoff distance is controlled by a balance between the chemical heat release and the heat feedback to the propellant surface. For a given binder thickness, as pressure increases the LEF shrinks, causing a decrease in chemical heat release. The larger amount of non-premixed reaction at higher pressures contributes to the premixed LEF shrinking. Additionally, the LEF shrinkage suggests that there is some limit to how close increasing pressure will push the flames to the propellant surface [79]. As the binder laminate thickens the LEF can form closer to the surface than otherwise due to the increased fuel supply. Though the LEF will still shrink, the outer diffusion flame, which also approaches the surface with increasing pressure, will contribute to the heat feedback and help stabilize the LEF [79]. As the LPDL is approached, the AP monopropellant flame becomes more dominant and the final diffusion flame extent and heat release increase [55].

Many of the results described up to this point have been for sandwiches with pure binder lamina. In an AP propellant the binder usually is oxygenated, or contains fine AP. Experiments with sandwich propellants showed that when the binder matrix is oxygenated the experimental diffusion flame becomes shorter than when the laminate is pure binder [54]. The LEF shift toward the matrix laminate rather than being located primarily above the AP/binder interface. If the AP particles in the binder laminate are small and pressure is low, mixing becomes more
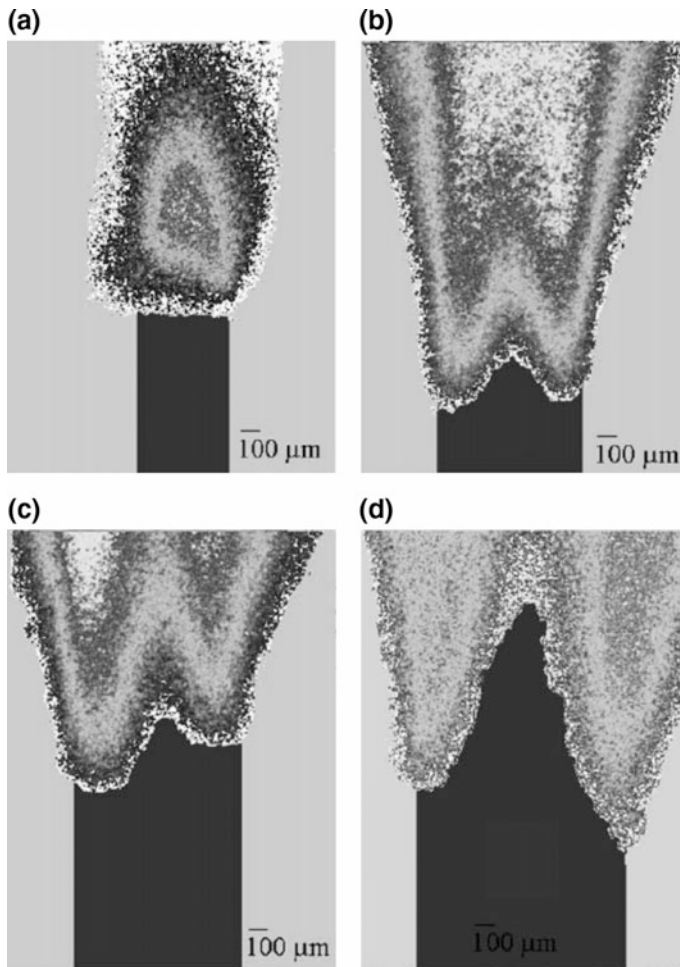
Fig. 8 Experimental images for fuel matrix at 15 atm and **a** 510 μm, **b** 790 μm, **c** 920 μm, and **d** 1150 μm. Figure from Ref. [54]. Used with permission. Here **a** shows a combined LEF while **b**–**d** show split LEF with a separate LEF occurring at each oxidizer/binder interface. The split LEF are expected to interact to some extent

complete in the LEF between the AP and binder matrix lamina. As pressure increases, or if the AP particles in the matrix laminate are large, the particles in the binder matrix laminate can form their own LEF [79]. The particle LEF can blanket the surface of the binder matrix laminate and connect the fuel-rich sides of the AP/binder lamina LEF, which increases the sandwich burning rate [82]. For a given fine AP/binder matrix formulation, LEF and the premixed flame from the fine AP/binder matrix are expected to form closer to the surface at elevated pressures [81]. If the stoichiometry is more fuel-rich, the gas-phase flame tends to move

farther away from the burning surface, causing the surface temperature to decrease, while flames that are more stoichiometric sit closer to the burning surface [82]. Flame height is also linked to binder laminate thickness [48, 81].

Adding aluminum to propellant laminates (sandwiches) has shown that the addition of aluminum does not significantly alter the AP/binder flame structure, though it does increase burning rate via heat feedback (significantly radiative) or decrease it via inert heat-sink effects [41]. The aluminum typically will not ignite until it reaches the flame between the outer AP laminate and the fine AP/binder matrix, as the pseudo-premixed flame is not always hot enough to be an ignition source. The effect of the aluminum was either as an inert heat sink before ignition (drawing energy from the AP/binder flame) or as a thermal source after ignition. At lower pressures the effect of the aluminum is noticeable on the burning rate, as the final AP diffusion flame is farther from the surface and any contribution of heat feedback will help increase the burning rate. Above about 5 atm, the final diffusion flame begins to move closer to the sandwich propellant surface. However, the aluminum flame height is only weakly dependent on pressure and its effect on propellant burning rate will decrease. Additionally, at higher pressures the inert heat sink effect of aluminum becomes more prominent for the conditions considered. The lessened effect of the aluminum flame height on burning rate combined with the increased heat sink effect results in a decrease in burning rate of the aluminized laminates compared to the non-aluminized laminates and a smaller pressure exponent for aluminized sandwich propellants [41], although this may be different in actual propellants.

As they are simpler to model than composite propellants, flame structure models have been created for sandwich propellants. The models take into account surface geometry, flame structure, burning rate for variations in pressure, particle size, binder width, and propellant formulation [80]. The flame structure is often characterized in terms of volumetric heat release, which provides information on condensed-phase pyrolysis, gas heat feedback, flame structure, and surface geometry. Model results indicate that low pressures result in recessed binder lamina while high pressures result in protruding binder lamina. Numerical predictions also indicate that a break in the pressure exponent occurs for sandwich propellants. At low pressures, the pressure exponent was calculated to be 0.4, indicating that the primary diffusion flame is important. However, as pressure increases, the pressure exponent was calculated to change to 0.74 above 0.7 MPa, indicating the final diffusion flame importance is increasing as it is pushed closer to the propellant surface [9].

4.4 Monomodal

Though simplified geometries are useful for modeling studies and understanding the basics of AP composite propellant flame structure, three-dimensional effects must be considered to fully understand propellant combustion [66]. The simplest

propellant formulation is one where the AP is mono- or unimodal, meaning it has only one size distribution. In this way the burning rate only depends on particle size and solids loading, and if the solids loading is held constant the burning rate can be directly related to particle size [83].

Flame structures for monomodal propellants depend on particle size. For fine particles at low pressures, the AP does not develop an attached diffusion flame and simply pyrolyzes and burns in the pseudo-premixed flame [84]. As pressure increases, the particle size below which premixed flames occur decreases and micro-scale flames begin to attach to individual AP particles [84]. Flames will also attach to individual AP particles as the particle size increases. The point at which diffusion flames begin to form above individual AP particles is known as the premixed limit. The premixed limit can be seen experimentally or computationally as an inflection point where the burning rate begins to decrease with increasing particle size, as seen in Fig. 9. Sandwich propellants with AP mixed into the binder have also displayed a premixed limit [9]. As particle size becomes large enough, the AP monopropellant limit is reached. In the AP monopropellant limit, where the particle size is large, combustion is dominated by the relatively cool AP mono-propellant flame and the propellant approaches the burning rate of pure AP. The monopropellant flame will control the burning rate, as it is much closer to the propellant surface than the final diffusion flame. The particle sizes at which the premixed limit, transitional diffusion zone, and monomodal limit regions begin depend on pressure and propellant formulation [44, 45].

Flame structures affect global burning rate. For propellants where particle sizes ranged from 20 to 800 μm, the visible flame structure can be divided into two categories at 1 atm as seen in Fig. 10 [77]. Propellants with fine AP (20–100 μm)
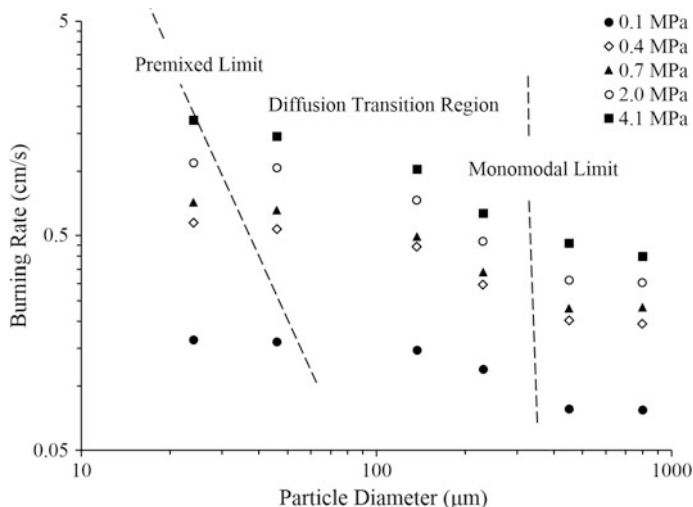
Fig. 9 Burning rate of propellants as a function of pressure and particle diameter. Modified from Ref. [61]. The locations of the premixed and monomodal limits are approximate but reasonable
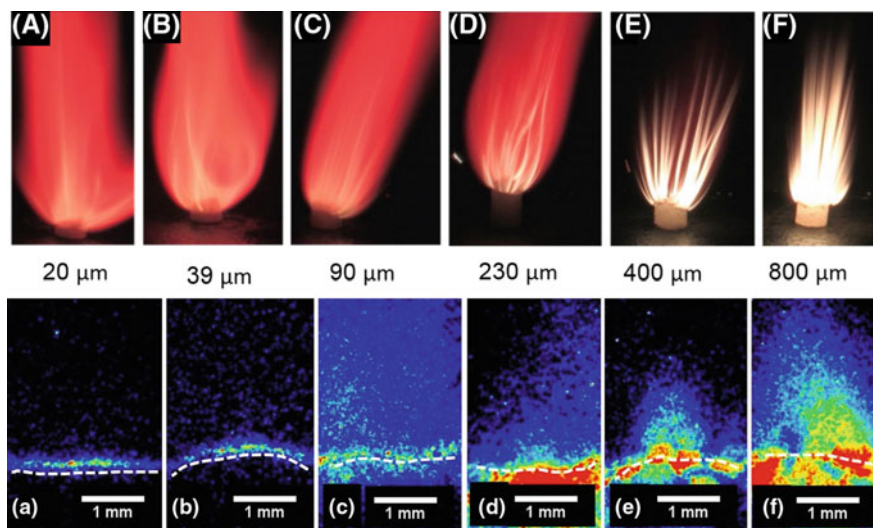
Fig. 10 Monomodal propellants at 1 atm. *Top row* shows visual propellant structure. *Bottom row* shows PLIF structure and is adapted from Ref. [77]

had a very uniform flame structure, both visually and using PLIF imaging. No defined flame sheet was visible, though that is most likely due to the lack of the required spatial resolution rather than the lack of a flame sheet. As AP diameter increased to above 200 μm bright flame tendrils began to be visible inside the coral sheath flame in the visible images. These tendrils correspond to diffusion flames. Similar flames are visible in the PLIF images. In the PLIF images (Fig. 10d–f), bright patches on the propellant surface correspond to coarse AP crystals. The flame structures seen above the coarse AP particles at 1 atm are uniformly jet-like in the PLIF images.

As AP crystal diameter increases at 1 atm, flame height increases (Fig. 11), as would be expected. Jet-like diffusion flames were visible above both individual AP crystals and groups of AP crystals. Group combustion of AP particles is analogous to the group combustion observed in droplet combustion [85]. When the AP crystals burn in groups, the flame structure is taller than that of an individual AP crystal. Group combustion is believed to occur partly due to interaction between leading-edge flames of individual particles. The LEF increase the heating rate of nearby coarse AP particles, causing an increase in particle burning rate. The increase in burning rate causes an increase in volumetric flow rate. As flame height is proportional to volumetric flow rate, groups burning together will lead to very tall flames [77].

As pressures increase above 1 atm, individual diffusion flames above the fine AP particles are expected to form. These flames have not yet been experimentally observed due to the lack of resolution in current experimental capabilities. However, the flame structures above the propellants with coarse AP have been
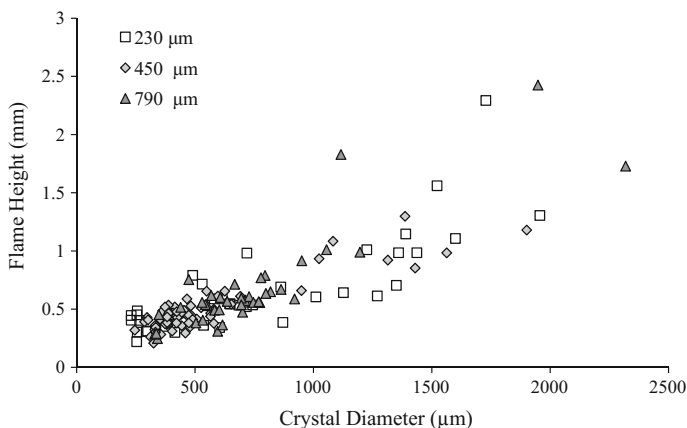
Fig. 11 Flame height as a function of crystal diameter in a monomodal propellant. Adapted from Ref. [77]. The legend refers to the average particle size of the monomodal propellant
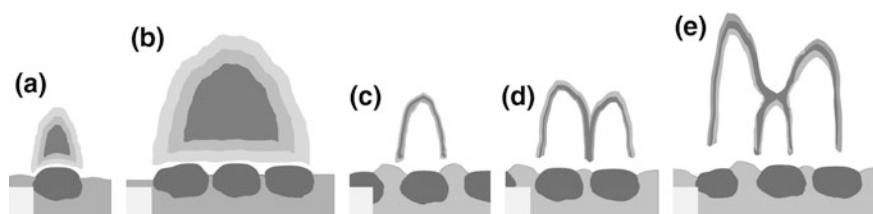
Fig. 12 Flame structures above solid propellants. Here, **a** represents underventilated jet-like flames above individual particles, **b** represents a group flame over a large number of particles, **c** is a single-arch flame, **d** is a double-arch flame, and **e** is a triple-arch flame. Though **a** have been observed at all pressures investigated (up to 1.0 MPa), group flames as in (**b**) have only been observed at 1 atm and arched flames as in (**c–e**) have only been observed at pressures above about 0.3 MPa

observed to change from jet-like underventilated flames [Figs. 10 and 12(a-b)] to lifted, arched, overventilated diffusion flames [Fig. 12(c-e)]. Flame structures observed above coarse monomodal propellants at elevated pressures were arched. Three distinct structures were seen: single arches, double arches, and triple arches. These flame structures can be seen in Fig. 12 along with examples of jet-like flames (Fig. 12a, b). Double-arch flames differ from two single-arch flames in close proximity as the arches in the double-arch flames share a center leg (Fig. 12d). The triple-arch flames consist of two tall flames with a shorter arch located between and below them. Flame structures are often found in close proximity to one another.

Figure 13 shows experimental PLIF images of monomodal propellant flame structures at 0.5 MPa [77]. Figure 13(1) shows a 20 μm AP monomodal propellant. The flame structure is not resolvable, though from burning rate measurements it is likely the propellant is still burning in the premixed regime and individual
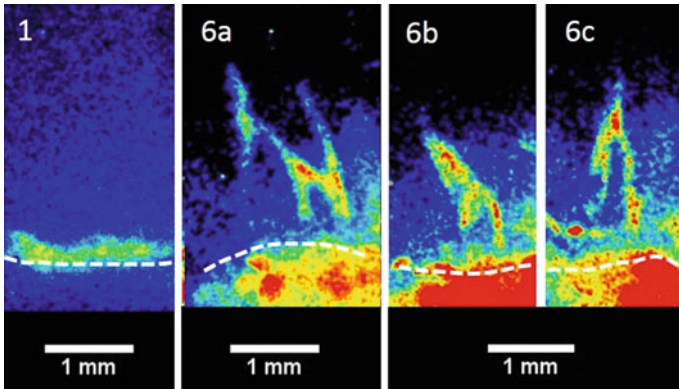
Fig. 13 Flame structures above monomodal propellants with (*1*) 20 μm and (*6*) 790 μm monomodal AP at 0.5 MPa. *White dashed lines* are placed immediately below the propellant surface. From Ref. [77]. Used with permission

structures above the fine AP particles have not yet developed. The other flame structures shown in Fig. 13 are above 790 μm AP propellants. In these images one can see arched diffusion flame structures. Figure 13(6a) shows the U-shaped region connecting the taller arches and two shorter center arches of a triple flame. Figure 13(6b, c) show single-arch flames. Interestingly, at 0.5 MPa, arched flame heights were equal for all propellants for which they were visible [77]. The thin reaction zones that are visible in the PLIF images are thought to be due to the overventilated condition, as these flames are known to have thinner reaction sheets than underventilated flames [86]. In Fig. 13(6b) one can see a second high concentration of OH slanting diagonally off the single-arch flame. This artifact is probably part of another flame that falls within the laser sheet enough to show that it exists, but not enough to capture the shape of the flame. Flame aspects like these reflect the highly heterogeneous and three-dimensional nature of the propellant flame structure.

The change in flame structure between 1 atm and elevated pressure combustion is thought to be due to the relative burning rates of the coarse AP particles [60]. At 1 atm, the propellants with fine AP burn with a pseudo-premixed flame in the premixed region. In propellants with coarse AP, the large particles burn relatively slower than the binder, as can be seen by the protrusion of the coarse AP above the surface. When the length scales become large enough, diffusion begins to become important and jet-like flames begin to form above the propellants. As pressure increases, AP chemical kinetics accelerate. Whether or not a monopropellant flame occurs at pressures below the LPDL in the propellant environment is as of yet unknown (but is strongly indicated by the results from opposed flow burners [68, 75]); regardless, the coarse AP decomposes faster at as pressure increases, even at pressures below the LPDL. The increased volumetric flux above the propellant causes the area near the decomposing AP crystal to become locally oxidizer rich.

The resulting lifted diffusion flame is hot, but located well above the surface. The increased flame height causes a decrease in heat flow back to the propellant surface and a corresponding decrease in burning rate. With a further increase in pressure, AP crystal burning rates are governed by the AP self-deflagration (monopropellant) flame, which is cooler than the diffusion flames formed between the finer AP and binder. The monopropellant flame is closer to the propellant surface than the final diffusion flame, but it is also about 1000 K cooler, causing a decrease in burning rate [69].

In summary, as described by the BDP model (which was initially formulated for a monomodal propellant), flame structure depends on particle size. The flame structures visible in Fig. 13 are the final diffusion flames, as the premixed, primary, and AP monopropellant (if present) flames were not resolvable. For propellants with small particle sizes, diffusion flames were not seen. Diffusion times for these particles were short enough that the fuel and oxidizer can mix prior to ignition [3]. As particle size increased, a decrease in burning rate and the appearance of diffusion flame structures occurred. Diffusion flames are expected to form above even the finest AP particles if the pressure is high enough [39, 44].

4.5 Bimodal

As monomodal propellants have poor packing efficiency and density, fielded propellants are typically multimodal. Using two or more oxidizer size distributions allows the finer particles to fill in the spaces between the larger particles. The burning rate of bimodal propellants is affected by the coarse AP content as well as the ratio of the coarse and fine AP diameters. In general, due to the effects of the coarse AP on combustion, the burning rates of bimodal propellants are lower than the burning rates of monomodal propellants with the same average particle size [83]. The addition of coarse AP will decrease the burning rate of the propellant, and the relatively low amount of fine AP, even if it is finer than the AP in the monomodal propellant, will not entirely compensate for the decrease in burning rate.

4.5.1 Coarse-to-Fine Ratio

Global Burning Rate

Global burning rate decreased with C/F ratio, as can be seen in Fig. 14. This is to be expected, as the burning rate of a bimodal propellant will change with the average oxidizer particle size, though not as directly as that of a monomodal propellant. One can change the average particle size in a multimodal propellant by either changing the particle sizes directly or by changing the coarse-to-fine (C/F) ratio of the propellant. As the C/F ratio changes, the flame structure will change, which in turn changes the burning rate. The presence of larger amounts of coarse AP will push the

Fig. 14 Burning rate of composite propellants with varying C/F ratio. Legend is in % coarse AP. Figure modified from Ref. [61]
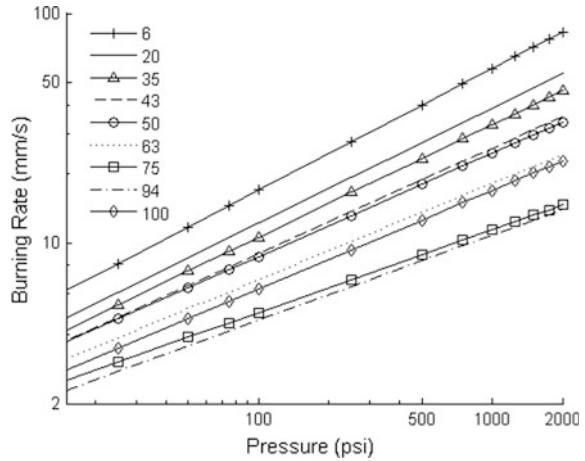
overall flame structure to be more diffusion-based while the pseudo-premixed flame will become more dominant if there is more fine AP. In a typical bimodal propellant, it is likely that both the diffusion and pseudo-premixed flames will be present. As might be expected, the coarse AP and fine AP/binder matrix do not burn independently. Leading-edge flames associated with coarse particle combustion occurs when the AP decomposition products burn with the fuel-rich products from the fine AP/binder matrix decomposition or flame. The final diffusion flame forms from the AP decomposition or monopropellant flame products and the fine AP/binder matrix flame products. The fine AP/binder matrix may be too fuel-rich to burn on its own and require heat flow from the leading-edge or final diffusion flames to decompose and sustain combustion.

When the coarse AP diameter is kept constant and the fine AP diameter varied, at a fixed C/F ratio of 7:3 global burning rate was observed to be almost insensitive to fine particle size except at high pressures [84]. Changes in burning rate because of C/F ratio are thought to be due in part to the distances between the coarse AP and therefore the interactions between the leading edge flames. If the distances between coarse AP particles are relatively small, as for high C/F ratio propellants, the LEF are thought to close over neighboring regions of the fine AP/binder matrix, as is seen in sandwich propellant combustion [55]. In these cases the heat feedback from the LEF is dominant over the heat feedback from the pseudo-premixed flame and the burning rate at a given pressure barely changes with fine AP particle size [84]. The insensitivity to fine AP particle size is also expected because AP diameters will be below the premixed limit up to a certain point. At higher pressures, a pseudo-premixed flame becomes less likely, resulting in a dependence of burning rate on fine AP particle size (again, with the coarse AP diameter held constant) [84]. Note that this result is important for propellant formulators. If fine AP diameter does not affect burning rate at high C/F ratios except at high pressures, a moderately large fine AP diameter may be chosen to increase propellant processability and safety.

As the amount of fine AP in the propellant increases, the burning rate becomes more sensitive to the average fine AP particle size [84]. With a decreasing amount of coarse AP in the propellant, the coarse AP LEF would not be expected to blanket the fine AP/binder matrix due to increased distances between the coarse particles. Additionally, as the amount of fine AP in the propellant increases, the pseudo-premixed flame will become closer to stoichiometric and therefore hotter. As the fine AP particle size increases, while remaining smaller than the coarse AP particle size, individual diffusion flames will form over the particles and the fine AP LEF will blanket the surface [84]. This will also occur as pressure increases. As C/F decreases the global burning rate is expected to increase in part due to the increased heating of the propellant surface from the hotter, more stoichiometric pseudo-premixed flame or the individual fine AP particle flames. Both of these flames have a short standoff distance and will provide significant heat feedback to the propellant surface.

Flame Structure

The flame structure above bimodal propellants is expected to follow the BDP model with the addition of the pseudo-premixed flame. For fine particles and low pressures the establishment of diffusion flames over individual particles does not occur and the pseudo-premixed flame forms over the propellant surface [84]. As particle size becomes large enough or pressure high enough, the leading-edge, monopropellant, and final diffusion flames form. Leading-edge flames are a small part of the overall flame but are important to combustion as they sit close to the propellant surface [84]. For bimodal propellants at low pressure, LEF may be attached only to locations on the surface where large areas of fuel and oxidizer are located close to each other, such as when coarse crystals are surrounded by a relatively large swath of binder. As pressure increases, the required dimensions of adjacent fuel and oxidizer patches decrease and conditions become more favorable for LEF flame-holding at smaller oxidizer particle sizes.

While the descriptions of LEF are at this point mostly theoretical, direct experimental observations have been made of the diffusion flames above bimodal composite propellants. Though propellant flames were found to be optically thick, LIF imaging was used to determine that flame height extended about 6 mm above the surface of an 87% solids loading AP/polybutadiene propellant. At 1 atm, the reaction zone is thought to occur within about 600 μm of the propellant surface based on CN concentrations. This reaction zone thickness was seen to be approximately constant for pressures between 0.1 and 3.5 MPa [59]. Using high-speed OH PLIF, high OH regions that appeared and disappeared from above the coarse crystals were visible, and these regions became more pronounced when the coarse crystals were being consumed [62]. The high OH regions are thought to
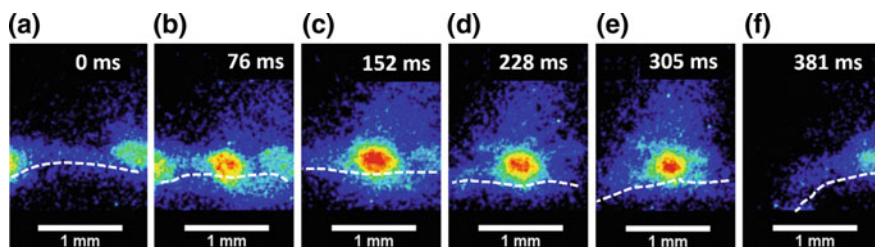
Fig. 15 A sequence of OH PLIF images is shown above. Gas phase OH concentration can be seen as well as the AP crystals on the surface. The *white dashed line* is placed just below the propellant surface as a reference point. Similar results have been seen by Hedman et al. [62] and Isert et al. [61]

be to the appearance and disappearance of jet-like underventilated diffusion flames above the propellant, and examples are shown in Fig. 15. Similar results were first seen by Hedman et al. [62].

Changes of the C/F ratio are accompanied by changes in coarse particle spacing and the O/F ratio of the fine AP/binder matrix, and consequently in the flame structure above the propellant [39]. At 1 atm underventilated jet-like diffusion flames similar to those seen in the monomodal propellant were observed using PLIF imaging for propellants with C/F ratios ranging from 1:16 to 16:1. The flame heights of the jet-like diffusion flames over individual coarse AP particles are statistically the same for all C/F ratios at about 0.54 ± 0.13 mm [61]. The flame height of the final diffusion flame did not vary significantly with C/F ratio at 1 atm as the particles are all approximately the same diameter, in similar environments, and will have the approximately the same burning rate and therefore volumetric oxidizer fluxes. Though the average flame heights were similar, it should be noted that there was about a 25% scatter in the flame heights. The scatter is from the innate heterogeneity of the propellants; though the coarse particles may have on average the same diameter, environment, and burning rate, in reality one or more of these may vary widely and cause a correspondingly different flame height.

Group combustion is not seen for propellants with very low C/F ratios as the coarse crystals are not in close enough proximity to one another for the LEF to interact. Flames that form over groups of coarse AP particles are underventilated jet-like flames similar to the individual particle flames, only taller [61]. Flame height increased with group diameter, but did not in general vary with C/F ratio (Fig. 16). The prevalence of group combustion can be linked to a decrease in propellant burning rate. Propellants with larger C/F ratios had more instances of group combustion due to the increased proximity of the coarse AP particles. The taller flames that result from group combustion will lead to decreased heat feedback to the propellant surface and consequently a lower burning rate.

At pressures above about 0.3 MPa, the AP decomposition kinetics increase, coarse particles begin to recess into the propellant surface, and flame structures began to transition from jet-like to lifted flames [63]. Though less commonly
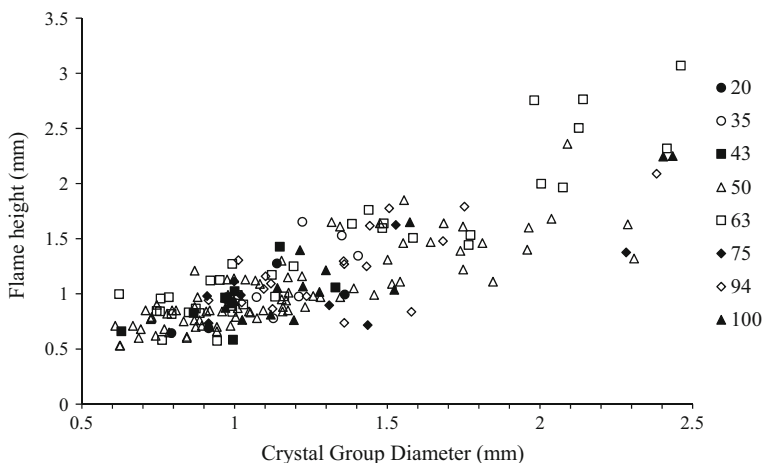
Fig. 16 Flame height as a function of AP coarse crystal group diameter. Legend is % coarse AP. From Ref. [61]. Used with permission

observed, jet-like flames are still visible even at pressures around 1.2 MPa, and flame heights are found to increase with pressure [63]. The lifted flame sheets become more noticeable as pressure increases, and their duration matches the coarse AP crystal burn times [63]. As pressure increases, the coarse AP begins to decompose and burn faster than the surrounding fine AP/binder matrix, releasing large amounts of oxidizer into the gas phase. The local excess of oxidizer causes the oxidizer and fuel to mix and burn far above the propellant surface, forming a lifted, overventilated, inverted (oxidizer in the center) diffusion flame, similar to those described for the monomodal propellants in Sect. 4.4. The flames stand well off the surface because the flow of oxidizer is large, and the standoff distance found to increase with pressure. Note that these observations are for propellants with large (400 μm) AP particles [63]. Diffusion flame heights were found to increase in height with increasing propellant burning rates, perhaps due to the large diffusional distances associated with large AP particles [27].

Pressure is not the only determining factor for whether a flame is arched. Lifted IOF occur when there is a local overventilation of the area, causing fuel and oxidizer to mix and burn farther above the surface. Such an overventilation can occur where there is a large concentration of coarse crystals. Experimentally, at elevated pressures jet-like flames were seen more frequently for propellants with low C/F ratios and arched flames for propellants with high C/F ratios. Arched flames are rarely seen for low C/F propellants (6–35% cAP), as the fine AP/binder matrix is still burning rapidly, preventing a local overventilation from the coarse crystals. A mix of jet-like and arched flames is seen for a 43% cAP propellants at 0.5 MPa [61]. The variety of flame structures in this propellant may occur because some coarse crystals or groups of crystals receive the necessary heat flux to increase the oxidizer volumetric flow rate and lift the flame, possibly due to heating from

Fig. 17 Flame heights above propellants at 0.5 MPa. From Ref. [61]. Used with permission
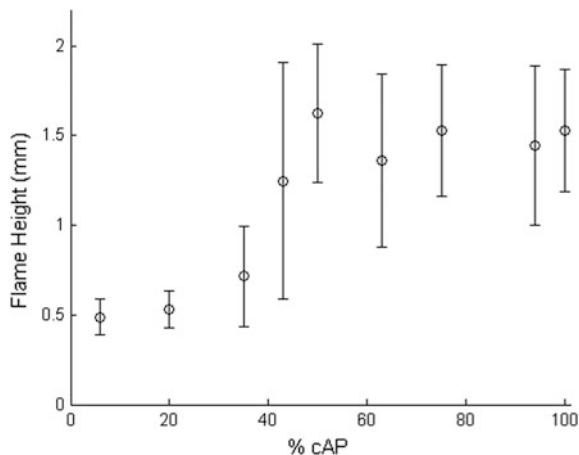
nearby LEF, while others do not [61]. Flames above propellants with 50–100% cAP were observed to be primarily arched flames with statistically equal heights. The similarity in flame heights may indicate that height is mostly a function of oxidizer size, though as the coarse AP has recessed below the propellant surface it cannot be determined how many particles are contributing to the flame. Figure 17 shows the flame heights of AP propellants with an 80% solids loading at 0.5 MPa [61]. The taller flame heights correspond visually to arched flames. When the flames are taller, heat release occurs farther above the propellant surface in the final diffusion flame. For the lower C/F ration propellants, on the other hand, heat release is primarily occurring in the pseudo-premixed fine AP/binder flame or in jet-like diffusion flames that sit closer to the propellant surface. The difference in flame structure between the lower and higher C/F ratio propellants is a factor in the burning rate decrease with increasing C/F ratio [61].

Coarse Crystal Burning Characteristics

In order to understand the coarse AP combustion in propellant environments, coarse AP burning rate, ignition delay, and lifetimes were measured, and qualitative observations were made about the coarse AP protrusion or recession. Isolated coarse AP particles were observed to burn in a two-step process where an ignition delay was followed by combustion of the coarse crystal [62]. The ignition delay varies not only with particle size [62], but also as the percentage of coarse AP in the propellant changes [61]. In general ignition delay is shorter for smaller AP particles and C/F ratios. The short ignition delays for the smaller C/F ratios may be attributed at least in part to the preheating effect of the fine AP/binder matrix flame. Coarse crystal burning rates were measured and the scatter was large, probably due in part to the heterogeneous nature of the propellant. The percent of coarse AP lifetime spent in ignition delay stays approximately constant at 70% despite changing C/F ratios [61].

The coarse particle burning rate was nearly constant at the pure AP combustion rate for individual particles between about 0.1–0.6 MPa and increased afterwards. At these pressures the coarse AP crystals were observed to protrude above the surrounding fine AP/binder matrix. The protrusion is caused by the rapid burning rate of the fine AP/binder matrix. In the 0.7–1.2 MPa range protrusion is modest and ignition delay cannot be measured as the coarse crystals regress whenever they are protruding. At this point the individual AP crystals burn at rates well above the pure AP combustion rates [62]. Above 1.2 MPa the AP particles burn much faster than the surrounding fine AP/binder matrix and become recessed into the surface [63]. Pressure is not the only factor in AP particle protrusion or recession; other factors include binder type, particle size, and propellant O/F ratio [39]. Protrusion is generally attributed to slower AP regression rates and higher binder (with or without fine AP) pyrolysis rates at low pressures. At higher pressures the AP decomposition kinetics accelerate and the monopropellant flame forms, causing the AP to regress faster than the binder matrix. The coarse crystals regress below the propellant surface, forming concave, dish-like shapes [87]. These explanations may be overly simplistic when one considers all the interactions that are going on in a propellant.

Early high-speed OH PLIF imaging led to the discovery that AP fluoresces under 283 nm UV laser light with good contrast between the coarse AP and the fine AP/binder matrix (Fig. 15) [62]. As this was the case, the particle lifetime, or the time between when the AP crystal first appeared on the propellant surface and when it disappeared, could be measured in the propellant environment. The coarse particle lifetime varied with C/F ratio [61]. The pseudo-premixed flame temperature, height of surrounding diffusion flames, distance between coarse crystals, and LEF will affect particle lifetime. Lower C/F ratio propellants have shorter particle lifetimes in part due to the hot pseudo-premixed flame supplying heat to the coarse AP. As the pseudo-premixed flame becomes cooler due to an increased percentage of coarse AP, diffusion flames becomes more dominant. The diffusion flames stand farther above the surface than the pseudo-premixed flame; that, combined with the decreased pseudo-premixed flame temperatures, results in a lower heat feedback to the propellant surface and longer coarse particle lifetimes. As C/F ratio increases, leading-edge flames from one coarse particle are more likely to interact with nearby particles, increasing coarse AP decomposition rates and shortening lifetimes. However, if the LEF do not provide a heat flux as large as that from the pseudo-premixed flame, coarse crystal lifetimes may be expected to be longer [61].

4.5.2   Catalysts

Catalysts are often used instead of changing the propellant C/F ratio to tailor a propellant with both the required burning rate and pressure exponent. The burning rates of solid rocket propellants increase as catalyst size decreases (higher surface area), with nano-sized catalysts causing faster burning rates than micron-sized catalysts. In sandwich combustion experiments using catalysts, results indicated

that the catalysts would be more effective as the oxidizer becomes finer due to the higher surface area of AP exposed to the catalyst [26]. Loading the AP with catalyst or coating the AP with catalyst has similar effects. Nano-sized catalysts have been used as a seed for AP crystal growth, resulting in the catalyst been surrounded by, or encapsulated in, the oxidizer [28, 37, 38, 60, 88]. Propellants with the nano-sized catalysts encapsulated into the fine AP had even higher burning rates than propellants with the nano-sized catalysts mixed directly into the binder [60, 88].

When micron- or nano-sized iron (III) or copper (II) oxide (CuO) were added to the composite propellant, burning rates of the composite propellants increased [27]. Catalysts were observed to significantly reduce the ignition delay times of the AP crystals [27]. The global propellant burning rate was seen to strongly depend on the lifetime of the coarse AP crystals. The fine AP/binder matrix burning rate is accelerated by the presence of catalysts, resulting in increased protrusion of the coarse AP above the propellant surface at 1 atm [27, 60]. At elevated pressures for a baseline propellant with no catalyst, coarse AP was not visible on the surface at 0.4 MPa. Adding catalyst to the propellant caused the fine AP/binder matrix burning rate to increase, resulting in exposed coarse particles even at elevated pressures, making coarse crystal lifetimes and burning rates measurable. Nano-iron oxide catalyzed propellants had shorter coarse crystal lifetimes than micron-iron oxide catalyzed propellants between 0.4 and 0.7 MPa [60]. There was no statistical difference in coarse crystal lifetime between propellants where the nano-catalyst was mixed directly or where it was encapsulated into the oxidizer [60]. The encapsulated catalyst is evidently still able to affect the coarse AP burning time, perhaps by being deposited on the propellant surface after fine AP combustion. The shorter coarse crystal lifetimes for the nano-catalyzed propellants are related to the fact that catalysis is a surface phenomenon. For an equal mass of catalyst, a nano-catalyst will have more surface area than a micron-catalyst. The increased surface area will increase the contact area between the oxidizer and catalyst, resulting in shorter particle lifetimes for the coarse AP particles.

Catalyzing the propellant causes the flame to move close to the propellant surface even at low pressures, resulting in higher burning rates. The imaged OH intensity using PLIF in regions with no coarse AP were observed to be higher for the catalyzed propellants; this would indicate higher OH concentrations. The higher concentration could be due to faster fine AP/binder matrix burning rates or increased OH generation due to altered kinetic pathways [27]. Flame structures of catalyzed propellants were observed to change with pressure, catalyst size and catalyst location. At 1 atm, jet-like flames at were visible above both catalyzed and uncatalyzed propellants. The jet-like flame heights at 1 atm were variously reported to be statistically the same [60] or taller [27] than the baseline propellant with the addition of catalysts; the variation can possibly be attributed to differences in the catalyst percentage and the equipment used. Flame heights and structures changed with pressure. For non-catalyzed propellants, flame structures were observed to change from jet-like to lifted arched flames between 1 atm and 0.4 MPa, and flame height stayed constant even with an increase in pressure to 0.7 MPa [60]. However, a micron-iron oxide catalyzed propellant transitioned from jet-like flames to lifted

Fig. 18 Flame heights as a function of pressure and catalyst size. Figure from Ref. [60]. Used with permission. Here Propellant 1 is the baseline (no catalyst) propellant, Propellant 2 contains 0.21% 53 μm iron oxide catalyst, Propellant 3 contains 0.21% 3 nm iron oxide catalyst, and Propellant 4 contains 0.21% 3 nm catalyst encapsulated inside the fine AP
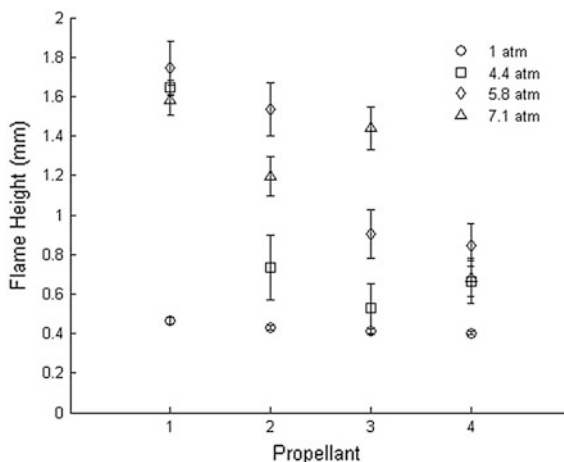
flames more gradually, with the lifted flames becoming more frequent than the jet-like flames around 0.6 MPa. Similarly, a propellant with nano-iron oxide catalyst began transitioning around 0.6 MPa but did not fully transition until 0.7 MPa. While these propellants exhibited mostly lifted flames at the maximum pressure observed, the propellant with encapsulated nano-iron oxide did not transition; a few lifted flames were seen, but the bulk of the flames were jet-like even at 0.7 MPa [60]. Flame heights for non-catalyzed, micron-iron oxide catalyzed, nano-iron oxide catalyzed, and encapsulated nano-iron oxide catalyzed propellants can be seen in Fig. 18.

The transition from jet-like flames to lifted flames is tied to the burning rate of the fine AP/binder matrix. As discussed previously in Sect. 4.4 and Section "Flame Structure", lifted flames occur when the coarse AP burns fast enough relative to the local fine AP/binder matrix to locally overventilate the area, causing fuel and oxidizer to mix and burn farther above the surface. The coarse crystals in an uncatalyzed propellant were generally recessed above 0.4 MPa, indicating that they are burning faster than the fine AP/binder matrix and locally overventilated conditions are present. One might expect in this case for the flames to be generally lifted flames, and the experimental data bear this out. On the other hand, propellants with micron-sized and nano-sized catalyzed were seen to exhibit a higher pressure transition from jet-like to lifted diffusion flames. In these cases, at lower pressures the fine AP/binder matrix is burning faster than the coarse AP due to the presence of the catalyst. As long as the fine AP/binder matrix is burning fast enough relative to the coarse AP particles, locally overventilated conditions cannot occur and the flames will be jet-like. When the coarse AP kinetics are increased to the point where the fine AP burns fast enough relative to the binder, the flames will be lifted. For the encapsulated catalyst, as the catalyst is in such intimate contact with the AP the coarse AP kinetics have not accelerated to the point that an excess of oxidizer can be produced, and the flames remain jet-like [60]. Note that the coarse AP does not

need to be recessed for the flames to be lifted, the burning rate of the coarse AP needs only be fast enough relative to the fine AP/binder matrix to locally over-ventilate the flame.

Burning rate is directly related to flame structure. At 0.7 MPa, the flames above a nano-iron oxide catalyzed propellant are lifted. For an encapsulated nano-iron oxide propellant, the fine AP/binder matrix burns fast enough to mitigate local overventilation and the flames are jet-like [60, 64]. A comparison of the burning rates between these two propellants shows that when the flames are lifted the burning rate about 12% slower than when the flames are jet-like and close to the surface, catalyst percentage and all other aspects of the propellants being equal [60]. When the flames are lifted, heat release occurs further above the propellant surface than if the flames are jet-like (see Fig. 18). The propellant that has less heat feedback to the propellant surface will have a slower burning rate. Though there are no doubt other reasons for the change in burning rate, flame structure is an important factor.

4.5.3 Binder

As discussed in Sect. 4.3, the type of binder used in a propellant has an effect on AP composite propellant flame structure and burning rate [64] Burning rates are observed to be progressively more sensitive to the binder (fuel) type as pressure increases [73]. This can be due to more obvious factors like the binder pyrolysis temperature, but other factors such as adhesion between the AP particles and binder can also have an effect on propellant combustion. Very fuel rich propellants (25–30% binder) can lead to abnormal burning or even complete extinction of the propellant strand due to the presence of a carbonized layer covering the AP particles on the propellant surface [89].

Limited experiments have been done to study how changing the binder changes flame structure. One study compared AP composite propellants with HTPB, PBAN, and dicyclopentadiene (DCPD) binders. As with other composite propellants discussed in this chapter, AP composite propellants using these binders exhibited jet-like diffusion flames below about 0.4 MPa [64]. The DCPD-based propellant had a consistently higher background OH PLIF signal above the propellant surface compared to the HTPB- and PBAN-based propellants, which had equivalent OH signals. The higher OH PLIF signal can possibly be attributed to a higher OH generation rate either from the binder combustion or from a stronger fine AP/binder flame. Transition from jet-like to lifted IOF was gradual and began near 0.4 MPa for all binder systems considered. The lifted flames formed flame sheets that were in general thinner than the jet-like flames and were visible as v-shaped regions in the gas phase [64]. Flame heights are reported to have a gradual increase with pressure, though this could be due to the transition from jet-like to diffusion flames. The flame heights did not appear to vary significantly with a change in binder, possibly

due to similar binder decomposition products. Alternatively, flame height could be more dependent on propellant O/F ratio, and as the coarse oxidizer particles are approximately the same size the propellants will be roughly the same height.

4.5.4 Aluminum

Adding aluminum or another metallic fuel to solid propellants is often used to increase the specific impulse by increasing the temperature of the burned gases Adding aluminum to a propellant changes the amount of energy released [89]. In solid propellant combustion, the aluminum will typically accumulate on the burning surface, detach, ignite, and burn slowly above the surface, surrounded by its own flame [90]. A large amount of aluminum oxide is typically produced upon aluminum combustion. Ignition of micron-sized aluminum particles may be induced by the LEF or final diffusion flame, as the temperatures required for their ignition is not usually found in the fine AP/binder matrix flame; however, ultra-fine aluminum (~100 nm diameter) has been observed to ignite in the fine AP/binder matrix flame [91].

Aluminum particle size affects the overall flame structure, and therefore the burning rate. In some cases, micron-sized powders have not been observed to increase burning rate. This is possibly due to the fact that the large particles burn well above the gas-phase flames of the AP flame structure and do not affect heat feedback to the propellant surface significantly, but are instead a thermal sink in the propellant [92, 93]. Ultra-fine or nanoscale powders, on the other hand, increase burning rate because they can burn in the fine AP/binder flame due to earlier ignition and rapid combustion [92]. Imaging of these flames shows the nano-aluminum reacting and burning within a thin, luminous layer adjacent to the propellant surface, providing a significant amount of heat feedback to the propellant surface [93]. Propellants with large amounts of fine AP have been observed to have less aluminum agglomeration than propellants with larger percentages of coarse AP; this is thought to be in part due to the presence of pseudo-premixed flames and a higher gas velocity that can lift the aluminum away from the propellant surface [94].

Flame structures of aluminized propellants can be difficult to investigate. No studies have been reported of PLIF on aluminized propellants, as the addition of aluminum creates high luminosity and optically thick flames. In some cases flames were observed to be essentially opaque above 0.8 MPa. At atmospheric pressure, however, a change in CN emission profile was seen between aluminized and non-aluminized propellants, with the CN profile being extended in the aluminized propellant as seen in Fig. 19 [95]. It is possible, and even probable, that there will be changes in other molecular profiles above the propellant surface, though measurement difficulties still stand.
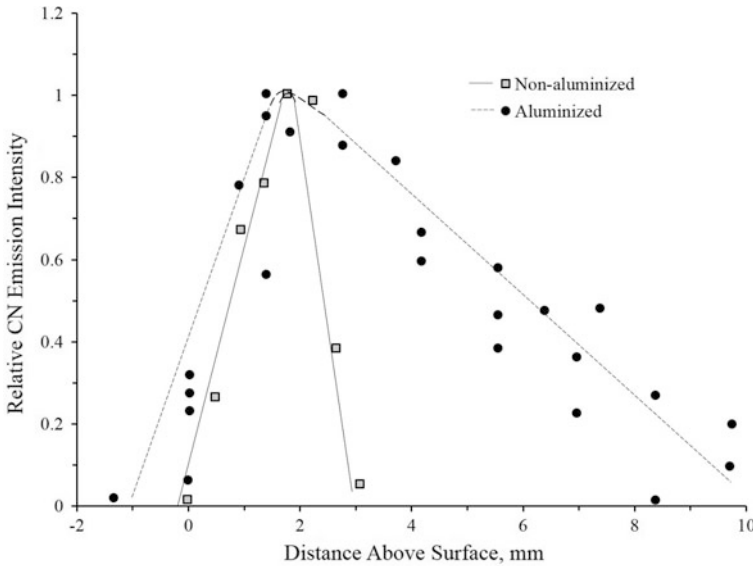
Fig. 19 CN emission intensity profiles for two AP propellants (1 atm N_2+). Figure is modified from Ref. [95]. Here AP1 is a non-aluminized propellant and AP2 is aluminized

5 Predicted Flame Structures

A complete model for the propellant combustion should take into consideration individual component burning rates, different oxidizer size distributions, propellant compositions, pressure, and burning surface geometry [87]. All three coupled flames of the BDP model are necessary for successful prediction of flame structure and burning rate [55]. Construction of propellant models is a non-trivial task and truly predictive propellant models are beginning to come into their own with the advent of high-power computing. This section will briefly describe results from current models. The ultimate goal is to develop a computer model that will be able to predict the burning rate of a composite solid propellant a priori using only boundary conditions and fundamental properties rather than empirically derived parameters from experiments.

Physical characteristics of propellants such as random packing of oxidizer particles in a fuel binder, unsteady 3D heat conduction, unsteady regression of the nonplanar surface, and unsteady 3D combustion fields sustained by fluxes from the surface are being modeled [96]. Combustion chemistry must be considered, which can be difficult as the flow is by nature unsteady, three-dimensional, and highly coupled between the solid and gas phases; however, detailed kinetics cannot be included because of current computational limitations as well as kinetic parameter uncertainties. Gas phase combustion must be considered as the gas phase flames provide heat feedback to the propellant surface. Solid phase reactions and phase

changes must also be considered. As AP composite propellants are heterogeneous, the burning surface will not in general be flat, which is affected in part by the different regression rates of the AP crystals and the fine AP/binder matrix. The gas phase model must be coupled to the solid phase model. To rigorously model many fielded propellants, aluminum combustion must be also considered. Finally, the model must be validated with experimental data.

A significant step in moving toward a complete model of AP composite propellant combustion was the development of random packing algorithms and corresponding combustion models. A model was created to make packs of bimodal spheres in a periodic cube and parameters like oxidizer fractions on the surface were determined [13]. These random packs were then compared to previously obtained experimental data [97] and used as a base for AP combustion [98]. Current cutting-edge models of AP/HTPB combustion use unsteady conditions and random packs of particles of general shapes [96, 99, 100]. Coarse AP particles were found to be able to protrude or recess depending on the amount of surrounding binder, the AP content in the fine AP/binder matrix, and the system pressure. If the propellant is fuel-rich recessed particles are expected [47].

The extremely small scale of AP/HTPB flame structure makes complete experimental resolution essentially impossible at practical pressures, so numerical models have been developed in part to understand combustion processes [45]. The size of the AP particles is decisive in dictating the burning behavior of the composite propellant [40]. Since not all scales can be resolved numerically with current computational capabilities, one must decide at which point fine AP can be considered to be homogeneous with the binder. In a homogenized AP/binder case, the individual flames above each fine AP particle are not modeled; this saves computational time and reduces complexity. The AP homogenization cutoff diameter decreases as pressure increases [45]. As particle sizes become smaller the primary flame extends out to cover the fine AP/binder matrix, the flame becomes essentially a combined premixed-like flame, and the temperature gradients across the fine AP particles are not as high as those above larger crystals [46].

At 1 atm kinetics are too slow to allow the monopropellant and premixed fine AP/binder flames to form [46], and the final diffusion flame is thought by Gross and Beckstead to be too far from the surface to have any substantial impact on the burning rate [45]. The final diffusion flame is formed from products that have reacted in one of the surface premixed flames and is predicted to be close enough to the surface to influence combustion below about 20 atm [46]. Standoff distances for the final diffusion flame were seen to increase with pressure above 400 μm coarse AP particles, while for other particle sizes standoff heights decrease. At elevated pressures, the final diffusion flame moves away from the surface due to an increased oxidizer mass flux; the oxidizer species are convected downstream before they are able to react. Other flames present move closer to the surface due to increased kinetics [46]. As standoff height increases with pressure the diffusion flame affects the surface less. For relatively coarse AP particles (400 μm, for example) AP monopropellant and fine AP/binder flames are formed away from the AP/binder interface. A leading-edge flame will form between the AP and binder
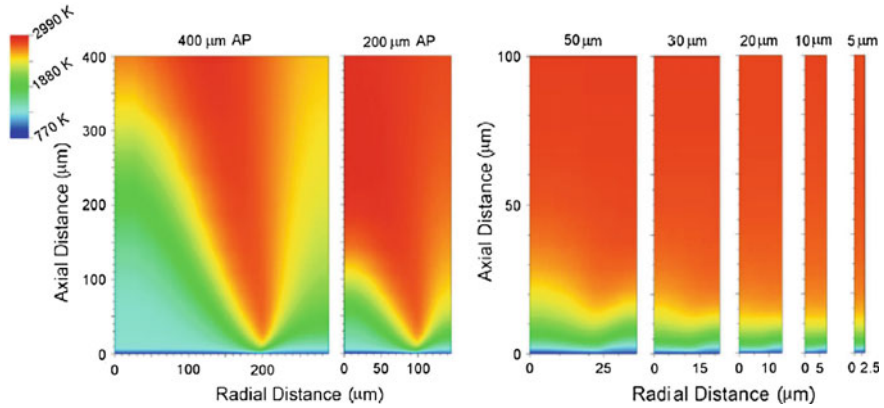
Fig. 20 Temperature profiles above the surface for 86% AP composite propellants at 20 atm varying the large AP particle size from 400 to 5 μm. Figure from Ref. [45]. Used with permission

condensed-phase decomposition products [45]. At pressures where it can form, the leading-edge flame is a very small part of the combustion field but is intense and has a noticeable effect on the propellant regression [101]. Computed temperature fields above a variety of AP particle sizes are shown in Fig. 20.

Computations show that the flame height of the AP monopropellant is about 1–2 orders of magnitude lower than that of the final diffusion flame at pressures above about 20 atm [40]. At rocket motor pressures, the AP deflagrates rapidly and the flame height is predicted to be about 1–2 μm high [40]. The effect of the leading-edge flame can be neglected because there is simply not enough time for the HTPB pyrolysis products to mix and burn with the AP monopropellant decomposition products [40]. As the flame moves closer to the surface, the heat feedback to the condensed phase increases and the burning rate increases as well [40, 46]. Maximum heat release is predicted to take place very close to the propellant surface and serve as a flame holder for the entire diffusion flame.

6 Conclusions

The burning rate of an AP composite solid propellant is known to depend mainly on three things: AP particle size, propellant formulation, and operating pressure. Flame structure experiments have shown that the flame structure above an AP composite propellant also depends in large part on those three things. Though AP particle size of course plays into propellant formulation, its effects are significant enough on their own that they must be considered. In the propellant environment, very small AP particles will burn with the binder in a pseudo-premixed flame. As particle size increases, the flame structure will change from premixed to a diffusion flame structure over individual or groups of AP particles. The diffusion flame structures

are higher above the surface than the pseudo-premixed flame. As particle size increases still further, the AP monopropellant flame will become more dominant, though the final diffusion flame will still be present. The change in flame structure will affect burning rate. As the flame becomes farther from the surface, heat feedback to the propellant surface will lessen and burning rate will decrease. As the monopropellant flame becomes more dominant the burning rate will decrease still further as it is cooler than the diffusion flame. Knowing where the flame structure transitions from premixed to diffusion to monopropellant-dominated can help propellant formulators. The fine AP used in the propellant can be made as large as possible while still remaining in the premixed limit. The larger AP particle sizes can help tailor the burning rate by selecting particle sizes to ensure the particles burn in the diffusion or monopropellant-dominated regimes for faster or slower burning rates, respectively. Modelers can also use flame structure data both to validate their models and to know when the pseudo-premixed assumption is valid or if the flame structures above individual AP particles must be modeled.

General propellant formulation is also an important factor in determining flame structure. Other than the AP particle size distribution, propellant formulation also includes coarse-to-fine ratio, percent solids loading, the type of binder, and whether or not metallic fuels and/or burning rate modifiers are present. Changing the coarse-to-fine ratio of the propellant can change flame structure as many coarse particles close to each other can burn together in group combustion. The corresponding increase in oxidizer flow rate can result in increased flame height. The same effect may be produced by increased solids loadings. Additionally, if a propellant has a larger percentage of fine AP, the flame structure will be more dominated by the pseudo-premixed flame over diffusion flames. A change in binder from HTPB to PBAN has not been observed to change the flame structure in the propellant environment; however, along with increased solids loadings, this area has only begun to be studied. Other binders, particularly energetic binders, have been observed to greatly change the propellant burning rate and the flame structure may be quite different as well. The inclusion of burning rate catalysts has been observed to change the flame structure, with uncatalyzed propellants developing taller flames at lower pressures than catalyzed propellants. More work should be done in this area, as thus far only catalysts have been investigated, while burning rate inhibitors have not. Adding a metallic fuel to the propellant will add another flame due to the combustion of the fuel, but has not been observed to explicitly change the flame structure of the base propellant. However, due to difficulties in making flame structure observations, it is quite possible that the base flame structure is changed in some way.

Flame structure for a given propellant formulation can change with pressure. At low pressures for coarse AP crystals, underventilated jet-like diffusion flames are the most commonly seen flame structures. As pressure increases, flame structure will transition to overventilated arched diffusion flames. The fine AP/binder matrix flame may also be expected to change with pressure. As pressure increases the required particle size for the fine AP/binder matrix to burn in a pseudo-premixed flame becomes smaller. This means that fine AP particles that burn in a

pseudo-premixed flame at lower pressures can form diffusion flames at higher pressures. The change from a pseudo-premixed to a diffusion flame may cause a decrease in burning rate as the flame height becomes taller and the heat release occurs farther from the propellant surface. Similarly, when all other things are equal, propellants with jet-like flames burn faster than propellants with arched flames as the heat release occurs close to the propellant surface. Changes in pressure will also produce changes in flame height and may increase burning rate because the flames are driven closer to the propellant surface.

The current state of the art, computationally, is three-dimensional modeling of propellant packs coupled with three-dimensional unsteady combustion with detailed kinetics and species transport. The propellant packs can be constructed with oxidizer particle packs of random shapes and arbitrary particle distributions. The combustion model uses detailed kinetics with fully coupled gas- and condensed-phase reactions. However, though the chemistry/transport models have been used to develop good understanding of AP/HTPB combustion, they come with high computational costs, which make it difficult to integrate them into larger simulations. Using particle packs opens the door to fully predictive models; however, at present the computational time required only allows small sections of the propellant to be simulated at any one time and some homogenization must be applied to the finest AP crystals. Though packs may be stacked [100], computational limitations do not permit full motor grains to be simulated at this time. Simplified models have been observed to predict burning rate to within about 20% about 90% of the time with only the inputs of pressure, AP particle size, and propellant formulation with minimal computational run time [102]. Researchers have been adding aluminum combustion into their models, which will bring them closer to being able to predict propellant burning rates [103, 104], but much remains to be done. For example, simulating aluminum combustion is complicated by aluminum agglomeration, as it cannot be easily predicted and more experimental data are needed to assist in modeling it.

Experimentally, 5 kHz OH PLIF has been used recently to gather qualitative information on in situ flame structure up to about 0.7 MPa. This has allowed for visualization of previously unseen flame structures, as well as insights into flame heights and the quantification of coarse AP crystal burning rates and ignition delays. The technique has also provided valuable information on how microscale flame structure and propellant burning rate are related, and how flame structure changes with propellant formulation. While this information is interesting, if the technique could be extended to higher pressures it would allow rocket pressure conditions to be considered, possibly by using more stoichiometric propellants or considering other species. Using PLIF imaging on other species, such as CN, will provide valuable insight into propellant flame structures. Preliminary work on using 3D PLIF to probe the propellant flame structure has been done but has yet to be implemented on a regular basis, but will prove useful in investigating the highly three-dimensional flame structures above solid rocket propellants.

Besides PLIF imaging of propellants in 3D and of other species on the baseline propellants, other propellant formulations must be considered. Though the effects of

iron oxide burning rate catalysts on flame structures have been investigated, it would be interesting to see if other catalysts have the same effects on the flame structure. This would allow further understanding into the method of operation of the catalysts on the propellants. Additionally, looking at the effect of burning rate inhibitors on flame structure has the potential to be very interesting—for example, do they prematurely lift the propellant flame? Another large area of investigation must how flame structures of different oxidizers are different from that of AP. Preliminary PLIF imaging of flame structures above ADN- and AN-based propellants at 1 atm indicates that the flame structure is quite different than that above AP propellants. With the current desire to move away from propellants containing perchlorates, knowledge of how different oxidizers and energetic material additives change solid propellant flame structures will help propellant formulators solve problems currently in the way of using these materials in fielded propellants. Other areas of interest including identifying systems that allow for better resolution of the microscale flames, perhaps including experimental visualization of the AP monopropellant flame, fine AP/binder matrix flame, and/or the leading-edge flames. As technology advances we can push the envelope and come closer to truly understanding how microscale flame structure affects solid propellant burning rate.

References

1. Sabadell AJ, Wenograd J, Summerfield M (1965) AIAA J 3:1580
2. Hermance CE (1966) AIAA J 4:1629
3. Summerfield M, Sutherland GS, Webb MJ, Taback HJ, Hall KP (1960) In: Solid propellant rocket research american institute of aeronautics and astronautics, Reston, VA, USA, p 141
4. Sparks JF, Friedlander MP III (1999) Fifty years of solid propellant technical achievements at Atlantic Research Corporation. In: 35th AIAA/ASME/SAE/ASEE joint propulsion conference and exhibit, Los Angeles, CA
5. Chaturvedi S, Dave PN (2015) Arabian J Chem (In press)
6. Chaturvedi S, Dave PN (2013) J Saudi Chem Soc 17:135
7. Kumari A, Mehilal, Jain S, Jain MK, Bhattacharya B (2013) J Energ Mater 31:192
8. Kuo KK, Acharya R (2012) In: Applications of turbulent and multiphase combustion. Wiley, Hoboken, p 1
9. Ramakrishna PA, Paul PJ, Mukunda HS, Sohn CH (2005) Proc Comb Inst 30:2097
10. Oommen C, Jain SR (1998) J Hazard Mater A67:253
11. Parr TP, Hanson-Parr DM (1996) Symp (Int) Comb 26:1981
12. Jeppson MB (1998) A kinetic model for the premixed combustion of a fine AP/HTPB composite propellant. Brigham Young University
13. Knott GM, Jackson TL, Buckmaster J (2001) AIAA J 39:678
14. McGeary RK (1961) J Am Ceram Soc 44:513
15. Sutton GP, Biblarz O (2001) Rocket propulsion elements. Wiley, New York, pp 475–519
16. Hill P, Peterson C (1992) Mechanics and thermodynamics of propulsion. Addison-Wesley Publishing Company, Inc., Prentice Hall
17. Brewster MQ, Hites MH, Son SF (1993) Combust Flame 94:178
18. Kishore K, Sunitha MR (1979) AIAA J 17:1118
19. Dey A, Athar J, Varma P, Prasant H, Sikder AK, Chattopadhyay S (2015) RCS Adv 5:1950

20. Huang C, Li C, Shi G (2012) Energy Environ Sci 5:8848
21. Li N, Cao M, Wu Q, Hu C (2012) CrystEngComm 14:428
22. Li N, Geng Z, Cao M, Ren L, Zhao X, Liu B, Tian Y, Hu C (2013) Carbon 54:124
23. Wanga B, Park J, Wang C, Ahn H, Wanga G (2010) Electrochim Acta 55:6812
24. Zhao J, Liu Z, Qin Y, Hua W (2014) CrystEngComm 16:2001
25. Chaturvedi S, Dave PN (2012) J Exp Nanosci 7:205
26. Strahle WC, Handley JC, Milkie TT (1973) Combust Sci Technol 8:297
27. Hedman TD, Reese DA, Cho KY, Groven LJ, Lucht RP, Son SF (2012) Combust Flame 159:1748
28. Ma Z, Li F, Chen A-S, Bai H-P (2004) Acta Chim Sinica 62:1252
29. Joshi SS, Patil PR, Krishnamurthy VN (2008) Defence Sci J 58:721
30. Chakravarthy SR, Price EW, Sigman RK (1997) J Propuls Power 13:471
31. Pittman CU Jr (1969) AIAA J 7:328
32. Patil PR, Krishnamurthy VN, Joshi SS (2006) Propellants Explos Pyrotech 31:442
33. Jayaraman K, Anand KV, Chakravarthy SR, Sarathi R (2009) Combust Flame 156:1662
34. Lu K-T, Yang T-M, Li J-S, Yeh T-F (2012) Combust Sci Technol 184:2100
35. Kohga M (2011) Propellants Explos Pyrotech 36:57
36. Krishnan S, Periasamy C (1986) AIAA J 24:1670
37. Reese DA, Son SF, Groven LJ (2012) Propellants Explos Pyrotech 37:635
38. Ma Z, Wi R, Song J, Li C, Chen R, Zhang L (2012) Propellants Explos Pyrotech 37:183
39. Price EW, Chakravarthy SR, Sigman RK, Freeman JM (1997) Pressure dependence of burning rate of ammonium perchlorate-hydrocarbon binder solid propellants. In: 33rd AIAA/ASME/SAE/ASEE Joint Propulsion Conference, Seattle, WA
40. Cai W, Thakre P, Yang V (2008) Combust Sci Technol 180:2143
41. Brewster MQ, Mullen JC (2011) Combust Explos Shock+ 36:200
42. Beckstead MW, Derr RL, Price CW (1970) AIAA J 8:2200
43. Beckstead MW (1993) Pure Appl Chem 65:297
44. Gross ML, Beckstead MW (2009) J Propul Power 25:74
45. Gross ML, Beckstead MW (2010) Combust Flame 157:864
46. Gross ML, Beckstead MW (2011) J Propul Power 27:1064
47. Gross ML, Hedman TD, Son SF, Jackson TL, Beckstead MW (2013) Combust Flame 160:982
48. Price EW, Sambamurthi JK, Sigman RK, Panyam RR (1986) Combust Flame 63:381
49. Renie JP, Condon JA, Osborn JR (1979) AIAA J 17:877
50. King MK (1978) Model for steady state combustion of unimodal composite solid propellants. AIAA 16th Aerospace Sciences Meeting, Huntsville, Alabama
51. Freeman JM, Jeenu R, Price EW, Sigman RK (1998) Effect of matrix variables on bimodal propellant combustion. In: Proceedings of the 35th JANNAF Combustion Subcommittee Meeting, Tucson, AZ
52. Sinditskii VP, Egorshev VY, Levshenkov AI, Serushkin VV (2005) Propellants Explos Pyrotech 30:269
53. Parr TP, Hanson-Parr DM (1992) In: Nonsteady burning and combustion stability of solid propellants, vol 148. American Institute of Aeronautics and Astronautics, Inc., Washington, DC, p 261
54. Fitzgerald RP, Brewster MQ (2004) Combust Flame 136:313
55. Fitzgerald RP, Brewster MQ (2008) Combust Flame 154:660
56. Chorpening BT, Knott GM, Brewster MQ (2000) Proc Combust Inst 28:847
57. Dyer MJ, Crosley DR (1982) Opt Lett 7:382
58. Edwards T (1989) In: Air force astronautics laboratory. Edwards Air Force Base, CA
59. Edwards T, Weaver DP, Campbell DH (1987) Appl Opt 26:3496
60. Isert S, Groven LJ, Lucht RP, Son SF (2015) Combust Flame 162:1821
61. Isert S, Hedman TD, Lucht RP, Son SF (2015) Combust flame (In press)
62. Hedman TD, Cho KY, Satija A, Groven LJ, Lucht RP, Son SF (2012) Combust Flame 159:427

63. Hedman TD, Groven LJ, Cho KY, Lucht RP, Son SF (2013) Proc Combust Inst 34:649
64. Hedman TD, Groven LJ, Lucht RP, Son SF (2013) Combust Flame 160:1531
65. Parr TP, Hanson-Parr DM (1991) Propellant diffusion flame structure. In: Proceedings of the 28th JANNAF Combustion Subcommittee Meeting, Los Alamos, NM
66. Parr TP, Hanson-Parr DM, Smooke MD, Yetter RA (2005) Proc Comb Inst 30:2113
67. Smooke MD, Yetter RA, Parr TP, Hanson-Parr DM (2000) Proc Combust Inst 28:839
68. Smooke MD, Yetter RA, Parr TP, Hanson-Parr DM, Tanoff MA, Colket MB, Hall RJ (2000) Proc Combust Inst 28:2013
69. Tanoff MA, Ilincic N, Smooke MD, Yetter RA, Parr TP, Hanson-Parr DM (1998) Symposium (International) on combustion proceedings vol 27, p 2397
70. Cho KY, Satija A, Pourpoint TL, Son SF, Lucht RP (2014) Appl Opt 53:316
71. Murphy JL, Netzer DW (1974) AIAA J 12:13
72. Edwards T, Weaver DP, Campbell DH, Hulsizer S (1986) J Propul Power 2:228
73. Powling J (1967) Proc Combust Inst 11:447
74. Johansson RH (2012) Investigation of solid oxidizer and gaseous fuel combustion performance using an elevated pressure counterflow experiment and reverse hybrid rocket engine. The Pennsylvania State University, State College, PA
75. Johansson RH, Connell TL Jr, Risha GA, Yetter RA, Young G (2012) Int J Energ Mat Chem Propuls 11:511
76. Young G, Roberts C, Dunham S (2012) Combustion behavior of solid oxidizer/gaseous fuel diffusion flames. In: 50th AIAA aerospace sciences meeting including the new horizons forum and aerospace exposition, Nashville, Tennessee
77. Isert S, Connell TL Jr, Risha GA, Hedman TD, Lucht RP, Yetter RA, Son SF (2015) Combust flame (In press)
78. Varney AM, Strahle WC (1972) Combust Sci Technol 4:197
79. Chakravarthy SR, Price EW, Sigman RK, Seitzman JM (2003) J Propul Power 19:56
80. Knott GM, Brewster MQ (2002) Combust Sci Technol 174:61
81. Lee S-T, Price EW, Sigman RK (1994) J Propul Power 10:761
82. Chakravarthy SR, Seitzman JM, Price EW, Sigman RK (2004) J Propul Power 20:101
83. Kohga M (2008) J Propul Power 24:499
84. Lee ST, Hong SW, Yoo KH (1993) Experimental studies relating to the combustion microstructure in heterogeneous propellants. In: 29th AIAA/ASME/SAE/ASEE joint propulsion conference and exhibit, Monterey, CA
85. Chiu HH, Liu TM (1997) Combust Sci Technol 17:127
86. Turns SR (2012) An introduction to combustion: concepts and applications. McGraw-Hill Education, New York
87. Bilger RW, Jia X, Li JD, Nguyen TT (1996) Combust Sci Technol 115:1
88. Ma Z, Li F, Bai H (2006) Propellants Explos Pyrotech 31:447
89. Cohen-Nir E (1974) Combust Sci Technol 9:183
90. Price EW, Sigman RK, Sambamurthi JK, Park CJ (1982) Georgia institute of technology: school of aerospace engineering. Atlanta, GA
91. Dokhan A, Price EW, Seitzman JM, Sigman RK (2003) The ignition of ultra-fine aluminum in ammonium perchlorate solid propellant flames. In: 39th AIAA/ASME/SAE/ASEE joint propulsion conference and exhibit, Huntsville, AL
92. Galfetti L, De Luca LT, Severini F, Meda L, Marra G, Marchetti M, Regi M, Bellucci S (2006) J Phys Condens Matter 18:S1991
93. De Luca LT, Galfetti L, Severini F, Meda L, Marra G, Vorozhtsov AB, Sedoi VS, Babuk VA (2005) Combust Explos Shock+ 41:680
94. Mullen JC, Brewster MQ (2008) Characterization of aluminum at the surface of fine-AP/HTPB composite propellants. In: 44th AIAA/ASME/SAE/ASEE Joint Propulsion Conference and Exhibit, Hartford, CT
95. Edwards T (1998) Air force astronautics laboratory. Edwards Air Force Base, CA
96. Jackson TL (2012) AIAA J 50:933

97. Miller RR (1982) Effects of particle size on reduced smoke propellant ballistics. In: AIAA/SAE/ASME 18th joint propulsion conference, Cleveland, OH
98. Jackson TL, Buckmaster J (2002) AIAA J 40:1122
99. Stafford DS, Jackson TL (2010) J Comput Phys 229:3295
100. Plaud M, Gallier S, Morel M (2015) Proc Comb Inst 35:2447
101. Massa L, Jackson TL, Buckmaster J (2005) J Propul Power 21:914
102. Gross ML, Hedman TD (2015) Int J Energ Mat Chem Propuls 14:399
103. Maggi F, Bandera A, De Luca LT, Thoorens V, Trubert JF, Jackson TL (2011) Prog Propuls Phys 2:81
104. Wang X, Hossain K, Jackson TL (2008) Combust Theor Model 12:45

PAFRAG Modeling and Experimentation Methodology for Assessing Lethality and Safe Separation Distances of Explosive Fragmentation Ammunitions

Vladimir M. Gold

Abstract The fundamental vision of the US Army Armaments Research, Design and Engineering Center, Picatinny Arsenal is that the fragmentation ammunition has to be safe for the soldier and lethal for the adversaries. PAFRAG (Picatinny Arsenal Fragmentation) is a combined analytical and experimental technique for determining explosive fragmentation ammunition lethality and safe separation distance without costly arena fragmentation tests. PAFRAG methodology integrates high-strain high-strain-rate computer modelling with semi-empirical analytical fragmentation modelling and experimentation, offering warhead designers and ammunition developers more ammunition performance information for less money spent. PAFRAG modelling and experimentation approach provides more detailed and accurate warhead fragmentation data for ammunition safe separation distance analysis, as compared to the traditional fragmentation arena testing approach.

1 Introduction: Fragmentation of Explosively Driven Shells

The subject of fragmentation of explosively driven shells has long been of interest in the military field and has recently commanded attention in a number of other applications including the design of fragment and blast resistant structures and protective facilities. A review of previous work shows that extensive studies on the subject were performed in the early 1940s. Historically, three names of ground-breaking researchers' stand out: Gurney has been credited for deriving a form of an empirical expression for prediction of fragment velocities as a function of the mass ratio between the explosive and the metal shell [1], Mott has been

V.M. Gold (✉)
U. S. Army ARDEC, Picatinny Arsenal, NJ 07806-5000, USA
e-mail: vladimir.m.gold.civ@mail.mil

credited for developing statistical models for predicting average fragment sizes and fragment mass distributions [2], and Taylor has been credited for developing models describing expanding shell dynamics and the state of stress at the time of fracture [3]. Most of this work, however, ceased shortly after the World War II and was not resumed until the 1960s.

Before the state-of-the-art high-strain-rate high-strain finite difference computer programs had become available to fragmentation munition designers, for nearly six past decades, modeling of explosive fragmentation munitions had relied for a large degree on analytical methods developed in 1940s, that is on the fragment velocity predictions based on Gurney [1] approximations and on the fragment mass distribution statistics based on Mott [2] and/or Gurney and Sarmousakis [4] fragmentation models. A brief overview of empirical fragmentation models widely used in 1960s and 1970s is given by Hekker and Pasman [5]. Mott's [2] approach to the dynamics of fracture activation has been successfully pursued starting in 1980s by Grady and Kipp resulting in significant advances in a number of dynamic fracture and fragmentation areas [6–9] including the high-velocity impact fragmentation [10, 11], shaped charge jet break-up [12], dynamic fragmentation of metal rings [6, 7, 13], spalling phenomena [14, 15], and rock blasting [16]. The extensive influence of Mott's concepts can be found in many other works including that of Hoggatt and Recht [17] and Wesenberg and Sagartz [18]. A comprehensive review of Mott's fragmentation concepts is given by Grady [19]. A perturbation stability approach to fragmentation of rapidly expanding metal rings is given by Mercier and Molinari [20]. A compilation of analytical techniques for assessment of effectiveness of fragmentation munitions can be found in Weiss [21] and a brief review of fragmentation models can be found in Grady [22]. Recently, there had been a number of reports of applying the state-of-the-art continuum hydrocode analyses to the explosive fragmentation problem utilizing Eulerian, Arbitrary-Lagrangian-Eulerian, Lagrangian, Peridynamics, SPH (Smooth Particle Hydrodynamics), and corpuscular model methods [23–27].

An attempt to apply the state-of-the-art continuum hydrocode analyses to the explosive fragmentation problem had been reported by Wilson et al. [28]. The work was performed employing the CTH computer program [29] with a "code-built-in" Grady–Kipp fragmentation model [11, 30] based on the Poisson statistics and the average fragment sizes as functions of the strain-rates $\dot{\varepsilon}$. To validate the model, Wilson et al. [28] compared the CTH code analyses with the experimental data, resulting in a good agreement in the average fragment sizes predictions, although the fragment mass distribution predictions were rather poor, in particular for fragments with masses below 2 grains. Since in many military explosive fragmentation applications including the anti-personnel fragmentation warheads, mines, grenades, and mortars the majority of lethal fragments have masses below 2 grains, an improved computational procedure enabling more accurate modeling and simulation of fragmentation munitions has been required.

A technique for predicting performance of explosive fragmentation munitions presented in this work is based on integrating the CALE computer program [31] with a semi-empirical fragmentation computer model PAFRAG (Picatinny Arsenal

FRAGmentation). CALE is a plane two-dimensional and three-dimensional axial symmetric high-rate finite difference computer program based on Arbitrary Lagrangian–Eulerian formulation of the governing equations. The mathematical description of the PAFRAG code is given in sections that follow. The geometries of three example problems considered in this work are shown in Figs. 1 and 11. As shown in Fig. 1, upon initiation of the high-explosive charges, rapid expansion of high-pressure high-velocity detonation products results in high-strain high-strain-rate dilation of the hardened steel shells, which eventually rupture generating a "spray" of high-velocity steel fragments. In the case of the Charge A, the dilation of the steel shell is accompanied by the implosion of the copper shaped charge liner that produces a high-speed metal jet moving along the charge's axis of symmetry z. In the case of the Charge B, in addition to the explosive charge, the hardened steel shell also encapsulates a tracer and a fuze that occupy significant volume of the munition payload. A threaded connection between the fuse and the fragmenting portion of the hardened steel case was also included into the CALE model. In order to allow a "slippage" along the joint, the threads were modeled with a few rows of computation cells employing ideally-plastic-zero-yield-strength material with the same hydrodynamic response parameters as steel. Following the expansion of the detonation products, the fuze section of the warhead is projected in the negative direction of the z-axis, without contributing to the lethality of the fragment spray. In addition to specification of the problem geometry and initial and boundary conditions, equations of state and constitutive equations for all materials have to be specified before the solution procedure can be initiated. The explosive was modeled using the Jones–Wilkins–Lee–Baker equation of state [32] employing a set of parameters resulting from thermo-chemical equilibrium analyses of deto-nation products with the JAGUAR code [33, 34] and calibrated with copper cylinder test expansion data. The hydrodynamic responses of the steel shell and the copper liner were modeled using a standard linear polynomial approximation usually employed for metals. The constitutive behavior of these metals was mod-eled using the Steinberg–Guinan yield-strength model [35] and the von Mises yielding criterion. A standard set of parameters based on measured stress and free-surface vs. time histories from shock wave experiments available from Steinberg et al. [35], Tipton [36], and Steinberg [37] had been employed in the analyses. The principal equations of the Steinberg–Guinan yield-strength model are given here for completeness and are as follows:

$$Y = Y_0 f(\varepsilon_p) \frac{G(p,T)}{G_0} \tag{1}$$

where

$$Y_0 f(\varepsilon_p) = Y_0 [1 + \beta(\varepsilon_p + \varepsilon_i)]^m \leq Y_{\max} \tag{1a}$$

and

$$G(p, T) = G_0[1 + \frac{Ap}{\eta^{1/3}} - B(T - 300)] \tag{1b}$$

In Eqs. (1a) and (1b) $G(p, T)$ is the shear modulus at pressure p and temperature T, G_0 is the initial shear modulus, Y_0 is the yield strength at the Hugoniot elastic limit, ε_p is the equivalent plastic strain, ε_i is the initial plastic strain, Y_{max} is the work hardening maximum yield-strength, β and m are work-hardening parameters, η is the compression, and parameters A and B represent dependence of the shear modulus on pressure and temperature, respectively.

Since the extent of dilation of the rapidly expanding steel shell is limited by its strength, at some point the shell ruptures generating a spray of steel fragments moving with trajectories at angles Θ with z-axis. Accordingly, the principal topic of this work is a numerical model for analytical description of parameters of the resulting fragment spray as functions of the "spray" angle Θ. In typical large-scale explosive fragmentation tests ("arena" tests) the tested munitions are positioned at the origin of the reference polar coordinate system and surrounded with series of velocity-measuring screens and fragment-catching witness panels, all at significant distances from the warhead. Accordingly, the fragmentation characteristics are
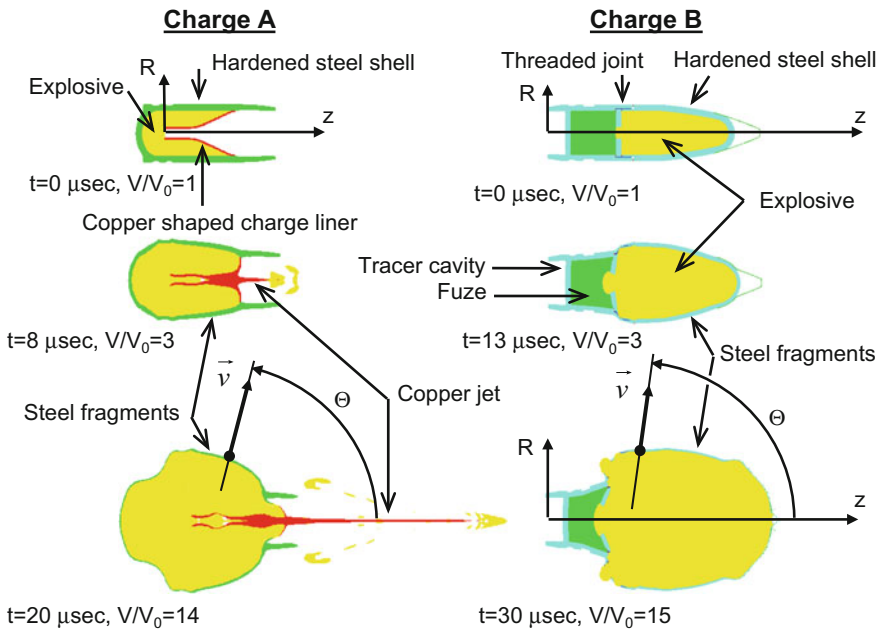
Fig. 1 Results of CALE-code modeling: initial configuration and CALE's predictions following the explosive detonation initiation

assessed as functions of polar angles Θ' identifying angular positions of these measuring devices.

Initially developed in 2001, for the past decade PAFRAG methodology had been applied in support of tens of US Army ARDEC's explosive fragmentation ammunition design, development, modernization, and characterizations programs resulting in comprehensive collection of PAFRAG code modules, fragmentation warhead analyses, and experimental data. This paper presents a few examples of PAFRAG applications, illustrating utility and versatility of the technique. Since the main objective of the PAFRAG procedure is to simulate the "data output" (i.e. warhead fragmentation performance information) from traditional fragmentation arena tests, a brief description of the fragmentation arena test methodology is given below for completeness.

2 The Fragmentation Arena Test Methodology

Basic principles and requirements governing fragmentation arena test procedures in the U.S.A. are stipulated in Joint Munition Effectiveness Manual [38]. In a typical fragmentation arena test set-up, tested munitions are positioned at the origin of the reference polar coordinate system and surrounded with series of velocity-measuring screens and fragment-catching witness panels, all at significant distances from the warhead. Defining the longitudinal axis of the munition as the polar axis z, the polar altitudinal angles Θ are measured from the munition's nose ($\Theta = 0°$) to the tail ($\Theta = 180°$), and the azimuthal angles ϕ are measured from an arbitrary projectile's feature ($\phi = 0°$) in a counterclockwise direction. In conventional fragmentation arena test procedures fragment sampling and fragment velocity measuring is usually limited to relatively small azimuthal sections, mainly because of enormous construction and data assessment costs associated with recovering fragments from the entire fragmenting shell. This sampling technique requires the assumption of isotropic fragmentation properties for all azimuthal angles ϕ throughout the entire Θ-angle zone, i.e. through a complete altitudinal region bounded by two polar angles. By sampling small azimuthal angles across all polar zones from the munition nose to tail and adjusting this sample data mathematically, a prediction for entire munition fragment characterization is obtained. Since only a small azimuthal section of the region is sampled and scaled up, even relatively small munition positioning errors may result in large deviations of the fragmentation data, routinely requiring repeated testing for statistical data stability.

According to PAFRAG modelling and experimentation methodology, the assessment of the ammunition fragmentation parameters is performed analytically employing the PAFRAG code which links three-dimensional axial symmetric high-strain high-strain-rate continuum analyses with a phenomenological fragmentation model validated through a series of experiments including flash radiography, Celotex^{TM} and water test rear fragments recovery, and sawdust total fragment spray recovery. In fragmentation arena tests, the ammunition

fragmentation characteristics are assessed as functions of polar angles Θ identifying angular positions of fragment-catching witness panels and velocity-measuring screens. In PAFRAG code analyses, positions of these devices are irrelevant, and the fragmentation characteristics are assessed in reference to the fragment trajectory angles Θ' calculated from the CALE code [31] cell velocities at the time of the shell break-up. Once the shell breaks up and fragments are formed, fragment velocities may change with time due to a number of reasons, including the air drag and the rigid body motion induced at the time of the shell break up. Assuming that the fragment trajectory angles Θ do not change with time (that is the rigid body motion and the lateral drift of fragments due to air resistance is relatively small) and that the definitions of angles Θ and Θ' are approximately identical, the PAFRAG model enables prediction of crucial characteristics of explosive fragmenting munitions including the number of fragments, the fragment size distribution, and the average fragment velocities.

3 The PAFRAG Fragmentation Model

Similarly to fragmentation arena test fragment sampling assumptions, the PAFRAG fragmentation model assumes that for any point within a fixed Θ_j-angle zone the fragment number distribution $N_j(m)$ is uniform and independent of the altitude and the azimuth angles Θ and ϕ, respectively. Hence, the total fragment number distribution is given by

$$N(m) = \sum_{j}^{L} N_j(m). \tag{2}$$

In Eq. (2) m is the fragment mass, L is the number of altitudinal Θ_j-angle zones, $0 \leq \Theta \leq \pi$, and $N_j(m)$ is the fragment number distribution function for the j-th zone. For convenience, all Θ-zones are assumed to have the same altitudinal lengths of $\Delta\Theta = \pi/(L-1)$, except for the first and the last "half-length" zones with lengths of $\frac{1}{2}\Delta\Theta$. In the fragmentation ammunition arena testing practice adopted at the US Army Armament Research Development and Engineering Center, the number altitudinal zones is usually $L = 37$, resulting in uniform Θ-angle resolution of $\Delta\Theta = 5°$. Accordingly, the Θ-zones are identified by the middle of the zone altitudinal angles Θ_j given by the following series

$$\Theta_j = \begin{cases} 1/4\Delta\Theta, & j = 1, \\ \Delta\Theta(j-1), & 2 \leq j \leq L-1, \\ \pi - 1/4\Delta\Theta, & j = L. \end{cases} \tag{3}$$

In the case of traditional fragmentation arena testing, all individual fragment number distribution functions $N_j(m)$ for all polar Θ-zones are determined directly

from the test data. The main drawback of this approach is the extremely high testing costs limiting the fragmentation arena testing to final ammunition fragmentation characterization. Alternatively, the PAFRAG modeling and experimentation is a relatively low-cost procedure enabling accurate assessment of the fragmenting munition performance at the research, design, and development phases. According to the PAFRAG approach the individual Θ-zone fragment number distribution functions $N_j(m)$ are computed analytically from the sawdust or water tank fragment recovery test data, $N(m)$. Mathematically, the PAFRAG fragmentation modeling is a solution of the inverse problem of Eq. (1), i.e. determining a series of individual $N_j(m)$'s for given $N(m)$. Since with PAFRAG approach, the $N(m)$ function is assessed based on approximately 98–99% fragment recovery data, the accuracy of PAFRAG predictions is high.

PAFRAG code is capable of modeling fragmentation of "natural" and "controlled", or "pre-formed" fragmentation warheads. In PAFRAG, natural fragmentation warheads are usually modeled using the PAFRAG-MOTT model, "controlled" or "pre-formed" fragmentation warheads are usually modeled using the PAFRAG-FGS2 model. The PAFRAG-MOTT natural fragmentation model is based on Mott's theory of break-up of cylindrical "ring-bombs" [39], in which the average length of the resulting circumferential fragments is a function of the radius and velocity of the ring at the moment of break-up, and the mechanical properties of the metal. Accordingly, in the PAFRAG-MOTT model the "random variations" in fragment sizes of natural fragmentation warheads are accounted through the following fragment distribution relationship

$$N(m) = \sum_{j}^{L} N_{0j} \mathrm{e}^{-\left(m/\mu_j\right)^{1/2}}. \tag{4}$$

In Eq. (4) N_{0j} and μ_j represent number of fragments and one half of the average fragment mass in the j-th Θ-zone, respectively, computed from the CALE-code data.

The PAFRAG-FGS2 fragmentation model based on Ferguson's multivariable curve representation [40] and is defined in parametric form as

$$\begin{bmatrix} N_k(\xi_k) \\ m_k(\xi_k) \end{bmatrix} = \begin{bmatrix} \sum_{j}^{L} \frac{m_j}{\sum_{j}^{L} m_j}(a_{N0k} + a_{N1k}\xi_k + a_{N2k}\xi_k^2 + a_{N3k}\xi_k^3) \\ a_{m0k} + a_{m1k}\xi_k + a_{m2k}\xi_k^2 + a_{m3k}\xi_k^3 \end{bmatrix}. \tag{5}$$

In Eq. (5) ξ_k is a non-dimensional parameter, $0 \le \xi_k \le 1$, k is the curve index, $k = 0,1$, and sixteen coefficients a_N's and a_m's are obtained by fitting two curve segments $k = 0$ and $k = 1$ with conditions of curve and tangent continuity at the adjacent ends. More detailed description and application examples for the PAFRAG-MOTT and PAFRAG-FGS2 models are given in sections that follow.

4   The PAFRAG-Mott Fragmentation Model

For a large part the PAFRAG-MOTT fragmentation model is based on the Mott's theory of break-up of cylindrical "ring-bombs" [39], in which the average length of the resulting circumferential fragments is a function of the radius and velocity of the ring at the moment of break-up, and the mechanical properties of the metal. A brief review of the Mott's theory is given here for completeness. Following Mott and Linfoot [19], the "random variations" in fragment sizes are accounted through the following fragment distribution relationship

$$N(m) = N_0 e^{-(m/\mu)^{1/2}} \tag{6}$$

In Eq. (6) $N(m)$ represents total number of fragments of mass greater than m, μ is defined as one half of the average fragment mass, $N_0 = M/\mu$, and M is the total mass of the fragments.

In attempting to evaluate the distribution of fragment sizes occurring in the dynamic fragmentation of expanding metal rings, Mott [39] introduced an idealized model in which the average circumferential fragment lengths are not random but determined by the interaction of stress release waves originating from instantaneous fractures in the body. A schematic of the Mott's model is shown in Fig. 2a. Assuming that a fracture in the ring is supposed to have occurred first at A_1 and that stress release waves have traveled to points B_1 and $\underline{B}_1$, further fractures can no longer take place in regions A_1B_1 and $\underline{A}_1\underline{B}_1$. On the other hand, in the regions B_1B_2 and $\underline{B}_1\underline{B}_2$ the plastic strain is increasing, which increases the probability of fractures at any point in these regions, especially at points near B_1, B_2, $\underline{B}_1$, and $\underline{B}_2$. Thus, according to Mott's theory the average size of fragments is determined by the rate at
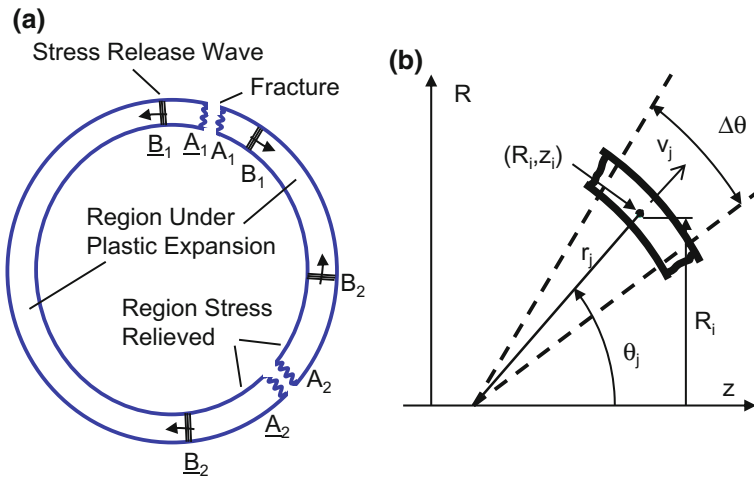
Fig. 2 The fragmentation model schematic

which stress relieved regions A_1B_1 and $\underline{A}_1\underline{B}_1$ spread through the plastically expanding ring.

At the moment of fracture, let r be the radius of the ring and V be the velocity with which the shell is moving outwards. Then, according to Mott [39], the average circumferential length of the resulting fragments is

$$x_0 = \left(\frac{2\sigma_F}{\rho\gamma'}\right)^{1/2} \frac{r}{V} \tag{7}$$

In Eq. (7) ρ and σ_F denote the density and the strength, respectively; and γ' is a semi-empirical statistical constant determining the dynamic fracture properties of the material.

As the shell expands radially, a series of radial fractures propagate along the length of the shell resulting in formation of relatively long splinter-like fragments that continue to stretch in the axial direction. Since the extent of the plastic deformation is limited by the shell strength, the splinter-liker fragments eventually break-up forming rugged shaped but approximately proportionally sized prism-shaped fragments. According to Mott [2], the ratios of the fragments' circumferential breadths and the lengths are approximately constant and the average cross-sectional areas are approximately proportional to

$$(r/V)^2 \tag{8}$$

Given that the rugged-shaped fragments can be idealized with simple geometric shapes such as parallelepipeds [2, 22] having longitudinal length l_0, breadth x_0, and thickness t_0, the average fragment mass takes the following form

$$\mu = \frac{1}{2}\alpha\rho x_0^3 \tag{9}$$

In Eq. (9), $\alpha = \frac{l_0}{x_0} \cdot \frac{t_0}{x_0}$. Substituting Eq. (7) into Eq. (9) results in

$$\mu = \frac{1}{2}\left(\frac{2\sigma_F}{\rho^{1/3}\alpha^{-2/3}\gamma'}\right)^{3/2}\left(\frac{r}{V}\right)^3 \tag{10}$$

Since the fragment distribution relationship, Eq. (6), warrants knowledge of the average fragment mass but not the shape, introducing

$$\gamma = \alpha^{-2/3}\gamma' \tag{11}$$

Equation (10) can be put in a simpler and more useful form

$$\mu = \frac{1}{2} \left(\frac{2\sigma_F}{\rho^{1/3}\gamma} \right)^{3/2} \left(\frac{r}{V} \right)^3 \tag{12}$$

A schematic for the technique implemented in the PAFRAG-MOTT model is shown in Fig. 2b. For computational purposes the shell is discretized into a finite number of short "ring" segments, N. For each discrete ring element j uniform field variables are assumed. Accordingly, the masses, the velocities and radii of ring segments j are defined by the mass averages of the respective parameters:

$$m_j = \sum_{L_j} m_i \tag{13}$$

$$V_j = \frac{\sum\limits_{L_j} V_i m_i}{m_j} \tag{14}$$

$$r_j = \frac{\sum_{L_j} R_i m_i}{m_j} \cdot \frac{1}{\sin \Theta_j} \tag{15}$$

$$\Theta_j - \frac{\pi}{2N} \leq \Theta_i < \Theta_j + \frac{\pi}{2N} \tag{16}$$

In Eqs. (13) through (16) m_i, V_i, and R_i denote the mass, the velocity, and the radial coordinate of the i-th computational cell from the CALE-code generated data. As shown in Fig. 2b, the shell is discretized into "ring" elements j in terms of Θ-angles and L_j denotes a number of computational cells contained in the j-th "ring" segment. Θ_j denotes the Θ-angle that corresponds to the j-th ring segment given by

$$\Theta_j = \frac{\pi}{2N} \cdot \left(j - \frac{1}{2} \right) \tag{17}$$

For each computational cell i, the velocity V_i and the Θ-angle Θ_i are calculated respectively by

$$V_i = \sqrt{V_{zi}^2 + V_{Ri}^2} \tag{18}$$

and

$$\Theta_i = \arctan \frac{V_{Ri}}{V_{zi}} \tag{19}$$

In Eqs. (18) and (19) V_{zi}, and V_{Ri} denote the axial and the radial velocity components from the CALE-code generated data.

Given that the velocities and the radii of ring segments j are determined through Eqs. (14) and (15), the resulting fragment size distributions in each segment j can be calculated through the following relationships

$$N_j(m) = N_{0j}e^{-(m/\mu_j)_{1/2}} \tag{20}$$

$$\mu_j = \sqrt{\frac{2}{\rho}\left(\frac{\sigma_F}{\gamma}\right)^{3/2}\left(\frac{r_j}{V_j}\right)^3} \tag{21}$$

$$N_{0j} = \frac{m_j}{\mu_j} \tag{22}$$

As the detonation wave travels along the shell length and the expanding detonation products rupture the shell, in the case of the idealized "long-pipe-bombs", the break-up radii r_j and the break-up velocities V_j of the individual segments j are approximately the same, regardless of the axial positions of the segments. Accordingly, taking $\mu \approx \mu_j$, the number of fragment distribution relationship is given by the original Mott's Eq. (6).

However, in the case of conventional explosive fragmentation munitions with shell geometries far from that of the idealized "long-pipe-bombs", the break-up radii r_j and the break-up velocities V_j vary along the shell length, so that the resulting variance in the average fragment half-weights μ_j of the individual segments j may be rather significant. The existence of significant differences in the average fragment sizes between the cylindrical and the curved portions of the shell had been experimentally confirmed in this work through flash radiography and high-speed photography. Accordingly, the following two fragment distribution relationships are introduced herein. The "shell-averaged" fragment distribution is defined as

$$N(m) = \tilde{N}_0 e^{-(m/\tilde{\mu}_0)1/2} \tag{23}$$

where $\tilde{N}_0$ and $\tilde{\mu}_0$ are defined as

$$\tilde{N}_0 = \sum_j N_{0j} \tag{24}$$

$$\tilde{\mu}_0 = \frac{\sum_j m_j}{2\tilde{N}_0} \tag{25}$$

The "ring-segment-averaged" fragment distribution is defined as

$$N(m) = \sum_j N_{0j}e^{-(m/\mu_j)1/2} \tag{26}$$

5   PAFRAG-Mott Model Validation: Charge a Analyses

The validation of the PAFRAG-MOTT fragmentation model was accomplished using existing ***Charge A*** arena test data. The fundamental assumption of all fragmentation analyses presented in this work was that the fragmentation occurs simultaneously throughout the entire body of the shell. Following Mott's critical fracture strain concept [39] and assuming that for given shell geometry and materials, the shell fragmentation time is a function of the plastic strain in the shell, the shell fragmentation time can be conveniently expressed in terms of the global shell dilatational properties. Given that in a typical fragmentation munition device the explosive is tightly confined inside the shell, the cumulative strains of the expanding explosive and the surrounding shell are nearly proportional. Accordingly, the critical fracture strain at the moment of the shell break-up may be conveniently measured in terms of the high explosive detonation products volume expansions, V/V_0.

Figure 3 shows the effect of the shell fragmentation time on the fragment spray velocity distribution function. The seemingly significant disagreement between the experimental velocities and the analyses for $\Theta \leq 15°$ is due to deliberate omission of the shaped charge jet data from the PAFRAG-MOTT fragmentation analyses, mainly because of the minimal contribution to the overall fragment-spray lethality. Accordingly, the copper shaped charge jet was neglected in all fragmentation analyses, although included in the CALE model in order to maintain proper explosive confinement parameters. As shown in Fig. 3, varying the shell fragmentation time from approximately 8 μs (at which the detonation products had expanded approximately 3 times its original volume, $V/V_0 \sim 3$) to approximately 20 μs ($V/V_0 \sim 14$), the resulting changes in the fragment spray angles Θ were rather small, while the fragment spray velocities were affected rather significantly. As shown in Fig. 3, delaying the moment of the shell break-up predicts considerable increases in the fragment spray velocities, apparently due to the prolonged "pressurized" interaction with expanding detonation products that increased the total momentum transferred to the shell.

Fig. 3 Fragment velocity distribution versus spray angle Θ. Charge A
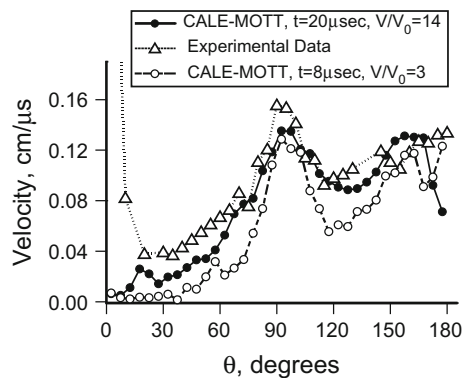
Figures 4 through 6 show plots of the number of fragments in the fragment spray as functions of the fragment size m/μ, the choice of the number of fragment distribution function model, Eqs. (23) and (26), the spray angle Θ, the shell fragmentation time, and the dynamic fracture parameter γ. As shown in the figures, increases in the parameter γ had resulted in increases of the number of fragments N, both for the N–m/μ and the N–Θ relationships. These results are in agreement with the Mott's theory [39], according to which the parameter γ defines the probability of fracture in the plastically expanding shell determining the number of breaks in the circumferential direction.

Figure 4 shows a plot of a series of curves given by Eq. (23), $N(m) = f_{(23)}(m, \gamma)$, all analyses repeated for two parameters considered: the shell fragmentation time assumed and the dynamic fracture constant, γ. For example, taking the 8 μs ($V/V_0 \sim 3.0$) fragmentation time with $\gamma = 12$ and the 20 μs ($V/V_0 \sim 14$) fragmentation time with $\gamma = 30$ resulted in nearly identical fragment distribution curves, both in good agreement with the data. The accepted shell fragmentation time had been determined from the high-speed photographic data of Pearson [41] which reasonably agreed with the CALE analyses. Following Pearson [41], the fragmentation of shells with the idealized cylindrical geometries occurs approximately at 3 volume expansions, the instant of fragmentation defined as the time at which the detonation products first appear emanating from the fractures in the shell. In the CALE analyses, the time of shell fragmentation was defined by the structural failure of the shell modeled with the Steinberg-Tipton failure model [31] with the strain work-hardening failure-limit condition $Y = Y_{max}$, Eq. (1a). Once the $Y = Y_{max}$ failure criterion was met, the yield-strength of the "failed" material was set to zero, which provided a reasonable approximation of structural failure of plastically expanding shell. CALE analyses showed that as the detonation wave propagated along the length of the charge and the shell continued to expand radially, the average shell failure strains were in the order of $\varepsilon \sim 0.5$–0.7 and at approximately 8 μs ($V/V_0 \sim 3.0$) the entire shell had failed. Accordingly, the accepted shell fragmentation time was approximately 8 μs ($V/V_0 \sim 3.0$).

Fig. 4 Cumulative number of fragments in the fragment spray versus the fragment size m/μ. Charge A
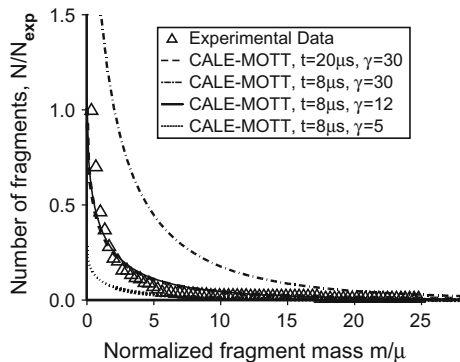
Figure 5 shows a plot of the cumulative number of fragments from the arena test data and the PAFRAG-MOTT analytic predictions employing $N(m) = f_{(23)}(m, \gamma)$ and $N(m) = f_{(26)}(m, \gamma)$ relationships, i.e. the overall "shell-averaged" fragment size distribution, Eq. (23), and the "ring-segment-averaged" fragment size distribution, Eq. (26), respectively. As shown in the plot, employing Eq. (23) resulted in consistently higher values of the cumulative numbers of fragments than that of Eq. (26), apparently because of the nature of the definition of the overall "shell-average" fragment mass $\breve{\mu}_0$, Eq. (25). As shown in the figure, two equally reasonable fits were obtained for both relationships considered, resulting in $\gamma = 12$ for Eq. (23) and in $\gamma = 14$ for Eq. (26) with the standard deviations of approximately $\sigma_{\gamma=12}(1.62) = 2\%$ and $\sigma_{\gamma=14}(1.62) = -2\%$, respectively. Both curves were fitted at a single point $m_0/\mu = 1.62$, which corresponds to the total number of fragments with mass greater than m_0; the aim was to replicate the overall lethality of the fragmenting spray, rather than focusing on the entire range of the m/μ values considered. Accordingly, the accepted shell fragmentation had been approximately 8 μs ($V/V_0 \sim 3.0$) and two values $\gamma = 12$ and $\gamma = 14$ were selected for all further analyses.

A comparison between empirical values of γ with "theoretical" values of γ' is of interest. According to Mott [39]:

$$\gamma' = 2 \ln(N\breve{V}) \frac{1}{n} \frac{d(\ln \sigma)}{d\varepsilon} \tag{27}$$

Equation (27) is based on the fundamental assumption that initiation of fractures in plastically expanding metal shells is due to microscopic flaws and cracks normally present in all metals, wherein fractures occur when the maximum principal stress reaches a value large enough to start a crack at the weak point for which the crack length is the largest. In Eq. (27) N represents a number of microscopic flaws
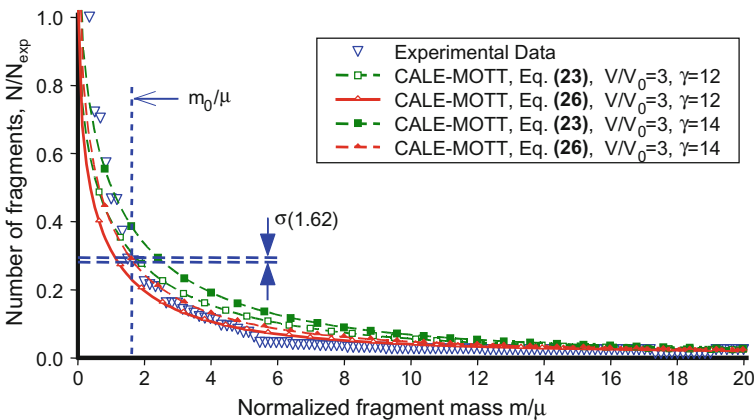
Fig. 5 Cumulative number of fragments versus m/μ for varying γ. CALE-MOTT analyses using Eqs. (19) and (22). Charge A

in a unit volume $\breve{V}$, parameter n is an exponent in the relationship between the stress σ at which the crack spreads and the length of the crack, and ε is the strain. Following Taylor [3], at the moment of fracture the circumferential stress at the outer surface of radially expanding ring is $\sigma_{\Theta\Theta} = Y$ and the radial stress is $\sigma_{rr} = 0$. Employing the Steinberg-Guinan yield-strength model, Eq. (1), and assuming that the initial strain in the shell $\varepsilon_i = 0$, and that the shell fractures when the principle strain reaches the value of ε_F, Eq. (27) takes following form:

$$\gamma' = 2 \ln(N\breve{V}) \frac{1}{n} \frac{m\beta}{1 + \beta\varepsilon_F} \tag{28}$$

Substituting Eq. (28) into Eq. (7) results in:

$$x_0 = \left(\frac{4 \ln(N\breve{V})}{\rho n} \frac{\sigma_F(1 + \beta\varepsilon_F)}{\beta m} \right)^{1/2} \frac{r}{v} \tag{29}$$

Equations (28) and (29) are useful for examining the relationship between the resulting fragment mass distribution and the principal physical properties of fragmenting metal shells. As evident from Eq. (29), modeling fragmentation of ductile high-strength metals with larger values of fracture stress σ_F and fracture strain ε_F, Mott's theory correctly predicts larger average fragments x_0 and fewer numbers of fragments N. Similarly, modeling high-fragmentation brittle metals with rapid strain hardening rates defined by parameters β and m, Eq. (29) correctly predicts larger numbers of fragments N and smaller average fragments x_0 because of the increased fracture probability γ', Eq. (28).

Given that for most metals and metal alloys the yield-strength is a function of strain-rate softening and strain hardening, Eqs. (6) and (10) model the number of fragments N and the average fragment mass μ_0 as a function of a ratio σ_F/γ' where fracture stress σ_F corresponds to the yield-strength Y at the time of fracture and fracture constant γ' defines the probability of shell's fracture or "brittleness". Accordingly, in fragmentation analyses, the value of fracture stress σ_F was set to the value $\sigma_F = Y_{\max}$, while values of γ had been obtained by fitting Eqs. (23) and (26) to experimental fragment distribution data. It is interesting to compare the experimental value of γ which includes the average fragment shape coefficient α with a theoretical value of γ' given by Eq. (28). For example, assuming SAE 4340 steel with Rockwell hardness C38 and the initial strain $\varepsilon_i = 0$, from Steinberg [37] values of work-hardening parameters β and m are $\beta = 2$ and $m = 0.5$. Given that at the moment of break-up, $V/V_0 \sim 3.0$, the average fracture strain ε_F in the shell is $\varepsilon_F \approx [(V/V_0)^{1/2} - 1] \sim 0.73$. Following Mott (1947) and assuming Griffith (1924) form of relationship between the stress and the crack length, the parameter $n = 1/2$. Value of N can be only guessed. For example, for N, Mott [39] assumed that average distances between microscopic flaws are approximately in order of 0.1 μm, hence $N\mathsf{V} = 10^{15}$. Assuming $n = 1/2$ and $N\breve{V} = 10^{15}$ Eq. (28) results in $\gamma' = 56$.

Substituting $\gamma' = 56$ in Eq. (11) results in α from 8 to approximately 10: for $\gamma = 14$, $\alpha \approx 8$; for $\gamma = 12$, $\alpha \approx 10.1$; which is in good agreement with the adopted fragment shape idealization model and with author's observations, although no quantitative assessment of values of α had been attempted. Precise statistical assessment of fragment shapes to obtain averaged values of α is quite laborious and costly, in particular for the state-of-the art high-fragmentation steels producing a large number of small fragments with weights less then 3 grains (0.2 g) which usually represents more then 70% of all "countable" fragments having weights greater then 0.3 grains (0.02 g). For relatively large fragments with weights greater then 5 grains (0.3 g), representative values of average aspect ratios of fragments lengths to circumferential breadth l_0/x_0 are available from the literature. For example, Mott [39] reports that for World War II British Service munitions, $l_0/x_0 \sim 5$, and for World War II German munitions, $l_0/x_0 \sim 2.5$ (Mott, 1943); Mock and Holt [42] report that for Armco iron cylinders, $l_0/x_0 \sim 5$, and for high-fragmentation HF-1 steel cylinders, $l_0/x_0 \sim 2.5$. Accordingly, considering idealized approximately square-shaped base parallelepiped fragments with aspect ratios $l_0/x_0 \approx t_0/x_0$, α $(l_0/x_0)^2$, yields for high-fragmentation steel cylinders $\alpha \approx 6.3$, which compares reasonably well with α approximately from 8 to 10 from this work.

Figure 6 shows a plot of the number of fragments with mass greater than 3 grains versus the spray angle Θ, which is the principal lethality parameter of the fragment spray of the munition. The disagreement between the analyses and small spikes at 45° and 60° is probably due to fragments from the shaped charge liner-retaining ring, which had not been included in the CALE model, mainly because of the minimal effect on the overall fragment lethality. The disagreement between the analyses and the spike at 155° is probably due to fragments from a rotating band that had not been included in the CALE model. As shown in the figure, even using a relatively crude assumption of the shell fragmentation time, the overall agreement between the analyses and the experimental data is very good.

Fig. 6 Number of fragments in the fragment spray: varying the shell fragmentation time and the γ. Charge A
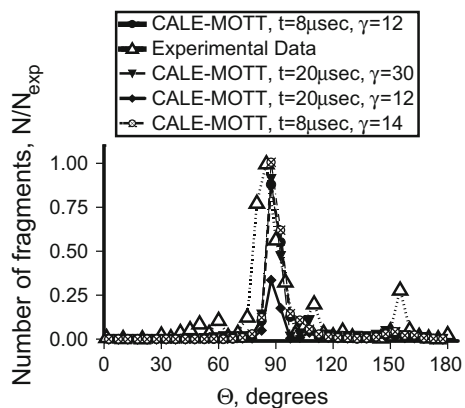
6 Charge B Modeling and Experimentation

After having established the crucial parameters of the model, ***Charge B*** shown in Fig. 1 was designed to maximize the total number of lethal fragments generated. Upon fabrication, the performance of the new charge was tested in a series of experiments including flash radiography, high-speed photography, and sawdust fragment recovery.

The flash radiography tests were performed using two 150 kV x-ray heads located approximately 74 in. in front of the round. Shortly after initiating the round, each of the two x-rays heads were flashed at the separate prescribed times and intervals several microseconds apart. Two flash radiography tests were conducted. Each test resulted in two dynamic images of the expanding fragmented steel shell, both images superimposed on the film.

The high-speed photography tests were performed employing Cordin Framing Camera Model No. 121 capable of recording up to 26 high-speed exposure frames with time intervals between individual frames of less than 1 μs apart. In the experiments, the round was placed on a test stand in front of a fiducial grid, surrounded with four Argon gas light bombs, all enclosed in a white paper tent. A total of two high-speed photography tests were conducted, each test resulting in over 20 dynamic images of the expanding and fragmenting shell, approximately one microsecond apart.

Figure 7 shows a comparison between the CALE code predictions and the images of the expanding and partially fractured shell obtained from the flash radiography and high-speed photography experiments. The figure shows that the model resulted in an accurate prediction of the shape of the expanding hardened steel shell, including the early break out of the detonation products through the joint between the fuze and the main charge. After the shell breaks up and the detonation products start moving through the air, the discrepancy between the position of the edge of the detonation products cloud observed from the high-speed photography and that from the CALE code simulations is relatively large and needs to be commented. The discrepancy is mainly due to modeling approximations in applying the idealized three-dimensional axisymmetric geometry assumption, the Steinberg-Tipton failure algorithm, and the JWLB equation of state to simulate a complex physical phenomenon of shell fracture coupled with high-rate high-pressure-gradient flow of detonation products through cracks into relatively low pressure regions of air surrounding the shell. Given an excellent overall prediction of the shape of the expanding fragmenting shell evident from flash radiographic images, the final impact of these modeling errors is minimal.

Referring to the flash radiographic image of the partially fragmented shell given in Fig. 7, it is important to note remarkable difference between shapes and sizes of fragments ejected from the cylindrical and the curved portions of the charge. As seen from both the 27 μs and from the 45 μs radiographic images, the majority of cracks in the cylindrical portion of the charge are in the axial direction, resulting in fragment spray with relatively large axially oriented splinter-like fragments. On the
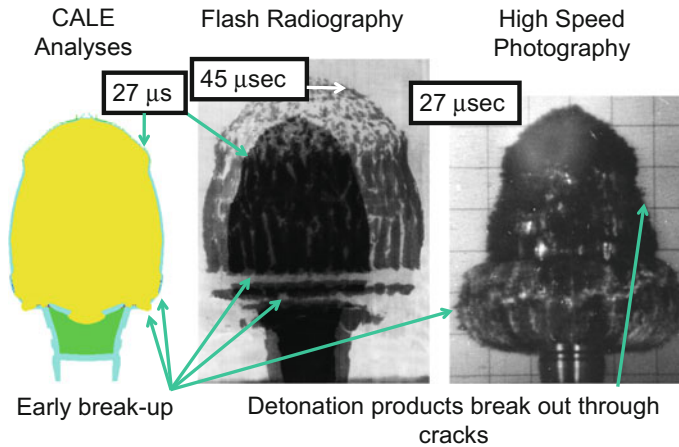
Fig. 7 CALE code modeling and experimentation. Charge B

contrary, in the curved nose portion of the shell, the orientation of cracks is random and distances between fissures are shorter, resulting in fragment spray of predominantly small compactly shaped fragments.

Figure 8 shows a series of high-speed photographic images of the state of the shell's surface as the warhead's hardened steel case expands and the detonation products emerge through cracks. As shown in the figure, visible fractures start to appear on the surface of the shell at approximately 9.4 μs after the detonation, which according to the CALE code analyses corresponds to approximately $V/V_0 = 1.8$. Examination of the entire series of images taken approximately one microsecond apart shows that as the shell expands, fractures develop first in the cylindrical portion of the shell. As the shell continues to expand, the developed fractures propagate mostly in the axial direction, occasionally linking-up by new cross-cracks in the circumferential direction, ultimately resulting in formation of large splinter-like fragments shown in the radiographic images of Fig. 7.

As the shell continues to expand, fractures gradually advance towards the curved nosed portion of the shell, and at approximately 19.8 μs, or at approximately 6.2 volume expansions, the entire shell is fully fragmented, the fragmentation being defined as the instant at which the detonation products first appear as they emanate from the fractures in the shell. Following the PAFRAG-MOTT model assumption that the critical fracture strain at the moment of the shell break-up is expressed in terms of the high explosive detonation products volume expansions, the "average" volume expansion at the time of the shell break-up is then approximately one-half of the value of volume expansions of the fully fragmented shell, hence $V/V_0 = 3.1$. It is interesting to note that the value of $V/V_0 = 3.1$ is in excellent agreement with that assumed initially based on the high-speed photographic data of Pearson [41] for an open ended SAE 1015 steel cylinders filled with Comp C-3 explosive. At a framing rate of 330,000 frames per seconds the recording time was about 75 μs,
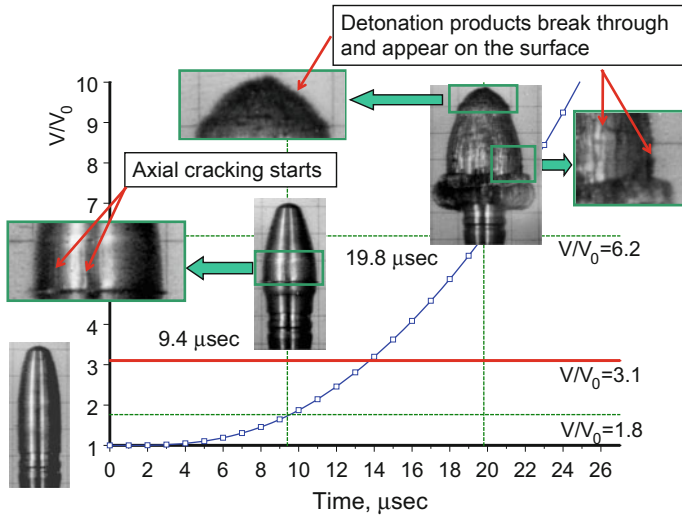
Fig. 8 Development of surface fractures in the expanding shell. Charge B

resulting in approximately the same number of high-speed images as in the this work. It is also interesting to note that changing initial test temperatures from normal 26 °C to −79 °C resulted in significant changes in the fragment cross-sectional shapes from the shear fracture mode to a combination of shear and brittle tensile fracture, but the value of the volume expansion at the time of the shell break-up remained approximately the same. More detailed information regarding the tests can be found in Pearson [41].

Figure 9 shows plots of PAFRAG-MOTT analytic predictions of the fragment velocity distribution function and the experimental data. The experimental data considered here were reduced from the radiographic images of the expanding and partially fractured shell. As shown in the figure, two analytical fragment velocity distribution functions were considered: *(i)* assuming that the entire shell fragments instantly at approximately at 13 μs ($V/V_0 = 3$), and *(ii)* assuming that the entire shell fragments instantly at approximately at 30 μs ($V/V_0 = 15$). Given that the explosive was modeled using a semi-empirical set of parameters calibrated with the experimental copper cylinder expansion data, the CALE predictions of the expanding (but not fractured) shell velocities should be reasonably accurate. As shown in the figure, the agreement between the data and the $V/V_0 = 3$ curve is significantly better than with the $V/V_0 = 15$ curve, suggesting that the shell fractured at approximately 3 volume expansions. In addition, given that (according to the high-speed photography) the entire shell had fully fractured at approximately 6.2 volume expansions, the assumption of the $V/V_0 = 3$ instantaneous fracture event is quite reasonable: once the detonation products start to escape through the cracks, any further gains in the velocities are relatively small and may be neglected.

Fig. 9 Fragment velocity distribution versus spray angle Θ. Design B
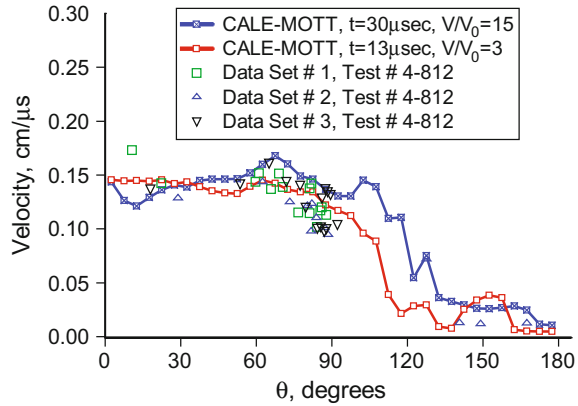
The fragment recovery tests considered in this work were performed employing disposable plastic containers measuring approximately 52 in. in diameter and 59 in. in height, filled with approximately 1000 lbs of sawdust. After inserting the tested round in an inflatable rubber balloon and filling the balloon with air, the balloon was positioned in the sawdust in the middle of the plastic container. After detonating the round, the resulting fragments were recovered employing a combination of the magnetic (for separating fragments from the sawdust) and the vacuum (for separating sawdust from the fragments) recovery techniques. Mass distribution of the collected fragments was analyzed employing an electronic high precision balance gauge interfaced with a computer system capable of automatic counting of fragments as they were manually placed on the scale and weighed. Weighing of the fragments was performed employing the Ohaus Voyager Balance model V14130 gauge with the maximum capacity of 410 g and the precision of 0.001 g. A total of two sawdust recovery tests were performed, each of the tests resulting in successful recovery of approximately over 99.8% of the mass of the steel shell.

Figure 10 shows plots of PAFRAG-MOTT analytic predictions of the cumulative number of fragments compared with the data from the fragment recovery tests. As shown in the figure, two analytic relationships had been considered: (i) the "shell-averaged" fragment size distribution, Eq. (23), and (ii) the "ring-segment-averaged" fragment size distribution, Eq. (26). As shown in the figure, the analytic prediction of Eq. (23) significantly disagrees with the experimental data, regardless of the value γ considered. The disagreement between the Eq. (23) predictions and the data is mostly because of the significant variance in fragment weights μ_j along the shell, ultimately resulting in over-predicting the "shell-averaged" fragment weight $\tilde{\mu}_0$, Eq. (26). On the contrast, the agreement between the data and the $\gamma = 14$ "ring-segment-averaged" fragment size distribution given by the Eq. (26) is quite good: $\sigma_{\gamma=14}(1.051) = -7.3\%$. Given relative simplicity of the model, the overall agreement between the analyses and the data is excellent.
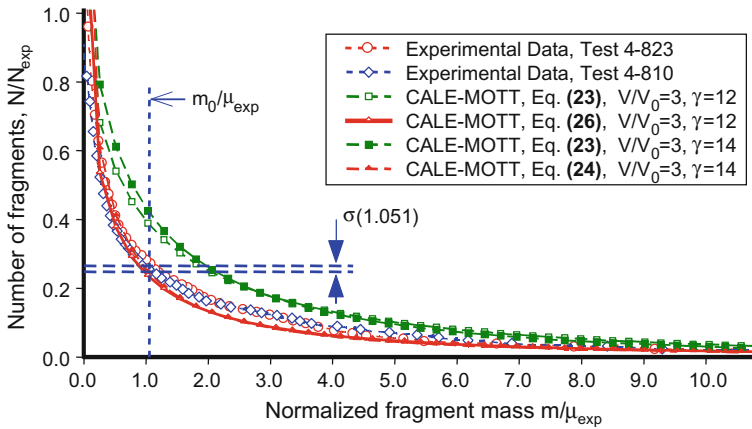
Fig. 10 Cumulative number of fragments versus normalized fragment mass m/μ_{exp}. Charge B

7 Charge C Modeling and Experimentation

Figure 11 shows results of high-strain high-strain-rate CALE modeling and flash radiographic images of a representative natural fragmentation warhead, Charge C, at 30 and 50 μs, and at 300 and 500 μs after detonation. As shown in the figure, upon initiation of the high explosive, rapid expansion of high-pressure high-velocity detonation products results in high-strain high-strain-rate dilation of the hardened fragmenting steel shell, which eventually ruptures generating a "spray" of high-velocity steel fragments. As shown in the Charge C model, the rear end of the warhead has a cylindrical cavity for the projectile tracer material. Following the expansion of the detonation products, the tracer holder fractures and the resulting fragments are projected in the negative direction of the z-axis, without contributing to the warhead lethality but posing potential danger to the gunner. As evidenced from the series of flash radiographic images shown in Fig. 11, the tracer holder section of the warhead breaks up into a number of relatively large fragments that may cause serious or fatal injuries to the gunner.

The Charge C CALE analyses had been conducted until approximately 30 μs after the charge initiation. As shown in the figure, CALE modeling results are in very good agreement with flash radiographic images of the fragmented warhead. As discussed in the previous sections, the fundamental assumption of all fragmentation analyses presented in this work was that the fragmentation occurs simultaneously throughout the entire body of the shell, at approximately at 3 volume expansions, the instant of fragmentation defined as the time at which the detonation products first appear emanating from the fractures in the shell. Accordingly, at approximately 3 volume expansions (12.5 μs), the Charge C fragmenting steel shell was assumed completely fractured, and the CALE-code cell flow field data was passed to PAFRAG-MOTT and PAFRAG-FGS2 fragmentation modeling.
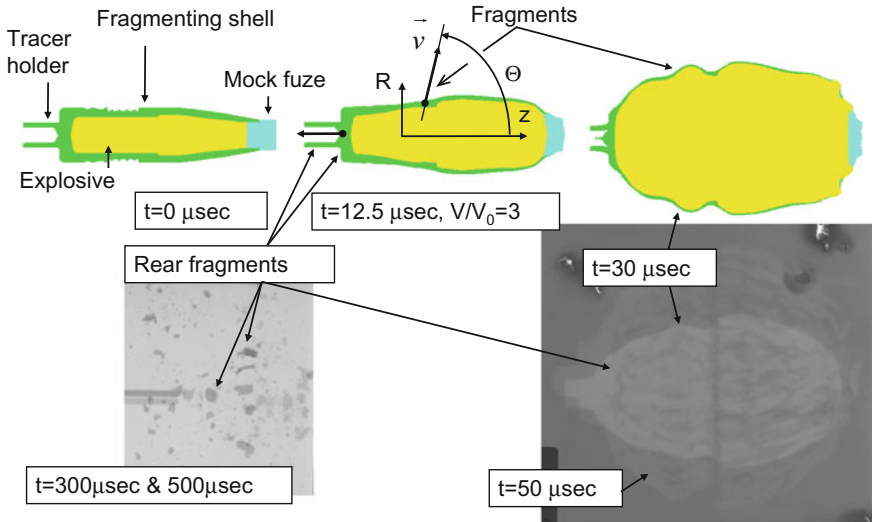
Fig. 11 Results of CALE modeling and flash radiographic images of a natural fragmentation warhead at 30 and 50 μs (test No. X-969), and at 300 and 500 μs (test No. Y-070) after detonation. Charge C

Results of PAFRAG modeling of the Charge C are given in Figs. 12, 13, 14 and 15. Figure 12 shows plots of the cumulative number of fragments versus fragment mass for small-to-moderate weight ($m/\mu_0 < 5.5$) and for relatively large ($m/\mu_0 > 5.5$) fragments calculated with PAFRAG-MOTT and PAFRAG-FGS2 models. As shown in the figure, attempting to fit the sawdust fragment recovery data with the PAFRAG-MOTT model by changing parameter γ "rotated" the curve, but did not yield an accurate fit to the data. Accordingly, more a "flexible" PAFRAG-FGS2 model was applied. As shown in the figure, using the PAFRAG-FGS2 model resulted in accurate fit throughout the entire range of data. Accordingly, PAFRAG-FGS2 model was used for all further Charge C analyses.

Figure 13 shows the PAFRAG model fragment velocity predictions compared with the experimental data. The experimental values of fragment velocities of the main fragment spay ($80° \leq \Theta \leq 100°$) were obtained from the flash radiographic images at 29.4 and 49.9 μs. Velocities of the rear fragments broken off from the tracer section of the shell (which move significantly slower than fragments from the main spray) were assessed from the flash radiographic images at 125.2, 300.0 and 310.9 μs. PAFRAG model prediction of the "average" Θ-zone fragment velocities was obtained from the momentum averaged CALE-code flow field cell velocities. As shown in the figure, the agreement between the PAFRAG model fragment velocities predictions and the data is good.

Figure 14 shows PAFRAG model predictions of the fragment mass distribution versus the spray angle Θ; the zonal fragment mass m_j and the cumulative fragment mass M distribution functions were computed from CALE-code cell flow field data.
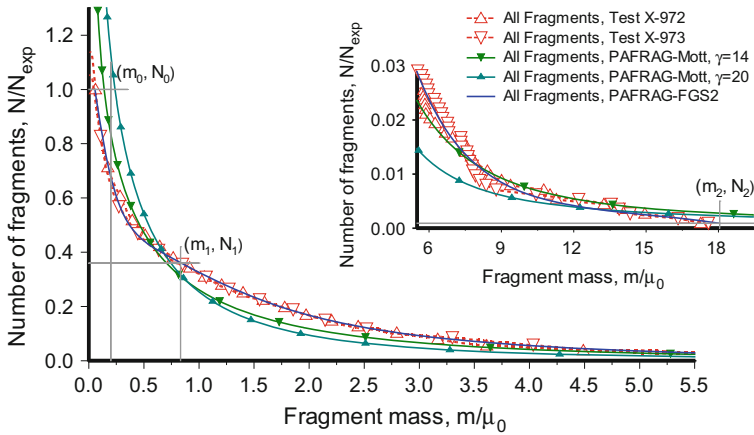
Fig. 12 Cumulative number of fragments versus fragment mass, $N = N(m)$, for small-to-moderate weight ($m/m_0 < 5.5$) and relatively large ($m/m_0 > 5.5$) fragments. Charge C
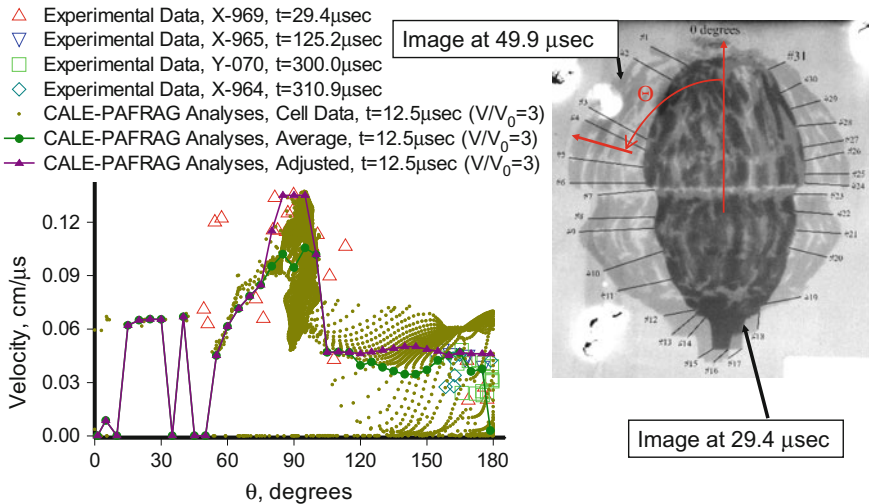
Fig. 13 Fragment velocities versus fragment spray angle Θ and flash radiographic images at 29.4 and 49.9 μs (test No. X-969) after detonation. Charge C

For representation clarity, the cumulative fragment mass function M is defined in terms of angle $180° - \Theta$, not the spray angle Θ. As shown in the figure, the PAFRAG model prediction of the cumulative fragment mass distribution M is in good agreement with the available experimental data at $\Theta = 161.6°$ (the Celotex™ and the water test fragment recovery) and at $\Theta = 180°$ (the sawdust fragment recovery).
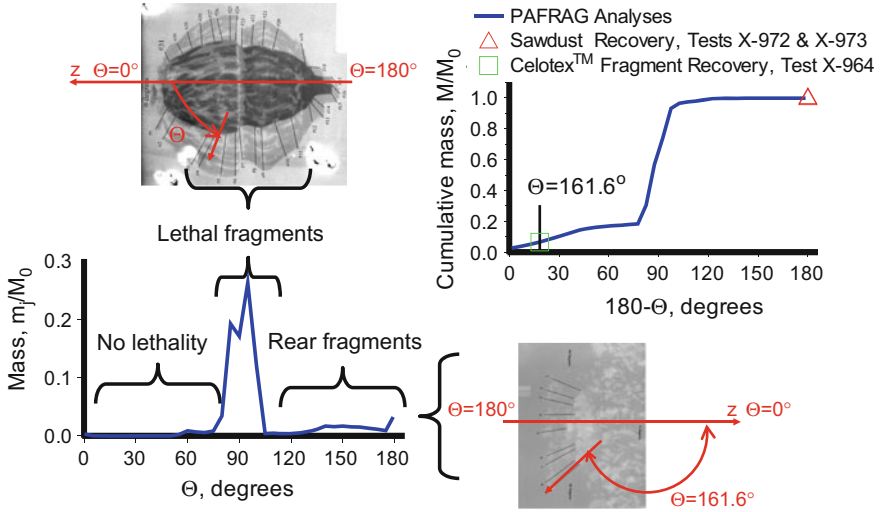
Fig. 14 PAFRAG analyses of fragment mass distribution versus Θ. Cumulative fragment mass distribution from PAFRAG analyses is in excellent agreement with experimental data. Charge C
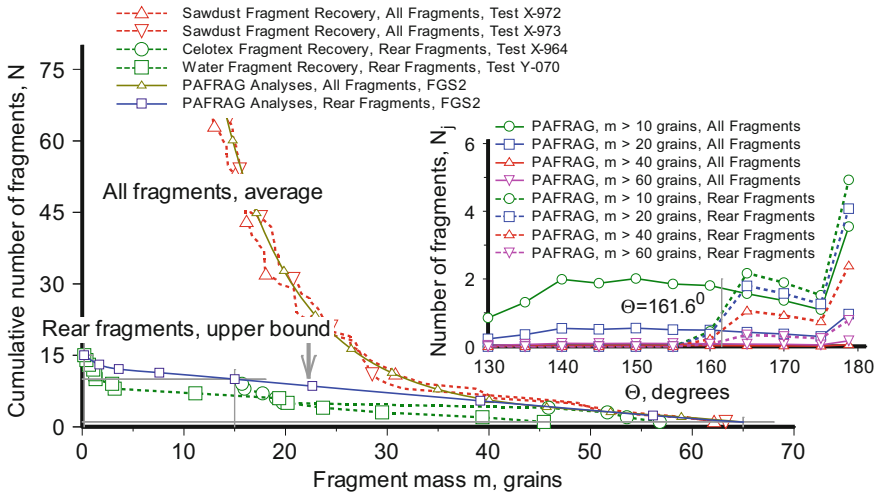
Fig. 15 Cumulative number of fragments versus fragment mass and number of fragments versus Θ, for total "all fragments" and "rear only" ($\Theta > 161.6°$) distributions. Charge C

As shown in Fig. 14, Charge C PAFRAG modeling predicts that the majority of the munition's fragment spray is projected into a relatively narrow Θ-zone in the direction perpendicular to the projectile's axis, approximately at angles $80° \leq \Theta \leq 100°$. This is in good agreement with the flash radiography data showing no fragments projected to the projectile's anterior region, $0° \leq \Theta \leq 50°$. The

fragment velocity "spikes" in the region of $0° \leq \Theta \leq 50°$ (see fragment velocity plot, Fig. 13), are due the numerical "noise" from a few "stray" mix-material computational cells from the CALE modeling. Because there is no considerable fragment mass in the front Θ-zones, the overall effect of these errors is negligible, and the "average" fragment velocity in the $0° \leq \Theta \leq 50°$ region should be disregarded.

As evidenced from the flash radiographic images presented in Fig. 14, the tracer holder portion of the warhead breaks up into a number of relatively large fragments projected in the negative z-axis direction, back towards the gunner. As shown in Fig. 14, in excellent agreement with the Celotex™ and the water test fragment recovery data, PAFRAG modeling predicts that approximately 7.2% of the total fragment mass is projected to the "rear", in the region of $161.6° \leq \Theta \leq 180°$. Since according to PAFRAG modeling and the flash radiography data, Fig. 13, the velocities of these fragments is approximately 0.05 cm/μs, the broke-up pieces of the projectile's tracer holder are capable of causing serious injuries or death to the gunner.

Figure 15 shows PAFRAG-FGS2 model predictions of the cumulative number of fragments versus fragment mass, $N = N(m)$, and of the Θ-zonal number of fragments versus Θ, $N_j = N_j(\Theta)$, for both the total "all fragments" and the "rear only" ($161.6° \leq \Theta \leq 180°$) modeling cases. The "all fragments" fragment distribution was assessed from the sawdust fragment recovery tests that included fragments from the tracer section together with all fragments from the entire shell. The "rear only" fragment distribution was obtained from the Celotex™ and from the water test fragment recovery experimentation and accounted only for fragments projected at angles greater than approximately 161.6°. The limiting rear fragment collection angle of $\Theta = 161.6°$ represents the altitudinal angle Θ covering the fragment recovery surface area.

As shown in Fig. 15, the "rear fragments" PAFRAG-FGS2 model fragment distribution was obtained by fitting Eq. (5) to the upper bound of the Celotex™ and water test recovery data, providing an additional "safety" margin for the safe separation distance analyses. Since in a typical fragmentation warhead only a few fragments are projected backward towards the gunner, establishing a statistically robust data base from the conventional fragmentation arena test requires repeated experimentation and is expensive. In contrast, the data from the PAFRAG modeling offers to munition designers more warhead performance information for significantly less money spent. The PAFRAG provides more detailed and more statistically accurate warhead fragmentation data for ammunition safe separation distance analysis, as compared to the traditional fragmentation arena testing approach.

8   Charge C PAFRAG Model Analyses: Assessment of Lethality and Safety Separation Distance

The safety separation distance analyses presented in this work were performed employing the JMEM/OSU Lethal Area Safety Program for Full Spray Fragmenting Munitions code [43] and the Wedge model computational module. According to Ref. [44], the safe separation distance is defined as fixed distance from the weapon's launch platform and personnel beyond which functioning of the munition presents an acceptable risk of a hazard to the personnel and the platform. Accordingly, the safe separation hazard probability had been calculated based on the warhead's fragment spray ability to strike and to penetrate exposed (bare) skin tissue of unprotected gun crew personnel. According to the Ref. [44], the maximum total risk to the munition crew at safe separation distance is generally accepted as 10^{-6}.

The input for the lethality and safe separation distance analyses included a range of possible ballistic projectile trajectories and the static PAFRAG FGS2 model predictions of the fragment spray blast characteristics. Figure 16 shows resulting plots of areas with $0.1 \leq P_i \leq 1$ and $P_i \leq 10^{-6}$ unprotected personnel risk hazards for varying projectile lunch velocities. As shown in Fig. 16, the projectile launch velocity has a significant effect on both the munition lethality $(0.1 \leq P_i \leq 1)$ and the safety $(P_i \leq 10^{-6})$. As shown in the figure, if the gun operates normally and launches the projectile with the nominal muzzle velocity of V_0, all fragments are projected in the forward direction, posing no danger to the gun crew. However, if the gun misfires $(V_z \ll V_0)$ and the munition is detonated, the results may be catastrophic.
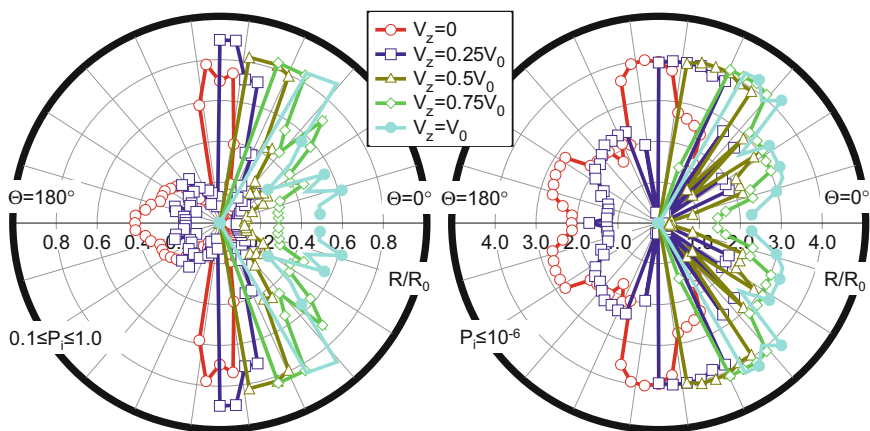
Fig. 16 Cumulative number of fragments versus fragment mass and number of fragments versus Θ, for total "all fragments" and "rear only" $(\Theta > 161.6°)$ distributions. Charge C

9 Summary

The fundamental vision of the US Army Armaments Research, Design and Engineering Center, Picatinny Arsenal is that the fragmentation ammunition has to be safe for the soldier and lethal for the adversaries. PAFRAG (Picatinny Arsenal FRAGmentation) is a combined analytical and experimental technique for determining explosive fragmentation ammunition lethality and safe separation distance without costly arena fragmentation tests. PAFRAG methodology integrates high-strain high-strain-rate computer modelling with semi-empirical analytical fragmentation modelling and experimentation, offering warhead designers and ammunition developers more ammunition performance information for less money spent. PAFRAG modelling and experimentation approach provides more detailed and accurate warhead fragmentation data for ammunition safe separation distance analysis, as compared to the traditional fragmentation arena testing approach.

References

1. Gurney RW (1943) The initial velocities of fragments from shells, bombs, and grenades. US Army Ballistic Research Laboratory Report BRL 405, Aberdeen Proving Ground, Maryland, Sept 1943
2. Mott NF (1943) A theory of fragmentation of shells and bombs. Ministry of Supply, A.C. 4035, May 1943
3. Taylor GI (1963) The fragmentation of tubular bombs, paper written for the Advisory Council on Scientific Research and Technical Development, Ministry of Supply (1944). In: Batchelor GK (ed) The scientific papers of Sir Geoffrey Ingram Taylor, vol 3. Cambridge University Press, Cambridge, pp 387–390
4. Gurney RW, Sarmousakis JN (1943) The mass distribution of fragments from bombs, shell, and grenades. US Army Ballistic Research Laboratory Report BRL 448, Aberdeen Proving Ground, Maryland, Feb 19431943
5. Hekker LJ, Pasman HJ (1976) Statistics applied to natural fragmenting warheads. In: Proceedings of the second international symposium on ballistics, Daytona Beach, Florida, 1976, p 311–24
6. Grady DE (1981) Fragmentation of solids under impulsive stress loading. J Geophys Res 86:1047–1054

7. Grady DE (1981) Application of survival statistics to the impulsive fragmentation of ductile rings. In: Meyers MA, Murr LE (eds) Shock waves and high-strain-rate phenomena in metals. Plenum Press, New York, pp 181–192
8. Grady DE, Kipp ME (1985) Mechanisms of dynamic fragmentation: factors covering fragment size. Mech Mat 4:311–320
9. Grady DE, Kipp ME (1993) Dynamic fracture and fragmentation. In: Asay JA, Shahinpoor M (eds) High-pressure shock compression of solids. Springer, New York, pp 265–322
10. Grady DE, Passman SL (1990) Stability and fragmentation of ejecta in hypervelocity impact. Int J Impact Eng 10:197–212
11. Kipp ME, Grady DE, Swegle JW (1993) Experimental and numerical studies of high-velocity impact fragmentation. Int J Impact Engng 14:427–438
12. Grady DE (1987) Fragmentation of rapidly expanding jets and sheets. Int J Impact Eng 5:285–292
13. Grady DE, Benson DA (1983) Fragmentation of metal rings by electromagnetic loading. Exp Mech 4:393–400
14. Grady DE (1988) Spall strength of condensed matter. J Mech Phys Solids 36:353–384
15. Grady DE, Dunn JE, Wise JL, Passman SL (1990) Analysis of prompt fragmentation Sandia report SAND90-2015, Albuquerque. Sandia National Laboratory, New Mexico
16. Grady DE, Kipp ME (1980) Continuum modeling of explosive fracture in oil shale. Int J Rock Mech Min Sci Geomech Abstr 17:147–157
17. Hoggatt CR, Recht RF (1968) Fracture behavior of tubular bombs. J Appl Phys 39:1856–1862
18. Wesenberg DL, Sagartz MJ (1977) Dynamic fracture of 6061-T6 aluminum cylinders. J Appl Mech 44:643–646
19. Grady DE (2005) Fragmentation of rings and shells. The legacy of N.F. Mott. Springer, Berlin
20. Mercier S, Molinari A (2004) Analysis of multiple necking in rings under rapid radial expansion. Int J Impact Engng 30:403–419
21. Weiss HK (1952) Methods for computing effectiveness fragmentation weapons against targets on the ground. US Army Ballistic Research Laboratory Report BRL 800, Aberdeen Proving Ground, Maryland, Jan 1952
22. Grady DE (1990) Natural fragmentation of conventional warheads. Sandia Report No. SAND90-0254. Sandia National Laboratory, Albuquerque, New Mexico
23. Vogler TJ, Thornhill TF, Reinhart WD, Chhabildas LC, Grady DE, Wilson LT et al (2003) Fragmentation of materials in expanding tube experiments. Int J Impact Eng 29:735–746
24. Goto DM, Becker R, Orzechowski TJ, Springer HK, Sunwoo AJ, Syn CK (2008) Investigation of the fracture and fragmentation of explosive driven rings and cylinders. Int J Impact Eng 35:1547–1556
25. Wang P (2010) Modeling material responses by arbitrary Lagrangian Eulerian formulation and adaptive mesh refinement method. J Comp Phys 229:1573–1599
26. Moxnes JF, Prytz AK, Froland Ø, Klokkehaug S, Skriudalen S, Friis E, Teland JA, Dorum C, Ødegardstuen G (2014) Experimental and numerical study of the fragmentation of expanding warhead casings by using different numerical codes and solution techniques. Defence Technol 10:161–176
27. Demmie PN, Preece DS, Silling SA (2007) Warhead fragmentation modeling with Peridynamics. In: Proceedings 23rd international symposium on ballistics, pp 95–102, Tarragona, Spain, 16–20 Apr 2007
28. Wilson LT, Reedal DR, Kipp ME, Martinez RR, Grady DE (2001) Comparison of calculated and experimental results of fragmenting cylinder experiments. In: Staudhammer KP, Murr LE, Meyers MA (eds) Fundamental issues and applications shock-wave and high-strain-rate phenomena. Elsevier Science Ltd., p 561–569
29. Bell RR, Elrick MG, Hertel ES, Kerley GI, Kmetyk LN, McGlaun JM et al (1992) CTH code development team. CTH user's manual and input instructions, Version 1.026. Sandia National Laboratory, Albuquerque, New Mexico, Dec 1992

30. Kipp ME, Grady DE (1985) Dynamic fracture growth and interaction in one-dimension. J Mech Phys Solids 33:339–415
31. Tipton RE (1991a) CALE User's manual, Version 910201. Lawrence Livermore National Laboratory
32. Baker EL (1991) An explosive products thermodynamic equation of state appropriate for material acceleration and overdriven detonation. Technical Report AR-AED-TR-91013. Picatinny Arsenal, New Jersey
33. Baker EL, Stiel LI (1998) Optimized JCZ3 procedures for the detonation properties of explosives. In: Proceedings of the 11th international symposium on detonation. Snowmass, Colorado; August 1998, p 1073
34. Stiel LI, Gold VM, Baker EL (1993) Analysis of Hugoniots and detonation properties of explosives. In: Proceedings of the tenth international symposium on detonation. Boston, Mass, July 1993, p 433
35. Steinberg DJ, Cochran SG, Guinan MW (1980) A constitutive model for metals applicable at high-strain rate. J Appl Phys 51:1498–1504
36. Tipton RE (1991b) EOS coefficients for the CALE-code for some materials. Lawrence Livermore National Laboratory
37. Steinberg DJ (1996) Equation of state and strength properties of selected materials. Technical Report UCRL-MA-106439. Lawrence Livermore National Laboratory, Livermore, California
38. Joint Munition Effectiveness Manual (1989) Testing and data reduction procedures for high-explosive munitions. Report FM 101-51-3, Revision 2, 8 May 1989
39. Mott NF (1947) F.R.S., Fragmentation of steel cases. Proc Roy Soc 189:300–308
40. Ferguson JC (1963) Multivariable curve interpolation. Report No. D2-22504, The Boing Co., Seattle, Washington
41. Pearson J. A fragmentation model for cylindrical warheads. Technical Report NWC TP 7124, China Lake, California: Naval Weapons Center; December 1990
42. Mock W Jr, Holt WH (1983) Fragmentation behavior of Armco iron and HF-1 steel explosive-filled cylinders. J Appl Phys 54:2344–2351
43. Joint Technical Coordination Group for Munitions Effectiveness (1991) Computer program for general full spray materiel MAE computations. Report 61 JTCG/ME-70-6-1, 20 Dec 1976, Change 1: 1 Apr 1991
44. (1999) Guidance for Army Fuze Safety Review Board safety Characterization. US Army Fuze Office, Jan 1999
45. Griffith AA (1920) The phenomena of rapture and flow in solids. Phil Trans Royal Soc Lond A221:163
46. Griffith AA (1924) The theory of rapture. In: Biezeno CB, Burgurs JM, Waltman Jr J (eds) Proceedings of the first international congress of applied mech, Delft, p 55
47. Mott NF, Linfoot EH (1943) A theory of fragmentation. Ministry of Supply, A.C. 3348, Jan 1943

Grain-Scale Simulation of Shock Initiation in Composite High Explosives

Ryan A. Austin, H. Keo Springer and Laurence E. Fried

Abstract Many of the safety properties of solid energetic materials are related to microstructural features. The mechanisms coupling microstructural features to safety, however, are difficult to directly measure. Grain-scale simulation is a rapidly expanding area which promises to improve our understanding of energetic material safety. In this chapter, we review two approaches to grain-scale simulation. The first is multi-crystal simulations, which emphasize the role of multi-crystal interactions in determining the response of the material. The second is single-crystal simulations, which emphasize a more detailed treatment of the chemical and physical processes underlying energetic material safety.

Keywords Shock initiation · Grain-scale simulation · Strength · Plasticity · HMX · Plastic bonded explosive · Microstructure

1   Introduction

High explosives are materials which release energy upon chemical reaction with sufficient rapidity to produce a supersonic shock wave, called a detonation. Explosive materials come in a wide variety of forms, including granular composites, liquids, suspensions, and gases. Granular composites, however, have the broadest current use in military and industrial applications [1].

In a granular composite explosive, most of the explosive mass is found in a crystalline phase. Some explosive materials are solidified directly from a molten phase [for example, 1,3,5-trinitro-toluene (TNT)] in which case the energetic is a single-phase polycrystal. In other common formulations, a crystalline phase is solidified in a slurry that contains a second crystalline phase with a higher melting

R.A. Austin · H.K. Springer · L.E. Fried (✉)
Lawrence Livermore National Laboratory, Energetic Materials Center,
Livermore, CA, USA
e-mail: fried1@llnl.gov

point. A good example of this is the widely used military explosive Composition B, in which TNT is solidified in a slurry containing RDX (1,3,5-trinitroperhydro-1, 3,5-triazine) [1].

One of the most common forms of solid explosive for precision military applications is the plastic bonded explosive (PBX) [2]. Plastic bonded explosives utilize a polymer component to bind crystals of the explosive material together, and may be machined into precision parts. Furthermore, the mechanical properties of a PBX may be dramatically affected by the polymer component (depending on the type and amount of plastic used), allowing for formulations with varying levels of stiffness, strength, and ductility.

The safety properties of high explosive (HE) materials are described by responses to a wide range of insults, including slow impacts, shocks, and heating. One of the most widely studied areas is shock initiation. In the process of shock initiation, a sample is subjected to a shock wave that compresses and heats the material. The explosive responses to shock initiation are typically more repeatable than responses found at lower velocity impacts. Nonetheless, the mechanisms responsible for the shock initiation of solid composites are not understood in detail.

It is known, however, that material defects play an important role in shock initiation [3–5]. When a composite is shocked, the entire material is heated by (bulk) compression. Regions with defects, however, are preferentially heated as compared to non-defective regions of the bulk. These regions of preferential heating are usually referred to as "hot spots". In solid (heterogeneous) explosive materials, there are multiple potential sources of localization that may contribute to temperature rise in the crystalline phase, including, for example, micro-jetting within collapsing pores, inelastic deformation, and frictional sliding along grain surfaces [6]. The mechanisms that are activated under shock wave loading depend on the material of interest, the underlying microstructure, and the rate/intensity of loading.

Although hot spots may occur in many forms, the dominant mechanisms are typically linked to void collapse. When a void collapses, stress-strain work is done on the surrounding material, which produces localized heating. This has been established experimentally by observing changes in shock sensitivity with porosity [7]. Typically, materials with lower porosity are more difficult to shock initiate than materials with higher porosity.

In a typical shock-loaded PBX, the hot spots sizes of interest range from about 0.1–10 μm [8]. These hot spots are formed during the shock rise time (~ 1 ns) and may go on to form self-propagating burn fronts or be quenched by heat diffusion on a sub-microsecond time scale. Given the time and length scales that are involved, it has been difficult to resolve the formation and evolution of hot spots by experimental methods. It has therefore been useful to study hot spot dynamics in HE materials via numerical methods (cf. Refs. [9–17] and work cited in Sect. 2). While it is recognized that numerical calculations are not a substitute for experimental observation and measurement, modeling efforts can help to (i) gain insights to the grain-scale behavior, (ii) identify potential material sensitivities, and (iii) develop hypotheses that can be tested in experiments.

There are several possible modeling approaches to grain-scale phenomena in energetic materials [18, 19]. In the following, we describe continuum-based models that have been developed to study hot spot formation at the length scale of (i) individual defects in single crystals, and (ii) crystal aggregates containing many crystals and many defects. Ultimately, we hope that numerical simulations will provide insights to the role of hot spots generated by pore collapse and other defects in HE shock initiation. Such information would be valuable in developing improved macroscopic models of shock initiation and in designing new explosives that are safer than existing materials.

2   Multi-crystal Simulations

Studies to date have mostly focused on the responses of crystal aggregates to shock wave loading. In order to simulate the coupled thermal/mechanical/chemical responses of multiple crystal domains, it is generally necessary to develop simplifications of the underlying physics and chemistry. This has allowed for the study of many-grain interactions and spatial extents that are comparable to the run-to-detonation distances in impact-loaded PBXs. Aggregate simulations are, furthermore, an important part of multi-scale strategies, as they provide information on (non-uniform) hot spot distributions and improved understanding of microstructure-property relationships. As such, this section focuses on the development of multi-crystal/pore simulation frameworks.

The microstructure of a typical PBX is highly heterogeneous. It is composed of crystal/binder phases with potentially disparate thermal/mechanical properties and an assortment of defects (e.g., pores and cracks). An example of a typical micrograph, showing the plastic-bonded explosive PBX-9501, is depicted in Fig. 1 [20]. To resolve hot spot distributions in a shock-loaded PBX, efforts are made to build initial configurations with varying levels of heterogeneity and defect structure. A key challenge associated with these multi-crystal studies is reconstructing realistic instantiations of the HE microstructure.

Fig. 1 A micrograph that illustrates the heterogeneous microstructure (grains, binder, internal flaws) of a typical HMX-based plastic bonded explosive, PBX-9501 [20]. The scale marker is 100 μm
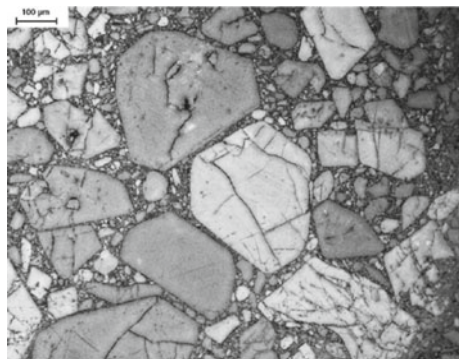
2.1 Microstructure Characterization and Reconstruction

The combination of novel explosive microstructure characterization techniques with advances in grain-packing software has allowed for the creation of large, realistic multi-crystal geometries for simulation purposes. In the following, some of the more popular characterization techniques are discussed, including current limitations and trade-offs.

Two-dimensional optical microscopy (cf. Fig. 1) and focused ion beam (FIB) techniques [21] provide highly resolved spatial data (tens of nanometers), which are needed for reconstructing realistic multi-crystal configurations. However, these techniques are destructive and the measurement itself can alter defect populations in the sample of interest. On the other hand, X-ray microtomography (cf. Fig. 2) is a non-destructive technique but resolutions are typically limited to one-thousandth of the field-of-view (e.g., 1 μm for a 1-mm thick sample). This can be insufficient for resolving critical defects when observing representative volume elements. Additionally, a lack of X-ray contrast between the crystal and binder phases can present challenges for resolving grain boundaries. Ultra small angle X-ray scattering [22] can provide information on very small pore structures, ranging from 1 nm to 1 μm, but this technique provides only averaged spatial information.

Grain-packing software tools [23–25] enable either direct initialization of HE composite geometries given suitable microstructural data (e.g., optical or X-ray microtomography data) or reconstruction via reduced sets of microstructure data when spacing or size information is missing (as in the case of ultra small angle X-ray scattering data). In the case of direct initialization, pixel or voxel data is painted onto a mesh. For reduced data sets, particle-packing and tessellation algorithms can be used to generate synthetic microstructures in lieu of explicit geometries.

Fig. 2 A typical X-ray microtomography image taken from an HMX-based PBX [74]. The cube size is 0.66 mm and *dark features* are voids
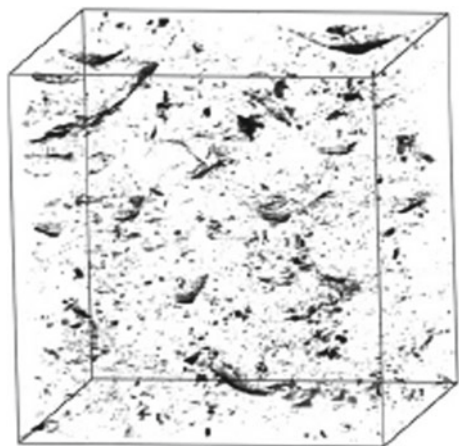
2.2 Survey of HE Shock Initiation Work

The earliest two-dimensional continuum simulations of multiple pore collapse were performed by Mader [26]. These calculations considered a regular array of pores and investigated shock responses both with and without chemical reactions. Despite computational limitations and highly idealized pore geometries, this seminal work demonstrated basic hot spot mechanisms: pore collapse, post-collapse reaction, and stress wave interactions with neighboring pores. Subsequent three-dimensional studies [27, 28] showed that the interactions between multiple collapsing pores is more likely to initiate HE materials, such as nitromethane, HMX, TATB, and PETN, than the collapse of a single pore subjected to the same shock stress.

Benson and Conley [10] considered the dynamic compression of HMX grain aggregates wherein the initial configurations (microstructures) were obtained from digitized experimental micrographs. These calculations were inert and neglected the presence of the polymeric binder. Other studies considered ordered arrays of uniform HMX grains and more-realistic packing structures with non-uniform grain sizes [11, 29]. These calculations showed that the more-realistic microstructures exhibit greater levels of temperature field heterogeneity (cf. Fig. 3) when compared to the case of uniform grain size and spacing.
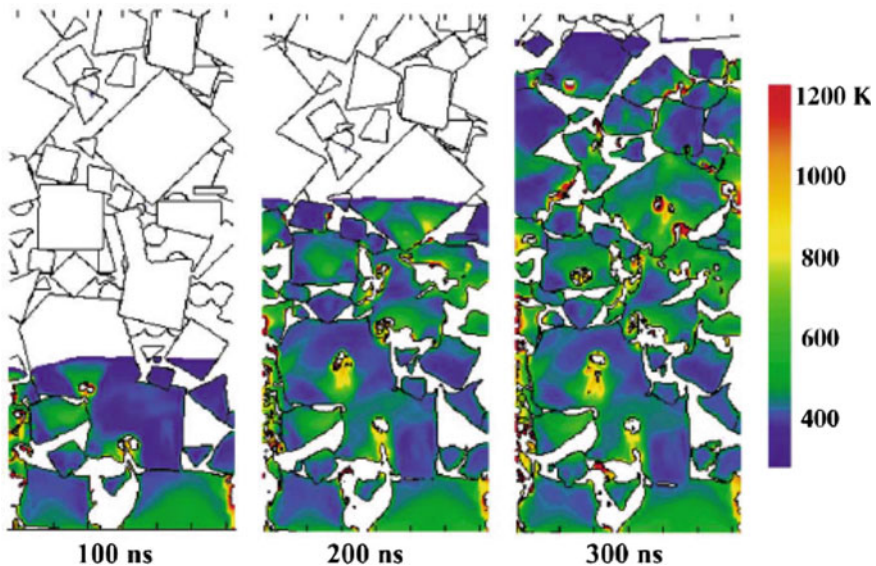
Fig. 3 The computed temperature fields for an HMX-based PBX impacted at 1000 m/s. In these images, the polyurethane binder and void space has been removed for clarity. The localized heating stems from the inelastic work of intergranular pore collapse and material jetting [11]

Cohesive finite element methods have been used to predict the fracture behavior of explosive grains, binder, and interfaces in an HMX-estane PBX subjected to overall strain rates on the order of 10000–100000 s^{-1} [30]. These studies showed that hot spots are formed primarily by viscoelastic heating of the polymeric binder during the early stages of deformation and frictional sliding along crack surfaces at later stages. In Fig. 4, the effects of overall strain rate, energetic volume fraction, and lateral confinement on computed hot spot temperature distribution are illustrated [31]. The temperature of the most frequent hot spots increases with strain rate; this effect is attributed to frictional dissipation. As the energetic volume fraction increases, the average binder thickness decreases and the peak stress increases. This results in earlier fracture and higher frictional dissipation.

Improved Lagrangian calculations employing granular frictional sliding and thermo-elastic-viscoplastic stress-strain response were used to study the compaction of HMX powder beds (85% energetic solid by volume, mean grain size of 60 μm) [32]. In these calculations, it was found that frictional work, not plastic work, is responsible for the highest temperature hot spots at impact speeds of 50–500 m/s. To assess chemical reactivity in these calculations, a critical hot spot size/temperature criterion [8] was evaluated to determine the induction time for various hot spot populations and loading conditions. This criterion was used in a number of other studies as well to establish ignition thresholds for various explosive microstructures [31, 33, 34].

A step forward in realism was achieved in the PBX modeling work of Reaugh [35] (Fig. 5). These simulations were fully three-dimensional, chemically reactive, and incorporated a more realistic description of the polymer/grain/void structure in an HMX-based PBX. From these grain-scale simulation results, a reactive flow macromodel [36] was parameterized to describe the ignition and growth of an assembly of hot spots. In this study, better agreement with detonation velocity data was demonstrated when using a pressure-dependent deflagration model, as compared to a multi-step Arrhenius kinetic, for hot spot growth. This was one of the earliest examples of using multi-crystal calculations to inform a continuum reactive
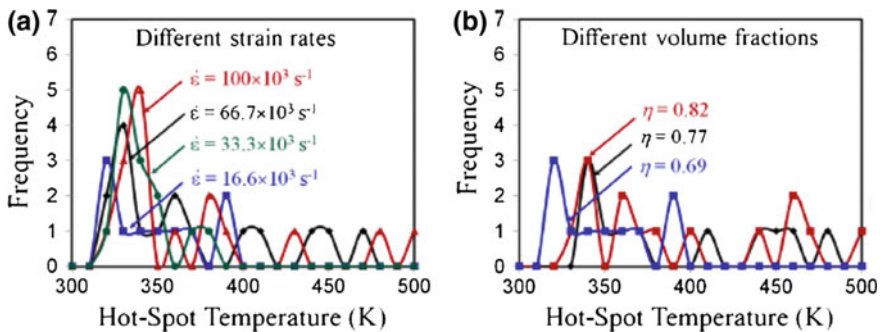
Fig. 4 The simulated effects of (**a**) strain rate and (**b**) energetic volume fraction on hot spot temperature distribution in an HMX-estane PBX under dynamic compression [31]

flow model. Bridging length scales is an important topic that needs to be addressed in future multi-scale studies.

Recent studies have sought to compare short-pulse shock initiation experiments with closely-coupled reactive multi-crystal simulations [16]. In this study, a Kapton flyer (127 μm) impacted LX-10 (95wt% HMX, 5wt% Viton A, 2% porosity) at speeds of 4.3–5.3 km/s. Grain-packing techniques [25] were used to reconstruct microstructures for these simulations, given the composition and grain/pore size distributions, wherein spherical pores were randomly positioned in the LX-10 domain. Porosity was varied from the 2% baseline value to 5, 10, and 20%. Pore radii of 5, 12.5, and 25 μm were used in calculations and resolved using sub-micron zone sizes. A single-step Arrhenius kinetic model [37] was used to describe reactivity. Figure 6 shows that for the baseline porosity of 2%, the relatively smaller, more numerous 5 μm radius pores are more effective at supporting a non-planar reaction front than the large but fewer 25 μm radius pores. The results demonstrate the effects of higher hot spot number density. Figure 7 shows that for a fixed pore radius of 5 μm, the reaction front and overall reaction rate were faster for the 10% porosity case, as compared to the 2% porosity case. At higher porosities, the hot spot density increases and greatly increases the reaction front speed and overall reactivity.
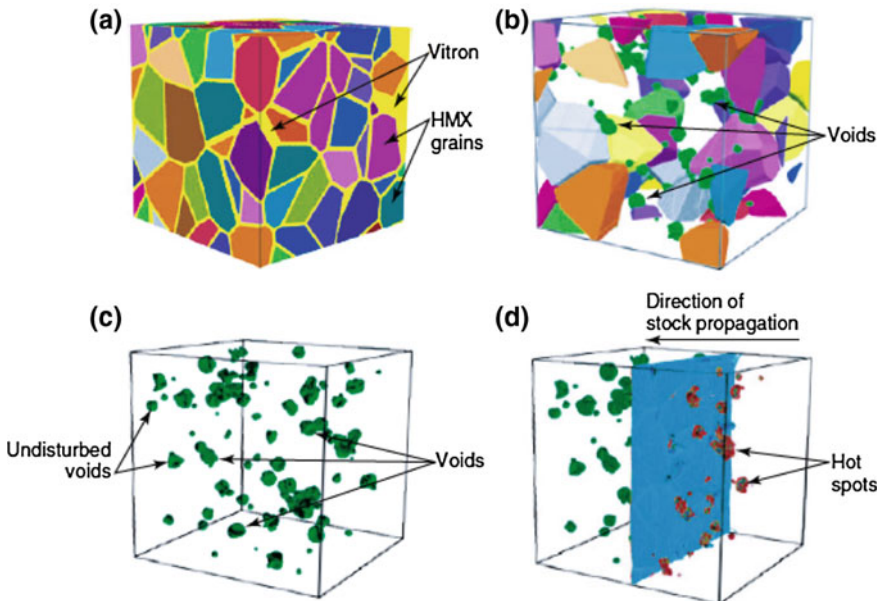
Fig. 5 The formation of hot spots under shock loading in a three-dimensional simulation with detailed microstructures [35]; **a** the faceted HMX grain structure with Viton binder, **b** internal void and grain structure, **c** void structure, and **d** shock wave propagation which induces void closure and hot spot production
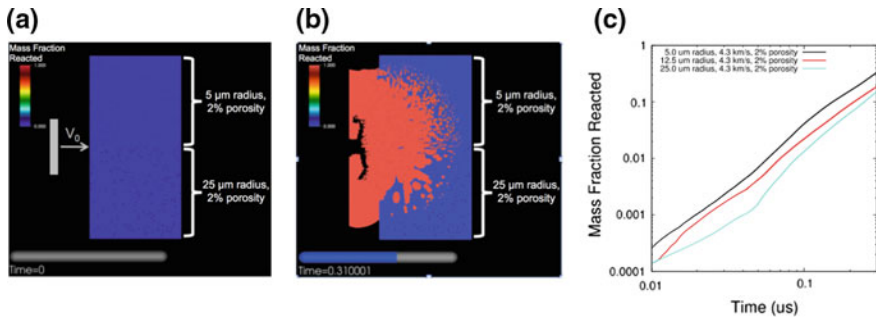
Fig. 6 Calculations of pore size effects (fixed 2% porosity) on non-planar reaction front propagation and overall reactivity of LX-10 impacted by a Kapton flyer (127 μm) at 4.3 km/s: **a** the initial impact conditions with 5 μm radius pores (*top half*) and 25 μm radius pores (*bottom half*), **b** product mass fractions fields, and **c** the time evolution of overall product mass fractions for different pore sizes [16]
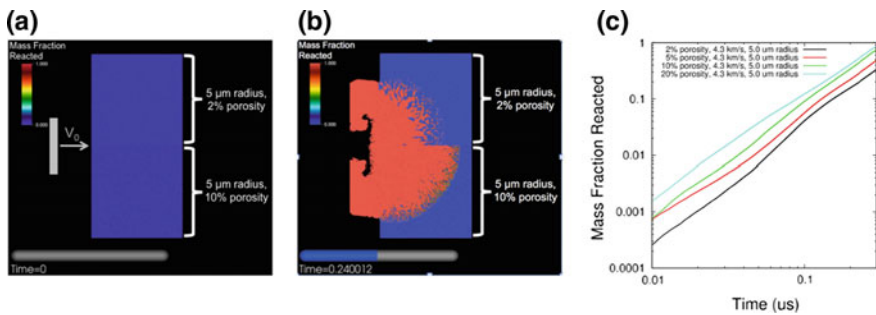
Fig. 7 Calculations of porosity effects (fixed 5 μm radius pores) on non-planar reaction front propagation and the overall reactivity of LX-10 impacted by a Kapton flyer (127 μm) at 4.3 km/s: **a** the initial impact conditions with 2% porosity (*top half*) and 10% porosity (*bottom half*), **b** product mass fraction fields, and **c** the time evolution of overall product mass fractions for 2–20% porosity [16]

Experimental validation of multi-crystal modeling efforts remains a key challenge. To this end, we simulated an HMX powder (1.24 g/cc) subjected to shock loading (1.3 GPa) and compared the calculations to embedded Manganin pressure gauge records [38]. As shown in Fig. 8, the calculations are in rough accord with the pressure gauge records, demonstrating an ability to reproduce run-to-detonation behavior in a multi-crystal simulation framework.

Fig. 8 In-situ pressure records (measured and simulated) from an impacted HMX powder (1.24 g/cc). Detonation is achieved by a run distance of ∼6 mm [38]
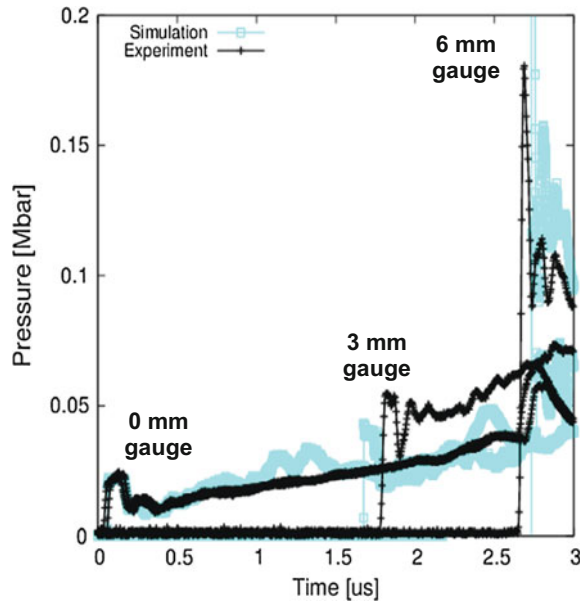
3 Single-Crystal Simulations

Further insight into the fundamental mechanisms of HE shock initiation can be obtained by considering the collapse of a single pore in a single HE crystal. Although the problem of pore collapse has been considered previously (see, for example, Ref. [12]) we believe continued study is warranted as improved models of grain-scale thermal/mechanical response emerge. In the following, we describe a material model that has been developed for the shock wave loading of HMX. The model is then employed in numerical simulations of pore collapse, with the purpose of investigating energy localization and the mechanisms of shock initiation [39]. The novel aspects of this modeling effort are the treatment of solid-phase strength behavior (a time-dependent anisotropic elastic/plastic formulation is adopted) and thermal decomposition reactions that are driven by the temperature field (i.e., the hot spots). In this regard, it will be shown that the simulated reactivity is sensitivite to the viscoplastic (strength) responses of both the solid and liquid phases. Although we focus on a continuum-based approach here, we would like to note that coarse-grained molecular dynamics [40] or very large scale molecular dynamics [41] are possible alternatives.

3.1   Continuum Model of HMX

The most stable phase of HMX at standard ambient temperature and pressure
(298 K, 1 atm) is the crystalline β phase [42, 43]. The β-phase crystal structure is
monoclinic, with two molecules per unit cell, as shown in Fig. 9. When porous
crystal is subjected to relatively weak shock wave loading, the dissipated energy of
inelastic work may be sufficient to melt parts of the crystal phase. At high enough
temperatures, the solid and/or liquid phases will undergo decomposition reactions if
given enough time. Therefore, the material model described herein addresses two
phase transformations: crystal melting ($\beta \rightarrow$ liq) and decomposition reactions that
yield gaseous products ($\beta +$ liq $\rightarrow$ gas). The $\beta \rightarrow \delta$ solid phase transformation is
ignored, as the loading conditions of interest involve pressures greater than a few
GPa [44] and the time scale of interest is short. The $\beta \rightarrow \phi$ transformation that is
observed at higher pressures (>27 GPa) [45] is also ignored. In the sections that
follow, we provide constitutive relations for the thermal/mechanical behavior of the
phases of interest (β, liquid, gas mixture) and an elementary description of the
reaction path and kinetics. For a review of HMX properties that have been mea-
sured or predicted by computations, one may refer to the literature [46].

3.1.1   Solid Phase

The thermo-elasto-viscoplastic behavior of the β phase is described using a crystal
model that was developed in previous work [13]. This model accounts for the
anisotropic nature of elastic/plastic deformation and the time-dependence of
material flow. A brief account of the crystal model is provided here. The literature
should be referenced for full model details and parameterization [13].

Following conventional crystal mechanics treatments, the crystal kinematics are
written using a multiplicative decomposition of the deformation gradient tensor,
i.e., $\boldsymbol{F} = \boldsymbol{V R F^p}$, where $\boldsymbol{F^p}$ describes the plastic shearing of the lattice, $\boldsymbol{R}$ is the

Fig. 9 The unit cell of β-
HMX (monoclinic crystal
structure) in space group
$P2_1/c$. The atoms are colored
as: C (*gray*), H (*white*), N
(*blue*), O (*red*). The HMX
molecules exhibit a chair-like
conformation in this phase
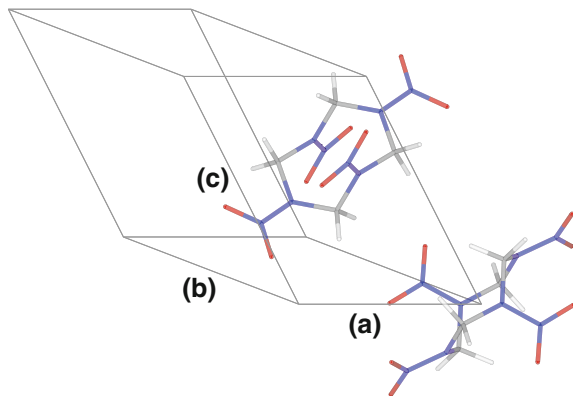
lattice rotation, and V is the thermoelastic lattice stretch tensor. In this treatment, plastic deformation is mediated by dislocation motion (crystallographic slip). As such, the velocity gradient in an intermediate configuration is written as,

$$\hat{L} = \dot{F}^p F^{p-1} = \sum \dot{\gamma}^\alpha \hat{s}^\alpha \otimes \hat{m}^\alpha \tag{1}$$

where $\dot{\gamma}^\alpha$ denotes the crystallographic shearing rates and $\hat{s}^\alpha$ and $\hat{m}^\alpha$ are unit vectors that define the slip direction and slip plane normal of the αth slip system, respectively. From the Orowan relation,

$$\dot{\gamma}^\alpha = \rho_\perp^\alpha b^\alpha \bar{v}^\alpha \tag{2}$$

where, with respect to a given slip system, $\rho_\perp^\alpha$ is the dislocation density, b^α is the Burgers vector magnitude, and $\bar{v}^\alpha$ is the mean dislocation velocity. The dislocation density is taken as an evolving internal state variable in this description. Constitutive relations have been postulated for the plasticity kinetics (dislocation mobility based on thermal activation and damped glide) and for the evolution of dislocation density [13].

In this work we include the two slip systems that have been experimentally identified, i.e., $(001)[100]$ and $(\bar{1}02)[201]$ in space group $P2_1/c$ [47, 48], and eight additional slip systems that were identified in atomistic calculations [13]. The flow resistance of each slip system scales with the square-root of the total dislocation density (in accordance with the Taylor form). As such, the dislocation density contributes to both the crystal strengthening and the ability to relax non-equilibrium shear stresses via plastic deformation.

The thermoelastic formulation combines the second-order elastic constants [49] with a Murnaghan equation-of-state (EOS) to account for non-linear volumetric response. The EOS parameters were selected to reproduce Hugoniot data from solvent-pressed HMX grain aggregates that are close to fully density [50] and isothermal compression data from diamond anvil cell experiments [45]. It is noted, however, that HMX compressibility data exhibits a wide range of scatter and that recent measurements call into question commonly-accepted parameterizations of the β-HMX EOS [51]. Improving the fidelity of the β-phase EOS is therefore a subject of ongoing work. To allow for melting of the β-phase, an energy-based melting criterion was derived from a Lindemann-type law. The crystal is fully transformed to the liquid phase when the internal energy exceeds the melt energy by an amount equal to the latent heat of melting. The melting behavior is included to account for the loss of static strength in molten regions.

3.1.2 Fluid Phases

The stress-strain responses of the liquid and product gas mixture phases are isotropic. The reference density and EOS of the liquid phase are taken to be identical to that of the β phase. This is assumed purely for expedience and it is recognized that accounting for the actual liquid density and compressibility would improve the model. The volumetric response of each component gas of the product gas mixture is described using a Buckingham exponential-6 potential [52]. The distortional responses of the liquid and gas phases are described using a Newtonian fluid law. In this description, the viscosity is constant (independent of the pressure and temperature). The nominal liquid viscosity is taken as 5.5 cP, which corresponds to the value computed from atomistic simulations performed at 800 K and 1 atm [53]. The gas mixture viscosity is assumed equal to that of the liquid phase for simplicity.

3.1.3 Thermal Properties

The inelastic work done on all phases (β, liquid, gas) is fully dissipated and converted to thermal energy. To compute phase temperatures, it is necessary to have reasonably accurate heat capacities over the temperature range of interest. The heat capacity of the β phase is described using a temperature-dependent Einstein relation, which respects the experimental data at lower temperatures [54] and the classical limit at higher temperatures (i.e., the Dulong-Petit law). The heat capacity of the liquid phase is assumed to be identical to that of the solid phase, for expedience., whereas the heat capacity of gas phase components are described using a set of temperature-dependent polynomials [52]. Thermal expansion effects in the solid and liquid phases are currently neglected.

In non-adiabatic calculations, heat conduction is modeled using Fourier's law. The thermal conductivity of the β phase is assumed to be constant, isotropic, and independent of pressure and temperature. Although analytical predictions suggest that the thermal conductivity tensor of the β phase is close to isotropic [55], refined treatments might incorporate the effects of temperature and pressure on solid-phase thermal conductivity [8, 55]. The thermal conductivities of the liquid and gas phases are assumed to be equal to that of the solid phase, for expedience.

3.1.4 Chemistry

The path and kinetics of decomposition reactions in HMX-based formulations have been investigated in a number of experimental and modeling efforts (cf. Refs. [8, 37, 56–60] and work cited therein). These efforts have focused on reactions initiated by relatively slow direct heating, with samples held under varying levels of confinement. This had led to the construction of a single-step (global) reaction scheme [37] and an assortment of multi-step reaction schemes [8, 37, 61]. However, the reaction path that is followed under shock wave loading has not been identified. In light of this uncertainty, the single-step reaction scheme [37] has been adopted for

its simplicity. The selected reaction addresses the decomposition of both β and liquid-phase HMX, i.e.,

$$\begin{array}{ccc} \text{HMX} \, (\beta + \text{liquid}) & \to & \text{Product gas mixture} \\ \text{C}_4\text{H}_8\text{N}_8\text{O}_8 & & 4 \, \text{CO} + 4 \, \text{H}_2\text{O} + 4 \, \text{N}_2 \end{array} \tag{3}$$
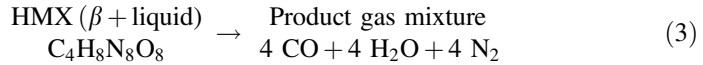
In this scheme, the chemical species to be tracked are HMX and the product gas mixture. The kinetics of this reaction are prescribed and handled using the thermochemical code, Cheetah [52]. In addition to the reaction given above, numerous fast reactions are allowed to occur among the product gas components. These reactions, which occur instantaneously, serve to maintain chemical equilibrium among the gas mixture components and the HMX species. As a result, the product gas mixture is adjusted to include other gases (for example, C, H_2, CO_2, HCN, NO_2, etc.). The current product gas composition is therefore not given exactly by (3), but rather that which is obtained by minimizing the Gibbs free energy of system subject to the kinetic constraint on HMX concentration. The species are held in pressure/temperature equilibrium in these calculations. As shown in Table 1, the formation of gaseous products involves a large exothermic heat release, which factors into the model temperature calculations.

The reaction rate law is taken as first-order with respect to the molar concentration of HMX. Therefore,

Table 1 The values of selected material properties and parameters used to model single-crystal HMX shock response

		β-HMX	Liquid-HMX	Product gas mixture
Mass density—ρ_0	g/cm^3	1.904	1.904[a]	–
Molar mass—M	g/mol	296.156	–	–
Bulk modulus—K_0	GPa	15.588	15.588[a]	–
Heat capacity—c_{v0}	J/g-K	0.995	0.995[a]	–
Volumetric CTE—α_0	1/K	0	0	–
Melting temperature—T_{m0}	K	550	–	–
Heat of formation—h_{f0}	J/g	253	489	–4760
Fluid viscosity—η	cP	–	5.5	5.5[b]
Thermal conductivity[c]—κ	W/m-K	0.5	0.5[a]	0.5[b]
Kinetic parameters of decomposition reaction: HMX (β + liquid) $\to$ product gas				
Arrhenius frequency factor —k_0	s^{-1}	5.6×10^{12}		
Activation temperature —E_a/R	K	17.9×10^3		

A subscripted zero refers to a property at standard ambient temperature and pressure
[a]Assumed equal to that of the solid phase
[b]Assumed equal to that of the liquid phase
[c]Set to zero in adiabatic simulations

$$\frac{d}{dt}[\text{HMX}] = -\frac{d}{dt}[\text{productgas}] = -k[\text{HMX}] \tag{4}$$

where the rate coefficient, k, displays an Arrhenius-type dependence on temperature. Despite its simplicity, the single-step reaction provides a reasonable approximation of experimentally-measured ignition times when the kinetic parameters of Henson [37] are utilized. As noted above, this formalism assumes the rates of decomposition from the solid and liquid phases are the same. While this seems to be a reasonable starting point, the model might be improved by distinguishing the kinetics of reactions in the solid and liquid phases [57]. Please refer to Table 1 for a partial listing of properties and parameters that are used in the single-crystal simulations.

3.2 Simulations of Intragranular Pore Collapse

The numerical simulations of pore collapse were performed using the multi-physics arbitrary Lagrangian-Eulerian finite element code ALE3D [62]. In this code, the material and mesh are permitted to undergo independent motions, with algorithms accounting for the advection of material among the computational zones (elements). In this way, the mesh is incrementally relaxed over the course of the deformation. This allows for the handling of large strains while avoiding severe mesh distortion.

The computational domain was rendered by locating a single air-filled pore near the center of a rectangular slab of β-HMX crystal. For the time being, work has been limited to 2D plane strain calculations. As such, the idealized flaw is cylindrical in shape. Two-dimensional axisymmetric simulations (for spherical pores) were not considered because the crystal lattice does not display this symmetry. Although full 3D calculations are certainly desirable, we believe such expensive calculations are premature given the developmental state of the material model.

To provide a more realistic description of the microstructure of the crystal phase, the initial dislocation density field is randomly distributed in space (cf. Refs. [13, 39] for details). This is done because the meshing requirements are such that one should expect fluctuations in dislocation density among the elements. The initial field is prescribed such that the initial dislocation density of the full sample is 0.0307 μm^{-2} [13], a value that would be considered typical for annealed metals. A planar shock wave is generated by prescribing the axial component of velocity on the left-hand surface of the crystal slab. The prescribed velocity rises instantaneously, similar to the conditions imposed at the impact face in a plate experiment. The top and bottom surfaces of the crystal sample are periodic and the right-hand

surface is restrained by a rigid frictionless wall. A single shock wave transit of the slab is simulated.

In the following, we examine predictions from the model for various load cases and material modeling assumptions. Of particular interest are the details of deformation localization and the initiation of chemical reactions. With this in mind, we consider the effects of stress wave amplitude, conductive heat transfer, solid-phase flow strength, and liquid-phase viscosity.

3.2.1 Basic Results for a Reference Case

As a reference case, consider a pore diameter of $d = 1\,\mu m$, an imposed boundary velocity of $u = 1\,\mu m/ns$ normal to the $(\bar{1}\bar{1}1)_{P2_1/c}$ plane (this generates a peak axial stress of $\sigma_{11} = 9.4\,GPa$), and locally adiabatic conditions. For this reference case, a mesh study indicated that 8-nm-zoning was needed for reasonable levels of convergence (cf. Ref. [39]). This amounts to rather fine meshing, as the pore diameter is spanned by 125 elements. To mesh the entire crystal sample $(25d \times 25d)$, about 10 million elements were required. A single pore collapse simulation run in parallel on 512 cores required about 72 h of wall clock time.

To illustrate the basic elements of material response, the pressure and temperature fields for the reference case are given, at three instants in time, in Fig. 10. In this figure, the observation windows are fixed in space and contain only the central portion of the sample. The times given for each snapshot are relative to the time at which the shock front arrives at the left-hand side of the pore. Behind the shock front, the nominal pressure (p) and deviatoric stress (s_{11}) are approximately 6.6 and 2.8 GPa, respectively. The high level of deviatoric stress is due to the rapid compression of the lattice, which produces large (elastic) strains that await relaxation by plastic flow. A release wave is emitted from the crystal-air interface (0.2 ns) as the shock front propagates across the pore. The release wave is followed by a secondary shock that is generated when the pore is fully closed (0.5 ns). This disturbance travels away from the initial pore and beyond the observation window (1.2 ns). The simulations are run until the secondary wave begins to interact with the boundaries, which allows for a post-collapse simulation time of approximately 2 ns.

The localization of deformation and energy is correlated with the development of hot spots in Fig. 10. The temperature fields indicate the formation of a central hot spot around the collapsed pore as well as narrow localization bands that grow away from the pore. These sheets of hot material are shear bands, which are filled with liquid-HMX. The inception and growth of these shear bands is driven by large non-equilibrium shear stresses in the crystal phase. As the shock begins to interact with the pore, the release of material into the pore allows for large shearing deformations in certain locations around the crystal-air interface. The mechanical work is sufficient to melt the crystal in some parts, and the flow strength and viscosity of the liquid phase are much lower than that of the crystal phase. As such,

shock direction ⟶
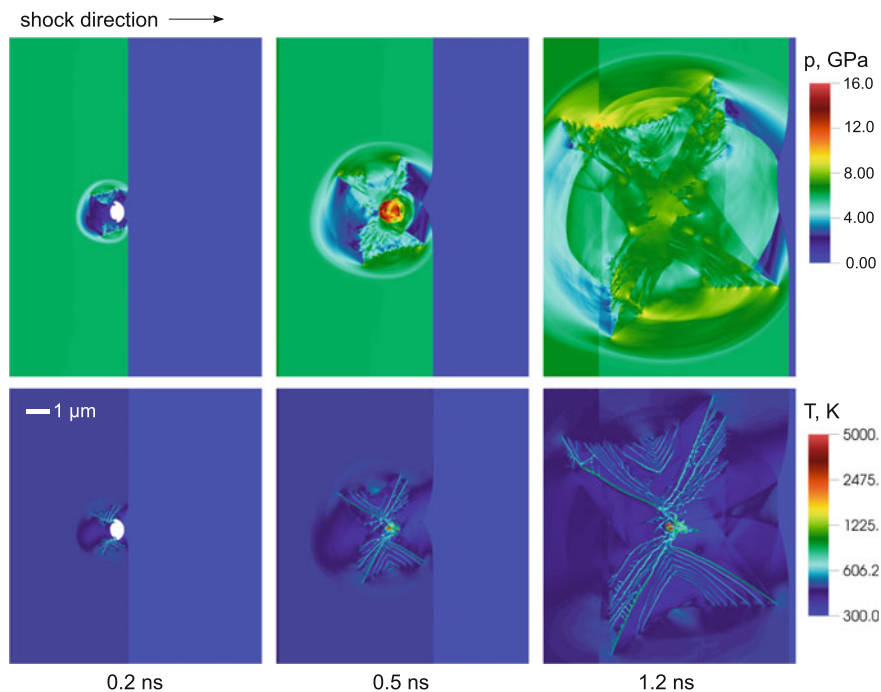
Fig. 10 The pressure and temperature fields that are generated when a shock wave (9.4 GPa) collapses a single pore (1 μm) in β-HMX crystal (reference case simulation parameters). The time origin coincides with the arrival of the shock wave at the left-hand side of the pore [75]

shearing loads that were once supported by the crystal phase are transferred onto the melt band tips and the surrounding material. The ensuing plastic deformation causes continued melting and propagation of bands that are filled with liquid-HMX. The shear bands may therefore be viewed as melt cracks, as the advancement of a band serves to reduce free energy (strain energy of the crystal lattice).

The shear banding (melt cracking) at stress wave amplitudes of 6.5, 9.4, and 10.7 GPa is illustrated in Fig. 11. In this figure, the shear bands are highlighted by plotting the phase fraction of liquid-HMX. At each stress level, a pool of liquid-HMX is formed around the collapsed pore. At 6.5 GPa, a few shear bands grow out of the pore collapse region and branch off to form finer localization bands. When the stress is increased to 9.4 GPa, the shear bands grow in four general directions and exhibit greater amounts of branching. At 10.7 GPa, the spacing of molten sheets is yet finer. In the reference case ($\sigma_{11} = 9.4$ GPa), the shear bands in the lower right-hand quadrant of the crystal sample are approximately 50 nm in width. These bands propagate at a rate of ~ 4.6 μm/ns and reach temperatures of 500–900 K. The simulated shear banding behavior indicates that the effects of internal flaws (or other material heterogeneities) may not be as localized as one might assume. As shown in Fig. 11, the hot spots generated by the growing shear bands are larger and more extended than
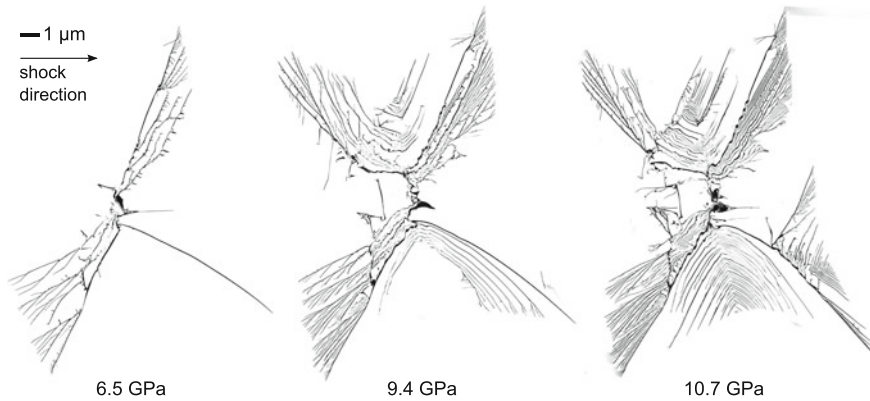
Fig. 11 The shear bands (melt cracks) that are produced when a crystal sample is shock-loaded to different peak stress levels. Here, the phase fraction of liquid-HMX is plotted on a grayscale (ranging from 0 to 1) [75]

the footprint of the original pore. It should be noted that true convergence of localization band behavior (i.e., mesh-independence of results) is not expected unless appropriate provisions are made for dissipative processes, such as heat diffusion or non-local stress-strain response. This should serve as a subject of future work.

Experimental work has documented the tendency of low-symmetry HE crystals to exhibit shear banding under shock wave loading. For example, RDX crystals that were shocked to ~ 13 GPa showed the presence of localization bands and beaded-up volumes of material on the surfaces of recovered samples [63, 64]. The beads are thought to be liquid-RDX that was squeezed out of the localization bands during the shock deformation and which resolidified on the surface of the recovered crystal sample. Shear banding is also predicted in atomistic simulations of shock wave propagation in α-HMX [65] and α-RDX [66]. In the atomistic simulations, the shear banding regions were found to be composed of an amorphous liquid-like phase. These experimental and computational results are encouraging, as this is similar to what is predicted in our continuum β-HMX simulations.

The deformation around the collapsing pore is highly non-uniform, involving the formation and interaction of multiple liquid jets within the pore. For a detailed illustration of the pore collapse process, one may refer to Ref. [39]. In the reference case, material jetting drives up the temperature enough to react a small amount of material in the pore collapse region. The sample reactivity was quantified by product relative mass, $\xi \equiv m_p/m_{pore}$, where m_p is the mass of the product phase and m_{pore} is the "pore mass" (i.e., the reference mass of crystal that would fit inside the initial pore). The reactivity of the low-stress case (6.5 GPa) was quite small on this time scale ($\xi < 0.002$). In the reference case (9.4 GPa), ξ reached a value of ~ 0.08 after a compression time of ~ 2 ns. Increasing the stress to 10.7 GPa did not significantly increase the simulated reactivity. Although the shear bands reach relatively high temperatures (800–900 K), they do not exhibit significant extents of

reaction on this time scale. For higher loads (>20 GPa) such as those observed in short-pulse initiation scenarios, bulk shock melting may occur and bypass localization bands associated with material strength.

We now consider a challenging numerical issue: artificial heat transfer among the species. Since we are employing an ALE method, solution variables need to be advected among the computational zones during the mesh relaxation stage. This numerical advection introduces errors, as solution variables tend to be smeared out in space. For example, if part of a hot (reacted) zone is advected into a neighboring zone that contains cold (unreacted) material, the temperature of the initially cold zone will be uniformly raised due to the mixing of hot and cold volumes. There is not a physical basis for this heat transfer; it is simply an error introduced by the numerical treatment. We attempted to avoid such mixing by shutting off advection in partially reacted zones [39]. This was not successful, however, as the reacting zones experience large volume expansions and require relaxation (advection) to avoid mesh tangling.

Instead of assuming an equilibrated mixture temperature, it may be useful to derive a non-equilibrium treatment that distinguishes the temperatures of the reactant and product species. Mixing among computational zones could then be handled on a species-by-species basis. In this way, when product gas is advected it would only be allowed to mix with other product gas and not serve to heat up the cold unreacted phase. A scheme like this has not yet been employed in our calculations, but should be an objective of future work. The fine zone size (8 nm) that is utilized in these calculations helps to mitigate against artificial heat transfer, as advection errors scale with mesh length. However, there is still some amount of artificial heat transfer among the species, which stems from numerical advection, and this remains an open issue.

3.2.2 Heat Conduction Considerations

The reference case was modeled as adiabatic to generate a baseline response in the absence of physical heat transfer effects. For the time scale considered here, the characteristic dimension of heat diffusion ($\sqrt{\kappa t / \rho c_v}$) is about 20 nm. Although this dimension is small in comparison to the central hot spot (around the collapsed pore), it is non-negligible when compared to the shear band width. Furthermore, the propagation of burn fronts initiated at hot spots depends on heat conduction. It is therefore of interest to assess the dependence of simulation results on assumptions pertaining to heat conduction.

To assess heat transfer effects, the pore collapse simulations were performed with Fourier heat conduction (all other aspects of the reference case remained the same). For a stress wave amplitude of 9.4 GPa, the temperature field that was

computed with heat conduction was rather similar to that computed using the adiabatic model [39]. The temperature gradients were, of course, less steep in the conductive case, but the central hot spots were of similar size and temperature. Peak temperatures in the shear bands were reduced by up to ~ 100 K. The flux of heat away from the central hot spot renders the conductive case slightly less reactive than the adiabatic case. For example, the computed extent of reaction (ξ) was reduced by less than 10% [39]. This indicates that the adiabatic assumption is reasonable when the simulation duration is limited to a few nanoseconds, as the results of interest are not changed in a substantial way when heat conduction is included. However, simulations that seek to address longer time scales (e.g., tens to hundreds of nanoseconds) and hot spot burning should treat heat conduction in a meaningful way.

We would like to note that the (macroscopic) Fourier law breaks down when the length scale of interest approaches the mean free path of the phonons. Since the pore collapse calculations involve strong temperature gradients over tens of nanometers, we believe it will be important to adopt a more sophisticated treatment of small-scale heat transfer. For example, one that accounts for phonon interactions [67].

3.2.3 Model Sensitivity to Solid Flow Strength

We now consider the dependence of simulation results on the flow strength of the solid phase. The crystal model, which has been used in all simulations up to this point, accounts for the elastic/plastic anisotropy of the β phase and the time-dependent nature of plastic deformation. The time- or rate-dependence of plasticity is thought to be important here because many solids exhibit a sharp increase in flow stress at higher rates. In regard to the problem of pore collapse, if the time scale of plastic relaxation is comparable to the time scale of pore collapse, high shear stresses will persist until they are relieved by inelastic deformation. These shear stresses factor into the mechanical work, which is responsible for a large fraction of the temperature rise.

To investigate effects related to solid flow strength, a pore collapse simulation was performed using a conventional isotropic/rate-independent strength model for the β phase. Here, the yield strength is taken as $Y = Y_0(1 + \beta \varepsilon^p)^n$, where Y_0 is the initial yield strength, ε^p is the effective plastic strain (a proxy for internal state), and β and n are hardening parameters. In the literature, it has been common to assume a constant yield strength in the range of 0.060–0.180 GPa [10, 11, 68]. To consider the effects of somewhat higher strength and weak strain-hardening behavior, the following parameters were selected: $Y_0 = 0.300$ GPa, $\beta = 0.060$, $n = 1$. All other aspects of the reference-case simulation remained the same.

The temperature fields that are computed from the isotropic/rate-independent model are shown in Fig. 12. The pore is now collapsed by a single smooth jet that produces a symmetric configuration of two hot spots. The appearance of these hot
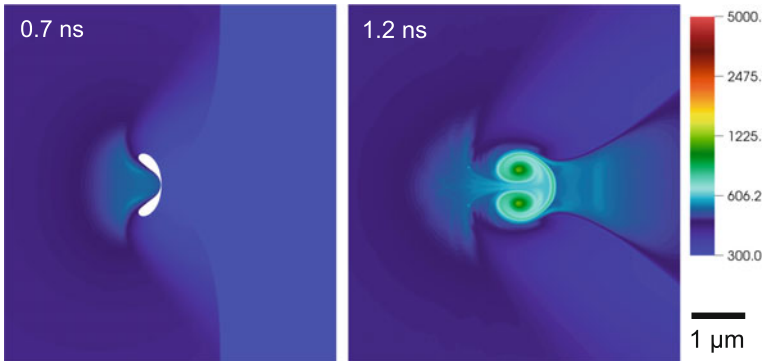
Fig. 12 The temperature fields that are obtained when pore collapse is simulated using a rate-independent/isotropic strength model (reference case simulation parameters, otherwise). The closure process and degree of localization are in sharp contrast to predictions from the rate-dependent/crystal model [75]

spots is largely due to vortical flows that are set up on either side of the impinging jet. These temperature fields may be compared to those computed earlier using the crystal model (Fig. 10). In the rate-dependent/crystal calculations, shear banding is a prominent feature of the deformation. In the rate-independent/isotropic calculations, energy localization is confined to the immediate surroundings of the pore and there is no shear banding.

The differences in localization behavior are largely attributed to the strain-rate-dependence of the strength model. Although rate-dependent flow stresses are often seen as tending to suppress localization (given that higher stresses are required to drive higher strain rates), this notion breaks down in the presence of thermal softening and melting. Such is the case in our rate-dependent calculations, where relatively large flow stresses and small plastic strains are sufficient to melt the material located at the tips of the localization bands. In the rate-independent case, the stress state is forced to remain on a strain-rate-independent yield surface and plastic strains are computed according to a consistency condition. For the parameters chosen above, the mechanical work is insufficient to trigger shear banding. It may be possible to induce shear banding in the rate-independent model by prescribing a higher yield strength. This, however, would be at odds with experimental stress-strain curves at quasistatic rates [69] and the observed relaxation behavior under shock wave loading [48]. It is, however, possible to induce shear banding by assigning sufficient strain-rate-dependence to an isotropic model. In this case, the bands form on the planes of maximum shear, whereas, in the crystal model, the details of plastic flow and band structuring are sensitive to the slip plane orientations.

To quantify the differences in thermal energy localization predicted by these models, temperature histograms were computed near the end of the simulation (cf. Fig. 13). These histograms were constructed by binning the sample mass according

to temperature and normalizing those bins by the pore mass. As shown in Fig. 13, the isotropic model is biased toward lower temperatures (notice the large peak in-between 400 and 500 K), whereas the crystal model predicts higher temperatures due to shear localization (600–1200 K) and exothermic reaction (>2000 K). For equivalent energies imparted to each sample, the crystal model predicts higher degrees of localization and, therefore, hot spots that are larger or higher in temperature. The extent of reaction that is predicted by the rate-independent model is effectively zero on this time scale, despite the formation of hot spot temperatures of greater than 1000 K. Therefore, the solid-phase strength law has a significant effect on the character of shock-induced plasticity, the peak temperatures that are generated, and the initiation of reactions due to pore collapse.

3.2.4 Model Sensitivity to Liquid Viscosity

The localization bands that grow out of the pore collapse region are filled with liquid-HMX (cf. Fig. 11). In this model, the liquid phase is treated as a simple Newtonian fluid. Although the viscosity of the liquid phase is expected to depend on the pressure and temperature (and perhaps strain rate as well), we assumed that the liquid viscosity is constant for the sake of simplicity. In the reference case, the liquid viscosity was taken as 5.5 cP, corresponding to the atomistic value at 800 K and 1 atm [53]. We now consider the sensitivity of the model to the assumed liquid viscosity. As a comparative case, the liquid viscosity was increased to 22.0 cP, which corresponds to the atomistic value at 700 K. All other aspects of the reference case remained the same.

The temperature field that is obtained when pore collapse is simulated using the higher liquid viscosity is given in Fig. 14. The shear bands are now wider, fewer in number, and hotter than those of the lower-viscosity case (Fig. 10). The shear band temperatures are higher in this case because of greater mechanical dissipation within the bands. The temperatures within the shear bands are now high enough to

Fig. 13 The temperature histograms that are computed (in log-log space) when pore collapse is simulated using a rate-independent/isotropic strength model and the rate-dependent/crystal model [75]
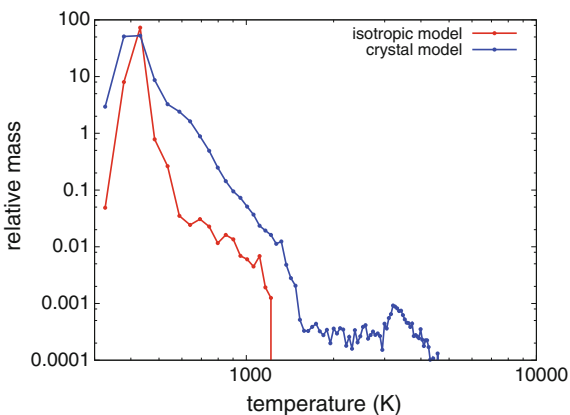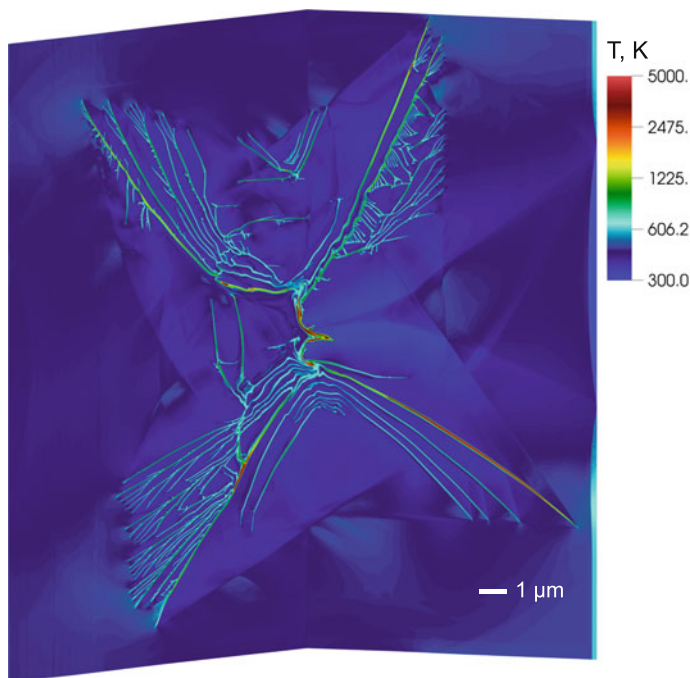
Fig. 14 The temperature field computed for the case of higher liquid viscosity (22.0 cP). Reactions now occur in both the central hot spot (pore collapse region) and the shear bands, due to increased mechanical dissipation [75]

drive decomposition reactions on this time scale (see, for example, the forward-most band in the lower right-hand quadrant of Fig. 14).

To illustrate sample reactivity, time histories of product relative mass (ξ) were computed for the lower- and higher-viscosity cases (cf. Fig. 15). The initial trajectory of the product curve is controlled by reactions that occur in the liquid phase around the central hot spot (pore collapse region). In the reference case, reactions are confined to the central hot spot, with roughly 10% of the pore mass reacted after a few nanoseconds. The higher-viscosity case exhibits higher reactivity from the start, due to increased mechanical dissipation around the central hot spot. At about 2 ns, however, the higher-viscosity case exhibits a sharp increase in overall reaction rate. This corresponds to the onset of chemical reactions in the shear bands. During a post-collapse simulation time of ~ 2 ns, ξ reaches a value of ~ 0.8. The appearance of rapidly-growing, reactive shear bands suggest that the initiation of HE crystals, such as HMX, may be dominated by planar burn waves emitted from localization bands, rather than spherical burn fronts from more compact sources.

The model predictions of reactivity are therefore quite sensitive to the viscosity of the liquid phase. This is because the liquid within a band can be subjected to exceptionally high shearing rates. Since the liquid phase experiences temperatures

Fig. 15 The product curves computed for lower and higher liquid viscosities. The sharp increase in reaction rate for the higher-viscosity case is due to the onset of reactions in the shear bands [75]
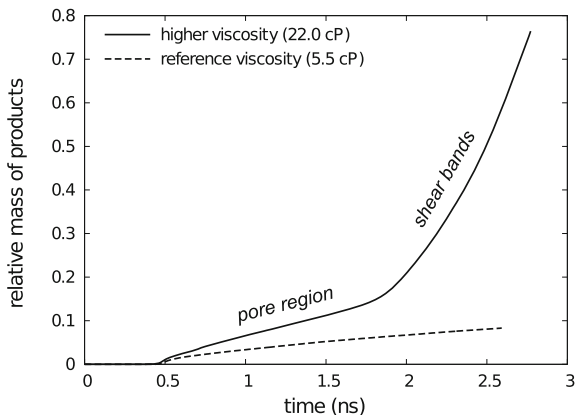
ranging from about 550 K (initial melting at 1 atm) to greater than 1000 K, future modeling efforts should incorporate the temperature-dependent liquid viscosity that was computed in atomistic simulations, i.e., $\eta = \eta_0 \exp(T_a/T)$, where $\eta_0 = 3.1 \times 10^{-4}$ cP and $T_a = 7800$ K [53]. The effect of pressure on liquid viscosity should also be considered, although we are not aware of any such data.

4 Concluding Remarks

The development of models for the grain-scale behavior of HE materials under dynamic loading conditions is an area of long-standing interest. Such efforts are needed to help elucidate the mechanisms of impact-induced hot spot formation and reaction initiation and should be viewed as complementary to experimental investigations, which are challenging to perform at the time/length scales of interest. Along these lines, we are enthusiastic about new ultra-fast measurement techniques that have been developed to probe the shock compression of HE crystals on sub-ns time scales [51]. These are truly grain-scale type measurements that may be used to further assess and refine the single-crystal model of Sect. 3 in the near future.

This article focused on the development of HE models at two length scales: (i) a coarser scale, which considers the shock responses of crystal aggregates with many defects/heterogeneities, and (ii) a finer scale, which considers single-crystal response and the behavior around a single defect (pore). In the latter, we described a continuum model that was developed for the thermal/mechanical/chemical responses of HMX. This model was used to simulate pore collapse in shock-loaded β-phase crystal and attendant energy localization modes. The single-crystal pore collapse results indicate: (i) a modest extent of reaction is achieved when an adiabatic reference case ($d = 1 \, \mu m$) is shock-loaded up to ~ 10 GPa and held for a few nanoseconds; (ii) the growth of shear bands is an important mode of localization;

(iii) hot spot dissipation via heat conduction is an important consideration for compressions longer than a few nanoseconds; (iv) the strain-rate-dependence of solid-phase strength behavior has a strong bearing on energy localization; and (v) the reactivity of impact-induced shear bands (melt cracks) is sensitive to the viscosity of the liquid phase.

Although the crystal model represents a step forward in realism, much remains to be done to improve the fidelity of model predictions. For example, the HMX material model would be improved by a better treatment of melting and liquid-phase behavior. In this regard, one might include kinetics for the $\beta \rightarrow$ liquid phase transformation, a more appropriate description of the liquid-phase EOS (i.e., one that is distinct from the solid phase), distinct kinetics for (faster) decompositions from the liquid phase [57], and a liquid phase viscosity that depends on pressure and temperature, as the simulated reactivity is quite sensitive to this property. Formulations that treat non-equilibrium species temperatures (within a given material point, or computational cell) may also prove valuable for mitigating against artificial heat transfer in various numerical settings.

The overall spatial extents that can be handled using the single-crystal model are obviously limited. To reach larger volume elements, which better reflect the heterogeneity of actual PBX microstructures, it is useful to consider aggregate calculations that employ coarsened descriptions of constituent behavior. Establishing a link between the single-crystal calculations and multi-crystal models (for example, by some information passing scheme) remains a major objective of ongoing work. A next step would then involve coarse-graining multi-crystal (aggregate) responses to obtain a PBX macromodel. However, much remains to be done to establish these connections.

Looking ahead, there are several long-standing questions for which the multi-crystal (aggregate) simulations may provide insight:

- How does defect size, spacing, morphology, and orientation influence hot spot formation and growth under shock loading conditions?
- What are the bounds on defect size that produce hot spots that are relevant to the shock initiation process?
- How does defect location in the explosive/binder system influence shock initiation behavior? For example, intragranular defects versus interfacial defects vs. binder defects.
- How does non-uniform binder coating thickness and explosive/binder impedance mismatch influence shock initiation behavior?
- How does explosive/binder microstructure and constituent properties (adhesion, flows strength) influence fragmentation, which is important to reaction violence in safety scenarios?

Such efforts must proceed with some level of experimental validation at appropriate time/length scales and this remains a major outstanding challenge.

In closing, we would like to note that multi-scale strategies that merge descriptions coming from the fine/intermediate length scales may provide a basis

for developing new PBX macromodels that incorporate microstructure-property information and, therefore, improve upon existing hot spot models [70–73]. We believe such microstructure-aware models would be valuable in designing high explosive materials for specific applications with tailored performance and safety.

References

1. Köhler J, Meyer R (1993) Explosives, fourth edition. VCH, Weinheim, FRG
2. Teipel U (2005) Energetic materials: particle processing and characterization. Wiley-VCH, Weinheim, FRG
3. Bowden FP, Yoffe AD (1952) Ignition and growth of explosions in liquids and solids. Cambridge University Press, UK
4. Campbell AW, Davis WC, Ramsay JB, Travis JR (1961) Shock initiation of solid explosives. Phys Fluids 4(4):511–521
5. Field JE, Swallowe GM, Heavens SN (1982) Ignition mechanisms of explosives during mechanical deformation. Proc Roy Soc Lond A Mat 382(1782):231–244
6. Field JE (1992) Hot spot ignition mechanisms for explosives. Acc Chem Res 25(11):489–496
7. Garcia F, Vandersall KS, Tarver CM (2014) Shock initiation experiments with ignition and growth modeling on low density HMX. J Phys: Conf Ser 500:052048
8. Tarver Craig M, Chidester Steven K, Nichols Albert L (1996) Critical conditions for impact- and shock-induced hot spots in solid explosives. J Phys Chem 100:5794–5799
9. Charles L Mader (1997) Numerical modeling of explosives and propellants. CRC press, USA
10. Benson DJ, Conley P (1999) Eulerian finite-element simulations of experimentally acquired HMX microstructures. Modell Simul Mater Sci Eng 7:333–354
11. Baer MR (2002) Modeling heterogeneous energetic materials at the mesoscale. Thermochim Acta 384:351–367
12. Menikoff R (2004) Pore collapse and hot spots in HMX. Proc APS Topical Group Shock Compression Condens Matter 706:393–396
13. Barton Nathan R, Winter Nicholas W, Reaugh John E (2009) Defect evolution and pore collapse in crystalline energetic materials. Modell Simul Mater Sci Eng 17:035003
14. Najjar FM, Howard WM, Fried LE, Manaa MR, Nichols A III, Levesque G (2012) Computational study of 3-D hot spot initiation in shocked insensitive high-explosive. Proc APS Topical Group Shock Compression Condens Matter 1426:255–258
15. Kapahi A, Udaykumar HS (2013) Dynamics of void collapse in shocked energetic materials: physics of void–void interactions. Shock Waves 23(6):537–558
16. Springer HK, Tarver CM, Reaugh JE, May CM (2014) Investigating short-pulse shock initiation in HMX-based explosives with reactive meso-scale simulations. J Phys: Conf Ser 500:052041
17. Kapahi A, Udaykumar HS (2015) Three-dimensional simulations of dynamics of void collapse in energetic materials. Shock Waves 25(2):177–187
18. Rice BM (2012) Multiscale modeling of energetic material response: Easy to say, hard to do. Shock Compression Condens Matter—2011, Parts 1 and 2 1426:1241–1246
19. Brennan JK, Lisal M, Moore JD, Izvekov S, Schweigert IV, Larentzos JP (2014) Coarse-grain model simulations of non-equilibrium dynamics in heterogeneous materials. J Phys Chem Lett 5:2144–2149

20. Skidmore CB, Phillips DS, Howe PM, Mang JT, Romero AJ (1999) The evolution of microstructural changes in pressed HMX explosives. In: 11th international detonation symposium, p 556
21. Wixom RR, Tappan AS, Brundage AL, Knepper R, Ritchey MB, Michael JR, Rye MJ (2010) Characterization of pore morphology in molecular crystal explosives by focused ion beam nanotomography. J Mater Res 25(7):1362
22. Willey TM, van Buuren T, Lee JR, Overturf GE, Kinney JH, Handly J, Weeks BL, Ilavsky J (2006) Changes in pore size distribution upon thermal cycling of TATB-based explosives measured by ultra-small angle X-ray scattering. Prop, Explos, Pyrotech 31(6):466
23. Torquato S (2002) Random heterogeneous materials: microstructure and macroscopic properties. Springer, New York
24. Kumar NC (2008) Reconstruction of periodic unit cells of multimodal random particulate composites using genetic algorithms. Comp Mater Sci 42:352
25. ParticlePack Friedman G, Manual User (2015) Version 3:1
26. Mader C L. The two-dimensional hydrodynamic hot spot, volume IV. *Los Alamos National Laboratory Technical Report*, LA-3771, 1967
27. Mader CL, Kershner JD (1967) Three-dimensional modeling of shock initiation of heterogeneous explosives. In: 19th International Combustion Symposium, p 685
28. Mader CL, Kershner JD (1985) The three-dimensional hydrodynamic hot-spot model. In: 8th International Detonation Symposium, p 42
29. Baer MR, Kipp ME, van Swol F (1999) Micromechanical modeling of heterogeneous energetic materials. In: International detonation symposium, p 788
30. Barua A, Zhou M (2011) A Lagrangian framework for analyzing microstructural level response of polymer-bonded explosives. Model Simul Mater Sci Eng 19:055001
31. Barua A, Horie Y, Zhou M (2012) Energy localization in HMX-estane polymer-bonded explosives during impact loading. J Appl Phys 111(5):054902
32. Panchadhara R, Gonthier KA (2011) Mesoscale analysis of volumetric and surface dissipation in granular explosive induced by uniaxial deformation waves. Shock Waves 21:43
33. Barua A, Kim S, Horie Y, Zhou M (2013) Ignition criteria for heterogeneous energetic materials based on hotspot size-temperature threshold. J Appl Phys 113:064906
34. Kim S, Barua A, Horie Y, Zhou M (2014) Ignition probability of polymer-bonded explosives accounting for multiple sources of material stochasticity. J Appl Phys 115(17):174902
35. Reaugh JE (2002) Grain-scale dynamics in explosives. Technical Report UCRL-ID-150388-2002, Lawrence Livermore National Laboratory
36. Lee EL, Tarver CM (1980) Phenomenological model of shock initiation in heterogeneous explosives. Phys Fluids 23(12):2362–2372
37. Henson BF, Asay BW, Smilowitz LB, Dickson PM (2001) Ignition chemistry in HMX from thermal explosion to detonation. Technical report LA-UR-01-3499, Los Alamos National Laboratory
38. Springer HK, Vandersall KS, Tarver CM, Souers PC (2015) Investigating shock initiation and detonation in powder HMX with reactive mesoscale simulations. In: 15th International detonation symposium
39. Ryan AA, Nathan RB, John ER, Laurence EF (2015) Direct numerical simulation of shear localization and decomposition reactions in shock-loaded HMX crystal. J Appl Phys 117 (18):185902
40. Moore JD, Barnes BC, Izvekov S, Lisal M, Sellers MS, Taylor DE (2016) A coarse-grain force field for RDX: density dependent and energy conserving. J Chem Phys 144(10):104501
41. Tzu-Ray S, Aidan PT (2014) Shock-induced hotspot formation and chemical reaction initiation in PETN containing a spherical void. J Phys: Conf Ser 500:172009
42. Cady HH, Larson AC, Cromer DT (1963) The crystal structure of alpha-HMX and a refinement of the structure of beta-HMX. Acta Cryst 16:617–623
43. Chang SC, Henry PB (1970) A study of the crystal structure of-cyclotetramethylene tetranitramine by neutron diffraction. Acta Cryst. B., 26(9):1235–1240, 1970

44. Elizabeth AG, Joseph MZ, Alan KB (2009) Pressure-dependent decomposition kinetics of the energetic material HMX up to 3.6 GPa. J Phys Chem A 113(48):13548–13555
45. Choong-Shik Y, Hyunchae C (1999) Equation of state, phase transition, decomposition of β-HMX (octahydro-1, 3, 5, 7-tetranitro-1, 3, 5, 7-tetrazocine) at high pressures. J Chem Phys 111(22):10229–10235
46. Ralph M, Thomas DS (2002) Constituent properties of HMX needed for mesoscale simulations. Combust Theor Model 6(1):103–125
47. Sheen DB, Sherwood JN, Gallagher HG, Littlejohn AH, Pearson A (1993) An investigation of mechanically induced lattice defects in energetic materials. Technical report, Final Report to the US Office of Naval Research
48. Dick JJ, Hooks DE, Menikoff R, Martinez AR (2004) Elastic-plastic wave profiles in cyclotetramethylene tetranitramine crystals. J Appl Phys 96(1):374–379
49. Thomas DS, Ralph M, Dmitry B, Grant DS (2003) A molecular dynamics simulation study of elastic properties of HMX. J Chem Phys 119(14):7417–7426
50. Marsh SP (1980) LASL Shock Hugoniot data. University of California Press, Berkeley, CA
51. Zaug JM, Armstrong MR, Crowhurst JC, Ferranti L, Swan R, Gross R, Teslich Jr NE, Wall MA, Austin RA, Fried LE (2014) Ultrafast dynamic response of single crystal PETN and beta-HMX. In: 15th international detonation symposium
52. Laurence EF, Howard WH (1998) An accurate equation of state for the exponential-6 fluid applied to dense supercritical nitrogen. J Chem Phys 109(17):7338–7348
53. Dmitry B, Grant DS, Thomas DS (2000) Temperature-dependent shear viscosity coefficient of octahydro-1, 3, 5, 7-tetranitro-1, 3, 5, 7-tetrazocine (HMX): a molecular dynamics simulation study. J Chem Phys 112(16):7203–7208
54. Baytos JF (1979) Specific heat and thermal conductivity of explosives, mixtures, and plastic-bonded explosives determined experimentally. Technical report LA-8034-MS, Los Alamos Scientific Laboratory
55. Long Y, Liu YG, Nie FD, Chen J (2012) A method to calculate the thermal conductivity of HMX under high pressure. Philos Mag 92(8):1023–1045
56. John Z, Rogers RN (1962) Thermal initiation of explosives. J Phys Chem 66(12):2646–2653
57. Rogers RN (1972) Differential scanning calorimetric determination of kinetics constants of systems that melt with decomposition. Thermochim Acta 3(6):437–447
58. McGuire RR, Tarver CM (1981) Chemical-decomposition models for the thermal explosion of confined HMX, TATB, RDX, and TNT explosives. In Proceedings of the 7th international detonation symposium, pp 56–64
59. Craig MT, Tri DT (2004) Thermal decomposition models for HMX-based plastic bonded explosives. Combust Flame 137(1):50–62
60. Jack JY, Matthew AM, Jon LM, Albert LN, Craig MT (2006) Simulating thermal explosion of octahydrotetranitrotetrazine-based explosives: model comparison with experiment. J Appl Phys 100(7):073515
61. Aaron PW, William MH, Alan KB, Albert LN III (2008) An LX-10 kinetic model calibrated using simulations of multiple small-scale thermal safety tests. J Phys Chem A 112(38):9005–9011
62. Albert LN (2007) ALE-3D user's manual
63. Coffey CS, Sharma J (2001) Lattice softening and failure in severely deformed molecular crystals. J Appl Phys 89(9):4797–4802
64. Sharma J, Armstrong RW, Elban WL, Coffey CS, Sandusky HW (2001) Nanofractography of shocked RDX explosive crystals with atomic force microscopy. Appl Phys Lett 78(4):457–459
65. Jamarillo E, Sewell TD, Strachan A (2007) Atomic-level view of inelastic deformation in a shock loaded molecular crystal. Phys Rev B 76:064112
66. Cawkwell MJ, Thomas DS, Lianqing Z, Donald LT (2008) Shock-induced shear bands in an energetic molecular crystal: application of shock-front absorbing boundary conditions to molecular dynamics simulations. Phys Rev B 78(1):014107
67. Minnich AJ (2015) Advances in the measurement and computation of thermal phonon transport properties. J Phys: Condens Matter 27(5):053202

68. Harry KS, Elizabeth AG, John ER, James K, Jon LM, Mark LE, William TB, John PB, Jennifer LJ, Tracy JV (2012) Mesoscale modeling of deflagration-induced deconsolidation in polymer-bonded explosives. In Proceedings of the APS topical group on shock compression of condensed matter, vol 1426, p 705

69. Rae PJ, Hooks DE, Liu C (2006) The stress versus strain response of single β-HMX crystals in quasi-static compression. In Proceeding of the 13th international detonation symposium, p 293–300

70. Kang J, Butler PB, Baer MR (1992) A thermomechanical analysis of hot spot formation in condensed-phase, energetic materials. Combust Flame 89:117

71. Massoni J, Saurel R, Baudin G, Demol G (1999) A mechanistic model for shock initiation of solid explosives. Phys Fl 11:710

72. Nichols III AL, Tarver CM (2003) A statistical hot spot reactive flow model for shock initiation and detonation of solid high explosives. 12th Int Det Symp 489

73. Nichols AL III (2006) Statistical hot spot model for explosive detonation. AIP Conf Proc 845:465

74. Willey TM, Lauderbach L, Gagliardi F, van Buuren T, Glascoe EA, Tringe JW, Lee JR, Springer HK, Ilavsky J (2015) Mesoscale evolution of voids and microstructural changes in HMX-based explosives during heating through β–δ phase transition. *J. Appl. Phys.*, 118:055901, 2015

75. Reproduced with permission from Austin RA, Barton NR, Reaugh JE, Fried LE J Appl Phys 117:185902. Copyright 2015, AIP Publishing LLC

Computational Modeling for Fate, Transport and Evolution of Energetic Metal Nanoparticles Grown via Aerosol Route

Dibyendu Mukherjee and Seyyed Ali Davari

Abstract Energetic nanomaterials have gained prominence in the development of solid-state propellants, explosives and pyrotechnics. Such interests stem from kinetically controlled ignition processes in nanoscale regimes resulting from larger specific surface areas, metastable structures and small diffusion length scales at fuel-oxidizer interfaces. To this end, numerous works have investigated the energetic properties of a large class of metal nanoparticles (NPs) that include Al, Si and Ti. Gas-phase synthesis of metal NPs involve rapid cooling of supersaturated metal vapor (monomers) that initiates free-energy-driven collisional process including condensation/evaporation, and finally, leads to nucleation and the birth of a stable critical cluster. This critical cluster subsequently grows via competing coagulation/coalescence processes while undergoing interfacial reactions including surface oxidation. A fundamental understanding of the thermodynamics and kinetics of these processes can enable precise controlling of the synthesis process parameters to tailor their sizes, morphology, composition and structure, which, in turn, tune their surface oxidation and, energetic properties. The complexity and extremely diverse time scales make experimental studies of these processes highly challenging. Thus, hi-fidelity computational tools and modeling techniques prove to be powerful for detailed mechanistic studies of these processes in an efficient and robust manner. The current chapter focuses on computational studies of fate, transport and evolution of metal NPs grown via aerosol routes. The chapter starts with the discussion on gas-phase homogeneous nucleation, and nucleation rates of critical clusters, followed by kinetic Monte-Carlo (KMC) based studies on non-isothermal coagulation/coalescence processes leading finally to the mass transport phenomena involving oxidation of fractal-like NPs.

Keywords Energetic nanomaterials · Metal nanoparticles · Kinetic Monte-Carlo simulation · Coagulation · Non-isothermal coalescence · Surface oxidation

D. Mukherjee (✉) · S.A. Davari
Nano-BioMaterials Laboratory for Energy, Energetics & Environment (nbml-E3),
Department of Mechanical, Aerospace & Biomedical Engineering,
University of Tennessee, Knoxville, USA
e-mail: dmukherj@utk.edu

1   Introduction

1.1   Energetic Nanomaterials: A Broad Overview

The last few decades have seen a large volume of research work focus on a class of novel materials that demonstrate enhanced energetic property and reactivity thereby finding application in the development of propellants, explosives and pyrotechnics. To this end, past studies involving various forms of aluminized solid propellants prepared with different mixtures of aluminum powders and oxidizers as heterogeneous, composite solid propellants have indicated high burning rates and enhanced ignition [1–5]. The conventional wisdom in such mixtures calls for the stoichiometric mixing of the fuel and oxidizer to maximize their energy density. But, the overall kinetics of the process demands an atomistic mixture of the two components to minimize the fuel-oxidizer diffusion length during the reaction. Thus, for larger particle grain size, and hence lower interfacial area between the oxidizer and fuel, the overall reaction speed reflects mass-transfer limitations. On the other hand, a substantially larger surface area arising from fuel-oxidizer interfaces in nanoscale regime promote kinetically controlled ignition processes. This drive towards enhanced ignition kinetics has motivated extensive research on the development of nanosized oxidizer and fuel material that offer the potential (high surface area) for applications demanding rapid energy release. In this regard, increased research effort has been invested towards the use of nano-aluminum in explosives [5–8]. There has been notable work [9] analyzing the unique combustion properties of various energetic composite materials at nano-scale as compared to their properties at micro-scale. The application of various nano-powders and nano-composites of explosive materials like ammonium nitrite, cyclotrimethylene trinitramine (RDX), and aluminum in studying heterogeneous combustion characteristics [10] have also been carried out. In light of the aforementioned research drive towards novel energetic nanomaterials, rational design and synthesis of metal (fuel) nanoparticles with tailored size, morphology and compositions play a pivotal role in tuning the reactivity of these classes of nanomaterials with high accuracy. Nanomaterials are known to exhibit unique physico-chemical properties as compared to their bulk counterparts in different applications. The high specific surface areas of nanomaterials endow them with significantly enhanced surface reactivity as compared to their bulk counterparts. Atomic forces being effective approximately up to 5 interatomic distances, interfacial atoms with unsaturated bonds up to ~ 1 nm in depth are highly reactive [11]. Moreover, usually the structures at these length scales are unbalanced and metastable due to their fast formation during manufacturing processes. Thus, while existing in their metastable state for long times under normal conditions, any perturbations sufficient enough for structural changes may result in the release of excess energy in the form of heat in an effort to relax to stable structural arrangements. Additionally, the diffusion length being exceedingly small in the nano-scale regime, the reaction rates are further increased by many orders of magnitude as compared to those the bulk state. These features have encouraged

researchers to investigate the enhanced energetic properties of a large class of metal nanoparticles. Traditionally, Aluminum (Al) with its large enthalpy of combustion ($\sim$1675 kJ/mol for bulk Al) has always been considered in the class of solid-state propellants and explosives [12]. But, considering that the enthalpy of combustion of an isolated Al atom is $\sim$2324 kJ/mol and the aforementioned interfacial energetic properties at nano-scale, nano-Al has been the center of attention in energetic nanomaterials. However, other fuels such as Si and Ti have also been studied by many researchers [13–15]. Thinner passivation layer, high flame temperature, and easy surface functionalizing are the advantages of Si. Numerous research works have also focused on elemental and structural variations of nanopowders to produce metastable intermolecular composites (MICs) [16–18]. Typically, MICs are constructed from nanosized reagents comprising fuels and oxidizers ideally mixed at atomic scale to reduce the diffusion paths between the two. While MICs stay stable under normal conditions, they are capable of interacting with each other under applied stimulations to release significant amount of energy [19]. Metal-metal oxide systems such as Al/Fe_2O_3, Al/Mo_3, Mg/CuO, etc. are examples of MICs. But, MICs are not limited to metal-oxide systems, since metal-metal systems such as Al/Ni, Al/Ti, B/Ti, etc. have also been studied rigorously. Moreover, studies have also investigated the role of different structures, and morphologies such as core shell [20], nanowires [21], nanoporous particles [22, 23], and multilayered nanofoils [24, 25] in the performance of MICs. To this end, manufacturing processes dictate much of the physical and chemical properties of nanoparticles and nanopowders such as shape, size distributions, elemental ratios, compositions, etc. Depending on the class (structure, composition) of nanomaterials that are required to be designed, different solution-phase and gas-phase synthesis techniques have been developed for the manufacturing of nanoparticles, and nanopowders. In relation to energetic metal NPs, one of the first methods proposed for production of nano-Al was based on the condensation of metal vapors generated by explosion of electrically induced wire [26]. This method is still widely used in the research community and nanopowders of many other elements have been produced by this technique [27, 28]. The mean particle sizes of the Al nanoparticles produced by this technique were in the 30–45 nm [29]. The other routes for the synthesis of energetic nanoparticles involve the chemical techniques. Sol-gel approach has been employed by researchers at Lawrence Livermore National Lab for the synthesis Al/Fe_2O_3 for the first time [30]. The process starts with polymerization of a solution containing precursors. The result is a dense three-dimensional cross-linked network. The energetic materials can be introduced during solution preparation or the gel stage of the process. Due to porous structure, the intimacy of the fuel-oxidizer components is significantly high. Specifically, lab-scale and industrial synthesis of metal nanoparticles typically employ rapid condensation of supersaturated metal vapor (monomer) that are generated from thermal evaporation of the bulk metal, electric arc discharge, laser ablation, flame reactors, plasma reactors, etc. During these gas-phase synthesis processes, rapid cooling ($\sim 10^3$–10^5 K/s) of the metal vapor initiates the saturated vapor to undergo the free-energy driven collisional process including condensation and evaporation, that finally leads to nucleation and the

birth of a stable cluster. This critical cluster subsequently grows via coagulation/coalescence and undergoes various interfacial reactions including surface oxidation. The thermodynamics and kinetics of each of the aforementioned events during the vapor-phase production of nanoparticles play significant role in tailoring their sizes, morphology, composition and structure, which, in turn, tune their extent of surface oxidation and hence, drive their energetic properties. The complexity of these processes combined with the extremely diverse time scales for the corresponding events during the vapor-phase evolution of nanoparticles makes it extremely challenging for a unified experimental study to capture the entire sequence of the fate, transport and growth of metal nanoparticles. To this end, the advent of hi-fidelity computational tools and modeling techniques provides a powerful advantage for the detailed mechanistic studies of these complex processes in an efficient and robust manner.

1.2 Modeling Work to Study Fate, Transport and Growth of Metal Nanoparticles

Numerous modeling studies have been developed over the years to investigate the vapor-phase synthesis of metal NPs. Generally speaking, these methods, and techniques can be broadly categorized into two different approaches. The first one involves the phenomenological models that approaches the problem based on macroscopic thermodynamic functions and solves the Smoluchowsky population balance equation by binning particle size domains into discrete sections and/or nodes to obtain size distributions in time, and space. In this direction, various sectional methods have been developed such as hybrid grid size [31], discrete-sectional [32, 33], and nodal methods [34]. Girshick et al. [35] studied the synthesis of Iron NPs in a plasma flame reactor using discrete-sectional method. Panda et al. [36] had developed very preliminary models for Al NP synthesis in aerosol flow reactors to show that low pressure, and temperature, and high cooling rate facilitate the formation of ultrafine NPs. Prakash et al. [37] developed a simple nodal model involving nucleation, surface growth, evaporation, and coagulation for synthesis of aluminum NPs. Mukherjee et al. [38] implemented a discrete-nodal model to account for size dependent surface tension in Al NPs. These methods are powerful, and robust to obtain the size distribution with low computation cost. However, they fail to capture the microscopic picture behind the chemical physics of the processes. Moreover, in general they suffer from significant numerical diffusion, which brings in numerical artifacts in the concentrations and particle size distribution data.

The second approach involves molecular level models, wherein Molecular Dynamics (MD) and Monte Carlo (MC) simulations are used to estimate the structural and free energy variations as well as the source terms resulting from nucleation process from the first principles. In classical MD, an initial position and

momentum is assigned for each atom/molecule, and then Newton's law is applied to molecules. An intermolecular potential is allocated to the system, and trajectories of molecules are traced in order to identify phase transition and nucleation rate. Zachariah et al. [39] used a MD simulation to validate their sintering model, and showed coalescence time is size dependent for solid particles. Yasuoka et al. [40] calculated the nucleation rate for Ar and showed that surface excess energy and entropy takes bulk value for clusters above 50. Lummen et al. [41] investigated homogenous nucleation of Platinum nanoparticles from vapor phase and extracted the nucleation rate and properties of critical cluster. While MD is a powerful technique for molecular scale simulation, it is limited to small time scale simulations. The typical time step required for a MD simulation is in the order of ~ 1 fs. Therefore, in order to accomplish a 1 s simulation, 10^{14} time steps are required, which is computationally expensive and beyond the typical machines capacity. Monte Carlo is a stochastic technique in which a random configuration is identified at each step, and system decides to accept or reject the configuration randomly. The fate of the system is determined through the random jumps in configurations. The simulation can be carried out to obtain the system free energy [42], structure of nanoparticles [43], evolution of size distribution [44] etc. Gillespie [45] developed a stochastic model for growth process and coalescence. Liffmann [46] developed a model for coagulation of particles to solve the Smoluchowski equation, and introduced a topping up method to account for particle loss during the simulation. Kruis et al. [47] developed a MC model for nucleation, surface growth, and coagulation and compared their results with analytical solutions. Mukherjee et al. [44] considered the effect of coalescence heat release during particles collision and formation for Silicon and Titania nanoparticles. Efendiev et al. [48] applied a hybrid MC simulation to the growth of SiO_2/Fe_2O_3 binary aerosol. Mukherjee et al. [49] developed a collision-coalescence model to study the effect of fractal morphology on surface oxidation of Aluminum (Al) nanoparticles.

In this chapter, we mainly focus on the KMC-based models to investigate the growth and evolution of metal nanoparticles synthesized as energetic nanomaterials via aerosol routes. The following sections in this chapter would develop into the various MC-based models that we have developed in capturing the detailed chemical-physics behind the formation of these particles that include processes such as nucleation, surface growth, coagulation, coalescence, and finally, their effects in driving the surface oxidation of metal nanoparticles. We consider each of the processes separately, starting with the earliest stage of nucleation, and tracing them up to coagulation/coalescence and finally, surface oxidation (see Fig. 1). The goal here is to provide a mechanistic study of each of these processes that can lead to a fundamental understanding on the role of these processes in tailoring the sizes, morphologies and extents of oxidation and hence, driving the energetic behavior of passivated metal or spent metal-oxide nanoparticles as shown by the schematics in Fig. 1.
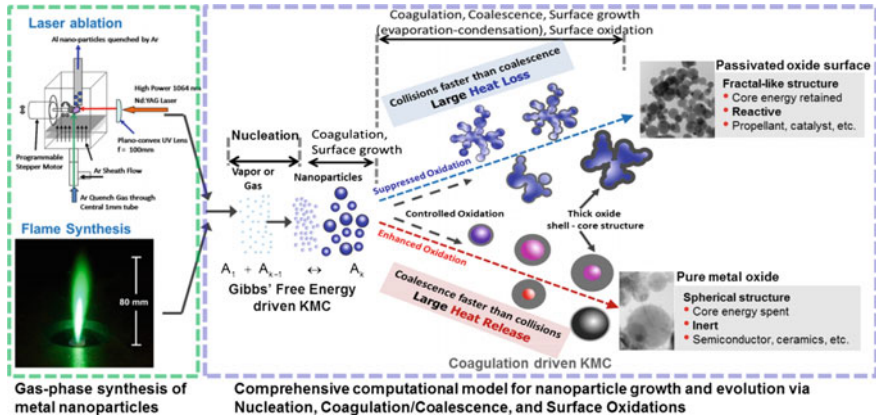
Fig. 1 Schematic representation of computational models studying the fate of metal nanoparticles grown and evolved from gas-phase synthesis via nucleation, coagulation/coalescence, and surface oxidation

2   Homogeneous Gas-Phase Nucleation of Metal Nanoparticles

Generally, nucleation can be realized as a first-order phase transition that marks the birth of a thermodynamically stable condensed phase in the form of a critical nucleus and is the precursor to the crystallization process, followed by subsequent growth of the critical cluster via coagulation and condensation/evaporation processes. In formation of particles, nucleation is the first physical process that occurs during system evolution. Based on existence of a foreign material, nucleation can be subcategorized into homogeneous, and heterogeneous nucleation. Atoms and molecules need nucleation sites in order to condense on the sites and create a new phase. The nucleation sites can be provided by the nucleating atoms, and molecules (self-nucleation) or by another material or surface. Homogeneous nucleation is defined as nucleation of specific phase of a material (vapor e.g.) on an embryos comprised of that material, while foreign materials do not play any role in terms of providing nucleation site in the process. On the other hand, heterogeneous nucleation is the nucleation of specific phase of a material (vapor e.g.) on an embryos comprised of another material. Homogeneous nucleation is a kinetically disfavored process that involves surmounting a nucleation barrier during the vapor-phase cooling of monomers leading to supersaturation where in clusters grow via collisions and/or condensation of monomers, or decompose into smaller clusters and monomers via evaporation. The aforementioned processes continue till the critical nucleus is formed as the new phase that resides on top of the nucleation barrier and undergoes barrier-less spontaneous growth under any perturbation. The presence of a free energy barrier in a first-order phase transition process makes nucleation a rare event whose exceedingly small length and time scales pose an insurmountable

challenge for designing experiments that can accurately monitor and/or control the in situ NP formation [50–52]. Homogeneous nucleation can occur in presence of supersaturated vapor phase. The extent of supersaturation of a material in a carrier gas at temperature T is determined by saturation ratio, which is defined as:

$$S = \frac{n_1}{n_s(T)} = \frac{p_1}{p_s(T)} \tag{1}$$

in which n_1, and p_1 are monomer concentration, and pressure respectively, and n_s, p_s are saturation monomer concentration, and pressure at temperature T. $S < 1$ indicates a relaxed system, $S = 1$ a saturated system (equilibrium), and $S > 1$ indicates a supersaturated system (tense). Sudden cooling down is a very common method for creating a supersaturated system during gas-phase synthesis of nanoparticles via aerosol routes. A sharp temperature gradient $\sim 10^3$–10^6 K/s is required for transition to supersaturation by sudden cooling. These types of temperature gradients can be provided by plasma ablation, thermal evaporation, and flame synthesis with precursors and subsequent cooling in a reactor cell for particle generation. The formation of particles occurs in two stages, the first being nucleation and the emergence of critical nucleus (or, critical cluster), and the second is the growth of the critical nucleus. During nucleation process the change in enthalpy is negative ($\Delta H < 0$), which is thermodynamically favorable. However, the change in entropy is negative as well ($\Delta S < 0$), thereby causing a competition between the two thermodynamic quantities. Usually there is an energy barrier in the first stage to be surmounted before the critical nucleus is formed. Figure 2 shows the typical Gibbs' free energy barrier as a function of cluster sizes that is encountered during the nucleation process. The Gibbs' free energy of formation increases up to a critical cluster size corresponding to the critical nucleus or cluster beyond which the formation energy decreases with size. The height of the free energy at the critical cluster size is called nucleation barrier that dictates the driving force behind nucleation and particle formation. The change in the free energy during a formation reaction is positive for clusters smaller than critical cluster (unfavorable), and after the critical cluster size, the change is negative (favorable). The process starts with monomer collisions. These collisions lead to small cluster formations that can, in turn, collide with each other or other monomers (condensation) to grow into larger clusters, and dissociate due to evaporation into smaller clusters. The cluster growth, and dissociation continue until a sufficiently large cluster size emerges and passes the nucleation barrier. The rate at which clusters pass the nucleation barrier is called nucleation rate. Beyond this critical stage, the free energy change for cluster formations being favorable, clusters that pass the barrier grow spontaneously resulting in rapid surface growth. The driving force at this stage is the difference between monomer concentration (n_1) and saturation monomer concentration over a particle ($n_{s,i}$) that is determined by the Kelvin relation:

Fig. 2 Typical Gibbs free
energy of formation, and
nucleation barrier.
Condensation and
evaporation occur on *left side*
of the barrier until the
nucleation onset at the top of
the barrier, followed by
spontaneous surface growth
and coagulation
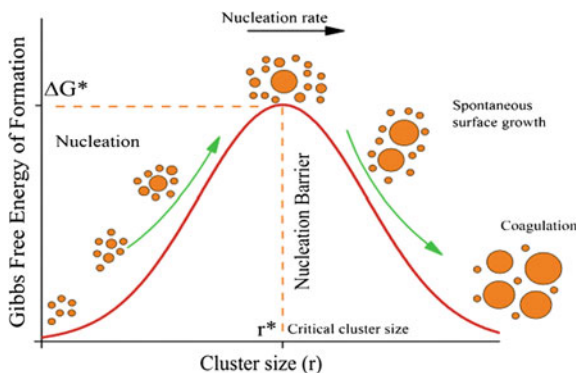
$$n_{s,i} = n_s \exp\left(\frac{4\sigma v_1}{d_i k_B T}\right) \tag{2}$$

in this equation n_s is saturation monomer concentration, σ surface tension, v_1
monomer volume, d_i diameter of the particle, T temperature, and k_B the Boltzmann
constant. The monomer concentration greater than saturated monomer concentra-
tion over the particle ($n_1 > n_{s,i}$) drives condensation on the particle whereas the
reverse ($n_{s,i} > n_1$) drives evaporation from the particle causing them to shrink via
monomer loss. The surface growth continues until the equilibration of monomer
concentration and saturated monomer concentration over particles ($n_{s,i} = n_1$)
wherein coagulation and subsequent coalescence becomes the dominant process for
the particle growth and evolution.

However, the presence of a free energy barrier in the aforementioned first-order
phase transition process makes nucleation a rare event whose exceedingly small
length and time scales pose an insurmountable challenge for designing experiments
that can accurately monitor and/or control the in situ NP formation [50–52]. Hence
hi-fidelity simulations that capture the mechanistic, detailed and yet, collective
picture of vapor-phase homogenous nucleation, through systemic modeling of the
chemical physics of the problem, become necessary for predictive synthesis of
tailored metal NPs. Here one needs to note that most homogenous vapor-phase
nucleation studies (specifically, for non-polar liquids and small organic molecules)
[35, 53–57] in the past have resorted to the Classical Nucleation Theory
(CNT) framework due to its ability to provide a robust yet, relatively accurate
investigation into the basic chemical physics of nucleation in a convenient and
elegant fashion. Thus, in the next sub-section we present a brief introduction to the
basic premises of the CNT.

2.1 Classical Nucleation Theory (CNT)

The reaction kinetics for the aforementioned processes can be represented as:

$$M + M \leftrightarrow M_2$$
$$M + M_2 \leftrightarrow M_3$$
$$M + M_3 \leftrightarrow M_4$$
$$\ldots$$
$$M + M_i \leftrightarrow M_{i+1}$$
$$\ldots$$
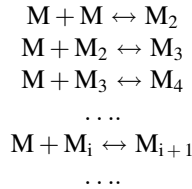
where M_i denotes a cluster containing i number of monomers (called i-mer). It describes a set of coupled reactions. Note that the set of reactions above does not include cluster-cluster collisions. Since the concentration of clusters in compare to monomer is relatively low, this type of collisions can be neglected. In order to investigate the kinetics behind the set of reactions, one needs to know the rate of reaction in forward, and backward direction. In the free molecular regime of kinetic theory, when clusters are smaller than the mean free path of the gas, the rate at which two clusters collide each other can be written as:

$$K_{ij}^F = K^F(V_i, V_j) = \left(\frac{3}{4\pi}\right)^{\frac{1}{6}}\left(\frac{6k_B T_p}{\rho_p}\right)^{\frac{1}{2}}\left(\frac{1}{V_i} + \frac{1}{V_j}\right)^{\frac{1}{2}}\left(V_i^{1/3} + V_j^{1/3}\right)^2 \quad (3)$$

K_{ij}^F collision kernel in free molecular regime, is the number of collisions between two clusters containing i, and j number of monomers per unit of time, k_B Boltzmann constant, ρ_M clusters density, and T_i, and v_i are temperature and volume of each cluster respectively. The backward rate is determined based on the principle of detailed balance (or microscopic reversibility) requiring the transition between two states to occur at the same rate at equilibrium. Thus, for the generalized reaction for the formation of an i-mer:

$$M + M_{i-1} \leftrightarrow M_i$$
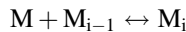
The rate of change of concentration for (i-1)-mer can be written as:

$$\frac{dn_{i-1}}{dt} = -k_{f,i-1}n_1 n_{i-1} + k_{b,i}n_i \quad (4)$$

where $k_{f,i-1}$ and $k_{b,i}$ are the forward and backward reaction rate respectively, and n_i is concentration of i-mer where under the assumption of all successful collisions in the system, $k_{f,i-1} = K_{i-1,1}^F$. Since the process is at the equilibrium:

$$\frac{dn_{i-1}}{dt} = 0 \rightarrow k_{f,i-1}n_1n_{i-1} = k_{b,i}n_i \tag{5}$$

Reaction constant, K_c, is defined as:

$$K_c = \frac{k_{f,i-1}}{k_{b,i}} = \frac{n_i}{n_1n_{i-1}} \tag{6}$$

Also, from thermodynamics, reaction equilibrium constant can be expanded as:

$$K_p = \frac{p_i/p_0}{p_{i-1}/p_0 \; p_1/p_0} = \exp\left(-\frac{\Delta G_{i,i-1}}{k_B T}\right) = K_c n_0 \tag{7}$$

where p_i, and $\Delta G_{i,i-1}$ are partial pressure of i-mer, and Gibbs free energy change for the forward reaction. Subscript "0" refers to the reference pressure, and concentration.

Therefore, the backward rate can be written as:

$$k_{b,i} = k_{f,i-1}n_0 \exp\left(+\frac{\Delta G_{i,i-1}}{k_B T}\right) \tag{8}$$

In order to evaluate the k_b, we need to know the Gibbs free energy change for the forward reaction, $\Delta G_{i,i-1}$.

Considering a particle in equilibrium with its vapor, and realizing that volume per atom in gas phase is greater than the particle phase ($v_{1,v} \gg v_{1,p}$), and assuming the vapor phase behaves as an ideal gas, the difference in chemical potential of particle (μ_p) and gas phase (μ_v) can be related through the Kelvin relation as:

$$\mu_v - \mu_p = \frac{2\sigma v_{1,p}}{r} = k_B T \ln\left(\frac{p(r)}{p_s}\right) = k_B T \ln(S) \tag{9}$$

where r is the radius of the particle, σ is the surface tension in the bulk regime, and p(r) is monomer vapor pressure over the particle. Based on the change in chemical potential at gas, and particle phase, the Gibbs free energy of formation of an i-mer from its vapor can be written as:

$$\Delta G_i = 4\pi\sigma r^2 - ik_B T \ln(S) \tag{10}$$

The first term in (10) represents the change in energy due to phase change. The second term shows the increase in energy due to formation of surface. The Gibbs free energy of formation is a function of size, temperature and saturation ratio of the system. For a specific saturation ratio above 1 (S > 1), the ΔG_i has maxima. Differentiating with respect to size, and equating to zero:

$$r^* = \frac{2\sigma v_{1,p}}{k_B T \ln(S)} \tag{11}$$

For cluster smaller than r* the Gibbs free energy of formation increases with size, and after that it decrease with size. The r* represents the radius of critical cluster. The Gibbs free energy of formation at this size represents the nucleation barrier, and can be written as:

$$\Delta G^* = \frac{16\pi}{3} \frac{v_{1,p}^2 \sigma^3}{(k_B T \ln(S))^2} \tag{12}$$

Analyzing (11) and (12), the critical cluster size, and nucleation barrier are reduced as the saturation ratio increases. Defining the dimensionless surface tension as:

$$\theta \equiv (36\pi)^{1/3} \frac{\sigma v_{1,p}^{2/3}}{k_B T} \tag{13}$$

thus, (10) can be rearranged as:

$$\frac{\Delta G_i}{k_B T} = \theta i^{2/3} - i \ln(S) \tag{14}$$

This equation relates the dimensionless Gibbs free energy of formation to the dimensionless surface tension, saturation ratio, and cluster size. The equilibrium concentration of clusters can be expressed as:

$$n_i^e = n_1 \exp\left(-\frac{\Delta G_i}{k_B T}\right) \tag{15}$$

Using the CNT expression for clusters formation energy, the equilibrium concentration becomes:

$$n_i^e = n_1 \exp\left(-\theta i^{2/3} + i \ln(S)\right) \tag{16}$$

examining (16), we realize by substituting $i = 1$, $n_1^e \neq n_1$, which clearly is incorrect. Moreover, one can observe that ΔG_i when $i = 1$ gives a nonzero value, while it is expected that the Gibbs free energy of formation for monomer be zero. So far, the obtained Gibbs free energy of formation showed inconsistencies in terms of monomer concentration, and formation energy. However, the greatest advantage of classical nucleation theory, namely simplicity, motivated researchers to adjust the Gibbs

free energy of formation to solve the inconsistency problem. Girshick et al. [35] suggested to replace $i^{2/3}$ with $(i^{2/3} - 1)$ to solve inconsistency in monomer concentration and Gibbs free energy of formation. The self-consistent form is written as:

$$\frac{\Delta G_i}{k_B T} = \theta\left(i^{2/3} - 1\right) - (i - 1)\ln(S) \tag{17}$$

Note the equilibrium concentration of clusters decreases with increase of size up to critical cluster. After that increasing the size shows increase in concentration, which physically is incorrect. Thus, the derived equilibrium concentration is valid only up to $i = i^*$.

Now going back to the set of coupled equation, we can write the change in concentration for an i-mer as:

$$M + M_{i-1} \leftrightarrow M_i + M \leftrightarrow M_{i+1}$$
$$\frac{dn_i}{dt} = \left(k_{f,i-1}n_1 n_{i-1} - k_{b,i}n_i\right) - \left(k_{f,i}n_1 n_i - k_{b,i+1}n_{i+1}\right) \tag{18}$$

It has been assumed that the only involved mechanisms that change the concentration of a cluster are condensation and evaporation. Since the concentration of clusters is significantly lower than monomers, collisions between clusters can be neglected. However, at high saturation ratios, where the concentration of clusters is considerable, this assumption becomes questionable. The first term in the RHS represents the ingoing flux to the i-mer, and the second term in the RHS represents outgoing flux from the i-mer. The nucleation current for each cluster, J_i, is defined as:

$$J_i = k_{f,i-1}n_1 n_{i-1} - k_{b,i}n_i \tag{19}$$

Therefore the rate of change in concentration for i-mer can be written in terms of nucleation current as:

$$\frac{dn_i}{dt} = J_i - J_{i+1} \tag{20}$$

It is usual to define a steady state for the all clusters in the system. In the steady state the concentration does not change in time and the income current and outgoing current are equal to steady state nucleation current, J_{ss}:

$$\frac{dn_i}{dt} = 0 \rightarrow J_i = J_{i+1} = J_{ss} \tag{21}$$

J_{ss} is called steady state nucleation rate, which can be derived as:

$$J_{ss} = \frac{n_1^2}{\sum_{i=1}^{i=M} \dfrac{1}{k_{f,i} \exp\left(-\dfrac{\Delta G_i}{k_B T}\right)}} \tag{22}$$

The steady state nucleation rate is related to the monomer concentration and Gibbs free energy of formation of clusters. If the number of terms in the summation is sufficiently large, then the summation can be replaced by integral. After a little mathematical manipulation the steady state nucleation obtained as:

$$J_{ss} = \frac{d_1^2}{6} \sqrt{\frac{2k_B T \theta}{m_1}} \frac{n_1^2}{S} \exp[\theta - \frac{4\theta^3}{27(\ln(S))^2}] \tag{23}$$

where d_1, and m_1 are the diameter and mass of monomer respectively. It can be observed, as the nucleation rate is a steep function of saturation ratio.

2.2 Modeling Nucleation: KMC Based Model and Deviations from CNT

Enormous numbers of studies have been carried out to verify the nucleation rates from classical nucleation theory. Generally speaking, the experimental set-ups for these studies comprise adiabatic expansion chamber [58, 59], upward diffusion chamber [54], laminar flow chamber [60, 61], turbulent mixing chamber [62, 63], etc. The main difference between these methods is how the supersaturated system is generated. Interestingly, the results for comparisons between nucleation rates from classical nucleation theory and experiments range from excellent agreement up to several order of magnitude differences. Wagner et al. [59] used an adiabatic expansion approach and studied nucleation rates of water and 1-propanol, and observed that classical nucleation theory over predicts the nucleation rate for water, while the measured nucleation rates for 1-propanol was considerably higher than what classical nucleation theory predicts (see Fig. 3). The discrepancies between measured nucleation rates and classical nucleation predictions become even more severe in the cases of metal vapors [64, 65]. To this end, Zhang et al. had carried out a comprehensive review on the topic [66].

The discrepancies between theory and experimental studies can be possibly explained in light of the fundamental assumptions made in the classical nucleation theory. It can be observed that the nucleation rate bears an exponential dependence on the Gibbs free energy of formation of clusters. Thus, any error in the Gibbs free energy of formation can change the nucleation rate drastically. To this end, the most significant assumption is introduced when the bulk properties are extended to the
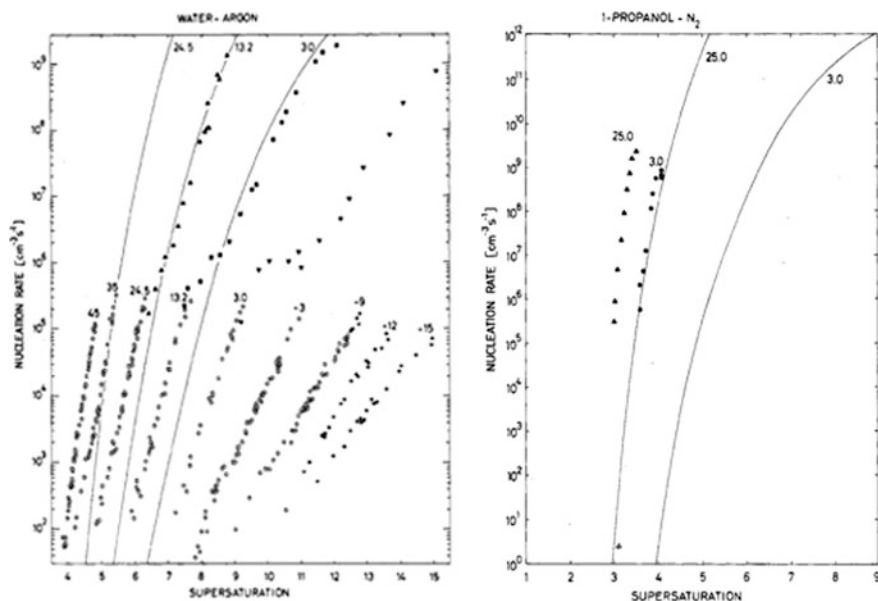
Fig. 3 Nucleation measurement of water and 1-propanol at different initial chamber temperature for different saturation ratio. Curves are predicted values from CNT (Adapted with permission from *J. Phys. Chem., 1981, 85 (18), 2694.* Copyright (1981) American Chemical Society)

smaller cluster sizes. The thermophysical properties of the bulk phase vary significantly from those for the nanophase materials. Previous studies have shown that material properties change as a function of size [67, 68]. Thus, Mukherjee et al. [38] had employed a size-dependent surface tension in their nucleation study that had resulted in the Gibbs free energy of formation for different cluster sizes to indicate multiple peak profiles. In the aforesaid study, the implementation of a size-dependent surface tension (non-capillarity approximation) in a hybrid nodal model had resulted in an earlier onset of nucleation than that predicted from classical nucleation theory (Fig. 4). The other questionable assumption lies in the morphology of the clusters. CNT assumes spherical cluster shapes. However, at the atomistic level, the geometry of a cluster with few atoms is barely spherical and hence, other geometric and electronic arrangements can generate lower energy structure that are more stable. Such structural stability of certain localized cluster sizes can possibly explain the existence of some cluster sizes with relatively higher concentrations as compared to those for their neighboring cluster sizes in experimental observations [69, 70]. In some literatures, these cluster sizes have been referred to as magic numbers. Furthermore, Li et al. [42, 71, 72] had also calculated the Gibbs free energy changes, and association rate constants using MC configuration integral and atomistic (MD) simulations, and showed that the Gibbs free energy of formation for Al clusters is different than what classical nucleation theory predicts (Fig. 5). Specifically, this work had explained the differences in the
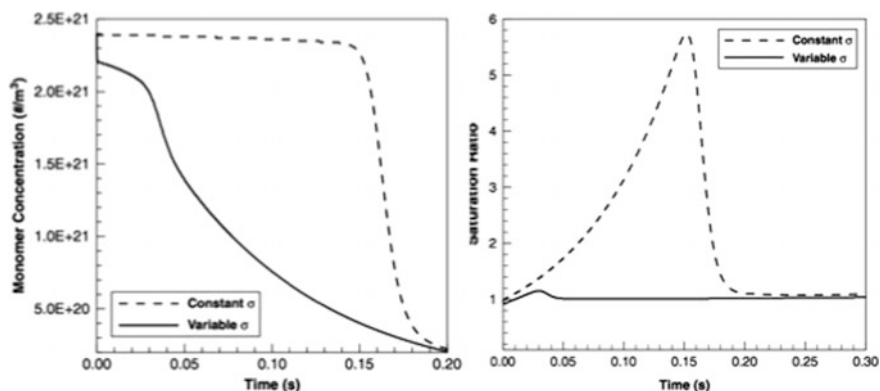
Fig. 4 Difference in onset of nucleation for constant and size-dependent surface tension. Sudden changes in monomer concentration and saturation ratio illustrate the onset of nucleation (Reprinted from *J. Aerosol Sci., 37, 1388 (2006)*. [38] Copyright (2006), with permission from Elsevier)
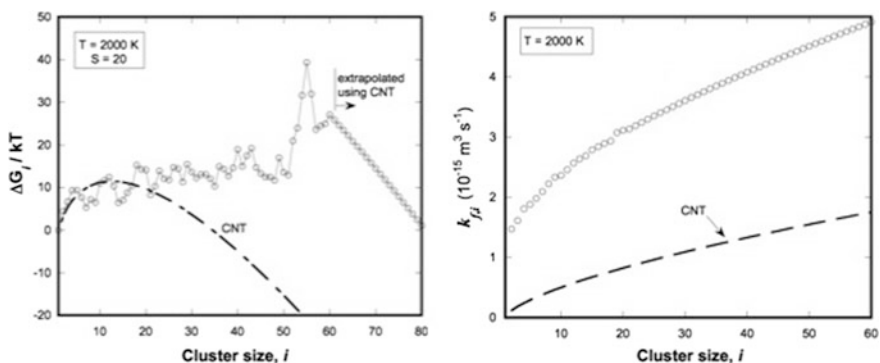
Fig. 5 Comparison between classical nucleation theory, and MC, MD simulations for Gibbs free energy and forward reaction rate of aluminum clusters considering structure of clusters (Reprinted from *J. Chem. Phys. 131, 134,305 (2009)* [72] with the permission of AIP Publishing)

forward reaction rates based on the open-shell structures of Al atoms in the clusters as compared to the conventional spherical assumptions in classical nucleation theory. One of the widely accepted outcomes of CNT-based studies is the derivation of the unified nucleation flux based on the inherent steady-state assumptions of cluster concentration invariance over relatively short period of time during cluster growth. To this end, MD studies by Yasuoka et al. [40] had observed that the steady-state nucleation rates are valid only for clusters above a certain size wherein the nucleation rate was found to be constant and size independent. However, it was noted that the clusters below that size do not reach steady-state and their concentrations change in time. Specifically, cluster concentrations decrease as cluster size increases up to a certain size beyond which the concentrations become

approximately invariant with size. Finally, beyond the aforesaid broad assumptions, CNT also assumes that all clusters and background gases are at the same temperature, thereby assuming the occurrence of an isothermal nucleation event. But, in order for isothermal nucleation to be established the pressure of background gas must be sufficiently high that results in the condensable vapor being dilute as compared to the background gas, thereby allowing the heat of condensation to be rapidly quenched by collisions with the background gas molecules. However, at high saturation ratio this assumption becomes questionable. Wyslouzil et al. [73] had investigated the effect of non-isothermal nucleation on the nucleation rate of water that revealed at low pressure conditions, non-isothermal nucleation rate is significantly lower than the isothermal counterpart and as background gas pressure increases, this difference is reduced. Similar behaviors were also observed by Barrett [74] for the nucleation studies carried out on Argon, *n*-butanol, and water. These results are represented in the nucleation rate plots in Fig. 6 for water (left) and Argon (right) under different background gas pressure conditions.

To address and fundamentally investigate the aforementioned discrepancies in nucleation studies, one requires more realistic models that can facilitate easy elimination of the aforesaid assumptions while capturing the ensemble physics of cluster growth and nucleation. Such robust models can provide deep physical understanding of the mechanistic picture behind nucleation. To this end, one would consider MD simulations as the first choice. However, as mentioned earlier, they are severely restricted by the time steps, and are not practical for analyzing ensemble processes that occur over vastly varying time scale ranges. Thus, stochastic-based KMC models with rate-controlled time steps become the preferred simulation technique that can capture an ensemble, statistically random and rare
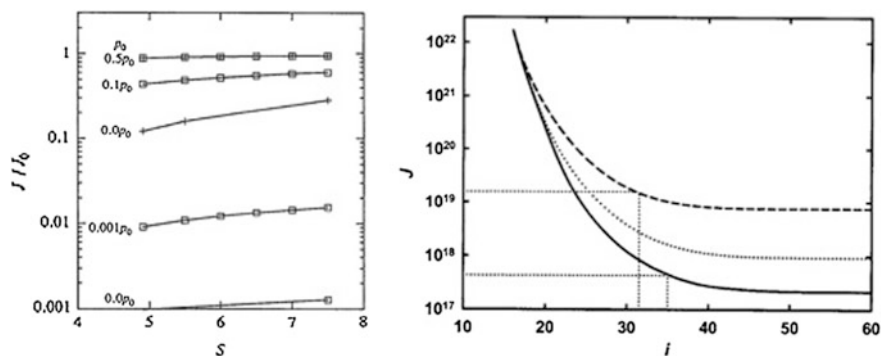
Fig. 6 Comparisons of isothermal, and nonisothermal nucleation rates. *Left* effect of pressure on the nucleation rate and comparison with classical nucleation theory for water as a function of saturation ratio, and background pressure [Reprinted from *J. Chem. Phys. 97, 2661 (1992)* [72] with the permission of AIP Publishing]. *Right* effect of background gas on the nucleation rate of Argon, (*dashed line*) classical nucleation theory, (*solid line*) absence of background gas, and (*dotted line*) low background gas (Reprinted from *J. Chem. Phys. 128, 164519 (2008)* [73] with the permission of AIP Publishing)

event like nucleation. Additionally, the simple yet elegant algorithm of MC models allows for easy implementation of additional physics without a priori assumptions been made.

As mentioned earlier, KMC models can provide realistic simulations to capture physico-chemical phenomena in a kinetically driven time step. They can solve multi-scale and multi-time systems without requiring any governing equation. Generally, the KMC models can be divided into two broad categories, constant-number, and constant-volume. The constant-number models keep the number of particles in the simulation box constant, and whenever a successful event is identified which changes the number of particles (e.g. coagulation, evaporation), the system needs to either add or remove a particle from the simulation. The other category is constant-volume methods. Usually, these methods can be divided into "time-driven" [75, 76], and "event-driven" [47, 77, 78] models. In the time-driven technique the time step is determined before the simulation, and based on the time step, system decides how many events, and which events become successful events. In the "event-driven" technique, first an event is identified, then an appropriate time step based on the rate of the identified event is calculated. The probability of the event should be related to the rate of event.

At each time step two clusters are chosen for the growth process. In the system of reactions (R1) the forward rate of reaction is based on the collision kernel in the free molecular regime. Therefore, the probability of the event can be written as:

$$p_{i,j} = \frac{k_{i,j}}{\sum_{i,j} k_{i,j}} \tag{24}$$

Summation over all possible kernels can be an expensive computational task. Instead, Matsoukas et al. [78] showed that the summation over all pairs can be replaced by the maximum kernel among particles without sacrificing the accuracy significantly.

$$p_{i,j} = \frac{k_{i,j}}{k_{max}} \tag{25}$$

The time step corresponds to the event then can be calculated based on the total number of particles in the simulation box, the volume of the simulation box, and the rate of events as:

$$\Delta T_f = \frac{V_{comp}}{\sum R_f} = \frac{V_{comp}}{\sum k_{i,j}} = \frac{2V_{comp}}{\langle k_{i,j} \rangle M(M-1)} \tag{26}$$

where, V_{comp} represents the volume of the simulation box, and $\langle k_{i,j} \rangle$ is the mean kernel of the system. The factor of "2" was introduced to prevent double counting of collision pairs. Calculating the mean kernel can be computationally expensive. Studies [44, 79] showed that one can replace the mean kernel by the kernel of the

identified kernel without introducing significant error in the results. The same logic can be implemented for the backward events such as evaporation. Growth and decomposition processes will change the total number of particles in the simulation. It has been shown [46] that the accuracy of MC simulation is proportional to $1/\sqrt{N}$, where N is the total number of particles in the simulation box. Therefore, in order to preserve the accuracy, whenever the total number of particles drops to half of the initial value, the entire simulation box is duplicated [46].

Recently, we have been actively involved with the development of a hi-fidelity KMC model to study the homogeneous nucleation of Al nanoparticles from vapor phase. [80] The model uses the self-consistent expression for the Gibbs free energy of formation as expressed in Eq. 17. To this end, based on the fundamental principles of Metropolis algorithm and detailed balancing, one can model the basic probabilities of condensation and evaporation during the cluster growth processes based on the Gibbs free energy changes during the reactions as:

$$P_c = \begin{cases} e^{-\frac{\Delta G_{i,i-1}}{k_B T}} & \Delta G_{i,i-1} > 0 \\ 1 & \Delta G_{i,i-1} \leq 0 \end{cases} \qquad (27)$$

$$P_e = \begin{cases} 1 & \Delta G_{i,i-1} > 0 \\ e^{-\frac{\Delta G_{i,i-1}}{k_B T}} & \Delta G_{i,i-1} \leq 0 \end{cases} \qquad (28)$$

Our current approach for the simulations involves modeling the cluster-cluster collisions based on the probability given by Eq. 25. On the other hand, Eqs. 27 and 28 aim to drive the process in presence of a nucleation barrier, wherein the probability of condensation is hindered by the change in the Gibbs free energy during condensation, while the probability of evaporation is unity. The rationale behind the model development is that the particles are driven by the free energy profile until they surmount and eventually, pass the nucleation barrier to form the critical cluster sizes. Once the critical clusters pass the barrier, their growth by condensation is favored ($p_c = 1$), while their evaporation is not favored anymore ($p_e < 1$). Preliminary results from our aforesaid KMC simulations indicate the nucleation rates to deviate from the steady-state values CNT prediction. [80] Specifically, smaller clusters (<10-mer size in Fig. 7) indicate higher nucleation rates as compared to larger clusters all the way up to the critical cluster size that finally attain a steady state constant flux at the onset of nucleation (Fig. 7). Such observations were also reported in previous MD simulations on vapor-phase nucleation of a Lennard-Jones fluid [40]. These results indicate that our KMC models can eliminate a priori CNT assumptions, while being not limited to the typical MD time steps. In doing so, one can envision a realistic nucleation model in future that can facilitate the elimination of all built in assumptions of CNT while accounting for other physical effects such as size-dependent properties and the effect of heat of condensation. This is an ongoing
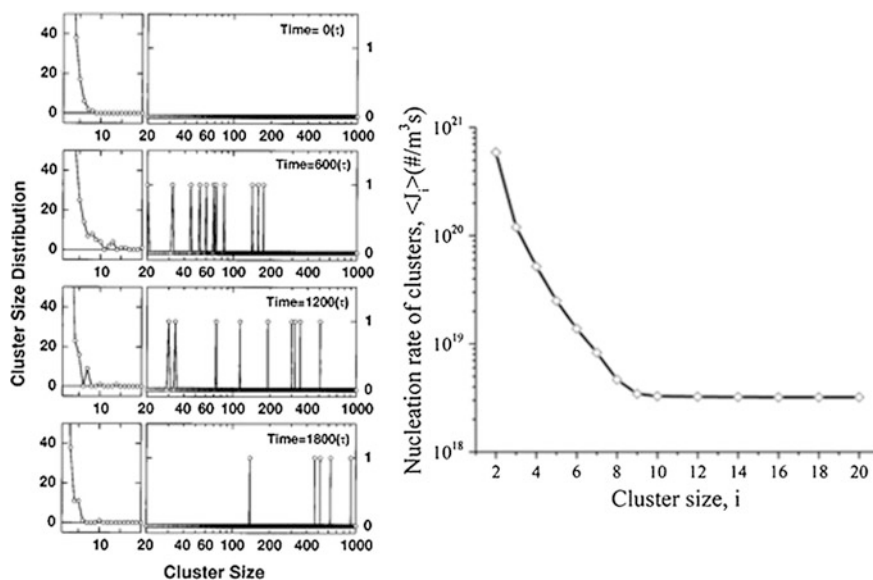
Fig. 7 Cluster distribution and nucleation rate based on: *Left* MD simulations for nucleation of Lennard-Jones fluid, (Reprinted from *J. Chem. Phys. 109, 8451 (1998)* [40] with the permission of AIP Publishing) and *Right* Our KMC simulation of Aluminum nanoparticle formation from vapor phase

research effort with the authors' groups that can eventually lead to fundamental understanding and hence, hitherto elusive comparisons with experimental results for nucleation process of metal nanoparticles.

3 Non-isothermal Coagulation and Coalescence

Coagulation refers to the growth mechanism of nanoparticles via collisional agglomeration that typically ensues following the nucleation of the critical cluster when the particles undergo barrier-less spontaneous growth during gas-phase synthesis. Coagulation is frequently followed by coalescence resulting in structural re-arrangements leading to surface area/energy reductions, and neck formations in the sintered aggregates. Here, "*agglomerates*" refer to an assembly of primary particles (i.e., physically joined together) whose total surface area does not differ appreciable from the sum of specific surface areas of primary particles, whereas "*aggregates*" refer to an assembly of primary particles that have grown together to form necks via sintering/re-arrangements whose total specific surface area is less than the sum of the surface areas of the primary particles. The study of coagulation and coalescence of nano-sized aerosols resulting in aggregate/agglomerate formation and the growth characteristics, morphology and size distributions of primary

particles in the aggregates/agglomerates have been an area of extensive study in both theoretical and experimental works. Coalescence of particles resulting in spherical particles can be of importance in predicting uniformity of particle sizes required for pigment synthesis, chemical vapor deposition, carbon black, etc. On the other hand, clusters of individual primary particles forming agglomerates of higher specific surface area are known to enhance catalytic activity [81] or the rate of energy release in propellants [82]. Indeed many thermal, mechanical and optical properties [83] are determined by the size of primary particles. Thus, the ability to predict and control primary particle sizes of nano-structured materials either in the free-state or stabilized in an aggregate or agglomerate is of paramount importance in the implementation of many of the engineering applications of nanomaterials that envisage a size dependent property, including energetic behavior of metal nanoparticles.

During many gas-phase aerosol processes, a high concentration of very small particles undergoes rapid coagulation. This may lead to the formation of fractal-like agglomerates consisting of a large number of spherical primary particles of approximately uniform diameter [84]. The size of the primary particles ultimately is determined by the relative rates of particle-particle collision and coalescence of a growing aerosol [85]. At very high temperatures, for example, particle coalescence occurs almost instantly on contact resulting in uniform spherical primary particles of relatively small surface area. At low temperatures, the rate of coalescence may be so slow that particles undergo many frequent collisions before the agglomerate can undergo structural re-arrangements, leading to fractal-like agglomerates consisting of very small primary particles, and thus larger surface area. Of particular interest are those intermediate conditions where neither process is rate controlling. Ultimately controlling the coalescence rate is only possible through knowledge of the material properties, and the use of a programmed and well-characterized time-temperature history of the growth environment [86].

Significant past efforts, of both experimental and theoretical nature, have been dedicated towards predicting primary particle sizes for nanoparticles grown from a vapor. These include the study of the sintering kinetics of Titania (TiO_2) nanoparticles in free jets and the use of a simple coalescence-collision time crossover model to determine the shapes of primary particles [87, 88]; TEM observations of TiO_2 primary particle sizes during sintering in heated gas flows [9]; or the analysis of growth characteristics of silica (SiO_2) [89–91] nanoparticles in aerosol reactor cells [92]. Models of nanoparticle coalescence in non-isothermal flames have been developed which employ population balance equations that are variants of the Smoluchowski equation [93]. Sectional models for aggregate aerosol dynamics accounting for gas-phase chemical reaction and sintering have also been developed to determine primary and aggregate particle size distributions under varying reactor temperatures [89].

It needs to be highlighted here that all of the afore-mentioned works on the prediction of primary particle sizes are primarily built on *the underlying assumption that particles were always at the background gas temperatures*. The only closest and earliest experimental work dealing with energy release during condensation of

aerosol clusters possibly carried out by Freund and Bauer [94] in their studies related to the homogeneous nucleation of metal vapors. Here, it will be critical to note that certainly on the experimental side, determination of particle temperature over extremely short time scales, as will be discussed in length in this section, would call for highly determined and involved experimental efforts to probe such effects.

Among some of the seminal works in relatively recent years, Lehtinen and Zachariah had shown [86, 95] that the exothermic nature of the coalescence process could significantly alter the sintering rate of nanoparticles. Moreover, they had demonstrated some unique results indicating that background gas pressures and volume loading of the material could significantly alter the overall temporal energy balance of coalescing particles, and could be used as effective process parameters to tailor primary particle sizes and the onset of aggregation [95]. The motivation for such novel observations stemmed from an earlier molecular dynamics (MD) study by Zachariah and Carrier [34] investigating the coalescence characteristics of silicon nanoparticles. This work had demonstrated a significant increase in nanoparticle temperature while undergoing coalescence. The formations of new chemical bonds between particles in the aftermath of collisions result in large heat release, and neck formations between the particles. This heat release may, under some conditions, result in an increase in particle temperature well above the background gas. Thus, the articles from Lehtinen and Zachariah [86, 95] had particularly reported that the particle coalescence is largely dominated by solid-state diffusion mechanism, which is an extremely sensitive function of temperature. Hence, the increase in particle temperature itself bears important effects on the coalescence dynamics. In fact, it was shown that for Si nanoparticle coalescence, in some cases, such effects could reduce the coalescence time by several orders of magnitude! *However, an important point of observation is that these studies did not consider ensemble aerosol effects, which led to the follow-up article by Mukherjee* et al. [44] *that developed a detailed KMC model to capture the ensemble effects of non-isothermal coagulation and coalescence on the growth dynamics of energetic nanoparticles. This will also constitute the main subject of this chapter*. Here, ensemble effects refer to random collision/coalescence processes between particle/aggregate pairs of any sizes and shapes, where simultaneous coalescence of all agglomerates that have undergone collisions at any instant of time are allowed to take place.

In light of the aforementioned observations, the following sub-sections in this chapter will largely focus on the work by Mukherjee et al. [44] that had developed a Monte Carlo based model in the lines of the earlier works of Efendiev and Zachariah [48] to extend their work on particle coagulation by incorporating non-isothermal finite rate coalescence processes. Through this work we will investigate here the inter-relationships of heat release and coalescence, as already proposed by Lehtinen and Zachariah [86, 95]. In doing so, we will present the details of a kinetic Monte Carlo (KMC) method developed and used by Mukherjee et al. [44] to study the effect of gas temperature, pressure and material volume loading on the heat release phenomenon during the time evolution of a nanoparticle cloud growing by random collision/coalescence processes. The significance of these

background process parameters in predicting the primary particle growth rates will also be discussed and analyzed. Largely, the role of non-isothermal coalescence process in controlling primary particle growth rates and aggregate formation for typical Si nanoparticles are discussed here. But, we will also present some significant highlights of findings from the titania (TiO_2) nanoparticle studies. The choice of these two materials is based on the large body of earlier works that have focused on them primarily due to the industrial importance of these particles, and their energetic behaviors.

3.1 Mathematical Model and Theory

3.1.1 Smoluchowski Equation and Collision Kernel Formulation

The particle size distribution of a poly-disperse aerosol undergoing coagulation can be described by the Smoluchowski equation as:

$$\frac{dN(t,V_j)}{dt} = \frac{1}{2} \int_0^{V_j} K(V_i, V_j - V_i)N(t,V_i)(t,V_j - V_i)dV_i - N(t,V_j) \int_0^\infty K(V_j, V_i)N(t,V_i)dV_i \tag{29}$$

where, t is the time, $K(V_i, V_j) = K_{i,j}$ is the kinetic coagulation kernel for the particles chosen with volume V_i and V_j and $N(t, V_j)$ is the number density of the j-cluster [85].

The appropriate form of the coagulation or collision kernel depends on the Knudsen size regime of the growth. The kernel for the free molecule regime takes the form [85]:

$$K_{ij}^F = K^F(V_i, V_j) = \left(\frac{3}{4\pi}\right)^{\frac{1}{6}} \left(\frac{6k_BT_p}{\rho_p}\right)^{\frac{1}{2}} \left(\frac{1}{V_i} + \frac{1}{V_j}\right)^{\frac{1}{2}} \left(V_i^{1/3} + V_j^{1/3}\right)^2 \tag{30}$$

where, k_B denotes the Boltzmann constant, T_p is the particle temperature considered for collision, ρ_p is the particle density (assumed constant).

For the work presented in this section, one has to bear in mind that in free molecular regime the temperature dependence of collision kernel ($K_{ij}^F \propto T_p^{1/2}$) arises from the mean thermal speed of the nano particles derived from kinetic theory and expressed in the form: $\bar{c}_i = \left(8k_BT_p/\pi_\rho pV_i\right)^{1/2}$. Although the kernel has a weak dependence on the temperature, in this case the particle temperatures can become significantly higher than the background gas temperature. While formulating the

collision kernel, the present model considers its dependence on the particle temperature during the coalescence process. Hence, the above collision kernel takes the form:

$$K_{ij}^F = K^F(V_i, V_j) = \left(\frac{3}{4\pi}\right)^{\frac{1}{6}} \left(\frac{6k_B}{\rho_p}\right)^{\frac{1}{2}} \left(\frac{T_i}{V_i} + \frac{T_j}{V_j}\right)^{\frac{1}{2}} \left(V_i^{1/3} + V_j^{1/3}\right)^2 \qquad (31)$$

where, T_i and T_j are the respective particle temperatures in the system considered for collision.

3.1.2 Energy Equations for Coalescence Process

During coalescence, a neck rapidly forms between the particles, which transforms into a spherule, and slowly approaches a sphere coupled with which is the particle temperature rise due to heat release as demonstrated by Zachariah and Carrier [39] and indicated by the schematic in Fig. 8.

Let us consider the case where, based on the collision probabilities, a typical collision event has successfully occurred between two spherical particles of sizes, V_i and V_j. Then upon coagulation it forms a new particle of volume $V_i + V_j$. It consists of N atoms or units which would essentially undergo the coalescence process and hence, would be used for formulating the typical energy equations and the corresponding heat release associated with modeling the entire process for all such particles. We assume that the energy E of a particle throughout the coalescence process can be described with bulk and surface contribution terms [96]:

$$E = \underbrace{N_W\left[\varepsilon b(0) + c_V T_p\right]}_{E_{bulk}} + \underbrace{\sigma_s a_p}_{E_{surf}} \qquad (32)$$

Fig. 8 Schematic representation of the temporal evolution of particle temperature and shape during nanoparticle coalescence
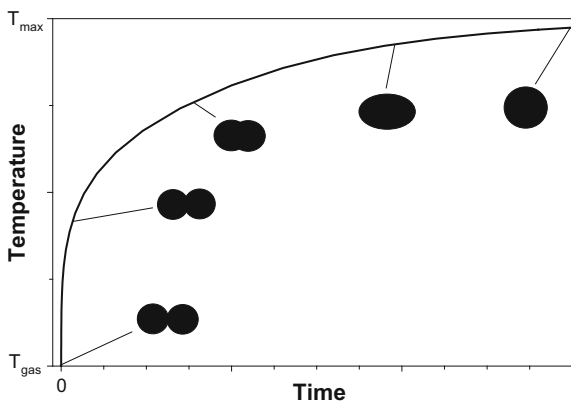
where, a_p is surface area of the coalescing particle pair, σ_s the surface tension, ε_b (0) the bulk binding energy (negative) at zero temperature, c_v the constant volume heat capacity (mass specific, J/kg-K) and N_w is the equivalent mass (kg) of N atoms in the particle pair undergoing coalescence. Under adiabatic conditions considered over a particle pair, the energy E would be constant, while the coalescence event will result in a decrease in the surface area, a_p and therefore an increase in particle temperature.

Any change in total energy, E of the particle (or, aggregate) can only result from energy loss to the surroundings, by convection, conduction to the surrounding gas, radiation, or, evaporation. Thus, for the temporal energy conservation equation for a particle (or, aggregate) we may write:

$$\frac{dE}{dt} = N_w c_v \frac{dT_p}{dt} + \sigma_s \frac{da_p}{dt} = -Z_c m_g c_g \left(T_p - T_g\right) - \varepsilon \sigma_{SB} a_p \left(T_p^4 - T_g^4\right) - \frac{\Delta H_{vap}}{N_{av}} Z_{ev}$$

(33)

where, T_p is the particle temperature, T_g is the gas temperature (K); c_g the mass specific heat capacity and m_g is the mass of gas molecules (kg). The emissivity of particles is ε, σ_{SB} is the Stefan-Boltzmann constant, ΔH_{vap} is the enthalpy of vaporization (J/mole) and N_{av} is the Avogadro number. Z_c is collision rate (s^{-1}) of gas-particle interactions in the free-molecule range and Z_{ev} is evaporation rate of surface atoms based on calculation of heterogeneous condensation rate (s^{-1}) of atoms on the particle surface.

The second term on the left hand side of Eq. 33 is the heat release due to coalescence arising from surface area reduction. The first and second terms on the right hand side of the equation are heat losses due to collisions with gas molecules, and radiation respectively, while the last term represents the heat loss due to evaporation from the particle surface.

The surface area reduction term in Eq. 33 is evaluated with the help of the well-known linear rate law [97] for final stages of coalescence:

$$\frac{da_p}{dt} = -\frac{1}{\tau_f} \left(a_p - a_{sph}\right)$$

(34)

where the driving force for area reduction is the area difference between the area of coalescing particles, a_p and that of an equivalent volume sphere, a_{sph}. Equation 34 has been widely used to model the entire process from spherical particles in contact to complete coalescence, since the overall sintering stage is rate controlled by the initial growth to a spheroid [97].

With the substitution, the non-linear differential equation for particle temperature can be expressed as:

$$N_w c_v \frac{dT_p}{dt} = \frac{\sigma_s}{\tau f}\left(a_p - a_{sph}\right) - Z_c m_g c_g\left(T_p - T_g\right) - \varepsilon\sigma_{SB} a_p\left(T_p^4 - T_g^4\right) - \frac{\Delta H_{vap}}{N_{av}} Z_{ev}$$

(35)

where, τ_f is characteristic coalescence, or fusion time defined as:

$$\tau_f = \frac{3k_B T_p N}{64\pi\sigma_s D_{eff}} \text{ where, } D_{eff} = D_{GB}\left(\frac{\delta}{d_{p\,(small)}}\right)$$

(36)

D_{eff} being the atomic diffusion coefficient that brings in significant non-linearity in the above equation as discussed in details later in this section. The above formulation for D_{eff} is derived based on the earlier works of Wu et al. [98]. D_{GB} is the solid-state grain boundary diffusion coefficient having the Arrhenius form: $D_{GB} = A\exp\left(-B/T_p\right)$, where σ_s is the particle surface tension, δ the grain boundary width (Table 1) and $d_{p(small)}$ is the diameter of the smallest particle in the coalescing cluster undergoing grain boundary diffusion process. The logic assumed here is that the smaller particle in any aggregate would coalesce faster into the larger ones, thereby determining the characteristic coalescence time. The values for pre- exponential factor A and activation energy term B are presented in Table 1.

Z_c, the gas–particle collision rate (s^{-1}) in the free-molecule regime results in conduction heat loss from the particle to the surrounding gas and is obtained from kinetic theory as:

$$Z_c = \frac{p_g a_p}{\sqrt{2\pi m_g k_B T_g}}$$

(37)

where a_p is the area of the coalescing particle pair and hence, varying in time according to the rate law (Eq. 34) and p_g is the background gas pressure.

Z_{ev}, the evaporation rate of surface atoms (s^{-1}) is determined by detailed balancing [99], and evaluated from the kinetic theory based calculation of the heterogeneous condensation rate on particle surface of area at the saturation vapor pressure given as [85]:

$$Z_{ev} = \frac{\alpha_c p_d a_p}{\sqrt{2\pi m k_B T_p}}$$

(38)

where, α_c is the accommodation coefficient assumed to be unity, p_d is the saturation vapor pressure over the droplet (spherical particle) and determined from the Kelvin effect.

Thus, for the evaporative heat loss term:

$$\frac{\Delta H_{vap}}{N_{av}} Z_{ev} = \frac{\Delta H_{vap}}{N_{av}}\left(\frac{\alpha_c a_p p_s}{\sqrt{2\pi m k_B T_p}}\right)\exp\left(\frac{4\sigma_s v_m}{d_p R T_p}\right)$$

(39)

Table 1 Thermodynamic, and diffusional properties for Silicon and Titania[a]

Properties	Silicon	Titania	Reference
Bulk melting point, T_m (K)	1683	2103	[151]
Density, ρ_p (kg/m^3)	2330	3840	[151, 160]
Solid surface tension, σ_s (J/m^2)	0.9	0.6	[88, 151]
Liquid surface tension, σ_l (J/m^2)	–	0.34	[93, 95]
Constant volume heat capacity, c_v(J/kg-K)	729	800	[151]
Heat of vaporization, ΔH_{vap} (J/mole)	384,000	598,712	[151, 157]
Heat of fusion, L (J/mole)	–	47,927	[95]
Diffusion coefficient parameters			
Pre-exponential factor, A (m^2/s)	4.69×10^{-7}	7.2×10^{-6}	[39, 161]
Activation energy, E_{ac} (kJ/mole)	62.84	286	[39, 161]
Normalised activation energy, B = (E_{ao} / 8.31) (K)	7562	34,416	
Saturation vapor pressure relations			
(a) Silicon			[100]
$\log_{10} p_s = a + \dfrac{b}{T_p} + c \log_{10} T_p$ $+ dT_p + eT_p^2$ (p_s in mm of Hg; T_p in K)			
a = 315.0687; $b = -7.1384 \times 10^4$; c = -89.68; d $= 8.3445 \times 10^{-3}$ and e = -2.5806×10^{-9}			
(b) Titania			
$\log_{10} p_s = a + \dfrac{b}{T_p} + cT_p$ (p_s in Pa or, N/m^2; T_p in K)			[157]
a = 16.20; b = -30361 and c = -0.492×10^{-3}			

[a]Reprinted from *J. Chem. Phys.* **119**, 3391 (2003) [44], with the permission of AIP Publishing

where, p_s is the saturation vapor pressure (Pa) over flat surface at the instantaneous particle temperature during coalescence [100] and v_m is the molar volume (m^3/mole). The equations for vapor pressure of Si and TiO$_2$ used in the present work have been given in Table 1. The exponential dependence on particle temperature implies that as the particles heat by coalescence, significant evaporative cooling might take place.

As discussed earlier, the coalescence process reduces the surface area according to the rate law equation given in Eq. 34, which result in surface energy loss. In an adiabatic case all this energy would be partitioned into the internal thermal energy of particles. However, losses to the surroundings will have a significant impact on the particle temperature and therefore its coalescence dynamics. A detailed

description of the coalescence dynamics and energy transfer is obtained by numerically solving the coupled Eqs. (34) and (35).

It is to be noted that Eq. 33 is highly non-linear in temperature through the exponential dependence of the solid-state atomic diffusion coefficient D_{GB} in the particle, which is expressed, as:

$$D_{GB} = A \exp\left(-\frac{B}{T_p}\right)$$ (40)

where, A and B are material dependent constants (Table 1). Thus, in typical solid-state sintering, if particle temperature increases due to heat release effects, then lower gas pressures, higher volume loadings (higher collision frequency) and high gas temperatures may result in particle heat generation being larger than heat loss to the surroundings. This, in turn, increases diffusion coefficient (D_{eff}), reduces characteristic coalescence time, τ_f and hence, further serves to increase the particle temperature.

A further complication that may occur during a coalescence event, is that before the resulting particle can relax back to the background gas temperature, it may encounter yet another collision. This would be the case when the characteristic coalescence time is larger than the collision time ($\tau_f > \tau_{coll}$), thereby generating aggregates. On the other hand, if $\tau_f < \tau_{coll}$, particles have sufficient time to coalescence and no aggregate is formed. Therefore, the formation of the often-observed aggregate structure is determined by the relative rates of collision and coalescence. However, the heat release from coalescence, if not removed efficiently from the particle, will keep the coalescence time small relative to the collision time and delay the onset of aggregate formation. Our goal is to understand the non-linear dynamics leading to the formation of aggregates and its effect in terms of growth characteristics of primary particles that go on to form these aggregates.

3.1.3 Effect of Lowered Melting Point of Nanoparticles on Coalescence

The diffusion mechanism in nano-sized particles might differ from bulk diffusion processes and has been previously studied [39]. Although, the phenomenon is not clearly understood, for most practical purposes of this work, one might assume that classical concepts of volume, grain boundary, and surface diffusion are applicable [98]. Grain boundary diffusion has been pointed out as the most significant solid-state diffusion process in polycrystalline nano-sized particles [39, 98], though the exact processes for atomic diffusion depend on the crystalline structures of particles.

The diffusion coefficient being very sensitive to the phase (molten or solid), care must be taken to track the phase changes during the growth process. Of particular importance, in the size range of interest, is the size dependence of the melting point

of ultrafine particles. The empirical relation approximating the melting point of nano particles is given as [101]:

$$T_{mp}(dp) = T_m \left[1 - \frac{4}{L\rho_p d_p} \left(\sigma_s - \sigma_1 \left(\frac{\rho_p^{2/3}}{\rho_1} \right) \right) \right] \qquad (41)$$

Here, T_m is the bulk melting point, L the latent heat of melting (J/kg), σ_s and σ_l are the surface tensions (J/m^2), and ρ_p and ρ_l are the respective solid and liquid phase densities (kg/m^3). The various material property values are presented in Table 1.

This effect of lowered melting point on particle coalescence process turns out to be of particular significance the case of titania growth studies, since these investigations are typically conducted in the 1600–2000 K range. Application of Eq. 41 would show that for titania that has a bulk melting point of 2103 K, the melting point drops to about 1913 K at 5 nm and 1100 K for a 1 nm particle. In such a scenario, at typical flame temperatures encountered in experiments, particles may coalesce under a viscous flow mechanism as opposed to a solid-state diffusion mechanism. It also implies that particles may encounter a phase transition during a coalescence event simply due to the energy release process, i.e., $T_p(t) > T_{mp}(d_p)$.

To take this into account, the diffusion process and corresponding characteristic coalescence times for the TiO$_2$ cases meed to be computed as follows: (1) when $T_p(t) < T_{mp}(d_p)$, a solid state grain boundary diffusion process was assumed to calculate coalescence time as given by Eq. 40 and (2) when $T_p(t) > T_{mp}(d_p)$, a viscous flow mechanism was used [102] as:

$$\tau_f = \frac{\mu d_{eff}}{2\sigma_l} \qquad (42)$$

where, μ is the viscosity at the particle temperature; σ_l is the liquid surface tension of particle and d_{eff} was taken to be proportional to the instantaneous effective particle diameter (V_p/a_p), i.e., $d_{eff} = 6V_p/a_p$.

The viscosity, μ is estimated from empirical relations [103] as a function of particle temperature T_p, and melting point for the corresponding particle size, $T_{mp}(d_p)$. The empirical relation for size dependent viscosity of nanoparticles is given as:

$$\mu = 10.87 \times 10^{-7} \frac{\left[M.T_{mp}(d_p) \right]^{1/2} \exp\left(\frac{L}{RT_p} \right)}{v_m \exp\left[\frac{L}{RT_{mp(d_p)}} \right]} \qquad (42a)$$

where, L is the latent heat of fusion (J/mole), R is the universal gas constant (J/mole-K), v_m is the molar volume (m^3/mole) and M is the molar weight (kg/mole).

3.1.4 Radiation Heat Loss Term for Nanoparticles: A Discussion

Thermal radiation from small particles is a subject of considerable interest and complexity and has been discussed by a number of earlier works [104–107]. The prime concern for this work is in the emissivity values needed in Eq. 35 to determine the effect of radiation heat loss in typical nanoparticles. However unlike bulk materials, for particles smaller than the wavelength of thermal radiation, the emissivity becomes a strong function of the characteristic dimension of the particle [108]. It is well known from Rayleigh scattering theory that the absorption efficiency: $Q_{abs} \propto X$, where, X is the non-dimensional particle size parameter given as: $X = \pi d_p / \lambda$, λ being the wavelength of emitted radiation considered. For very fine particles and for the wavelength range of 800 nm or greater (for thermal radiation), the values for absorption efficiency (Q_{abs}) are extremely small (around 10^{-5}–10^{-7}).

Now, from Kirchhoff's law for radiation from spherical particles: $Q_{abs} = \varepsilon$ [109]. Hence, we conclude that emissivity for thermal radiations from nanoparticles in the Rayleigh limit ($d_p \ll \lambda$) are negligible unless we operate at extremely high temperatures. Thus, for all practical purposes, the radiation heat loss term for the present study can be assumed to be negligible and dropped from Eq. 35 to give its final form as:

$$N_w c_v \frac{dT_p}{dt} = \frac{\sigma_s}{\tau_f}\left(a_p - a_{sph}\right) - Z_c m_g c_g \left(T_p - T_g\right) - \frac{\Delta H_{vap}}{N_{av}} Z_{ev} \qquad (43)$$

3.2 Modeling Non-isothermal Coagulation and Coalescence: Coagulation Driven KMC Model

Monte Carlo (MC) methods have recently been shown to be a useful tool for simulating coagulation-coalescence phenomena. They have the advantage that both length and time scale phenomena can be simultaneously solved without a single unifying governing multi-variate equation. Furthermore, MC methods provide an intuitive tool in simulating the random coagulation process without any a priori assumption of the aerosol size distribution. To this end, Rosner and Yu [110] have used MC methods to demonstrate the "self-preserving" asymptotic pdf for bivariate populations in free molecular regime. Kruis et al. [47] have used MC methods to establish its suitability for simulating complex particle dynamics. These works have clearly demonstrated the statistical accuracy of MC method by comparing it with the theoretical solutions for aggregation and the asymptotic self-preserving particle-size distribution [85] for coagulation. In a parallel work, Efendiev and Zachariah [48] had also demonstrated the effectiveness of the method, by developing a hybrid MC method for simulating two-component aerosol coagulation and internal phase-segregation. Furthermore, it has been shown rigorously by Norris [111] that the MC approach approximates the aerosol coagulation equation for

number concentration of particles of any given size as a function of time. The kinetic Monte Carlo (KMC) model, presented here from Mukherjee et al. [44], has been primarily based on the earlier works of Liffman [46] Smith and Matsoukas [78] and the recently developed hybrid MC method of Efendiev and Zachariah [48].

Among a vast number of existing MC techniques developed for simulating the growth of dispersed systems, the two primary ones fall under the category of Constant-Number (*Constant-N*) and the Constant-Volume (*Constant-V*) methods. The classical *Constant-V* method samples a constant volume system of particles, and with the advancement of time reduces the number of particles in the sample due to coagulation. This is the same approach as any other time-driven numerical integration and hence it does not offer a uniform statistical accuracy in time. This reduction in the sample usually needs simulation for large number of initial particles to ensure an acceptable level of accuracy in the results. This might lead to an under-utilization of the computational resources [112]. This problem can be over-come by a *Constant-N* method by refilling the empty sites of the particle array in the system, with copies of the surviving particles. This method has been shown to be more efficient, and has been employed by Kostoglou and Konstandopoulos [112], Smith and Matsoukas [78] and Efendiev and Zachariah [48] for simulation of particle coagulation.

To overcome this loss of accuracy due to continuously decreasing particle number arising from coagulation a discrete refilling procedure, as proposed by Liffman [46], was used in which whenever the particle number dropped to a suf-ficiently small value (50% of the initial number) the system was replicated. The *Constant-N* approach can be implemented in two general ways. The first approach is to set a time interval, Δt and then use the MC algorithm to decide which and how many events will be realized in the specified time interval [46, 113]. This essentially amounts to integrating the population balance forward in time and requires dis-cretization of the time step. In the second approach, a single event is chosen to occur and the time is advanced by an appropriate amount to simulate the phe-nomenon associated with the event [45, 114]. This approach does not require explicit time discretization, and has the advantage that the time step, being calcu-lated during the simulation, adjusts itself to the rates of the various processes.

The work presented in this section employs the second approach for describing particle coagulation, while the first approach is used for simulating particle coa-lescence, once a coagulation event has been identified. Thus, more precisely, first a single coagulation event is identified to occur for the particles in the system and then, the mean inter-event time required, ΔT for the next coagulation event to occur is computed. Then, during this time interval, the coalescence process is simulated along with the associated energy release for all the particles in our system. It is worth mentioning for clarity that at any identified inter-event time between two successive particle (or, aggregates) collisions, there will be coalescence taking place for other system particles that had collided earlier in time.

It is important to recognize that the mean characteristic collision time ($\tau_{coll} \approx \tau_c$) essentially signifies the mean time interval that any particular particle (or, aggre-gate) has to wait before it encounters another collision, while the mean inter-event

time represents the time between any two successive collision events (ΔT) amongst any two particles (or, aggregates) in the system. The latter, also becomes the MC simulation time-step for the current model.

3.2.1 Implementation of MC Algorithm: Determination of Characteristic Time Scales for Coagulation

The MC algorithm presented here is developed based on Mukherjee et al.'s work [44] wherein a simulation system with initial particle concentration of C_0 is considered. A choice of the number of particles N_0 that can be efficiently handled in the simulation, defines the effective computational volume: $V_0 = N_0/C_0$. To connect the simulations to real time, the inter-event time between any two successive collisions or the MC time step, ΔT_k is inversely proportional to sum of the rates of all possible events:

$$\Delta T_k = \frac{V_0}{\sum_l R_l} = \frac{2N_0}{C_0 \sum_{i=1}^{N_{k-1}} \sum_{i=1}^{N_{k-1}} K_{ij}^F} \tag{44}$$

where, $R_l = K_{ij}$ is the rate of event l, defined as the coagulation of the pair (i, j), K_{ij} is the coagulation kernel for sizes i and j, and $V_0 = N_0/C_0$ is the actual volume represented in the simulation system for particle concentration, C_0 and number of simulation particles, N_0. For computational time efficiency, a mean coagulation probability, $\left\langle K_{ij}^F \right\rangle$ is defined as:

$$\left\langle K_{ij}^F \right\rangle = \frac{\sum_{i=1}^{N_{k-1}} \sum_{j=1}^{N_{k-1}} K_{ij}^F}{N_{k-1}(N_{k-1} - 1)} \tag{45}$$

Hence, the final form for the Monte Carlo time step can be given as:

$$\Delta T_k = \frac{2N_0}{C_0 \left\langle K_{ij}^F \right\rangle N_{k-1}(N_{k-1} - 1)} \tag{46}$$

Now, for each collision event, we use the inter-event time (ΔT_k or, simply ΔT) determined above, to simulate the coalescence process for *all particles* by integrating the surface area reduction and the energy equations. Then based on the mean values of the area, volume and temperature of the particles in the system calculated at the end of each MC time step, the mean characteristic collision time (τ_c) in the free molecular regime is estimated from the self-preserving size distribution theory of Friedlander [85] as:

$$\tau_c = 3/B \text{ where } B = (\alpha/2)\left(\frac{6k_B\overline{T}_p}{\rho_p}\right)^{1/2}\left(\frac{3}{4\pi}\right)^{1/6}\phi\overline{V}_p^{(-5/6)} \tag{47}$$

where, $\overline{T}_p$ and $\overline{V}_p$ stands for the mean particle temperature and volume, α, a dimensionless constant equal to 6.55 [115], ρ_p is the density of the particle material (assumed to be temperature independent) and ϕ is the material volume loading in the system considered.

Thus, for each inter-event time ΔT, an integration time step Δt for the coalescence process is defined as:

$$\Delta t = \frac{\Delta T}{n_{max}}, \quad \text{and} \quad n_{max}\frac{\Delta T}{\tau_f} \times p \tag{48a, b}$$

where, n_{max} is the number of iterative loops for the numerical integration in time; τ_f is the characteristic coalescence time previously defined in Eq. 42 and p is any integer value normally chosen as: $p = 10$. This method of choosing the numerical time step ensures sufficient discretization of time step to obtain desired resolution for simulating the coalescence process over the particular inter-event collision time and characteristic sintering time, both of which are sensitive to size and temperature.

In order to implement the numerical computation, the coagulation probability is defined as:

$$p_{ij} = \frac{K_{ij}^F}{K_{max}^F} \tag{49}$$

where, K_{max}^F is the maximum value of the coagulation kernel among all droplets. At each step two particles are randomly selected and a decision is made whether a coagulation event occurs based on p_{ij}. If the event takes place, then the inter event time, ΔT us calculated as shown earlier and the subsequent coalescence process is simulated. As indicated earlier by Smith and Matsoukas [78] as well as Efendiev and Zachariah [48], this probability should, in principle, be normalized by the sum of all K_{ij} but the choice of K_{max}^F is commonly employed in order to increase the acceptance rate while maintaining the relative magnitude of probabilities.

In the current implementation of the KMC model, a coagulation event occurs only if a random number drawn from a uniform distribution is smaller than the coagulation probability, p_{ij}. If the coagulation is rejected, two new particles are picked and the above steps are repeated until a coagulation condition is met. Upon successful completion of this step the selected particles with volumes V_i and V_j are combined to form a new particle with volume $V_i + V_j$ and total number of particles in the system is decreased by unity.

When the number of particles due to this repeated coagulation process drops to half of the initial value, the particles in the system are replicated. In order to

preserve the physical connection to time, the topping up process must preserve the average behavior of the system like the volume loading or the particle number density corresponding to the time prior to the topping up. In such time-driven MC processes, one ensures that the inter-event time for particle collisions stays the same by increasing the effective simulation volume, V_0 in proportion to the increase in particle number in the topped up system.

In relating the MC simulation to the real physics of the coalescence process, the schematic indicating the role of different time scales of events is helpful and is shown in Fig. 9. This figure, shows the relative magnitudes of the three time scales: the characteristic cooling time (τ_{cool}), characteristic collision time (τ_c) and characteristic coalescence or fusion time (τ_f) that are critical in determining whether a particle colliding would undergo complete sintering, release more heat and grow into a larger uniform primary particle or, would quickly quench and lose heat to form aggregates with larger surface area, but smaller primary particle sizes. If a criteria is met where by $\tau_{cool} > \tau_c > \tau_f$, one should expect to see fully sintered primary particles with large heat release. Whereas, if $\tau_c < \tau_f$, then the particles cannot fully sinter before they encounter the next collision, and this gives rise to the formation of aggregates.

3.2.2 Model Metrics and Validation for the KMC Algorithm

The number of MC particles required to achieve statistical accuracy in the system under study were determined from analyses of the characteristic collision and fusion times, temperature rise and other properties for two systems consisting of 1000 and 10,000 particles. Although computation time increases significantly, there is insignificant change in the mean results for characteristic collision times, fusion times and particle temperature of these two systems indicating the attainment of statistical equilibrium. Thus, all results presented in the following section on results from the current KMC simulation have been obtained by using systems of 1000

Fig. 9 Schematic diagram indicating the various time scales; mean inter-event time (ΔT), characteristic coalescence/fusion (τ_f), characteristic collision (τ_c) and the mean cooling time for particles (τ_{cool})
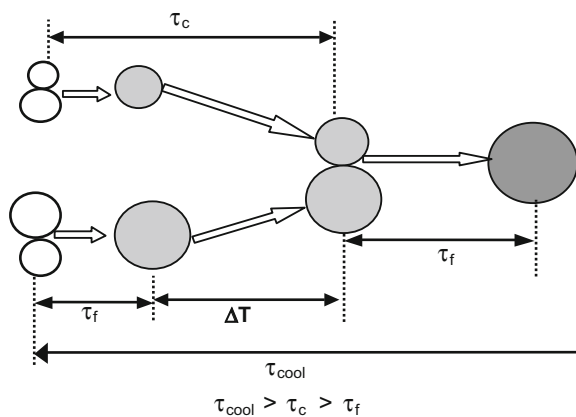
particles. It may be recalled here that the use of topping up technique, as proposed by Liffman [46], also reduces the statistical errors in the simulations even with a smaller number of particles, while requiring lesser computer memory. For all the studies presented here, the average simulation time for a 1000 particles system with a volume loading of 10^{-4} was anywhere between 15 and 2 h (depending on the parameters of the case study) while running on IBM–SP machines at the Minnesota Supercomputing Institute with eight 1.3 GHz power4 processors sharing 16 GB of memory.

For ease of scaling, the simulations presented in the following sections starts with the assumption of a monodisperse system of 1 nm diameter particles. Also, it was observed that the increase in background gas temperature due to heat release from coalescence is insignificant and hence, gas temperature was assumed to be constant throughout in all the simulation results discussed here. The representative results presented here for the discussions are for silicon and titania nanoparticles. The thermodynamic properties of Si and TiO_2, including density, heat capacity, latent heat of fusion/melting and surface tension are assumed to be particle size independent [91, 96], and are reported in Table 1.

The MC algorithm presented here was validated for the coagulation study, the details for which can be found in Mukherjee et al. [44], and its accuracy was found to be in excellent agreement with sectional model simulations of Lehtinen and Zachariah [34]. As the model metrics, we present here, as seen in Fig. 10, the particle size distributions at long times, which when compared with the numerical results of Vemury et al. [116], showed very good agreement with the known self-preserving size distribution seen for coagulating aerosols.

Fig. 10 Self-preserving size distribution for coagulation from Monte Carlo method compared with numerical results of Vemury et al. [43] and plotted as dimensionless number density, $\psi(\eta) = N(t, V_p) \overline{V}_p / N_\infty$ versus dimensionless volume, $\eta = V_p / \overline{V}_p$. Silicon at $T_g = 320$ K was considered assuming free molecular regime collision kernel
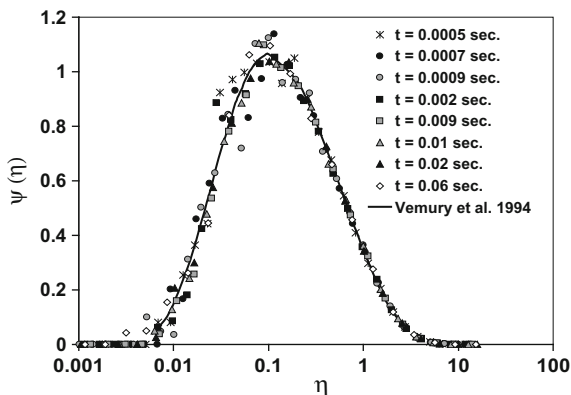
3.3 Results and Discussions: Effects of Process Parameters on Nanoparticle Growth via Coagulations and Non-isothermal Coalescence

3.3.1 Effect of Background Gas Temperature

The competing effects of heat release and bath gas cooling were assessed with simulations for Si nanoparticle growth carried out at gas temperatures of 325, 500 and 800 K with background gas pressure, $P_g = 100$ Pa and material volume loading, $\phi = 10^{-6}$. Shown in Fig. 11 are plots adopted from the results of Mukherjee et al. [44] that indicate the characteristic collision and coalescence times as a function of growth time. Such a plot has been proposed by Windeler et al. [87] to assess the competition between these two times and their crossing point. In Fig. 11a, the heavy dotted line represents the characteristic collision time, which is relatively independent of temperature and increases in time for a coagulation process because of the net decrease in particle number concentration. The coalescence time is a function of particle size and temperature as discussed before. For the work considered here, the coalescence energy release and the losses to the surrounding can significantly alter this time. The crossing point, as suggested by Windeler et al. [87], defines the onset of aggregation and enables primary particle size prediction. However we show later that the use of the crossing point between τ_f and τ_c to predict primary particle sizes might not be universally applicable. For the various gas temperatures studies presented here, we found that with increasing residence time, τ_f initially decreases, reaches a minimum, and then monotonically increases.

The decrease in the characteristic coalescence (fusion) time τ_f is actually associated with an increase in the particle temperature and is shown in Fig. 11b. Here we see that the particle temperature takes an abrupt and very rapid rise to a value well in excess of 1200 K. This is an indication that the characteristic cooling time under these conditions is slow relative to the fusion time, τ_f implying larger heat generation. Higher background temperatures show an earlier onset of elevated temperatures and a prolonged dwell time at higher temperatures due to the lower driving force for cooling. At the same time, delayed onset of heat release effects, generate larger aggregates trying to coalesce fully, which cause a stronger driving force for the heat generation arising from the surface area reduction term and hence, an increase in the net rise in particle temperature. Referring back to Fig. 11a, we see the minimum in the coalescence time roughly corresponds to the peak particle temperature achieved. Also, with increasing gas temperatures, for the same particle size distribution, the relative values of τ_f decrease but τ_c remains relatively unchanged. In the context of the current discussions on the comparison of characteristic times, we see from Fig. 11a, b that after the initial drop the coalescence time eventually rises, coupled with heat loss from particles, till it crosses the collision time curve. At this point one can reasonably conclude that aggregate formation has been triggered. Beyond this, in the region where $\tau_f > \tau_c$, the particles do not get sufficient time to fully sinter before the next collision takes place thereby

Fig. 11 Variations of
a characteristic fusion (τ_f) and
collision (τ_c) times, **b** mean
particle temperature ($<T_p>$),
and **c** normalized area (*left
axis*) and mean volume
equivalent diameters (*right
axis*) with residence times for
various background gas
temperatures for Silicon;
(P_g = 100 Pa and $\phi = 10^{-6}$).
*Here, $A_{(i)}$: Particle area and
$A_{sph(i)}$: Equivalent spherical
area of corresponding
particle*
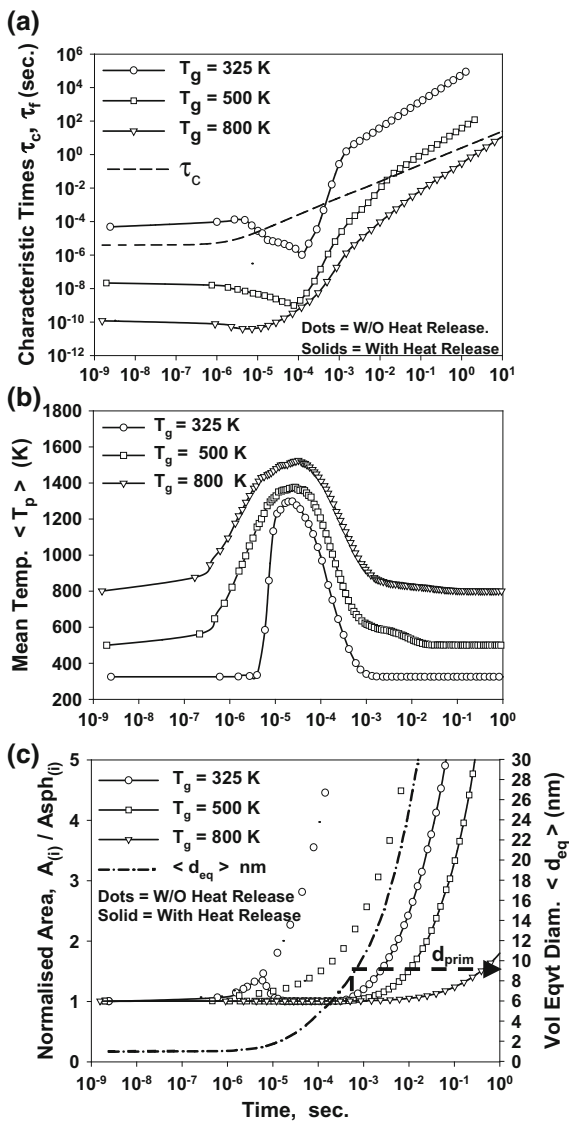
forming aggregates. Eventually, the particles get sufficiently larger so that their heat capacity is large enough as to negate any significant temperature rise associated with coalescence and the growing particles return to the background temperature.

Higher background temperatures show an earlier onset of elevated temperatures and a prolonged dwell time at higher temperatures due to the lower driving force for cooling. At the same time, delayed onset of heat release effects, generate larger aggregates trying to coalesce fully, which cause a stronger driving force for the heat generation arising from the surface area reduction term and hence, an increase in the

net rise in particle temperature. Referring back to Fig. 11a, we see the minimum in the coalescence time roughly corresponds to the peak particle temperature achieved. Also, with increasing gas temperatures, for the same particle size distribution, the relative values of τ_f decrease but τ_c remains relatively unchanged. In the context of the current discussions on the comparison of characteristic times, we see from Fig. 11a, b that after the initial drop the coalescence time eventually rises, coupled with heat loss from particles, till it crosses the collision time curve. At this point one can reasonably conclude that aggregate formation has been triggered. Beyond this, in the region where $\tau_f > \tau_c$, the particles do not get sufficient time to fully sinter before the next collision takes place thereby forming aggregates. Eventually, the particles get sufficiently larger so that their heat capacity is large enough as to negate any significant temperature rise associated with coalescence and the growing particles return to the background temperature.

It is possible that with higher temperatures as $d\tau_f/dt$ approaches $d\tau_c/dt$ (at the crossing point, i.e., $\tau_f \approx \tau_c$), oblong particles with long necks and strong bonds are formed that would eventually go on to form aggregates. However, at lower temperature the crossing occurs within the heat generation regime and $d\tau_f/dt \gg d\tau_c/dt$ (at $\tau_f \approx \tau_c$). Thus, in this case, uniform spherical particles held together by weak Van der Waals' forces in the agglomerates are formed. This theory was also found to be consistent with the earlier work of Windeler et al. [87].

3.3.2 Effect of Background Gas Pressure

The conventional wisdom has held that background gas pressure has no role in the heat transfer during collision/coalescence process. This presumption has held sway because until very recently prior work had neglected the exothermic nature of coalescence. Lehtinen and Zachariah [86, 95] were the first to recognize this effect and conclude that gas pressure P_g, should have an impact on primary particle size.

The effect of P_g on τ_f at constant gas temperature for silicon ($T_g = 500$ K, $\phi = 10^{-6}$) is shown in Fig. 12a. Corresponding mean particle temperatures are shown in Fig. 12b. At 101 kPa the effect of heat release is negligible as the heat losses to the surroundings are evidently sufficiently facile. As one decreases the pressure however, the lowered heat loss term through conduction enables the particles to experience elevated temperatures. In these cases the lower the pressure the higher the particle temperatures. This self-heating is also reflected in the lowering of the characteristic sintering time seen in Fig. 12a. At the highest pressure simulated the role of heat release is unimportant, while with decreasing pressure we see a monotonic increase in primary particle size from roughly about 3 nm at 101 kPa to 13 nm 100 Pa. This increase clearly establishes the effect of gas pressure on the primary particle growth rates and as seen from Fig. 12b, reflects the higher particle temperatures experienced at lower pressures resulting from a lower heat loss rate by conduction. It is clearly noticed that the fusion and collision times presented in Fig. 12a show a crossing point independent of pressure! This result indicates that the crossing point may not be the best criteria for assessing the

spherical primary particle size, especially beyond the heat generation regime where the relative gradients of the characteristic times, i.e., $d\tau_f/dt$ and $d\tau_c/dt$ at the crossing point are close to each. The two gray points in Fig. 12a mark a noticeable change in $d\tau_f/dt$ indicating the time where the normalized surface area deviates from unity ($A/A_{sph} > 1$), and was used for determining the spherical primary particle sizes. Beyond this point, and before the particles are agglomerated (i.e., the

Fig. 12 Variations of a characteristic coalescence/fusion (τ_f) and collision (τ_c) times, and b mean particle temperature ($<T_p>$) with residence time along with heat release effects on primary particle sizes (d_{prim}) for various background gas pressures, P_g. ($T_g = 500$ K and $\phi = 10^{-6}$). Grey point marks gradient change when $A_{(i)}/A_{sph(i)} \geq 1$; Results are for Si
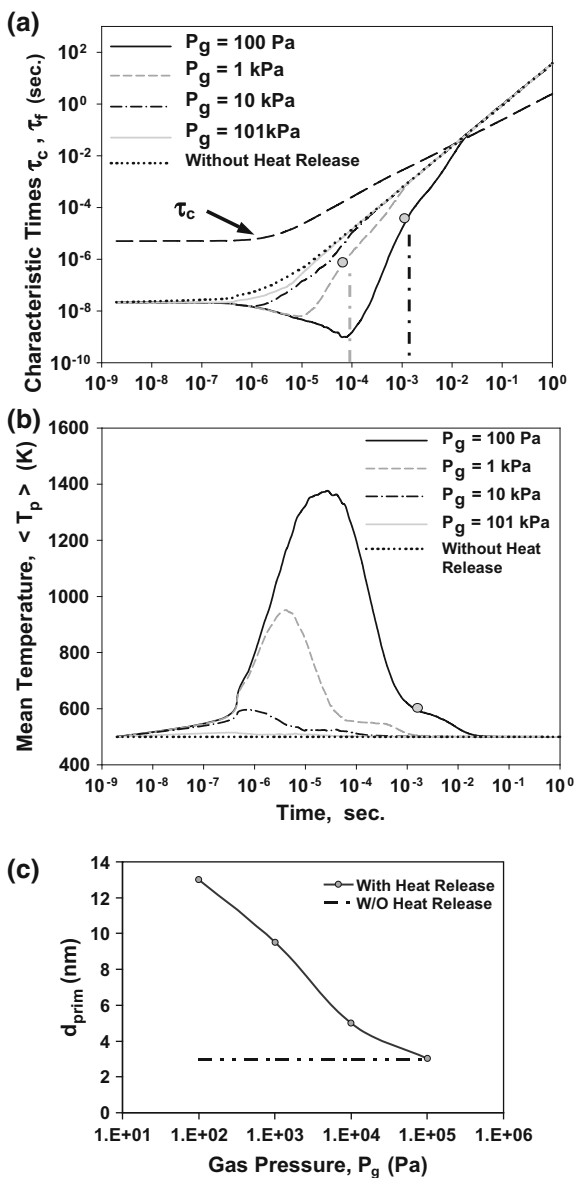
crossing point between τ_f and τ_c) the primary particles are non-spherical (possibly oblong with large necks) mainly due to the slow crossing point of τ_f and τ_c, as discussed in details earlier [87]. Thus, we estimate the primary particle size (d_{prim}) from the normalized area term ($A/A_{sph} > 1$) and the corresponding volume equivalent diameter as discussed earlier (not shown here) at the point of agglomeration. These results are presented in Fig. 12c.

The aforementioned model was also applied to TiO_2 nanoparticle growth under different gas pressures (P_g = 100 Pa, 1, 10 and 101 kPa) at T_g = 1600 K. The choice for the operating temperature was based on the process parameters used in the industry for TiO_2 production. It needs to be highlighted here that the present simulations trace the coagulation/coalescence of particles from the time precursor reactions leading to 100% conversion of precursors (TiCl$_4$ or, TTIP) to TiO_2 nanoparticles have been achieved, so that we have a sufficiently large particle number concentration and growth rates are purely due to collision/coalescence process without any nucleation effects.

We would like mention that the focus of the current chapter being energetic metal nanoparticles, we would briefly touch upon the significant results from the TiO_2 nanoparticle case studies. For further details on the TiO_2 case studies, the readers should refer to article by Mukherjee et al. [44]. The most significant aspect of the studies on the TiO_2 nanoparticle systems was that the results are able to capture the role of phase transition on growth along with the effect of size dependent melting point of nanoparticles. We rely on Eq. 41 to determine, for a given particle, if we are above or below the melting point at any instant in the coalescence process and use the appropriate sintering model (solid-state or viscous flow). This becomes essential since viscous flow characteristic times are 2–3 orders of magnitude lower than that for solid-state diffusion.

The heat release, and the rise in particle temperature in time due to the competing characteristic times of τ_f and τ_c are evident form Fig. 13a. Here, it needs to be pointed out that initially for small particle sizes (1 nm), $T_p(t) > T_{mp}(d_p)$ (from Eq. 41), particles are in molten state and hence, the characteristic coalescence time (τ_f) is very small so that particles coalesce almost instantly on contact and undergo rapid evaporative cooling. But as particle sizes increase due to coagulation/coalescence, corresponding melting points also increase and rise above the particle temperature, i.e., $T_p(t) < T_{mp}(d_p)$ and the particles shift over to the much slower solid-state diffusion mechanism followed by slow conductive losses only. These processes are clearly observed from the gradient changes in the τ_f and T_p during the particle energy relaxation periods in Fig. 13a, b. In line with our earlier discussions from the Si nanoparticle case studies, the size for the spherical primary particles at the cross-over point for τ_f and τ_c (see Fig. 13a) were determined from the criteria of $d\tau_f/dt \gg d\tau_c/dt$ for all the pressure case studies of 100 Pa–101 kPa. Furthermore, from Fig. 13b, it can be seen that the peak rise in particle temperature (i.e., in the region of viscous diffusion mechanism) does show significant variations for the different gas pressures. However, when the particle temperature relaxers (i.e., in solid-state diffusion region), the particle temperatures are higher for the P_g = 100 Pa case due to lesser heat loss resulting in a prolonged

Fig. 13 Variations of
a characteristic fusion (τ_f) and
collision (τ_c) times, and
b mean particle temperature
($<T_p>$) with residence times
for various background gas
pressures, P_g, *Open circle*
indicates abrupt change in
gradient corresponding to
phase change from molten to
solid-state; **c** Heat release
effects on primary particle
sizes (d_{prim}) for the aforesaid
case. ($T_g = 1600$ K and
$\phi = 10^{-3}$). *Results are for*
TiO$_2$
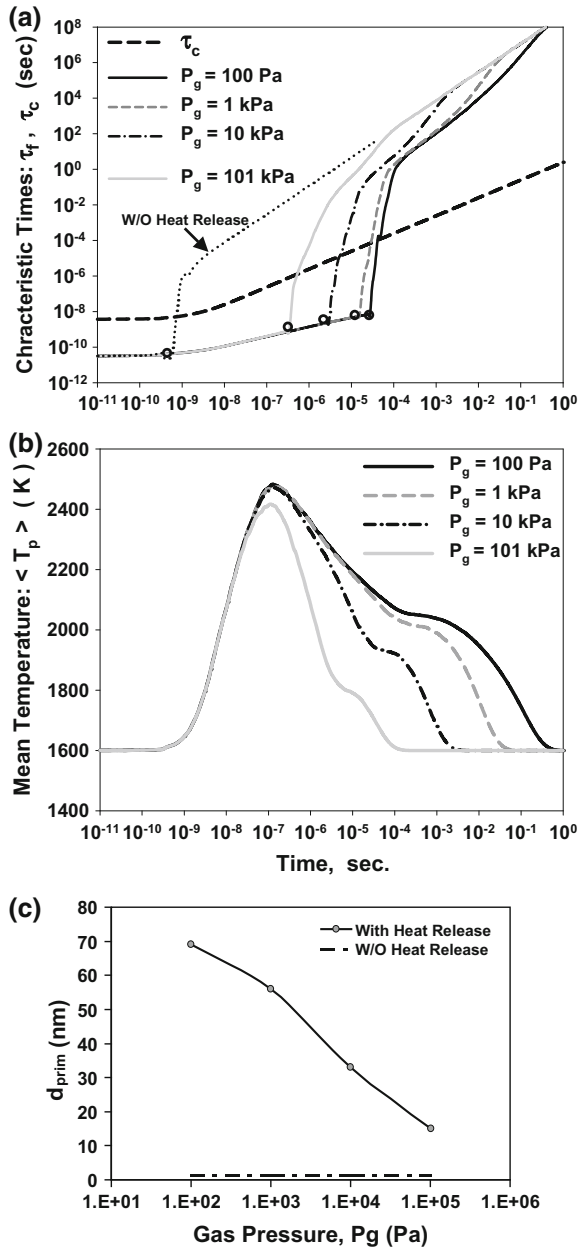
and enhanced sintering mechanism over the time that competes with the heat loss
terms in the energy balance. Finally, they cool down to background gas temperature
indicated by the merging of all the fusion time gradients where τ_f keeps on
increasing purely due to aggregate growth. Figure 13c illustrates the spherical

primary particle sizes as function of different gas pressures and shows the use of background pressure to alter primary particle size.

3.3.3　Effect of Volume Loading

Volume loading is another important process parameter that typically is not considered for detailed analysis in many studies of primary particle size predictions for nanoparticle coalescence processes. Common laboratory experiments are usually limited to low volume fractions ($\phi = 10^{-6}$) for ease of experimentation, particularly for those who use in situ optical probes. Industrial practice of course seeks to maximize production rate and typically operates at much higher volume fractions ($\phi = 10^{-3}$). Without the consideration of the exothermic nature of coalescence, it is natural to expect no role for the volume fraction. On the other hand, with heat release considered we might expect that under rapid coalescence conditions, where heat release is faster than energy loss to the surroundings, a higher collision rate might magnify the effect.

The model has been applied to various laboratory and industrial volume loadings in the range of $\phi = 10^{-6}$–10^{-3} for Si (Fig. 14). Here the Si example is most reflective of what might occur in typical low-pressure plasma synthesis of metal nanopartciels. In Fig. 14a, it is seen that all volume loadings considered result in elevated particle temperatures, however increased volume fraction results in higher temperatures for prolonged time period. This reflects the fact that if the characteristic fusion time is much less than the collision time, there is opportunity to enhance the coalescence process by increasing the collision rate through larger volume loading. In doing so, one essentially enhances the heat release rate by shortening the time interval between the process of cooling that a sintered particle undergoes and another collision that it encounters before cooling down completely, thereby heating up the particle even more. The corresponding primary particle sizes predicted for various volume loadings are seen in Fig. 14b. It clearly shows enhanced primary particle sizes as volume loading is increased.

4　Surface Oxidation

The fate, growth and evolution of nanoparticles leading to complex surface restructuring and reactivity, including surface oxidation, during their manufacturing via flame synthesis [117, 118] plasma processing [119] or flow reactors [120, 121] has been extensively studied. The motivation for such studies resides in the directed fabrication of nano-structured materials and thin films with controlled porosity, specific surface coatings and catalytic properties. Structural rearrangements during nanoparticle evolution can lead to the formation of either compact spherical nanoparticles with low surface area (electronic device fabrications, sensors, etc.) or, fractal-like aggregates with high surface area (nanocatalysts, energetic materials, H_2

Fig. 14 Effect of different particle volume loading ($\phi = 10^{-4}, 10^{-5}, 10^{-6}$) on **a** the temporal variation of the mean particle temperature ($<T_p>$); and **b** the prediction of primary particle sizes (d_{prim}) for Si nanoparticle coalescence ($T_g = 500$ K and $P_g = 100$ Pa). Primary particle size predicted without heat release effect has also been indicated
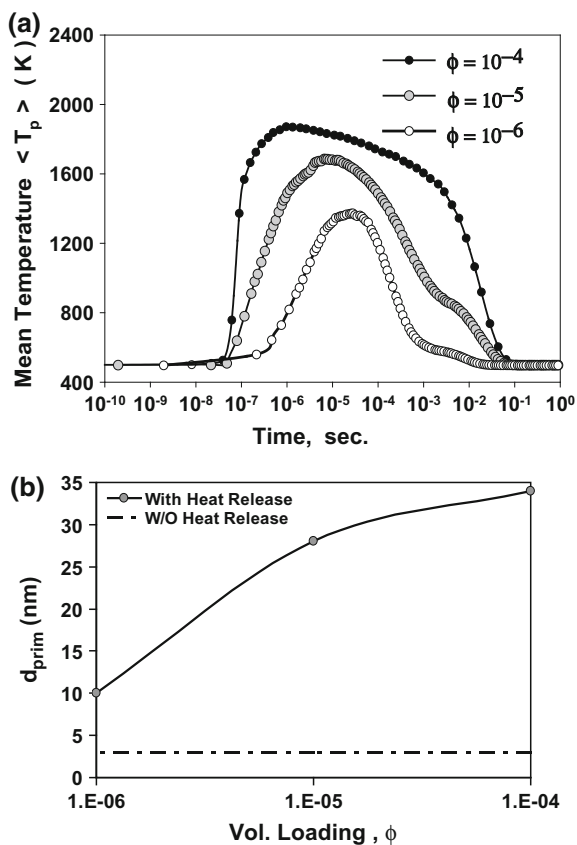
storage, etc.). Yet, the complex interplay between the various physical pathways such as collision/coalescence as discussed in the previous sections, and chemical kinetics of their surface reactivity during gas-phase synthesis of these structures is not clearly understood.

Aerosol dynamics based sectional/ nodal models [37, 38, 122], method of moments [123, 124] or, models for particle laden flows [125, 126] have been widely used to study nanoparticle evolution in the past. But, only recently Monte Carlo (MC) based stochastic models, as developed in our earlier sections, have been able to simulate nanoparticle coagulation, aggregation, surface growth and restructuring [47, 79] without resorting to a single unifying governing multivariate equation [44]. Specifically, MC simulations of nanoparticle aggregation and restructuring via coalescence/sintering [102] have provided great insight into the role of process parameters in controlling the structures of gas-phase synthesized nanoparticles [127]. Furthermore, the highly exothermic and energetic nature of coalescence due to self-reinforcing atomic diffusions at nano-scale [39, 95] have prompted recent kinetic MC (KMC) studies to elucidate the role of non-isothermal

coalescence in tailoring the size and shape of nanoparticles generated via collision-coalescence events [44]. The implications of a competing, non-isothermal collision-coalescence event leading to complex nanoparticle shapes are far-reaching in regards to the thermal and morphological activation of the interfacial chemistry of these nanostructured materials.

The aforementioned studies have encouraged systematic characterizations of complex fractal-like structures of nano-aggregates, in lieu of the commonly used equivalent spherical shapes [128, 129]. Such modifications significantly alter the inter-particle collision frequency function [130] and hence their growth dynamics. The excess surface area of fractal-like nanostructures, when coupled with the exothermic nature of coalescence, makes the chemical physics of surface energy-driven interfacial processes such as oxidation and coagulation-coalescence in nanoparticles [131] highly complex and intriguing. Yet, to date a comprehensive study of the non-linear coupling between all of the aforementioned energetic processes in the framework of synthesizing fractal-like nano-structures has not been performed.

Understanding these complex energetic processes is essential for establishing the process guidelines for synthesis of tailored nanostructures with controlled oxide layers for surface passivation, energetic or, specific catalytic and electronic applications [132–134]. Specifically, the energetic properties of metal nanoparticles (<100 nm) with large surface-to-volume ratio and energy densities [135–137] have attracted much attention from the combustion community (e.g., solid propellant or, pyrotechnique research). To this end, oxidation kinetics of Al NPs have been investigated using thermogravimetric analysis (TGA), Rutherford backscattering spectrometry (RBS) studies [138], single particle mass spectrometry (SPMS) [139] and laser-induced breakdown spectroscopy (LIBS) [140] techniques.

Recent phenomenological models [12] and Molecular Dynamics (MD) simulations [141, 142], although simplistic in assuming spherical particle shapes, have provided critical insight into metal nanoparticle oxidation. But, due to computational limitations, they fail to account for the exothermic effects of the competing collision-coalescence processes during nanoparticle growth mechanism [44]. The motivation behind the investigations discussed in this section stems from the fact that most studies on metal nanoparticle oxidation rely on the simplified assumption of spherical particles while looking at size evolution and/or surface oxidation of single particle [12], uniformly sized particles [143] or, ensemble particle size distributions [144]. Thus, here we present our recently developed KMC model that efficiently accounts for coagulation-coalescence events coupled with particle energy balance and surface oxidation during the synthesis of metal nanoparticles with fractal-like structures under typical processing conditions dictated by background gas pressure (p_g), temperature (T_g) and material volume loading (ϕ). This model for the first time allowed the investigation of the role of morphological complexity defined by surface fractal dimensions of metal nano-aggregates in their growth mechanism, energetic activities, extents of oxidation and structural/ compositional changes. Specifically, due to the wealth of high quality experimental data [135–140], we specifically report the investigation of

gas-phase synthesis of Al nanoparticles undergoing simultaneous oxidation (i.e., Al/Al_2O_3 system) as a case study to demonstrate the efficacy of the KMC model.

4.1 Mathematical Model and Theory

4.1.1 Morphology: Surface Fractal Dimension

The present study is focused on interfacial processes such as coalescence and surface oxidation, and hence, uses the surface fractal dimension D_s [145] to describe particle morphology. Based on the scaling law relation [146] between particle surface area (A_p) and volume (V_p): $A_p \propto V_p^{D_s/3}$ for fractal-like surfaces, D_s is estimated from the slope of a linear fit to $\ln(A_p)/A_0$ vs. $\ln(V_p)/V_0$ for the ensemble particle system as per the normalized area-to-volume relationship with their primary particles [145]:

$$\frac{A_p}{A_0} = \left(\frac{V_p}{V_0}\right)^{\frac{D_s}{3}} \tag{50}$$

Theoretically, $2 \leq D_s \leq 3$, where $D_s = 2$ represents perfect smooth spheres; $2 < D_s < 3$ represents self-similar fractal-like aggregates undergoing partial coalescence and, $D_s = 3$ represents completely open-chained fractal aggregates (Fig. 15). In using Eq. 50, it needs to be mentioned that the choice of initial monomers as primary particles in the system, as used earlier [112], is not valid when collision-coalescence mediated growth ($\tau_f \ll \tau_{coll}$) generates significantly large, uniform spherical particles that act as the primary particles in newly formed aggregates. Hence, subject to a log-normal distribution of aggregates coalescing into uniform spherical particles (discussed later), log mean diameter of the particle ensemble is assigned as the characteristic primary particle dimension. At the onset of aggregation, the primary particle size estimated from the most recent particle ensemble is used for the D_s estimation of all future aggregates. In addition, the validity of Eq. 1 for $D_s > 2$ requires a substantial number of primary particles (>10–20) in any cluster to minimize error arising from the spherical primary particle morphology ($D_s = 2$).

4.1.2 Collision Kernel and Characteristic Collision Time

Based on Eqs. 3 and 30 in the earlier Sects. 2.1 and 3.1.1, the free molecular form of the collision kernel between two particles i and j of any shapes and cluster sizes, varying particle temperatures [44] and densities (due to compositional variations), can be represented as [145]:
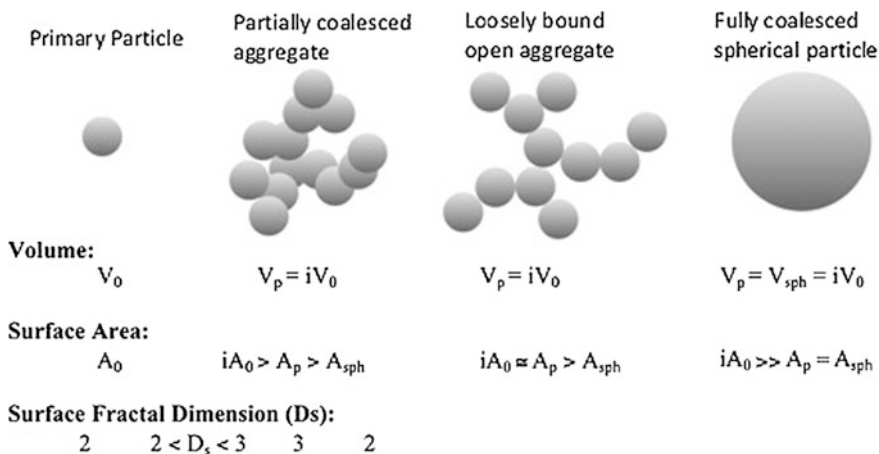
Fig. 15 Schematic indicating particle morphology variations

$$\beta_{ij} = \frac{1}{4}\left(\frac{8k_b}{\pi}\right)^{1/2}\left(\frac{T_i}{\rho_i V_i} + \frac{T_i}{\rho_j V_j}\right)^{1/2}\left[(s_i A_i)^{1/2} + (s_j A_j)^{1/2}\right]^2 \tag{51}$$

$$s_i = (D_s - 2)\left(\frac{2}{i}\right)^{1-\chi} + (3 - D_s) \tag{52}$$

where, it is noted that when $D_s = 2$ for dense spheres, $s_i = 1$ and χ is experimentally determined to be 0.92 for typical nanoparticle aggregation [147, 148].

In terms of β_{ij} (Eq. 51) and aerosol self-preserving size distribution (SPD) theory [85] based non-dimensional particle volumes, $\eta_i = N_\infty V_i/\phi$ and size distributions, $\psi(\eta_i) = N_i\phi/N_\infty^2$ (as also presented in Fig. 10 in Sect. 3.2.2.), rate of change in particle number concentration is given as:

$$\frac{dN_\infty}{dt} = -\frac{a}{2}\Omega N_\infty^{5/2} I(\eta_i, \eta_j) \text{ where, } I(\eta_i, \eta_j) = \int_0^\infty \int_0^\infty F(\eta_i, \eta_j)\psi(\eta_i)\psi(\eta_j)d\eta_i d\eta_j \tag{53}$$

and

$$F(\eta_i, \eta_j) = \left(\frac{1}{\eta_i} + \frac{1}{\eta_j}\right)^{1/2}\left[\eta_i^{\gamma/2}\left\{1 + (b\theta/a)\eta_i^{1-\chi}\right\}^{1/2} + \eta_j^{\gamma/2}\left\{1 + (b\theta/a)\eta_j^{1-\chi}\right\}^{1/2}\right]^2 \tag{53a}$$

where,

$$\Omega = \left(\frac{2k_b\overline{T}}{\pi\overline{\rho}\phi}\right)^{\frac{1}{2}}\left(\frac{A_0}{2^\chi\eta_0^\gamma}\right); \gamma = (D_s/3 + \chi - 1); a = (D_s - 2); b = (3 - D_s); \theta$$
$$= (2\eta_0)^{\chi-1}$$

$\eta_0 = N_\infty V_0/\phi$ The volume integral over the entire population in Eq. 53 justifies the use of an ensemble averaged particle density and temperature, $\overline{\rho}$ and $\overline{T}$, whereas the statistical nature of the problem provides support for the use of D_s, obtained from the linear fit of Eq. 50 over the particle ensemble, to represent the surface morphology of individual particles.

Here $I(\eta_i, \eta_i)$, which has been numerically solved for homogeneous forms of $F(\eta_i, \eta_j)$ at different volume fractal dimensions [85] (D_f), becomes analytically intractable and numerically intensive due to the non-homogeneous form of $F(\eta_i, \eta_j)$ in Eq. 53a. Thus, asymptotic solutions of $\left\{1 + (b\theta/a)\eta_i^{1-\chi}\right\}^{1/2} \cong 1$ when, $(b\theta/a) \ll 1$ $(D_s \to 2)$ and $\left\{1 + (b\theta/a)\eta_i^{1-\chi}\right\}^{1/2} \cong (b\theta/a)^{1/2}\eta_i^{1-\chi/2}$ when, $(b\theta/a) \gg 1$ $(D_s \to 3)$ (Note: $(b\theta/a)$ ranges over several orders of magnitude, whereas $\eta_i^{1-\chi} \sim 0.5 - 1.0$) lead to the homogenous forms of $I(\eta_i, \eta_j)$. Upon numerical integration, $I(\eta_i, \eta_j)$ converges to the average values ~ 6.576 and 6.577 over the respective ranges of $D_s = 2.4$–3.0 and $D_s = 2.0$–2.6 (see Table 2). Finally, using an average value of $I(\eta_i, \eta_j) = 6.577$ in Eq. 53, the characteristic collision time τ_{coll} (time taken by a particle to double its volume and hence, N_∞ to drop to $N_\infty/2$ via coagulation) in the respective D_s regimes is estimated from:

$$\tau_{coll} = \frac{N_\infty^{(\gamma-3/2)}\left(1 - 0.5^{(\gamma-3/2)}\right)}{Ya(\gamma - 3/2)I(\eta_i, \eta_j)} \quad \text{for } D_s \to 3 \text{ (approaching fractal)} \tag{54}$$

$$\tau_{coll} = \frac{N_\infty^{(\gamma-\chi-1/2)}\left(1 - 0.5^{(\gamma-\chi-1/2)}\right)}{Yb(\gamma - \chi - 1/2)\left(\frac{2V_0}{\phi}\right)^{\chi-1}I(\eta_i, \eta_j)} \quad \text{for } D_s \to 2 \text{ (approaching sphere)} \tag{55}$$

where, the intermediate coefficient,

$$Y = -\frac{1}{2}\left(\frac{2k_b\overline{T}}{\pi\overline{\rho}\phi}\right)^{\frac{1}{2}}\left(\frac{A_0}{2^\chi}\right)\left(\frac{\phi}{V_0}\right)^\gamma. \tag{56}$$

The final τ_{coll}, as constructed from Eqs. 5 and 6 in the respective particle morphology regimes of $D_s \to 2$ (earlier times) and $D_s \to 3$ (later times), exhibit the

Table 2 Numerical values of the integral $I(\eta_i; \eta_j)$ in Eq. 4 for $D_s \rightarrow 2$ and $D_s \rightarrow 3$[a]

D_s	2.0	2.1	2.2	2.3	2.4	2.5	2.6	2.7	2.8	2.9	3.0	Mean
$I(\eta_i; \eta_j)\ D_s \rightarrow 3$	6.739	6.702	6.657	6.624	6.576	6.578	6.569	6.546	6.576	6.572	6.615	6.576
$I(\eta_i; \eta_j)\ D_s \rightarrow 2$	6.624	6.576	6.578	6.569	6.546	6.576	6.572	6.615	6.651	6.694	6.744	**6.577**

[a]Adapted from *AIChE J., 58, 3341 (2012)* [49] with copyright permission from Wiley

expected escalation in τ_{coll} at later stages due to larger collision cross-sections of fractal-like aggregates.

4.1.3 Coalescence

Coalescence can be approximated by the Eq. (34) in Sect. 3.1.2 to model the surface area reduction rate [85]. In this case, the variations in mean characteristic fusion time, τ_f (i.e., time needed to reduce the excess agglomerate surface area, $(A_p - A_{sph})$ by 63%) has to be accounted for due to the formation of composite phase segregated nanoparticles as a result of metal (M) $\rightarrow$ metal oxide (MO_x) phase transitions. In doing so, τ_f is estimated from individual $\tau_{f(M)}$ and $\tau_{f(MOx)}$ weighted by respective metal (M)/metal oxide (MOx) volume fractions:

$$\tau_f = \tau_{f(M)}^{\varphi_M} \tau_{f(MOx)}^{\varphi_{MOx}} \tag{57}$$

to account for the predominant diffusion rates due to dynamical variations in the M and MOx composition within the particle. Depending on particle temperatures T_p, melting points $T_{m(x)}$ and physical states of material, individual $\tau_{f(x)}$ (x = M or, MOx) are calculated as: (1) $\tau_{f(x)} = \frac{3k_b T_p n_x}{64\pi\sigma_S(X)D_{eff}}$ for grain boundary diffusion (solid state sintering when $T_p < T_{m(x)}$ [98]) where, D_{eff} is the effective diffusion coefficient [44] ($m^2 \ s^{-1}$) and, (2) $\tau_{f(x)} = \frac{\mu_x d_{p(eff)}}{2\sigma_{1(x)}}$ for viscous diffusion (molten state liquid sintering when $T_p \geq T_{m(x)}$ [102]) where, $d_{p(eff)} = 6V_p/A_p$ accounts for multiple sintering necks on one particle [44].

    $T_{m(x)}$ (x = M or, MOx), being highly sensitive to particle sizes (d_p) at nano-scale, is determined from the expression for size-dependent melting point of nanomaterials [149]:

$$T_{m(x)}(d_p) = T_{b(x)} \left\{ 1 - \frac{4}{h_L \rho_{s(x)} d_p} \left[\sigma_{s(x)} - \sigma_{1(x)} \left(\frac{\rho_{s(x)}}{\rho_{1(x)}} \right)^{2/3} \right] \right\} \tag{58}$$

    The respective thermochemical and physical properties used in Eq. 58 are specifically reported in Table 3 for the Al/Al_2O_3 case-study.

4.1.4 Surface Oxidation: Transport Model and Species Balance

The surface oxidation model has the following features: (1) Uniform oxide shell formation, based on the *shrinking core like model* [150], hence the core shrinks in size while maintaining the same morphology (given by D_s) as the external particle surface (Fig. 16); (2) Only surface oxidation of solid and liquid material leads to solid oxide (ash) formation; (3) O_2 diffuses through the ash layer to oxidize the

Table 3 Thermochemical and physical properties of Al and $Al_2O_3^a$

Properties	AL (Ref.)	Al_2O_3 (Ref.)
Solid density, $\rho_{S(X)}$ (kg/m³)	2700 [151]	3980 [151]
Solid surface tension, $\sigma_{s(X)}$ (J/m²)	1.14 [151]	1.12 [151]
Liquid density, $\rho_{l(X)}$ (kg/m³)	2377 [152]	2930 [153]
Liquid surface tension, $\sigma_{l(X)}$ (J/m²)	1.05 [154]	0.64 [153]
Molecular weight (g/mol)	27	102
Molar volume, v_{mol} (m³/mol)	1×10^{-5}	2.56×10
Heat of vaporization, h_v (kJ/mol)	294 [151]	346.94 [155]^b
Latent heat of melting, h_L (kJ/mol)	10.7 [151]	109 [153]
Heat capacity, $c_{p(X)}$ [J/(kg°C)]	917 [151]	775 [151]
Bulk melting point, $T_{m(X)}$ (K)	933[151]	2327[151]
Viscosity, μ_x (Pa-s)	$4.97 \times 10^{-4} \left[T_m/(T_p - T_m)\right]^{0.5714}$ [156]	$(3.2 \times 10^{-3}) \exp\left[4.32 \times 10^4/(R_u T_p)\right]$ [153]
Grain boundary diffusion coefficient, D_{GB} (m²/s)	$(\alpha/\delta) \exp\left[-\beta/(R_u T_p)\right]$ [151]	$(\alpha/\delta) \exp\left[-\beta/(R_u T_p)\right]$ [151]
δ: Grain boundary width = 0.5 nm	$\alpha = 3 \times 10^{-14}$ m²/s; $\beta = 6 \times 10^4$ J/mol	$\alpha = 3 \times 10^{-3}$ m²/s; $\beta = 4.77 \times 10^5$ J/mol
Saturated vapor pressure, p_{sat} (Pa)	$\exp(13.07 - 36,373/T_p)$ [12]	$101325. \exp(13.42 - 27,320/T_p)$ [157]
Other thermochemical properties		
Enthalpy of reaction (kJ/mol)	2324 [139]	
Temperature dependent surface tension (N/m)	$\sigma_{Al}(T_p) = 0.001\left[860 - 0.134(T_p - 933)\right]$ [158]	
Thermal conductivity of Al_2O_3, k_{ash} [W/(m-K)]		$\alpha + \beta \exp\left[-\gamma(T_p - \theta)\right]/\left[(T_p - \theta) + \varepsilon\right]$ [159] $\alpha = 5.85$; $\beta = 15,360$; $\gamma = 0.002$; $\theta = 273.13$
First-order reaction rate coefficient, k_f (m/s) $d_p < 50$nm 50nm $< d_p < 100$nm 100nm $< d_p$	$24. \exp\left[-31.8 \times 10^3/(R_u T_p)\right]$ $180. \exp\left[-56.9 \times 10^3/(R_u T_p)\right]$ $(5.4 \times 10^7) \exp\left[-174.6 \times 10^3/(R_u T_p)\right]$ [139]	

(continued)

Table 3 (continued)

Properties	AL (Ref.)		Al$_2$O$_3$ (Ref.)	
Heterogeneous diffusion coefficient (m^2/s)	$O_2 \rightarrow Al_2O_3$		$Al_2 \rightarrow Al_2O_3$	
	$D_{O_2|Ash} = \alpha \exp\left[-\beta/(R_u T_p)\right]$	[139]	$D_{Al_2|Ash} = \alpha \exp\left[-\beta/(R_u T_p)\right]$	[157]
	$\alpha = 1.72 \times 10^{-9}$ m^2/s; $\beta = 69.5$ J/mol		$\alpha = 2.8 \times 10^{-3}$ m^2/s; $\beta = 477.3$ J/mol	

[a]Adapted from *AIChE J., 58, 3341 (2012)* [49]

[b]h_v (kJ/mol) for Al$_2$O formation is considered by assuming the pathway for Al$_2$O$_3$ evaporation as: 4/3 Al + 1/3 Al$_2$O$_3$ $\rightarrow$ Al$_2$O(g) $\rightarrow$ 2Al(g) + 1/2 O$_2$(g; [155]

metal at shell-core interface (Fig. 16); (4) Molten metal from unreacted core diffuses in opposite direction through the ash layer to react with O_2 at particle surface (Fig. 16); (5) Pressure gradient in nanoparticle core opposing the inward diffusion of O_2 and resulting in rupturing or thinning of ash layer [12] is not considered; (6) D_s driven shape parameter factors account for particle morphology.

The Damköhler number (Da) determines the relative roles of reaction (Da $\ll$ 1) or, diffusion limited (Da $\gg$ 1) oxidation mechanisms. It is defined for reacting species (m = O_2 or, metal) diffusing through mediums (n = gas film or, ash layer) as:

$$Da_{(m|n)} = \frac{\tau_{diff(m|n)}}{\tau_{rxn}} \tag{59}$$

Characteristic reaction time τ_{rxn} for surface oxidation of nanoparticles is defined as:

$$\tau_{rxn} = \frac{1}{\zeta_{SV}k_f\left(T, d_p\right)} \tag{60}$$

where, $\zeta_{SV} = A_p/V_p$ is surface-to-volume ratio (m^{-1}) and $k_f\left(T, d_p\right)\left[\sim \alpha_{oxid}\exp\left(-E_{oxid}/k_bT_p\right)\right]$ is the temperature and size (based on Al nanoparticle oxidation studies in size regimes of: <50 nm, 50–100 nm and >100 nm [139]) dependent first-order reaction rate coefficient (see Table 3). Characteristic diffusion time $\tau_{diff(m|n)}$ for species, m diffusing through medium, n is defined as:

$$\tau_{diff(m|n)} = \frac{1}{\zeta_{SV}^2 D_{(m|n)}} \tag{61}$$

In this study, the following oxidation routes are considered:
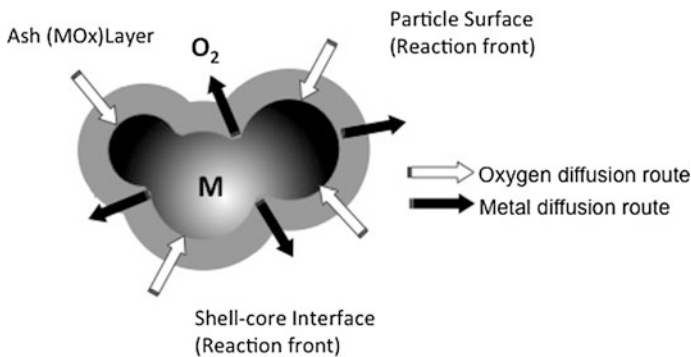
Fig. 16 Schematic for shell-core oxidation model

a. Bare metal particle: Diffusion of O_2 through the gas film: For all cases studied, characteristic $Da_{(O_2|Gas)} \ll 1$ (where $\tau_{diff(O_2|Gas)}$ is determined from Eq. 61 using $D_{O_2|Gas}$) for O_2 diffusion to the bare particle surface indicates the process to be always reaction controlled. Hence, the reaction rate is expressed as:

$$\dot{\omega}_{O_2|Gas} = -\frac{dn_{O_2}}{dt} = A_p k_f C_{O,\infty} \tag{62}$$

b. Oxide coated particle: Oxide shell formation prompts the following parallel processes: (i) *Diffusion of O_2 through oxide shell to core surface:* Net oxidation rate, mainly governed by the reaction at the *core metal surface* (Fig. 16), is derived as:

$$\dot{\omega}_{O_2|Ash} = -\frac{dn_{O_2}}{dt} = \frac{A_p k_f C_{O,\infty}}{1 + \dfrac{Da_{(O_2|Ash)}}{Z_{O_2}}} \tag{63}$$

and, (ii) *Diffusion of molten metal through oxide shell to particle surface:* Net oxidation rate, mainly governed by the reaction at the *particle surface* (Fig. 17), is derived as:

$$\dot{\omega}_{M|Ash} = -\frac{dn_M}{dt} = \frac{A_p k_f C_{M,c}}{1 + \dfrac{Da_{(M|Ash)}}{Z_M}} \tag{64}$$
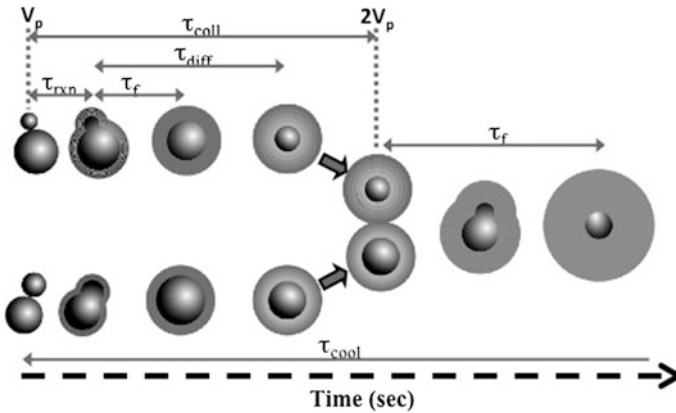
Fig. 17 Schematic of the relative time scales of events during nanoparticle synthesis undergoing surface oxidation and simultaneous collision-coalescence processes where in for typical energetic oxidation processes: $\tau_{cool} > \tau_{coll} > \tau_f > \tau_{diff} > \tau_{rxn}$

Equations 63 and 64 are derived using the scaling law relations: $A_p/A_c = \left(V_p/V_c\right)^{D_s/3}$ (self-similar shrinking core assumption in feature 1 above and Fig. 16) between the particle and its core surface area and volume such that the morphological complexity are accounted for through the non-dimensional shape parameters: $Z_{O_2} = \sqrt{\frac{4\pi}{A_p} \frac{\lambda^2}{\zeta_{sv}(\lambda-1)}}$ (for O_2 diffusing out through the ash layer) and $Z_M = \frac{1}{\lambda^2} Z_{O_2}$ (for metal diffusing in through the ash layer) along with $\lambda = \left(V_p/V_c\right)^{D_s/6}$. The boundary conditions used for O_2 concentrations [150] in Eq. 63 are: $C_o\left(A_p\right) = C_{o,\infty}$; $C_o(A_c) = 0$ while those for the metal concentrations in Eq. 64 are: $C_M(A_c) = C_{M,c}$; $C_M\left(A_p\right) = 0$. Characteristic $Da_{(O_2|Ash)}$ (O_2 diffusion through the ash layer) and $Da_{(M|Ash)}$ (metal diffusion through the ash layer) are calculated from Eqs. 59 and 60 using the respective $\tau_{diff(O_2|Ash)}$ and $\tau_{diff(M|Ash)}$ (Eq. 61) as estimated from $D_{O_2|Ash}$ and $D_{M|Ash}$. It is noted that Eqs. 63 and 64, by their mechanistic design, shall drive the oxidation to be reaction limited or, diffusion limited based on the expressions: $\frac{Da_{O_2|Ash}}{Z_{O_2}}$ and $\frac{Da_{M|Ash}}{Z_M}$ being $\ll 1$ or, vice versa respectively.

Specifically, for the Al/Al_2O_3 case-study used here to discuss the results obtained from the present model, the extent of conversion α (i.e., amount of Al converted to Al_2O_3) is defined as [139, 140, 150]:

$$2Al + \frac{3}{2}\alpha O_2 \rightarrow (1-\alpha)Al + \alpha Al_2O_3 \text{ where, } \alpha = \frac{2n_{Al_2O_3}}{2n_{Al_2O_3} + n_{Al}} \tag{65}$$
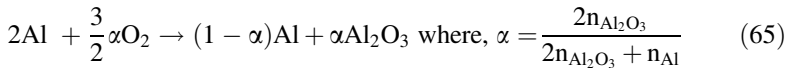
Finally, the stoichiometric species balance results in the net oxidation rate as:

$$\dot{\omega}_{O_2} = \dot{\omega}_{O_2|Ash} + \frac{3}{4}\dot{\omega}_{Al|Ash} \tag{66}$$

Also, to account for compositional changes, mean particle density, ρ_p and surface tension, σ_p used throughout the simulations for the Al/Al_2O_3 system are estimated as:

$$\rho_p = \varphi_{Al}\rho_{Al} + \left(1 - \varphi_{Al_2O_3}\right)\rho_{Al_2O_3}$$
$$\sigma_p = \varphi_{Al}\sigma_{Al} + \left(1 - \varphi_{Al_2O_3}\right)\sigma_{Al_2O_3}$$

where, ρ_{Al} and $\rho_{Al_2O_3}$ are taken to be the bulk solid densities: $\rho_{s(Al)}$ and $\rho_{s(Al_2O_3)}$, whereas surface tension of Al, σ_{Al} is calculated from $\sigma_{Al}(T_p)$ and $\sigma_{(Al_2O_3)}$ is taken as $\sigma_{s(Al_2O_3)}$ or, $\sigma_{l(Al_2O_3)}$ for $T_p < T_{m(Al2O3)}$ or, vice versa respectively (refer to Table 3).

4.1.5 Energy Balance

The net rate of bulk energy increase E_p, in a nanoparticle/aggregate due to coalescence and oxidation, compensated by the rate of heat losses by conduction and evaporation (radiation being negligible in nano-sized particles [44]) is given as:

$$\frac{dE_p(T_p)}{dt} = \left(m_M c_{p(M)} + m_{MOx} c_{p(MOx)}\right)\frac{dT_p}{dt} = \dot{E}_{coal} + \dot{E}_{oxid} - \dot{E}_{cond} - \dot{E}_{evap} \quad (67)$$

$\dot{E}_{coal}$, based on coalescence rate (Eq. 34) for surface energy reduction, is given as [44]:

$$\dot{E}_{coal} = -\sigma_p \frac{dA_p}{dt} = \frac{\sigma_p}{\tau_f}\left(A_p - A_{sph}\right) \quad (68)$$

$\dot{E}_{oxid}$ is calculated from oxygen consumption rate $\dot{\omega}_{O_2}$ obtained from Eq. 66 as:

$$\dot{E}_{oxid} = \dot{\omega}_{O_2} \frac{H^{\circ}_{rxn}}{N_{av}} \quad (69)$$

where, H°_{rxn} is the enthalpy of metal oxidation (kJ mol^{-1}).

$\dot{E}_{cond}$ for the rate of heat loss via conduction is given as:

$$\dot{E}_{cond} = \frac{R_{kin}\left(T_p - T_g\right)}{1 + \left(\dfrac{R_{kin}}{R_{Ash}}\right)} \quad (70)$$

where, $R_{Ash} = k_{ash}\frac{\sqrt{4\pi A_p}}{\lambda - 1}$ is the resistance term for heat conduction through the ash layer whereas, $R_{Kin} = m_g c_g \frac{p_g A_p}{\sqrt{2\pi m_g k_b T_g}}$ accounts for collisions with gas molecules at the particle surface as derived from kinetic theory [44]. Here, the assumption of lumped heat in the metal core is valid for $c_{p(M)} > c_{p(MOx)}$.

Finally, $\dot{E}_{evap}$ for the rate heat loss via evaporation is formulated as:

$$\dot{E}_{evap} = \frac{\varepsilon_{kin}(h_v/N_{av})A_p}{1 + \left(\dfrac{\varepsilon_{Kin}}{\varepsilon_{Diff}}\right)} \quad (71)$$

where, $\varepsilon_{Diff} = D_{M|Ash}C_{M,c}\frac{\sqrt{4\pi A_p}}{\lambda - 1}$ is the contribution from molten core metal diffusing through ash layer which competes with $\varepsilon_{Kin} = \frac{p_{drop}}{\sqrt{2\pi k_b T_p m_M}}$ due to evaporation of the molten metal from particle surface [12] where vapor pressure on a droplet is related to that on a flat surface at temperature, T_p via Kelvin relation:

$$p_{drop} = p_{sat}(T_p) \exp\left(\sqrt{\frac{\pi}{A_p}} \frac{4\sigma_p v_{mol}}{R_u T_p} \right) \tag{72}$$

For completely oxidized particles, $\dot{E}_{evap}$ is calculated from the ε_{Kin} term only based on h_v, p_{drop} and p_{sat} of pure metal oxide. The temperature ranges in the present study makes oxide shell evaporation, although built into the model as a safeguard against exceedingly high particle temperatures, negligible due to the fact that $T_{mp(M)} \ll T_{mp(MOx)}$ as well as p_{sat} being extremely low for most metal oxides. All thermochemical and physical properties used in the aforementioned equations for the simulation of Al/Al_2O_3 system in the present study are charted out in Table 3. All notations used here are reported at the end of the article.

4.2 Modeling Surface Oxidation: Coagulation Driven KMC Model

The KMC model presented here is built on the earlier coagulation driven constant-number (*constant-N*) MC with periodic boundary conditions as developed in [112] and described in details in the previous Sect. 3.2. As also mentioned before, the current MC algorithm operates based on the probability of occurrence of a coagulation (p_{ij}) event as represented by Eq. 49 under Sect. 3.2, wherein the MC particles undergoing coagulation are replenished by replicating the system with copies of the surviving particles whenever the particle number drops to 50% of the initial number, thereby enabling a computationally efficient method without loss of accuracy. Here the $\beta_{max} = f(V_p, \rho_p, T_p, D_s)$, as per Eq. 51, is estimated from all particles in the system. At any step, for $p_{ij} \geq R \in [0, 1]$, a collision event between two randomly chosen particles (i and j) is accompanied by an advancement of the MC time-step ΔT_{MC} (mean inter-event time between successive coagulations), as calculated from the inverse of the sum of the rates of all possible collision events and represented by Eqs. 44–46 in the previous Sect. 3.2.

Here in simulating the surface of the fractal-like aggregates, within each ΔT_{MC}, Eqs. 34 and 62 [bare metal particles] or, 66 [oxide coated particles] and 67 are numerically solved for coalescence, oxidation and energy/species conservations for the ensemble particles. The schematic in Fig. 17 elucidates the characteristic time scales governing the inter-play between the aforementioned processes i.e., collision (τ_{coll}), fusion (τ_f) and diffusion (τ_{diff}) or, reaction (τ_{rxn}) limited oxidation in relation to the characteristic time taken to quench the energetic processes in a particle (τ_{cool}). To capture the real physico-chemical processes, the rate-determining characteristic time, τ_{Char} is taken as the fastest amongst τ_{coll}, τ_f, τ_{diff} and τ_{rxn}, and it is used as the time step Δt within each ΔT_{MC} as:

$$\Delta t = \frac{\Delta T_{MC}}{k_{max}} \text{ where, } k_{max} = \frac{\Delta T_{MC}}{\tau_{Char}} \times k \qquad (73)$$

where, k_{max} is the number of iteration loops for the numerical integrations ($k \sim 10$, or 100 to ensure accuracy). Typical particle temperature profiles obtained from simulations with $N_{MC} = 5000$ and 10,000 showed negligible variations. Since the computational time for 5000 particles is ~ 3 days as compared to ~ 3–5 weeks for 10,000 particles, all results presented henceforth are for $N_{MC} = 5000$ particles.

4.3 Effect of Morphology and Non-isothermal Coalescence on Surface Oxidation of Metal Nanoparticles: Results from the Study

All results presented here are for the representative case-study of the oxidation and evolution of Al/Al$_2$O$_3$ nanoparticles during gas-phase synthesis.

4.3.1 Estimation of Primary Particle Size

For the estimation of the mean primary particle size, the particle ensemble is assumed to be "mostly spherical" when the ensemble averaged normalized excess surface area $\langle (A_p - A_{sph})/A_{sph} \rangle < 0$. As an example, for $T_g = 800$ K, the primary particle size is fixed at $t = 7.52 \times 10^{-5}$ s when $\langle (A_p - A_{sph})/A_{sph} \rangle > 0$ (Fig. 18a) which corresponds to the crossing point between τ_f and τ_{coll} marking the onset of aggregation [85] such that spherical particles formed for $\tau_f \ll \tau_{coll}$ constitute the aggregates formed when $\tau_f > \tau_{coll}$ (collisions faster than coalescence). Keeping in mind that the slow approach of τ_f towards τ_{coll} ($d\tau_f/dt \ll d\tau_{coll}/dt$) at the crossing point might lead to the formation of oblong particles with long necks [44] we strictly use $\langle (A_p - A_{sph})/A_{sph} \rangle > 0$ as the criterion for primary particle size selection to ensure the choice of spherical primary particles only. Furthermore, due to periodic boundary conditions, sufficient collisions ensure a log-normal distribution for the uniform spherical particles formed before the onset of aggregation, beyond which the log-mean diameter of the most recent particle distributions is fixed as the primary particle size for the rest of the particle evolution study. This is corroborated by the probability distribution function of particle sizes in Fig. 18b at $t = 7.5 \times 10^{-5}$ s (corresponding to $\langle (A_p - A_{sph}/A_{sph}) \rangle \geq 0$ in Fig. 18a indicating a log-normal distribution with estimated log-mean diameters of <d$_{prim}$> ~ 3.8 nm ($\sigma_g = 1.93$) which is commensurate with <d$_{prim}$> (marked on Fig. 18a) used as the primary particle size (A_0, V_0) for the future particle evolution studies.
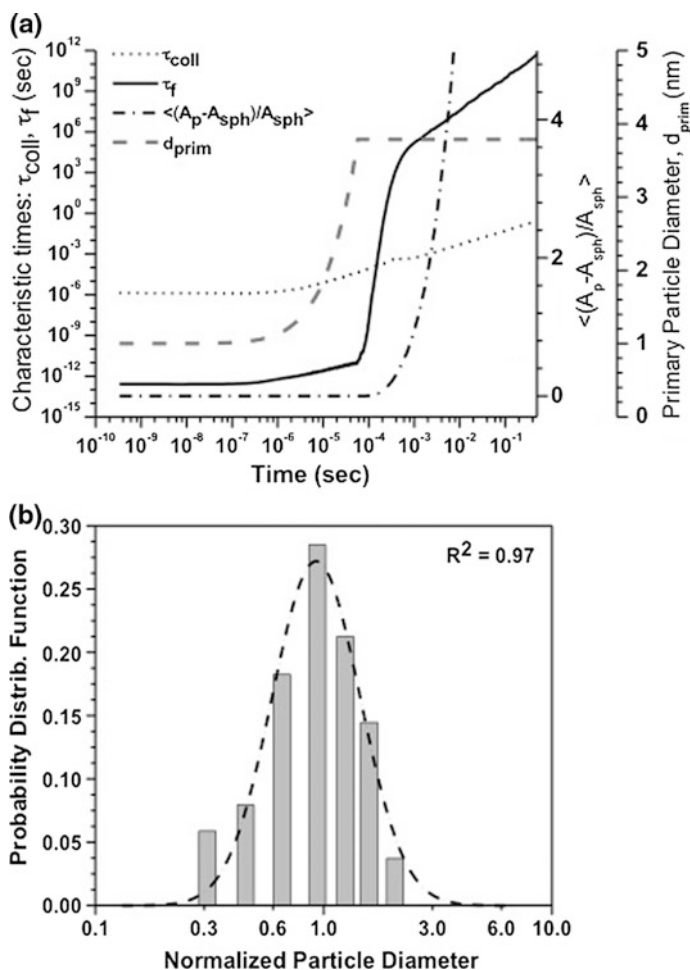
Fig. 18 **a** Determination of primary particle size, d_{prim} (nm) corresponding to cross-over point of characteristic fusion (τ_f) and collision (τ_{coll}) times; **b** Corresponding probability distribution function of primary particle sizes along with a peak fit indicating that the primary particles follow log-normal distribution with $\langle d_{prim} \rangle \sim 3.8$ nm and $\sigma_g = 1.93$ ($T_g = 800$ K; $p_g = 1$ atm and $\varphi = 10^{-6}$)

4.3.2 Estimation of Particle Morphology

Using A_0 and V_0 in Eq. 50, $D_s = 2.35$ and 2.94 at two different stages of particle evolution are estimated from the slopes of the two typical linear fits to $\ln(A_p/A_0)$ versus $\ln(V_p/V_0)$ plots (Fig. 19) for $T_g = 800$ K, $p_g = 1$ atm and $\varphi = 10^{-6}$. The temporal variation of D_s in Fig. 20 depicts the particle morphology evolution in relation to the different characteristic time scales τ_f, τ_{coll}, τ_{rxn} and $\tau_{diff(O_2|Ash)}$ for the

Fig. 19 Typical plots of ln (V_p/V_0) vs $\ln(A_p/A_0)$ indicating good linear fits used to determine D_s from their slopes as described by Eq. (3). Representative case studied for $T_g = 800$ K, $p_g = 1$ atm and $\varphi = 10^{-6}$
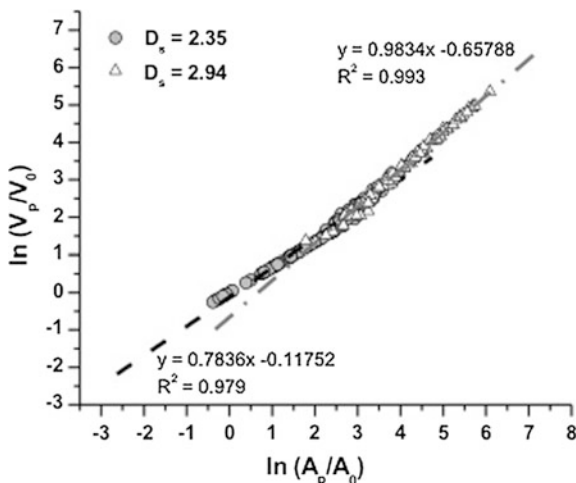
Fig. 20 Temporal evolution of typical characteristic times, τ_f, τ_{coll}, τ_{rxn} and $\tau_{diff(O_2|Ash)}$ and the significance of their cross-over points with respect to the fractal dimension, D_s of nanoparticles studied at $T_g = 800$ K; $p_g = 1$ atm and $\varphi = 10^{-6}$
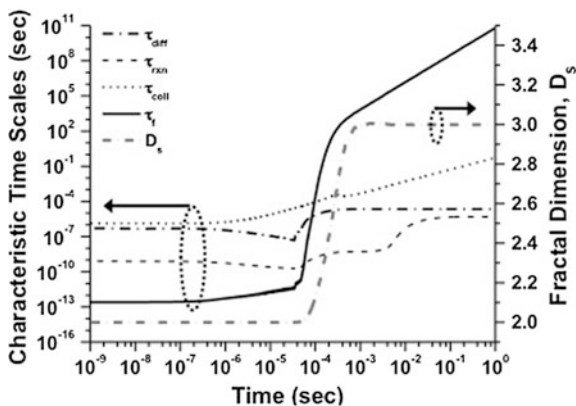
aforementioned operating conditions. Rapid coalescence at initial times, as compared to collision, oxidation due to surface reaction or, diffusion through the ash layer ($\tau_f \ll \tau_{coll}$, τ_{rxn} or $\tau_{diff(O_2|Ash)}$), generates spherical particles ($D_s = 2$). But hard oxide shell formation slows down self-diffusion, and hence coalescence. Thus, the particles transition from the molten viscous to the solid state diffusion regime as τ_f rapidly crosses τ_{rxn} and $\tau_{diff(O_2|Ash)}$ followed by τ_{coll}, hereby quenching the exothermic coalescence-oxidation processes. Corresponding to these crossing points D_s rapidly deviates from 2 (spheres) towards $D_s > 2$ (non-spherical) leading to aggregate formations ($D_s \sim 3$ at later stages in Fig. 20). At lower T_g cases, surface oxidation due to extremely retarded metal diffusion through oxide layer is negligible.

4.3.3 Surface Oxidation and Evolution of Fractal-like Al/Al$_2$O$_3$ Nanoparticles

Simulation results presented in this section are based on the case studies from Mukherjee et al.'s study [44] depicting typical laboratory or, industrial gas-phase synthesis of Al nanoparticles under standard processing conditions of: $T_g = 400$, 600, 1000, 1400 K; $p_g = 0.1$ and 1 atm; and $\phi = 10^{-6}$ and 10^{-8}. Specifically, here we will focus on the case studies for varying background gas temperatures (T_g) to elucidate the role of exothermic coagulation/coalescence mediated surface oxidation on the energetic behavior of fractal-like nano-aggregates. For further details on similar studies describing the role of other processing parameters such as gas pressure and volume loadings, the readers can refer to Mukherjee et al.'s [44] work. Unless mentioned otherwise, all simulation results presented here are for the MC system with initial particle diameters, $d_{ini} = 1$ nm in 5000 particles system.

In contrast to the previous coalescence studies [44] the non-linear energetic coupling between coalescence and oxidation is manifested here through the drastic rise in mean particle temperature $\langle T_p \rangle$ for $T_g = 400$ K giving rise to the unique bi-modal temperature profiles for $T_g = 1000$ and 1400 K (Fig. 21a). An early rise in $\langle T_p \rangle$ (bold arrow in Fig. 21a) is followed by a subsequent reduction and the formation of a second peak that finally equilibrates to T_g. In early stages, higher T_g promotes thermally activated processes such as: (1) non-isothermal coalescence due to competing collision-coalescence events ($\tau_f \ll \tau_{coll}$ in Fig. 21b) and (2) O$_2$ and molten Al (in this case) diffusion through relatively thin oxide layers. Specifically, when $\langle T_p \rangle > 1000$ K, enhanced Al diffusion promotes rapid oxidation leading to hard oxide shell formation, which, in turn, retards coalescence and results in the temporary reduction of $\langle T_p \rangle$. But the oxide shell insulation also retards conductive and evaporative heat losses from the Al core which, for small cluster sizes ($d_{prim} = 4.7$ and 8.4 nm for $T_g = 1000$ and 1400 K respectively from Fig. 21b), activate a second heat release mechanism dominated by the combined metal-metal oxide sintering (Fig. 21a and $\tau_f \ll \tau_{coll}$ in Fig. 21b). Thick oxide shells hinder both Al and O$_2$ diffusion and quench coalescence ($\tau_f > \tau_{coll}$ in Fig. 21b) through the final oxidation stages. Eventually, fractal-like structures with large surface-to-volume ratio, ζ_{SV} (Fig. 22) promote evaporative and conductive heat losses that relax $\langle T_p \rangle$ back to T_g.

In relation to the sequence of aforementioned events, the morphological evolution (Fig. 22a) indicates that increasing T_g delays the cross-over points between τ_f and τ_{coll}. This concurs with the formation of non-spherical clusters ($D_s > 2$) with larger d_{prim} (Fig. 21b) and lower ζ_{SV} (Fig. 22a). While an earlier onset of fractal-like structures ($D_s > 2$) coincides with the peak in $\langle T_p \rangle$ for $T_g = 400$ K, particles continue to coalesce into spheres ($D_s = 2$) until the second peak in $\langle T_p \rangle$ (Fig. 21a) for $T_g = 1000$ and 1400 K. Finally, fractal-like aggregates ($D_s = 3$) form to reduce ζ_{SV} to a constant lower bound value except for $T_g = 1400$ K, where $d\tau_f/dt \approx d\tau_{coll}/dt$ (see Fig. 21b) promotes the formation of partially sintered non-spherical particles ($D_s < 2.25$ in Fig. 22a).
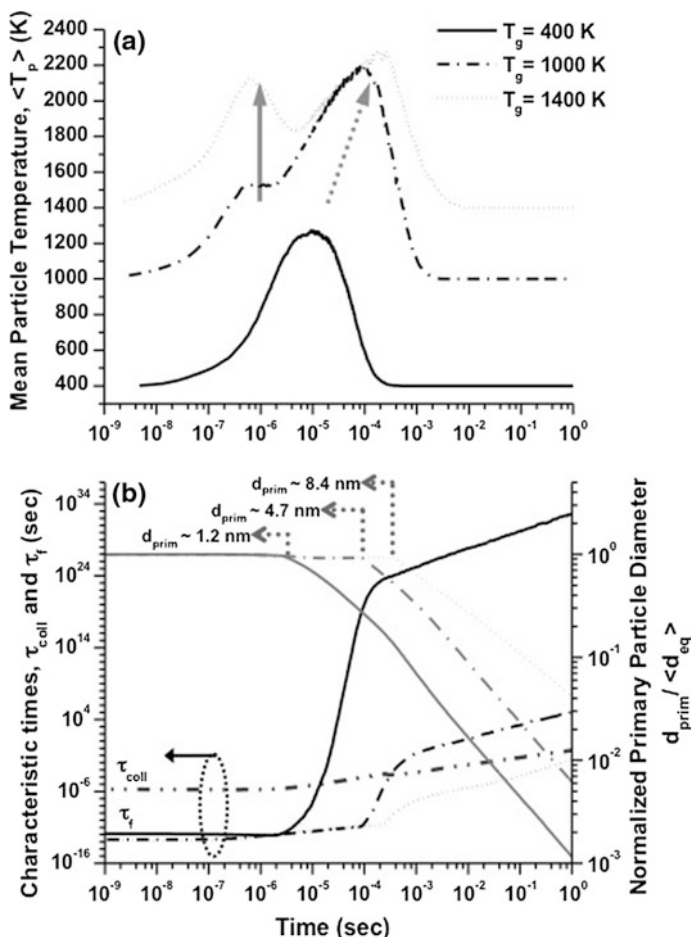
Fig. 21 Temporal variation of **a** mean particle temperatures, $\langle T_p \rangle$ and **b** characteristic collision (τ_{coll}), fusion (τ_f) times (*black lines*; left Y-axis) and primary particle diameters normalized by volume equivalent diameters, $d_{prim}/\langle d_{eq} \rangle$ (*gray lines*; right Y-axis) for $T_g = 400$, 1000 and 1400 K ($p_g = 1$ atm and $\varphi = 10^{-6}$). Corresponding d_{prim} values when $d_{prim}/\langle d_{eq} \rangle > 1$ for each of the T_g cases are indicated

In Fig. 22b, the extent of oxidation, α for $T_g = 400$ K indicates that spherical particles ($D_s = 2$) oxidize until 4×10^{-6} s (Fig. 22a) to form a critical shell ($\alpha = 0.3$ in Fig. 22b), beyond which partially sintered non-spherical particles with excess surface area ($D_s \sim 2$–2.5 in Fig. 22a) drive α to a maximum ($\alpha = 0.59$ and $d\alpha/dt \approx 0$ in Fig. 22b). But for $T_g = 1000$ and 1400 K, subsidence of the first peak in $\langle T_p \rangle$ (Fig. 21a) in unison with $\alpha = 0.3$ (Fig. 22b) indicates surface oxidation as the dominant exothermic contributor until this point. In the later stages, the formation of spherical particles ($D_s = 2$) until $\sim 10^{-4}$ s (Fig. 22a) implies a dominant coalescence (as discussed earlier), wherein most of the oxidation ($> 85\%$) has
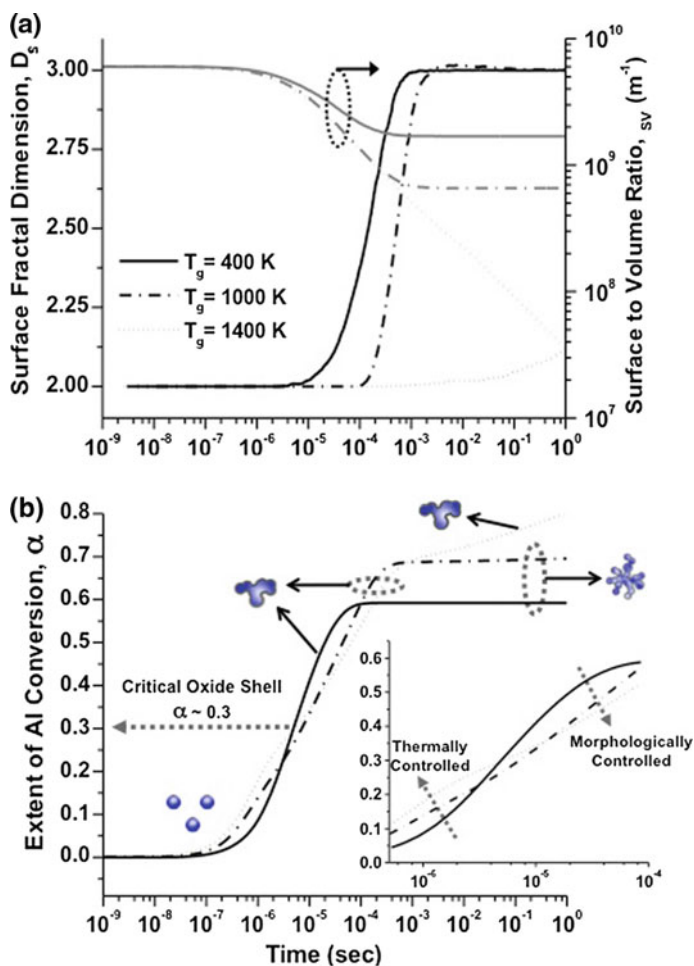
Fig. 22 Temporal variation of **a** surface fractal dimension, D_s (*black lines*; left y-axis); surface-to-volume ratio, ζ_{SV} (*gray lines*; right y-axis) and **b** extents of Al conversion, α in NPs synthesized at $T_g = 400$, 1000 and 1400 K ($p_g = 1$ atm and $\varphi = 10^{-6}$). Schematics indicate corresponding morphology during different stages of particle evolution (*Inset* Blow-up of α around the inflexion point, i.e., critical oxide shell, $\alpha \sim 0.3$)

already ensued (Fig. 22b). Eventually, while non-spherical particles ($D_s \sim 2$–2.5) attain the maximum α and fractal-like structures ($D_s = 3$) at later times ($>10^{-4}$ s) for $T_g = 1000$ K. In contrast, for $T_g = 1400$ K, the particles continue to exhibit a steady rise in α (Fig. 22b). The inflexion at $\alpha = 0.3$ (inset in Fig. 22b and prominent for $T_g = 1400$ K) separates the two energetic regimes: (1) thermally controlled oxidation prompting higher α with increasing T_g before the critical oxide shell formation and (2) morphologically controlled oxidation beyond this point, wherein non-spherical particles for $T_g = 400$ K ($D_s = 2$–2.5 from Fig. 22a

and $\langle T_p \rangle > 1000$ K from Fig. 21a) attain higher α than those for the other T_g ($D_s = 2$ till $\sim 10^{-4}$ s from Fig. 22a, while $\langle T_p \rangle > 1200$ K from Fig. 21a). This is specifically exemplified by the $T_g = 1400$ K case (Fig. 22b).

To probe into the roles of classical oxidation mechanisms, Fig. 23 compares residence times from KMC simulations (t_{MC}) with those for typical reaction ($t_{Reaction}$) and diffusion ($t_{Diffusion}$) limited processes theoretically determined based on characteristic times for complete conversion via diffusion ($T_{Diffusion}$) or reaction ($T_{Reaction}$) as [150]:

$$\frac{t_{Reaction}}{T_{Reaction}} = 1 - (1 - \alpha)^{1/3}; \quad T_{Reaction} = \frac{\rho_{mol(Al)} d_p}{(8/3) k_f C_{O,\infty}} \tag{74a}$$

$$\frac{t_{Diffusion}}{T_{Diffusion}} = 1 - 3(1 - \alpha)^{2/3} + 2(1 - \alpha); \quad T_{Diffusion} = \frac{\rho_{mol(Al)} d_p^2}{32 D_{O_2|Ash} C_{O,\infty}} \tag{74b}$$

where, $\rho_{mol(Al)}$ is the molar density of Al (mol m^{-3}). For $T_g = 400$ K, unlike common nanoparticle oxidation models [12, 139] the mechanism starts off as

reaction-limited but shifts between diffusion and reaction limited regimes (morphology controlled) as the particle evolves whereas for $T_g = 1400$ K, immediately after the initial oxide shell formation, t_{MC} uniformly follows the diffusion-limited mechanism trend (thermally activated with dominant coalescence) leading to continuous increase in α as discussed above.

Similar studies were also carried out for different background gas pressures (p_g) and volume loadings (ϕ). These studies also indicate the familiar bi-modal temperature profile depicting the energetic behavior of the fractal-like Al nanoparticles during their exothermic coalescence mediated surface oxidations. The energetic behavior for the aggregates were enhanced for lower gas pressure and lower volume loadings due to the lack of gas molecules to facilitate the heat dissipation from the nanoparticles in the former case, and the reduced collisions from lower particle concentrations promoting the exothermic coalescence in the latter. For further details on these studies, the readers can refer to Mukherjee et al. [49].

4.3.4 Implications of Coalescence-Driven Fractal like Morphology on the Surface Oxidation of Al/Al$_2$O$_3$ Nanoparticles

The unique contribution of the study presented here can be realized by comparing results for Al nanoparticle oxidation starting with an initial diameter, $d_{ini} \sim 1$ nm at $T_g = 400$ K and $p_g = 1$ atm while accounting for: (1) exothermic coalescence mediated morphological evolution of non-spherical nanoparticles generated via collision-coalescence mechanisms and (2) no morphological variations or, exothermic coalescence under the assumption of instant coalescence of colliding particles into spheres. As seen from Fig. 24a, b for $T_g = 400$ K, as particles in case 1 evolve from spherical shapes ($D_s = 2$) into fractal-like structures ($D_s = 3$), the extents of oxidation, α for case 1 is significantly higher than that for case 2 (black lines for case 1 and gray lines for case 2). In conjunction to this, final ζ_{SV} (Fig. 24b) for particles with complex morphology and larger surface area (case 1) is significantly higher than that for spherical particles (case 2), thereby supporting the enhanced α for case 1. Moreover, in case 1 the onset of fractal-like aggregates ($D_s > 2$ in Fig. 24a) generates particles with larger volume equivalent diameters $<d_{eq}>$ (Fig. 24b) as compared to their instantly coalesced spherical counterparts. It is noted that for case 1 significant amount of oxidation ($\alpha \sim 0.59$) ensues in the size regime of $<d_{eq}> <10$ nm ($t \sim 10^{-4}$ s.). Enhanced coalescence mediated thermal activities in spherical particles dominate the early stages till $<d_{eq}> \sim 1.5$ nm ($t \sim 4 \times 10^{-6}$ s) beyond which, until $<d_{eq}> \sim 10$ nm ($t \sim 10^{-4}$ s), coalescence mediated non-spherical morphology drives the final stages of particle oxidation, i.e., $\alpha \sim 0.3$–0.59 as $D_s \sim 2$–2.5 (as discussed earlier). In comparison, case 2 shows much slower and yet, continuous rise all through its evolution, irrespective of particle size or morphology.

Fig. 24 KMC simulations comparing temporal variations of: **a** Extents of conversion, α (*solid lines* on left y-axis) and surface fractal dimension, Ds (*dash-dot lines* on right y-axis); **b** volume equivalent diameter, <deq> (*solid line* on left y-axis) and surface to volume ratio, ζ$_{SV}$ (*dash-dot line* on right y-axis) (dini = 1 nm, Tg = 400 K, pg = 1 atm, and φ = 10^{-6}) for particles undergoing exothermic coalescence mediated morphological evolution (*all black lines*) and particles assumed to be spherical without any coalescence (*all gray line*)
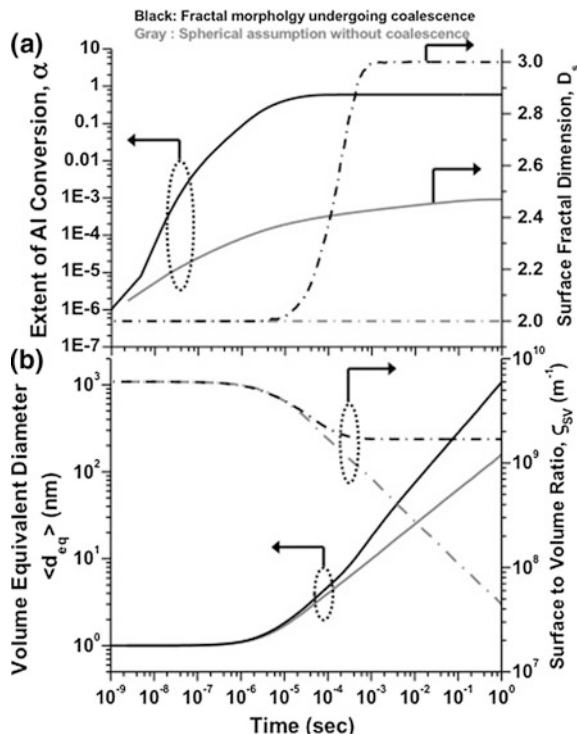
5 Conclusion

In this chapter, we discussed the development of various computational models to study the fate, transport and evolution of metal NPs grown via aerosol routes. The results and discussions indicated the role of process parameters during gas-phase synthesis of metal NPs in tailoring their final sizes, shapes, compositions and structures, which, in turn, tune their surface reactivity and energetic behaviors. Homogeneous nucleation derived from CNT assumptions was introduced as the first step towards the inception of critical clusters as the new nanophase structures. Furthermore, a discussion on models that deviate from CNT was invoked that included the role of size-dependent surface tension as well as the breakdown of steady-state assumptions for small cluster sizes as revealed by our recently developed Gibbs' free energy-driven KMC model for vapor-phase nucleation studies. The sizes, shapes, and rates of formation of critical clusters determine the subsequent growth mechanisms, via surface growth and coagulation, for the seeding NPs.

We presented a KMC model that accounted for the ensemble effects of NP collision/coalescence phenomena, without any a priori constraint on the particle size distribution. The heat generation during typical non-isothermal coalescence phenomena was shown to bear a strong effect on the coalescing dynamics of metal

NPs that, in turn, played a significant role in dictating their final morphologies and sizes. Finally, the KMC model was further extended to study the effect of surface oxidation on the formation and growth of fractal-like nano-aggregates. These results elucidated the role of process parameters (background gas temperatures, gas pressures and particle volume loadings) in tailoring the energetic properties of metal/metal oxide nanostructures generated via gas phase synthesis. Specifically, results for non-isothermal coalescence in fractal-like particle morphology, when compared to those obtained with the assumption of instantly coalescing spherical particles clearly indicated the significant impact of the former case on surface oxidation of non-spherical metal NPs.

The computational studies consolidated in this chapter pave the path for our on-going efforts in developing a unified KMC-based model to simulate NP life-cycles from their inception to final growth and evolution into oxidized (surface passivated) fractal-like aggregates. Such studies will lay the foundation for fundamental theoretical understanding and, hitherto elusive comparisons with experimental results for the fate of metal NPs generated from vapor-phase synthesis.

References

1. Renie J et al (1982) Aluminum particle combustion in composite solid propellants. Purdue University, West Lafayette, Ind
2. Bakhman N, Belyaev A, Kondrashkov YA (1970) Influence of the metal additives onto the burning rate of the model solid rocket propellants. Phys Combust Explos 6:93
3. Chiaverini MJ et al (1997) *Instantaneous regression behavior of HTPB solid fuels burning with GOX in a simulated hybrid rocket motor.* Int J Energ Mat Chem Propul 4(1–6)
4. Mench M, Yeh C, Kuo K (1998) Propellant burning rate enhancement and thermal behavior of ultra-fine aluminum powders(Alex). Energ Mat-Prod, Process Charac 30–1
5. Ritter H, Braun S (2001) High explosives containing ultrafine aluminum ALEX. Propellants, Explos, Pyrotech 26(6):311–314
6. Ilyin A et al (2002) Characterization of aluminum powders I. Parameters of reactivity of aluminum powders. Propellants Explos Pyrotech 27(6):361–364
7. Brousseau P, Anderson CJ (2002) Nanometric aluminum in explosives. Propellants, Explos, Pyrotech 27(5):300–306
8. Weiser V, Kelzenberg S, Eisenreich N (2001) Influence of the metal particle size on the ignition of energetic materials. Propellants, Explos, Pyrotech 26(6):284–289
9. Pantoya ML, Granier JJ (2005) Combustion behavior of highly energetic thermites: nano versus micron composites. Propellants, Explos, Pyrotech 30(1):53–62
10. Pivkina A et al (2004) Nanomaterials for heterogeneous combustion. Propellants, Explos, Pyrotech 29(1):39–48
11. van der Heijden AEDM et al (2006) Processing, application and characterization of (ultra) fine and nanometric materials in energetic compositions. Shock Compression Condens Matter Pts 1 and 2 845:1121–1126

12. Rai A et al (2006) Understanding the mechanism of aluminium nanoparticle oxidation. Combust Theor Model 10(5):843–859
13. Mason BA et al (2013) Combustion performance of several nanosilicon-based nanoenergetics. J Propul Power 29(6):1435–1444
14. Piekiel NW et al (2013) Combustion and material characterization of porous silicon nanoenergetics. In: 26th Ieee international conference on micro electro mechanical systems (Mems 2013) p 449–452
15. Thiruvengadathan R et al (2012) Combustion characteristics of silicon-based nanoenergetic formulations with reduced electrostatic discharge sensitivity. Propellants, Explos, Pyrotech 37(3):359–372
16. Prakash A, McCormick AV, Zachariah MR (2005) Synthesis and reactivity of a super-reactive metastable intermolecular composite formulation of Al/KMnO$_4$. Adv Mat 17(7):900–
17. Perry WL et al (2004) Nano-scale tungsten oxides for metastable intermolecular composites. Propellants, Explos, Pyrotech 29(2):99–105
18. Perry WL et al (2007) Energy release characteristics of the nanoscale aluminum-tungsten oxide hydrate metastable intermolecular composite. J Appl Phys 101(6)
19. Berner MK, Zarko VE, Talawar MB (2013) Nanoparticles of energetic materials: synthesis and properties (review). Combust Explosion Shock Waves 49(6):625–647
20. Prakash A, McCormick AV, Zachariah MR (2005) Tuning the reactivity of energetic nanoparticles by creation of a core-shell nanostructure. Nano Lett 5(7):1357–1360
21. Zhang KL et al (2007) Synthesis of large-area and aligned copper oxide nanowires from copper thin film on silicon substrate. Nanotechnology 18(27)
22. Prakash A, McCormick AV, Zachariah MR (2004) Aero-sol-gel synthesis of nanoporous iron-oxide particles: A potential oxidizer for nanoenergetic materials. Chem Mater 16 (8):1466–1471
23. Subramanian S et al (2008) Nanoporous silicon based energetic materials, DTIC Document
24. Blobaum KJ et al (2003) Deposition and characterization of a self-propagating CuO$_x$/Al thermite reaction in a multilayer foil geometry. J Appl Phys 94(5):2915–2922
25. Ma E et al (1990) Self-propagating explosive reactions in Al/Ni multilayer thin-films. Appl Phys Lett 57(12):1262–1264
26. Gen M, Ziskin M, Petrov I (1959) A study of the dispersion of aluminium aerosols as dependent on the conditions of their formation. Doklady Akademii Nauk SSSR 127(2):366–368
27. Kwon YS et al (2003) Passivation process for superfine aluminum powders obtained by electrical explosion of wires. Appl Surf Sci 211(1–4):57–67
28. Kwon YS et al (2007) Properties of powders produced by electrical explosions of copper-nickel alloy wires. Mater Lett 61(14–15):3247–3250
29. Sarathi R, Sindhu TK, Chakravarthy SR (2007) Generation of nano aluminium powder through wire explosion process and its characterization. Mater Charact 58(2):148–155
30. Tillotson TM et al (2001) Nanostructured energetic materials using sol-gel methodologies. J Non-Cryst Solids 285(1–3):338–345
31. Jacobson MZ, Turco RP (1995) Simulating condensational growth, evaporation, and coagulation of aerosols using a combined moving and stationary size grid. Aerosol Sci Technol 22(1):73–92
32. Biswas P et al (1997) Characterization of iron oxide-silica nanocomposites in flames. 2. Comparison of discrete-sectional model predictions to experimental data. J Mater Res 12 (3):714–723
33. Landgrebe JD, Pratsinis SE (1990) A discrete-sectional model for particulate production by gas-phase chemical-reaction and aerosol coagulation in the free-molecular regime. J Colloid Interface Sci 139(1):63–86
34. Lehtinen KEJ, Zachariah MR (2001) Self-preserving theory for the volume distribution of particles undergoing Brownian coagulation. J Colloid Interface Sci 242(2):314–318
35. Girshick SL, Chiu CP (1989) homogeneous nucleation of particles from the vapor-phase in thermal plasma synthesis. Plasma Chem Plasma Process 9(3):355–369

36. Panda S, Pratsinis SE (1995) Modeling the synthesis of aluminum particles by evaporation-condensation in an aerosol flow reactor. Nanostruct Mater 5(7–8):755–767
37. Prakash A, Bapat AP, Zachariah MR (2003) A simple numerical algorithm and software for solution of nucleation, surface growth, and coagulation problems. Aerosol Sci Technol 37(11):892–898
38. Mukherjee D, Prakash A, Zachariah MR (2006) Implementation of a discrete nodal model to probe the effect of size-dependent surface tension on nanoparticle formation and growth. J Aerosol Sci 37(10):1388–1399
39. Zachariah MR, Carrier MJ (1999) Molecular dynamics computation of gas-phase nanoparticle sintering: a comparison with phenomenological models. J Aerosol Sci 30 (9):1139–1151
40. Yasuoka K, Matsumoto M (1998) Molecular dynamics of homogeneous nucleation in the vapor phase. I. Lennard-Jones fluid. J Chem Phys 109(19):8451–8462
41. Lummen N, Kraska T (2005) Molecular dynamics investigation of homogeneous nucleation and cluster growth of platinum clusters from supersaturated vapour. Nanotechnology 16 (12):2870–2877
42. Li ZH et al (2007) Free energies of formation of metal clusters and nanoparticles from molecular simulations: Al-n with n = 2–60. J Phys Chem C 111(44):16227–16242
43. McGreevy RL (2001) Reverse Monte Carlo modelling. J Phys-Condens Matter 13(46): R877–R913
44. Mukherjee D, Sonwane CG, Zachariah MR (2003) Kinetic Monte Carlo simulation of the effect of coalescence energy release on the size and shape evolution of nanoparticles grown as an aerosol. J Chem Phys 119(6):3391–3404
45. Gillespie DT (1975) Exact method for numerically simulating stochastic coalescence process in a cloud. J Atmos Sci 32(10):1977–1989
46. Liffman K (1992) A direct simulation Monte-Carlo method for cluster coagulation. J Comput Phys 100(1):116–127
47. Kruis FE, Maisels A, Fissan H (2000) Direct simulation Monte Carlo method for particle coagulation and aggregation. AIChE J 46(9):1735–1742
48. Efendiev Y, Zachariah MR (2002) Hybrid Monte Carlo method for simulation of two-component aerosol coagulation and phase segregation. J Colloid Interface Sci 249(1):30–43
49. Mukherjee D, Wang M, Khomami B (2012) Impact of particle morphology on surface oxidation of nanoparticles: a kinetic Monte Carlo based study. AIChE J 58(11):3341–3353
50. Auer S, Frenkel D (2001) Prediction of absolute crystal-nucleation rate in hard-sphere colloids. Nature 409(6823):1020–1023
51. Valeriani C et al (2007) Computing stationary distributions in equilibrium and nonequilibrium systems with forward flux sampling. J Chem Phys 127(11)
52. Allen RJ, Valeriani C, Ten Wolde PR (2009) Forward flux sampling for rare event simulations. J Phys-Condens Matter 21(46)
53. Katz JL et al (1976) Condensation of a supersaturated vapor. III. The homogeneous nucleation of CCl4, CHCl3, CCl$_3$F, and C$_2$H$_2$C$_{14}$. J Chem Phys 65(1):382–392
54. Katz JL (1970) Condensation of a Supersaturated Vapor. I. The homogeneous nucleation of the *n*-alkanes. J Chem Phys 52(9):4733–4748
55. Oxtoby DW (1992) Homogeneous nucleation: theory and experiment. J Phys: Condens Matter 4(38):7627
56. Rusyniak M et al (2001) Vapor phase homogeneous nucleation of higher alkanes: dodecane, hexadecane, and octadecane. 1. Critical supersaturation and nucleation rate measurements. J Phys Chem B 105(47):11866–11872
57. Finney EE, Finke RG (2008) Nanocluster nucleation and growth kinetic and mechanistic studies: a review emphasizing transition-metal nanoclusters. J Colloid Interface Sci 317(2):351–374
58. Schmitt JL (1981) Precision expansion cloud chamber for homogeneous nucleation studies. Rev Sci Instrum 52(11):1749–1754

59. Wagner P, Strey R (1981) Homogeneous nucleation rates of water vapor measured in a two-piston expansion chamber. J Phys Chem 85(18):2694–2698

60. Hameri K, Kulmala M (1996) Homogeneous nucleation in a laminar flow diffusion chamber: the effect of temperature and carrier gas on dibutyl phthalate vapor nucleation rate at high supersaturations. J Chem Phys 105(17):7696–7704

61. Anisimov MP, Hameri K, Kulmala M (1994) Construction and test of laminar-flow diffusion chamber–homogeneous nucleation of Dbp and N-hexanol. J Aerosol Sci 25(1):23–32

62. Wyslouzil BE et al (1991) Binary nucleation in acid water-systems. 2. Sulfuric-acid water and a comparison with methanesulfonic-acid water. J Chem Phys 94(10):6842–6850

63. Viisanen Y, Kulmala M, Laaksonen A (1997) Experiments on gas-liquid nucleation of sulfuric acid and wafer. J Chem Phys 107(3):920–926

64. Fisk JA et al (1998) The homogeneous nucleation of cesium vapor. Atmos Res 46 (3–4):211–222

65. Ferguson FT, Nuth JA (2000) Experimental studies of the vapor phase nucleation of refractory compounds. V. The condensation of lithium. J Chem Phys 113(10):4093–4102

66. Zhang RY et al (2012) Nucleation and growth of nanoparticles in the atmosphere. Chem Rev 112(3):1957–2011

67. Lu HM, Jiang Q (2005) Size-dependent surface tension and Tolman's length of droplets. Langmuir 21(2):779–781

68. Lai SL et al (1996) Size-dependent melting properties of small tin particles: nanocalorimetric measurements. Phys Rev Lett 77(1):99–102

69. Tomanek D, Schluter MA (1986) Calculation of magic numbers and the stability of small Si clusters. Phys Rev Lett 56(10):1055–1058

70. Boustani I et al (1987) Systematic ab initio configuration-interaction study of alkali-metal clusters: Relation between electronic structure and geometry of small Li clusters. Phys Rev B 35(18):9437

71. Li ZH, Truhlar DG (2008) Cluster and nanoparticle condensation and evaporation reactions. Thermal rate constants and equilibrium constants of $Al(m) + Al(n-m) <-> Al(n)$ with n = 2–60 and m = 1–8. J Phys Chem C 112(30):11109–11121

72. Girshick SL, Agarwal P, Truhlar DG (2009) Homogeneous nucleation with magic numbers: aluminum. J Chem Phys 131(13)

73. Wyslouzil BE, Seinfeld JH (1992) Nonisothermal homogeneous nucleation. J Chem Phys 97 (4):2661–2670

74. Barrett JC (2008) A stochastic simulation of nonisothermal nucleation. J Chem Phys 128(16)

75. Domilovsky ER, Lushnikov AA, Piskunov VN (1979) Monte-Carlo simulation of coagulation processes. Izvestiya Akademii Nauk Sssr Fizika Atmosfery I Okeana 15 (2):194–201

76. Debry E, Sportisse B, Jourdain B (2003) A stochastic approach for the numerical simulation of the general dynamics equation for aerosols. J Comput Phys 184(2):649–669

77. Garcia A et al (1987) A Monte Carlo method of coagulation. Phys A 143:535–546

78. Smith M, Matsoukas T (1998) Constant-number Monte Carlo simulation of population balances. Chem Eng Sci 53(9):1777–1786

79. Efendiev Y, Zachariah MR (2003) Hierarchical hybrid Monte-Carlo method for simulation of two-component aerosol nucleation, coagulation and phase segregation. J Aerosol Sci 34(2):169–188

80. Davari SA, Mukherjee D (2017) Kinetic Monte Carlo simulation for homogeneous nucleation of metal nanoparticles during vapor phase synthesis. AIChE J. Accepted. doi:10. 1002/aic.15887

81. Pratsinis SE (1998) Flame aerosol synthesis of ceramic powders. Prog Energy Combust Sci 24(3):197–219

82. Mench MM et al (1998) Comparison of thermal behavior of regular and ultra-fine aluminum powders (Alex) made from plasma explosion process. Combust Sci Technol 135(1–6):269–292

83. Ozaki Y, Ichinose N, Kashū S (1992) Superfine particle technology. Springer, Berlin

84. Megaridis CM, Dobbins RA (1990) Morphological description of flame-generated materials. Combust Sci Technol 71(1–3):95–109
85. Friedlander SK (1977) Smoke, dust and haze: Fundamentals of aerosol behavior. Wiley-Interscience, New York, vol 333, p 1
86. Lehtinen KEJ, Zachariah MR (2001) Effect of coalescence energy release on the temporal shape evolution of nanoparticles. Phys Rev B 63(20)
87. Windeler RS, Lehtinen KEJ, Friedlander SK (1997) Production of nanometer-sized metal oxide particles by gas phase reaction in a free jet. 2. Particle size and neck formation - Comparison with theory. Aerosol Sci Technol 27(2):191–205
88. Windeler RS, Friedlander SK, Lehtinen KEJ (1997) Production of nanometer-sized metal oxide particles by gas phase reaction in a free jet. 1. Experimental system and results. Aerosol Sci Technol 27(2):174–190
89. Tsantilis S, Pratsinis SE (2000) Evolution of primary and aggregate particle-size distributions by coagulation and sintering. AIChE J 46(2):407–415
90. Ehrman SH, Friedlander SK, Zachariah MR (1998) Characteristics of SiO_2/TiO_2 nanocomposite particles formed in a premixed flat flame. J Aerosol Sci 29(5–6):687–706
91. Schweigert IV et al (2002) Structure and properties of silica nanoclusters at high temperatures. Phys Rev B 65(23)
92. Kruis FE et al (1993) A simple-model for the evolution of the characteristics of aggregate particles undergoing coagulation and sintering. Aerosol Sci Technol 19(4):514–526
93. Xing YC, Rosner DE (1999) Prediction of spherule size in gas phase nanoparticle synthesis. J Nanopart Res 1(2):277–291
94. Freund HJ, Bauer SH (1977) Homogeneous nucleation in metal vapors. 2. Dependence of heat of condensation on cluster size. J Phys Chem 81(10):994–1000
95. Lehtinen K, Zachariah M (2001) Energy accumulation during the coalescence and coagulation of nanoparticles. Phys Rev B 63(20):205402
96. Zachariah MR, Carrier MJ, BlaistenBarojas E (1996) Properties of silicon nanoparticles: a molecular dynamics study. J Phys Chem 100(36):14856–14864
97. Koch W, Friedlander SK (1990) The effect of particle coalescence on the surface-area of a coagulating aerosol. J Colloid Interface Sci 140(2):419–427
98. Wu MK et al (1993) Controlled synthesis of nanosized particles by aerosol processes. Aerosol Sci Technol 19(4):527–548
99. Martin DL, Raff LM, Thompson DL (1990) Silicon dimer formation by three-body recombination. J Chem Phys 92(9):5311–5318
100. Yaws C (1994) Handbook of vapor pressure. Gulf Pub. Co., Houston
101. Buffat P, Borel JP (1976) Size effect on the melting temperature of gold particles. Phys Rev A 13(6):2287
102. Tandon P, Rosner DE (1999) Monte Carlo simulation of particle aggregation and simultaneous restructuring. J Colloid Interface Sci 213(2):273–286
103. Iida T et al (2000) Equation for estimating viscosities of industrial mold fluxes. High Temp Mater Processes (London) 19(3–4):153–164
104. Hansen K, Campbell EEB (1998) Thermal radiation from small particles. Phys Rev E 58(5):5477–5482
105. Kumar S, Tien CL (1990) Dependent absorption and extinction of radiation by small particles. J Heat Transfer-Trans Asme 112(1):178–185
106. Tomchuk PM, Tomchuk BP (1997) Optical absorption by small metallic particles. J Exp Theor Phys 85(2):360–369
107. Altman IS et al (2001) Experimental estimate of energy accommodation coefficient at high temperatures. Phys Rev E 64(5)
108. Bohren CF, Huffman DR (1983) Absorption and scattering by a sphere. Absorption Scattering Light Small Part 82–129
109. Siegel R, Howel J (1992) Thermal radiation heat transfer. Hemisphere Publishing Corp, Washington DC

110. Rosner DE, Yu SY (2001) MC simulation of aerosol aggregation and simultaneous spheroidization. AIChE J 47(3):545–561
111. Norris JR (1999) Smoluchowski's coagulation equation: uniqueness, nonuniqueness and a hydrodynamic limit for the stochastic coalescent. Ann Appl Probab 9(1):78–109
112. Kostoglou M, Konstandopoulos AG (2001) Evolution of aggregate size and fractal dimension during Brownian coagulation. J Aerosol Sci 32(12):1399–1420
113. Gooch JRV, Hounslow MJ (1996) Monte Carlo simulation of size-enlargement mechanisms in crystallization. AIChE J 42(7):1864–1874
114. Shah BH, Ramkrishna D, Borwanker JD (1977) Simulation of particulate systems using concept of interval of quiescence. AIChE J 23(6):897–904
115. Friedlander SK, Wu MK (1994) Linear rate law for the decay of the excess surface-area of a coalescing solid particle. Phys Rev B 49(5):3622–3624
116. Vemury S, Kusters KA, Pratsinis SE (1994) Time-lag for attainment of the self-preserving particle-size distribution by coagulation. J Colloid Interface Sci 165(1):53–59
117. Rosner DE (2005) Flame synthesis of valuable nanoparticles: Recent progress/current needs in areas of rate laws, population dynamics, and characterization. Ind Eng Chem Res 44 (16):6045–6055
118. Strobel R, Pratsinis SE (2007) Flame aerosol synthesis of smart nanostructured materials. J Mater Chem 17(45):4743–4756
119. Bapat A et al (2004) Plasma synthesis of single-crystal silicon nanoparticles for novel electronic device applications. Plasma Phys Controlled Fusion 46:B97–B109
120. Holunga DM, Flagan RC, Atwater HA (2005) A scalable turbulent mixing aerosol reactor for oxide-coated silicon nanoparticles. Ind Eng Chem Res 44(16):6332–6341
121. Kommu S, Wilson GM, Khomami B (2000) A theoretical/experimental study of silicon epitaxy in horizontal single-wafer chemical vapor deposition reactors. J Electrochem Soc 147(4):1538–1550
122. Gelbard F, Tambour Y, Seinfeld JH (1980) Sectional representations for simulating aerosol dynamics. J Colloid Interface Sci 76(2):541–556
123. Frenklach M, Harris SJ (1987) Aerosol dynamics modeling using the method of moments. J Colloid Interface Sci 118(1):252–261
124. Whitby ER, McMurry PH (1997) Modal aerosol dynamics modeling. Aerosol Sci Technol 27(6):673–688
125. Kommu S, Khomami B, Biswas P (2004) Simulation of aerosol dynamics and transport in chemically reacting particulate matter laden flows. Part I: algorithm development and validation. Chem Eng Sci 59(2):345–358
126. Garrick SC, Lehtinen KEJ, Zachariah MR (2006) Nanoparticle coagulation via a Navier-Stokes/nodal methodology: Evolution of the particle field. J Aerosol Sci 37(5):555–576
127. Tsantilis S, Pratsinis SE (2004) Soft- and hard-agglomerate aerosols made at high temperatures. Langmuir 20(14):5933–5939
128. Wu MK, Friedlander SK (1993) Enhanced power-law agglomerate growth in the free-molecule regime. J Aerosol Sci 24(3):273–282
129. Maricq MM (2007) Coagulation dynamics of fractal-like soot aggregates. J Aerosol Sci 38(2):141–156
130. Zurita-Gotor M, Rosner DE (2002) Effective diameters for collisions of fractal-like aggregates: Recommendations for improved aerosol coagulation frequency predictions. J Colloid Interface Sci 255(1):10–26
131. Schmid HJ et al (2006) Evolution of the fractal dimension for simultaneous coagulation and sintering. Chem Eng Sci 61(1):293–305
132. Zhou L et al (2008) Ion-mobility spectrometry of nickel nanoparticle oxidation kinetics: application to energetic materials. J Phys Chem C 112(42):16209–16218
133. Dikici B et al (2009) Influence of aluminum passivation on the reaction mechanism: flame propagation studies. Energy Fuels 23:4231–4235
134. Wang CM et al (2009) Morphology and electronic structure of the oxide shell on the surface of iron nanoparticles. J Am Chem Soc 131(25):8824–8832

135. Rai A et al (2004) Importance of phase change of aluminum in oxidation of aluminum nanoparticles. J Phys Chem B 108(39):14793–14795
136. Sun J, Pantoya ML, Simon SL (2006) Dependence of size and size distribution on reactivity of aluminum nanoparticles in reactions with oxygen and MoO3. Thermochim Acta 444(2):117–127
137. Trunov MA et al (2005) Effect of polymorphic phase transformations in Al_2O_3 film on oxidation kinetics of aluminum powders. Combust Flame 140(4):310–318
138. Aumann CE, Skofronick GL, Martin JA (1995) Oxidation behavior of aluminum nanopowders. J Vac Sci Technol, B 13(3):1178–1183
139. Park K et al (2005) Size-resolved kinetic measurements of aluminum nanoparticle oxidation with single particle mass spectrometry. J Phys Chem B 109(15):7290–7299
140. Mukherjee D, Rai A, Zachariah MR (2006) Quantitative laser-induced breakdown spectroscopy for aerosols via internal calibration: application to the oxidative coating of aluminum nanoparticles. J Aerosol Sci 37(6):677–695
141. Alavi S, Mintmire JW, Thompson DL (2005) Molecular dynamics simulations of the oxidation of aluminum nanoparticles. J Phy Chem B 109(1):209–214
142. Vashishta P, Kalia RK, Nakano A (2006) Multimillion atom simulations of dynamics of oxidation of an aluminum nanoparticle and nanoindentation on ceramics. J Phys Chem B 110(8):3727–3733
143. Zhang F, Gerrard K, Ripley RC (2009) Reaction mechanism of aluminum-particle-air detonation. J Propul Power 25(4):845–858
144. Trunov MA et al (2006) Oxidation and melting of aluminum nanopowders. J Phys Chem B 110(26):13094–13099
145. Xiong Y, Pratsinis SE (1993) Formation of agglomerate particles by coagulation and sintering. 1. A 2-dimensional solution of the population balance equation. J Aerosol Sci 24(3):283–300
146. Mandelbrot BB (1983) The fractal geometry of nature 173 (Macmillan)
147. Meakin P, Witten TA (1983) Growing interface in diffusion-limited aggregation. Phys Rev A 28(5):2985–2989
148. Schmidtott A (1988) New approaches to insitu characterization of ultrafine agglomerates. J Aerosol Sci 19(5):553–563
149. Buffat P, Borel JP (1976) Size effect on melting temperature of gold particles. Phys Rev A 13(6):2287–2298
150. Levenspiel O (1999) Chemical reaction engineering. Ind Eng Chem Res 38(11):4140–4143
151. German RM (1996) Sintering theory and practice. Wiley, New York
152. Assael MJ et al (2006) Reference data for the density and viscosity of liquid aluminum and liquid iron. J Phys Chem Ref Data 35(1):285–300
153. Paradis P-F, Ishikawa T (2005) Surface tension and viscosity measurements of liquid and undercooled alumina by containerless techniques. Jpn J Appl Phys 44:5082–5085
154. Sarou-Kanian V, Millot F, Rifflet JC (2003) Surface tension and density of oxygen-free liquid aluminum at high temperature. Int J Thermophys 24(1):277–286
155. Blackburn PE, Buchler A, Stauffer JL (1966) Thermodynamics of vaporization in the aluminum oxide-boron oxide system. J Phys Chem 70(8):2469–2474
156. Polyak EV, Sergeev SV (1941) Compt Rend (Doklady) Acad Sci URSS 33
157. Samsonov G (1982) The oxide handbook. Springer, New York
158. Jensen JE et al (1980) Brookhaven national laboratory selected cryogenic data notebook, U. S.D.O.E. Brookhaven National Laboratory Associated Universities Inc., Editor. Brookhaven national Laboratory Associated Universities: UptUUpton, NY
159. Munro RG (1997) Evaluated material properties for a sintered alpha-alumina. J Am Ceram Soc 80(8):1919–1928
160 Weast RC (1989) CRC handbook of chemistry and physics. CRC Press, Boca Raton, FL
161 Astier M, Vergnon P (1976) Determination of the diffusion coefficients from sintering data of ultrafine oxide particles. J Solid State Chem 19(1):67–73

Physical Properties of Select Explosive Components for Assessing Their Fate and Transport in the Environment

Veera M. Boddu, Carmen Costales-Nieves, Reddy Damavarapu, Dabir S. Viswanath and Manoj K. Shukla

Abstract Information on physical properties of munitions compounds is necessary for assessing their environmental distribution and transport, and predict potential hazards. This information is also needed for selection and design of successful physical, chemical or biological environmental remediation processes. This chapter summarizes physicochemical properties relevant to distribution of select explosive components in the three environmental matrices namely, soil, water and air. Physicochemical properties including melting point (MP), boiling point (BP), aqueous solubility (S_w), water-octanol partition coefficient (K_{OC}), Henry's law constant (K_H), vapor pressure (VP) and enthalpy of vaporization (ΔH) obtained from literature using model predictions and experimental studies are listed for a total of 16 energetic compounds. The explosive compounds included are dinitroanisole (DNAN), *n*-methyl-*p*-nitroaniline (MNA), nitro-triazolone (NTO), triaminotrinitrobenzene (TATB), cyclotetramethylene-tetranitramine (HMX), cyclotrimethylene-trinitramine (RDX), trinitrotoluene (TNT), Chinalake-20 (CL-20), Diamino-Dinitroethylene (DADE), 1,3,3-Trinitroazetidine (TNAZ), Pentaerythritol tetranitrate (PETN),

V.M. Boddu (✉)
Plant Polymer Research Unit, National Center for Agriculture Utilization Research, Agricultural Research Service, US Department of Agriculture, NCAUR/ARS/USDA, 1815 N. University St., Peoria, IL 61604, USA
e-mail: Veera.Boddu@ars.usda.gov

C. Costales-Nieves
Environmental Processes Branch, US ARMY ERDC-CERL, Champaign, IL, USA

R. Damavarapu
Energetics and Warheads Division, U.S. Army—Armament Research, Development and Engineering Center, Picatinny Arsenal, NJ, USA

D.S. Viswanath
Nuclear Science and Engineering Institute, University of Missouri, Columbia, MO, USA, and J.J. Pickle Research Center, University of Texas at Austin, Austin, TX, USA

M.K. Shukla
Environmental Laboratory, US Army Engineer Research and Development Center, Vicksburg, MS, USA

343

2,4-Dinitrophenol (DNP), 1-Methyl-2,4,5-trinitroimidazole (MTNI), Triacetone Triperoxide (TATP), 2,4,6-trinitrophenyl-N-methylnitramine (TETRYL), and Bis (2,2,2-trinitroethyl)-3,6-diaminotetrazine (BTAT). The prediction models considered are limited to the EPI suite, SPARC and group contribution and COSMOtherm. Results of model predictions are compared with available experimental data. This chapter is not an exhaustive review of all available literature data.

Keywords Henry's law constant · Water-octanol partition coefficient · EPI suite · Vapor pressure · Solubility in water

1 Introduction

The fate and distribution of an explosive compound released into the environment are primarily governed by: (1) the physicochemical properties of the compound, (2) the prevailing environmental conditions at the points of release, and (3) the degradation and transformation of the explosive. Thus, accurate determination of physicochemical properties is critical in developing valid environmental predictions and remediation approaches. Physicochemical properties such as melting point (MP), boiling point (BP), and vapor pressure (VP) are important in understanding a munition's dispersion and fate within the environment. Often, these properties are difficult to measure experimentally in a laboratory due to the special safety and handling concerns associated with the explosive components. Hence, model predictions are often relied upon for estimating the physical properties of explosives. This chapter presents experimental values and model predictions for 16 select explosive components. Select explosive compounds (Fig. 1) are dinitroanisole (DNAN), *n*-methyl-*p*-nitroaniline (MNA), nitro-triazolone (NTO), triaminotrinitrobenzene (TATB), cyclotetramethylene-tetranitramine (HMX), cyclotrimethylene-trinitramine (RDX), trinitrotoluene (TNT), Chinalake-20 (CL-20), Diamino-Dinitroethylene (DADE), 1,3,3-Trinitroazetidine (TNAZ), Pentaerythritol tetranitrate (PETN), 2,4-Dinitrophenol (DNP), 1-Methyl-2,4,5-trinitroimidazole (MTNI), Triacetone Triperoxide (TATP), 2,4,6-trinitrophenyl-N-methylnitramine (TETRYL), and Bis (2,2,2-trinitroethyl)-3,6-diaminotetrazine (BTAT). The models considered for prediction are limited to the EPI suite [1], SPARC [2] and COSMOtherm [3]. Results of model predictions are compared with available experimental data, and the data gaps are identified. However, this chapter is not an exhaustive review of all available data in the literature, and all the properties are not included for each compound.

In general chemical constituents with similar structures, and physical and chemical characteristics will show similar transformation, transport, or attenuation behavior in the environment. Aqueous solubility, vapor pressure, chemical partitioning coefficients, degradation rates, and Henry's Law Constants provide information that can be used to evaluate contaminant mobility in the environment. High aqueous solubility and low degradation and transformation rate is an indication that the explosive can be easily transported to surface and groundwater bodies.
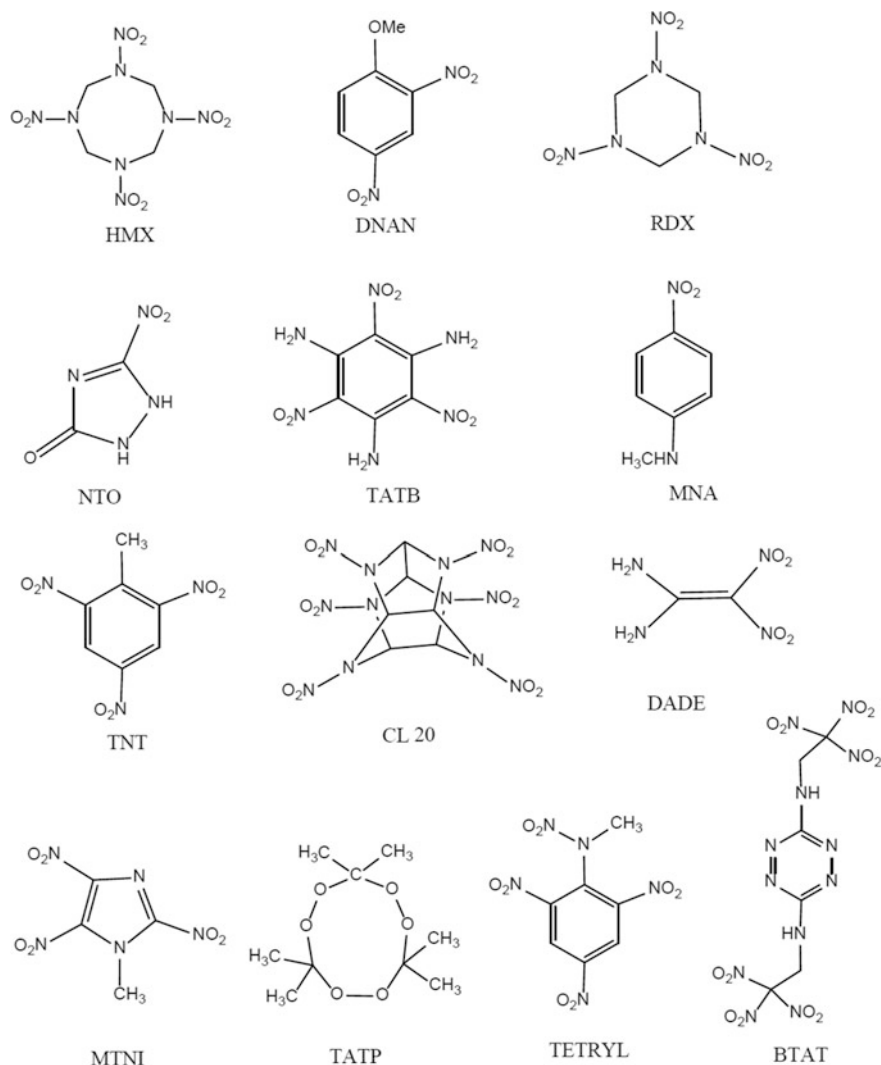
Fig. 1 Chemical structures of select explosive compounds

The BP of a munition is the temperature at which the VP of the liquid equals the environmental pressure surrounding the liquid. The higher the VP of a liquid at a given temperature, the lower the normal boiling point of the liquid. Partitioning coefficients are used to assess the relative affinities of the compounds absorption in solutions or solid phase adsorption. Additional details of these select physical properties are described below.

Solubility in water (S_w): One of the most important physical properties related to the environmental behavior of an organic compound is its aqueous solubility.

Solubility is an equilibrium property defined as the maximum solute concentration possible at equilibrium and it can also function as a limiting factor in concentration dependent processes [4]. The water solubility is the maximum (saturated) concentration of the compound in water at a given temperature and pressure. The aqueous solubility of a compound also indicates its hydrophilic or hydrophobic nature. The solubility may vary due to the presence of other salts, pH and other constituents of the water body and its temperature. The tendency for a compound to be transported by groundwater is directly related to its solubility and inversely related to both its tendencies to adsorb to soil and volatilize from water [5]. Compounds with high water solubilities tend to desorb from soils and sediments, are more likely to stay in water.

The octanol-water partition coefficient (K_{ow}) is the ratio of the concentration of a chemical in the n-octanol phase of a two-phase system to the concentration in the water phase. The K_{ow} is an equilibrium property and is a function of temperature. The octanol-water partition coefficient can be used to estimate the tendency of a chemical to partition between environmental phases of different polarity [6, 7]. Compounds with log K_{ow} values less than 1 are highly hydrophilic, while compounds with log K_{ow} values greater than 4 will partition to soil particles and also tend to bioaccumulate as these are lipophilic [8]. Octanol is an organic solvent that is used as a surrogate for natural organic matter. The K_{OW} is used in many environmental studies to determine the fate of chemicals in the environment. It is particularly useful in the prediction of bioaccumulation, (bioconcentration factor, BCF), lethal dose 50% mortality rates, water solubility, and organic carbon-water partitioning. It is assumed that the molecular speciation of the solute is the same in both solvents and that the solutions are sufficiently dilute [9]. K_{ow} predicts the migration of dissolved hydrophobic organic compounds in soil and groundwater. If it is more hydrophobic, the material will more likely be absorbed by fat. This value correlates well with bioconcentration factor since the octanol-water coefficient is also important in estimating the compound's toxicity and biological uptake. The BCF is important to predict of the explosive's tendency to build up in marine/biological organisms because of an explosive's presence in the surroundings.

The water/organic carbon partition coefficient (K_{oc}) is a measure of the tendency of a compound to partition between soil and water. The K_{oc} is defined as the ratio of the absorbed compound per unit weight of organic carbon to the aqueous solute concentration. This coefficient can be used to estimate the degree to which a compound will adsorb to soil and thus not migrate with groundwater. The higher the K_{oc} value, the greater the tendency of the compound to partition into soil [5]. The K_{oc} value depends on temperature, pH, particle size distribution, concentration, ratio between solids and solution, volatility of the compound, degradation of the compound, and contact time.

The soil sorption coefficient (K_d) is calculated from the K_{oc} coefficient by multiplying the K_{oc} value by the fraction of organic carbon in the soil ($K_d = K_{oc} *$ Organic fraction) [1, 10, 11].

The Henry's Law Constant (K_H) is a measure of the ratio of the compound's vapor pressure to its aqueous solubility. The K_H value can be used to make general predictions about the compound's tendency to volatilize from water and to be an air pollutant. Substances with K_H values less than 10^{-7} atm-m^3/mol will generally volatilize slowly, while compounds with a K_H greater than 10^{-3} atm-m^3/mol will volatilize rapidly [8, 12].

LC_{50} is important to predict the toxicity of a munition compound to aquatic organisms. It is the lethal concentration required to kill 50% of the test species or population. Dermal permeability is important to predict the extent of a toxic munition can penetrate the skin of animals and its affects upon organisms. Hydrolysis rate constants are important to predict how fast a compound will undergo hydrolysis at various pHs of solution. This information would aid in developing efficient methods for treatment of wastewater from industrial facilities and other contaminated aqueous bodies. Biodegradation probability is important to predict the life of a compound within the environment if left untreated [7].

Vapor Pressure (VP) is the pressure at which a compound and its vapor are in equilibrium. The value can be used to determine the extent to which a compound would travel in air, as well as the rate of volatilization from soils and solution [5]. In general, compounds with vapor pressures lower than 10^{-7} mm mercury will not be present in the atmosphere or soil air in significant amounts, while compounds with vapor pressures higher than 10^{-2} mm mercury will exist in the air [13].

Melting Point (MP) and Boiling Point (BP)

Prediction of melting points and boiling points are important in finding thermal behavior of the explosive compound. The MP and BP indicate relative purity and physical state of the material. The boiling point also indicates the volatility of a compound. Results of model predictions are compared with available experimental vapor pressure and meting point data, and the data gaps are identified [10, 13, 14].

2 Model Predictions

In this chapter, we have considered basically three physical property prediction approaches. These are the Estimation Programs Interface (EPI) Suite, SPARK, and the COSMOtherm [1–3]. Boddu and co-workers have presented additional details elsewhere [15–18], however, the estimated properties are included in this chapter.

2.1 Physical Properties Prediction Using Estimation Programs Interface (EPI) Suite

When experimental physicochemical property data are not available to assess environmental risk, a possible way to estimate the necessary values is the use of estimation models. The EPI program was developed to help environmental

scientists to prepare profiles for a wide array of chemical profiles for the National Library of Medicine's Hazardous Substance Data Bank (EPA). The EPI program simply requires the chemical structure or the Chemical Abstracts Service (CAS) registry number to predict or retrieve experimental property values.

Chakka et al. [10, 15]. have reported estimated physical properties of solubility (S_W), octanol-water partition coefficient (K_{ow}), Henry's Law Constant (K_H), organic carbon adsorption (K_{oc}), bioconcentration factors (BCF), aquatic toxicity (LC_{50}), dermal permeability coefficient (K_p), the hydrolysis rate constant, biodegradation probability, boiling point (BP), vapor pressure (VP), and melting point (MP) using the EPI Suite program. They have reported the data of six energetic materials and compared with literature values. Included in the study are the explosive compounds dinitroanisole (DNAN), n-methyl-p-nitroaniline (MNA), nitro-triazolene (NTO), triaminotrinitrobenzene (TATB), cyclotetramethylene-tetranitramine (HMX), cyclotrimethylene-trinitramine (RDX) and trinitrotoluene (TNT).

The water solubility S_W of an organic compound can also be estimated by utilizing the K_{ow} and the chemical structure [19]. EPI suite presents two correlations Eqs. (1) and (2) for prediction of aqueous solubility. "MW" is the molecular weight, "MP" is the melting point, and "cf" is the correction factor. The first equation is based upon a validation set of 85 substances and an experimental log (K_{ow}) but no melting point. The second equation is based upon 817 compounds with measured water solubilities and melting points.

$$\log S \,(\text{mol/l}) = 0.796 - 0.854 \log K_{ow} - 0.00728 MW + cf \tag{1}$$

$$\log S \,(\text{mol/l}) = 0.693 - 0.96 \log K_{ow} - 0.0092(MP - 25) - 0.00314 MW + cf \tag{2}$$

The K_{ow} value is calculated by, using Eq. (3), taking the ratio of a chemical's concentration in the octanol-phase to concentration in the aqueous phase of a two-phase system at equilibrium. In Eq. (3), $\sum(f_i n_i)$ is the summation of f_i (the coefficient for each atom or fragment) multiplied by n_i (the number of times, the atom/fragment occurs in the structure). $\sum(c_j n_j)$ is the summation of c_j (the coefficient for each correction factor) multiplied by n_j (the number of times, the correction factor occurs or is applied in the structure). The atom/fragment contribution method was developed by multiple linear regressions of experimental log (K_{ow}) values performed in two sets. The first set corresponded to the log (K_{ow}) values and the second set corresponded to the correlated correction factors. The log (K_{ow}) was then estimated by summing up the values from the chemical structure of the chemical compound [7].

$$\log K_{ow} = \sum (f_i n_i) + \sum (c_j n_j) + 0.229 \tag{3}$$

The K_H values are calculated by using both the group contribution and the bond contribution methods of Hine and Mookerjee [20] over the temperature range of 0 to 50 °C [12]. EPI Suite furthers on this calculation by developing new fragment

constants from experimental data [6]. K_H estimations are based upon group and bond contributions which are derived from experimentally measured log ($K_{air\text{-}water}$) values.

$$K_H = \text{vapor pressure} \times \text{molecular weight} / \text{water solubility} \; [\text{Pa.m}^3/\text{mol}] \quad (4)$$

The K_{oc} values are calculated using the ratio of the chemical adsorbed per unit weight of organic carbon in the soil to the concentration of the chemical in solution at equilibrium. The chemical structure is provided following the SMILES notation and the molecular connectivity indices and the correction factors. Depending on the organics' chemical class [20]. "OC" in the following Eq. (6) is the organic carbon content's partition coefficient.

$$K_d = \text{Concentration sorbed to soil} / \text{Mean concentration in aqueous solution} \quad (5)$$

$$Koc = (K_d / OC\%) \times 100 \quad (6)$$

The EPI suite estimates the BCF data from a file that contains information on measured BCF and Log (K_{OW}) values. The substances of ionic nature were further divided into carboxylic acids, sulfonic acids and their salts, and quaternary N compounds. Log BCF for non-ionics is estimated from log (K_{ow}) and a series of correction factors specific to each chemical [11], where "a" is the lipid fraction actually ranging from 0.02 to 0.20.

$$BCF = a \times K_{ow} \quad (7)$$

EPI suite derives LC50 values from a collection of experimental data submitted by industry based on measured test data or other sources for chemicals with similar structures. By combining experimental aquatic toxicity values and estimated K_{ow} values, regression equations are developed for each class of chemicals. The toxicity values for new chemicals are calculated by putting the estimated K_{ow} value into the regression equation Eq. (8) and adjusting the result based on the molecular weight of the compound [7].

$$\log \text{LC50 (96h)} = -0.73 \log(K_{ow}) - 2.16 \quad (8)$$

The MP value can be estimated using both the Joback group contribution method [21] and by a correlation drawn between the MP and BP values [22]. The two MP values derived by both methods are then compared to the chemical structure of the organic compound and the magnitude of the difference of both values and a suggested MP is reported. The BP is estimated by the Stein method [23], where "g_i" is the group increment value and "n_i" is the number of times the group occurs in the compound. The resulting BP is then corrected with either Eqs. (2) or (3) based on the temperature.

$$BP = 198.2 + \sum ni \, gi \tag{9}$$

$$BP(corr.) = BP - 94.84 + 0.5577 \, BP - 0.0007705 \, (BP)^2 \quad [BP \leq 700K] \tag{10}$$

$$BP(corr.) = BP + 282.7 - 0.5209 \, BP \, [BP > 700 \, K] \tag{11}$$

The VP values are estimated by the Antoine method, the modified Grain method, and the Mackay method [22]. The Antoine equation works best for liquids that boil below 200 °C and have vapor pressures above 10^{-2} kPa and 25 °C. The Antoine equation is the most reliable three-parameter equation for representing vapor pressure as a function of temperature from the melting point to 85% of the critical temperature and provides and adequate fit for pressures in the range 1–100 kPa. L (x) is the isothermal retention index. A, B, and C are constants that depend on the substance and the stationary base used for Antoine's equation.

$$L(x) = A + \frac{B}{T_C + C} \tag{12}$$

2.2 Physical Properties Prediction Using SPARC Performed Automated Reasoning in Chemistry (SPARC) Package

SPARC modeling system has been developed to predict physical and chemical properties of different classes of organic chemicals from molecular structure. It is developed by the USEPA's Ecosystems Research Division [2, 24, 25]. Due to recent trends in regulatory strategies and the widespread detection of new contaminants in water and soil, the EPA developed a modeling system that is able to predict physical properties at different conditions of solvent, temperature, pressure, and pH. The following summary is based on comparison of physical properties of select explosive components using the SPARC model and EPI Suite [16].

SPARC has the capability to calculate a variety of physical properties including vapor pressure (as a function of temperature), boiling point (as a function of pressure), molar volume, diffusion coefficient, electron affinity, density, refractive index, Henry's law constant and K_{ow} (as a function of temperature), solubility, activity coefficient, and distribution coefficient. To estimate these variety of physical properties, SPARC uses a combination of models including Linear Free Energy Relationships (LFER), Structure Activity Relationships (SAR), and Perturbation Molecular Orbital (PMO) theory. The program requires the user input on molecular structure such as the Simplified Molecular Input Line Entry Specification (SMILES) notations and conditions of interest such as solvent, temperature, and pressure [24]. However, if the SMILES notation of a chemical is unavailable, it is possible to generate it by providing the chemical molecular structure. In order to calculate vapor pressure or solubility, the program requires the melting point of the

Table 1 SMILES notation for compounds of select explosive compounds

Explosive	SMILES notation
RDX	C1N(CN(CN1[N+](=O)[O-])[N+](=O)[O-])[N+](=O)[O-]
HMX	C1N(CN(CN(CN1[N+](=O)[O-])[N+](=O)[O-])[N+](=O)[O-])[N+](=O)[O-]
TATP	CC1(C)(OOC(C)(C)OOC(C)(C)OO1)
DADE	N(=O)(=O)C(N(=O)(=O))=C(N)N
NTO	O=C(NN=1)NC1N(=O)(=O)
TATB	C1(=C(C(=C(C(=C1[N+](=O)[O-])N)[N+](=O)[O-])N)[N+](=O)[O-])N
CL-20	O=N(=O)N(C(N(N(=O)=O)C1C23)C4N3N(=O)=O)C(N4N(=O)=O)C(N1N(=O)=O)N2N(=O)=O
DNAN	c(cc(c1)N(=O)=O)c(OC)c1N(=O)=O
BTAT	n(nc(n1)NC(N(=O)=O)(N(=O)=O)N(=O)=O)c(n1)NC(N(=O)=O)(N(=O)=O)N(=O)=O

compound. When using a well-known compound such as RDX, SPARC is capable of suggesting melting point values from its databank. However, when predicting properties of a new compound the melting point needs to be provided by the user. Costales-Nieves et al. [16]. have estimated the physical properties such as vapor pressure, aqueous solubility, octanol-water partition coefficient, and Henry's constant are predicted at temperatures from 15 to 100 °C. Other physical properties including boiling points, enthalpy of vaporization (ΔH_{vap}), and activity coefficients (γ) are also included. In addition, the results generated from the SPARC program are compared with experimental data available in literature and also with the results from USEPA's EPI Suite model [10].

Physical properties of explosives and propellants including cyclotrimethylenetrinitramine (RDX), cyclotetramethylene-tetranitramine (HXM), triacetone triperoxide (TATP), Dinitro-diaminoethene (DADE, FOX 7), Nitrotriazolene (NTO), Triaminonitrobenzene, (TATB), 2,4,6,8,10,12-hexanitro-2,4,6,8,10,12-hexaazaisowurtzitane (CL-20), Dinitroanisole (DNAN), and Bis(2,2,2-trinitroethyl)-3,6-diaminotetrazine (BTAT) are estimated using the SPARC program. SMILES of the compounds are shown in Table 1.

2.3 Theoretical Background for SPARC Approach for Calculating Physical Properties

SPARC uses the following general Free Energy equation and relates it to physical properties of a compound.

$$\Delta G_{process} = \Delta G_{interaction} + \Delta G_{other} \tag{13}$$

where, $\Delta G_{interaction}$ describes the change in energy associated with the intermolecular interactions in the liquid phase. These interaction mechanisms are

calculated from molecular structures. The summation of all the interactions is expressed by the following equation:

$$\Delta G_{interaction} = \Delta G_{dispersion} + \Delta G_{induction} + \Delta G_{dipole-dipole} + \Delta G_{H-bond} \quad (14)$$

Dispersion interactions are present in all molecules, including polar and non-polar molecules. Induction interactions are present between two molecules when at least one of them has a local dipole moment. Dipole-dipole interactions exist when both molecules have local dipole moments. H-bond interactions exist when $\alpha_i \beta_j$ or $\alpha_j \beta_i$ products are non-zero, where α represents the proton donation strength and β represents the proton acceptor strength [25].

2.4 SPARC approach for estimation of Water Solubility (S_w) and Activity Coefficient (γ)

The water solubility is calculated from the activity coefficient model. SPARC estimates molecular solubility from the infinite dilution activity coefficient γ^{∞} as,

$$-RT\log\left(\gamma^{\infty}\right) = \sum_{Interaction}^{All} \Delta G_{ij}(Interaction) + RT\left(-\log\frac{Vi}{Vj} + \frac{\frac{Vi}{Vj} - 1}{2.303}\right) \quad (15)$$

When $\log \gamma^{\infty}$ is greater than 2, the mole fraction solubility can be estimated as

$$x^{sol} \approx \frac{1}{\gamma^{\infty}} \quad (16)$$

When $\log \gamma^{\infty}$ is less than 2, the above approximation underestimates the solubility because γ^{∞} is greater than γ^{sol} for these cases. However, SPARC can employ an iterative calculation for these cases by setting the initial guess of the solubility as $x_{guess} = 1/\gamma^{\infty}$. Specifically, SPARC models a mixture where the solute and solvent are defined as x_{guess} and $1-x_{guess}$ respectively. SPARC recalculates γ^{∞} until it converges or goes to 1 (i.e. miscible) [25].

2.5 SPARC Approach for Estimation of Vapor Pressure (VP)

Vapor pressure (P_i) of a pure solute i, can be calculated as a function of the intermolecular interactions as,

$$\log P_i = \frac{-\Delta G_{ii}(Interaction)}{2.303RT} + Log\,T + C \tag{17}$$

where, ΔG_{ii}(Interaction): represents the intermolecular interaction mechanisms (dispersion, induction, dipole-dipole and H-bonding), Log (T) + C: describes the change in the entropy contribution associated with the volume change in transition from the liquid to the gas phase.

For molecules that are solids at 25 °C, the crystal energy contribution becomes important. For each intermolecular interaction, SPARC assumes a different but constant ratio of enthalpic to entropic contributions. SPARC estimates the crystal energy contributions assuming ΔG_{ii} = 0 at the melting point [24].

2.6 SPARC Approach for Estimation of Boiling Point (BP)

SPARC estimates boiling point by an iterative approach. It varies and calculates the vapor pressure. When the vapor pressure equals the desired (or set) pressure, then that temperature corresponds to the boiling point at that pressure. The normal boiling point is calculated by setting the pressure to 760 Torr. Boiling points at a reduced pressure can be calculated by setting the pressure to a different value. The dipole-dipole and H-bond interactions become less important and decrease significantly above the boiling point [25].

2.7 SPARC Approach for Estimation of Octanol-Water Partition Coefficient (K_{ow})

The octanol-water partition coefficient K_{ow} can be calculated as a function of the activity coefficient at infinite dilutions (γ^{∞}) of the molecular species in each of the liquid phases as,

$$\log K_{\frac{liq1}{liq2}} = \log \gamma_{liq2}^{\infty} - \log \gamma_{liq1}^{\infty} + \log R_m \tag{18}$$

where, γ^{∞}: are the activity coefficient at infinite dilution of the compound of interest in the two liquid phases, R_m: is the ratio of molecularites of the two phases (M_1/M_2). In addition, SPARC has the capability of estimating a compound's liquid-liquid partition coefficient for any two immiscible phases. The phases may also be mixed solvents [25].

2.8 SPARC Approach for Estimation of Henry's Law Constant (K_H)

Henry's constant can be calculated as,

$$H_x = P_i^{\circ}\, \gamma_{ij}^{\infty} \tag{19}$$

where, P_i°: represents the vapor pressure of pure solute i (liquid or subcooled liquid), γ_{ij}^{∞}: describes the activity coefficient of solute (i) in the liquid phase (j) at infinite dilution.

SPARC vapor pressure and activity coefficient models can be used to calculate the Henry's constant for any solute out of a mixed solute-solvent liquid phase [2].

2.9 SPARC Approach for Estimation of Enthalpy of Vaporization (ΔH_{vap})

The enthalpy of vaporization, known also as heat of vaporization can be calculated as a function of the intermolecular interactions as,

$$\log \Delta H(vap) = \frac{-\Delta G_{ii}^{H}(Interaction)}{2.303RT} - Log\, T + C^{H} \tag{20}$$

where, ΔG_{ii}^{H}: is the free energy change of the self-interactions modified for the enthalpic contribution, $Log\, T + C^{H}$: describes the change in entropy associated with the change in volume going from the liquid to gas phase upon on vaporization, and C^{H} is independent of temperature and represents the Clausius-Clapeyron integration constant [24].

3 Group Contribution and COSMOtherm Approach

Toghiani et al. [14, 18] used group contribution methods and COSMOtherm to predict vapor pressures for 7 compounds (Table 2). These predictions following Eq. (12) are much larger than those found in experimental reported data and the variance between the data points indicates that low volatility compounds are difficult to gather vapor pressure data from experimental studies. This data for RDX are summarized in Fig. 2.

Table 2 Antoine coefficients generated using COSMOtherm [18]

Compound	A_i	B_i	C_i
DNAN	18.01	7087.5	−43.94
DNP	17.72	7092.4	−60.25
MNA	18.19	6757.9	−61.43
MTNI	17.99	7080.5	−41.10
NTO	20.63	7334.04	−76.29
TATB	18.27	6756.2	−62.45
ε-CL20	18.74	9247.9	−38.79
RDX	18.56	7718.5	−42.65
HMX	20.24	11,881.4	−35.96
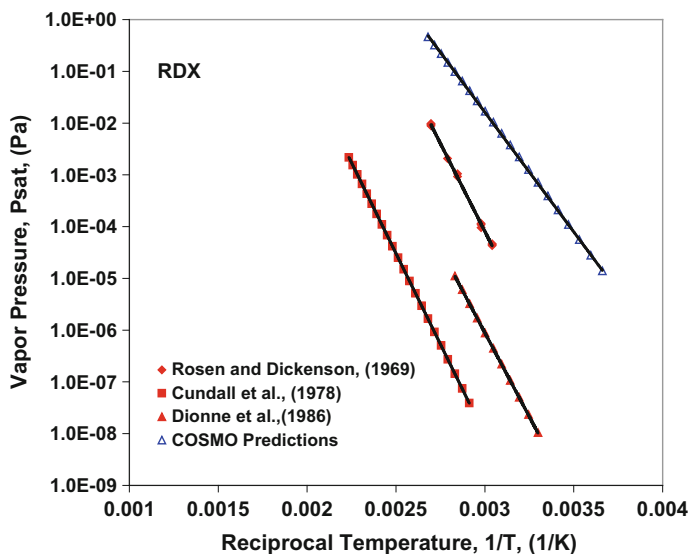
Fig. 2 Vapor pressure of RDX—comparison with literature data

For higher boiling, less volatile substances, the Grain method gives more reliable estimates. The Grain method is also more reliable to find the vapor pressures for solids as it finds the vapor pressure lowering upon solidification of the supercooled liquid [26]. The Grain method uses an approximation to the Watson expression for the temperature dependence of enthalpy, which takes care of the problem that is caused when the Antoine equation introduces unreasonable assumptions about the change in enthalpy with temperature [19, 26]. The program then calculates a suggested VP based on which method is recommended for the chemical's class.

4   Experimental Approaches

Experimental approach for measuring Aqueous Solubility S_w: The aqueous solubility, in general, is measured by dissolving excess amount of a compound in pure water. The amount of the explosive compound in the water is measured by quantitative chemical analysis, such as a chromatographic method. An approach used by Boddu et al. [27, 28] is described here. S_w was obtained by adding an excess amount of the solid explosive component to glass flasks containing 8 mL solutions of deionized water. The vials were screwed tightly to prevent evaporation of water. Experiments were conducted in a shaker water bath and the temperature was controlled within $\pm 0.5^\circ$ C. Experiments were conducted at 10 K intervals between 288 and 313 K. The flasks were stirred at 150 rpm for 24–8 h. When the solute was saturated with solution after 24+ h of shaking, the solution appeared transparent with the excess explosive particles sitting at the bottom of the vials. Once thermal equilibrium was established at a given temperature, one 1 mL sample was taken from each sample and placed into clean glass vials where they were each diluted with 1 mL deionized water to avoid precipitation. To avoid the explosive adsorption losses on the glassware during experimentation, all the glassware were soaked in their respective explosive compounds solution for about 24 h and rinsed with deionized water several times to remove excess munition compound prior to the experiment. To avoid re-crystallization of the explosive, the hardware used for sampling and filtration was equilibrated at the test temperature. The concentration of the explosive compounds was determined by using the HPLC method [27].

4.1   *Experimental Approach For Measuring Octanol-Water Partition Coefficient (K_{ow})*

A method described by Boddu et al. [27, 28]. is described here. A stock solution of excess explosive component in 1-octanol was prepared, this concentration being well above the solubility limit. The concentration of the solution was determined. The experiments were conducted in 8 mL vials with silicone septa. The two solvents, octanol and water, were mutually saturated at the temperature of the experiment before adding munition compound dissolved in 1-octanol. To prevent loss of material due to volatilization, the vials were completely filled with the two-phase system. Experiments were conducted at 10 K intervals between 288 and 313 K. The vials were shaken in the shaker water bath at a desired temperature controlled to ± 0.5 K. The contents were then allowed to equilibrate at the set temperature for about 24–48 h. The aqueous phase from each vial was withdrawn using a syringe with a removable stainless steel needle. The syringe was filled partially with air and gently expelled while passing through the octanol layer. Once the syringe had an adequate quantity of the aqueous phase, it was quickly withdrawn and the needle was removed. This process of withdrawing the aqueous phase

eliminated the risk of contamination with traces of 1-octanol. Both the phases were analyzed for the explosive concentration. The octanol-water partition coefficient was obtained as the ratio of concentration of the explosive component in the organic and aqueous phases.

4.2 Vapor Pressure (VP)

The vapor pressure is important in evaluating the distribution of a compound into the environmental compartments of soil, air, and water and its life within these compartments. Theoretical basis of a method using Thermogravimetry (TGA) procedure is the Langmuir equation [29], where $\left(\frac{1}{a}\right)\frac{dm}{dt}$ is the rate of mass loss per unit area ($kgs^{-1}\,m^{-2}$), p the vapor pressure (Pa), M the molecular weight of the vapor of the evaporating compounds ($kgmol^{-1}$), R the gas constant ($JK^{-1}mol^{-1}$), T the absolute temperature, and α is the vaporization coefficient.

$$\left(\frac{1}{a}\right)\frac{dm}{dt} = p\alpha\sqrt{\frac{M}{2\pi RT}} \tag{21}$$

Rearranging the Langmuir equation gives the following equation, where v is calculated from the TGA data and k is given as a straight line plot of p against v.

$$p = kv \tag{22}$$

Where:

$$k = \frac{\sqrt{2\pi R}}{\alpha} \quad v = \frac{1}{a}\frac{dm}{dt}\sqrt{\frac{T}{M}} \quad \log p = A + \frac{B}{T_C + C}$$

From the Clausius-Clapeyron equation, a plot of $\ln p$ against $1/T$ gives a straight line plot of slope, $\Delta H/R$. Also a plot of $\ln v$ against $1/T$ should give a straight line plot of slope, $\Delta H/R$.

$$\ln p = A - \frac{\Delta H}{RT} \tag{23}$$

Rosen and Dickenson [29] determined VP by the Langmuir method from measurements of the rates of sublimation at constant temperature. They calculated VP values for RDX, HMX, and TATB from the observed weight loss of the heated sample in a vacuum using the expression below, where P is pressure in terms of torr, G is weight loss in grams/cm^2/sec., T is the absolute temperature, and M is molecular weight.

$$P = 17.14G\sqrt{\frac{T}{M}} \qquad (24)$$

Vapor pressure of the explosive components was obtained following the approach using the weight loss information obtained from the TGA measurements. The VPs taken for RDX, HMX, and TATB were determined by the Langmuir method from measurements of the rates of sublimation at constant temperature as described by Rosen and Dickenson [29]. Vapor pressures were then computed from the observed weight loss of the heated sample in a vacuum using the equation Eq. (24). The BPs taken from Toghiani et al. [14, 17, 18]. for CL-20, RDX, HMX, DNAN, DNP, MNA, MTNI, NTO, and TATB were estimated by the Stein-Brown modification of the Joback method. The modification incorporates additional functional groups, including nitrogen groups in a ring [18]. Thermogravimetry and Differential Scanning Calorimetry are used to obtain melting point, boiling point and enthalpy changes.

Chakka et al. [13]. have carried out experimental measurements to obtain, MP, BP and VP of select munitions compounds using Differential Scanning Calorimetry (DSC) and Thermogravimetric Analyzer (TGA). Their approach involves 10 °C min^{-1} (or at a set heating rate 5–10 °C) heating rate of TGA. Constant sample mass of 3 ± 0.1 mg was used for the explosive component experiments and 5 ± 0.1 mg was used for adipic acid and dimethyl oxalate experiments. Each sample was placed into an aluminum hermetic cell and was sealed with an aluminum lid when run on the DSC. The samples were spread thinly and uniformly in the cell completely covering the bottom surface. Samples were run with aluminum hermetic cells with pierced lids and with crimped aluminum cells. The heat flow and temperature calibrations of the DSC were done using indium and zinc standards, and then were verified with indium standard. Thermograms were obtained with 5 °C min^{-1} heating rate. Each sample was placed into an open aluminum cell when run on the TGA. The samples were spread thinly and uniformly in the cell completely

Table 3 Experimental and model predictions of boiling points (BP), vapor pressure (VP), and melting points (MP) of select explosive compounds

	BP (°C)	VP (mmHg)	MP (°C)
DNAN	588 [14] 319.62 [23] 206 @ 12 mmHg[(a)]	29,936.32 @ 532.85 °C [14] 0.000145 [8, 26]	359.9 [30] 96.56[(b)] 94.5[(a)]
MNA	527 [14] 259.24 [23]	31,286 @ 474.85 °C [14] 0.000839 [8, 26]	425.15 [31] 60.96[(b)] 152[(a)]
NTO	568 [14] 389.94 [23]	64521 @ 555.85 °C [14] 5.83E-7 [8, 26]	539.35 [32] 547.9 [33] 161.19[(b)]

<div align="right">(continued)</div>

Table 3 (continued)

	BP (°C)	VP (mmHg)	MP (°C)
TATB	481.26 [23]	42391 @ 639.85 °C [14] 0.733E7 @ 129.3 °C [29] 0.746E7 @ 129.3 °C [29] 1.83E7 @ 136.2 °C [29] 1.93E7 @ 136.2 °C [29] 10.3E7 @ 150.0 °C [29] 9.42E7 @ 150.0 °C [29] 9.73E7 @ 150.0 °C [29] 32.2E7 @ 161.4 °C [29] 32.3E7 @ 161.4 °C [29] 45.8E7 @ 166.4 °C [29] 167E7 @ 177.3 °C [29] 1.58E-11 [8, 26] 3.00E-3 @ 175 °C[a]	594–599 [34] 203.85[b] 350[a]
HMX	709 [14] 436.41 [23]	39765 @ 640.85 °C [14] 0.0324E7 @ 97.6 °C [29] 0.164E7 @ 108.2 °C [29] 0.390E7 @ 115.6 °C [29] 0.385E7 @ 115.6 °C [29] 0.419E7 @ 115.6 °C [29] 2.83E7 @ 129.3 °C [29] 2.87E7 @ 129.3 °C [29] 2.41E-8 [8, 26] 3.3E-14[a]	553.15 [35] 182.89[b]
RDX	627 [14] 353.43 [23]	43516 @ 569.85 °C [14] 3.5E7 @ 55.7 °C [29] 3.24E7 @ 55.7 °C [29] 3.42E7 @ 55.7 °C [29] 8.21E7 @ 62.6 °C [29] 7.14E7 @ 62.6 °C [29] 8.63E7 @ 62.6 °C [29] 69.3E7 @ 78.2 °C [29] 78.7E7 @ 78.2 °C [29] 155E7 @ 85.3 °C [29] 735E7 @ 97.7 °C [29] 667E7 @ 97.7 °C [29] 702E7 @ 97.7 °C [29] 1.34E-6 [8, 26] 4.1E-8[a]	478.5 [36] 205.5[a]
TNT	364.14 [23]	1.72E-5 [8, 26] 8.02E-6[a]	124.36[b] 80.1[a]
CL-20	862 [14]	36688 @ 784.85 °C [14]	513 [37]

(continued)

covering the bottom surface. Constant sample mass of 3 ± 0.1 mg was used for the experiments. All samples were in a nitrogen atmosphere at a flow rate of 20 ml min^{-1}. The experimental results were compared with available experimental

Table 3 (continued)

	BP (°C)	VP (mmHg)	MP (°C)
TATP	712 [14] 168.45 [23]	$\ln P(atm) = 22.73 - 9695.5/T$ @ 12–97 °C [38] $\ln P(atm) = 15.29 - 6978.8/T$ @ T > 97 °C [38] $\text{Log}_{10}P(Pa) = 19.791 - 5780/T$ @ 12–60 °C [39] 2.24 [8, 26]	13.07[b]
DNP	575 [14] 332.13 [23]	51994 @ 543.85 °C [14] 1.29E-5 [8, 26] 3.9E-4 @ 20 °C[a]	363-364 [40] 118.46[b] 115.5[a]
TNAZ	311.56 [23]	0.000221 [8, 26]	95.15[b] 101 [41]
PETN	363.86 [23]	4.21E-6 [8, 26] 5.45E-9	119.48[b] 140.5[a]
MTNI	629 [14] 402 [23]	41040 @ 571.85 °C [14] 4.14E-7 [8, 26]	355.15 [42] 148.36[b]
TETRYL	432.11 [23]	1.17E-7 [8, 26]	159.69[b] 131.5[a]
DADE	287.51 [23]	0.00104 [8, 26]	83.37

[a]Exp., unreported, Boddu and co-workers
[b]Weighted average of several exp. results
Note Most of the literature data in the table are experimental values. However, some model predictions are also included. The reader is referred the literature for details

literature values, and predicted values using EPI suite and the SPARC models [15, 16] are presented in Tables 3 and 4. The vapor pressure data for about nine explosive compounds predicted using the SPARC approach are included in Fig. 3.

5 Conclusion

Physical property data included in this chapter are measured values for aqueous solubility, octanol-water partition coefficients, Henry's law constants, boiling and melting points and vapor pressures for select explosive compounds. The data are compared with EPI, COSMOtherm, and SPARC models. These models enable prediction of the concentrations and behavior of the explosive compounds water and wastewater and other environmental matrices. Literature review shows that aqueous solubility, octanol-water partition coefficient, vapor pressure and boiling and melting point data for many explosive materials is very limited. The review also shows many data gaps. The experimental measurements, by nature, are difficult and lead us to rely on model predictions. At least few experimental measurements are

Table 4 Summary of Physical Properties of explosives at different temperatures[a]

Explosive	T (°C)	VP (Pa)	S_w (mg/L)	K_{ow} (Log)	K_H (PaM³/mole)	BP (°C)	MP (°C)	(ΔHvap) (kcal/mol) 25 °C	γ (log) 25 °C
RDX	15	2.84E-12 3.91E-10 [43]	26.63 23.32 [15, 16] 29.67 [44]	0.13 0.917 [15, 16]	2.37E-11	546.3 353.43 [1]	205.5 [15, 16] 132.76 [1] 205.35 [36]	35.02	4.8
	25	7.02E-11 1.79E-04 [1] 2.42e-9 [43]	30.47 40.94 [15, 16] 59.7 [1] 56.35 [44]	0.39 0.89 [15, 16] 0.87 [1]	5.11E-10 2.04E-06 [1] 0.90 @ 21 (°C) [44]				
	35	1.08E-09 1.32E-08 [43]	33.4 55.01 [15, 16]	0.64 0.864 [15, 16]	7.18E-09				
	40	3.58E-9	34.9 61.57 [15, 16]	0.75 0.855 [15, 16]	2.27E-8				
	45	1.10E-08 6.51E-08 [43]	36.85	0.85	6.65E-08				
	55	8.77E-08 2.90E-07 [43]	41.21	1.03	4.72E-07				
	65	5.74E-07 1.188E-06 [43]	46.62	1.19	2.73E-06				
	75	3.20E-06 4.47E-06 [43]	53.24	1.33	1.33E-05				
	85	1.55E-05 1.56E-5 [43]	61.26	1.44	5.63E-05				
	90	3.27E-05 2.85E-5 [43]	65.88	1.49	1.1E-04				
	100	1.33E-04 9.05E-5 [43]	76.49	1.58	3.87E-04				

(continued)

Table 4 (continued)

Explosive	T (°C)	VP (Pa)	S_w (mg/L)	K_{ow} (Log)	K_H (PaM³/mole)	BP (°C)	MP (°C)	(ΔHvap) (kcal/mol) 25 °C	γ (log) 25 °C
HMX	15	6.91E-18	4.11	0.2	4.98E-16	462.4	276–286[15, 16]	46.75	5.36
	25	3.57E-16 0.21E-06 [1] 6.33e-13 [46]	3.84 58 [1] 4.46 [44] 2370 [47] 6.6 @ (20 °C) [45]	0.55 0.16 [1] 0.165 @ (21 °C) [44]	2.75E-14 8.78E-05 [1] 2.5e-14 @ (20 °C) [47] 0.165 @ (21 °C) [44]	436.41 [15, 16] 179 [29]	182.89 [1] (−56) [29] 286 [45] 280 [46]	26.05 [45]	
	35	1.04E-14	3.63	0.87	8.49E-13				
	45	1.76E-13	3.44	1.15	1.52E-11				
	55	2.20E-12	3.34	0.55	1.95E-10				
	65	2.20E-11	3.35	1.61	1.94E-09				
	75	1.82E-10	3.45	1.8	1.57E-08				
	85	1.29E-09	3.63	1.96	1.06E-07				
	100	1.90E-08	4.08	2.16	1.38E-06				
TATP	15	144.8	2.78	4.88	11600	175.9	91 [15, 16]	11.06	6.19
	25	292.9 1.26 [1]	4.35 3.725 [1]	4.71 4.63 [1]	14900	263.59 [1]	64.56 [1]		
	35	498.7	6.9	4.54	16100				
	45	868.7	10.82	4.38	17900				
	55	1490	16.76	4.22	19700				
	65	2490	25.61	4.07	21600				
	75	4060	38.6	3.92	23400				
	85	6450	57.39	3.78	25000				
	100	11600	94.56	3.59	27200				

Table 4 (continued)

Explosive	T (°C)	VP (Pa)	S_w (mg/L)	K_{ow} (Log)	K_H (PaM³/mole)	BP (°C)	MP (°C)	(ΔHvap) (kcal/mol) 25 °C	γ (log) 25 °C
DADE	15	1.69	3940	2.37	0.0634	249.1	83.37 [15, 16]	15.38	2.87
	25	5.36 0.139 [1]	6130 1,000,000 [1]	2.19 −2.86 [1]	0.13 1.45E-7 [1]	287.51 [1]	83.37 [1]		
	35	9.99	6790	2.16	0.22				
	45	20.35	8070	2.09	0.37				
	55	41.37	9910	2.01	0.62				
	65	82.05	12400	1.92	0.98				
	75	157.9	15500	1.83	1.51				
	85	290.2	19200	1.76	2.24				
	100	614.2	23500	1.64	3.87				
NTO	15	3.22E-07	129.5	−1.84	3.23E-07	276.2	161.19 [15, 16]	16.06	4.23
	25	3.79E-06 2.13E-4 [1]	180.6 131,000 [1]	−1.49 −2.17 [1]	2.73E-06 4.12 E-8 [1]	379.34 [1]	144.89 [1] 266.2 [32] 274.75 [33]		
	35	2.85E-05	184.3	−1.08	2.01E-05				
	45	0.000173	225.8	−0.78	9.99E-05				
	55	0.000925	297.5	−0.53	4.04E-04				
	65	0.00513	469	−0.29	0.00142				
	75	0.0246	715.6	−0.0971	0.00447				
	85	0.1	1060	0.07	0.0128				
	100	0.73	1810	0.28	0.0526				

(continued)

Table 4 (continued)

Explosive	T (°C)	VP (Pa)	S$_w$ (mg/L)	K$_{ow}$ (Log)	K$_H$ (PaM^3/mole)	BP (°C)	MP (°C)	(ΔHvap) (kcal/mol) 25 °C	γ (log) 25 °C
TATB	15	4.37E-06	68.74	2.55	1.64E-05	462.4	350 [15, 16]	21.79	3.99
	25	2.73E-05 2.11E-09 [1] 1.16e-15 [48] 1.79e-9 [47]	120.8 262,600 [1] 160 [18], 197 [18] 32 [47]	2.42 −1.28 [1]	5.84E-05 8.72 E-12 [1] 5.8e-12 @ (20 °C) [47]	481.28 [1] 669.5 [48]	350 [49] 203.85 [1] 320.85 – 325.85 [18]	23.51 [48]	
	35	5.35E-05	103.2	2.55	1.34E-04				
	45	1.24E-04	108.4	2.59	3.03E-04				
	55	3.11E-04	128.8	2.59	6.24E-04				
	65	7.55E-04	164.1	2.56	1.19E-03				
	75	0.00178	216.9	2.5	0.00212				
	85	0.0041	291.5	2.44	0.00363				
	100	0.0135	456.5	2.34	0.00765				
CL–20	15	9.14E-30	7.35E-06 6.4 [15, 16] 2.48 [44]	−0.38 0.01 [15, 16]	5.45E-22	1020 588.63 [1]	240 [15, 16] 240 [50] 239.85 [37] 254 [1]	74.38	11.08
	25	3.28E-27 6.22E-11 [1]	7.73E-06 5.4 [15, 16] 899.9 [1] 3.65 [44]	0.3 −0.05 [15, 16] 0.34 [1] 1.92 @ 21 °C [44]	1.86E-19 1.42E-9 [1]				
	35	2.35E-24	1.09E-05 6.14 (interpolation) [44] 4.3 [15, 16]	0.84 0.275 [15, 16]	9.42E-17				
	45	3.28E-22	1.29E-05 9.51 (interpolation) [44]	1.36 −0.425 [15, 16]	1.11E-14				
	55	1.55E-20	1.40E-05 15.05 (interpolation) [44]	1.83	4.86E-13				

Table 4 (continued)

Explosive	T (°C)	VP (Pa)	S_w (mg/L)	K_{ow} (Log)	K_H (PaM³/mole)	BP (°C)	MP (°C)	(ΔHvap) (kcal/mol) 25 °C	γ (log) 25 °C
	65	4.45E-19	1.53E-05	2.25	1.28E-11				
	75	9.00E-18	1.72E-05	2.62	2.30E-10				
	85	1.39E-16	1.98E-05	2.94	3.06E-09				
	100	5.58E-15	2.59E-05	3.34	9.44E-08				
DNAN	15	0.017	232.3 155 [51]	2.48	0.0145	308 319.62 [1] 376.2 [48]	94.5 [15, 16] 96.56 [1] 94.5 [48] 86.75 [38]	18.31 14.33 [48]	4.18
	25	0.0771 0.0194 [1] 0.0021 [48]	368.7 632.1 [1] 140 [18], 159 [52] 276.2 [28]	2.39 1.71 [1] 1.70, 1.38, 1.92 [52] 1.612 [28]	0.0414 0.0305 [1] 1.366 [28]				
	35	0.16	324.8 399.2 [28]	2.54 1.549 [28]	0.0977 1.397 [28]				
	45	0.37	336.2 560.0 [28]	2.62 1.472 [28]	0.22 1.442 [28]				
	55	0.9	381.3	2.65	0.47				
	65	2.07	456.4	2.65	0.9				
	75	4.56	563.4	2.63	1.6				
	85	9.61	707.2	2.61	2.69				

(continued)

Table 4 (continued)

Explosive	T (°C)	VP (Pa)	S_w (mg/L)	K_{ow} (Log)	K_H (PaM³/mole)	BP (°C)	MP (°C)	(ΔHvap) (kcal/mol) 25 °C	γ (log) 25 °C
	100	25.91	960.7	2.55	5.34				4.64
BTAT	15	2.71396E-14 4.73799E-07 [15, 16]	65.5	2.68	3.02E-09	459.8 502.89 [1]	184 [15, 16] 213.95 [1]	36.08 3.65E-24 [1]	
	25	2.71E-14 6.42117E-07 [15, 16] 3.02E-08 [1]	111.2 1,000,000 [1]	2.6 −5.17 [1]	2.75E-08 3.65E-24 [1]				
	35	1.83E-12 8.7012E-07 [15, 16]	53.9	3.01	2.47E-07				
	45	1.02477E-11 1.17943E-06 [15, 16]	41.2	3.23	1.28E-06				
	55	5.53491E-11 1.59835E-06 [15, 16]	40.19	3.35	1.00E-05				
	65	2.70833E-10 2.16667E-06 [15, 16]	45.06	3.39	4.38E-05				
	75	1.19369E-09 2.93619E-06 [15, 16]	54.56	3.4	1.60E-04				
	85	4.93806E-09 3.97898E-06 [15, 16]	69.16	3.39	5.20E-04				
	100	3.64302E-08	102.5	3.34	2.59E-03				

[a]*Note* Most of the literature data in the table are experimental values. However, some model predictions are also included. The reader is referred to the literature for details
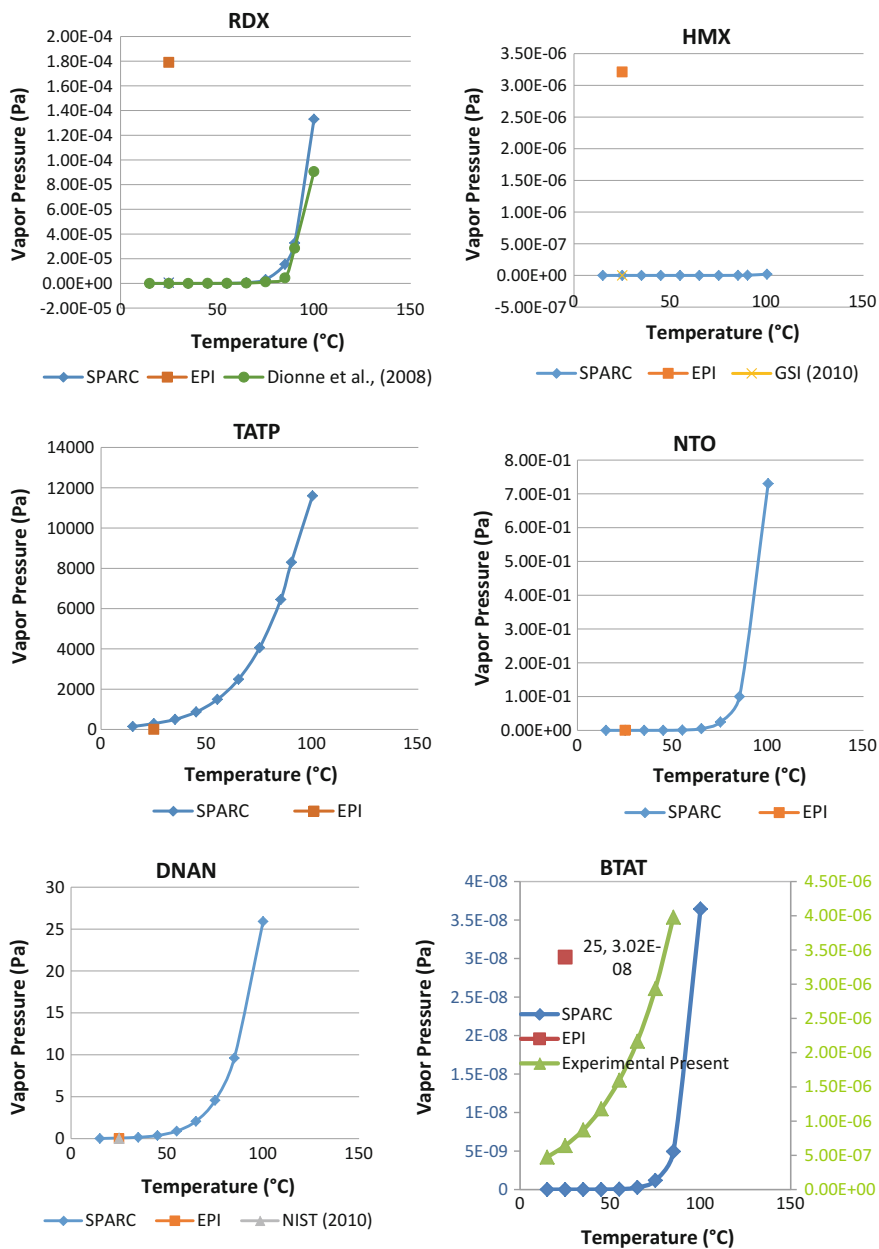
Fig. 3 Vapor pressure graphs for select explosive compounds
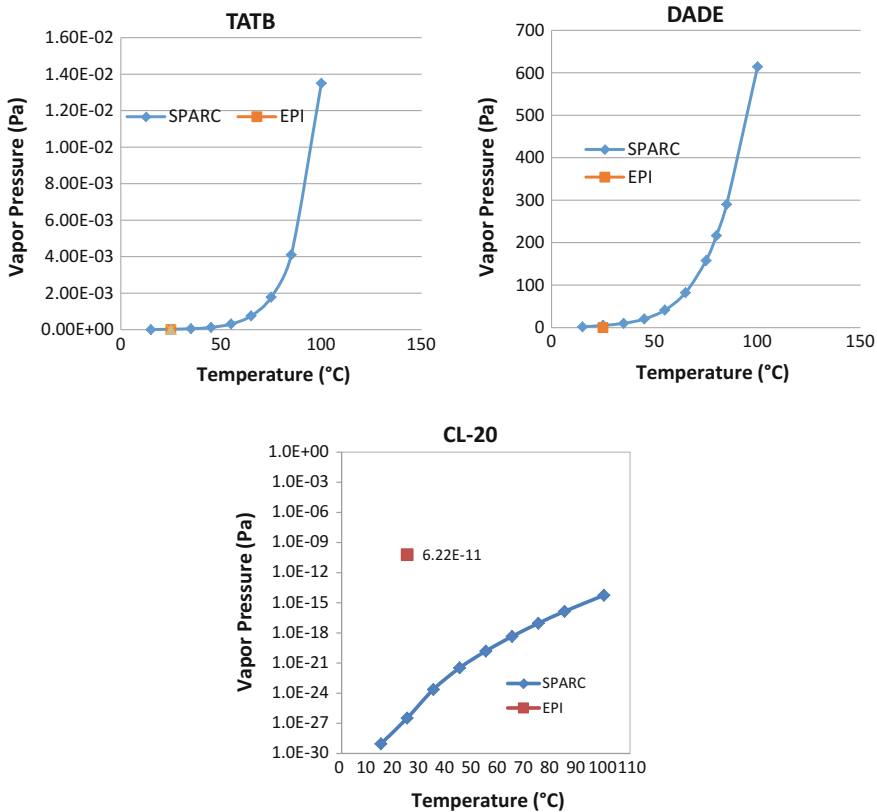
Fig. 3 (continued)

needed to verify the models and model predictions. The discrepancy between the model predictions and available experimental data is rather significant in case of some models, and further experimental data is necessary to make corrections to the predictive models.

References

1. EPI Suite, Estimation Programs Interface, (EPI) (2009) EPI suite: EPA's office of pollution toxics and syracuse research corporation. http://www.epa.gov/opptintr/exposure/pubs/episuitedl. htm). Accessed Nov 2009
2. Hilal SH, Karickhoff SW, Carreira LA (2003b) Verification and validation of the SPARC model. USEPA report number: EPA/600/R-03/033, Georgia, Athens
3. http://www.cosmologic.de/products/cosmotherm.html
4. Yalkowsky SH, Banerjee S (1992) Aqueous solubility-methods of estimation for organic compounds. Marcel Dekker, New York
5. OGE (O'Brien & Gere Engineers. Inc.), Hazardous waste site remediation (1988) Hazardous waste site remediation: the engineer's perspective. In: Bellandi R (ed) Van Nostrand Reinhold. New York
6. Meylan WM, Howard PH (1995) Atom/fragment contribution method for estimating octanol-water partition coefficients. J Pharm Sci 84(1995):83–92
7. Meylan WM, Howard PH, Boethling RS (1996) Improved method for estimating water solubility from octanol/water partition coefficient. Environ Toxicol Chem 15:100–106
8. Lyman WJ, Rosenblatt DH, Reehl WJ (1990) Handbook of chemical property estimation methods: environmental behavior of organic compounds. American Chemical Society, Washington, D.C.
9. Stanger J (1997) Octanol-water partition coefficients—fundamentals and physical chemistry. Wiley, New York
10. Chakka S, Boddu VM, Maloney SW, Damavarapu R (2010) Prediction of Physicochemical Properties of Energetic Materials via EPI Suite. In: Energetic materials: thermophysical properties, predictions and experimental solubility and experimental measurements, chapter 5. CRC Press, pp 77–92
11. Meylan W, Howard PH, Boethling RS (1992) Molecular topology/fragment contribution method for predicting soil sorption coefficients. Environ Sci Technol 26:1560–1567
12. Meylan WM, Howard PH (1991) Bond contribution method for estimating Henry's law constants. Environ Toxicol Chem 10:1283–1293
13. Chakka S, Costales-Nieves C, Boddu VM, Damavarapu R (2011) Physical properties of munitions compounds—Chinalake-20 (CL-20), diamino-dinitroethylene (DADE), cyclotetramethylenetetranitramine (HMX), and cyclotrimethylenetrinitramine (RDX). In: Conference Proceedings, AIChE Conference Proceedings, Annual Meeting, Minneapolis, MN, October 2011
14. Toghiani RK, Toghiani H, Maloney SW, Boddu VM (2010) Prediction of physicochemical properties of energetics materials, Chapter 10. In: Energetic materials: thermophysical properties, predictions and experimental solubility and experimental measurements. CRC Press, pp 171–198
15. Chakka S, Boddu VM, Maloney SW, Toghiani RK, Damavarapu R (2009) Vapor pressures and melting points of select munitions compounds. In: 2009 AIChE Annual Meeting Conference Proceedings
16. Costales-Nieves C, Boddu VM, Maloney SW, Chakka R, Damavarapu R, Viswanath DS (2010) SPARC prediction of physical properties of explosive compounds. In: AIChE Annual Meeting Conference Proceedings, Nov 2010
17. Toghiani RK, Toghiani H (2009) Prediction of physciochemical properties of energetic materials for identification of treatment technologies for generated waste streams. Project Report to US Army ERDC-CERL. Mississippi State University, July 2009
18. Toghiani RK, Toghiani H, Maloney SW, Boddu VM (2008) Prediction of physicochemical properties of energetics materials. Fluid Phase Equilib 264:86–92
19. U.S. Environmental Protection Agency, General Sciences Corporation (1987) GEMS User's Guide, Laurel, MD, USA

20. Hine J, Mookerjee PK (1975) The intrinsic hydrophilic character of organic compounds. Correlations in terms of structural contributions. J Org Chem 40:292–298
21. Joback KG, Reid RC (1987) Estimation of pure-component properties from group-contributions. Chemical Engineering Communications 57:233–243
22. Poling BE, Pausnitz JM, O'Connell JP (2004) The properties of gases and liquids, 5th edn. McGraw Hill, NY
23. Stein SE, Brown RL (1994) Estimation of normal boiling points from group contributions. J Chem Inf Comput Sci 34:581–587
24. Hilal SH, Karickhoff SW, Carreira LA (2003) Prediction of the vapor pressure boiling point, heat of vaporization and diffusion coefficient of organic compounds. QSAR & Combinational Science 22:565–574
25. Hilal SH, Karickhoff SW, Carreira LA (2004) Prediction of solubility, activity coefficient and liquid/liquid partition coefficient of organic compounds. QSAR Comb Sci 23:709–720
26. Boethling RS, Mackay D (2000) Boiling Point. In: Handbook of Property Estimation Methods for Chemicals Environmental and Health Sciences. CRC Press, Florida, pp 33
27. Boddu VM, Abburi K, Maloney SW, Damavarapu R (2008) Physicochemical properties of an insensitive compound, N-methyl-4-nitroaniline (MNA). J Haz Mat 155:288–294
28. Boddu VM, Abburi K, Maloney SW, Damavarapu R (2008) Thermophysical properties of an insensitive munitions compound, 2,4-dinitroanisole (DNAN). J Chem Eng Data 53:1120–1125
29. Rosen JM, Dickinson C (1969) Vapor pressures and heats of sublimation of some high melting organic explosives. J Chem Eng Data 1:120–124
30. Beringer FM, Brierley A, Drexler M, Gindler EM, Lumpkin CC (1953) Diaryliodonium salts II. The phenylation of organic and inorganic bases. J Am Chem Soc 75:2708
31. N-Methyl-4-nitroaniline; MSDS No. 261586 [Online]; J&K Scientific Ltd.: Beijing, China, 11 Jan 2010. http://www.laborservice-bb.de/pdf/312/261586_en.pdf. Accessed 24 Feb 2017
32. Liu ZR, Shao YH, Yin CM, Kong YH (1995) Measurement of the eutectic composition and temperature of energetic materials. Part 1. The phase diagram of binary systems. Thermochim Acta 250:65–76
33. Kim KJ, Kim MJ, Lee JM, Kim SH, Him HS, Park BS (1998) Solubility, density, and metastable zone width of the 3-nitro-1,2,4-triazol-5-one+ water system. J Chem Eng Data 43, 65–68
34. Zeman S (1993) The thermoanalytical study of some Aminoderivatives of 1,3,5-trinitrobenzine. Thermochim Acta 216:157–168
35. Maksimov YY (1992) Boiling points and heats of evaporation of liquid hexogen and octogen. Zh Fiz Khim 66:540–542
36. Hall PG (1971) Thermal decomposition and phase transitions in solid nitramines. Trans Faraday Soc 67:556–562
37. Andelkovic-Lukic M (2000) New high explosive-polycyclic nitramine hexanitrohexaaza-isowu- rtzitane (HNIW, CL-20). Naucno-Tehnicki Pregled 50:60–64
38. Egorshev V, Sinditiskii V, Smironov S, Glinkovsky E, Kuzmin VA (2009) Comparatice study on cyclic acetone peroxides. In: Proceeding of the New Trends in Research of Energetic Materials, Czech Republic
39. Oxley JC, Smith JL, Shinde K, Moran J (2005) Determination of the vapor density of Triacetone Triperoxide (TATP) using a gas chromatography headspace technique. Propellants, Explos, Pyrotech 30:127–130
40. Katritzky AR, Scriven EFV, Majumder S, Akhmedova RG, Akhmedova NG, Vakulenko AV (2005) Direct nitration of five membered heterocycles. ARKIVOC iii:179–191
41. Sikder N, Sikder AK, Bulakh NR, Gandhe BR (2004) 1,3,3-Trinitroazetidine (TNAZ), a melt-cast explosive: synthesis, characterization and thermal behavior. J Hazard Mater 113: 35–43
42. Cho JR, Kim KJ, Cho SG, Kim JK (2002) Synthesis and characterization of 1-methyl-2,4,5-trinitroimidazole (MTNI). J Heterocycl Chem 29:141–147

43. Dionne BC, Rounbehler DP, Archer EK, Hobbs JR, Fine DH (1986) Vapor pressure of explosives. J Energ Mater 4:447–472
44. Montiel-Rivera F, Paquet L, Deschamps S, Balakrishnan VK, Beaulieu C, Hawari J (1025) Physico-chemical measurements of cl-20 for environmental applications comparison with RDX and HMX. J Chromatogr 2004:125–132
45. Bausum HT (1989) Recommended Water Quality Criteria for Octahydro-1,3,5,7-Tentranito-1,3,5,7-Tetrazocin (HMX). U.S. Army Biomedical Research and Development Laboratory, Report Number: A165852
46. Makisimov YY, Russ J (1992) J Phys Chem 66: 280–281 (as cited in ref. 18)
47. GSI Environmental Inc., (2010) Triaminotrinitrobenzene. Retrieved May 2010, from http://www.gsi-net.com/
48. NIST Chemistry Web Book. Retrieved May 2010, from http://webbook.nist.gov
49. Encyclopedia of Chemistry, TATB. Chemie.DE Information Service GmbH. Retrieved May 2010 from http://www.chemie.de/lexikon/e/TATB/
50. Global Security. Global Security.org. Retrieved May 2010, from http//www.globalsecurity.org/military/systtems/munitions/Explosives-nitramines.htm, (2000–2010)
51. Myrdal P, Ward GH, Dannenfelser RM, Mishra D, Yalkowsky SH (1992) AQUAFAC 1: aqueous functional group activity coefficients; application to hydrocarbons. Chemosphere 24:1047–1061
52. Spectrum Laboratories I (2203) Chemical fact sheet: HMX. Retrieved May 2010, from http://www.speclab.com/compound/c2691410.htm

High Explosives and Propellants Energetics: Their Dissolution and Fate in Soils

Katerina Dontsova and Susan Taylor

Abstract Live-fire military training scatters energeticcompounds onto range soils. Once deposited on soil the explosives andpropellants ingredients can dissolve in water, experience complexinteractions with soil constituents, and migrate to groundwater.While in contact with soil these chemicals are also subject to biotic and abiotic (hydrolysis, photolysis, and reaction with metals) transformation both in the solid and in the aqueous state. In this chapter we summarize the current state of knowledge on how energetic residues are deposited on range soils, what the residues look like and how quickly they dissolve. We also describe the key physico-chemical properties (aqueous solubility (S_w), pH, octanol-water partitioning coefficient, (K_{ow})) of the energetic compounds in high explosives and propellants and how these parameters influence their biogeochemical interactions with soil. Knowing the reaction routes of these chemicals will help us understand their fate, their ecological impact, and how to enhance in situ remediation.

Keywords High explosives · Dissolution · Soil interactions · Reactive transport

List of Acronyms and Definitions

2-ADNT	2-amino-4,6-dinitrotoluene
4-ADNT	4-amino-2,6,-dinitrotoluene
2,4-DANT	2,4-diamino-6-nitrotoluene
2,6-DANT	2,6-diamino-4-nitrotoluene
2,4-DNT	2,4-dinitrotoluene
2,6-DNT	2,6-dinitrotoluene

K. Dontsova (✉)
Biosphere 2, University of Arizona, Tucson, AZ 85721-0158, USA
e-mail: dontsova@email.arizona.edu

S. Taylor
Cold Regions Research and Engineering Laboratory, Hanover, NH 03766, USA

ATSDR	Agency for Toxic Substances and Disease Registry
CEC	Cation exchange capacity
Comp B	Composition B, a high explosive composed of 60-39-1, RDX-TNT-wax
DoD	Department of Defense
DNX	Hexahydro-3,5-dinitroso-1-nitro-1,3,5-triazine
EDAX	Energy dispersive X-ray spectrometer
EOD	Explosives ordnance disposal
EPA	Environmental Protection Agency
ERDC	Engineer Research and Development Center
ER	Environmental restoration
HE	High explosive
HMX	Octahydro-1,3,5,7-tetranitro-1,3,5,7-tetrazocine
HPLC	High performance liquid chromatography
K_d	Soil adsorption coefficient
K_{ow}	Octanol-water partition coefficient
K_{OC}	Organic carbon adsorption coefficient
MC	Munitions constituent
MNX	Hexahydro-1-nitroso-3,5-dinitro-triazine
NC	Nitrocellulose
NC or NC + 2,4-DNT	Single-base propellant
NC + NG	Double-base propellant
NC + NG + NQ	Triple-base propellant
NDAB	Nitro-2,4-diazabutanal
NG	Nitroglycerin
NQ	Nitroguanidine
NT	Nitrotoluene
OC	Organic carbon
OM	Organic matter
pK_a	Acid disassociation constant
RDX	Hexahydro-1,3,5-trinitro-1,3,5-triazine
S_w	Aqueous solubility
TAT	2,4,6-triaminotoluene
TNT	2,4,6-trinitrotoluene
TNX	Hexahydro-1,3,5-trinitroso-1,3,5-triazine
Tritonal	Explosive made from $\sim$80% TNT and 20% aluminum
UXO	Unexploded ordnance

1   Introduction

Explosives and propellants are highly energetic nitrogen-based chemicals that rapidly release large amounts of energy and gaseous products when detonated or burned. Because of their explosive properties, these chemicals are extensively used by the military and by the construction and mining industries [1, 2]. The US military commonly uses the nitroaromatic TNT (2,4,6-trinitrotoluene), and the cyclic nitroamines RDX (hexahydro-1,3,5-trinitro-1,3,5-triazine) and HMX (octahydro-1,3,5,7-tetranitro-1,3,5,7-tetrazocine) in explosives, and DNT (2,4-dinitrotoluene), NG (trinitroglycerine) and NQ (nitroguanidine) in propellants (Fig. 1).

Live-fire military training scatters energetic compounds onto range soils. Once deposited on soil, the explosives and propellants ingredients can dissolve in precipitation and are subject to abiotic (hydrolysis, photolysis, and reaction with metals) and biotic (aerobic and anaerobic biotransformation) reactions both in the solid and in the aqueous state (Fig. 2). If on-site ecological receptors are threatened or contaminated groundwater migrates off a military base, political and regulatory actions can lead to training range closure.

Here we describe the deposition, dissolution and soil adsorption of explosives and energetic compounds and summarize how their key physicochemical properties influence their dissolution and biogeochemical interactions and transport in soil. These data are of interest for two reasons. First, these chemicals are variably toxic
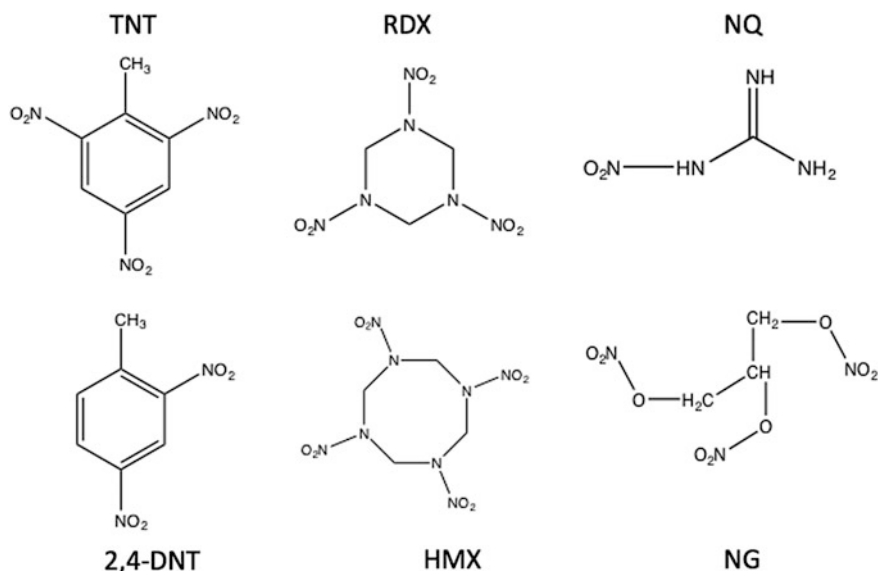
Fig. 1 Chemical structure of common munitions constituents
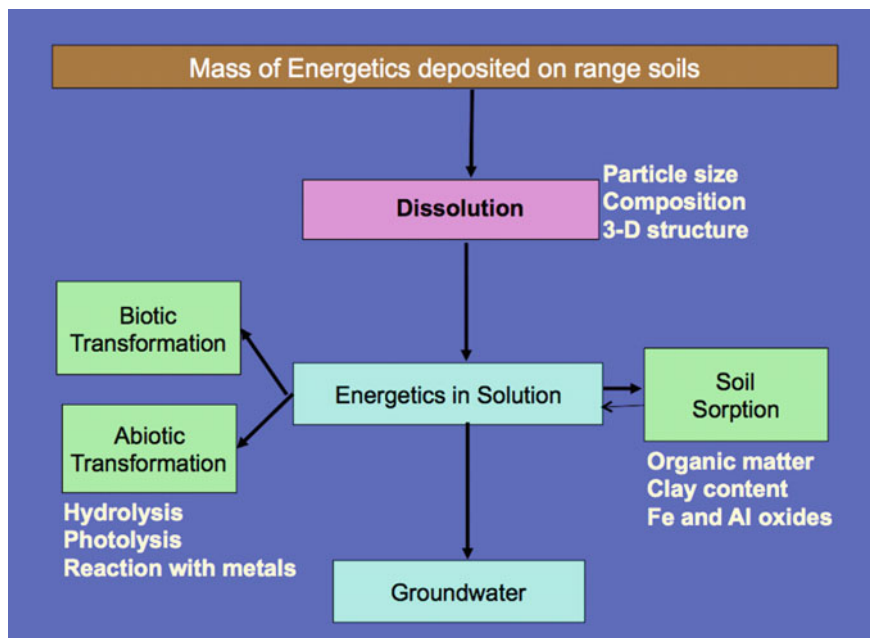
Fig. 2 Schematic showing the processes that affect the environmental fate of explosives deposited on training range soils

and can be deleterious to human, animal and plant health to varying degrees [3]. Second, these compounds can migrate through subsurface soil and contaminate groundwater [4]. Understanding the reaction routes of these chemicals will help us to understand their fate, their ecological impact, and help design remediation strategies.

2 Field Deposition

Military training scatters explosive and propellant compounds onto the soil surface. The mass of the scattered materials depends on the type of round fired and the manner in which it detonated: high-order, low-order (partial), unexploded ordnance (UXO), or blow-in-place detonations of UXO. Table 1 lists compounds found in commonly used explosives and propellants.

Table 1 Energetic chemicals found in military propellants and explosives

Compound	Uses	Chemicals of concern
Propellant formulations		
Single base	Howitzers (M1)	2,4-DNT
Double base	Small arms, mortars, howitzers	NG
Triple base	Howitzers (M31)	NG and NQ
Explosive formulations		
Comp B	Howitzers; mortars	RDX, TNT
C4	Demolition explosive	Military-grade RDX
Tritonal	Aerial bombs	TNT, Al
Comp A4	40-mm grenades	RDX
TNT	Howitzers	TNT
Comp H-6	Aerial bombs	RDX and TNT, Al
Octol	Antitank rockets	HMX and TNT

Note that military grade RDX contains $\approx$ 10% HMX and military-grade TNT contains $\approx$ 1% other TNT isomers and technical grade DNT contains $\approx$ 90% 2,4-DNT and 10% 2,6-DNT

2.1 Propellants

Propellants are generally composed of nitrocellulose (NC) impregnated with either 2,4-dinitrotoluene (called single-base), nitroglycerin (called double-base) or nitroglycerin and nitroguanidine (called triple-base). Propellant residues are partially burned and unburned particles of the solid propellant deposited on the soil surface. The shape of the original propellant grain and the presence or absence of perforations (made to increase the burn rate) dictates the appearance of the residue [5]. For example, propellant grains with a single perforation leave rings or crescent shaped residues (Fig. 3a), those with multiple perforations leave slivers (Fig. 3b) and those without perforations leave residues that are smaller versions of the original propellant (Fig. 3c). The size range of propellant residues is constrained by the size of the original propellant grains, many of which are millimeters in size.

Tests where small arms, mortars, artillery, and shoulder-fired antitank rockets were fired and the residues quantified, show that the mass of NG and 2,4-DNT deposited varies substantially for different munitions (Table 2). For example, the mass of NG deposited for a 155-mm howitzer was estimated at 1.2 mg per round fired, while the NG deposition for an 84-mm AT4 shoulder-fired rocket was 20,000 mg per rocket fired. Most of this deposition occurs as NC particles, with NG or 2,4-DNT located in the NC matrix [6]. NQ-containing propellants appear to leave little residue when used to fire 155-mm howitzer rounds [7].

The patterns of distribution for the residues vary depending on how the propellants are used. At fixed firing positions the propellant residues decrease downrange, except for residues from shoulder-fired rockets, where residues are deposited rearward from the firing positions. For small arms, propellant residues are generally within 5–30 m of the firing position (Table 2). For artillery, propellants are found
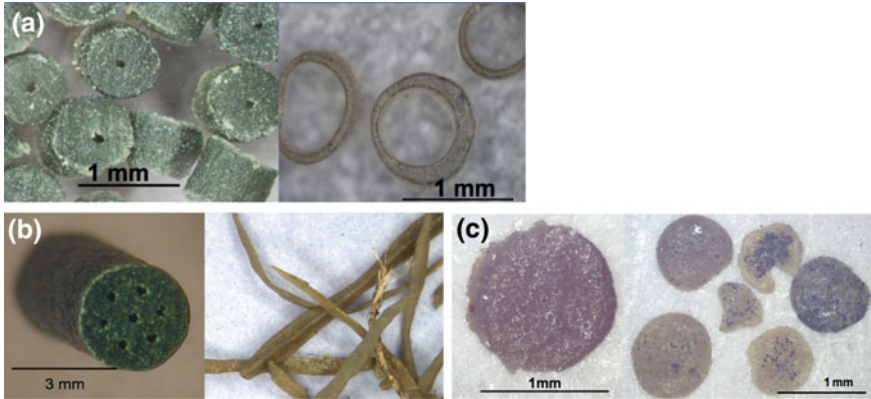
Fig. 3 Single perforated M45 propellant grains and residues (**a**), a multi-perforated M1 propellant and residues (**b**), and an M9 grain and residues (**c**) from Taylor et al. [5]

up to 75 m downrange. For shoulder-fired rocket the residues reside largely in a zone about 30 m behind the firing position. For antitank rockets, propellant residues are also present at the impact area, as all the propellant has generally not been expended before the rocket hits the target.

Pieces of propellant are often visible on training range soils and although the propellant particles are usually not transported, the 2,4-DNT, NG, and NQ, initially within the NC propellant matrix, can dissolve in precipitation and travel with the water into the soil. Taylor et al. [8] found that for unfired grains any NG near the surface of the propellant is readily dissolved. However, energetics in the center of the grain take time to diffuse through the insoluble NC matrix. Disposal of unused propellants by burning bags on the soil can scatter partially burned grains and contaminate the soil. A burn pan designed for this purpose is a much cleaner option [9].

2.2 High Explosives

Pieces of high explosives are scattered onto soils when rounds are detonated. For high order detonations 99.99% of the mass in these rounds is consumed in the detonation (Table 3) and the small amounts of residue deposited are µm-size particles [10, 11]. Low-order or partial detonations, on the other hand, deposit some fraction of the fill (Table 3) as particles and chunks (Fig. 4). These large pieces can deposit from 10,000 to 100,000 times more residue per round than high-order detonations [7]. The percentage of fired rounds that undergo low-order detonations varies from one munition type to another and was studied by Dauphin and Doyle [12].

When fired, some rounds do not detonate and result in UXO that will eventually release all of their explosives into the environment if they are not removed or

Table 2 Mass of propellant energetic constituent deposited during firing

Weapon system	Propellant	Constituent	Rounds fired	Residues/round (mg)	Deposition distance (m)	References
Howitzers						
105-mm	M1-I and II	2,4-DNT	71	34		[66]
105-mm	M1	2,4-DNT	22	6.4		[6, Ch. 4]
155-mm	M1	2,4-DNT	60	1.2		[67]
Mortars						
60-mm	Ignition cartridge	NG	40	0.09	12	[68]
81-mm	M9 (illuminator)	NG	61	1000	50	[68]
120-mm	M45	NG	40	350		[69]
Shoulder-fired rocket						
84-mm Carl Gustov	AKB 204/0	NG	39	1055	30[a]	[28, Ch. 4]
84-mm AT4	AKB 204	NG	5	20,000	50[a]	[66]
Tank (Leopard)						
105-mm	M1	2,4-DNT	90	6.7		[70]
Grenade						
40-mm HEDP	M2	NG	144	76	5	[71]
40-mm TP	F15080	NG	127	2.2	5	–
Small arms						
5.56-mm rifle	WC844	NG	100	1.8	10	[72]
5.56-mm MG	WC844	NG	200	1.3	30	–
7.62-mm MG	WC846	NG	100	1.5	15	–
9-mm pistol	WPR289	NG	100	2.1	10	–
12.7-mm MG (0.50 cal)	WC860 & 857	NG	195	11	40	–

[a]Major deposition is behind the firing line for shoulder-fired rocket

destroyed (Fig. 5). UXO are sometimes destroyed using blow-in-place practices by military Explosive Ordnance Disposal (EOD) technicians or contractor UXO technicians. Currently, military EOD personnel use C4, a demolition explosive that is 91% RDX, for blow-in-place operations. Thus, even if RDX was not present in the UXO, it is often present in soils when rounds have been blown in place. Blow-in-place operations that detonate UXO high order are almost as clean as high-order detonations of fired rounds. A blow-in-place detonation, however, can also result in a partial detonation that deposits a significant fraction of its explosive fill (Table 3).

Table 3 Mass of explosives residues deposited from high-order and partial detonations of TNT and Comp B-filled rounds

High-order detonations	Analyte	# Rounds sampled	Ave. HE fill deposited (%)	References
Mortars—Comp B				
60-mm	RDX	11	3×10^{-5}	[73]
	TNT	11	1×10^{-5}	
81-mm	RDX	5	2×10^{-3}	[73]
	TNT	5	3×10^{-4}	
120-mm	RDX	7	2×10^{-4}	[69]
	TNT	7	2×10^{-5}	
Hand grenades—Comp B				
M67	RDX	7	2×10^{-5}	[73]
	TNT	7	Not detected	
Howitzers—Comp B				
105-mm	RDX	9	7×10^{-6}	[74]
	TNT	9	2×10^{-5}	
155-mm	RDX	7	5×10^{-6}	[67]
	TNT	7		
Partial-detonations				
Mortars—Comp B				
60-mm	RDX + TNT	6	35	[51]
81-mm	RDX + TNT	4	42	[51]
120-mm	RDX + TNT	4	49	[51]
Howitzers—Comp B and TNT				
105-mm	RDX + TNT	15	27	[51]
155-mm	TNT	12	29	[51]
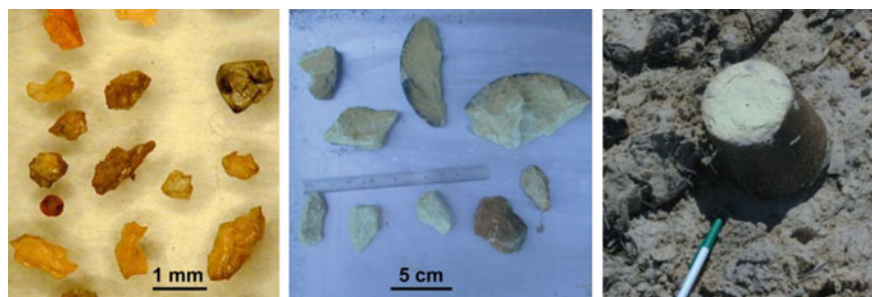
Fig. 4 Comp B pieces from a single partial detonation [11]

Fig. 5 Explosive fill exposed by corrosion of unexploded ordnance (UXO) casings [65]

At antitank rocket ranges, the distance from the firing position to the target is only a few hundred meters and, so, most rounds detonate, or rupture, near the targets. The highest concentrations are next to targets and decrease with distance from the target [13]. Unlike antitank ranges, soils near artillery targets have much lower concentrations of residues and there is no concentration gradient with distance from the targets. The much larger distances between artillery firing positions and their targets results in a much larger impact area around the targets. This situation also exists for mortar targets that often are used for both artillery and mortar testing and training.

Unlike propellants, there is generally no well-defined depositional pattern for high explosive residues. The largest sources of scattered explosives at impact areas derive from partial detonations (low-order), UXO ruptured by shrapnel from nearby live-fire detonations, or blow-in-place activities that produce low order detonations. Residues from these sources produce a localized zone of high concentration, 'point sources', that are not correlated across the range. Because the number of UXO and partial detonations is poorly known, it is difficult to estimate the mass of HE present at an impact area even if the number and type of rounds fired are known. The values provided by Dauphin and Doyle [12] can be used as a guide, but the mass of residues deposited needs to be determined by sampling.

Deposition patterns for energetic residues and how to sample for these on different types of ranges are discussed in [14, 15]. For other types of contaminants resulting from firing (e.g., metals) one would need to consider how these are deposited and any patterns in their spatial distributions [8, 16].

3 Dissolution of Energetic Compounds

Dissolution is thought to be the rate-limiting step for aqueous transport of energetic compounds to groundwater. Figure 6 shows experimental techniques that measure the dissolution of individual post-detonation HE particles, both in the laboratory and in an outdoor setting [17]. Each technique isolated dissolution from the confounding effects of soil interaction and scaled dissolution directly with drip rate (lab tests) or with the precipitation rate (outdoor tests). These tests mimic field conditions on training ranges, where residues are scattered on the soil surface and whose constituents are dissolved by precipitation. Such tests were successfully used to measure and model dissolution of high explosives [18].

3.1 Propellants

Single-base propellants containing 2,4-DNT are used to fire artillery, mainly 105- and 155-mm rounds from Howitzers. From drip tests Taylor et al. [5] showed that 2,4-DNT dissolved from unfired grains slowly but at a constant rate: after 500 days the maximum DNT loss was only 10%. The larger propellant grains lost more DNT than the smaller grains but a smaller percentage of what they contained. The residues from M1 seven-perforation propellant (12 fibers) lost the highest percentage of their 2,4-DNT owing the their large surface to volume ratios. The mass loss curves were not linear. They initially rose rapidly and then became more linear but still had a positive slope.

Double-base propellants are the most common type of propellant and are used to fire small arms, mortars, and rockets. In the drip tests, unfired double-base propellants show initial rapid dissolution of NG followed by much slower dissolution. Most double base propellants lost NG in proportion to how much NG they contained. For example, the M9 propellant with 40% NG lost a greater percentage of its NG than a propellant that contained less. Taylor et al. [5] found that the mass of NG
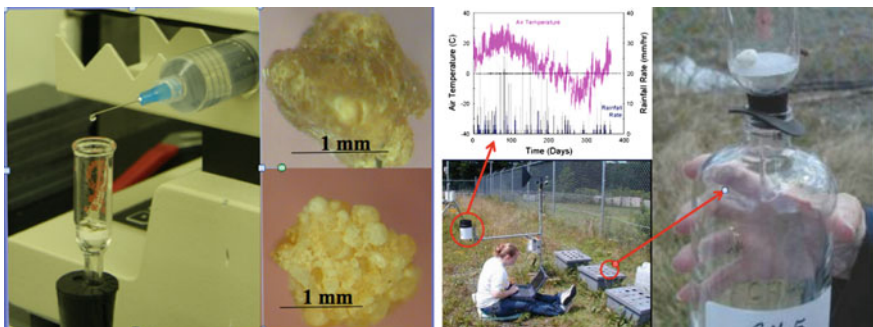
Fig. 6 Laboratory drip tests (*left*) and outdoor dissolution tests (*right*) [24]

Fig. 7 a Plot showing the % NG dissolved normalized by the NG/NC ratio versus time. All of the data from NG containing propellants, except for the small arms, are plotted on this figure. **b** Plot of the percent NG dissolved versus time for unfired (*top*) and fired (*bottom*) of the same four small arms propellants
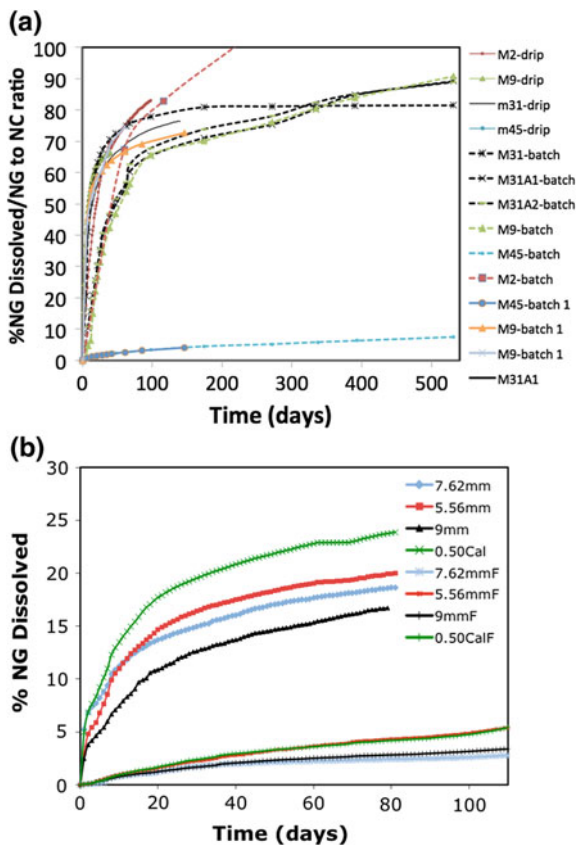
dissolved was a function of the NG/NC ratio in the propellant (Fig. 7a). Clustering of the data using this normalization technique suggests that NC binds 10–20% of the NG and that any extra NG is easily dissolved.

Exceptions from this trend were the ball propellants, used to fire small arms, and the M45 propellant used to fire mortars. The ball propellants all contained ∼10% NG, yet variable amounts of NG were dissolved independent of their NC content. The M45 propellant also contained 10% NG yet it lost less than 1% during the drip tests (Fig. 7a). The M45 is a squat grain with a central perforation, which should increase its NG loss. The low NG loss suggests that the nitrocellulose in M45 was not fully nitrated when it was manufactured so that the NG was effectively bound to the NC.

Dissolution data were collected from both fired residue and unfired grains from double-base ball propellants used to fire small arms. The concentrations of NG in the unfired grains were within the variability given in the technical manuals whereas the fired residues contained about 80% of the original NG on a mass basis. Figure 7b shows that more NG was dissolved from the unfired propellants

(15–20%) than from their residues (3–7%). For the unfired propellants the cumulative mass loss versus time curves were consistent with rapid loss of the NG from the surface of the grain followed by slower diffusion of the NG from the interior of the grain. The high aqueous solubility (S_w) of NG suggests it could be rapidly dissolved by contact with water if it existed as fine liquid droplets within an NC matrix. Droplets at the grain surface would quickly be dissolved by precipitation leaving the NG within the grain that would need to diffuse ($\sim 10^{-14}$ cm^2 s^{-1}) through the NC matrix to reach the water [19]. Late time dissolution would thus be limited by molecular diffusion.

Diffusion-limited dissolution also qualitatively accounts for the much lower dissolution rates observed for fired grains. Firing likely burns or volatilizes surface NG droplets so dissolution would be limited by molecular diffusion of NG from deeper within the NC matrix. The linear shape of the cumulative mass loss curves, the slower dissolution rate of NG from the fired residues and their 20% lower NG concentration compared to unfired grains are explained if NG near the surface is consumed during firing.

Triple base propellants are also used to fire artillery and contain NQ in addition to NG. Although there is more NQ than NG in the M31 propellant, and NQ is more soluble than NG (Table 4), both by mass and by percentage, more NG is dissolved (Fig. 8) [19]. This occurs because during manufacture of the propellant, NG is added as a liquid, whereas NQ is mixed in as a solid. The NQ, therefore, has to dissolve before it can leave the propellant.

Tests to measure how well the components in triple-based propellants were mixed [20] showed that NG is not as well mixed as NC and NQ and that there is more NG near the surface and less in the interior of the grain. Yazici et al. suggest that after a certain threshold (27% NG for a 12.2% nitrated NC) the NG does not effectively bond to the NC and it migrates to the propellant surface as a low

Table 4 Some physicochemical properties of explosives

Compound	Formula	Mol wt.	Density (g cm^{-3})	S_w at 25 °C (g L^{-1})	Log K_{ow} at 25 °C
TNT	$C_7H_5N_3O_6$	227	1.65	0.10[c]	1.86–2.00[d]
2,4-DNT	$C_7H_6N_2O_4$	182	1.52	0.28[d]	1.98[d]
RDX	$C_3H_6N_6O_6$	222	1.82	0.060[e]	0.87[e], 0.81–0.87[d]
HMX	$C_4H_8N_8O_8$	296	1.81	0.0045[f]	0.17[f]
NG	$C_3H_5N_3O_9$	227	1.6	1.95[g]	1.62[g]
NQ	$CH_4N_4O_2$	104	1.71	2.6[i], 4.4[j]	−0.89[i], 0.148[i]

Data from [c]Ro et al. [75], [d]Rosenblatt et al. [76], [e]Banerjee et al. [77], [f]Monteil-Rivera et al. [78], [g]U.S. Army Materiel Command [79], [i]Haag et al. [80], [j]Van der Schalie [81]

Fig. 8 Percent NG and NQ dissolved (Ave. ±1 sigma, n = 8) versus time for unfired M31 single-perforation propellants [5]
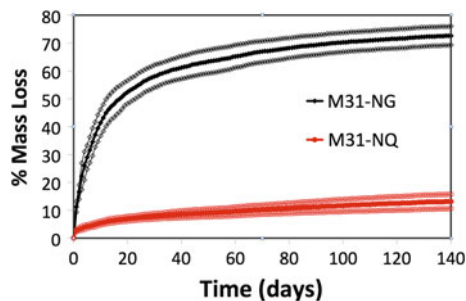
viscosity fluid. This migration would make liquid NG available near the surface of the propellant where it would be removed when in contact with water.

A HYDRUS-2D simulation was able to model dissolution of NG and NQ from the M31 propellant using a combination of diffusion and adsorption of energetics to the NC matrix (Fig. 9). Diffusion only did not adequately describe the experimental results. However, adding kinetic adsorption significantly improved the fit (Fig. 9) and decreased the error for parameter estimates. For NG, adsorption to two types of kinetic sites (one slow and one fast) better described the data than one adsorption site only, but for NQ one kinetic site was sufficient. If no adsorption was modeled, fitted diffusion coefficients were lower than determined in simulations that included kinetic adsorption, as slow release was attributed to diffusion. If we included sorption, slow release was explained partially by slow desorption. The diffusion coefficients ($2.09 \times 10^{-8} \pm 4.39 \times 10^{-9}$ cm^2 s^{-1} for NG and $1.78 \times 10^{-9} \pm 3.74 \times 10^{-10}$ cm^2 s^{-1} for NQ) were higher than found for small arms propellants [8, 19] but in general agreement with numbers reported by Levy [21] for nitroglycerin in cellulose acetate, 5.2×10^{-9} cm^2 s^{-1}. The fact that HYDRUS-2D simulations require an
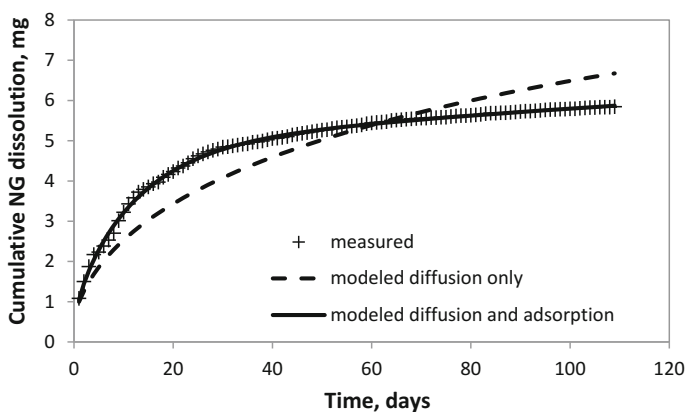
Fig. 9 Observed (*crosses*) and HYDRUS-1D generated cumulative dissolution curves for NG from M31 propellant particle in drip studies without soil: diffusion only (*dashed line*) and diffusion and adsorption on two kinetic sites in NC (*solid line*) [5]

adsorption term to describe energetic dissolution from propellants, supports observations by Yazici and Kalyon [22] that NG in propellant particles is adsorbed and held by NC preventing its movement within the particle.

3.2 High Explosives

The dissolution of pieces and particles of TNT, Comp B, and Tritonal was measured in the laboratory [17] and in the field [23]. Observations showed the TNT particles becoming smoother and smaller but retaining their original shapes as they dissolved. The Comp B particles became noticeably bumpier and "sugary-looking" as dissolution of the surface TNT revealed the larger (~ 0.1 mm), slower-dissolving RDX crystals. The Tritonal particles became smaller and slightly bumpier as TNT dissolved exposing the aluminum grains (Fig. 10a, b).

The outdoor dissolution tests showed that Comp B, Tritonal, and TNT particles all turned rust red with occasional shiny, almost iridescent, black patches. Following heavy rains, the reddish product washed off some surface areas, exposing the lighter-colored explosive beneath. Four of the 34 HE chunks split naturally during the tests and others spalled small flakes or cracked (Figs. 10c and 11b).

The cumulative mass losses for TNT pieces are shown in Fig. 11a. Data for Comp B, Tritonal and C4 are in Taylor et al. [24]. Except for the particles that split
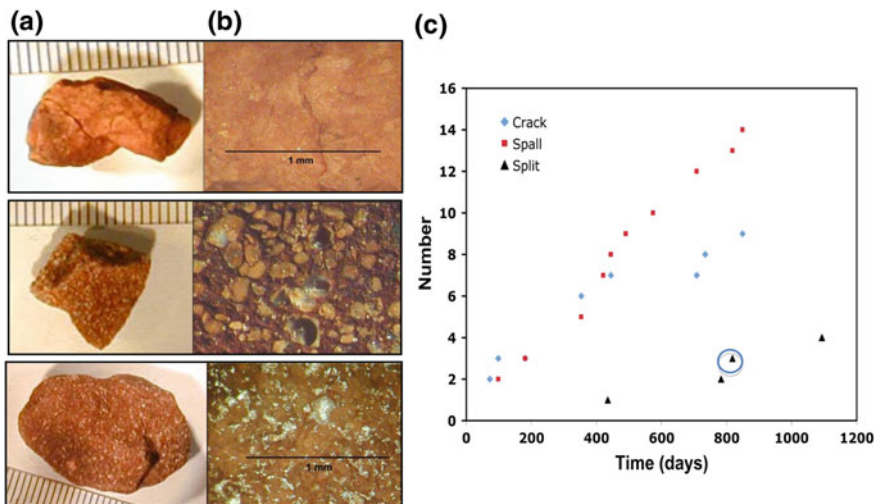
Fig. 10 **a** Photograph of particle and **b** close-up of its surface for TNT, Comp B and tritonal; **c** Number of HE chunks that cracked, spalled off a 1 mm piece, or split into multiple millimeter-sized pieces over the three-year test. For example, the *circled triangle* indicates that 3 of the 34 chunks had split by day 810 of the test
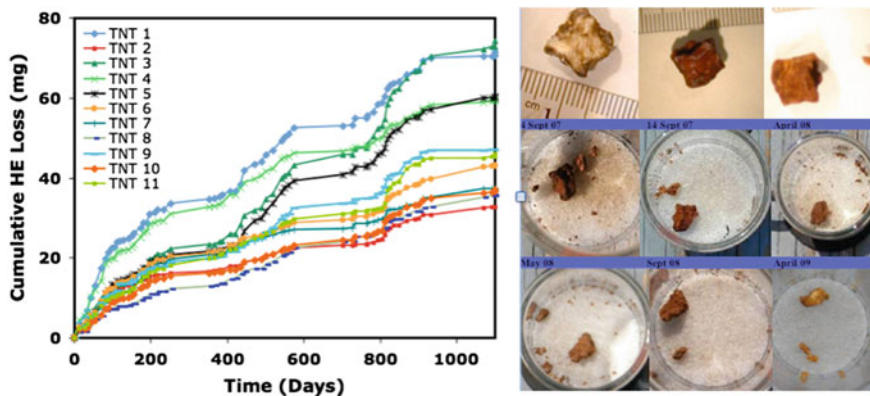
Fig. 11 *Left* cumulative mass loss of TNT (mg) versus time as measured by HPLC; *right* images of TNT particle # 3 over the course of the experiment

(TNT 3 and 5) the shapes of the cumulative mass loss curves are similar among all the particles. Although the largest particles lost the most mass, the small HE chunks lost a larger percentage of their initial mass due to a larger ratio of surface area to mass.

A dissolution model for explosives was developed and validated using data from both the laboratory and outdoor experiments [18, 23, 24]. The key input parameters are particle size, HE type, annual rainfall, and average temperature. Given those parameters, the model offers a simple and accurate way to predict aqueous-phase HE influx into range soils (Fig. 12).
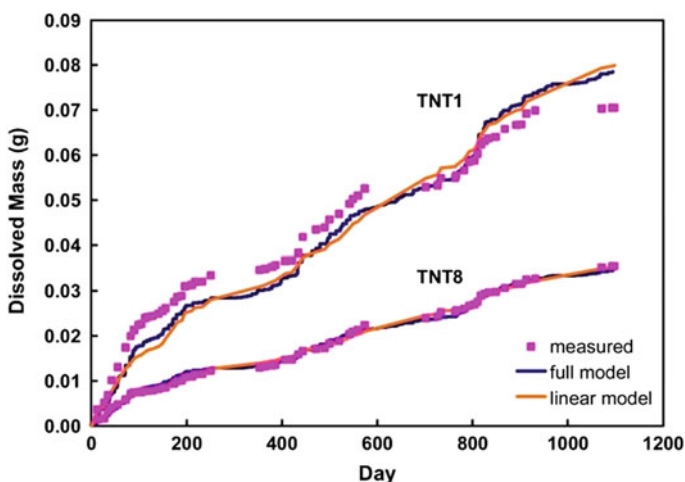
Fig. 12 Dissolved TNT mass measured for TNT 1 (1.9 g) and TNT 8 (0.36 g) along with predictions from full and linear drop-impingement models [24]
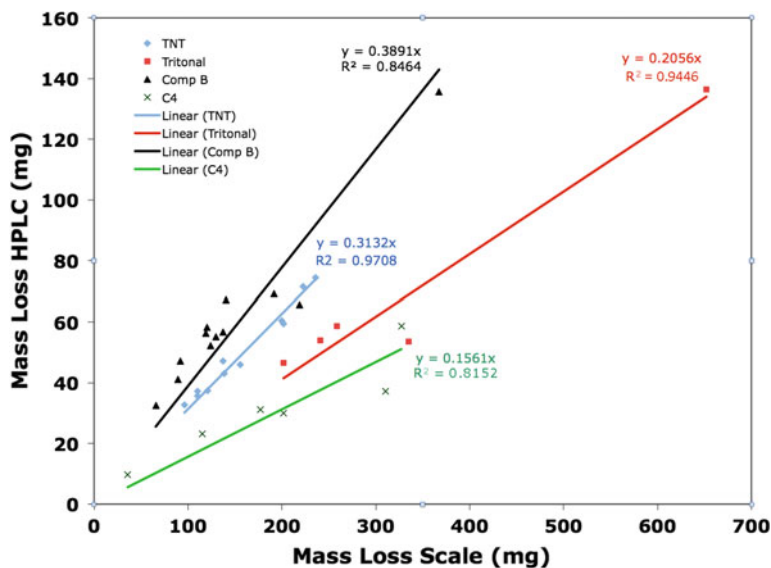
Fig. 13 Over 60% of the mass lost from the HE pieces, as measured by electronic balance, was not measured as dissolved explosives by the HPLC. The unaccounted for masses were larger than dissolved explosive masses, they scaled closely with surface area of each particle and increased with time

The mass loss for each HE chunk after three years is shown in Fig. 13. Note that two types of measurements are plotted against each other: mass loss measured by electronic balance, and cumulative dissolved mass obtained via high performance liquid chromatography (HPLC) analysis. Mass losses measured with the electronic balance were larger than dissolved masses, and the losses grew with time. These results were unexpected because both measurement methods had low uncertainties, and there were very good mass balances for TNT, Tritonal, and Comp B in the laboratory tests [17, 18].

Mass balance discrepancies could be due to formation of transformation products unquantified by HPLC caused by photolysis of the particle's surface or by hydrolysis on the wetted surface of the particle. Photo-transformation is inherent to outdoor weathering of explosives. TNT containing explosives and aqueous solutions are known to turn red and RDX also degrades [25]. TNT was found to produce 2-amino-4,6-dinitrobenzoic acid and a red product, both of which are stable, soluble, polar and elute chromatographically in the pre-solvent peak [24]. The 2-amino-4,6-dinitrobenzoic acid was found in concentrations similar to those measured for TNT and could account for about half of the missing mass. The poor mass balance of RDX was attributed to its photo-destruction as formaldehyde and nitrate, which were detected in photo-degradation studies [24, 25]. On training ranges, these transformation products likely constitute additional HE-based contaminant influx into range soils.

4 Physicochemical Properties of Explosive and Propellant Constituents

Insight into the fate of energetic compounds in the environment can be derived from their physicochemical properties, including solubility in water (S_w), partitioning between water and non-polar solvents (octanol-water partition coefficient, K_{ow}), and acid dissociation constant (pK$_a$). Table 4 summarizes key physicochemical parameters of studied explosives. The aqueous solubility is a measure of how much of a compound can dissolve in water at a given temperature, pH and ionic strength. The solubility of the compound is related to the size and polarity of the molecule, with smaller more polar molecules having higher solubility. Some energetics in propellants, such as NG, and NQ, are soluble (Table 4) and have low health screening levels for drinking water. NG, for example, has a solubility limit of approximately 1500 mg L^{-1} at 20 °C in water [26] and a screening level of 1.5 μg L^{-1} in residential water [27]. Nitrocellulose, NC, on the other hand, is insoluble and has no known health or environmental risks, so its deposited mass is not estimated [28].

Energetic compounds in high explosives such as RDX, HMX and TNT have low solubility. HMX is almost insoluble in water (4 mg L^{-1}), adsorbs to soils, and does not migrate to the subsurface, while RDX and TNT, which are more soluble, have been detected in subsurface environments and in the groundwater of contaminated sites [29]. As Table 4 shows, solubility changes drastically between each of the following classes: nitroaromatics (TNT, DNT), cyclic nitroamines (HMX, RDX), nitrate esters (NG) and nitroimines (NQ).

Octanol-water partitioning coefficient is a measure of the polarity of the molecule, which affects its geo-biochemical interactions in the environment in a variety of ways. Less polar molecules have a higher affinity for octanol, a non-polar solvent, and for lipids, while more polar molecules have an affinity for water, a polar solvent. Therefore, compounds with high log K_{ow} values partition into lipids, while those with low log K_{ow} values partition into water. Because non-polar interactions are involved, explosives with high log K_{ow} values tend to partition into soil organic matter (OM). High partitioning to soil OM usually means high soil sorption and decreased migration through the subsurface to groundwater. High log K_{ow} also promotes diffusion through a cellular membrane potentially causing damage to the biological receptor. As environmental contaminants become more lipophilic (up to log K_{ow} of 3 to 4) their uptake increases [30].

Of the explosives, TNT with its three –NO$_2$ groups partitions into OM and is the most hydrophobic ($1.8 <$ log $K_{ow} < 2.0$). Transformation of TNT to its amine derivatives, i.e. replacing –NO$_2$ groups by –NH$_2$ groups, reduces its hydrophobicity and affinity for soil organic matter and increases its water solubility. Reduced TNT amine products, therefore tend to migrate through the subsurface soil unless their migration is slowed down by immobilization mechanisms, e.g. chemisorption by forming –NH–C(O)—covalent bonds with soil OM [31].

5 Soil Interactions

Explosives are N-based organics that are rich in functional groups, a property that promotes biogeochemical interactions in the environment. Soil constituents, including organic matter, phyllosilicate clays, iron and aluminum oxides and hydroxides, can all adsorb energetic compounds, due to their high surface areas and their various functionalities, or interfere with adsorption (e.g. [32]). The soil type can, therefore, drastically influence the extent of soil—contaminant interactions (Table 5). Interactions of explosive constituents with soil affect their environmental fate and the risk associated with their use in the field.

When the $-NO_2$ functional group(s) in explosives transform to the corresponding $-NH_2$ (amino-) group(s) under various environmental redox conditions [2, 37] different products have different physicochemical properties (S_w, pK_a, K_{ow}) influencing their soil adsorption [31, 38–40]. For example, Haderlein et al. [36] reported that reversible sorption to montmorillonite decreased with the number of nitro groups and followed the order TNT > DNT > NT (nitrotoluene).

Soil adsorption coefficient (K_d), a ratio between concentration of compound in the soil and solution, is used to characterize affinity of energetics for soil. As K_d values increase, the chemicals tend to reside mostly on the solid surface and little is transported downward in the moving pore water. Since the majority of adsorption of organic contaminants in soils is attributed to soil OM, K_d values are often normalized to soil organic carbon (OC) content. The resulting K_{OC} parameter (soil OC adsorption coefficient) can then be used to calculate adsorption of these compounds to other soils based on their carbon content. For example, RDX tends to partition to organic carbon [32, 33] and its behavior can be predicted using K_{OC}. However, TNT exhibits very complex sorption behavior. In addition to being adsorbed to both polar and non-polar regions of organic matter [34, 35], TNT can intercalate and be adsorbed between clay layers [36].

5.1 TNT, DNT and Their Transformation Products

Nitroaromatic compounds, such as TNT and DNT, interact both with organic matter and with phyllosilicate clays in the soil. Haderlein et al. [36] showed that K-saturated clays have very high affinities for both TNT and DNT but that their affinities decreased by several orders of magnitude when clays were saturated with other cations. Although K^+ is usually not a dominant cation in soils, experiments indicate that soil clays do adsorb nitroaromatics, but that adsorption is decreased by mixed clay mineralogy, the cation composition, and organic and oxide coatings on soil clays [32, 41].

Table 5 List of soil adsorption coefficients, K_d, for energetic compounds interacting with soils and minerals

Soils	Clay (%)	OC (%)	K_d (L kg^{-1})					
			TNT	2,4-DNT	RDX	HMX	NG	NQ
Newport	5.6	3.5	2.3[h]	–	–	–		
Lonestar	10.0	0.06	2.5[h]	–	–	–		
Cornhuskers	20.0	0.83	4.1[h]	–	–	–		
Crane	20.6	2.8	3.7[h]	–	–	–		
Joliet	23.8	3.6	6.8[h]	–	–	–		
Holston B	43.8	1.2	3.0[h]	–	–	–		
Sharkey Clay	54.4	2.4	11[h]	–	–	–		
K$^+$-LAAP D[a]	32	0.20	167[i]	12.5	0.66[i]	1.73[i]		
Aqua-gel	>87	ND[c]	130[j]	130[j]	6.6[j]	8.9[j]		
Sassafras loam	11[d] 16.4[l]	0.33[d] 1.30[l]	–	2.34[l]		0.7[d]	0.26[i]	0.60[l]
Catlin silt loam	15.7[l] 18[n]	3.75[l] 4.23[n]	17.9[n]	15.30[l]	2.03[n]		1.27[l]	0.24[l]
Kenner muck	55	35.4	285.2[n]		36.19[n]			
Benndale fine sandy loam	20	0.89	1.77[n]		0.78[n]			
Adler silt loam	4.5[m]	0.29	2.4[m]		0.48[m]	0.48[m]	0.08[p]	
Plymouth sandy loam	14.4[l] 5.0[m]	1.72[l]	1.6[m]	5.06[l] 0.28–2.01[o]	0.65[m]	0.43[m]	1.41[l]	0.44[l]
Yokena/Sharkey clay	48.7	2.4	10[q]	12.5[s] 9.43[g]	3.5[h]	12.1[t]		0.43[r]
Picatinny	5	0.63		2.06[g]		4.25[t]	3.8[f]	
Grange Hill	10	0.29		0.43[g]		0.12[t]		0.15[r]
Varennes	4	8.4	4.2[e]		1.9[e]	2.5[d]		
LAAP A[a]	6	0.31	1.09[i]			1[i]		
LAAP C[a]	12	0.08	1.06[i]					
LAAP D[a]	32	0.2	1.67[i]	1.67[s]	0.3[i]	2.4[i]		

(continued)

Table 5 (continued)

Soils	Clay (%)	OC (%)	K_d (L kg^{-1})					
			TNT	2,4-DNT	RDX	HMX	NG	NQ
Minerals								
K$^+$-montmorillonite	NA[b]	ND	21500[k]	7400[k]	1.2[k]			
K$^+$-illite	NA	ND	12500[k]	3650[k]				
K$^+$-kaolinite	NA	ND	1800[k]	690[k]				
Ca^{2+}-montmorillonite	NA	ND	1.7[k]					
Ca^{2+}-illite	NA	ND	1.2[k]					
Ca^{2+}-kaolinite	NA	ND	0.3[k]					
K$^+$-montmorillonite	NA	ND	414[i]		3.17[i]	22.1[i]		

[a]*LAAP* Louisiana army ammunition plant
[b]*NA* non applicable
[c]*ND* not determined

Data from [d]Monteil-Rivera et al. [78], [e]Sheremata et al. [82], [f]Pennington et al. [83], [g]Pennington et al. [84], [h]Pennington and Patrick [37]; [i]Price et al. [85], [j]Leggett [86], [k]Haderlein et al. [36], [l]Taylor et al. [5], [m]Dontsova et al. [47], [n]Dontsova et al. [32], [o]Dontsova et al. [56], [p]Dontsova et al. [52], [q]Townsend et al. [59], [r]Pennington et al. [53], [s]Pennington et al. [87], [t]Brannon et al. [88]
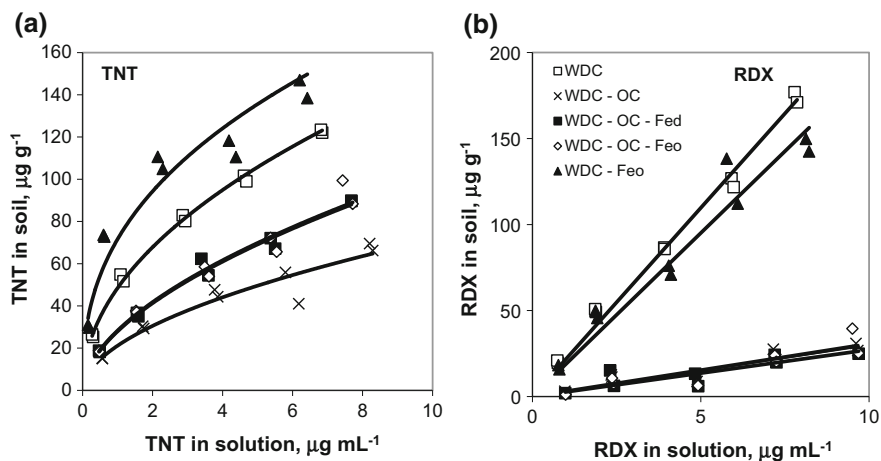
Fig. 14 Adsorption isotherms for TNT in Catlin (**a**) and RDX in Kenner (**b**) water-dispersible clay (WDC). WDC samples were then treated to remove carbonates, organic matter (–OM), non-crystalline aluminosilicates and hydrous oxides (–Fe_o), and free iron-aluminum oxides and hydroxides (–Fe_d) [32]

Organic matter also affects adsorption of TNT in soils (Fig. 14). Octanol-water partitioning coefficients for nitroaromatic compounds (Table 4) suggest nonspecific hydrophobic partitioning to OM [42]. This mechanism was thought to be important for particulate organic matter [34] while more polar soluble organic carbon interacts with TNT and its transformation products through bonds with functional groups present in humic substances [34, 42]. The non-linear shape of adsorption isotherms for TNT in soils (Fig. 14a) suggests that mechanisms other than OM partitioning are contributing to its retention.

Pure iron oxides (e.g., magnetite, hematite, lepidocrocite, and goethite) do not adsorb TNT or other nitroaromatics [43]. Ainsworth et al. [44] showed a negative relationship between dithionite-citrate extractable iron (Fe_d) in soils and TNT adsorption. Removal of poorly-crystalline iron oxides (oxalate extractable) increased adsorption of TNT by soil clays (Fig. 14a). The likely reason for the negative effect of iron oxides on TNT adsorption is that they cover clay surfaces and interfere with adsorption onto the clay minerals.

Once the nitro groups in TNT and DNT are reduced to amino groups, the latter can irreversibly adsorb to OM through covalent bonds [31, 45]. The mechanism involves the amino-transformation products of TNT [2-ADNT; 4-ADNT; 2,4-DANT; 2,6-DANT and TAT (2,4,6-triaminotoluene)] undergoing nucleophilic addition reactions with quinone and other carbonyl groups in the soil humic

acid to form both heterocyclic and nonheterocyclic condensation products. Earlier studies also revealed that monoamino- and diamino derivatives of TNT, ADNT and DANT, experienced reversible adsorption in soils [46, 47]. The strongest indicator of TNT adsorption was the cation exchange capacity (CEC) that accounted for both OM and clay content in the soil, as well as clay mineralogy (Fig. 15). For 2,4-DNT, adsorption to the clays was lower (Table 5) and OC was a better predictor of adsorption to soils (Fig. 15).
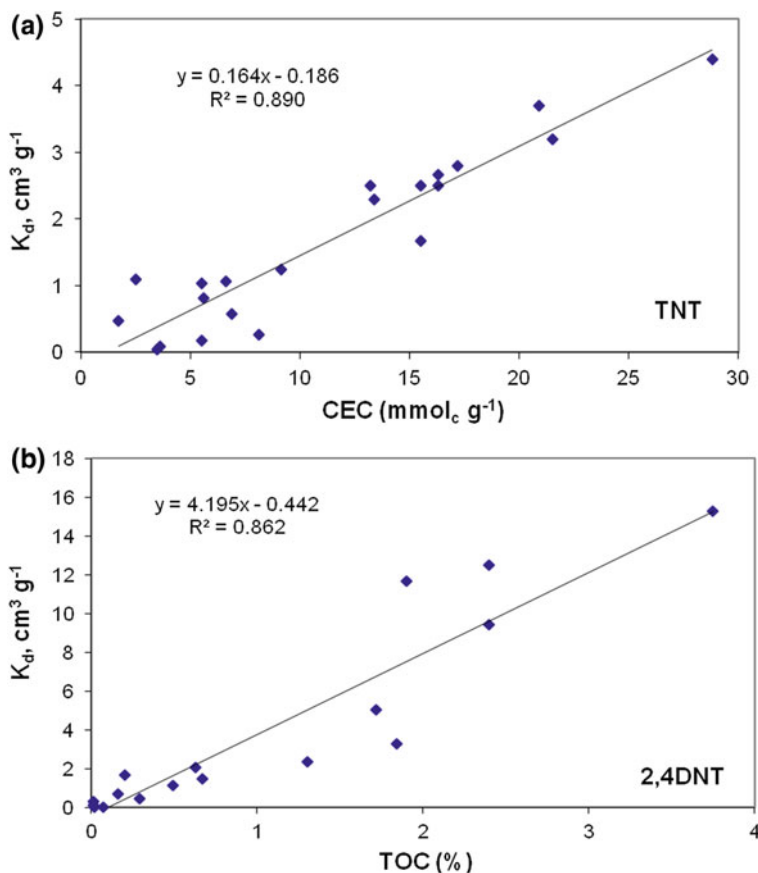
Fig. 15 Linear correlation between **a** measured TNT soil adsorption coefficients (K_d) and cation exchange capacity (CEC) that accounts for clay and OM in the soil ($P = 1.5 \times 10^{-10}$; data are from Brannon and Pennington [46]) and **b** measured 2,4-DNT K_d values and percent organic carbon (OC) in the soil ($P = 7.61 \times 10^{-8}$; data from Brannon and Pennington [46] and Taylor et al. [5]). P values smaller than 0.01 indicate a highly significant correlation
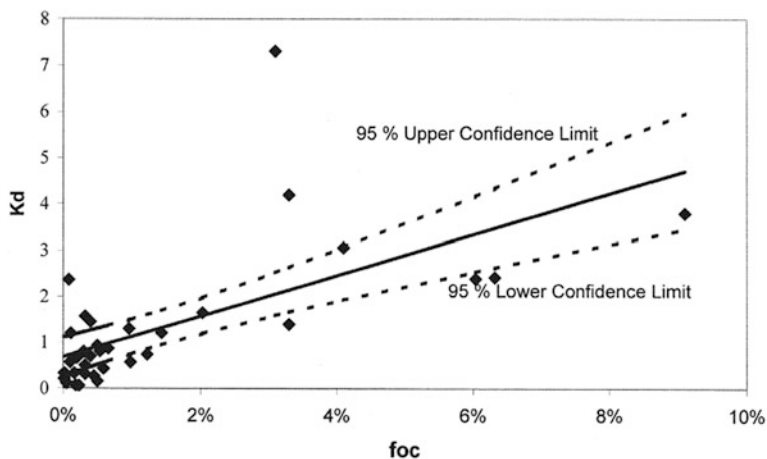
Fig. 16 Linear correlation between percent organic carbon in the soil and adsorption coefficients (K_d), L kg^{-1}, for RDX [33]

5.2 RDX and HMX

RDX and HMX are heterocyclic compounds. They are more polar and have smaller K_{ow} values than the nitro-aromatic TNT and DNT (Table 4). They do not adsorb to clay minerals [36], and have a lower affinity for soils that is determined primarily by OM (Figs. 14b and 16).

Measured soil adsorption coefficients were reviewed by Brannon and Pennington [46] and Tucker et al. [33]. Significant linear regression between RDX K_d values and soil OC content was observed by Tucker et al. [33] (Fig. 16) indicating that adsorption to organic matter is the main way RDX interacts with the soils. Adsorption isotherms for RDX are generally linear and reversible [32, 33] (Fig. 14b) confirming partitioning as the principal sorption mechanism. Haderlein et al. [36] showed that RDX does not exhibit specific adsorption to clay surfaces as shown for nitroaromatic compounds; however, it can participate in hydrogen bonding with clays [44]. Similarly to nitroaromatics, RDX does not adsorb to iron oxides. Szecsody et al. [48] observed no dependence of RDX adsorption on iron oxide content in studied sediments; and removal of iron oxides (both amorphous and crystalline) did not affect adsorption of RDX by soil fines [32]. HMX has a similar behavior to RDX but higher K_d values (Table 5).

5.3 Nitroglycerine

Reported nitroglycerin soil adsorption coefficients range from 0.08 to 3.8 cm^3 g^{-1} (Table 5), lower than the ones determined for 2,4-DNT. This agrees with a factor of

two lower K_{ow} values (Table 4), though a larger difference was measured in K_d values than in K_{ow} values for the two compounds. NG adsorption coefficients are not correlated with organic matter content (P = 0.4945), suggesting that other mechanisms are responsible for adsorption. NG is a polar molecule [49] and may form dipole-dipole and hydrogen bonds with polar moieties in the soils.

5.4 Nitroguanidine

NQ is a highly polar compound. However, reported pKa values (12.8) indicate that it is not protonated in environmental pH ranges [50]. It has low sorption and degradation in soils and is very mobile. Batch studies report K_d values between 0.15 and 0.60 cm^3 g^{-1} [5, 51]. Column transport studies also showed limited potential for NQ adsorption, with K_d values ranging from 0 to 0.14 cm^3 g^{-1} [52]. Calculated log K_{oc} values for NQ are similar: 1.25–2.12 for [53], 0.82–1.66 for [5] and 1.83–2.22 for [52]. However, NQ adsorption coefficients do not correlate with OC content in the soil (P = 0.1585) indicating a lack of partitioning behavior. This is likely related to the polar nature of the NQ molecule with negative log K_{ow} values (Table 4), which results in low affinity for non-polar organic matter in the soils.

5.5 Reactive Transport

A number of studies have evaluated the transport of explosives and propellants compounds in soils [5, 47, 52, 54–60]. These studies measured both transport of prepared aqueous solutions and of solutions from dissolving particles. The latter combines dissolution and transport to observe leaching patterns and to evaluate the effect of varying concentrations of energetics, due to dissolution and compound interactions, on transport. Here we discuss solution-phase transport of explosives and propellants, combined dissolution and transport, and colloidal and particulate transport of explosive compounds.

Figures 17a, b show examples of breakthrough curves observed for aqueous solutions of TNT and RDX in a sandy soil. Note that RDX is little affected by interaction with the soil and elutes soon after the unreactive aqueous tracer, while TNT elutes later than the tracer and at a diminished concentration. Figure 17c, d show the transport behavior of Comp B when added as an aqueous solution (c) and as small particles on the surface of the column (d). The second scenario is representative of the particles dissolving on a soil surface as would be expected for the field conditions. When Comp B is added in solution, the RDX concentration in the leachate was much higher compared to all other solutes due to higher content of RDX in Comp B and the fast transformation of TNT in soil. In contrast, when Comp B particles are used, the concentrations of TNT and RDX are much closer in magnitude. The differences between these breakthrough curves exist because TNT
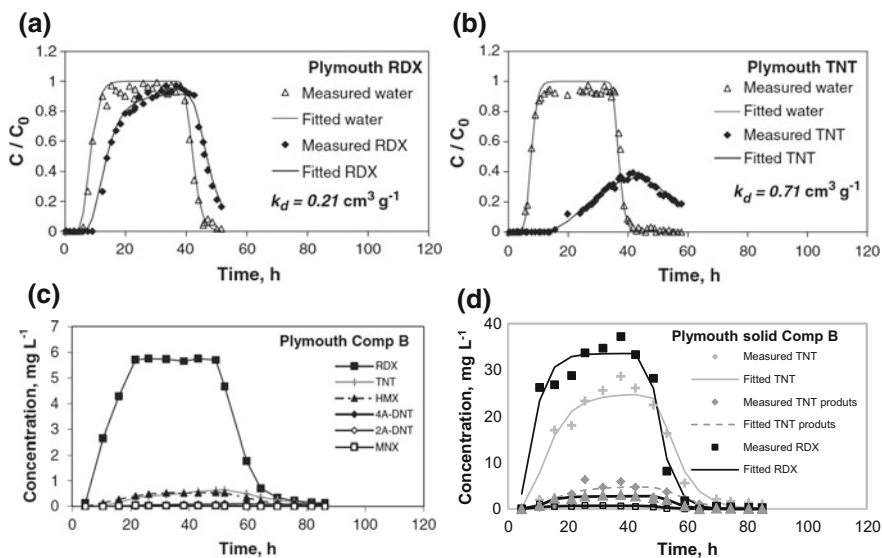
Fig. 17 Breakthrough curves for ^3H_2O tracer, as well as ^{14}C-RDX (**a**), ^{14}C-TNT (**b**), liquid phase Comp B (**c**), and solid phase Comp B (**c**) for continuous flow experiments. Tests used Plymouth loamy sand from Camp Edwards, MA and typical rainfall rate for the area [47]

dissolves faster than RDX. Overall for Comp B particles, dissolution was relatively steady and highly significant linear relationships were found among dissolution rates determined by HYDRUS-1D simulations for TNT, RDX and HMX eluting from the particles [47].

The transport behavior of propellants in solution is a function of their affinity for the soils. 2,4-DNT and NG are adsorbed and transformed in soils and therefore are retarded during transport, while NQ, which does not adsorb to soils and is very persistent, tends to travel through the soils with the water. Dissolution and therefore elution patterns of propellants are very different from explosives. While explosives followed approximately zero-order kinetics of dissolution, propellants are characterized by very high initial dissolution from the particles followed by steady state or quasi steady state dissolution. The pattern is explained by diffusion-limited dissolution from the insoluble NC matrix as discussed in Sect. 3.1. If the flow is interrupted and then restarted (as may happen between rainfall events), the effluent concentrations increase again (Fig. 18). Both the peak and the steady-state concentrations are highly dependent on the compound. For NQ there is a very sharp spike in concentration followed by low steady-state concentrations, while NG does not have a sharp peak but tends to maintain a higher concentration in the effluent over time (Fig. 18c) even when the concentration of NQ in the propellant is higher than for NG (19.5% NG and 55% NQ in M31 propellant). Very large changes in concentration result in non-linear adsorption behavior with soils having lower affinity for the propellants initially as the first elution wave moves through the soil
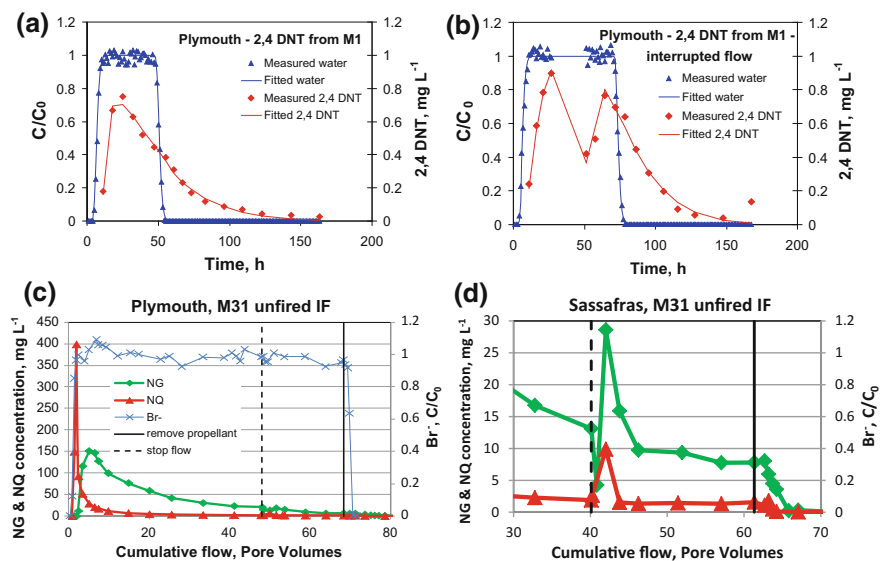
Fig. 18 Breakthrough curves for ³H₂O tracer, as well as NG, NQ, and 2,4-DNT for continuous flow experiments in Plymouth and Sassafras soils and interrupted flow (segment) using solid propellants. The decrease in concentration of NG upon flow interruption is attributed to transformation, followed by an increase in concentration due to time-limited dissolution. NQ experiences only the increase in concentration when flow is interrupted because it does not transform

profile and higher affinity when the concentrations are lower later. Little 2,4-DNT was observed in the effluent of columns with M1 propellant [5, 56] due to low dissolution rates and high adsorption and transformation in soils. For all studied propellants higher effluent concentrations were observed for unfired propellants compared to the fired residues. Increase in the flow rate resulted in a decrease in the NG concentration indicating dissolution limitation on the propellant constituent flux. Slow dissolution of energetics in propellants results in their long residence in NC particles and lack of ground water contamination [61].

A mechanism of transport that is not often considered but can influence movement of energetics in soils is colloidal or facilitated transport. Colloids are 0.001–1 μm particles that are potentially mobile and have a high affinity for dissolved explosives due to their high surface areas. If an energetic is strongly adsorbed by the colloid, colloid-facilitated transport can become a significant part of the overall movement of this chemical. Because water samples are routinely filtered through 0.45 μm filters when analyzed for explosives, a part of colloid-adsorbed explosives could be included in water analyses. The fraction >0.45 μm represents explosives that are potentially mobile but not routinely analyzed, while the fraction <0.45 μm are explosives included in routine water analysis. However, the behavior of colloid-adsorbed explosives in the water would differ from the behavior of pure explosives in solution. Since the mobility of the

colloids is influenced by the ionic strength of the solution, these and their HE "passengers" could be moved by low electrolyte rainwater. The HE might also be precipitated out by any salt in the aqueous solution.

To determine the contribution of colloidal transport the effluent from soil columns receiving solutions of TNT and RDX was analyzed. The effluent was either filtered (0.45 μm), not filtered, or flocculated using alum and filtered to remove colloids. No difference was found between the filtered and unfiltered samples, indicating that the explosives are either attached to colloids <0.45 μm in size or are fully dissolved. However, the results of filtering after addition of alum to flocculate colloids indicated that there was a significant amount of explosives in the filtered material that was transported with colloidal particles or dissolved organic matter (Fig. 19; Table 6).

The contribution of colloidal transport to the total transport of energetics depended on soil type and on solution chemistry (Table 6). High electrolyte concentration resulted in a smaller contribution of colloidal transport. For RDX in all soils and conditions and for TNT without salt in all soils and with salt in Benndale
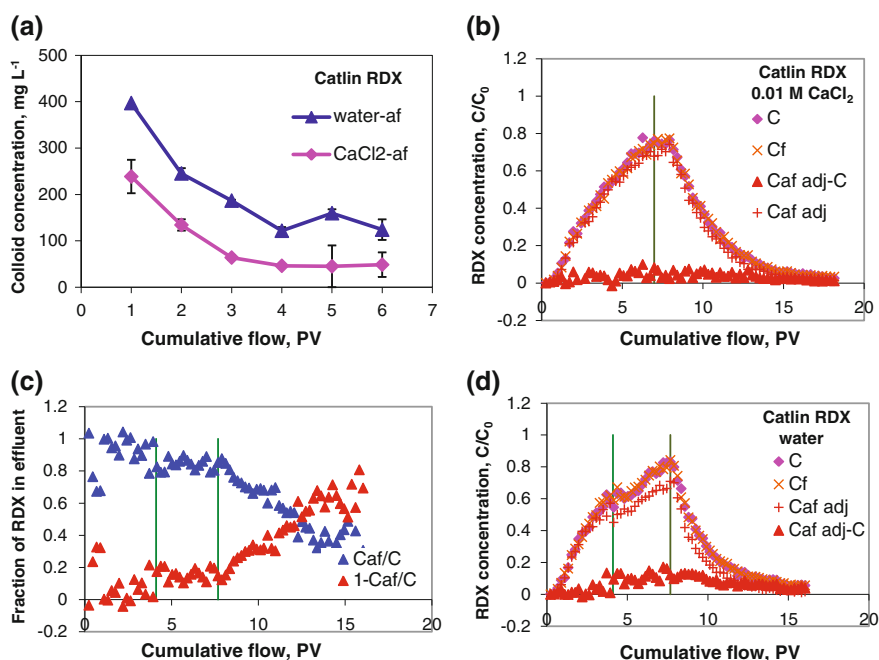
Fig. 19 Colloid concentration in solution (**a**), and breakthrough curves for RDX in Catlin soil in the presence of 0.01 M CaCl$_2$ (**b**) and in water (**d**), as well as a fraction of RDX in solution and adsorbed to colloids (**c**). *Vertical lines* indicate timing of flow interruption and when the RDX solution was switched back to the background solution without RDX. C–^{14}C-RDX in unfiltered samples, C$_f$–^{14}C-RDX in samples filtered through 0.45 μm filter, C$_{afadj}$–^{14}C-RDX in samples that were filtered through 0.45 μm filter after addition of alum. "*Adj*" refers to correction for dilution of the sample through alum addition

Table 6 Percent of total explosives in solution moved through soil with colloidal particles

	Catlin silt loam 4.2% OC 18% clay 16% WDC[a]		Benndale fine sandy loam 0.9% OC 20% clay 8% WDC[a]		Kenner muck 35.3% OC 55% clay 7% WDC[a]	
	Mean	CI	Mean	CI	Mean	CI
TNT						
0.01 M $CaCl_2$	1.37	1.65	0.49	0.16	0.43	0.54
Water	2.08	1.07	1.43	1.05	0.70	0.01
RDX						
0.01 M $CaCl_2$	4.11	1.20	0.97	0.31	1.34	0.05
Water	6.56	0.84	1.36	0.00	2.61	0.38

[a]*WDC* water-dispersible clay

soil, colloidal transport was significantly different from zero. For RDX but not TNT there was a significant difference between the mass of explosive transported with 0.01 M $CaCl_2$ and without salt. At low electrolyte concentrations, the contribution of colloidal transport to the transport of explosives is greater because at higher concentrations colloids are flocculated and immobilized (Fig. 19a).

The largest amount transported (6.56%) was for RDX in mineral soil with high organic matter content (4.2% OC). Natural rainfall has a low salt content so no salt treatment realistically represents field conditions. The significant colloid transport observed for high OM soil may be exaggerated due to the use of repacked columns as repacking could mobilize more colloids. However, if we consider that the HE particles that serve as the source of energetics are deposited in impact areas, disturbances of the soils would be expected.

The contribution of colloidal transport varied during the course of the experiment (Fig. 19c). The largest quantity contributed was expected in the beginning of the tests because this is when colloid concentrations in the effluent were the largest (Fig. 19a). However, the colloid transport was largest during the desorption stage of the isotherm and colloidal transport is responsible in large part for the tailing observed in transport experiments.

Another way explosives can be transported is if micron-sized explosives residues, resulting from detonations or particle weathering, move through soils [62]. Fuller et al. [63] showed that 20–45 μm sized particles of Comp B moved through sand resulting in increased transport compared to mm-sized particles. Similar results were obtained for transport of 2,6-DNT particles ground to 2–50 μm size in sand and glass beads [64]. The contribution of particulate transport of explosives should be more significant in coarse sediments with large pores and fast pore water velocities, while in finer soils micrometer sized particles would likely dissolve before they are transported due to their high surface area per mass.

5.6 Conclusions

A critical problem facing range managers is determining if live-fire training is likely to contaminate groundwater under their ranges. Off-base migration of energetic contaminants may trigger federal regulatory actions that can close bases or restrict training. To predict the likelihood of off-base contamination, one needs to know the following:

- the mass, type and spatial distribution of explosives on the range;
- the dissolution rates of each HE type as a function of piece size, rainfall and temperature;
- the interaction of aqueous-phase HE with different types of soil; and
- the amount of transport through the vadose zone to the groundwater.

Good progress has been made in quantifying and characterizing the residues deposited by live fire training. The key environmental physicochemical parameters (dissolution, the octanol-water partitioning coefficient, and soil adsorption coefficient) have also been measured for TNT, RDX, HMX, 2,4-DNT, NG, and NQ and a robust dissolution model developed for TNT and RDX, if their particle sizes are known.

In regards to groundwater contamination, TNT bio- and photo-degrades and is less likely to reach groundwater than RDX, which is stable and has a low affinity for soils. The energetics in propellant residues, 2,4-DNT, NG and NQ, tend to dissolve slowly from their nitrocellulose matrix and the NG/NC ratio appears to control the amount of NG dissolved. Because 2,4-DNT and NG interact strongly with soils and have high adsorption and transformation rates, they are unlikely to reach groundwater. NQ, on the other hand, has a low soil adsorption and does not degrade or transform in the soil and could travel to groundwater.

Probably the largest source of uncertainty in estimating HE aqueous influx into range soils results from poorly quantified mass of HE residues on ranges. The number and sizes of these particles depends on many factors including the munitions used, their firing rates, their detonation probabilities (high-order, low-order, or dud) and weathering and mechanical disaggregation. If we had a better estimate of the mass of HE particles, this information could be used to predict the HE aqueous influx to soils. When coupled to a vadose transport model, these data would provide a first-order estimate of the HE mass reaching groundwater.

References

1. Jenkins TF, Hewitt AD, Grant CL, Thiboutot S, Ampleman G, Walsh ME, Ranney TA, Ramsey CA, Palazzo AJ, Pennington JC (2006) Identity and distribution of residues of energetic compounds at army live-fire training ranges. Chemosphere 63:1280–1290

2. Spain JC, Hughes JB, Knackmuss H-J (2000) Biodegradation of nitroaromatic compounds and explosives. Lewis Publishers, Boca Raton, FL

3. ATSDR (1995) Toxicological profile for 2,4,6-trinitrotoluene and RDX. US Department of Health and Human Services, Public Health Service, Agency for Toxic Substances and Disease Registry, Atlanta, GA

4. Environmental Protection Agency. In the Matter of Training Range and Impact Area, Massachusetts Military Reservation. Administration Order for Response Action; EPA Docket Number SDWA-1-2000-0014; U. S. EPA Region 1: 2000

5. Taylor S, Dontsova K, Bigl S, Richardson C, Lever J, Pitt J, Bradley JP, Walsh M, Šimůnek J (2012) Dissolution rate of propellant energetics from nitrocellulose matrices. Cold Regions Research and Engineering Laboratory, Hanover, NH

6. Jenkins TF, Pennington JC, Ampleman G, Thiboutot S, Walsh MR, Diaz E, Dontsova KM, Hewitt AD, Walsh ME, Bigl SR, Taylor S, MacMillan DK, Clausen JL, Lambert D, Perron NM, Lapointe MC, Brochu S, Brassard M, Stowe R, Farinaccio R, Gagnon A, Marois A, Gilbert D, Faucher D, Yost S, Hayes C, Ramsey CA, Rachow RJ, Zufelt JE, Collins CM, Gelvin AB, Saari SP (2007) Characterzation and fate of gun and rocket propellant residues on testing and training ranges: interim report 1. Engineer Research and Development Center

7. Walsh ME, Thiboutot S, Walsh ME, Ampleman G, Martel R, Poulin I, Taylor S (2011) Characterzation and fate of gun and rocket propellant residues on testing and training ranges. ERDC/CRREL TR-11-13

8. Taylor S, Jenkins TF, Rieck H, Bigl S, Hewitt AD, Walsh ME, Walsh MR (2011) MMRP guidance document for soil sampling of energetics and metals. Cold Regions Research and Engineering Laboratory, Hanover, NH

9. Walsh ME, Thiboutot S, Walsh ME, Ampleman G (2012) Controlled expedient disposal of excess gun propellant. J Hazard Mater 15:219–220

10. Taylor S, Campbell E, Perovich L, Lever J, Pennington J (2006) Characteristics of composition B particles from blow-in-place detonations. Chemosphere 65:1405–1413

11. Taylor S, Hewitt A, Lever J, Hayes C, Perovich L, Thorne P, Daghlian C (2004) TNT particle size distributions from detonated 155-mm howitzer rounds. Chemosphere 55:357–367

12. Dauphin L, Doyle C (2000) Study of ammunition dud and low-order detonation rates. Aberdeen proving ground, U.S. Army Environmental Center report SFIM-ACE-ET-CR-200049, MD

13. Thiboutot S, Ampleman G, Gagnon A, Marois A, Jenkins TF, Walsh ME, Thorne PG, Ranney TA (1998) Characterzation of antitank firing ranges at CFB Valcartier, WATC Wainwright and CFAD Dundurn. Report DREV-R-9809

14. Hewitt AD, Bigl SR, Walsh ME, Brochu S (2007a) Processing of training range soils for the analysis of energetic compounds. ERDC/CRREL TR-07-15

15. Hewitt AD, Jenkins TF, Walsh ME, Walsh MR, Bigl SR, Ramsey CA (2007b). Protocols for collection of surface soil samples at military training and testing ranges for the characterization of energetic munitions constituents. ERDC-CRREL TR-07-10

16. Clausen JL, Richardson J, Perron N, Gooch G, Hall T, Butterfield E (2012) Evaluation of sampling and sample preparation modifications for soil containing metallic residues, ERDC TR-12-1

17. Taylor S, Lever JH, Fadden J, Perron N, Packer B (2009) Simulated rainfall-driven dissolution of TNT, tritonal, Comp B and Octol particles. Chemosphere 75:1074–1081

18. Lever JH, Taylor S, Perovich L, Bjella K, Packer B (2005) Dissolution of composition B detonation residuals. Environ Sci Technol 39:8803–8811

19. Taylor S, Richardson C, Lever JH, Pitt JS, Bigl S, Perron N, Bradley JP (2011) Dissolution of nitroglycerin from small arms propellants and their residues. Int J Energ Mater Chem Propuls 10:397–419
20. Yazici R, Kalyon DM, Fair D (1998) Microstructure and mixing distribution analysis in M30 triple-base propellants. U.S. Army Armament Research, Development and Engineering Center, Warheads, Energetics and Combat-support Armaments Center, Picatinny Arsenal, New Jersey
21. Levy ME (1955) Microscopic studies of ball propellant, Frankford Arsenal report. Pitman-Dunn Laboratories, Philadelphia, PA, USA
22. Yazici R, Kalyon DM (1998) Microstructure and mixing distribution analysis in M30 triple-base propellants
23. Taylor S, Lever JH, Fadden J, Perron N, Packer B (2009) Outdoor weathering and dissolution of TNT and tritonal. Chemosphere 77:1338–1345
24. Taylor S, Lever JH, Walsh ME, Fadden J, Perron N, Bigl S, Spanggord R, Curnow M, Packer B (2010) Dissolution rate, weathering mechanics and friability of TNT, Comp B, tritonal, and Octol. ERDC/CRREL
25. Bedford CD, Carpenter PS, Nadler MP (1996) Solid-state photodecomposition of energetic nitramines (RDX and HMX). Naval Air Warfare Center Weapons Division, China Lake, CA 93555-6001
26. Yinon J (1999) Forensic and environmental detection of explosives. John Wiley, Chichester, UK
27. U.S. Environmental Protection Agency (2012) Region 9 human health screening levels
28. Jenkins TF, Ampleman G, Thiboutot S, Bigl SR, Taylor S, Walsh MR, Faucher D, Martel R, Poulin I, Dontsova KM, Walsh ME, Brochu S, Hewitt AD, Comeau G, Diaz E, Chappell MA, Fadden JL, Marois A, Fifield LNR, Quemerais B, Simunek J, Perron NM, Gagnon A, Gamache T, Pennington JC, Moors V, Lambert DJ, Gilbert MD, Bailey RN, Tanguay V, Ramsey CA, Melanson L, Lapointe MC (2008) Strategic environmental research and development program (SERDP) Characterization and fate of gun and rocket propellant residues on testing and training ranges: final report
29. Paquet L, Monteil-Rivera F, Hatzinger PB, Fuller ME, Hawari J (2011) Analysis of the key intermediates of RDX (hexahydro-1,3,5-trinitro-1,3,5-triazine) in groundwater: occurrence, stability and preservation. J Environ Monit 13:2304–2311
30. Gobas FAPC, Moore MM, Hermens JLM, Arnot JA (2006) Bioaccumulation reality check. SETAC Globe 7(5):40–41
31. Thorn KA, Kennedy KR (2002) 15N NMR investigation of the covalent binding of reduced TNT amines to soil humic acid, model compounds, and lignocellulose. Environ Sci Technol 36:3787–3796
32. Dontsova KM, Hayes C, Pennington JC, Porter B (2009) Sorption of high explosives to water-dispersible clay: influence of organic carbon, aluminosilicate clay, and extractable iron. J Environ Qual 38:1458–1465
33. Tucker WA, Murphy GJ, Arenberg ED (2002) Adsorption of RDX to soil with low organic carbon: laboratory results, field observations, remedial implications. Soil Sediment Contam 11:809–826
34. Eriksson J, Skyllberg U (2001) Binding of 2,4,6-trinitrotoluene and its degradation products in a soil organic matter two-phase system. J Environ Qual 30:2053–2061
35. Zhang D, Zhu D, Chen W (2009) Sorption of nitroaromatics to soils: comparison of the importance of soil organic matter versus clay. Environ Toxicol Chem 28:1447–1454
36. Haderlein SB, Weissmahr KW, Schwarzenbach RP (1996) Specific adsorption of nitroaromatic explosives and pesticides to clay minerals. Environ Sci Technol 30:612–622
37. Pennington JC, Patrick WH (1990) Adsorption and desorption of 2,4,6-trinitrotoluene by soils. J Environ Qual 19:559–567
38. Elovitz MS, Weber EJ (1999) Sediment-mediated reduction of 2,4,6-trinitrotoluene and fate of the resulting aromatic (poly)amines. Environ Sci Technol 33:2617–2625

39. Haderlein SB, Schwarzenbach RP (1995) Environmental processes influencing the rate of abiotic reduction of nitroaromatic compounds in the subsurface. In: Spain JC (ed) Biodegradation of nitroaromatic compounds. Springer Science+Business Media, New York, pp 199–225

40. Rieger P-G, Knackmuss HJ (1995) Basic knowledge and perspectives on biodegradation of 2,4,6-trinitrotoluene and related nitroaromatic compounds in contaminated soil. In: Spain JC (ed) Biodegradation of nitroaromatic compounds. Plenum Press, New York, pp 1–18

41. Weissmahr KW, Hildenbrand M, Schwarzenbach RP, Haderlein SB (1999) Laboratory and field scale evaluation of geochemical controls on groundwater transport of nitroaromatic ammunition residues. Environ Sci Technol 33:2593–2600

42. Li AZ, Marx KA, Walker J, Kaplan DL (1997) Trinitrotoluene and metabolites binding to humic acid. Environ Sci Technol 31:584–589

43. Weissmahr KW, Haderlein SB, Schwarzenbach RP (1998) Complex formation of soil minerals with nitroaromatic explosives and other pi-acceptors. Soil Sci Soc Am J 62:369–378

44. Ainsworth CC, Harvey SD, Szecsody JE, Simmons MA, Cullinan VI, Resch CT, Mong GM (1993). Relationship between the leachability characteristics of unique energetic compounds and soil properties. U.S. Army Biomedical Research and Development Laboratory, Fort Detrick, Frederick, MD

45. Thorn KA, Pennington JC, Kennedy KR, Cox LG, Hayes CA, Porter BE (2008) N-15 NMR study of the immobilization of 2,4- and 2,6-dinitrotoluene in aerobic compost. Environ Sci Technol 42:2542–2550

46. Brannon JM, Pennington JC (2002) Environmental fate and transport process descriptors for explosives. US Army Corps of Engineers, Engineer Research and Development Center, Vicksburg, MS

47. Dontsova KM, Yost SL, Simunek J, Pennington JC, Williford CW (2006) Dissolution and transport of TNT, RDX, and composition B in saturated soil columns. J Environ Qual 35:2043–2054

48. Szecsody JE, Girvin DC, Devary BJ, Campbell JA (2004) Sorption and oxic degradation of the explosive CL-20 during transport in subsurface sediments. Chemosphere 56:593–610

49. Winkler DA (1985) Conformational analysis of nitroglycerin. Propellants Explos Pyrotech 10:43–46

50. Spanggord RJ, Chou TW, Mill T, Haag W, Lau W (1987) Environmental fate of nitroguanidine, diethyleneglycol dinitrate, and hexachloroethane smoke. Final report, phase II. SRI International, Menlo Park, CA, p 67

51. Pennington JC, Jenkins TF, Ampleman G, Thiboutot S, Brannon JM, Hewitt AD, Lewis J, Brochu S, Diaz E, Walsh MR, Walsh ME, Taylor S, Lynch JC, Clausen J, Ranney TA, Ramsey CA, Hayes CA, Grant CL, Collins CM, Bigl SR, Yost SL, Dontsova KM (2006) Distribution and fate of energetics on DoD test and training ranges: final report. Engineer Research and Development Center, Vicksburg, MS

52. Dontsova KM, Pennington JC, Yost S, Hayes C (2007) Transport of nitroglycerin, nitroguanidine and diphenylamine in soils. Characterization and fate of gun and rocket propellant residues on testing and training ranges: interim report 1. Engineer Research and Development Center, Vicksburg, MS

53. Pennington JC, Jenkins TF, Ampleman G, Thiboutot S (2004) Distribution and fate of energetics on DoD test and training ranges: interim report 4. U.S. Army Engineer Research and Development Center, Vicksburg, MS

54. Alavi G, Chung M, Lichwa J, D'Alessio M, Ray C (2011) The fate and transport of RDX, HMX, TNT and DNT in the volcanic soils of Hawaii: a laboratory and modeling study. J Hazard Mater 185:1600–1604

55. Dontsova KM, Chappell M, Šimunek J, Pennington JC (2008) Dissolution and transport of nitroglycerin, nitroguanidine and ethyl centralite from M9 and M30 propellants in soils. Characterization and fate of gun and rocket propellant residues on testing and training ranges: final report. ERDC TR-08-1. U.S. Army Engineer Research and Development Center, Vicksburg, MS

56. Dontsova KM, Hayes C, Šimunek J, Pennington JC, Williford CW (2009) Dissolution and transport of 2,4-DNT and 2,6-DNT from M1 propellant in soil. Chemosphere 77:597–603
57. Gutiérrez JP, Padilla IY, Sánchez LD (2010) Transport of explosive chemicals when subjected to infiltration and evaporation processes in soils. Ingeniería y Competitividad 12:117–131
58. Townsend DM, Adrian DD, Myers TE (1996) RDX and HMX sorption in thin disk soil columns. Waterways Experiment Station, US Army Corps of Engineers, p 33
59. Townsend DM, Myers TE, Adrian DD (1995) 2,4,6-Trinitrotoluene (TNT) transformation/sorption in thin-disk soil columns. US Army Corps of Engineers, Waterways Experiment Station, p 58
60. Yamamoto H, Morley MC, Speitel GE, Clausen J (2004) Fate and transport of high explosives in a sandy soil: adsorption and desorption. Soil Sediment Contam 13:459–477
61. Bordeleau G, Martel R, Ampleman G, Thiboutot S, Poulin I (2012) The fate and transport of nitroglycerin in the unsaturated zone at active and legacy anti-tank firing positions. J Contam Hydrol 142–143:11–21
62. Fuller ME, Schaefer CE, Andaya C, Fallis S (2015) Production of particulate composition B during simulated weathering of larger detonation residues. J Hazard Mater 283:1–6
63. Fuller ME, Schaefer CE, Andaya C, Fallis S (2014) Transport and dissolution of microscale composition B detonation residues in porous media. Chemosphere 107:400–406
64. Lavoie B (2010) Transport of explosive residue surrogates in saturated porous media. In: Geology. The University of Tennessee, Knoxville
65. Taylor S, Bigl S, Packer B (2015) Condition of in situ unexploded ordnance. Sci Total Environ 505:762–769
66. Walsh MR, Walsh ME, Hewitt AD (2009) Energetic residues from the expedient disposal of artillery propellants. ERDC/CRREL TR-09-8
67. Walsh MR, Taylor S, Walsh ME, Bigl S, Bjella K, Douglas T, Gelvin A, Lambert D, Perron N, Saari S (2005a) Residues from live fire detonations of 155-mm howitzer rounds. U. S. Army Engineer Research and Development Center, Cold Regions Research and Engineering Laboratory, Hanover, NH
68. Walsh MR, Walsh ME, Ramsey CA, Rachow RJ, Zufelt JE, Collins CM, Gelvin AB, Perron NM, Saari SP (2006) Energetic residues from a 60-mm and 81-mm live fire exercise
69. Walsh MR, Walsh ME, Collins CM, Saari SP, Zufelt JE, Gelvin AB, Hughes JB (2005b) Energetic residues from live-fire detonations of 120-mm Mortar rounds. ERDC/CRREL TR-05-15
70. Ampleman G, Thiboutot S, Marois A, Gagnon A, Gilbert D, Walsh MR, Walsh ME, Woods P (2009) Evaluation of the propellant, residues emitted during 105-mm leopard tank live firing at CFB Valcartier, Canada. Defence R&D Canada-Valcartier, TR 2009-420
71. Walsh MR, Walsh ME, Hug JW, Bigl SR, Foley KL, Gelvin AB, Perron NM (2010) Propellant residues deposition from firing of 40-mm grenades. ERDC/CRREL TR-10-10
72. Walsh MR, Walsh ME, Bigl SR, Perron NM, Lambert DJ, Hewitt AD (2007) Propellant residues deposition from small arms munitions. Cold Regions Research and Engineering Laboratory, U.S. Army Engineer Research and Development Center, Hanover, NH
73. Hewitt AD, Jenkins TF, Walsh ME, Walsh MR, Taylor S (2005) RDX and TNT residues from live-fire and blow-in-place detonations. Chemosphere 61:888–894
74. Walsh ME, Collins CM, Hewitt AD, Walsh MR, Jenkins TF, Stark J, Gelvin A, Douglas TS, Perron N, Lambert D, Bailey R, Myers K (2004) Range characterization studies at Donnelly training area, Alaska: 2001 and 2002. ERDC/CRREL TR-04-3
75. Ro KS, Venugopal A, Adrian DD, Constant D, Qaisi K, Valsaraj KT, Thibodeaux LJ, Roy D (1996) Solubility of 2,4,6-trinitrotoluene (TNT) in water. J Chem Eng Data 41:758–761
76. Rosenblatt DH, Burrows EP, Mitchell WR, Parmer DL (1991) Organic explosives and related compounds. In: Hutzinger O (ed) The handbook of environmental chemistry. Springer, Berlin, pp 195–234

77. Banerjee S, Yalkowsky SH, Valvani C (1980) Water solubility and octanol/water partition coefficients of organics. Limitations of the solubility-partition coefficient correlation. Environ Sci Technol 14:1227–1229

78. Monteil-Rivera F, Paquet L, Deschamps S, Balakrishnan V, Beaulieu C, Hawari J (2004) Physico-chemical measurements of CL-20 for environmental applications. Comparison with RDX and HMX. J Chromatogr A 1025:125–132

79. U.S. Army Materiel Command (1971) Properties of explosives of military interest. In: Engineering design handbook. Explosives series, AMC pamphlet 706-177, Washington, DC, 29 Jan 1971

80. Haag WR, Spanggord R, Mill T, Podoll RT, Chou T-W, Tse DS, Harper JC (1990) Aquatic environmental fate of nitroguanidine. Environ Toxicol Chem 9:1359–1367

81. Van der Schalie WH (1985) The toxicity of nitroguanidine and photolyzed nitroguanidine to freshwater aquatic organisms. U.S. Army Medical Bioengineering Research and Development Laboratory, Fort Detrick, Fredrick, MD

82. Sheremata TW, Halasz A, Paquet L, Thiboutot S, Ampleman G, Hawari J (2001) The fate of the cyclic nitramine explosive RDX in natural soil. Environ Sci Technol 35:1037–1040

83. Pennington JC, Jenkins TF, Ampleman G, Thiboutot S, Brannon JM, Lynch J, Ranney TA, Stark JA, Walsh ME, Lewis J, Hayes CA, Mirecki JE, Hewitt AD, Perron N, Lambert D, Clausen J, Delfino JJ (2002) Distribution and fate of energetics on DoD test and training ranges: interim report 2. Army Corps of Engineers, Washington, DC, U.S, p 126

84. Pennington JC, Thorn KA, Hayes CA, Porter BE, Kennedy KR (2003) Immobilization of 2,4- and 2,6-dinitrotoluenes in Soils and Compost. US Army Engineer Research and Development Center, Vicksburg, MS

85. Price CB, Brannon JM, Yost SL, Hayes CA (2000) Adsorption and transformation of explosives in low-carbon aquifer soils. Engineer Research and Development Center Environmental Laboratory, Vicksburg, MS, p 26

86. Leggett DC (1985) Sorption of military explosive contaminants on bentonite drilling muds. CRREL report 85-18

87. Pennington JC, Brannon JM, Berry TE Jr., Jenkins TF, Miyares PH, Walsh ME, Hewitt AD, Perron N, Ranney TA, Lynch J, Delfino JJ, Hayes CA (2001) Distribution and fate of energetics on DoD test and training ranges: interim report 1. U.S. Army Engineer Research and Development Center, Vicksburg, MS

88. Brannon JM, Deliman PN, Gerald JA, Ruiz CE, Price CB, Hayes C, Yost S, Qasim M (1999) Conceptual model and process descriptor formulations for fate and transport of UXO. U.S. Army Engineer Waterways Experiment Station, Vicksburg, MS

Insensitive Munitions Formulations: Their Dissolution and Fate in Soils

Susan Taylor, Katerina Dontsova and Marianne Walsh

Abstract New explosive compounds that are less sensitive to shock and high temperatures are being tested as replacements for TNT (2,4,6-trinitrotoluene) and RDX (hexahydro-1,3,5-trinitro-1,3,5-triazine). Two of these explosives, DNAN (2,4-dinitroanisole) and NTO (3-nitro-1,2,4-triazol-5-one), have good detonation characteristics and are the main ingredients in a suite of insensitive munitions (IM) explosives. Both compounds, however, are more soluble than either TNT or RDX. Data on their fate could help determine if DNAN and NTO have the potential to reach groundwater and be transported off base, an outcome that could create future contamination problems on military training ranges and trigger regulatory action. In this chapter, we describe how quickly IM constituents (DNAN, NTO, nitroguanidine, RDX and ammonium perchlorate) dissolve from three IM formulations (IMX-101, IMX-104 and PAX-21) and how solutions of IM compounds interact with different types of soils. This information, coupled with the mass of IM formulations scattered on a range, will allow estimates of the dissolved IM mass loads, their subsequent transport and fate, and their likelihood of reaching groundwater.

Keywords High explosives · Dissolution · Soil interactions

1 Introduction

New explosive compounds that are less sensitive to shock and high temperatures are being tested as replacements for TNT (2,4,6-trinitrotoluene) and RDX (hexahydro-1,3,5-trinitro-1,3,5-triazine). Two of these explosives, DNAN (2,4-dinitroanisole) and NTO (3-nitro-1,2,4-triazol-5-one), have good detonation

S. Taylor (✉) · M. Walsh
Cold Regions Research and Engineering Laboratory, Hanover, NH 03766, USA
e-mail: Susan.Taylor@erdc.dren.mil

K. Dontsova
Biosphere 2, University of Arizona, Tucson, AZ 85721-0158, USA

characteristics and are the main ingredients in a suite of insensitive munitions (IM) formulations that are being fielded (Table 1). Both compounds, however, are more soluble than either TNT or RDX (Table 2) and research has shown that both have some human and environmental toxicity. Toxicology data for DNAN show that it is more toxic to mammals than TNT [1–3], can inhibit seed germination and plant growth [4] and is toxic to bacteria and earthworms [5]. While NTO has low mammalian toxicity [6], both DNAN and NTO can form toxic transformation products [3, 7, 8].

Explosives are released onto training range soils when unexploded ordnance (UXO) casings fail and after incomplete (partial) detonations during training with explosive-filled munitions and from blow-in-place operations. Partial detonations are estimated to deposit most of the explosive mass available for dissolution on ranges today [9]. The solid particles of IM explosives, scattered by incomplete detonations, are dissolved by precipitation and can then travel to groundwater. What compounds reach grosundwater is determined by their rates of dissolution, photo-transformation (both in solid form and in aqueous solution), and complex interactions of the aqueous explosive solutions with soil constituents during transport through the vadose zone.

Solubility, along with particle size and climatic conditions (rainfall and temperature), controls the dissolution rate of solid explosives [10–12]. The solubility of DNAN and nitroguanidine (NQ) increases by a factor of two between 20 and 40 °C and almost doubles for NTO (Fig. 1). The dissolution of DNAN and NTO, when part of a formulation, will depend not only on their individual solubility but also on the fraction of each component exposed to water. This process has been documented and modeled for high explosives [13, 14, 10, 11, 12]) but is different for DNAN-based IM formulations. The latter have constituents with order of magnitude differences in solubility, resulting in, not smaller diameter particles as occurs for HE, but hole-riddled particles with the same initial diameter [15, 16]. DNAN composes the matrix of IM formulations and, as it is one of the least soluble components, it persist as porous particles subject to photo-transformation. It is likely that their surfaces will photo-transform in the environment and, if the products are soluble, that these compounds could travel with the precipitation into the soil and possibly to groundwater.

Table 1 Compositions of IM formulations (IMX-101, IMX-104 and PAX-21) that contain DNAN and NTO and that we studied

IM	Components	Used in
IMX-101	DNAN, NQ, NTO	Qualified as the main fill in the 155 mm projectile
IMX-104	NTO, DNAN, RDX	Used by the U.S. Army for 60, and 81 mm mortars
PAX-21	DNAN, AP, RDX	No longer being fired during training or testing on US ranges

RDX contains about 10% HMX (octahydro-1,3,5,7-tetranitro-1,3,5,7-tetrazocine) as a manufacturing impurity. Data are from Fung et al. [17], Wilson [18], Pelletier et al. [19], and Coppola [20]

Table 2 Properties of DNAN, NTO and other compounds found in IM formulations

Energetic	Aqueous solubility[a]	Density	Formula	Reference
DNAN	276	1.34	$C_7H_6N_2O_5$	[21]
NTO	16,642	1.93	$C_2H_2N_4O_3$	[22]
TNT	128	1.65	$C_7H_5N_3O_6$	[23]
RDX	56	1.82	$C_3H_6N_6O_6$	[24]
HMX	4.5	1.81	$C_4H_8N_8O_8$	[24]
NQ	2600 ± 100	1.55	$CH_4N_4O_2$	[25]
AP	217,000	1.95	NH_4ClO_4	[26]

[a]mg L^{-1} at 25 °C

Fig. 1 Aqueous solubility of **a** DNAN, **b** NQ and **c** NTO plotted as a function of temperature
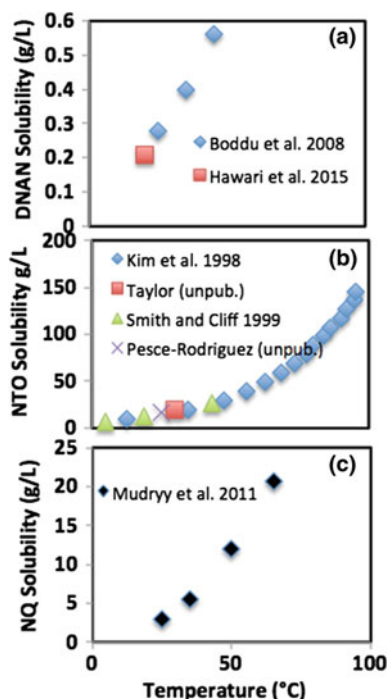
2   Field Deposition

Military training scatters explosive and propellantcompounds onto the soil surface. As was discussed for HE[13], the mass of the scattered materials depends on the type of round fired and the manner in which it detonated: high-order, low-order (partial), or blow-in-place detonations. IM formulations are mainly being used to fill mortar rounds and artillery projectiles (Table 1). Table 3 summarizes detonation test results for similar caliber rounds filled with either IM or HE. For the high order tests, rounds were either fired or command detonated using a fuze simulator [27].

Table 3 Comparison of IM and HE residues deposited after high-order and blow-in-place detonations, data from Walsh et al. [28, 29, 30, 27, 31]. The high order detonation residues were collected from either fired rounds or command detonations that initiated the normal detonation chain of the round. The blow in place detonations used one or more C4 blocks placed on the outside of the round-the current EOD practice

| | | Residue deposited | | | | High Order | | | blow-in-place | | | | | | |
	Caliber	Dodic	# sampled	Exp. Fill	Compounds	Mass (g)	Residues (mg)	Exp. Consumed Efficiency (%)	Dodic	# sampled	Exp. Fill	Compounds	Mass (g)	Residues (mg)	Exp.Consumed Efficiency
Mortar	60-mm	M888	7	Comp B	TNT RDX+HMX	153 230	nd 0.073	100.000 100.000	M888 Block C4	7	Comp B	TNT RDX+HMX	750	200	99.973
		M888	5	Comp B	TNT RDX+HMX	153 230	nd 0.074	100.000							
		M768	7	PAX 21	DNAN RDX+HMX AP Total	120 130 91 341	7.1 9.2 14,000 14016.3	99.994 99.993 84.615 95.890	M768 Block C4	7	PAX 21	DNAN RDX+HMX AP Total	120 130 91 341	7.1 9.2 14,000 14016.3	99.994 99.993 84.615 95.890
			7	IMX-104	DNAN NTO RDX+HMX Total	110 180 75 365	5.3 2200 4.5 2209.8	99.995 98.778 99.994 99.395	No dodic Block C4	7	IMX-104	DNAN NTO RDX+HMX Total	110 180 600 890	20120 89000 8300 117420	81.709 50.556 98.617 86.807
	81-mm	M374	14	Comp B	TNT RDX+HMX	400 600	nd 8.5	99.999	M374 block C4	7	Comp B	TNT RDX+HMX	1100	150	99.986
		M374	3	Comp B	TNT RDX+HMX	400 600	nd 10	99.998							
		M821A2 12g C4	7	IMX-104	DNAN NTO RDX+HMX Total	260 430 150 840	27 1900 16 1943	99.990 99.558 99.989 99.769	M821A2 block C4	7	IMX-104	DNAN NTO RDX+HMX Total	260 430 680 1370	45000 230000 20000 295000	82.692 46.512 97.059 78.467
		M821A2 18g C4	5	IMX-104	DNAN NTO RDX+HMX Total	260 430 160 850	7.8 540 7.6 555.4	99.997 99.874 99.995 99.935	M821A2 block C4	7	IMX-104	DNAN NTO RDX+HMX Total	260 430 860 1550	5000 45000 2100 52100	98.077 89.535 99.756 96.639
		M821A2 18g C4	1	IMX-104	DNAN NTO RDX+HMX Total	260 430 160 850	13 1150 3.8 1166.8	99.995 99.733 99.998 99.863							
		M821A2 18g C4	2	IMX-104	DNAN NTO RDX+HMX Total	260 430 160 850	17 720 4.1 741.1	99.993 99.833 99.997 99.913							
	120-mm	M933	7	Comp B	TNT RDX+HMX	1800	19	99.999	M933 Block C4	7	Comp B	TNT RDX+HMX	2300	25	99.999

(continued)

Table 3 (continued)

		Residue deposited				High Order			blow-in-place					
Caliber	Dodic	# sampled	Exp. Fill	Compounds	Mass (g)	Residues (mg)	Exp. Consumed		# sampled	Exp. Fill	Compounds	Mass (g)	Residues (g)	Exp. Consumed
Howitzer 105-mm	M1	9	Comp B	TNT RDX+HMX	1300	0.095	100.000	M1 Block C4	7	Comp B	TNT RDX+HMX	1800	50	99.997
155-mm	M107	7	Comp B	TNT RDX+HMX	4200	0.3	100.000	M107 Block C4	7	Comp B	TNT RDX+HMX	4700	15	100.000
155-mm practice	M107	7	TNT	TNT	6600	nd	100.000	M107 Block C4	7	TNT	TNT RDX	6600 520	5.9 5.9	100.000 99.999
	M1122 40-g C4	1	IMX-101	DNAN NTO NQ RDX+HMX Total	480 230 430 40 700	5900 40000 170000 18 210018	98.771 82.609 60.465 99.955 69.997	M1122 Block C4	3	IMX-104	DNAN NTO NQ RDX+HMX Total	480 230 430 710 1370	5300 15000 100000 21 115021	98.896 93.478 76.744 99.997 91.604
	M1122 50-g C4	7	IMX-101	DNAN NTO NQ RDX+HMX Total	480 230 430 50 710	2400 15000 130000 12 145012	99.500 93.478 69.767 99.976 79.576							
	M1122 60-g C4	1	IMX-101	DNAN NTO NQ RDX+HMX Total	480 230 430 50 710	660 14000 120000 10 134010	99.863 93.913 72.093 99.980 81.125	M1122 2 blocks C4	3	IMX-104	DNAN NTO NQ RDX+HMX Total	480 230 430 1200 1860	21000 24000 100000 46 124046	95.625 89.565 76.744 99.996 93.331
120-mm	100-g C4	5	PAX-21	DNAN NTO RDX+HMX Total	1700 1100 740 3540	nd 23 nd 23	99.998 99.999	5 blocks C4	5	PAX-21	DNAN NTO RDX+HMX Total	1700 1100 3300 6100	53000 410000 3800 466800	96.882 62.727 99.885 92.348

TNT (2,4,6-trinitrotoluene), RDX (hexahydro-1,3,5-trinitro-1,3,5-triazine), HMX (octahydro-1,3,5,7-tetranitro-1,3,5,7-tetrazocine), NQ (nitroguanidine), NTO (3-nitro-1,2,4-triazol-5-one), DNAN (2,4-dinitroanisole). Explosive fill (Exp. Fill) refers to the type of explosive formulation in the round

C4 in the simulator is detonated using a blasting cap and this blast initiates the detonation train of the round. For the blow-in-place tests, C4 blocks were placed on the outside of the round following the procedure used by explosive ordnance disposal personnel. The data show that more IM residue is deposited than HE residue for similar detonation conditions. For HE high order detonations 99.99% of the mass in the rounds is consumed but this percentage is slightly lower for most IM detonations and much lower for their individual constituents-values in bold highlight the lower percentage of ammonium perchlorate consumed (84%) in PAX-21, and the lower percentage of NTO (83–94%) and NQ (60–72%) consumed for IMX-101-filled rounds. The NTO consumed in IMX-104 rounds was consistently higher (>99.5%) for high order detonations but much lower and more variable for the blow-in-place detonations (47–90%). The IM blow-in-place detonations left more residues, particularly their crystal constituents AP, NQ and NTO, than did the HE blow-in-place (Table 3). It should be noted that the US Army has discontinued training using PAX21-filled rounds because of the amount of AP they deposit.

The field deposition of IM formulations differs from that of HE in two significant ways. First of all, IM rounds are designed to be more difficult to detonate and they leave more residues. Secondly, a fraction of the NTO, NQ and AP crystals in the DNAN matrices is deposited on the soil, even during high order detonations (Table 3). Micro computed tomographic (μCT) images show that the constituent crystals are de-bonded from the DNAN matrix during detonation, allowing some fraction of the crystals to be scattered (Fig. 2) [15].
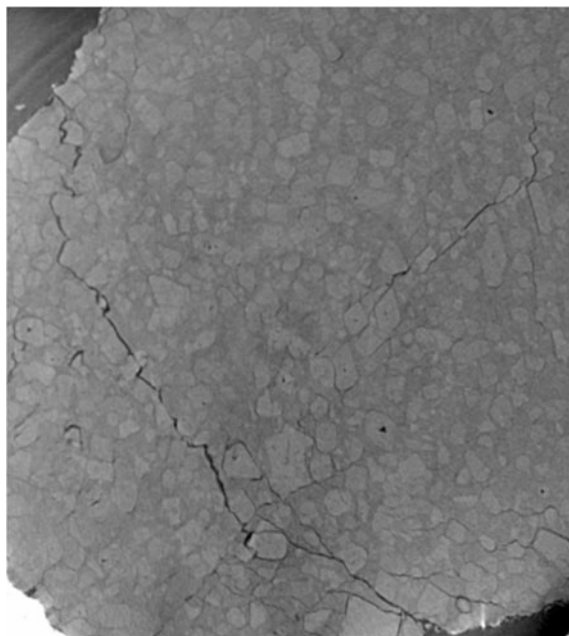
Fig. 2 A micro computed tomography (μCT) image of an IMX-101 particle from a partial detonation. Note that the fractures tend to travel through the DNAN matrix and around the periphery of both the NTO and NQ crystals
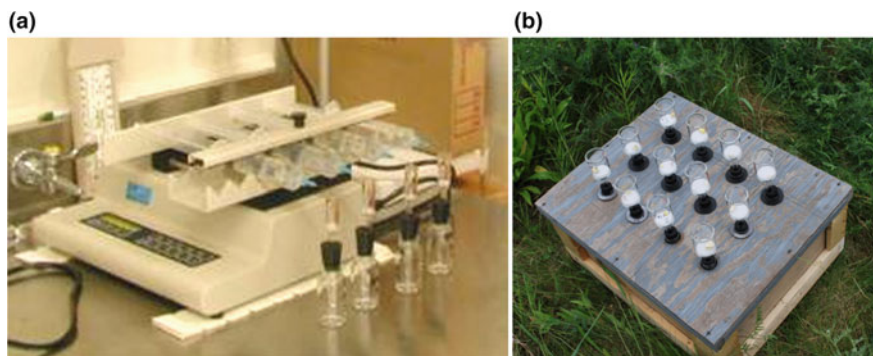
Fig. 3 Photos of **a** the laboratory drip tests and **b** the outdoor setup where glass liter jars in the box collect the effluent from precipitation interacting with explosive pieces in the glass funnels

3 Dissolution of IM Detonation Residues

3.1 Indoor Drip Tests

Taylor et al. [32] used well-controlled laboratory drip experiments to obtain dissolution data on field collected particles of IMX-101, IMX-104, and PAX-21 from detonation experiments [29, 31]. The laboratory tests used massed individual mm-size pieces of the explosive placed on a glass frit and dripped on by water at a 0.5 mL/h (Fig. 3a), after which the effluent was analyzed using HPLC. The laboratory tests on IMX-101 particles showed that NTO was the first compound to dissolve followed by NQ, and DNAN, (Fig. 4 top) consistent with the solubility of each component (Table 2; Fig. 1). NTO was lost quickly as indicated by a steep rise in the mass loss curve followed by a flat plateau. NQ had a less steep initial rise but also reached a plateau. DNAN was the last component to dissolve. The mass loss curves for the four IMX-104 particles (Fig. 4 bottom) show that NTO was again dissolved rapidly. The percent mass loss curves for the DNAN matrix were fairly linear with a larger percentage of DNAN dissolving early in the test and a larger fraction of RDX dissolving later in the test. These results agree with those obtained on a single, 150 mg piece of IMX-101 that was similarly dissolved [32, 33].

The mass balances for the indoor IMX-101 and IMX-104 tests show that the formulations are not being significantly photo- or bio-transformed in the laboratory because most of the mass ($100 \pm 5\%$) was recovered [15]. If these IM formulations were transforming into new, unknown compounds, the mass balance would be poor.
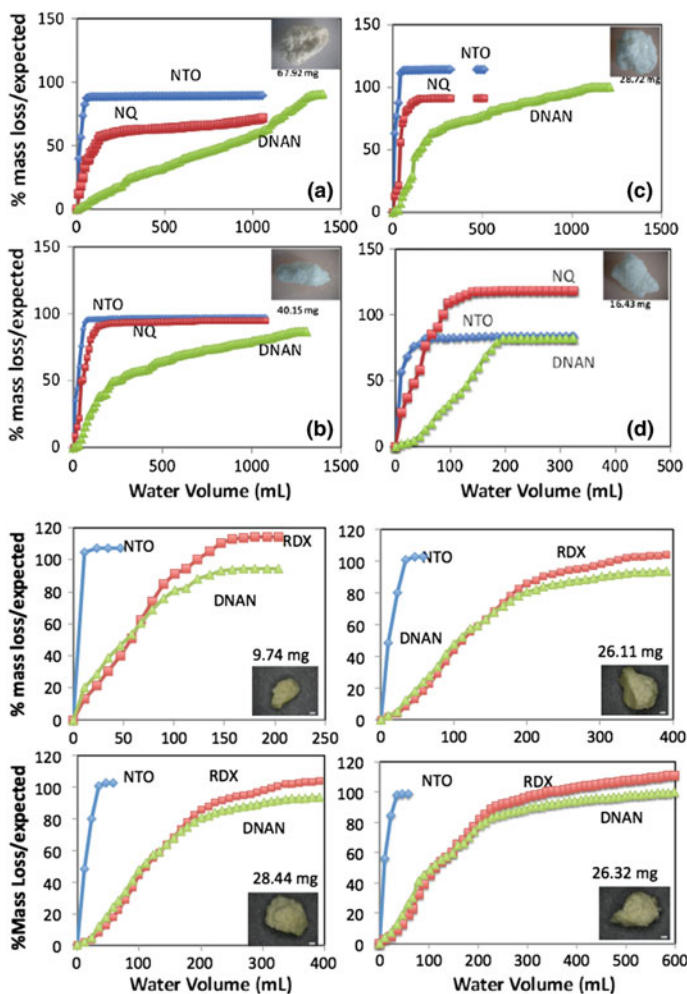
Fig. 4 Top four panels show the percent of mass dissolved for compounds in IMX-101 versus water volume (mL) and the bottom four panels show the same information for IMX-104. The y-axis plots the percent mass loss measured by HPLC relative to the expected mass (mass of initial particle multiplied by the percent contribution of each constituent in the formulation). Drip rate was 0.5 mL/h [25]

3.2 Outdoor Dissolution Tests

For the outdoor dissolution tests millimeter to centimeter-size chunks of detonated IM explosives were placed outside to weather under natural conditions (Fig. 3b); five particles of IMX-101 (#1 to #5), five particle of IMX-104 and two particles of PAX-21. The experiment ran for 864 days during which time the samples were wetted by 147 cm of precipitation. These tests simulated the dissolution of isolated

IM pieces on range soils and can be scaled based on rainfall rates at other locations. No soil was involved in any of the tests, yielding dissolution as a function of the particle mass and the water volume, average 3.7 ± 0.27 L, interacting with each particle [15, 16, 32].

The formulations were initially white (IMX-101), cream colored (IMX-104) and yellow (PAX-21) but their surfaces turned yellow after two weeks and orange to brick red after a year of exposure to sunlight (Fig. 5). During the 864 day long dissolution test all of the IM chunks split and all shed mm-sized particles, a much faster splitting rate than observed during similar tests on TNT, Comp B and Tritonal (TNT + aluminum) (Fig. 6) [34]. The friability of the IM formulations could be due to: (1) the large, ~ 300 µm, crystals they contain; (2) the voids left when the crystals dissolve or; (3) to fractures produced during detonation (Fig. 7) [32]. All of these features could weaken the IM formulations. The µCT images of an IMX-101 and an IMX-104 chunk taken before, part way through, and at the end of the outdoor tests (Fig. 7a, b) show that IMX-101 has lost crystals in its interior and periphery but less so than IMX-104 where all the NTO crystals dissolved.

Figure 8 shows the percent cumulative mass dissolved for each constituent in the IM formulation plotted against the cumulative volume of water collected. The mass loss data for the five IMX-101 chunks show that NTO dissolves first, followed by NQ and finally DNAN (Fig. 8a). The dissolution rates of NTO and NQ are higher at
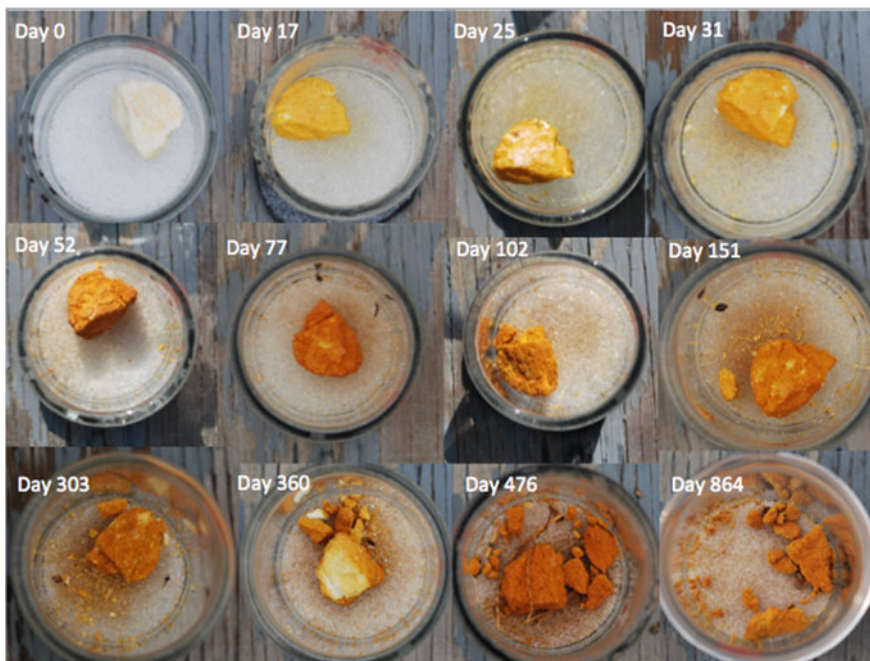
Fig. 5 IMX-101#1, set outside to weather and dissolve, shows changes to the appearance of the particle over the 864 days of the experiment
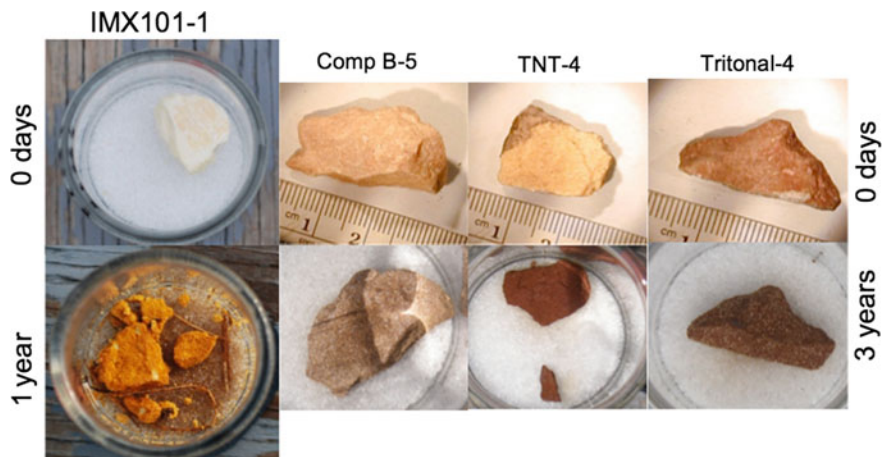
Fig. 6 IM formulations are very friable compared to traditional explosives
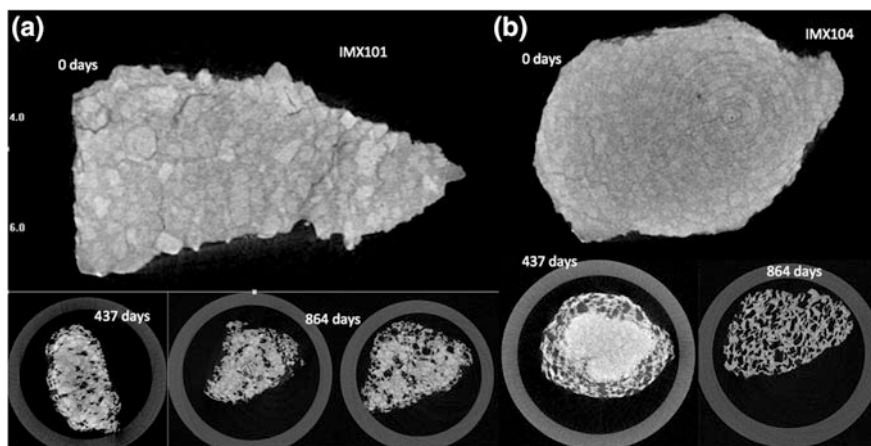
Fig. 7 Micro computed tomography (μCT) cross-sections of IMX-101 (**a**), and IMX-104 (**b**) taken at 0 and 437 and 864 days. These particles split during the test so the images taken at day 437 and 864 are the largest fragments of the original chunk

the start of the test and decrease with time. The shape of the NTO mass loss with water volume curve is more clearly seen for IMX-104, which contains no NQ (Fig. 8b). Figure 8c shows that the AP in PAX 21 dissolved in the first water sample indicating that water was able to access the interior of the PAX-21 particle.

As was found for laboratory experiments [33, 32], the constituents of the formulations dissolve in the order of their solubility. None of these chunks had completely dissolved after 864 days.
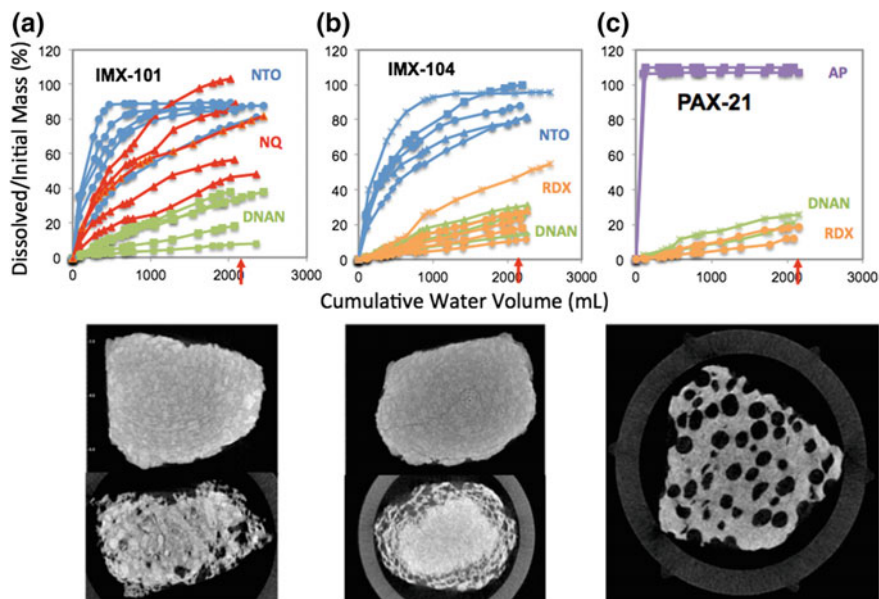
Fig. 8 Dissolved mass versus precipitationvolume for 5 IMX-101 (**a**), 5 IMX-104(**b**) and 2 PAX-21 (**c**) chunks placed outside, NTO (*blue*), NQ (*orange*), DNAN (*green*), RDX (*red*), AP (*purple*) [16]. Micro computed tomography images were taken at the beginning and near the end of the tests (*red arrows*). No initial µCT image for the PAX-21 is shown because the AP crystals appear very bright and produce artifacts and a poor quality image

Unlike TNT and Comp B, IM formulations dissolve throughout their volumes due to their soluble crystals constituents. One cannot, therefore, use dissolution models that assume dissolution from the surface [10] to calculate particle lifetimes. In these formulations, however, DNAN (and RDX) dissolve at a semi-constant rate; the mass loss is fairly linear when plotted against water volume (Fig. 9). The best linear fits to the DNAN data have slopes ranging from 0.0114 to 0.0572 and goodness of fit measures (R^2) between 0.94 and 0.99. As DNAN constitutes the matrix, its quasi-linear dissolution can be used to estimate chunk lifetimes. IMX-101 particles of 0.3–3.5 g (0.6–1.4 cm) are estimated to need 6–27 L (240–1080 cm) of precipitation to dissolve so their persistence can be estimated from local rainfall records. Values are similar for IMX-104, where 0.2–2 g (0.5–1.1 cm) particles require 4–15 L (160–600 cm) of precipitation to dissolve and for PAX-21 where 0.2–1.3 g (0.5–1 cm) particles would need 7–11 L (280–1080 cm) of precipitation to dissolve.

Quasi-linear dissolution does not occur for the NTO or NQ, for mm-sizes particles of these formulations [15, 16], or for Comp B and TNT [12]. In all these cases the explosive pieces lose more mass initially when soluble constituents are at or near the surface of the chunk, and then mass loss decreases as constituents are depleted or as water has a harder time contacting the constituents. For DNAN, its
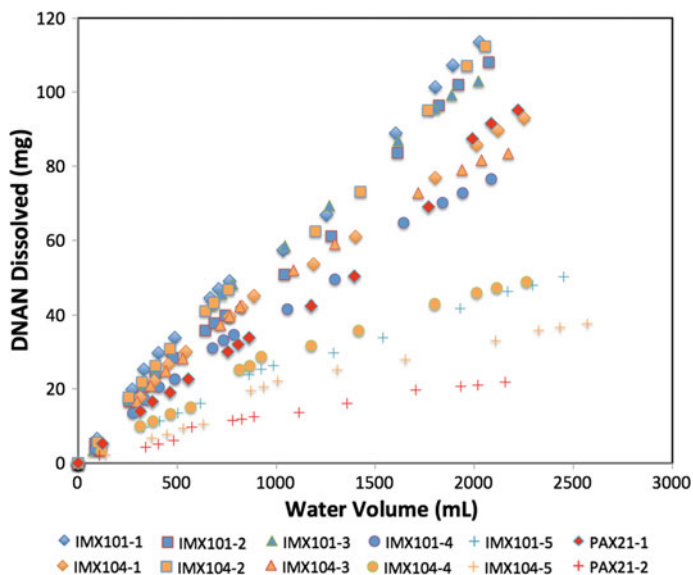
Fig. 9 Dissolved DNAN plotted against water volume for outdoor samples of IMX-101, IMX-104 and PAX-21 [11]

low solubility coupled with increases in its surface area explains the linear mass loss. When the IM chunks split, the numerous fragments that result increase the DNAN surface area and dissolution. This idea is supported by the fact that more fragments result in a better linear fit to the mass loss versus water volume data [15, 16]. Although fragmentation also affects the dissolution of NTO, NQ and AP none of these show quasi-linear dissolution because the time scales over which these compounds dissolve are shorter than the fragmentation rate.

3.3 Mass Balance for Outdoor Tests

Table 4 lists the initial and final masses for the IM particles, the difference between these masses, and how much explosive mass was found in the effluent samples. The same data for the high explosives (HE) outdoor tests is also shown. For IM, the difference between the initial and final masses averaged 0.8 ± 0.6 g and about 80% of this value was recovered in the effluent samples suggesting a 20% loss via photo-transformation. The conventional explosives (TNT, Comp B, Tritonal and C4) lost less mass, the difference between the initial and ending mass averaged 0.2 ± 0.08 g (constituents less soluble and particle less friable) but of this only about 20% was recovered in the effluent samples. This suggests that $\sim 80\%$ was photo-transformed into compounds not analyzed for in the effluent samples [34].

Table 4 Results of mass balance calculation for IM and high explosive formulations

Insensitive munition formulations							High explosive formulations						
Sample	M_i (g)	M_f (g)	Diff (g)	M_{diss} (g)	M_{miss} (g)	M_{diss} (Diff)	Sample	M_i (g)	M_f (g)	Diff (g)	M_{diss} (g)	M_{miss} (g)	M_{diss} (Diff)
IMX-101-1	3.55	1.43	2.12	1.65	0.48	0.78	TNT-1	1.97	1.75	0.22	0.071	0.15	0.32
IMX-101-2	1.39	0.28	1.11	0.75	0.36	0.68	TNT-2	0.4	0.31	0.10	0.033	0.06	0.34
IMX-101-3	0.63	0.02	0.61	0.49	0.12	0.80	TNT-3	0.52	0.28	0.24	0.074	0.16	0.32
IMX-101-4	0.53	0.04	0.49	0.38	0.11	0.77	Comp B-1	0.78	0.65	0.13	0.065	0.06	0.50
IMX-101-5	0.31	0.05	0.26	0.23	0.03	0.89	Comp B-2	0.43	0.31	0.11	0.056	0.06	0.50
IMX-104-1	2.00	0.70	1.30	1.15	0.15	0.88	Comp B-3	5.07	4.85	0.22	0.066	0.15	0.30
IMX-104-2	1.42	0.13	1.29	0.99	0.30	0.77	Trit-1	2.97	2.77	0.20	0.047	0.16	0.23
IMX-104-3	0.99	0.23	0.76	0.65	0.11	0.86	Trit-2	5.32	4.99	0.33	0.054	0.28	0.16
IMX-104-4	0.49	0.13	0.36	0.33	0.03	0.91	Trit-3	2.47	2.22	0.24	0.054	0.19	0.22
IMX-104-5	0.22	0.01	0.21	0.18	0.03	0.85	C4-1	4.93	4.62	0.31	0.037	0.27	0.12
PAX-21-1	1.28	0.41	0.87	0.67	0.20	0.77	C4-2	3.97	3.64	0.33	0.059	0.27	0.18
PAX-21-2	0.25	0.08	0.17	0.14	0.03	0.80	C4-3	2.30	2.10	0.20	0.030	0.17	0.15

Initial (M_i) and final (M_f) masses of the particles

Diff = $M_i - M_f$

M_{diss} = Mass determined from effluent samples via HPLC

M_{miss} = Mass missing = $M_i - (M_f + M_{diss})$

HPLC mass/mass not recovered = $(M_{diss})/(M_i - (M_f + M_{diss}))$

3.4 Photo-Transformation of IM

Photo-transformation is an important process because sunlight might chemically alter the surface of a compound to produce other compounds with different solubilities or toxicities. Hydrolysis studies found that without sunlight, DNAN and NTO are stable over a range of neutral, acidic, and basic conditions that can be encountered in natural environment and hydrolyze only at pH $\geq$ 12 (R. Pesce-Rodriguez, unpublished data [35, 36].

DNAN transformation pathways and products have been reported for several matrices including cell cultures, soil microcosms, sludge bioassays, treated wastewater, toxicity test organisms, irradiated aqueous solutions, and oxic aqueous solutions [8]. Few studies have been reported on the photo-transformation of the surface of solid pieces of DNAN or IM compositions [15]. Unknown peaks in the HPLC chromatograms of outdoor samples suggest that the particle surfaces are photo-degrading and forming new compounds; note the many additional peaks in Fig. 10. Some of the unknown peaks were not consistently present in effluent from these outdoor samples suggesting they were transient and actively transforming into other compounds.

A few studies report on photo-transformation products in DNAN aqueous solutions. Both Hawari et al. [37] and Rao et al. [38] found 2-methoxy-5-nitrophenol and 2,4-dinitrophenol as intermediates, and nitrate and, or nitrite or both (the analytical

Fig. 10 NovaPak C8 column chromatograms (absorbance at 230 nm) for; **a** an IMX-104 indoor drip sample (no sunlight exposure) and **b** an IMX-104 outdoor test. DNAN, RDX and HMX peaks are present but there are many unknown peaks and a large pre-solvent peak (*arrow*) in the outdoor sample
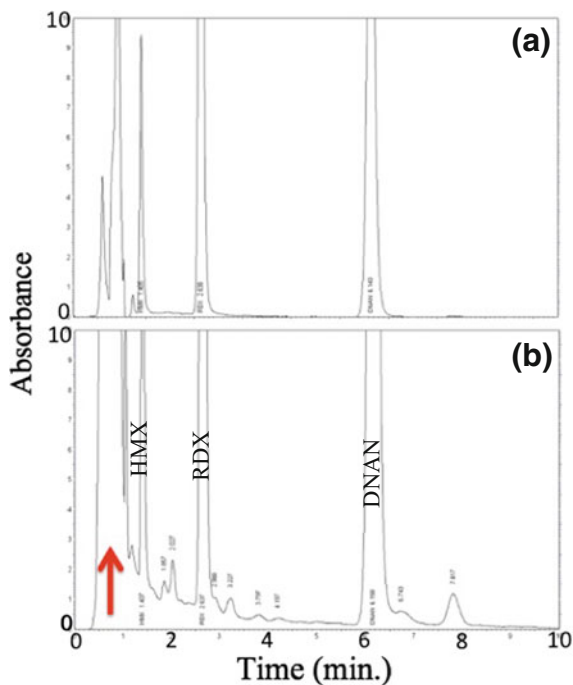
techniques could not separate the compounds). Hawari et al. [37] also reported for-mamide derivatives as intermediates of the transformation of amino-nitroanisole and amino-nitrophenol. The final products of a DNAN aqueous solution photolyzed over 21 days were, nitrate anion (0.7 mol), ammonium (1 mol), and formaldehyde/formic acid (0.9 mol, compounds also not separated), per mole of DNAN degraded [37]. Rao et al. [38] observed photo-transformation and a half-life ranging between 0.11 and 1.51 days. Observed products of photo-transformation for NTO, according to Le Campion et al. [39], include nitrites, nitrates, and carbon dioxide.

Taylor et al. [40] investigated thephoto-transformation of DNAN both as a pure solid and as a componentof solid IM formulations, IMX-101, IMX-104 and PAX-21. The latterwere samples placed outside to dissolve and transform as part of atwo and a half year dissolution study [16]. Taylor et al. [40] saw transient peaks in the chromatograms indicating intermediate, unstable products but consistently found methoxy nitrophenols and methoxy nitroanilines. One unknown product, possibly nitrosobenzene, was also found in most of the samples. The concentrations of transformation products found were small, <1% of the dissolved DNAN con-centration, suggesting that DNAN, not its transformation products, will be the main compound entering the soil.

The effect of temperature, pH, and dissolved organic matter on photo-transformation of DNAN and NTO in solution was examined by Dr. R. Pesce-Rodriguez [41]. The NTO transformation rates depended on the solution pH (Fig. 11a), with the lowest rates observed at neutral pH. The NTO photo-transformation rate doubled in the presence of humic acid (Fig. 11b), but was not affected by temperature (Fig. 12). Photo-transformation of DNAN in solution, on the other hand, was not sensitive to pH or natural organic matter but increased with increasing temperature (Fig. 12) a finding also reported by Rao et al. [38]. This suggests that DNAN may be less persistent in hot climates. The calculated acti-vation energy for DNAN photo-transformation was 27.8 kJ mol^{-1} [41].
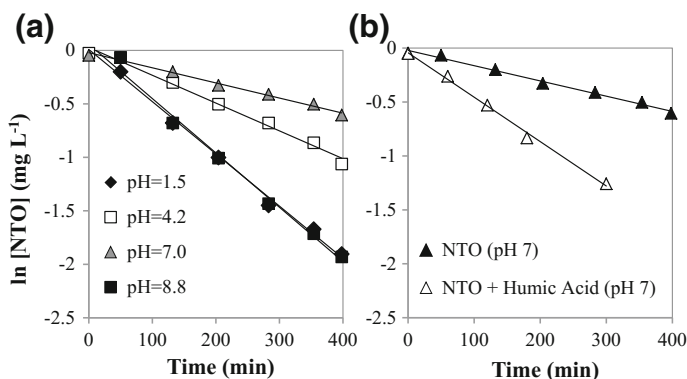
Fig. 11 Photo-transformation of NTO as affected by **a** solution pH and **b** the presence of natural organic matter [41]

Fig. 12 Measured (*solid*) and calculated (*hollow*) half-lives of NTO and DNAN as a function of temperature in aqueous solutions exposed to simulated sunlight [41]
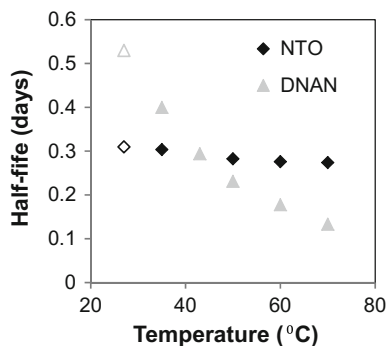
Fig. 13 Plot showing the relationship between NTO concentration and pH for indoor drip samples and outdoor samples [15]
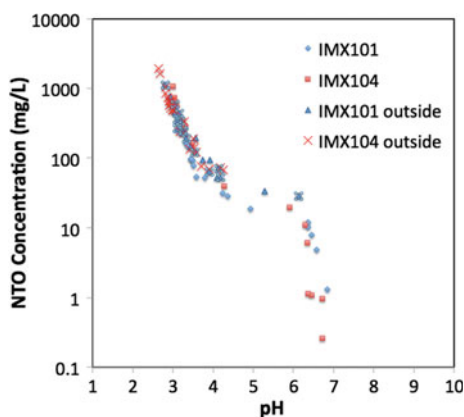
Studies to determine photo-transformation products that form on the surface of IM formulations or on solid pieces of DNAN, as well as experiments under different climatic conditions are underway. Evidence that IM particle surfaces photo-transform include color changes of the outdoor IM pieces (Figs. 6 and 7), the presence of unknown peaks in their HPLC chromatographs (Fig. 12b), and the absence of unknown peaks and good mass balances ($100 \pm 5\%$) in the indoor drip tests [16]. Some of these photo-produced compounds color the water samples and, therefore, are soluble.

3.5 PH of the IM Solutions

NTO is known to be acidic in solution $pK_a = 3.8$ [42, 43], and pH measurements of both the drip and the outdoor water samples show how pH changed during dissolution of the particle (Fig. 13). For the IMX-101 drip samples pH values were initially in the low 3 range and increased to neutral as the NTO concentration decreased to 10 mg L^{-1}. The pH of the IMX-104 samples showed a similar trend

with the difference being that, because IMX-104 contains proportionally more NTO than does IMX-101, the concentrations were higher and the pH levels lower for the first few IMX-104 samples. Figure 13 shows that there is a good correlation between NTO concentration and pH values between 2 and 5. At NTO concentrations below 20 mg L^{-1}, the pH is between 4 and 6; and at NTO concentrations below 10 mg L^{-1}, the pH of the solution is close to neutral. The color of the solution was also found to correlate with the NTO concentration—the most yellow colored solutions had the highest NTO concentrations and the lowest pH values. This property has been used to estimate concentration [44].

4 Physiochemical Properties of Insensitive Munitions Formulations

Once in solution, IM constituents and their transformation products experience reactive transport through the soil. En route to ground water, they can undergo irreversible and reversible adsorption by different mineral and organic phases in the soil, transformation, volatilization, and bio-uptake. The importance of each of these processes for the fate of a compound can be evaluated using the octanol-water partition coefficients (K_{ow}), acid dissociation constant (pK_a), Henry's Law constant (K_H), the one-electron standard reduction potential (E_m), the first-order transformation rate constant (k), linear (K_d) or Freundlich (K_f) soil adsorption coefficients, and soil organic carbon absorption coefficients (K_{OC}), among others. While some of these parameters are specific to the individual soil and depend on soil conditions (K_d, k, and partially K_{OC}), others are a function of the compounds' structure only but are linked to its environmental behavior (solubility, K_{ow}, K_H, pK_a, and E_m). Table 5 provides values for some of these parameters for compounds in IM and HE formulations.

The octanol–water partition coefficient is a measure of the tendency of the chemical to bio-accumulate and an indicator of its affinity for soil organic matter. Relatively low reported K_{ow} values (Table 5) indicate that these compounds are not strongly adsorbed by organic matter in soils through non-polar interactions. However, they can still experience specific sorption to soil organic matter, as has been shown for TNT and the DNTs (2,4- and 2,6-dinitrotoluene) [45, 46]. Based on the K_{ow} values, one would expect NTO to be more mobile than DNAN and to exhibit similar environmental behaviors to RDX.

Unlike most other explosives, which are polar but non-ionic compounds, NTO is an acid with pK_a of 3.7–3.76 [42, 43] and will be negatively charged at environmentally relevant pHs [47]. As both organic and mineral soil surfaces tend to have a net negative charge, NTO should have a low affinity for soils and a greater mobility in the environment. Relatively low volatility (ability to transfer from an aqueous phase to a gas phase) as measured by Henry's constants (log K_H of −3.25 to −4.40 for DNAN and −11.38 for NTO, [48], indicates that transport in a gas phase will not be important.

Table 5 Environmentally relevant chemical and physical properties, solubility at 25 °C, octanol-water partition coefficient (K_{ow}), acid dissociation constant (pKa), Henry's Law constant (K_H), one-electron standard reduction potentials (E_m), and soil organic carbon adsorption coefficient (K_{oc}) for DNAN, NTO, NQ, RDX, and TNT

Property	DNAN	NTO	NQ	RDX	TNT
Solubility (mg L^{-1})	276.2[a] [21], 213[a] [37],	16,642.0[c] [52]	2600[a] [25]	59.9[a] [53]	100.5[a] [53]
Log K_{ow}	1.58[a] [37], 1.64[a] [48], 1.70–1.92[b] [48]	0.37–1.03[b] [48]	−0.89 to 0.156 [54]	0.81–0.87 [55]	1.6–1.84 [55]
pKa		3.76[a] [47]	12.8[b] [25]		
Log K_H	−3.25 to −4.40[b] [48]	−11.38[b] [47]	−5.15[a] [25]	−10.71[b] [53]	−7.96[b] [53]
E_m (V)	−0.40[a] [49]			−0.55[a] [49]	−0.30[a] [49]
Log K_{oc}	2.2[a] [56], 2.2[b] [57]	1.1[a] [58], 2.1[b] [57]	1.3[a] [59]	2.3 [53]	3.2 [53]

[a]Measured; [b]Estimated; [c]Interpolated from measured values

One-electron standard reduction potential (E_m) is a measure of how easily nitro groups in these compounds reduce to amino groups [49], a common first step in transforming many explosive compounds. Boparai et al. [50] observed faster reduction for explosives having more positive one-electron reduction potentials. Measured electron standard reduction potential for DNAN (−0.40 V) is similar to 2,4-DNT, which is readily reduced in soil environments. Note that transformation products of the compound can have different environmental and toxicity properties than the original contaminant so they are important to identify and study.

5   Soil Interactions

While solubility, K_{ow}, K_H, pK_a, and E_m can be measured independently and used to predict environmental behavior of a contaminant, K_d, k, and K_{OC} need to be measured for soils found at specific locations in order to predict the fate and transport of the IM compounds at those locations. Alternatively these parameters can be measured for a selection of soils and then related to soil properties to extend predictions to other locations and soils.

The soil adsorption, or partitioning, coefficient, K_d, quantifies the absorption of energetics onto soil surfaces. In particular, organic matter, phyllosilicate clays, and iron and aluminum oxides and hydroxides adsorb organic compounds due to their high surface areas [51]. As values of K_d increase, the chemical resides mostly on soil surfaces and little is transported in the moving pore water. Usually, most of the adsorption of organic contaminants in soils can be attributed to soil organic carbon, and K_d values are normalized to soil organic carbon content, described by the soil organic carbon adsorption coefficient (K_{OC}). This parameter can be either derived

from K_{ow} or measured for the energetic in a particular soil, or set of soils. The obtained coefficient can then be used to calculate K_ds and predict the energetic's adsorption to other soils using their carbon contents. For compounds that are adsorbed mostly to organic matter in the soils through non-polar (hydrophobic) interactions K_{OC} can be a good estimate of a compound's adsorption across a range of soil environments.

However, organic matter is not the only soil component that can affect adsorption of energetics in soils. Studies using mineral soil components, phyllosilicate clays and iron and manganese oxides [60], indicated that similarly to TNT [61] DNAN is strongly adsorbed by phyllosilicate clays. The types of cations present on exchange sites in the clays influence the amount of adsorption, with K^+ resulting in the largest adsorption among the cations commonly present in soils. The mechanism of adsorption is based on the interaction between exchangeable cations and nitro-groups of DNAN. DNAN was not adsorbed by either iron or manganese oxides. NTO, on the other hand, experienced negative adsorption (repulsion) by phyllosilicates, as both are negatively charged at environmentally relevant pHs. NTO was strongly adsorbed by birnessite, a manganese oxide, which is positively charged.

Soil adsorption coefficients are measured using kinetic and equilibrium batch soil sorption experiments [62]. In these experiments, soils are mixed with solutions of NTO or DNAN and allowed to equilibrate for a predetermined amount of time. The soil is then separated from the solution and the supernatant analyzed to determine the amount of NTO or DNAN remaining in solution.

Transformation rates (k) of organic compounds in soils are influenced by both inherent soil properties and current soil conditions and therefore are more difficult to extrapolate to different environments and soils. Organic compound transformation is usually microbially driven, though there is some evidence of abiotic transformation catalyzed by soil minerals [60]. During microbial transformation, organic contaminants are either used as a source of energy by the microorganisms or co-metabolized by them, with other sources of carbon fueling their growth. Because of this, microbial transformation can be influenced by amount of the target compound (if it is metabolized) as well as by availability of labile organic carbon (if it is co-metabolized). At the same time, organic contaminants can also be toxic to the soil microorganisms [5, 63], suppressing their growth and decreasing transformation. In addition, since transformation of nitrated compounds commonly involves nitro-group reduction to amino-group, it is also very sensitive to redox state of the soil, which in turn is influenced by soil saturation and amount of available carbon [64]. Because of the factors described above, laboratory estimates of transformation rates (k) are useful for comparisons between different soils or between studied compounds but cannot serve as a reliable estimate of the field transformation rates [56].

Mark et al. [58] and Arthur et al. [56] tested soils collected on military ranges across the United States (Fig. 14). The soils belonged to multiple soil orders, including Entisols, Inceptisols, Mollisols, Aridisols, and Ultisols. Table 6 summarizes the physical and chemical properties for the 11 soils selected for these studies, as well as several other studies that examined NTO and DNAN interaction

Fig. 14 Soils collected from these locations were used for the insensitive munitions batch and column studies by Mark et al. [54] and Arthur et al. [52]

with soils. Soils used by Mark et al. [58] and Arthur et al. [56] had a wide range of OC concentrations (0.34–2.28%), soil pH (4.23–8.00), cation exchange capacity (CEC) (2.9–21.4 cmol kg^{-1}); and particle sizes (loamy sand to clay loam). Soils also varied in the mineral composition of the clay fraction [58].

5.1 Batch Soil Adsorption Studies

5.1.1 NTO

Mark et al. [58] observed that NTO adsorbed very weakly to the studied soils as can be expected for a negatively charged compound in a matrix that also possesses a net negative charge. The determined K_d values were less than 1 cm^3 g^{-1} (Table 6). For most soils, both Freundlich and linear adsorption isotherms described the observed adsorption well (Fig. 15a). Freundlich isotherms usually resulted in a slightly better fit (Table 6) but the Freundlich parameter n was not significantly different from one for the majority of the soils indicating a linear isotherm. When n was significant it was smaller than one [58] indicating a lower affinity for soils at higher NTO concentrations.

Soil pH was the strongest indicator of NTO soil adsorption (Fig. 15b). There was a highly significant negative relationship between linear adsorption coefficients and soil pH. There was no relationship between K_d values and OC, clay, or specific

Table 6 Measured physical and chemical properties of soils used in soil interaction experiments and fate and transport parameters for NTO and DNAN determined in these soils: Freundlich adsorption parameters, K_f and n; soil adsorption coefficient, K_d; log of adsorption coefficient normalized to fraction of OC in soils, log K_{OC}; transformation rate constant, k; half-life, $t_{1/2}$; and R^2 values for linear regressions used to determine these parameters

Soil	Texture	Clay %	pH[a]	OC[c] %	CEC[d] (cmol_c kg^{-1})		K_f	n	R^2	K_d (cm^3 g^{-1})	R^2	Log K_{oc} (cm^3 g^{-1})	k (h^{-1})	$t_{1/2}$ (days)	R^2	Reference
Catlin	Silt loam	25.6	7.31	5.28	21.4	NTO	0.21	1.03	0.94	0.21	0.92	0.6	0.0221	1.3	0.84	[2]
						DNAN	34	0.62	0.98	5.95	0.92	2.1	0.0047	6.1	0.88	[56]
Fort Harrison	Sandy loam	8.7	6.67	3.88	18	NTO	0.27	1.07	0.98	0.35	0.95	1.0	0.0021	13.8	0.98	[2]
						DNAN	13.86	0.77	0.9	6.32	0.93	2.2	0.001	28.9	0.45	[56]
Arnold AFB	Silt loam	11.4	6.66	2.68	8.7	NTO	0.58	0.86	0.98	0.34	0.94	1.1	0.0044	6.6	0.94	[2]
						DNAN	14.4	0.68	0.93	3.39	0.78	2.1	0.0022	13.1	0.92	[56]
Plymouth	Loamy sand	4.4	4.23	2.45	6.8	NTO	0.82	0.89	0.99	0.5	0.96	1.3	0.0043	6.7	0.97	[2]
						DNAN	10.05	0.83	0.98	4.38	0.94	2.3	0.007	4.1	0.51	[56]
Camp Butner	Sandy loam	7.7	6.69	2.42	6.1	NTO	0.74	0.54	0.77	0.12	0.72	0.7	0.0021	13.8	0.98	[2]
						DNAN	15.35	0.56	0.91	2.05	0.92	1.9	0.0018	16.0	0.67	[56]
Limestone	Sandy loam	11.2	7.54	1.99	13	NTO	0.33	0.88	0.92	0.21	0.92	1.0	0.0123	2.3	0.6	[2]
						DNAN	10.75	0.77	0.96	4.96	0.92	2.4	0.0019	15.2	0.78	[56]
Sassafras	Loam	16.4	4.4	1.3	7.9	NTO	0.9	0.86	0.99	0.48	0.96	1.6	0.008	3.6	0.99	[2]
						DNAN	2.26	0.97	0.85	1.89	0.72	2.4	0.0013	22.2	0.54	[56]
Camp Gruber	Clay loam	32.3	5.39	0.83	14.3	NTO	0.54	0.99	1	0.51	0.99	1.8	0.0025	11.6	0.98	[2]
						DNAN	7.62	0.72	0.84	1.99	0.91	2.4	0.0073	4.0	0.29	[56]
Camp Guernsey	Loam	4.1	8.21	0.77	2.9	NTO	0.06	0.48	0.18	0.02	0.21	0.4	0.0004	72.2	0.75	[2]
						DNAN	1.72	0.85	0.93	0.93	0.97	2.1	0.0041	7.0	0.85	[56]
Florence MR	Loam	26.8	8	0.45	12.2	NTO	0.09	0.77	0.55	0.06	0.57	1.1	0.0005	57.8	0.91	[2]
						DNAN	6.59	0.74	0.98	1.91	0.94	2.6	0.0007	41.3	0.35	[56]
Camp swift	Sandy clay loam	23.7	7.83	0.34	6.5	NTO	0.1	0.84	0.92	0.04	0.59	1.1	0.0009	32.1	0.93	[2]
						DNAN	1.27	0.84	0.7	0.6	0.84	2.2	0.0006	48.1	0.96	[56]
Petawawa		44.1[e]	4.9	2.5	<10	DNAN				9.1		2.7				[37]
Topsoil		0.4	6.1	34	35.0	DNAN				73		2.3				[37]

(continued)

Table 6 (continued)

Soil	Texture	Clay %	pH[a]	OC[c]%	CEC[d] (cmol_c kg^{-1})		K_f	n	R^2	K_d (cm^3 g^{-1})	R^2	Log K_{oc} (cm^3 g^{-1})	k (h^{-1})	$t_{1/2}$ (days)	R^2	Reference
DRDC-09		1.5	6.7	2.08	13.2	NTO				<0.1						[65]
						DNAN				2.27		2.0				[65]
Sandy clay loam	Sandy clay loam	21	6.6	1	14	NTO	1.39	1.33								[19]
						DNAN	0.68	1.28								[19]
Sand	Sand	0.03				NTO	0.34	1.04								[19]
						DNAN	0.17	1.18								[19]

[a]In 1:1 soil:water; [b]*OC* Organic carbon; [c]*CEC* Cation Exchange Capacity; [d]Includes silt
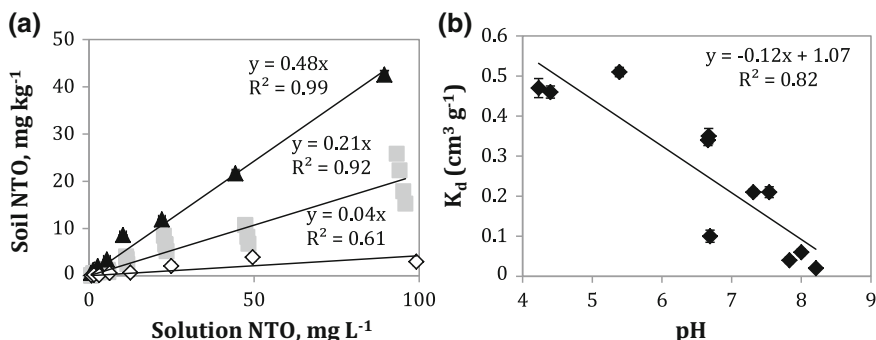
Fig. 15 a Adsorption isotherms for NTO in Sassafras, Catlin, and Camp Swift soil (listed highest to lowest adsorption); **b** Measured NTO adsorption coefficients (K_d) plotted against soil pH. $P = 0.00011$ [54]

surface area (SSA). The K_f values had similar but slightly weaker ($R^2 = 0.7818$, $P = 0.00030$) negative linear relationship with pH.

For Catlin soil that has a high pH and a high OC content, NTO was absorbed about 10 times less than RDX, K_d of 0.21 versus 2.03 cm^3 g^{-1} [51], while for Plymouth soil (low pH, less OC) the difference was smaller, 0.50 versus 0.65 cm^3 g^{-1} [14]. These results indicate that RDX and NTO are adsorbed through different mechanisms and that OC content is not a good predictor of NTO adsorption. The log K_{OC} for NTO in tested soils (1.06 ± 0.40 cm^3 g^{-1}) was significantly smaller compared to the literature value for RDX (2.26 ± 0.56 cm^3 g^{-1}) [53]. The K_{OC} values also had a higher percent standard deviation (102.7%) than K_d values from which they were calculated (72.8%) indicating that normalizing to OC did not decrease the variability.

The low NTO adsorption measured by Mark et al. [58] agreed with measurements by Hawari et al. [65] and Richard and Weidhaas [33]. We suggest that NTO adsorption may be either attributed to limited positive sites in the soils, such as birnessite or amino-groups in organic matter, or to interactions between non-charged NTO molecules at low pHs and non-charged soil sites. Linear isotherms support the second mechanism for NTO adsorption.

NTO also transformed in the soils [58]. Mass balance calculations (Fig. 16) indicated that after 24 h of equilibration there was little or no difference in NTO mass recovered between sterilized and non-sterilized soils. After 120 h, however, non-sterilized samples lost more NTO, indicating removal by microorganisms. In high OC soil (Catlin) the majority of NTO was transformed. Even in sterilized Catlin soil about 50% of NTO was lost from the solution in 120 h, probably due to abiotic transformation. This finding indicates a strong potential for natural attenuation.

Microbial transformation studies of NTO in soils show nitro-reduction followed by oxidative ring cleavage of the primary amine, 5-amino-1,2,4-triazol-3-one
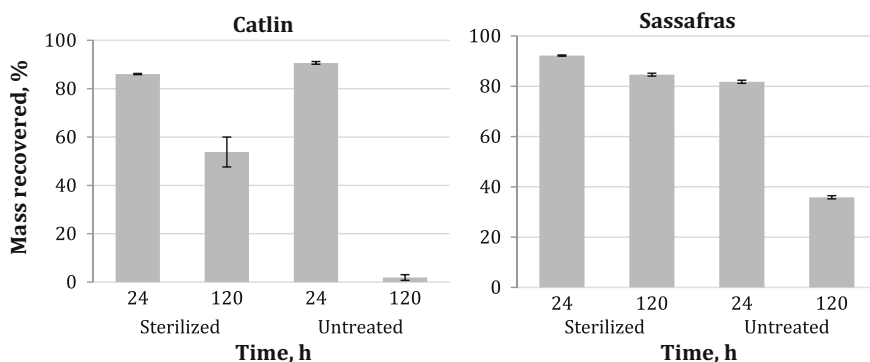
Fig. 16 Batch experiments for Sassafras and Catlin soils comparing mass (%) associated with solution and soil for sterilized (autoclaved) versus untreated soils. Soils and NTO solutions were reacted for 24 and 120 h. Error bars equal one standard error of the mean [54]

Fig. 17 Correlation between measured NTO transformation rate constants (k) and soil OC. $P = 0.02250$ [54]
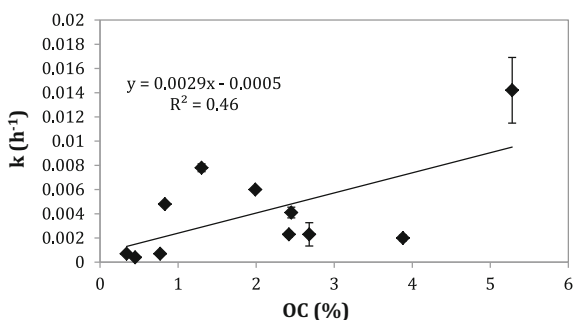
(ATO) forming a number of inorganic compounds [66, 7]. Mn oxide (birnessite) can abiotically oxidize ATO [60].

First-order rate coefficient estimates for transformation reactions range between 0.0004 h^{-1} in Camp Guernsey and 0.0221 h^{-1} in Catlin soil [58]. Measured transformation rates were lower for soils with less OC, such as Camp Guernsey, Florence MR, and Camp Swift. There was a positive relationship between the percent OC present in the soil and the measured transformation rate constant k (probability, $P = 0.02$), however, R^2 was low at 0.46 (Fig. 17). Other soil parameters, such as clay content, pH, and SSA, poorly correlated with k. The NTO transformation rate constant in Plymouth soil, 0.0043 h^{-1}, was about three times smaller than one measured previously for RDX in the same soil (0.013 h^{-1}) [14].

5.1.2 DNAN

Unlike NTO, DNAN adsorbes to the soils [56] indicating that natural attenuation may be an important mechanism for DNAN remediation. For all studied soils, the
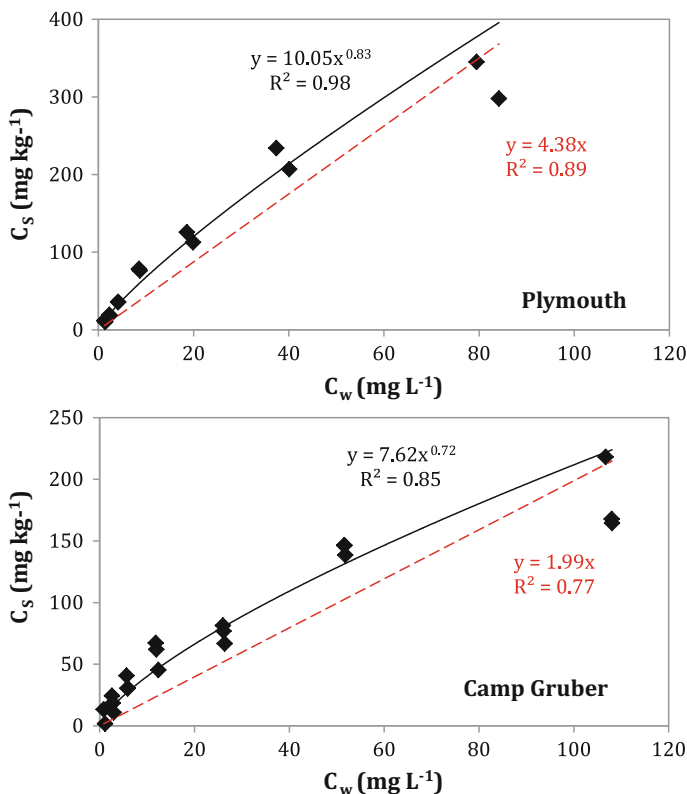
Fig. 18 Adsorption isotherms calculated for DNAN in Plymouth and Camp Gruber soils. The *red dashed line* indicates the linear adsorption isotherm fit to the measured adsorption data (equation is in *red*) while the *solid black line* is a fit of the Freundlich isotherm with the equation presented in *black* [41]

Freundlich isotherm resulted in a highly significant fit to the data (Table 6; Fig. 18). The mean value of the Freundlich parameter, *n,* across all the soils was equal to 0.76 ± 0.21. The 95% confidence intervals of *n* estimates overlapped for the majority of the soils, indicating that they were not significantly different from each other. For three soils, Sassafras, Camp Guernsey and Camp Swift, *n* was not significantly different from 1 (resulting in a linear isotherm).

Linear regressions for the isotherms were also highly significant (Table 6). For the majority of soils, a Freundlich isotherm described DNAN adsorption the best, but for four soils, Fort Harrison, Sassafras, Camp Guernsey, and Camp Swift, a linear isotherm resulted in a better fit to the data (Fig. 18). Normalizing estimated K_d values to OC content in the soil (K_{OC}) resulted in a decrease in the percent standard deviation of the estimates from 61 to 49%. The mean log K_{OC} value was 2.24 ± 0.20 similar to 2.33 ± 0.35 measured by Hawari et al. [37, 65].
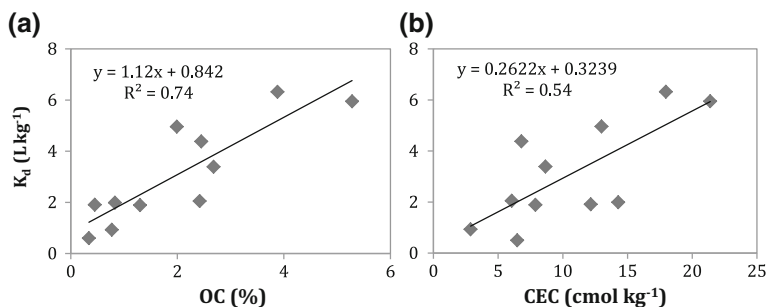
Fig. 19 Correlation between measured DNAN adsorptions coefficients (K_ds) and percent organic carbon in soil (OC) ($P = 0.00061$) (**a**) and cation exchange capacity (CEC) ($P = 0.0095$) (**b**) [52]

The determined DNAN adsorption coefficients, K_ds, resulted in highly significant positive relationships with percent OC in the soil (Fig. 19a) and CEC (Fig. 19b). Similarly significant linear relationships were observed between K_fs and OC and CEC [56]. No other measured soil properties, such as clay content, pH, or SSA, correlated with K_d or K_f values.

Lower DNAN K_{ow} and K_{OC} values (Table 5) indicate that it would have less affinity for soils than TNT. Comparing DNAN with TNT adsorption coefficients for Catlin and Plymouth soils [52] confirmed this trend for Catlin soil: K_d values were higher for TNT than DNAN (17.9 vs. 5.95) [51], though Freundlich parameters were similar for the two compounds ($K_f = 34.00$, n = 0.62 for DNAN and $K_f = 32.67$, n = 0.60 for TNT). However, in Plymouth soil DNAN adsorbed more strongly than TNT (K_d of 4.38 cm^3 g^{-1} for DNAN and 0.63–1.6 cm^3 g^{-1} for TNT, depending on the method used) [14].

Mechanisms of DNAN adsorption in soils likely include adsorption to phyllosilicate clays and interactions with organic matter. Evidence of the latter comes from a strong correlation between OC and adsorption coefficients (Fig. 19a) that indicates OC and K_ds are linked [56], while the former is supported by direct experiments with clays [60] and correlations between cation exchange capacity (CEC) and DNAN adsorption coefficients (Fig. 19b) [56]. We suggest that DNAN interacts with soil organic matter through hydrophobic partitioning and specific adsorption, as is seen for TNT [67]. The non-linear shape of the adsorption isotherms supports the contribution of specific adsorption. In addition to direct DNAN reactions with soils, DNAN reduction products can adsorb irreversibly to soil organic matter, similar to amino-products of TNT transformation [37].

To study the effect of microbial transformation, two sterilized and unsterilized soils with different OC concentrations were equilibrated with DNAN for 24 and 120 h. For the sterilized Sassafras soil the 24 and 120-h recoveries were similar and close to 100% (Fig. 20) [56]. For the unsterilized Sassafras soil the 120-h recovery was lower than when sterilized. These results indicate that the significant mass loss observed for the unsterilized Sassafras soil is due to biotic transformation, with minor contributions by abiotic transformation or irreversible adsorption; biotic
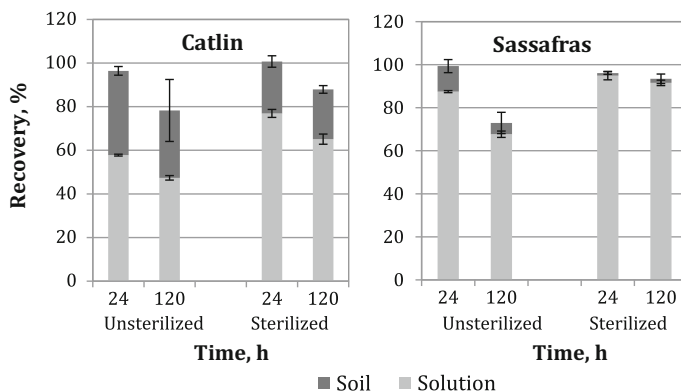
Fig. 20 Mass balance of DNAN in unsterilized and sterilized Catlin (5.28% OC) and Sassafras (1.30% OC) soils for 24 and 120 h of contact. Error bars equal confidence interval of the mean [56]

transformation was also seen in soils by Olivares et al. [8]. Conversely, for the sterilized Catlin soil, the 120-h recovery is significantly lower than the 24-hr recovery, indicating a contribution of abiotic transformation or irreversible adsorption or both.

The transformation rate constant, k, ranged between 0.0006 and 0.0073 h^{-1} for Camp Swift and Camp Gruber soils, resectively [56]. Although k appears to increase with OC, the trend is not statistically significant ($P = 0.78101$). This study found that other soil parameters, such as pH, clay content, and SSA, did not correlate with k. No known products of DNAN tranformation were measured in the solutions.

DNAN transformation observed in batch studies [56] was significantly slower than observed for TNT. For Plymouth soil, the TNT transformation rate constant was 0.21 h^{-1} [14] while the DNAN constant was 0.0070 h^{-1}. The environmental behaviors of NQ and RDX are described in Dontsova and Taylor [13].

5.2 Solution Transport for NTO and DNAN and HYDRUS-1D Modeling Results

HYDRUS-1D is a widely used numerical model that simulates variably saturated water flow and solute transport in porous media. We have used the HYDRUS-1D model to analyze breakthrough curves of a nonreactive tracer to determine the physical parameters characterizing the column experiments, and then, with fixed physical parameters, to analyze breakthrough curves of reactive compounds to determine the chemical and reaction processes involved. We compare the reaction parameters determined from the model to the same parameters independently measured in soil batch studies and drip tests. Agreement between the two sets of values indicates how well the determined relationships characterize the release and transport of IM components in soils.
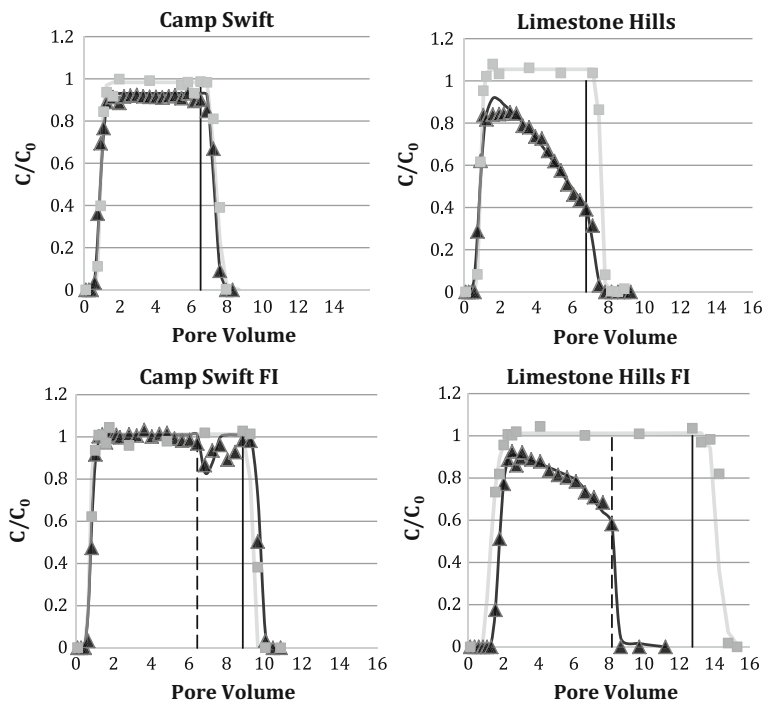
Fig. 21 Measured (*points*) and HYDRUS-simulated (*lines*) breakthrough curves for NTO (*black*) and Br– tracer (*grey*) in Camp Swift and Limestone Hills soils under conditions of continuous flow and flow interruption (FI). The *thin dashed black vertical line* shows the start of 24 h when the flow was interrupted. The *thin solid black line* indicates the time when the solution was changed back to 0.005 M CaCl$_2$ to observe the desorption phase of the isotherm [64]

To resolve non-equilibrium processes, column transport studies were conducted with continuous flow and 24-h flow interruption. In these experiments NTO or DNAN was added to the column with 0.005 M CaBr$_2$, where Br$^-$ served as a conservative tracer. After flow interruption the solution was switched to only 0.005 M CaCl$_2$ to observe desorption of NTO and DNAN from soils. A subset of the soils used in the batch experiments was used for the column tests. NTO had low retardation (Figs. 21 and 22; Table 7), in agreement with low K_ds measured in batch experiments, but experienced transformation in the soils. First order transformation kinetics (manifested by constant effluent concentration during steady-state conditions) was observed for half of the studied soils (Sassafras (Fig. 22), Camp Guernsey, Florence MR, and Camp Swift (Fig. 21)) in agreement with batch experiments. Transformation rate constants, however, were higher than determined in batch studies [58]. In these soils, flow interruption decreased effluent concentration, but concentrations recovered after the flow was restarted (Fig. 21, Camp Swift).
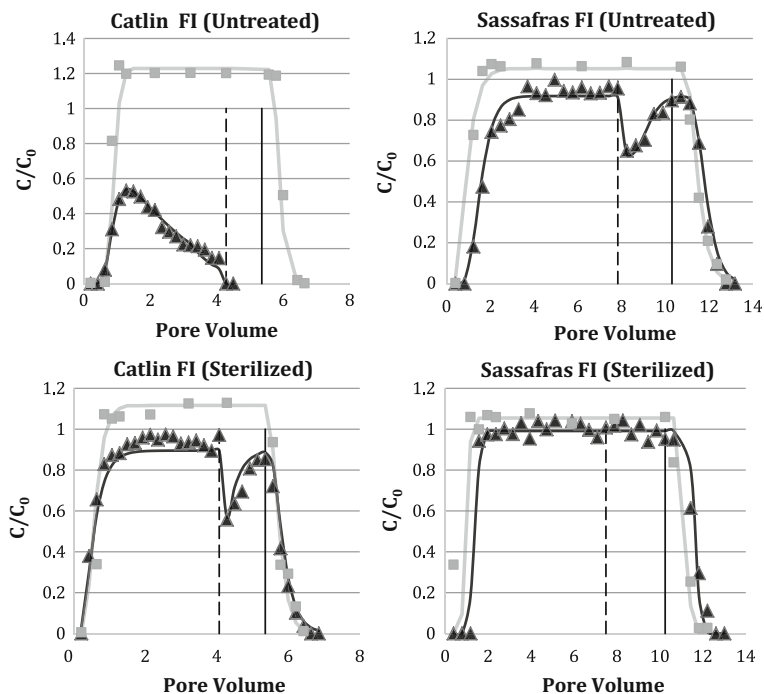
Fig. 22 Measured (*points*) and HYDRUS-simulated (*lines*) breakthrough curves for NTO (*black*) and Br– tracer (*grey*) in untreated and autoclaved Catlin and Sassafras soils. *Thin dashed black vertical line* indicates timing of 24-h flow interruption. *Thin solid black vertical line* indicates time when solution was changed back to 0.005 M CaCl$_2$ to observe desorption phase of the isotherm (modified from [64])

For the other soils, Catlin (Fig. 22), Arnold AFB, Camp Butner, and Limestone Hills (Fig. 21), effluent concentration decreased with time, indicating a change in the transformation rate constant. It was determined that Monod kinetics successfully described breakthrough curves for these soils. For these soils, when flow was interrupted concentrations decreased below the detection limit and did not recover when flow was restarted. This behavior was associated with soils that had higher OC contents than soils that had 1st rate kinetics of transformation (Table 7). To test if the pattern could be explained by microbial activity in the soils, Mark et al. [64] sterilized two soils, Catlin with high OC content (Table 5) and decreasing eluent concentrations with time, and Sassafras with lower OC and steady-state concentrations of NTO in the effluent. As a result of sterilization, Catin soil also had steady-state concentrations of NTO in the effluent (Fig. 22) confirming that microbial activity was responsible for the difference in patterns.

Fast transformation of NTO could result if reducing conditions develop in the soil. This could occur if microbial activity increased due to organic matter and water flow in the soils. The consumption of oxygen by microorganisms would

Table 7 NTO fate and transport parameters determined by HYDRUS-1D, linear adsorption coefficients, K_d, 1st order transformation rate constants, k, and initial Monod transformation rate, with average rate shown in parentheses

Soil	K_d (cm^3 g^{-1})		k (h^{-1})		Monod transformation rate (h^{-1})		R^2
	Estimate	95% CI	Estimate	95% CI	Estimate	95% CI	
Catlin	0.15	0.04			0.058 (0.123)	0.016	0.97
Catlin FI	0.04	0.04			0.046 (0.133)	0.017	0.96
Arnold AFB	0.17	0.02			0.072 (0.121)	0.008	0.99
Arnold AFB FI	0.13	0.02			0.067 (0.133)	0.010	0.98
Camp Butner	0.12	0.01			0.207 (0.259)	0.023	0.99
Camp Butner FI	0.06	0.01			0.100 (0.183)	0.011	0.99
Limestone Hills	0.00	0.01			0.038 (0.154)	0.011	0.99
Limestone Hills FI	0.15	0.01			0.034 (0.186)	0.009	0.99
Sassafras	0.05	0.01	0.100	0.008			0.99
Sassafras FI	0.40	0.32	0.076	0.064			0.96
Camp Guernsey	0.03	0.01	0.009	0.009			0.98
Camp Guernsey FI	0.05	0.01	0.064	0.010			0.98
Florence MR	0.03	0.01	0.065	0.012			0.98
Florence MR FI	0.04	0.01	0.041	0.003			0.97
Camp Swift	0.00	0.00	0.040	0.008			0.98
Camp Swift FI	0.04	0.01	0.009	0.004			0.99

Soils are listed in order of decreasing OC% (modified from [64]. FI = flow interruption
CI = 95% confidence interval

decrease the redox potential in the solution causing NTO to be reduced to ATO. In turn, Linker et al. [60] showed that ATO can be oxidized by Mn oxide to form a variety of organic and inorganic products. Thus, NTO could be completely attenuated in high OC soils under field conditions.

Similarly to NTO, DNAN experienced higher transformation rates in column transport than in batch experiments (Fig. 23) [56]. In addition, while no DNAN transformation products were detected in batch experiments, both 2-methoxy-5-nitroanisole and 4-methoxy-3-nitroanisole were measured in the column effluent. Even in the two low OC soils used in column expreriments (Camp Swift and Camp Gruensey) DNAN was significantly retarded and transformed.

5.3 Dissolution and Transport of IM Formulations

Dissolution and transport studies for IMX-101 and IMX-104 were performed using Camp Swift and Camp Guernsey soils [41]. These soils were selected because of
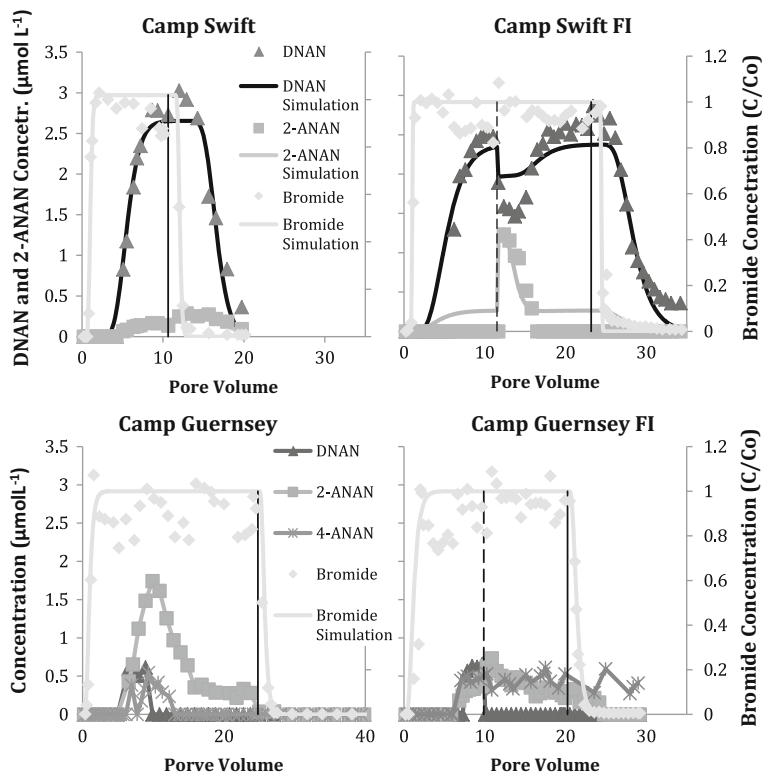
Fig. 23 Breakthrough curves for DNAN, 2-methoxy-5-nitroaniline (2-ANAN), 4-methoxy-3-nitroaniline (4-ANAN), and Br^{-1} tracer in Camp Swift and Camp Guernsey soils for continuous flow and flow interruption (FI). DNAN inflow concentration was 2.87 and 2.64 μmol L^{-1} in Camp Swift, and 2.71 and 2.78 μmol L^{-1} in Camp Guernsey respectively for continuous and interrupted flow experiments. *Vertical dashed line* indicates time of flow interruption and *solid line* indicates time when input solution was switched back to 0.005 M $CaCl_2$ [56]

their low organic matter content that provides a conservative estimate for IM constituents' attenuation in soils (Table 6). IM particles were placed on the soil surface and subjected to water flow until steady-state concentrations of IM constituents were measured in the effluent; then particles were removed and water flow continued to observe IM desorption.

Breakthrough curves were observed for all IMX-101 components. In addition, 2-methoxy-5-nitroaniline, a DNAN transformation product, was detected in the effluent at concentrations about 2 orders of magnitude lower than DNAN. Dissolution of all IM components was successfully simulated in HYDRUS-1D given: that the maximum dissolution occurred right after the initial exposure of IM101 particles to the flow and; that the dissolution rate decreased at an exponential rate until a steady-state rate was reached. This model was previously used to
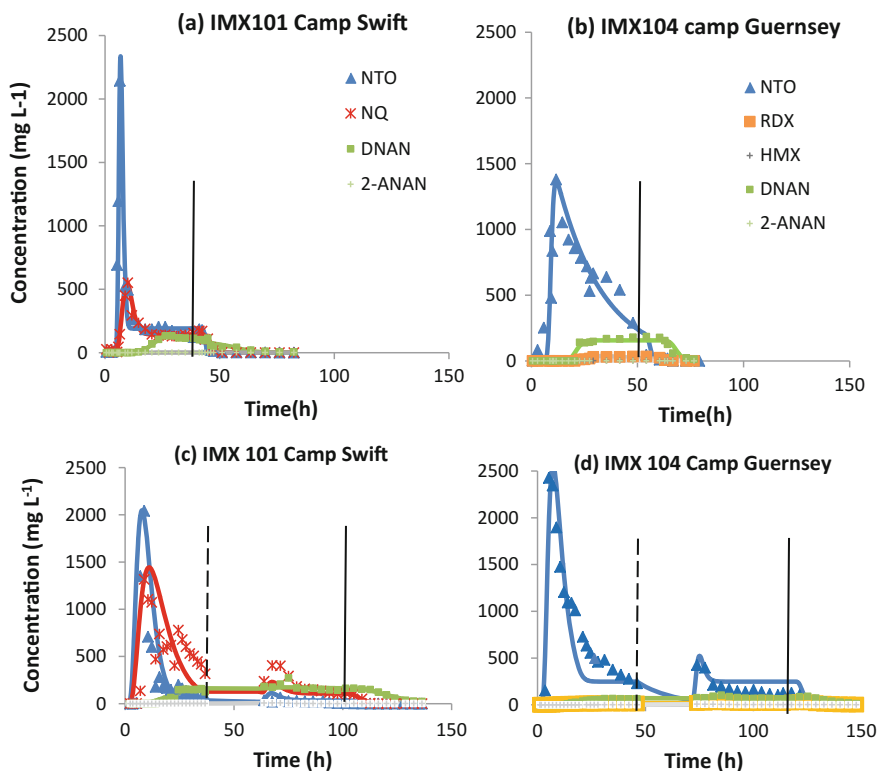
Fig. 24 Measured (*points*) and HYDRUS-1D simulated (*lines*) breakthrough curves for NTO, NQ, RDX, HMX, DNAN, and DNAN's transformation product, 2-methoxy-5-nitroaniline (2-ANAN). **a** IMX-101 particle dissolved on Camp Swift soil. **b** IMX-104 particles on Camp Gruensey soil. **c, d** Corresponding flow interruption experiments. *Vertical dashed line* indicates time of flow interruption and solid line indicates time when input solution was switched back to 0.005 M CaCl$_2$ and IM particle removed

describe dissolution of propellants from nitrocellulose matrices [59] and can be applied to melt-cast IM particles due to the large difference in solubility between the DNAN matrix and the crystal constituents of the IM formulations.

The shape of the breakthrough curves and the measured concentrations varied appreciably between IM constituents (Fig. 24a). NTO had the highest initial effluent concentrations despite representing only about 20% of the total IMX-101 mass. This agrees with NTO results from drip and outdoor studies [16, 32]. Although NTO concentrations were initially very high, they quickly decreased to smaller steady-state effluent concentrations. For NQ, initial concentrations were smaller than for NTO (despite higher content of NQ in IMX-101 but in agreement with lower NQ solubility), and transition to steady state was slower. For DNAN, effluent concentrations were stable over time indicating a near-constant dissolution rate. The DNAN concentrations were much smaller than peak concentrations for

either NTO or NQ but similar to the steady-state concentrations of these compounds.

The behavior of NTO, DNAN, and NQ dissolving from IM particles and transported to soils was consistent with previously measured fate and transport parameters [56, 58]. NTO experienced minimal retardation in the soils and was the first compound to break through. Early NTO breakthrough is consistent with low measured adsorption coefficients for both studied soils (0.02 and 0.04 cm^3 g^{-1} for Camp Guernsey and Camp Swift, respectively). Nitroguanidine, similarly to NTO, is a relatively inert compound in soil environments. Nitroguanidine K_d values for Sassafras, Plymouth, and Catlin soils were 0.60, 0.44, and 0.24 cm^3 g^{-1} [59] compared to 0.48, 0.50, and 0.21 cm^3 g^{-1} measured for NTO in the same soils. Breakthrough curves, however, indicated a slightly later arrival of NQ compared to NTO and a delay in desorption, indicating that NQ has a higher affinity for these soils than does NTO. DNAN was the last IM constituent to breakthrough. It also had a corresponding delay in desorption.

For IMX-104 similar trends were observed (Fig. 24b): NTO dissolved 1st, had the highest initial effluent concentrations that decreased sharply over time, and exibited minimal retardation in soils, while DNAN had stable dissolution, lower concentrations, and higher retardation in soils. RDX had lower concentrations than DNAN and experienced intermediate retardation, while HMX eluted at about a 10 times smaller concentrations than RDX and was strongly adsorbed. In interrupted flow experiments there was an increase in NTO concentration after flow resumption, consistent with continued dissolution during flow interruption (Fig. 24c, d).

6   Summary

The solubility of the individual constituents of IM formulations differs by orders of magnitude and produce porous particles as they dissolve. This process increases both the surface areas and the dissolution rates of the particles. Both the dissolution results and the µCT data show that the components in these explosive formulations dissolve sequentially and in the order predicted by their solubility i.e. NTO, NQ and DNAN. We expect the low pH of water containing dissolved NTO and the contaminant mixtures of the effluent to affect microbial communities in ways that are currently unknown.

The good mass balances measured for the laboratory drip tests indicate that the dissolved formulations do not significantly photo- or bio-transform when not exposed to sunlight. Photo-transformation does occur outdoors as evidenced by (1) DNAN changing color and (2) unknown peaks appearing in the HPLC chromatograms of the effluent from outdoor dissolution tests. Although photo-transformation products are present they were found to be small relative to the dissolved DNAN.

Both NTO and DNAN photo-transform when in solution. In pure water, DNAN photo-transformed more than NTO. However, rates were sensitive to solution

chemistry. NTO photo-transformation was enhanced in acidic and basic solutions. NTO photo-transformation rates also increased by a factor of three in the presence of organic matter that commonly occurs in soil solutions and in surface waters. Dissolved organic matter did not affect DNAN photo-transformation. We found the photo-transformation of NTO to be relatively insensitive to temperature between 35 and 70 °C. For DNAN, on the other hand, photo-transformation rates increased with increasing temperature.

Both NTO and DNAN experienced adsorption and transformation in soils. NTO was weakly adsorbed, with adsorption coefficients lower than those measured for RDX, the explosive compound it is replacing, and the explosive that has been found in groundwater beneath training ranges. NTO adsorption was not influenced by organic carbon in the soil but was strongly affected by soil pH. Adsorption decreased as soil pH increased, probably due to changes in protonation (and therefore charge) of both the soil surfaces and NTO. DNAN adsorption was similar to TNT and positively correlated with organic carbon.

Column studies supported batch-determined parameters that indicated increased transformation as soil becomes slightly anaerobic. NTO transformation rates increased with increases in soil organic carbon. NTO had little affinity for soils, making it more mobile in the environment than DNAN, and as it is also more soluble, we can expect it to reach ground water faster. DNAN is easily photo-transformed and adsorbed in the soil, making it less mobile in the environment. The solubility of most IM constituents is higher than that of TNT and RDX, increasing the likelihood that they will reach groundwater.

References

1 Mirecki JE, Porter B, Weiss CA (2006) Environmental transport and fate process descriptors for propellant compounds. U.S. Army Engineer Research and Development Center, Vicksburg, MS
2 Walsh MR, Walsh ME, Ramsey CA, Thiboutot S, Ampleman G, Diaz E, Zufelt JE (2014) Energetic residues from the detonation of IMX-104 insensitive munitions. Propellants, Explos, Pyrotech 39:243–250
3 Olivares CI, Abrell L, Khatiwada R, Chorover J, Sierra-Alvarez R, Field JA (2016) (Bio)transformation of 2,4-dinitroanisole (DNAN) in soils. J Hazard Mater 304:214–221
4 Lee K-Y, Chapman LB, Cobura MD (1987) 3-Nitro-1,2,4-triazol-5-one, a less sensitive explosive. J Energ Mater 5:27–33
5 Fung V, Price D, LeClaire E, Morris J, Tucker N, Carrillo A (2010) Further development and optimization of IM ingredients at Holston Army Ammunition Plant. In: 2010 insensitive munitions and energetic materials technology symposium, Munich, Germany
6 Walsh MR, Walsh ME, Taylor S, Ramsey CA, Ringelberg DB, Zufelt JE, Thiboutot S, Ampleman G, Diaz E (2013) Characterization of PAX-21 insensitive munition detonation residues. Propellants, Explos, Pyrotech 38:399–409
7 Taylor S, Dontsova K, Walsh ME, Walsh MR (2015) Outdoor dissolution of detonation residues of three insensitive munitions (IM) formulations. Chemosphere 134:250–256
8 Rao B, Wang W, Cai Q, Anderson T, Gu B (2013) Photochemical transformation of the insensitive munitions compound 2,4-dinitroanisole. Sci Total Environ 443:692–699

9 Uchimiya M, Gorb L, Isayev O, Qasim MM, Leszczynski J (2010) One-electron standard reduction potentials of nitroaromatic and cyclic nitramine explosives. Environ Pollut 158:3048–3053

10 Walsh MR, Walsh ME, Ramsey CA, Thiboutot S, Ampleman G, Dowden J (2015) Energetic residues from the detonation of IMX101 and IMX-104 munitions. ERDC/CRREL TR-15-3

11 Arthur JD, Mark NW, Taylor S, Šimunek J, Brusseau ML, Dontsova KM (2017) Batch soil adsorption and column transport studies of 2,4-dinitroanisole (DNAN) in soils. J Contam Hydrol 199:14–23

12 Chakka S, Boddu VM, Maloney SW, Damavarapu R (2008) Prediction of physicochemical properties of energetic materials via EPI suite. American Institute of Chemical Engineers Annual Meeting, Philadelphia, PA

13 Wilson A (2007) Explosive ingredients and compositions for the IM M795 In: Artillery ammunition. 2007 insensitive munitions and energetic materials technology symposium, Miami, FL

14 Boddu VM, Abburi K, Maloney SW, Damavarapu R (2008) Thermophysical properties of an insensitive munitions compound, 2,4-dinitroanisole. J Chem Eng Data 53:1120–1125

15 Smith MW, Cliff MD (1999) NTO based explosive formulations: a technology review. Weapons Systems Division, Aeronautical and Maritime Research Laboratory

16 Taylor S, Dontsova K, Bigl S, Richardson C, Lever J, Pitt J, Bradley JP, Walsh M, Šimůnek J (2012) Dissolution rate of propellant energetics from nitrocellulose matrices. Cold Regions Research and Engineering Laboratory, Hanover, NH

17 Monteil-Rivera F, Paquet L, Deschamps S, Balakrishnan V, Beaulieu C, Hawari J (2004) Physico-chemical measurements of CL-20 for environmental applications. Comparison with RDX and HMX. J Chromatogr A 1025:125–132

18 Krzmarzick MJ, Khatiwada R, Olivares CI, Abrell L, Sierra-Alvarez R, Chorover J, Field JA (2015) Biotransformation and degradation of the insensitive munitions compound, 3-nitro-1,2,4-triazol-5-one, by soil bacterial communities. Environ Sci Technol 49:5681–5688

19 Taylor S, Walsh ME, Becher JB, Ringelberg DB, Mannes PZ, Gribble GW (2017) Photo-degradation of 2,4-dinitroanisole (DNAN): an emerging munitions compound. Chemosphere 167:193–203

20 Le Campion L, Vandais A, Ouazzani J (1999) Microbial remediation of NTO in aqueous industrial wastes. FEMS Microbiol Lett 176:197–203

21 Lotufo GR, Biedenbach JM, Sims JG, Chappell P, Stanley JK, Gust KA (2015) Bioaccumulation kinetics of the conventional energetics TNT and RDX relative to insensitive munitions constituents DNAN and NTO in Rana pipiens tadpoles. Environ Toxicol Chem 34 (4):880–886

22 Taylor S, Park E, Bullion K, Dontsova K (2015) Dissolution of three insensitive munitions formulations. Chemosphere 119:342–348

23 Le Campion L, Giannotti C, Ouazzani J (1999) Photocatalytic degradation of 5-nitro-1,2,4-triazol-3-one NTO in aqueous suspention of TiO_2. Comparison with Fenton oxidation. Chemosphere 38:1561–1570

24 Hill FC, Sviatenko LK, Gorb L, Okovytyy SI, Blaustein GS, Leszczynski J (2012) DET M06-2X investigation of alkaline hydrolysis of nitroaromatic compounds. Chemosphere 88:635–643

25 Haag WR, Spanggord R, Mill T, Podoll RT, Chou T-W, Tse DS, Harper JC (1990) Aquatic environmental fate of nitroguanidine. Environ Toxicol Chem 9:1359–1367

26 Salter-Blanc AJ, Bylaska EJ, Ritchie JJ, Tratnyek PG (2013) Mechanisms and kinetics of alkaline hydrolysis of the energetic nitroaromatic compounds 2,4,6-trinitrotoluene (TNT) and 2,4-dinitroanisole (DNAN). Environ Sci Technol 47:6790–6798

27 Haderlein SB, Weissmahr KW, Schwarzenbach RP (1996) Specific adsorption of nitroaromatic explosives and pesticides to clay minerals. Environ Sci Technol 30:612–622

28 Roy WR, Krapac IG, Chou SFJ, Griffin RA (1992) Batch-type procedures for estimating soil adsorption of chemicals. Risk Reduction Engineering Laboratory, Cincinnati, OH, p 100

29 Liang J, Olivares C, Field JA, Sierra-Alvarez R (2013) Microbial toxicity of the insensitive munitions compound, 2,4-dinitroanisole (DNAN), and its aromatic amine metabolites. J Hazard Mater 262:281–287

30 Mark N, Arthur J, Dontsova K, Brusseau M, Taylor S, Šimůnek J (2017) Column transport studies of 3-nitro-1,2,4-triazol-5-one (NTO) in soils. Chemosphere 171:427–434

31 Hawari J, Perreault N, Halasz A, Paquet L, Radovic Z, Manno D, Sunahara GI, Dodard S, Sarrazin M, Thiboutot S, Ampleman G, Brochu S, Diaz E, Gagnon A, Marois A (2012) Environmental fate and ecological impact of NTO, DNAN, NQ, FOX-7, and FOX-12 considered as substitutes in the formulations of less sensitive composite explosives. National Research Council Canada

32 Thorn KA, Pennington JC, Hayes CA (2001) Transformation of TNT in an aerobic compost: Structure and reactivity effects in the covalent binding of aromatic amines to organic matter. Abstr Pap Am Chem Soc 41:628–632

33 Chipen GI, Bokalder RP, Grinstein VY (1966) 1,2,4-triazol-3-one and its nitro and amino derivatives. Chem Heterocycl Compd 2:110–116

34 Mark N, Arthur J, Dontsova K, Brusseau M, Taylor S (2016) Adsorption and attenuation behavior of 3-nitro-1,2,4-triazol-5-one (NTO) in eleven soils. Chemosphere 144:1249–1255

35 Taylor S, Lever JH, Fadden J, Perron N, Packer B (2009) Outdoor weathering and dissolution of TNT and Tritonal. Chemosphere 77:1338–1345

36 Nandi AK, Singh SK, Kunjir GM, Singh J, Kumar A, Pandey RK (2012) Assay of the insensitive high explosive 3-nitro-1,2,4- triazol-5-one (NTO) by acid-base titration. Cent Eur J Energ Mater 2:4–5

37 Taylor S, Lever JH, Bostick B, Walsh MR, Walsh ME, Packer B (2004) Underground UXO: are they a significant source of explosives in soil compared to low- and high- order detonations? ERDC/CRREL technical report TR-04-23

38 Dontsova K, Taylor S, Pesce-Rodriguez R, Brusseau M, Arthur J, Mark N, Walsh M, Lever J, Šimůnek J (2014) Dissolution of NTO, DNAN, and insensitive munitions formulations and their fates in soils. Cold Regions Research and Engineering Laboratory, Hanover, NH, p 92

39 Dontsova KM, Yost SL, Simunek J, Pennington JC, Williford CW (2006) Dissolution and transport of TNT, RDX, and composition B in saturated soil columns. J Environ Qual 35:2043–2054

40 Thorn KA, Pennington JC, Kennedy KR, Cox LG, Hayes CA, Porter BE (2008) N-15 NMR study of the immobilization of 2,4- and 2,6-dinitrotoluene in aerobic compost. Environ Sci Technol 42:2542–2550

41 Pelletier P, Lavigne D, Laroche I, Cantin F, Phillips L, Fung V (2010) Additional properties studies of DNAN based melt-pour explosive formulations. In: 2010 insensitive munitions and energetic materials technology symposium, Munich, Germany

42 London JO, Smith DM (1985) A toxicological study of NTO. Los Alamos National Laboratory Report

43 Dontsova K, Taylor S (this volume) High explosives: their dissolution and fate in soils. In: Shukla M, Boddu V, Steevens J, Reddy D, Leszczynski J (eds) Energetic materials: from cradle to grave

44 Hawari J, Monteil-Rivera F, Perreault NN, Halasz A, Paquet L, Radovic-Hrapovic Z, Deschamps S, Thiboutot S, Ampleman G (2015) Environmental fate of 2,4-dinitroanisole (DNAN) and its reduced products. Chemosphere 119:16–23

45 Boparai H, Comfort S, Satapanajaru T, Szecsody J, Grossl P, Shea P (2010) Abiotic transformation of high explosives by freshly precipitated iron minerals in aqueous FeII solutions. Chemosphere 79:865–872

46 Dontsova KM, Hayes C, Pennington JC, Porter B (2009) Sorption of high explosives to water-dispersible clay: influence of organic carbon, aluminosilicate clay, and extractable iron. J Environ Qual 38:1458–1465

47 Spear RJ, Louey CN, Wolfson MG (1989) A preliminary assessment of 3-nitro-1,2,4-triazol-5-one (NTO) as an insensitive high explosive. DSTO Materials Research Laboratory, Maribyrnong, Australia, p 38

48 Brannon JM, Pennington JC (2002) Environmental fate and transport process descriptors for explosives. US Army Corps of Engineers, Engineer Research and Development Center, Vicksburg, MS

49 Linker BR, Khatiwada R, Perdrial N, Abrell L, Sierra R, Field JA, Chorover J (2015) Adsorption of novel insensitive munitions compounds at clay mineral and metal oxide surfaces. Environ Chem 12:74–84

50 Davies PJ, Provatas A (2006) Characterisation of 2,4-dinitroanisole: an ingredient for use in low sensitivity melt cast formulations. Weapons Systems Division, Defence Science and Technology Organisation

51 Coppola EN (2007) Treatment technologies for perchlorate. In: Global demil symposium

52 Sokkalingam N, Potoff JJ, Boddu VM, Maloney SW (2008) Prediction of environmental impact of high-energy materials with atomistic computer simulations. In: ADM002187. Proceedings of the army science conference (26th) held in Orlando, Florida on 1–4 Dec 2008

53 Dumitras-Hutanu CA, Pui A, Jurcoane S, Rusu E, Drochioiu G (2009) Biological effect and the toxicity mechanisms of some dinitrophenyl ethers. Rom Biotechnol Lett 14:4893–4899

54 Taylor S, Lever JH, Walsh ME, Fadden J, Perron N, Bigl S, Spanggord R, Curnow M, Packer B (2010) Dissolution rate, weathering mechanics and friability of TNT, Comp B, Tritonal, and Octol. ERDC/CRREL

55 Eriksson J, Skyllberg U (2001) Binding of 2,4,6-trinitrotoluene and its degradation products in a soil organic matter two-phase system. J Environ Qual 30:2053–2061

56 Stanley JK, Lotufo GR, Biedenbach JM, Chappell P, Gust KA (2015) Toxicity of the conventional energetics TNT and RDX relative to new insensitive munitions constituents DNAN and NTO in Rana pipiens tadpoles. Environ Toxicol Chem 34(4):873–879

57 Dodard SG, Sarrazin M, Hawari J, Paquet L, Ampleman G, Thiboutot S, Sunahara GI (2013) Ecotoxicological assessment of a high energetic and insensitive munitions compound: 2,4-dinitroanisole (DNAN). J Hazard Mater 262:143–150

58 Taylor S, Ringelberg DB, Dontsova K, Daghlian CP, Walsh ME, Walsh MR (2013) Insights into the dissolution and the three-dimensional structure of insensitive munitions formulations. Chemosphere 93:1782–1788

59 Yoon JM, Oliver DJ, Shanks JV (2005) Plant transformation pathways of energetic materials (RDX, TNT, DNTs). In: Eaglesham A, Bessin R, Trigiano R, Hardy RWT (eds) Agricultural biotechnology: beyond food and energy to health and the environment, national agricultural biotechnology council report 17. Ithaca, New York, National Agricultural Biotechnology Council, pp 103–116

60 Walsh MR, Walsh ME, Ramsey CA, Brochu S, Thiboutot S, Ampleman G (2013) Perchlorate contamination from the detonation of insensitive high-explosive rounds. J Hazard Mater 262:228–233

61 Motzer WE (2001) Perchlorate: problems, detection, and solutions. Environ Forensics 2:301–311

62 Le Campion L, Adeline MT, Ouazzani J (1997) Separation of NTO related 1,2,4-triazole-3-one derivatives by a high performance liquid chromatography and capillary electrophoresis. Propellants, Explos, Pyrotech 22:233–237

63 Walsh MR, Walsh ME, Poulin I, Taylor S, Douglas TA (2011) Energetic residues from the detonation of common US ordnance. Int J Energ Mater Chem Propul 10:169–186

64 Richard T, Weidhaas J (2014) Dissolution, sorption, and phytoremediation of IMX-101 explosive formulation constituents: 2,4-dinitroanisole (DNAN), 3-nitro-1,2,4-triazol-5-one (NTO), and nitroguanidine. J Hazard Mater 280:561–569

65 Lever JH, Taylor S, Perovich L, Bjella K, Packer B (2005) Dissolution of composition B detonation residuals. Environ Sci Technol 39:8803–8811

66 Taylor S, Lever JH, Fadden J, Perron N, Packer B (2009) Simulated rainfall-driven dissolution of TNT, Tritonal, comp B and Octol particles. Chemosphere 75:1074–1081

67 Park J, Comfort SD, Shea PJ, Machacek TA (2004) Remediating munitions-contaminated soil with zerovalent iron and cationic surfactants. J Environ Qual 33:1305–1313

Toxicity and Bioaccumulation of Munitions Constituents in Aquatic and Terrestrial Organisms

Guilherme R. Lotufo

Abstract Explosives and their transformation products are present in terrestrial and aquatic environments around the globe and have the potential to cause toxicity to the biota inhabiting contaminated environments. This chapter summarizes the available data on the toxicity of explosives and their transformation products to microbes, soil and aquatic invertebrates, terrestrial plants, aquatic autotrophs, and terrestrial plants, as well as data on their potential to bioaccumulate. While RDX (hexahydro-1,3,5-trinitro-1,3,5-triazine) and HMX (octahydro-1,3,5,7-tetranitro-1,3,5,7-tetrazocine) typically remain untransformed, nitroaromatic explosives undergo fast transformation when added to soils and sediment, posing challenges when establishing concentration-response relations. The cyclic nitramines RDX and HMX typically caused no or minor adverse effects on biological receptors whereas 2,4,6-trinitrotoluene (TNT) caused lethal effects to most species investigated, in addition to sublethal effects on growth and reproduction reported for some species. Overall, nitroaromatic explosives are expected to pose greater risk to terrestrial and aquatic biota at contaminated sites compared to nitramine explosives. The toxicity of other explosives compounds was also summarized. As predicted mainly on the basis of their low hydrophobicity, bioaccumulation studies confirmed the low potential of explosives to accumulate in plants, fish, and invertebrates.

Keywords Explosives · Toxicity · Microbes · Invertebrates · Plants · Microalgae · Fish · Invertebrates · Water · Soil · Sediment · Bioaccumulation

G.R. Lotufo (✉)
U.S. Army Engineer Research and Development Center,
3909 Halls Ferry Road, Vicksburg, MS 39180, USA
e-mail: guilherme.lotufo@usace.army.mil

445

1 Introduction

Historically, manufacturing, open burning or detonation, and improper disposal in landfills have caused the release of explosives and related compounds to terrestrial and aquatic environments [1]. Explosives and related compounds are also present in terrestrial and aquatic environments around the world due to testing, training and combat operations. Explosives packaged into shells as well as fragments of explosives formulations remaining following incomplete detonations may be present in surface soils and in aquatic habitats. Unexploded ordnances (UXO) in the environment pose risks resulting from the release of explosives due to blow-in-place detonation, corrosion, and breaching, in both terrestrial and aquatic sites [2–4]. In addition, until the 1970s, it was accepted practice to dispose of wastes, including excess, obsolete and unserviceable munitions, in deep water areas, further contributing to the contamination of aquatic environments [5].

Thousands of sites throughout the world are potentially contaminated with explosives and related compounds in soil, sediment, groundwater or surface water of inland habitats, at concentrations that span several orders of magnitude [6–8]. Areas containing explosives in soil or sediment are sometimes extensive [3, 4]; however, the residues found in these areas are typically heterogeneous in distribution [3, 4, 6, 9]. Environmental contamination with explosives and related materials may pose unacceptable environmental risks and potentially jeopardize the long-term sustainability of ranges and training sites [10].

This chapter provides an updated overview of the toxicity and bioaccumulation potential of explosives and related compounds, especially in tadpoles, fish, aquatic and soil invertebrates and aquatic and terrestrial autotrophs. The toxicity of chemicals of military concern to terrestrial wildlife was extensively addressed in Williams et al. [11]. This chapter focuses on organismal-level effects, such as survival, growth and reproduction. An overview of sublethal biochemical effects of explosives was provided in Kuperman et al. [12] for soil invertebrates and plants and in Lotufo et al. [13] for fish and aquatic invertebrates. Overviews of the environmental fate of explosives are provided in Chaps. 10 and 11 of this book and also in Monteil-Rivera et al. [1], Lotufo et al. [14, 15], Chappell et al. [16] and Pichtel [9].

Evaluation of the effects of explosives to soil and aquatic organisms has focused on the toxicity of TNT, RDX, and HMX, but recent studies have addressed the toxicity of insensitive munitions (IM) explosives. Because unintentional detonation of munitions and munition stockpiles has caused losses to life, equipment, and infrastructure, the U.S. Department of Defense (DOD) has made concerted efforts to improve the safety by developing insensitive munitions for use in future and existing weapon systems [17].

2   Toxicity to Soil Microorganisms and Invertebrates

Reviews of the effects of explosives and related compounds to soil microorganisms and invertebrates were provided in Talmage et al. [8] and Kuperman et al. [12]. Most studies used spiked artificial soils as exposure media.

The nitroaromatic explosive TNT adversely affected microbial activity and certain components of the soil microbial community at lower concentrations (e.g., [18–20]), potentially causing long-term changes in composition and diversity of the microbial community [21, 22]. A concentration of approximately 30 mg/kg was submitted as a reasonable estimate of the TNT concentration in soil likely to significantly impair critical microbially mediated functions in soil ecosystems [12]. 2,4-dinitroanisole (DNAN), a component of IM explosives formulations, appears to be somewhat less toxic than TNT to microorganisms and microbial reductive transformation may reduce the inhibitory impact of DNAN [23]. The cyclic nitramine explosives RDX, HMX, and CL-20 (China Lake compound 20; hexanitrohexaazaisowurtzitane; an emerging polynitramine energetic material) have been shown to cause no or minor adverse effects on soil microbes [24–29].

The lethal and sublethal toxicity of TNT-spiked soils, investigated for earthworms, enchytraeids, and collembolans [10, 30–39] was widely variable, with toxicity varying with soil type, test species and exposure type [10, 12]. Decrease in survival and in juvenile production typically occurred within the 30–500 mg/kg concentration range (Table 1). TNT is rapidly transformed to the reduced amino-nitrotoluene products aminodinitrotoluenes (ADNTs) and diaminonitrotoluenes (DANTs) in aerobic soils [1, 12]. In spiked soils, concentrations promoting decreased survival were similar for TNT and 4-ADNT but were higher for 2-ADNT and DANTs [40] (Table 1). Kuperman et al. [41] reported that the lethal toxicity of dinitrotoluenes (2,4-DNT and 2,6-DNT), and of 1,3,5-trinitrobenzene (TNB) was greater than that of TNT when exposed to the same soil type. Dinitrotoluenes are components of many single-base propellants and TNB has been produced for use as an explosive.

RDX and HMX have been shown to have no effects on earthworm, potworm, and springtail survival or growth at high concentrations in spiked soils (e.g., no effect on earthworm mortality at 756 mg/kg for RDX), but decreased various reproduction parameters of fecundity at much lower concentrations (e.g., reduced earthworm juvenile production at 15 mg/kg for RDX) [10, 37, 39, 43–45, 48] (Table 1). CL-20 has been shown to be comparatively more toxic to earthworms and enchytraeids than RDX and HMX [46, 47] (e.g., decreased potworm reproduction at 0.1 mg/kg) (Table 1). Strong evidence for the synergistic toxic effect of the mixture of TNT, RDX, and HMX on earthworm survival has been reported [34].

Weathering and aging caused substantial decrease in the concentration of TNT spiked to soils with different characteristics likely due to rapid transformation to aminated products and to sorption to the soil matrix and decrease in bioavailability [10, 33, 44, 49]. Contrastingly, RDX concentrations in those soils did not appreciably decrease during the weathering and aging process [10, 29].

Table 1 Lethal and sublethal toxicity data for soil invertebrates exposed to explosives and their transformation products

MC	Species	Soil[a]	Duration	Biological endpoint[b]	Statistical endpoint[c]	Concentration (mg/kg)	Reference
TNT	*Eisenia andrei*	AFS	14	S	LC50	365	[35]
TNT	*Eisenia andrei*	AFS	14	S	LC25	331	[35]
TNT	*Eisenia andrei*	NFS	14	S	LC50	222	[35]
TNT	*Eisenia andrei*	AFS	28	S	NOEC (U)	881	[36]
TNT	*Eisenia andrei*	AFS	28	ABD	EC25/EC50	495/660	[36]
TNT	*Eisenia andrei*	AFS	28	JBD	EC25/EC50	102/529	[36]
TNT	*Eisenia andrei*	NFS	28	S	NOEC (U)	136	[37]
TNT	*Eisenia andrei*	NFS	28	ABD	EC20/EC50	39/56	[37]
TNT	*Eisenia andrei*	NFS	28	JPD	EC20	52	[37]
TNT	*Eisenia andrei*	NFS	14	S	LC50	132	[40]
TNT	*Eisenia fetida*	F	28	ABD	EC20	4	[31]
TNT	*Eisenia fetida*	NFS	14	S	LC50	277	[34]
TNT	*Enchytraeus albidus*	AFS	21	S	LC50	422	[32]
TNT	*Enchytraeus albidus*	AFS	42	JPD	EC50	111	[32]
TNT	*Enchytraeus crypticus*	F	42	S	LOEC	4	[31]
TNT	*Enchytraeus crypticus*	NSA	7	S	LC50	1290	[39]
TNT	*Enchytraeus crypticus*	NSA	28	JPD	EC50	480	[39]
TNT	*Enchytraeus crypticus*	F	7	S	LC50	570	[39]
TNT	*Enchytraeus crypticus*	F	28	JPD	EC50	360	[39]
TNT	*Enchytraeus crypticus*	NFS	28	JPD	EC20/EC50	77/98	[33]
TNT	*Enchytraeus crypticus*	NSW	28	JPD	EC20/EC50	37/48	[33]
TNT	*Enchytraeus crypticus*	NFS	14	S	LC50	117	[10]
TNT	*Enchytraeus crypticus*	NSW	14	S	NOEC (U)	238	[10]

(continued)

Table 1 (continued)

MC	Species	Soil[a]	Duration	Biological endpoint[b]	Statistical endpoint[c]	Concentration (mg/kg)	Reference
TNT	*Enchytraeus crypticus*	NFS	28	JPD	EC50	84	[10]
TNT	*Enchytraeus crypticus*	NSW	28	JPD	EC50	41	[10]
TNT	*Enchytraeus crypticus*	NFS	28	JPD	EC20/EC50	71/84	[10]
TNT	*Enchytraeus crypticus*	NSW	28	JPD	EC20/EC50	26/41	[10]
TNT	*Folsomia candida*	F	7	S	LC50	185	[39]
TNT	*Folsomia candida*	F	28	JPD	EC50	110	[39]
TNT	*Folsomia candida*	NSA	7	S	LC50	420	[39]
TNT	*Folsomia candida*	NSA	28	JPD	EC50	315	[39]
4-ADNT	*Eisenia andrei*	NFS	14	S	LC50	105	[40]
2-ADNT	*Eisenia andrei*	NFS	14	S	LC50	215	[40]
2,4 or 2,6-DANT	*Eisenia andrei*	NFS	14	S	NOEC (U)	100	[40]
TNB	*Enchytraeus crypticus*	NFS	14	S	LOEC	107	[41]
TNB	*Enchytraeus crypticus*	NSW	14	S	LOEC	176	[41]
TNB	*Enchytraeus crypticus*	NFS	14	JPD	EC20/EC50	42,501	[41]
TNB	*Enchytraeus crypticus*	NSW	14	JPD	EC20/EC50	42,633	[41]
2,4-DNT	*Enchytraeus crypticus*	NFS	14	S	LOEC	55	[41]
2,4-DNT	*Enchytraeus crypticus*	NSW	14	S	LOEC	72	[41]
2,4-DNT	*Enchytraeus crypticus*	NFS	14	JPD	EC20	19	[41]
2,4-DNT	*Enchytraeus crypticus*	NSW	14	JPD	EC20/EC50	14/36	[41]
2,4-DNT	*Enchytraeus crypticus*	NSW	14	JPD	EC50	27	[41]
2,6-DNT	*Enchytraeus crypticus*	NFS	14	S	NOEC (U)	64	[41]
2,6-DNT	*Enchytraeus crypticus*	NSW	14	S	LOEC	108	[41]

(continued)

Table 1 (continued)

MC	Species	Soil[a]	Duration	Biological endpoint[b]	Statistical endpoint[c]	Concentration (mg/kg)	Reference
2,6-DNT	*Enchytraeus crypticus*	NFS	14	JPD	EC20/EC50	37/57	[41]
2,6-DNT	*Enchytraeus crypticus*	NSW	14	JPD	EC20/EC50	18/29	[41]
DNAN	*Eisenia andrei*	NFS	14	S	LC50	47	[42]
RDX	*Eisenia andrei*	AFS	28	S	NOEC (U)	756 (U)	[36]
RDX	*Eisenia andrei*	AFS	28	JPD	LOEC	95	[36]
RDX	*Eisenia andrei*	NFS	28	S	NOEC (U)	201	[37]
RDX	*Eisenia andrei*	NFS	28	ABD	EC20	117	[37]
RDX	*Eisenia andrei*	NFS	28	JPD	EC20	15	[37]
RDX	*Eisenia fetida*	NFS	14	S	LC50	586	[34]
RDX	*Eisenia fetida*	F	28	S	NOEC (U)	1253	[30]
RDX	*Eisenia fetida*	F	28	ABD	LOEC	1253	[30]
RDX	*Enchytraeus crypticus*	F	42	S	NOEC (U)	1253	[30]
RDX	*Enchytraeus crypticus, E. albidus*	NFS	14–42	S, JPD	NOEC (U)	658	[43]
RDX	*Enchytraeus crypticus*	NFS	7	S	NOEC (U)	1000	[39]
RDX	*Enchytraeus crypticus*	NFS	28	JPD	NOEC (U)	1000	[39]
RDX	*Enchytraeus crypticus*	NFS	14	S	NOEC (U)	21,383	[44]
RDX	*Enchytraeus crypticus*	NSW	14	S	NOEC (U)	18,347	[44]
RDX	*Enchytraeus crypticus*	NFS	14	JPD	EC20/EC50	3715/51,413	[44]
RDX	*Enchytraeus crypticus*	NSW	14	JPD	EC20/EC50	8797/142,356	[44]
RDX	*Enchytraeus crypticus*	NFS	7	S	LC50	241	[45]
RDX	*Enchytraeus crypticus*	NFS	28	JPD	EC50	530	[45]
RDX	*Enchytraeus crypticus*	NFS	14	S	LC50	7511	[10]

Table 1 (continued)

MC	Species	Soil[a]	Duration	Biological endpoint[b]	Statistical endpoint[c]	Concentration (mg/kg)	Reference
RDX	Enchytraeus crypticus	NSW	14	S	NOEC (U)	15,236	[10]
RDX	Enchytraeus crypticus	NFS	28	JPD	EC20/EC50	4300/5610	[10]
RDX	Folsomia candida	NFS	7	S	NOEC (U)	1000	[39]
RDX	Folsomia candida	NFS	28	JPD	NOEC (U)	1000	[39]
RDX	Folsomia candida	NFS	7	S	NOEC (U)	4000	[45]
RDX	Folsomia candida	NFS	28	JPD	EC50	176	[45]
HMX	Eisenia andrei	NFS	28	S	NOEC (U)	711	[37]
HMX	Eisenia andrei	NFS	28	ABD	LOEC	16	[37]
HMX	Eisenia andrei	NFS	28	JPD	LOEC	16	[37]
HMX	Eisenia fetida	NFS	14	S	LC50	842	[34]
HMX	Enchytraeus crypticus	NFS	7	S	NOEC (U)	1000	[39]
HMX	Enchytraeus crypticus	NFS	28	JPD	NOEC (U)	1000	[39]
HMX	Enchytraeus crypticus	NFS	14	S	NOEC (U)	21,750	[44]
HMX	Enchytraeus crypticus	NSW	14	S	NOEC (U)	17,498	[44]
HMX	Enchytraeus crypticus	NFS	14	JPD	NOEC (U)	21,750	[44]
HMX	Enchytraeus crypticus	NSW	14	JPD	NOEC (U)	17,498	[44]
HMX	Enchytraeus crypticus, E. albidus	NFS	14–42	S, JPD	NOEC (U)	918	[43]
HMX	Folsomia candida	NFS	7	JPD	NOEC (U)	1000	[39]
HMX	Folsomia candida	NFS	28	JPD	NOEC (U)	1000	[39]
CL-20	Eisenia andrei	NFS	28	S	EC20/EC50	25.3/53.4	[46]
CL-20	Eisenia andrei	NFS	56	S	EC50	0.05	[46]
CL-20	Enchytraeus crypticus	NFS	14	S	LC20/LC50	0.003–0.3/0.1–0.7	[43]

(continued)

Table 1 (continued)

MC	Species	Soil[a]	Duration	Biological endpoint[b]	Statistical endpoint[c]	Concentration (mg/kg)	Reference
CL-20	*Enchytraeus crypticus*	NFS	28	JPD	EC50	0.08–0.62	[43]
CL-20	*Enchytraeus crypticus*	NFS	14	S	LC50	18	[47]
CL-20	*Enchytraeus crypticus*	NSW	14	S	NOEC (U)	6.8	[47]
CL-20	*Enchytraeus crypticus*	NFS	28	JPD	EC20/EC50	0.1/3	[47]
CL-20	*Enchytraeus crypticus*	NSW	28	JPD	EC20/EC50	0.035/0.1	[47]

[a]*AFS* Artificial, freshly spiked; *F* Field-obtained; *NFS* Natural, freshly spiked; *NSW* Natural, spiked, weathered; *NSA* Natural, spiked, aged

[b]*S* Survival; *ABD* Adult biomass decrease; *JBD* Juvenile biomass decrease; *JPD* Juvenile production decrease

[c]LC50 = estimated lethal concentration for 50% of the organisms tested (median); LC25 = estimated lethal concentration for 25% of the organisms tested; LC20 = estimated lethal concentration for 20% of the organisms tested; EC25 = estimated concentration causing 25% inhibition of measured response; EC50 = estimated concentration causing 50% inhibition of measured response; NOEC (U) = no-observed-effect concentration, unbounded (highest concentration tested); LOEC = lowest-observed-effect concentration

Weathering and aging significantly increased the toxicity of TNT, 2,6-DNT (2,6-dinitrotoluene), and CL-20 to enchytraeids, while the toxicities of 2,4-DNT or TNB were unaffected [33, 41, 47] (Table 1). The main factors affecting the TNT bioavailability in soils were soil organic matter content, clay contents, and cation exchange capacity [10, 49]. Both clay and organic matter contents of the soil were found to influence the effect on TNT on enchytraeid exposed to spiked and weathered soils, with organic matter content as the dominant factor [10]. No effect of weathering and aging on the toxicity spiked soils to invertebrates were reported for RDX or HMX [44, 48].

3 Toxicity to Terrestrial Plants

Reviews of the toxicity of explosives and related compounds to terrestrial plants were provided by Kuperman et al. [12] and more recently by Via and Zinnert [50], the latter limited to TNT and RDX. Nitroaromatic explosives, especially TNT and its transformation products, were shown to be toxic to terrestrial plants [51–59], and significant decrease in growth typically occurred at soil concentrations ranging from 10 to 100 mg/kg for a variety of species (Table 2). In addition to decreased growth, TNT has caused detrimental effects on germination and emergence [55–57, 60], and damage to photosynthetic functioning and plant-water relations [61, 62] (Table 2). The most prominent reported effects of TNT were inhibition of new roots and destroyed root hairs, corresponding to the part of the plant where bioaccumulation has been reported to preferentially occur [50]. The mono-amino breakdown products of TNT was similarly phytotoxic as the parent compound, but di-amino products were less toxic [59]. Weathering and aging significantly decreased the phytotoxicity of TNT, TNB or 2,6-DNT spiked to a sandy loam based on seedling emergence, but significantly increased the toxicity of those contaminants based on shoot growth [58] (Table 2). DNAN promoted growth inhibition of ryegrass at 7 mg/kg [42] (Table 2).

The nitramine explosives RDX, HMX and CL-20 have been shown to cause no adverse effects on the growth of various species of terrestrial plants (e.g., [19, 30, 34, 57, 65]), even at concentrations exceeding 9000 mg/kg (Table 2). However, RDX has been shown to inhibit seedling germination, decrease growth, alter leaf morphology, and to decrease photosynthesis in some plant species [62–64, 66] (Table 2). The most prominent reported effects of RDX on plants were on leaf and stem morphology, corresponding to the parts of the plant where bioaccumulation has been reported to preferentially occur [50]. Nitroglycerin (propane-1,2,3-triyl trinitrate) decreased growth of alfalfa, barnyard grass, and ryegrass at concentrations in spiked soils at median effective concentrations as low as 23 mg/kg [67]. Nitroglycerin is used in the manufacture of dynamite, gunpowder and rocket propellants.

Table 2 Lethal and sublethal toxicity data for terrestrial plants exposed to explosives and their transformation products

Chemical	Species	Soil[a]	Duration (d)	Biological endpoint[b]	Statistical endpoint[c]	Concentration (mg/kg)	Reference
TNT	*Avena sativa*	NFS	14	BD	NOEC (U)	1600	[51]
TNT	*Hordeum vugare*	NSA	14	SBD	IC20	139	[57]
TNT	*Hordeum vugare*	ASA	14	SBD	IC20	1200	[57]
TNT	*Lactuca sativa*	ASA	5	ED	IC20	3113	[57]
TNT	*Lepidium sativum*	NFS	14	SBD	LOEC	54	[51]
TNT	*Lolium perenne*	F	55	BD	EC20	4	[31]
TNT	*Medicago sativa*	NFS	16	SBD	EC20	41	[58]
TNT	*Medicago sativa*	NSA	16	SBD	EC20	3	[58]
TNT	*Morella cerifera*	NFS	7	DP	LOEC	30	[62]
TNT	*Morella cerifera*	NFS	7 or 56	DG, MA	NOEC (U)	900	[63]
TNT	*Myrica cerifera*	NFS	63	SCD, PD	LOEC	100	[61]
TNT	*Oriza sativa*	NFS	40	BD	NOEC (U)	500	[60]
TNT	*Oriza sativa*	NFS	8	GD	LOEC	500	[60]
TNT	*Triticum aestivum*	NFS	14	SBD	LOEC	50	[51]
TNT	*Triticum aestivum*	NFS	19	SBD	LOEC	100	[34]
TNT	*Trifolium pratense*	NFS	19	SBD	LOEC	180	[34]
TNB	*Medicago sativa*	NFS	16	SBD	EC20	38	[58]
TNB	*Medicago sativa*	NSA	16	SBD	EC20	20	[58]
2,4-DNT	*Medicago sativa*	NFS	16	SBD	EC20	11	[58]
2,4-DNT	*Medicago sativa*	NSA	16	SBD	EC20	7	[58]

(continued)

Table 2 (continued)

Chemical	Species	Soil[a]	Duration (d)	Biological endpoint[b]	Statistical endpoint[c]	Concentration (mg/kg)	Reference
2,6-DNT	*Medicago sativa*	NFS	16	SBD	EC20	1	[58]
2,6-DNT	*Medicago sativa*	NSA	16	SBD	EC20	2	[58]
RDX	*Baccharis halimifolia*	NFS	42	SCD, PD	LOEC	100	[64]
RDX	*Lolium perenne*	F	55	BD	NOEC (U)	1540	[30]
RDX	*Lolium perenne*	NFS	21	BD	NOEC (U)	9586	[65]
RDX	*Medicago sativa*	F	55	BD	NOEC (U)	1540	[30]
RDX	*Morella cerifera*	NFS	7	DP	LOEC	750	[62]
RDX	*Morella cerifera*	NFS	21	GD	LOEC	100	[63]
RDX	*Morella cerifera*	NFS	56	MA	LOEC	200	[63]
RDX	*Onobrychis viciifolia*	NFS	42	BD	LOEC	46	[66]
RDX	*Trifolium pratense*	NFS	19	SBD	NOEC (U)	1000	[34]
RDX	*Triticum aestivum*	NFS	19	SBD	NOEC (U)	1000	[34]
HMX	*Hordeum vugare*	NSA	14	SBD	NOEC (U)	3321	[57]
HMX	*Hordeum vugare*	ASA	14	SBD	NOEC (U)	1866	[57]
HMX	*Lolium perenne*	NFS	21	BD	NOEC (U)	9282	[65]
HMX	*Trifolium pratense*	NFS	19	SBD	NOEC (U)	1000	[34]
HMX	*Triticum aestivum*	NFS	19	SBD	NOEC (U)	1000	[34]
CL-20	*Lolium perenne*	NFS	21	SBD	NOEC (U)	10,000	[27]
CL-20	*Lolium perenne*	NFS	21	BD	NOEC (U)	9604	[65]
CL-20	*Medicago sativa*	NFS	19	SBD	NOEC (U)	10,000	[27]

(continued)

Table 2 (continued)

Chemical	Species	Soil[a]	Duration (d)	Biological endpoint[b]	Statistical endpoint[c]	Concentration (mg/kg)	Reference
DNAN	*Lolium perenne*	NSA	19	BD	EC50	7	[42]
Nitroglycerin	*Medicago sativa*	NFS	16	BD	EC20	23	[67]
Nitroglycerin	*Echinochloa crusgalli*	NFS	16	BD	EC20	9	[67]
Nitroglycerin	*Lolium perenne*	NFS	19	BD	EC20	16	[67]

[a] *AFS* Artificial, freshly spiked; *F* Field-obtained; *NFS* Natural, freshly spiked; *NSW* Natural, spiked, weathered; *NSA* Natural, spiked, aged
[b] *BD* decreased biomass; *ED* decreased emergence; *GD* decreased germination; *SCD* decreased in stomatal; conductance; *PD* decreased photosynthesis; *SBD* decreased seedling biomass; *SBD* decreased shoot biomass; *MA* morphological alternation
[c] NOEC (U) = no-observed-effect concentration, unbounded (highest concentration tested); LOEC = lowest-observed-effect concentration; EC20 = estimated concentration causing 20% inhibition of measured response; EC50 = estimated concentration causing 50% inhibition of measured response

4   Toxicity to Aquatic Autotrophs

The toxicity of nitroaromatic explosives to cyanobacteria and micro-and macro-algae has been summarized in [68]. TNT caused decreased population growth of cyanobacteria and green microalgae, at concentrations ranging from 0.75 to 18 mg/L (e.g., [69–71]). Overall, mono-amino transformation products of TNT exhibited lower toxicity to microalgae compared to the parent compound [71]. The nitroaromatic compounds 2,4-DNT and 2,6-DNT caused decreased population growth of microalgae at a range (0.9–16.5 mg/L) similar to that reported for TNT (e.g., [69]). The toxicity of various nitroaromatic explosives and their transformation products to sea lettuce zoospore germination was investigated by Nipper et al. [72], who reported nitroaromatics causing toxicity at concentrations ranging from 0.05 to 4.4 mg/L, with 1,3,5-TNB being the most toxic compound tested, followed by TNT, 2,4-DNT, and 2,6-DNT.

Cyanobacteria and algae were relatively tolerant to the effects of RDX, with effects on population growth reported at 12.0–36.7 mg/L [71–73]. Exposure to HMX at reported concentrations that approached or exceeded its solubility limit failed to decrease population growth of cyanobacteria and microalgae [71, 74].

Aquatic autotrophs were relatively tolerant to picric acid (2,4,6-trinitrophenol) [75], but sensitive to tetryl (trinitrophenylmethylnitramine), with sublethal effects reported at 61 mg/L and higher concentrations and 0.43 mg/L, respectively [75, 76]. Picric acid was used in grenades and mine fillings and tetryl was used in booster charges, detonator charges, and as a component of explosives mixture. Both picric acid and tetryl are considered obsolete military explosives.

Exposure of freshwater microalgae to nitroglycerin resulted in decreased population growth and reduction in chlorophyll *a* at concentrations as low as 0.4 mg/L [77, 78]. Exposure to DEGN (diethyleneglycol dinitrate) caused decreased population growth of a microalga at 58 mg/L and nitroguanidine caused decreased population growth and reduction in chlorophyll at 508 mg/L or higher concentrations [79].

5   Toxicity to Tadpoles and Fish

Broad overviews of the effects of explosive compounds to aquatic organisms were provided in Talmage et al. [8], Juhasz and Naidu [80], Nipper et al. [68], and more recently in Lotufo et al. [13]. Numerous aquatic toxicity studies have reported that TNT, its aminated transformation products or the related compounds TNB, 2,4-DNT and 2,6-DNT caused decreased survival to tadpoles [81–83], freshwater fish (e.g., [78, 84, 85]), and marine and estuarine fish [72, 86]. Except for 2,4-DANT, that was not toxic at the highest concentration tested (50 mg/L), fish survival was reduced within the range of 0.4–28 mg/L (Table 3). Survival of tadpoles was significantly decreased at concentrations as low as 0.003 mg/L for TNT

[83] and 0.13 and 0.21 mg/L for 2,4-DNT and 2,6-DNT, respectively [81] during chronic exposures (Table 3), suggesting that larval amphibians may be much more sensitive than fish to the long-term effects of nitroaromatic explosives.

The nitramine RDX caused lethal (Table 3) or sublethal impacts to freshwater [92, 94, 98, 99], and estuarine fish [93] at concentrations ranging from 2 to 28 mg/L. Studies with freshwater fish [74] demonstrated that larval fathead minnows were susceptible to the effects of HMX at exposure solutions saturated with HMX (Table 3). Except for the report of toxicity to fathead minnows by Bentley et al. [74], all other species of freshwater [74, 100] and estuarine fish investigated were unaffected by the highest concentrations of HMX tested (Table 3). The highest no-effect concentration reported in those studies were higher than the reported aqueous solubility limit of HMX.

When comparing the toxicity of eight explosives and related compounds to embryos of a marine fish, Nipper et al. [72], reported that tetryl was the most toxic compound overall, with toxicity occurring at 1 mg/L. It was also the most degradable compound, often being reduced to very low or below-detection levels at the end of the test exposure. In contrast to the high toxicity of tetryl, the nitrophenolic explosive picric acid was lethally toxic to fish at much higher concentrations [72, 95] (Table 3).

The range of toxicity of nitroglycerin to fish overlaps with that reported for TNT [77, 78] (Table 3). Lethal effects to freshwater fish exposed to nitroglycerin occurred at 1.9 and 3.6 mg/L [78]. The toxicity of DEGN was much higher than that of TNT and nitroglycerin, with lethal effects to fish occurring at >250 mg/L [96]. Fish were tolerant to the lethal effects of nitroguanidine, with no significant toxicity occurring at exposure concentrations exceeding 1500 mg/L [78] (Table 3). DNAN was lethally toxic to tadpoles [83] and fathead minnows [97] at concentrations ranging from 2.4 to 10 mg/L. NTO (3-nitro-1,2,4-triazol-5-one), a component of IM explosives formulations, decreased tadpole survival at 5.0 mg/L or higher concentrations [83] (Table 3).

6 Toxicity to Aquatic Invertebrates in Aqueous Exposures

Numerous aquatic toxicity studies have reported that TNT, its aminated transformation products or the related compounds TNB, 2,4-DNT and 2,6-DNT caused decreased survival to freshwater (e.g., [70, 78, 101–105]) and marine and estuarine invertebrates [72, 102, 106–108]. Toxicity to most species occurred within the range of 1 and 6 mg/L (Table 4). Decrease in offspring production at concentrations lower than those promoting mortality was reported for a cladoceran exposed to 2,4-DANT [103], for a cladoceran and a rotifer exposed to TNT [78, 105] and for a polychaete exposed to TNT, 1,3,5-TNB, 2,4-DNT, or 2,6-DNT [72] (Table 4).

A variety of aquatic invertebrate species, both marine and freshwater, were tolerant to the lethal effects of RDX at the maximum concentration tested, such as exposure to RDX at 7.2 mg/L failing to elicit mortality of coral [109] and exposure

Table 3 Lethal toxicity data for tadpoles and fish exposed to explosives and their transformation products

Spiked MC	Species	Habitat[a]	Duration (d)	Statistical endpoint[b]	Concentration (mg/kg)	Reference
Tadpole						
TNT	*Xenopus laevis*	FW	4	LC50	3.8	[82]
TNT	*Rana catesbeiana*	FW	4	LC50	40.3	[81]
TNT	*Rana catesbeiana*	FW	90	LOEC	0.12	[81]
TNT	*Rana pipiens*	FW	4	LC50	4.4	[83]
TNT	*Rana pipiens*	FW	28	LC50	0.003	[83]
2-ADNT	*Xenopus laevis*	FW	4	LC50	32.7	[82]
4-ADNT	*Xenopus laevis*	FW	4	LC50	22.7	[82]
2,4-DNT	*Rana catesbeiana*	FW	4	LC50	79.3	[81]
2,4-DNT	*Rana catesbeiana*	FW	90	LOEC	0.13	[81]
2,6-DNT	*Rana catesbeiana*	FW	4	LC50	92.4	[81]
2,6-DNT	*Rana catesbeiana*	FW	90	LOEC	0.21	[81]
DNAN	*Rana pipiens*	FW	4	LC50	24.3	[83]
DNAN	*Rana pipiens*	FW	28	LOEC	2.4	[83]
NTO	*Rana pipiens*	FW	28	LOEC	5.0	[83]
Fish						
TNT	*Lepomis macrochirus*	FW	4	LC50	2.6	[87]
TNT	*Ictalurus punctatus*	FW	4	LC50	2.4	[87]
TNT	*Pimephales promelas*	FW	10	LC50	2.2	[88]
TNT	*Oncorhynchus mykiss*	FW	4	LC50	0.8	[89]
TNT	*Sciaenops ocellatus*	M/E	2	LC50	7.6	[72]
TNT	*Cyprinodon variegatus*	M/E	5	LC50	1.7	[86]
2-ADNT	*Pimephales promelas*	FW	4	LC50	14.8	[85]
2-ADNT	*Cyprinodon variegatus*	M/E	5	LC50	8.6	[86]
4-ADNT	*Pimephales promelas*	FW	4	LC50	6.9	[85]
2,4-DANT	*Cyprinodon variegatus*	M/E	5	NOEC (U)	50	[86]

<div align="right">(continued)</div>

Table 3 (continued)

Spiked MC	Species	Habitat[a]	Duration (d)	Statistical endpoint[b]	Concentration (mg/kg)	Reference
TNB	*Lepomis macrochirus*	FW	4	LC50	0.85	[90]
TNB	*Ictalurus punctatus*	FW	18	LC50	0.38	[90]
TNB	*Pimephales promelas*	FW	4	LC50	0.49	[90]
TNB	*Oncorhynchus mykiss*	FW	18	LC50	0.43	[90]
TNB	*Sciaenops ocellatus*	M/E	2	LC50	1.20	[72]
TNB	*Cyprinodon variegatus*	M/E	5	LC50	1.20	[86]
2,4-DNT	*Lepomis macrochirus*	FW	4	LC50	13.5	[89]
2,4-DNT	*Pimephales promelas*	FW	4	LC50	24.3	[91]
2,4-DNT	*Oncorhynchus mykiss*	FW	4	LC50	16.3	[89]
2,4-DNT	*Sciaenops ocellatus*	FW	2	LC50	48	[72]
2,6-DNT	*Sciaenops ocellatus*	FW	2	LC50	28.0	[72]
RDX	*Lepomis macrochirus*	FW	4	LC50	3.6	[92]
RDX	*Ictalurus punctatus*	FW	4	LC50	4.1	[92]
RDX	*Pimephales promelas*	FW	4	LC50	5.8	[92]
RDX	*Oncorhynchus mykiss*	FW	4	LC50	6.4	[92]
RDX	*Cyprinodon variegatus*	M/E	10	LC50	9.9	[93]
RDX	*Danio rerio*	FW	4	LC50	23	[94]
HMX	*Pimephales promelas*	FW	4	LC50	15	[74]
HMX	*Oncorhynchus mykiss*	FW	4	NOEC (U)	32	[74]
HMX	*Ictalurus punctatus*	FW	4	NOEC (U)	32	[74]
Picric acid	*Oncorhynchus mykiss*	FW	4	LC50	110	[95]
Picric acid	*Sciaenops ocellatus*	M/E	2	LC50	127	[72]

Table 3 (continued)

Spiked MC	Species	Habitat[a]	Duration (d)	Statistical endpoint[b]	Concentration (mg/kg)	Reference
Tetryl	*Sciaenops ocellatus*	M/E	2	LC50	1.1	[72]
NG	*Pimephales promelas*	FW	4	LC50	3.6	[78]
NG	*Oncorhynchus mykiss*	FW	4	LC50	1.9	[78]
NQ	*Pimephales promelas*	FW	4	NOEC (U)	3,320	[78]
NQ	*Oncorhynchus mykiss*	FW	4	NOEC (U)	1,550	[78]
DEGDN	*Pimephales promelas*	FW	4	LC50	491	[96]
DEGDN	*Oncorhynchus mykiss*	FW	4	LC50	284	[96]
DNAN	*Pimephales promelas*	FW	7	LC50	10.0	[97]

[a]*FW* freshwater; *M/E* Marine or estuarine
[b]LC50 = estimated lethal concentration for 50% of the organisms tested (median); NOEC (U) = no-observed-effect concentration, unbounded (highest concentration tested); LOEC = lowest-observed-effect concentration

to RDX concentrations approaching its solubility in water (28 mg/L or higher concentrations) failing to elicit significant mortality in marine invertebrates [72, 102, 107] (Table 4). However, RDX caused lethal impacts or decreased reproduction at sublethal concentrations in some freshwater [78, 92] and marine invertebrate species [72] (Table 4). All freshwater [74, 100] and marine invertebrate [107] species investigated were unaffected by the highest concentrations of HMX tested, which were as values exceeding the aqueous solubility limit of that explosive (Table 4).

When comparing the toxicity of eight explosives and related compounds to marine invertebrates, Nipper et al. [72], reported that tetryl was the most toxic compound overall, with toxicity occurring at 1 mg/L or lower concentrations. Picric acid was lethally toxic at much higher concentrations to freshwater and marine invertebrates [72, 95, 102, 116] (Table 4). Picric acid promoted significant decrease of sea urchin embryonic development and copepod hatching success at relatively high concentrations, but which were lower than their respective lethal concentrations [72, 76].

Lethal effects of nitroglycerin to freshwater invertebrates exposed to nitroglycerin occurred at 17–18 mg/L [78]. The toxicity of DEGN was much higher than that of TNT and nitroglycerin, with lethal effects occurring at 90 mg/L and higher concentrations mg/L [96] (Table 4). For a copepod and a cladoceran, the single species of aquatic organism investigated for the toxicity of PETN (pentaerythritoltetranitrate),

Table 4 Lethal and sublethal toxicity data for aquatic invertebrates exposed to explosives and their transformation products

Spiked MC	Species	Habitat[a]	Duration (d)	Biological endpoint[b]	Statistical endpoint[c]	Concentration (mg/kg)	Reference
RDX	*Acropora formosa*	M/E	4	S	NOEC (U)	7.2	[109]
RDX	*Americamysis bahia*	M/E	4	S	NOEC (U)	47	[72]
RDX	*Arbacia punctulata*	M/E	2	ED	NOEC (U)	75	[72]
RDX	*Daphnia magna*	FW	2	I	NOEC (U)	55	[102]
RDX	*Ceriodaphnia dubia*	FW	7	OP	LOEC	6.0	[78]
RDX	*Daphnia magna*	FW	21	OP	LOEC	4.8	[92]
RDX	*Dinophilus gyrociliatus*	M/E	7	S	NOEC (U)	49	[72]
RDX	*Dinophilus gyrociliatus*	M/E	7	OP	LOEC	23.7	[72]
RDX	*Mytilus galloprovincialis*	M/E	2	ED	NOEC (U)	28	[107]
RDX	*Nitocra spinipes*	M/E	4	S	NOEC (U)	36	[102]
HMX	*Daphnia magna*	FW	28	S	NOEC (U)	3.9	[100]
HMX	*Daphnia magna*	FW	28	OP	NOEC (U)	3.9	[100]
HMX	*Mytilus galloprovincialis*	FW	4	S	NOEC (U)	28.4	[107, 110]
HMX	*Mytilus galloprovincialis*	FW	2	ED	NOEC (U)	2.0	[107, 110]
TNT	*Americamysis bahia*	M/E	4	S	LC50	0.26	[72]
TNT	*Arbacia punctulata*	M/E	2	ED	EC50	12.0	[72]
TNT	*Branchionus calyciflorus*	FW	1	S	LC50	5.6	[111]
TNT	*Ceriodaphnia dubia*	FW	2	S	LC50	4.0	[78]
TNT	*Ceriodaphnia dubia*	FW	7	OP	EC50	3.3	[103]
TNT	*Chironomus dilutus*	FW	4	S	LC50	1.9	[101, 112]
TNT	*Daphnia magna*	FW	4	S	LC50	1.0	[113]
TNT	*Dinophilus gyrociliatus*	M/E	7	S	LC50	5.6	[72]
TNT	*Dinophilus gyrociliatus*	M/E	7	OP	EC50	1.1	[72]

(continued)

Table 4 (continued)

Spiked MC	Species	Habitat[a]	Duration (d)	Biological endpoint[b]	Statistical endpoint[c]	Concentration (mg/kg)	Reference
TNT	*Hyalella azteca*	FW	4	S	LC50	3.6	[104]
TNT	*Lumbriculus variegatus*	FW	2	S	LC50	5.2	[89]
TNT	*Mytilus galloprovincialis*	M/E	4	S	LC50	19.5	[107, 110]
TNT	*Mytilus galloprovincialis*	M/E	2	ED	EC50	0.8	[107, 110]
TNT	*Tubifex tubifex*	FW	4	S	LC50	7.7	[101, 112]
2-ADNT	*Hyalella azteca*	FW	4	S	LC50	3.8	[104]
2-ADNT	*Ceriodaphnia dubia*	FW	7	OP	EC50	3.1	[103]
2-ADNT	*Ceriodaphnia dubia*	FW	7	S	LC50	4.9	[103]
2-ADNT	*Daphnia magna*	FW	4	S	LC50	1.06	[113]
4-ADNT	*Hyalella azteca*	FW	4	S	LC50	9.2	[104]
4-ADNT	*Ceriodaphnia dubia*	FW	7	OP	EC50	5.1	[103]
4-ADNT	*Ceriodaphnia dubia*	FW	7	S	LC50	6.6	[103]
4-ADNT	*Daphnia magna*	FW	4	S	LC50	5.1	[113]
2,4-DANT	*Hyalella azteca*	FW	4	S	LC50	1.70	[104]
2,4-DANT	*Ceriodaphnia dubia*	FW	7	OP	EC50	0.05	[103]
2,6-DANT	*Ceriodaphnia dubia*	FW	7	OP	EC50	0.33	[103]
TNB	*Hyalella azteca*	M/E	4	S	LC50	2.30	[104]
TNB	*Ceriodaphnia dubia*	FW	7	OP	EC50	1.41	[103]
TNB	*Americamysis bahia*	M/E	4	S	LC50	0.74	[72]
TNB	*Dinophilus gyrociliatus*	M/E	7	OP	EC50	0.40	[72]
TNB	*Dinophilus gyrociliatus*	M/E	7	S	LC50	1.60	[72]
TNB	*Arbacia punctulata*	M/E	2	ED	EC50	1.30	[72]
2,4-DNT	*Americamysis bahia*	M/E	4	S	LC50	4.4	[72]

(continued)

Table 4 (continued)

Spiked MC	Species	Habitat[a]	Duration (d)	Biological endpoint[b]	Statistical endpoint[c]	Concentration (mg/kg)	Reference
2,4-DNT	*Dinophilus gyrociliatus*	M/E	7	OP	EC50	5.2	[72]
2,4-DNT	*Dinophilus gyrociliatus*	M/E	7	S	LC50	20.0	[72]
2,4-DNT	*Arbacia punctulata*	M/E	2	ED	EC50	51.0	[72]
2,4-DNT	*Daphnia magna*	FW	21	I	EC50	0.6	[114]
2,4-DNT	*Daphnia magna*	FW	2	S	LC50	35.0	[115]
2,4-DNT	*Daphnia magna*	FW	2	S	LC50	47.5	[70]
2,6-DNT	*Schizopera knabeni*	M/E	4	HS	EC50	55.0	[76]
2,6-DNT	*Schizopera knabeni*	M/E	4	S	LC50	65.0	[76]
2,6-DNT	*Americamysis bahia*	M/E	4	S	LC50	5.0	[72]
2,6-DNT	*Dinophilus gyrociliatus*	M/E	7	OP	EC50	2.1	[72]
2,6-DNT	*Dinophilus gyrociliatus*	M/E	7	S	LC50	13.0	[72]
2,6-DNT	*Arbacia punctulata*	M/E	2	ED	EC50	6.7	[72]
2,6-DNT	*Daphnia magna*	FW	2	S	LC50	21.8	[70]
Picric acid	*Americamysis bahia*	M/E	4	S	LC50	13	[72]
Picric acid	*Crassostrea virginica*	M/E	6	SD	EC50	28	[95]
Picric acid	*Crassostrea virginica*	M/E	6	S	LC50	255	[95]
Picric acid	*Dinophilus gyrociliatus*	M/E	7	OP	EC50	155	[72]
Picric acid	*Dinophilus gyrociliatus*	M/E	7	S	LC50	265	[72]
Picric acid	*Nitocra spinipes*	M/E	4	S	LC50	95	[102]
Picric acid	*Arbacia punctulata*	M/E	2	ED	EC50	281	[72]
Picric acid	*Daphnia magna*	FW	2	S	LC50	85	[116]
Tetryl	*Americamysis bahia*	M/E	4	S	LC50	0.37	[72]
Tetryl	*Dinophilus gyrociliatus*	M/E	7	OP	EC50	0.010	[72]

(continued)

Table 4 (continued)

Spiked MC	Species	Habitat[a]	Duration (d)	Biological endpoint[b]	Statistical endpoint[c]	Concentration (mg/kg)	Reference
Tetryl	*Dinophilus gyrociliatus*	M/E	7	OP	EC50	0.008	[72]
Tetryl	*Dinophilus gyrociliatus*	M/E	7	S	LC50	0.030	[72]
Tetryl	*Arbacia punctulata*	M/E	2	ED	EC50	0.050	[72]
NG	*Ceriodaphnia dubia*	FW	2	S	LC50	17.8	[78]
NG	*Hydra littoralis*	FW	2	S	LC50	17.4	[78]
DEGN	*Hexagenia bilinata*	FW	2	S	LC50	343	[96]
DEGN	*Paratanytarsus parthenogeneticus*	FW	2	S	LC50	160	[96]
DEGN	*Daphnia magna*	FW	2	S	LC50	90	[96]
PETN	*Nitocra spinipes*	M/E	4	S, OP	NOEC (U)	32	[102]
PETN	*Daphnia magna*	FW	4	S, OP	NOEC (U)	49	[102]
NQ	*Ceriodaphnia dubia*	FW	2	S	LC50	2698	[78]
NQ	*Ceriodaphnia dubia*	FW	7	OP	LOEC	440	[78]
NQ	*Hydra littoralis*	FW	2	S	LC50	2061	[78]
DEGDN	*Daphnia magna*	FW	2	S	LC50	90.1	[96]
DNAN	*Ceriodaphnia dubia*	FW	6	S	LC50	6.7	[97]
DNAN	*Ceriodaphnia dubia*	FW	6	OP	IC25	2.8	[97]
DNAN	*Daphnia pulex*	FW	9 to 11	S	LC50	13.7	[97]
DNAN	*Daphnia pulex*	FW	9 to 11	OP	IC25	2.3	[97]
NTO	*Ceriodaphnia dubia*	FW	7	OP	IC50	57	[117]

[a]*FW* freshwater; *M/E* Marine or estuarine
[b]*S* Survival; *ED* Embryo development; *I* Immobilization; *OP* Offspring production; *HS* Hatching success; *SD* Shell deposition
[c]*NOEC* (U) NOEC = no-observed-effect concentration, unbounded (highest concentration tested); *LOEC* = lowest-observed-effect concentration; *LC50* = estimated lethal concentration for 50% of the organisms tested (median); *EC50* = estimated concentration causing 50% inhibition of measured response; IC25 = inhibition concentration, 25% reduction; IC50 = inhibition concentration, 50% reduction

no lethal or sublethal effects were observed at the highest concentration tested, 32 and 49 mg/L, respectively [102]. Aquatic invertebrates were relatively tolerant to nitroguanidine, with significant toxicity occurring at 440 mg/L or higher concentrations [78, 102]. Studies with nitrocellulose indicated no toxicity at concentrations up to 1000 mg/L to freshwater invertebrates [118]. The overall lack of toxicity of nitrocellulose is likely a result of its insolubility in water. DNAN was lethally toxic to cladocerans [97] at concentrations ranging from 2.4 to 42 mg/L and NTO caused decreased cladoceran reproduction at 57 mg/L [117] (Table 4).

7   Toxicity of Photo-Transformation Products

A review of the toxicity of photo-transformation products of explosives was provided in Nipper et al. [68]. Rosenblatt et al. [119] reported that photolysis of TNT reduced its toxicity to freshwater fish and cladocerans, but promoted no change in its toxicity to amphipods and midges. Irradiation of TNT-spiked water with UV light promoted no change in toxicity to both species [102]. The mixture of chemicals produced by the photolysis of nitroguanidine caused a dramatic two orders of magnitude increase in toxicity to a cladoceran and to sheepshead minnows [78, 79]. RDX decreased the reproduction of a cladoceran species at 6 mg/L [120], but photolysis under sunlight for 28 d resulted in no effect survival and reproduction at 10 mg/L for under the same exposure conditions [121].

In addition to the demonstrated evidence for the toxicity of photo-transformation products to aquatic organism, several studies reported the potential for the photo-activation of explosives and their transformation products accumulated in the tissues of aquatic invertebrates [68]. Irradiation of water spiked with 2,4-DNT with UV light for 2 h at the end of a toxicity test resulted in significantly increased acute toxicity to a cladoceran but not to an estuarine copepod [102]. Co-exposure with near-UV light only caused increased toxicity of 2-ADNT (10-fold) to a planarian, but not TNT and 4-ADNT [113]. Co-exposure of sea urchin eggs or embryos to near-UV light increased the toxicity of TNT, 2,4-DNT, and 2,6-DNT relative to exposure to those compounds in the dark [106]. In the above studies, both photo-transformation and photo-activation of bioaccumulated compounds could have contributed to the observed enhancement of toxicity compared to the no-UV treatments.

8   Toxicity to Aquatic Invertebrates and Fish in Exposures to Spiked Sediment

Contamination of sediments within military facilities has occurred mainly as a result of contaminated runoff, effluent from manufacturing facilities, liquid waste lagoons, and spills [8]. Cracked or corroded underwater UXOs also have potential

to contaminate surrounding sediments [2, 122]. Rapid transformation, disappearance of transformation products, and partitioning to overlying water following initiation of whole-sediment toxicity testing has been reported for TNT and its amino transformation products [101, 112, 123–128], for TNB [123, 127, 128] and for 2,6-DNT, picric acid and tetryl [76, 129]. The rapidly changing concentration of explosives and their transformation products in exposures to sediment presents unique challenges to the process of developing accurate toxicity data for the evaluation of risks at contaminated sediment sites [76, 112, 130]. Toxicity evaluations of nitroaromatic explosives spiked to sediments should use exposure conditions (e.g., duration, water quality requirements) that minimize degradation of the parent compound and that do not require water changes during the experimental period [112].

Compared to investigations addressing explosives and related compounds in soil exposures, relatively few studies addressed the toxicity of sediment-associated explosives to freshwater [112, 127, 128], and to marine invertebrates [76, 102, 123, 126, 129, 131]. A single study investigated the toxicity of an explosive to fish in exposures to spiked sediments [124]. A review of the fate and toxicity of explosives and related compounds amended to sediments was provided in Lotufo et al. [14] and expanded in Lotufo et al. [13].

The toxicity of sediment amended with TNT has been reported for a polychaete and a estuarine amphipod species [126, 131], for a freshwater midge and amphipod species [127, 128], for oligochaetes [101, 112], and for an estuarine fish [124]. Toxicity to most species occurred within a wide range (37–508 mg/kg) of concentrations. The observed variability in the effects concentrations was due at least in part to challenges associated with accurately characterizing the exposure concentrations [14, 112]. The toxicity of transformation products of TNT spiked to sediments was evaluated for marine and estuarine [123] and for freshwater [127, 128] invertebrates, and revealed that although the species investigated varied widely in responsiveness, TNT, 2-ADNT and TNB caused toxicity at relatively similar concentrations to each species. The toxicity of sediments spiked with 2,6-DNT was examined using a marine amphipod [129]. No significant lethal effects were observed in any treatment and because the highest 2,6-DNT measured concentration in sediments was relatively low (5 mg/kg), the effects of that compound at higher concentrations remain unknown.

The toxicity of sediments spiked with RDX and HMX was reported for a polychaete and two marine amphipod species [123, 126], and for a freshwater midge and amphipod species [127]. No significant mortality was observed in sediment concentrations of RDX ranging from 102 to over 2000 mg/kg, and HMX concentrations ranging from 115 to 353 mg/kg, suggesting high tolerance of benthic invertebrates to those explosives. The toxicity of picric acid and tetryl spiked to sediments was examined using a marine amphipod. Significant lethal effects in exposures to spiked sandy sediment were observed at picric acid concentrations similar to lethal concentrations reported for marine amphipods exposed to TNT, but tetryl promoted significant lethal effects at concentrations as low as 4 mg/kg [129].

9   Bioaccumulation in Soil Invertebrates and Terrestrial Plants

The potential for soil invertebrates and terrestrial vascular plants to uptake and bioaccumulate explosives and related compounds has been reviewed by Johnson et al. [132]. Explosive compounds are weakly hydrophobic and therefore their bioaccumulative potential is expected to be low, which was confirmed by studies addressing the bioaccumulation of TNT, RDX, HMX, and DNAN in soil invertebrates. Uptake of TNT in earthworms resulted in extensive biotransformation of the parent compound and bioaccumulation of extractable reduced transformation products ADNTs and DANTs [40, 133, 134] as well as of non-identified nonextractable compounds (i.e., bound residues), which have lower rates of elimination than the parent compound [135]. Bioaccumulation of non-identified nonextractable transformation products of RDX in earthworms were also reported [136]. "Nonextractable" implies that solvents that readily extract the parent compound and primary metabolites did not extract metabolites bound to organic molecules, likely proteins [135]. Differently from TNT, exposures to RDX resulted in bioaccumulation of mostly the parent compound in earthworm tissues [30, 136, 137]. Bioaccumulation of DNAN and its transformation products in earthworms was reported by Dodard et al. [42] and [138–140]. Nitroaromatic and nitramine explosives are unlikely to be trophically transferred from soil invertebrates to their predators because of their rapid transformation, excretion and lack of potential for continuous exposure [132].

Evaluations of the distribution of TNT in terrestrial vascular plants have demonstrated that it is stored almost exclusively in the root (e.g., [53, 141–143]). Most (95%) of the material found in the root tissue of yellow nutsedge was in the form of mono-amino transformation products of TNT that resisted organic solvent extraction [54]. In contrast, RDX is highly mobile within plants and have been shown to preferentially concentrate in aboveground tissues, mostly in the leaves and flowers and in the form of the parent compound [141, 143–145]. However, contrasting to finding from studies with all other plants investigated, RDX was predominantly retained in the roots of coniferous trees [146]. Relatively fewer studies addressed the bioaccumulation of explosives other than TNT and RDX in terrestrial plants. The nitramine explosive HMX was reported to have low potential to bioaccumulate in plants and was found chiefly in leaf tissues [147, 148]. Exposure to tetryl resulted in extensive degradation of the parent compound in the bush bean tissues leading to low bioaccumulation of parent compound [149]. When perennial ryegrass was exposed to soil spike with nitroglycerin, the parent compound was not found in the tissues but accumulated as dinitroglycerin in the roots and shoots [67]. Accumulation of DNAN and their aminated transformation products in grasses grown in DNAN-amended soil has been reported [42, 150]. Exposure of grasses to NTO resulted in no detection of NTO in roots or shoots [150].

9.1 Bioaccumulation in Fish and Aquatic Invertebrates

According to predictive models, explosives and related compounds have low potential to bioaccumulate in aquatic organisms [15, 138–140, 151]. Bioconcentration factors (the ratio of a chemical concentration in an aquatic organism to that in the surrounding water) were reported for tadpoles, fish and aquatic invertebrates exposed in the laboratory to TNT and its mono-amino transformation products [88, 107, 110, 112, 138–140, 152–157], 2,4-DNT [158, 159], 2,6-DNT [159], RDX [98, 110, 151, 152, 154, 155, 157, 160], HMX [110, 157], and DNAN [155].

Measured bioconcentration factor (BCF) values were overall higher for nitroaromatics (0.3–23.5 L/kg) than for nitroaminines (0.3–4.4 L/kg) and generally agreed with model predicted values [13, 151]. Extensive biotransformation in fish and aquatic invertebrates has been reported for TNT [88, 107, 110, 112, 152] and RDX [151]. The formation and prevalence of nonextractable residues compared to extractable TNT and aminated transformation products has been reported for aquatic invertebrates and fish [138–140, 153, 154, 156]. Investigations of the relevance of the dietary route for the bioaccumulation of explosives in fish [153, 160–162] concluded that aqueous exposure is likely the dominant route of exposure for TNT, RDX and similar compounds, with the dietary uptake route providing only minimal, if any, contribution to the net bioaccumulation of those explosives.

10 Summary and Conclusions

The cyclic nitramine explosives RDX, HMX, and CL-20 have been shown to cause no or minor adverse effects on soil microbes, whereas the nitroaromatic explosive TNT adversely affected microbial activity and certain components of the soil microbial community at relatively lower concentrations. Soil amended with TNT caused lethal and sublethal effects to soil invertebrates, but toxic concentrations varied widely with test species and soil type, in part because TNT is rapidly transformed to reduced amino-nitrotoluene products after spiking. Weathering and aging significantly decreased the concentration of the spiked nitroaromatic compound, and increased toxicity of TNT and 2,6-DNT, but did not affect the toxicity of soils spiked with 2,4-DNT or TNB. Soil organic matter content, clay contents, and cation exchange capacity were found to affect the TNT bioavailability in soils. RDX and HMX, even at exceedingly high concentrations (e.g., no effect on earthworm mortality at 756 mg/kg for RDX), have been shown to have no effect on the survival or growth of soil invertebrates, but have caused decrease in reproduction at relatively low concentrations. The cyclic nitramine explosives RDX is highly mobile within the plant and concentrate in leaf and flower tissue, while TNT is stored almost exclusively in the root and undergoes substantial transformation. RDX has been shown to cause morphological effects on some plant species but not

in others, even at exceedingly high concentrations in the soil. All plant species investigated tolerated exposure to high concentration of HMX and CL-20 in soil. TNT and other nitroromatic explosives and their degradation products have also been shown to decrease plant growth, and impact germination and emergence, as well as promote adverse physiological effects. Phytotoxicity has also been reported for nitroglycerin and DNAN.

The effects of explosives on fish and aquatic invertebrates and autotrophs has been extensively investigated. In most species tested, exposure to RDX and HMX near or at the maximum solubility resulted in no or minor biological responses, whereas TNT, its aminated transformation products and the related compounds TNB and 2,4-DNT and 2,6-DNT decreased survival in fish and invertebrates, offspring production in invertebrates, population growth of cyanobacteria and microalgae, and the zoospore germination of a macroalga. Survival of tadpoles was significantly decreased at ultralow concentrations of TNT, 2,4-DNT and 2,6-DNT during chronic exposures, suggesting that larval amphibians may be much more sensitive than fish to the long-term effects of nitroaromatic explosives. Tetryl was highly toxic and nitroglycerin was moderately toxic to fish and aquatic invertebrates whereas picric acid and nitroguanidine were toxic substantially less toxic. Similar to observations in soils, nitroaromatic explosives undergo fast transformation when added to sediment resulting in major decreases in the concentrations of explosives and their transformation products. Sediments spiked with the explosives TNT, TNB, picric acid, tetryl, and TNT transformation products promoted significant invertebrate mortality in laboratory exposures. However, exposure of benthic invertebrates to sediments spiked with RDX and HMX did not elicit lethal toxicity, even at exceedingly high concentrations.

Explosive compounds are weakly hydrophobic and therefore their bioaccumulative potential is expected to be low, which was confirmed for plants, fish, and invertebrates in soil or water exposures. Uptake of TNT in earthworms, fish and invertebrates resulted in extensive biotransformation of the parent compound and accumulation of extractable and nonextractable transformation products. For fish, aqueous exposure was shown to be the dominant route of exposure for explosive compounds, with dietary uptake providing only minimal contribution.

Substantial progress in explosives ecotoxicology over the last decades has generated a large set of data, sufficient to provide an adequate characterization of the potential hazards associated with the presence of explosives and their transformation products in terrestrial and aquatic environments. Comparison of toxicity values determined in laboratory tests summarized in this chapter with the limited information on the concentrations reported in field contaminated sites suggests a low risk from exposure to explosives to for fish and aquatic invertebrates (e.g., [163]). Differently, higher concentration of explosives reported for soils at contaminated sites [7, 30] suggest higher potential for risk from exposure to explosives to plants and soil invertebrates. A relevant knowledge gap exists for toxicity of explosives to plants and soil invertebrates inhabiting water-limited environments, as all the available information have been generated using species and soils from mesic habitats.

References

1. Monteil-Rivera F, Halasz A, Groom C, Zhao JS, Thiboutot S, Ampleman G, Hawari J (2009) Fate and transport of explosives in the environment. In: Sunahara GI, Lotufo GR, Kuperman RG, Hawari J (eds) Ecotoxicology of explosives. CRC Press, Boca Raton, FL

2. Lewis J, Martel R, Trepanier L, Ampleman G, Thiboutot S (2009) Quantifying the transport of energetic materials in unsaturated sediments from cracked unexploded ordnance. J Environ Qual 38:2229–2236

3. Taylor S, Bigl S, Packer B (2015) Condition of in situ unexploded ordnance. Sci Total Environ 505:762–769

4. Voie ØA, Mariussen E (2016) Risk assessment of sea dumped conventional munitions. Prop. Explos, Pyrot In Press

5. Carton G, Jagusiewicz A (2009) Historic disposal of munitions in US and European coastal waters, how historic information can be used in characterizing and managing risk. Mar Technol Soc J 43:16–32

6. Jenkins TF, Pennington JC, Ranney TA, Berry TE, Miyares PH, Walsh ME (2001) Characterization of explosives contamination at military firing ranges. ERDC TR-01-5. US Army Engineer Research and Development Center, Hanover, NH

7. Simini M, Wentsel RS, Checkai RT, Phillips CT, Chester NA, Majors MA, Amos JC (1995) Evaluation of soil toxicity at joliet army ammunition plant. Environ Toxicol Chem 14: 623–630

8. Talmage SS, Opresko DM, Maxwell CJ, Welsh CJ, Cretella FM, Reno PH, Daniel FB (1999) Nitroaromatic munition compounds: environmental effects and screening values. Rev Environ Contam Toxicol 161:1–156

9. Pichtel J (2012) Distribution and fate of military explosives and propellants in soil: a review. Appl Environ Soil Sci 2012:33p

10. Kuperman RG, Checkai RT, Simini M, Phillips CT, Kolakowski JE, Lanno R (2013) Soil properties affect the toxicities of 2,4,6-trinitrotoluene (TNT) and hexahydro-1,3,5-trinitro-1,3,5-triazine (RDX) to the enchytraeid worm *Enchytraeus crypticus*. Environ Toxicol Chem 32:2648–2659

11. Williams M, Reddy G, Quinn M, Johnson M (2015) Wildlife toxicity assessments for chemicals of military concern. Elsevier Inc., Oxford, UK

12. Kuperman RG, Simini M, Siciliano S, Gong P (2009) Effects of energetic materials on soil organisms. In: Sunahara GI, Lotufo GR, Kuperman RG, Hawari J (eds) Ecotoxicology of explosives. CRC Press, Boca Raton, FL

13. Lotufo GR, Rosen G, Wild W, Carton G (2013) Summary review of the aquatic toxicology of munitions constituents. ERDC/EL TR-13-8. US Army Engineer Research and Development Center, Vicksburg, MS

14. Lotufo GR, Nipper M, Carr RS, Conder JM (2009) Fate and toxicity of explosives in sediment. In: Sunahara GI, Lotufo GR, Kuperman RG, Hawari J (eds) Ecotoxicology of explosives. CRC Press, Boca Raton, FL

15. Lotufo GR, Lydy MJ, Rorrer GL, Cruz-Uribe O, Cheney DP (2009) Bioconcentration, bioaccumulation and biotransformation of explosives and related compounds in aquatic organisms. In: Sunahara GI, Lotufo GR, Kuperman RG, Hawari J (eds) Ecotoxicology of explosives. CRC Press, Boca Raton, FL

16. Chappell MA, Price CL, Miller LF (2011) Solid-phase considerations for the environmental fate of nitrobenzene and triazine munition constituents in soil. Appl Geochem 26:S330–S333

17. Duncan K (2002) Insensitive munitions and the army: improving safety and survivability. Army Logistician 34:16–17

18. Gong P, Siciliano SD, Greer CW, Paquet L, Hawari J, Sunahara GI (1999) Effects and bioavailability of 2,4,6-trinitrotoluene in spiked and field-contaminated soils to indigenous microorganisms. Environ Toxicol Chem 18:2681–2688

19. Gong P, Gasparrini P, Rho D, Hawari J, Thiboutot S, Ampleman G, Sunahara GI (2000) An in situ respirometric technique to measure pollution-induced microbial community tolerance in soils contaminated with 2,4,6-trinitrotoluene. Ecotoxicol Environ Saf 47:96–103

20. Meyers SK, Deng SP, Basta NT, Clarkson WW, Wilber GG (2007) Long-term explosive contamination in soil: effects on soil microbial community and bioremediation. Soil Sed Contam 16:61–77

21. Fuller ME, Manning JF (1998) Evidence for differential effects of 2,4,6-trinitrotoluene and other munitions compounds on specific subpopulations of soil microbial communities. Environ Toxicol Chem 17:2185–2195

22. George IF, Liles MR, Hartmann M, Ludwig W, Goodman RM, Agathos SN (2009) Changes in soil acidobacteria communities after 2,4,6-trinitrotoluene contamination. FEMS Microbiol Lett 296:159–166

23. Liang J, Olivares C, Field JA, Sierra-Alvarez R (2013) Microbial toxicity of the insensitive munitions compound, 2,4-dinitroanisole (DNAN), and its aromatic amine metabolites. J Hazard Mater 262:281–287

24. Anderson JAH, Canas JE, Long MK, Zak JC, Cox SB (2010) Bacterial community dynamics in high and low bioavailability soils following laboratory exposure to a range of hexahydro-1,3,5-trinitro-1,3,5-triazine concentrations. Environ Toxicol Chem 29:38–44

25. Gong P, Hawari J, Thiboutot S, Ampleman G, Sunahara GI (2001) Ecotoxicological effects of hexahydro-1,3,5-trinitro-1,3,5-triazine on soil microbial activities. Environ Toxicol Chem 20:947–951

26. Gong P, Hawari J, Thiboutot S, Ampleman G, Sunahara GI (2002) Toxicity of octahydro-1,3,5,7-tetranitro-1,3,5,7-tetrazocine (HMX) to soil microbes. Bull Environ Contam Toxicol 69:97–103

27. Gong P, Sunahara GI, Rocheleau S, Dodard SG, Robidoux PY, Hawari J (2004) Preliminary ecotoxicological characterization of a new energetic substance, CL-20. Chemosphere 56:653–658

28. Juck D, Driscoll BT, Charles TC, Greer CW (2003) Effect of experimental contamination with the explosive hexahydro-1,3,5-trinitro-1,3,5-triazine on soil bacterial communities. FEMS Microbiol Ecol 43:255–262

29. Sunahara GI, Robidoux PY, Gong P, Lachance B, Rocheleau S, Dodard S, Sarrazin M, Hawari J, Thiboutot S, Ampleman G, Renoux AY (2001) Laboratory and field approaches to characterize the soil ecotoxicology of polynitro explosives. In: Greenberg BM, Hull RN, Roberts MHJ, Gensemer RW (eds) Environmental toxicology and risk assessment ASTM. West Conshohocken, PA

30. Best EPH, Geter KN, Tatem HE, Lane BK (2006) Effects, transfer, and fate of RDX from aged soil in plants and worms. Chemosphere 62:616–625

31. Best EPH, Tatem HE, Geter KN, Wells ML, Lane BK (2008) Effects, uptake, and fate of 2,4,6-trinitrotoluene aged in soil in plants and worms. Environ Toxicol Chem 27:2539–2547

32. Dodard SG, Renoux AY, Powlowski J, Sunahara GI (2003) Lethal and subchronic effects of 2,4,6-trinitrotoluene (TNT) on *Enchytraeus albidus* in spiked artificial soil. Ecotoxicol Environ Saf 54:131–138

33. Kuperman RG, Checkai RT, Simini M, Phillips CT, Kolakowski JE, Kurnas CW (2005) Weathering and aging of 2,4,6-Trinitrotoluene in soil increases toxicity to potworm *Enchytraeus crypticus*. Environ Toxicol Chem 24:2509–2518

34. Panz K, Miksch K, Sojka T (2013) Synergetic toxic effect of an explosive material mixture in soil. Bull Environ Contam Toxicol 91:555–559

35. Robidoux PY, Hawari J, Thiboutot S, Ampleman G, Sunahara GI (1999) Acute toxicity of 2,4,6-trinitrotoluene in earthworm (*Eisenia andrei*). Ecotoxicol Environ Saf 44:311–321

36. Robidoux PY, Svendsen C, Caumartin J, Hawari J, Ampleman G, Thiboutot S, Weeks JM, Sunahara GI (2000) Chronic Toxicity of energetic compounds in soil determined using the earthworm (*Eisenia andrei*) reproduction test. Environ Toxicol Chem 19:1764–1773

37. Robidoux PY, Hawari J, Bardai G, Paquet L, Ampleman G, Thiboutot S, Sudahara GI (2002) TNT, RDX, and HMX decrease earthworm (*Eisenia andrei*) life-cycle responses in a spiked natural forest soil. Arch Environ Contam Toxicol 43:379–388

38. Robidoux PY, Svendsen C, Sarrazin M, Thiboutot S, Ampleman G, Hawari J, Weeks JM, Sunahara GI (2005) Assessment of a 2,4,6-trinitrotoluene-contaminated site using *Aporrectodea rosea* and *Eisenia andrei* in mesocosms. Arch Environ Contam Toxicol 48:56–67

39. Schafer R, Achazi RK (1999) The Toxicity of soil samples containing TNT and other ammunition derived compounds in the enchytraeid and collembola-biotest. Environ Sci Pollut R 6:213–219

40. Lachance B, Renoux AY, Sarrazin M, Hawari J, Sunahara GI (2004) Toxicity and bioaccumulation of reduced TNT metabolites in the earthworm *Eisenia andrei* exposed to amended forest soil. Chemosphere 55:1339–1348

41. Kuperman RG, Checkai RT, Simini M, Phillips CT, Anthony JS, Kolakowski JE, Davis EA (2006) toxicity of emerging energetic soil contaminant CL-20 to Potworm *Enchytraeus crypticus* in freshly amended or weathered and aged treatments. Chemosphere 62:1282–1293

42. Dodard SG, Sarrazin M, Hawari J, Paquet L, Ampleman G, Thiboutot S, Sunahara GI (2013) Ecotoxicological assessment of a high energetic and insensitive munitions compound: 2,4-dinitroanisole (DNAN). J Hazard Mater 262:143–150

43. Dodard SG, Sunahara GI, Kuperman RG, Sarrazin M, Gong P, Ampleman G, Thiboutot S, Hawari J (2005) Survival and reproduction of enchytraeid worms, oligochaeta, in different soil types amended with energetic cyclic nitramines. Environ Toxicol Chem 24:2579–2587

44. Kuperman RG, Checkai RT, Simini M, Phillips CT, Kolakowski JE, Kurnas CW, Sunahara GI (2003) Survival and reproduction of *Enchytraeus crypticus* (Oligochaeta, Enchytraeidae) in a natural sandy loam soil amended with the nitro-heterocyclic explosives RDX and HMX. Pedobiologia 47:651–656

45. Schafer R, Achazi R (2004) Toxicity of Hexyl to *F. candida* and *E. crypticus*. J Soils Sed 4:157–162

46. Robidoux PY, Sunahara GI, Savard K, Berthelot Y, Dodard SG, Martel M, Gong P, Hawari J (2004) Acute and chronic toxicity of the new explosive CL-20 to the earthworm (*Eisenia andrei*) exposed to amended natural soils. Environ Toxicol Chem 23:1026–1034

47. Kuperman RG, Checkai RT, Simini M, Phillips CT, Kolakowski JE, Kurnas CW (2006) Toxicities of dinitrotoluenes and trinitrobenzene freshly amended or weathered and aged in a sandy loam soil to Enchytraeus crypticus. Environ Toxicol Chem 25:1368–1375

48. Simini M, Checkai RT, Kuperman RG, Phillips CT, Kolakowski JE, Kurnas CW, Sunahara GI (2003) Reproduction and survival of *Eisenia fetida* in a sandy loam soil amended with the nitro-heterocyclic explosives RDX and HMX. Pedobiologia 47:657–662

49. Huang Q, Liu BR, Hosiana M, Guo X, Wang TT, Gui MY (2016) Bioavailability of 2,4,6-trinitrotoluene (TNT) to earthworms in three different types of soils in China. Soil Sediment Contam 25:38–49

50. Via SM, Zinnert JC (2016) Impacts of explosive compounds on vegetation: a need for community scale investigations. Environ Pollut 208:495–505

51. Gong P, Wilke BM, Fleischmann S (1999) Soil-based phytotoxicity of 2,4,6-Trinitrotoluene (TNT) to terrestrial higher plants. Arch Environ Contam Toxicol 36:152–157

52. Krishnan G, Horst GL, Darnell S, Powers WL (2000) Growth and development of smooth bromegrass and tall fescue in TNT-contaminated soil. Environ Pollut 107:109–116

53. Palazzo AJ, Leggett DC (1986) Effect and disposition of TNT in a terrestrial plant. J Environ Qual 15:49–52

54. Palazzo AJ, Leggett DC (1986) Effect and disposition of TNT in a terrestrial plant and validation of analytical methods. CRREL-86-15. Cold Regions Research and Engineering Lab Hanover, NH

55. Peterson MM (1996) TNT and 4-Amino-2,6-dinitrotoluene influence on germination and early seedling development of tall fescue. Environ Pollut 93:57–62

56. Peterson MM, Horst GL, Shea PJ, Comfort SD (1998) Germination and seedling development of switchgrass and smooth bromegrass exposed to 2,4,6-trinitrotoluene. Environ Pollut 99:53–59

57. Robidoux PY, Bardai G, Paquet L, Ampleman G, Thiboutot S, Hawari J, Sunahara GI (2003) Phytotoxicity of 2,4,6-trinitrotoluene (TNT) and octahydro-1,3,5,7-tetranitro-1,3,5,7-tetrazocine (HMX) in spiked artificial and natural forest soils. Arch Environ Contam Toxicol 44:198–209

58. Rocheleau S, Kuperman RG, Martel M, Paquet L, Bardai G, Wong S, Sarrazin M, Dodard S, Gong P, Hawari J, Checkai RT, Sunahara GI (2006) Phytotoxicity of nitroaromatic energetic compounds freshly amended or weathered and aged in sandy loam soil. Chemosphere 62:545–558

59. Picka K, Friedl Z (2004) Phytotoxicity of some toluene nitroderivatives and products of their reduction. Fresenius Environ Bull 13:789–794

60. Vila M, Lorber-Pascal S, Laurent F (2008) Phytotoxicity to and uptake of TNT by rice. Environ Geochem Health 30:199–203

61. Naumann JC, Anderson JE, Young DR (2010) Remote detection of plant physiological responses to TNT soil contamination. Plant Soil 329:239–248

62. Via SM, Zinnert JC, Butler AD, Young DR (2014) Comparative physiological responses of Morella cerifera to RDX, TNT, and composition B contaminated soils. Environ Exper Bot 99:67–74

63. Via SM, Zinnert JC, Young DR (2015) Differential effects of two explosive compounds on seed germination and seedling morphology of a woody shrub, Morella cerifera. Ecotoxicology 24:194–201

64. Zinnert JC (2012) Plants as phytosensors: physiological responses of a woody plant in response to RDX exposure and potential for remote detection. Int J Plant Sci 173:1005–1014

65. Rocheleau S, Lachance B, Kuperman RG, Hawari J, Thiboutot S, Ampleman G, Sunahara GI (2008) Toxicity and uptake of cyclic nitrarnine explosives in ryegrass Lolium perenne. Environ Pollut 156:199–206

66. Winfield LE, Rodgers JH, D'Surney SJ (2004) The responses of selected terrestrial plants to short (<12 days) and long term (2, 4 and 6 weeks) hexahydro-1,3,5-trinitro-1,3,5-triazine (RDX) exposure. Part I: growth and developmental effects. Ecotoxicology 13:335–347

67. Rocheleau S, Kuperman RG, Dodard SG, Sarrazin M, Savard K, Paquet L, Hawari J, Checkai RT, Thiboutot S, Ampleman G, Sunahara GI (2011) Phytotoxicity and uptake of nitroglycerin in a natural sandy loam soil. Sci Total Environ 409:5284–5291

68. Nipper M, Carr RS, Lotufo GR (2009) Aquatic toxicology of explosives. In: Sunahara GI, Lotufo GR, Kuperman RG, Hawari J (eds) Ecotoxicology of explosives. CRC Press, Boca Raton, FL

69. Dodard SG, Renoux AY, Hawari J, Ampleman G, Thiboutot S, Sunahara GI (1999) Ecotoxicity characterization of dinitrotoluenes and some of their reduced metabolites. Chemosphere 38:2071–2079

70. Liu DH, Spanggord RJ, Bailey HC, Javitz HS, Jones DCL (1983c) Toxicity of TNT wastewaters to aquatic organisms. Final report. Vol. I. Acute toxicity of LAP wastewater and 2,4,6-trinitrotoluene. AD A142144. SRI International, Menlo Park, CA

71. Sunahara GI, Dodard S, Sarrazin M, Paquet L, Ampleman G, Thiboutot S, Hawari J, Renoux AY (1998) Development of a soil extraction procedure for ecotoxicity characterization of energetic compounds. Ecotoxicol Environ Saf 39:185–194

72. Nipper M, Carr RS, Biedenbach JM, Hooten RL, Miller K, Saepoff S (2001) Development of marine toxicity data for ordnance compounds. Arch Environ Contam Toxicol 41:308–318

73. Burton DT, Turley SD, Peters GT (1994) The toxicity of hexahydro-1,3,5-trinitro-1,3,5-triazine (RDX) to the freshwater green alga Selenastrum capricornutum. Water Air Soil Pollut 76:449–457

74. Bentley RE, Leblanc GA, Hollister TA, Sleight BH (1977) Laboratory evaluation of the toxicity of nitrocellulose to aquatic organisms. AD A037749. US Army Medical Research and Development Command, Washington, DC

75. Bringmann G, Kuhn R (1978) Testing of substances for their toxicity threshold: model organisms *Microcystis (Diplocystis) aeruginosa* and *Scenedesmus quadricauda*. Mitt Int Ver Theor Angew Limnol 21:275–284

76. Nipper M, Carr RS, Biedenbach JM, Hooten RL, Miller K (2005) Fate and effects of picric acid and 2,6-DNT in marine environments: Toxicity of degradation products. Mar Pollut Bull 50:1205–1217

77. Bentley RE, Dean JW, Ellis SJ, Leblanc GA, Sauter S, Buxter KS, Sleight BH (1978) Laboratory evaluation of the toxicity of nitroglycerine to aquatic organisms. AD-A061739 ed

78. Burton DT, Turley SD, Peters GT (1993) Toxicity of nitroguanidine, nitroglycerin, hexahydro-1,3,5-trinitro-1,3,5-triazine (RDX), and 2,4,6-trinitrotoluene (TNT) to selected freshwater aquatic organisms report. AD A267467). The University of Maryland, Agricultural Experiment Station. Queenstown, MD

79. van der Schalie WH (1985) The toxicity of nitroguanidine and photolyzed nitroguanidine to freshwater aquatic organisms. Technical report 8404. AD-A153045. US Army Medical Bioengineering Research and Development Laboratory, Fredrick, MD

80. Juhasz AL, Naidu R (2007) Explosives: fate, dynamics, and ecological impact in terrestrial and marine environments. Rev Environ Contam Toxicol 191:163–215

81. Paden NE, Smith EE, Maul JD, Kendall RJ (2011) Effects of chronic 2,4,6,-trinitrotoluene, 2,4-dinitrotoluene, and 2,6-dinitrotoluene exposure on developing bullfrog (*Rana catesbeiana*) tadpoles. Ecotoxicol Environ Saf 74:924–928

82. Saka M (2004) Developmental toxicity of p, p′-dichlorodiphenyltrichloroethane, 2,4,6-trinitrotoluene, their metabolites, and benzo[a]pyrene in Xenopus laevis embryos. Environ Toxicol Chem 23:1065–1073

83. Stanley JK, Lotufo GR, Biedenbach JM, Chappell P, Gust KA (2015) Toxicity of the conventional energetics TNT and RDX relative to new insensitive munitions constituents DNAN and NTO in *Rana pipiens* tadpoles. Environ Toxicol Chem 34:873–879

84. Bailey HC, Spanggord RJ, Javitz HS, Liu DH (1985) Toxicity of TNT wastewaters to aquatic organisms. Final report, vol III. Chronic toxicity of LAP wastewater and 2,4,6-Trinitrotoluene. AD-A164 282. SRI international, Menlo Park, CA

85. Pearson JG, Glennon JP, Barkley JJ, Highfill JW (1979) An Approach to the Toxicological Evaluation of a Complex Industrial Wastewater. In: Marking LL, Kimerle RA (eds) Aquatic toxicology and hazard assessment: sixth symposium, ASTM STP, 667th edn. American Society for Testing Materials, Philadelphia, PA

86. Lotufo GR, Blackburn W, Gibson AB (2010) Toxicity of trinitrotoluene to sheepshead minnows in water exposures. Ecotoxicol Environ Saf 73:718–726

87. Liu DH, Bailey HC, Pearson JG (1983a) Toxicity of a complex munitions wastewater to aquatic organism. In: Bishop WE, Cardwell RD, Heidolph BB (eds) Aquatic toxicology and hazard assessment: sixth symposium, ASTM STP 802. American Society for Testing Materials, Philadelphia, PA

88. Yoo LJ, Lotufo GR, Gibson AB, Steevens JA, Sims JG (2006) Toxicity and bioaccumulation of 2,4,6-trinitrotoluene in fathead minnow (*Pimephales promelas*). Environ Toxicol Chem 25:3253–3260

89. Liu DH, Spanggord RJ, Bailey HC, Javitz HS, Jones DCL (1983b) Toxicity of TNT wastewaters to aquatic organisms. Final report. VoI. II. Acute toxicity of condensate wastewater and 2,4-dinitrotoluene. DSU-4262. SRI International, Menlo Park, CA

90. van der Schalie WH (1983) The acute and chronic toxicity of 3,5-dinitroaniline, 1,3-dinitrobenene, and 1,3,5-trinitrobenzene to freshwater aquatic organisms. Technical Report 8305. U.S. Army Medical Bioengineering Research and Development Laboratory, Fort Derick, MD

91. Broderius SJ, Kahl MD, Elonen GE, Hammermeister DE, Hoglund MD (2005) A comparison of the lethal and sublethal toxicity of organic chemical mixtures to the fathead minnow (*Pimephales promelas*). Environ Toxicol Chem 24:3117–3127

92. Bentley RE, Leblanc GA, Hollister TA, Sleight BH (1977) Acute toxicity of -1,3,5,7-tetranitro-octahydro-1,3,5,7-tetrazocine (HMX) to aquatic organisms. Final report. AD A061 730. EG & G Bionomics, Wareham, MA

93. Lotufo GR, Gibson AB, Leslie YJ (2010) b Toxicity and bioconcentration evaluation of RDX and HMX using sheepshead minnows in water exposures. Ecotoxicol Environ Saf 73:1653–1657

94. Mukhi S, Pan XP, Cobb GP, Patino R (2005) Toxicity of hexahydro-1,3,5-trinitro-1,3,5-triazine to larval zebrafish (*Danio rerio*). Chemosphere 61:178–185

95. Goodfellow WL Jr, Burton DT, Graves WC, Hall LW Jr, Cooper KR (1983) Acute toxicity of picric acid and picramic acid to rainbow trout, *Salmo gairdneri*, and American oyster, *Crassostrea virginica*. Water Resour Bull 19:641–648

96. Fisher DJ, Burton DT, Paulson RL (1989) Comparative acute toxicity of diethyleneglycol dinitrate to freshwater aquatic organisms. Environ Toxicol Chem 8:545–550

97. Kennedy AJ, Laird JG, Lounds C, Gong P, Barker ND, Brasfield SM, Russell AL, Johnson MS (2015) Inter- and intraspecies chemical sensitivity: a case study using 2,4-dinitroanisole. Environ Toxicol Chem 34:402–411

98. Mukhi S, Patino R (2008) Effects of hexahydro-1,3,5-trinitro-1,3,5-triazine (RDX) in zebrafish: general and reproductive toxicity. Chemosphere 72:726–732

99. Warner CM, Gust KA, Stanley JK, Habib T, Wilbanks MS, Garcia-Reyero N, Perkins EJ (2012) A systems toxicology approach to elucidate the mechanisms involved in RDX species-specific sensitivity. Environ Sci Technol 46:7790–7798

100. Bentley RE, Petrocelli SR, Suprenant DC (1984) Determination of the toxicity to aquatic organisms of HMX and related wastewater constituents. Part III. Toxicity of HMX, TAX and SEX to aquatic organisms. Final report. AD A172 385. Springborn Biomomics, Wareham, MD

101. Conder JM, Lotufo GR, Turner PK, La Point TW, Steevens JA (2004) Solid phase microextraction fibers for estimating the toxicity and bioavailability of sediment-associated organic compounds. Aquat Ecosyst Health Manag 7:387–397

102. Dave G, Nilsson E, Wernersson A-S (2000) Sediment and water phase toxicity and UV-activation of six chemicals used in military explosives. Aquat. Ecosyst. Health Manag 3:291–299

103. Griest WH, Vass AA, Stewart AJ, Ho CH (1998) Chemical and toxicological characterization of slurry reactor biotreatment of explosives-contaminated soils. Technical report SFIM-AEC-ETCR-96186. U.S. Army Environmental Center, Aberdeen, MD

104. Sims JG, Steevens JA (2008) The role of metabolism in the toxicity of 2,4,6-trinitrotoluene and its degradation products to the aquatic amphipod *Hyalella azteca*. Ecotoxicol Environ Saf 70:38–46

105. Snell TW, Moffat BD (1992) A 2-d life cycle test with the totifer *Brachionus calyciflorus*. Environ Toxicol Chem 11:1249–1257

106. Davenport R, Johnson LR, Schaeffer DJ, Balbach H (1994) Phototoxicology. 1. Light-enhanced toxicity of TNT and some related compounds to *Daphnia magna* and *Lytechinus variagatus* embryos. Ecotoxicol Environ Saf 27:14–22

107. Rosen G, Lotufo GR (2007) Bioaccumulation of explosive compounds in the marine mussel, *Mytilus galloprovincialis*. Ecotoxicol Environ Saf 68:237–245

108. Won WD, DiSalvo LH, Ng J (1976) Toxicity and mutagenicity of 2,4,6-trinitrotoluene and its microbial metabolites. Appl Environ Microbiol 31:576–580

109. Gust KA, Najar FZ, Habib T, Lotufo GR, Piggot AM, Fouke BW, Laird JG, Wilbanks MS, Rawat A, Indest KJ, Roe BA, Perkins EJ (2014) Coral-zooxanthellae meta-transcriptomics reveals integrated response to pollutant stress. BMC Genom 15:591

110. Rosen G, Lotufo GR (2007) Toxicity of explosive compounds to the marine mussel, *Mytilus galloprovincialis*, in aqueous exposures. Ecotoxicol Environ Saf 68:228–236

111. Toussaint MW, Shedd TR, van der Schalie WH, Leather GR (1995) A comparison of standard acute toxicity tests with rapid-screening toxicity tests. Environ Toxicol Chem 14(5):907–915

112. Conder JM, La Point TW, Steevens JA, Lotufo GR (2004) Recommendations for the assessment of TNT toxicity in sediment. Environ Toxicol Chem 23:141–149
113. Johnson LR, Davenport R, Balbach H, Schaeffer DJ (1994) Phototoxicology. 3. Comparative toxicity of trinitrotoluene and aminodinitrotoluenes to *Daphnia magna*, *Dugesia dorotocephala*, and sheep erythrocytes. Ecotoxicol Environ Saf 27:34–49
114. Deneer JW, Seinen W, Hermens JL (1988) Growth of *Daphnia magna* exposed to mixtures of chemicals with diverse modes of action. Ecotoxicol Environ Saf 15:72–77
115. Liu DH, Spanggord RJ, Bailey HC (1976) Toxicity of TNT wastewater (pink water) to aquatic organisms. ADA0310. US Army Medical Research and Development Command, Washington, DC
116. LeBlanc GA (1980) Acute toxicity of priority pollutants to water flea (*Daphnia magna*). Bull Environ Contam Toxicol 24:684–691
117. Haley MV, Kuperman RG, Checkai RT (2009) Aquatic toxicity of 3-Nitro-1,2,4-Triazol-5-one. ECBC-TR-726. US Army Research, Development and Engineering Command, Edgewood Chemical Biological Center, Aberdeen Proving Ground, MD
118. Bentley RE, Dean JW, Ellis SJ, Hollister TA, Leblanc GA, Sauter S, Sleight BH (1977) Laboratory evaluation of the toxicity of cyclotrimethylene trinitramine (RDX) to aquatic organisms. ADA 061730. US Army Medical Bioengineering Research and Development Laboratory, Fort Detrick, MD
119. Rosenblatt DH, Burrows EP, Mitchell WR, Parmer DL (1991) Organic explosives and related compounds. In: Huntzinger O (ed) The handbook of environmental chemistry—anthropogenic compounds, vol 3 Part G. Springer, Berlin
120. Peters GT, Burton DT, Paulson RL, Turley SD (1991) The acute and chronic toxicity of hexahydro-1,3,5-trinitro-1,3,5-traizine (RDX) to three freshwater invertebrates. Environ Toxicol Chem 10:1073–1081
121. Burton DT, Turley SD (1995) Reduction of hexahydro-1,3,5-trinitro-1,3,5-triazine (RDX) toxicity to the cladoceran *Ceriodaphnia dubia* following photolysis in sunlight. Bull Environ Contam Toxicol 55:89–95
122. Dave G (2003) Field test of ammunition (TNT) dumping in the ocean. In: M Munawar (ed) Quality assessment and management: insight and progress. Aquatic Ecosyst Health Manag Soc 213–220
123. Lotufo GR, Farrar JD, Inouye LS, Bridges TS, Ringelberg DB (2001) Toxicity of sediment-associated nitroaromatic and cyclonitramine compounds to benthic invertebrates. Environ Toxicol Chem 20:1762–1771
124. Lotufo GR, Blackburn W, Marlborough SJ, Fleeger JW (2010) Toxicity and bioaccumulation of TNT in marine fish in sediment exposures. Ecotoxicol Environ Saf 73:1720–1727
125. Nipper M, Qian Y, Carr RS, Miller K (2004) Degradation of picric acid and 2,6-DNT in marine sediments and waters: the role of microbial activity and ultra-violet exposure. Chemosphere 56:519–530
126. Rosen G, Lotufo GR (2005) Toxicity and fate of two munitions constituents in spiked sediment exposures with the marine amphipod *Eohaustorius estuarius*. Environ Toxicol Chem 24:2887–2897
127. Steevens JA, Duke BM, Lotufo GR, Bridges TS (2002) Toxicity of the explosives 2,4,6-trinitrotoluene, hexahydro-1,3,5-trinitro-1,3,5-triazine, and octahydro-1,3,5,7-tetranitro-1,3,5,7-tetrazocine in sediments to *Chironomus tentans* and *Hyalella azteca*: Low-dose hormesis and high-dose mortality. Environ Toxicol Chem 21:1475–1482
128. Lotufo GR, Farrar JD (2005) Comparative and mixture sediment toxicity of trinitrotoluene and its major transformation products to a freshwater midge. Arch Environ Contam Toxicol 49:333–342
129. Nipper M, Carr RS, Biedenbach JM, Hooten RL, Miller K (2002) Toxicological and chemical assessment of ordnance compounds in marine sediments and porewaters. Mar Pollut Bull 44:789–806

130. Pascoe GA, Kroeger K, Leisle D, Feldpausch RJ (2010) Munition constituents: Preliminary sediment screening criteria for the protection of marine benthic invertebrates. Chemosphere 81:807–816

131. Green AS, Moore DW, Farrar D (1999) Chronic toxicity of 2,4,6-trinitrotoluene to a marine polychaete and an estuarine amphipod. Environ Toxicol Chem 18:1783–1790

132. Johnson MS, Salice CJ, Sample BE, Robidoux PY (2009) Bioconcentration, bioaccumulation, and biomagnification of nitroaromatic and nitramine explosives in terrestrial systems. In: Sunahara GI, Lotufo GR, Kuperman RG, Hawari J (eds) Ecotoxicology of explosives. CRC Press, Boca Raton, FL

133. Dodard SG, Powlowski J, Sunahara GI (2004) Biotransformation of 2,4,6-trinitrotoluene (TNT) by enchytraeids (*Enchytraeus albidus*) in vivo and in vitro. Environ Pollut 131:263–273

134. Renoux AY, Sarrazin M, Hawari J, Sunahara GI (2000) Transformation of 2,4,6-trinitrotoluene in soil in the presence of the earthworm E*isenia andrei*. Environ Toxicol Chem 19:1473–1480

135. Belden JB, Lotufo GR, Chambliss CK, Fisher JC, Johnson DR, Boyd RE, Sims JG (2011) Accumulation of ^{14}C-trinitrotoluene and related nonextractable (bound) residues in *Eisenia fetida*. Environ Pollut 159:1368

136. Sarrazin M, Dodard SG, Savard K, Lachance B, Robidoux PY, Kuperman RG, Hawari J, Ampleman G, Thiboutot S, Sunahara GI (2009) Accumulation of hexahydro-1,3,5-trinitro-1,3,5-triazine by the earthworm *Eisenia andrei* in a sandy loam soil. Environ Toxicol Chem 28:2125–2133

137. Savard K, Sarrazin M, Dodard SG, Monteil-Rivera F, Kuperman RG, Hawari J, Sunahara GI (2010) Role of soil interstitial water in the accumulation of hexahydro-1,3,5-trinitro-1,3,5-triazine in the earthworm *Eisenia andrei*. Environ Toxicol Chem 29:998–1005

138. Lotufo GR, Farrar JD, Biedenbach JM, Laird JG, Krasnec MO, Lay C, Morris JM, Gielazyn ML (2016) Effects of sediment amended with deepwater horizon incident slick oil on the infaunal amphipod *Leptocheirus plumulosus*. Mar Pollut Bull 109:253–258

139. Lotufo GR, Coleman JG, Harmon AR, Chappell MA, Bednar AJ, Russell AL, Smith JC, Brasfield SM (2016) Accumulation of 2,4-dinitroanisole in the earthworm *Eisenia fetida* from chemically spiked and aged natural soils. Environ Toxicol Chem 35:1835–1842

140. Lotufo GR, Belden JB, Fisher JC, Chen SF, Mowery RA, Chambliss CK, Rosen G (2016) Accumulation and depuration of trinitrotoluene and related extractable and nonextractable (bound) residues in marine fish and mussels. Environ Pollut 210:129–136

141. Brentner LB, Mukherji ST, Walsh SA, Schnoor JL (2010) Localization of hexahydro-1,3,5-trinitro-1,3,5-triazine (RDX) and 2,4,6-trinitrotoluene (TNT) in poplar and switchgrass plants using phosphor imager autoradiography. Environ Pollut 158:470–475

142. Schneider K, Oltmanns J, Radenberg T, Schneider T, Pauly-Mundegar D (1996) Uptake of nitroaromatic compounds in plants. Environ Sci Pollut R 3:135–138

143. Vila M, Lorber-Pascal S, Laurent F (2007) Fate of RDX and TNT in agronomic plants. Environ Pollut 148:148–154

144. Chen D, Liu Z, Banwart W (2011) Concentration-dependent RDX uptake and remediation by crop plants. Environ Sci Pollut Res 18:908–917

145. Price RA, Pennington JC, Larson SL, Neumann D, Hayes CA (2002) Uptake of RDX and TNT by agronomic plants. Soil Sed Contam 11:307–326

146. Schoenmuth B, Mueller JO, Scharnhorst T, Schenke D, Buttner C, Pestemer W (2014) Elevated root retention of hexahydro-1,3,5-trinitro-1,3,5-triazine (RDX) in coniferous trees. Environ Sci Pollut R 21:3733–3743

147. Groom CA, Halasz A, Paquet L, Olivier L, Dubois C, Hawari J (2002) Accumulation of HMX (octahydro-1,3,5,7-tetranitri-1,3,5,7-tetrazocine) in indigenous and agricultural plants grown in HMX-contaminated anti-tank firing-range soil. Environ Sci Technol 36:112–118

148. Yoon JM, Van Aken B, Schnoor JL (2006) Leaching of contaminated leaves following uptake and phytoremediation of RDX, HMX, and TNT by Poplar. Int J Phytoremediat 8:81–94

149. Harvey SD, Fellows RJ, Cataldo DA, Bean RM (1993) Analysis of the explosive 2,4,6-trinitrophenylmethylnitramine (tetryl) in bush bean plants. J Chromatogr A 630:167–177

150. Richard T, Weidhaas J (2014) Dissolution, sorption, and phytoremediation of IMX-101 explosive formulation constituents: 2,4-dinitroanisole (DNAN), 3-nitro-1,2,4-triazol-5-one (NTO), and nitroguanidine. J Hazard Mater 280:561–569

151. Ballentine ML, Ariyarathna T, Smith RW, Cooper C, Vlahos P, Fallis S, Groshens TJ, Tobias C (2016) Uptake and fate of hexahydro-1,3,5-trinitro-1,3,5-triazine (RDX) in coastal marine biota determined using a stable isotopic tracer, ^{15}N—[RDX]. Chemosphere 153:28–38

152. Ballentine M, Tobias C, Vlahos P, Smith R, Cooper C (2015) Bioconcentration of TNT and RDX in coastal marine biota. Arch Environ Contam Toxicol 68:718–728

153. Belden JB, Lotufo GR, Lydy MJ (2005) Accumulation of hexahydro-1,3,5-trinitro-1,3,5-triazine in channel catfish (*Ictalurus punctatus*) and aquatic oligochaetes (*Lumbriculus variegatus*). Environ Toxicol Chem 24:1962–1967

154. Lotufo GR (2011) Whole-body and body-part-specific bioconcentration of explosive compounds in sheepshead minnows. Ecotoxicol Environ Saf 74:301–306

155. Lotufo GR, Biedenbach JM, Sims JG, Chappell P, Stanley JK, Gust KA (2015) Bioaccumulation kinetics of the conventional energetics TNT and RDX relative to insensitive munitions constituents DNAN and NTO in *Rana pipiens* tadpoles. Environ Toxicol Chem 34:880–886

156. Ownby DR, Belden JB, Lotufo GR, Lydy MJ (2005) Accumulation of trinitrotoluene (TNT) in aquatic organisms: Part 1—Bioconcentration and distribution in channel catfish (*Ictalurus punctatus*). Chemosphere 58:1153–1159

157. Lotufo GR, Lydy MJ (2005) Comparative toxicokinetics of explosive compounds in sheepshead minnows. Arch Environ Contam Toxicol 49:206–214

158. Lang PZ, Wang Y, Chen DB, Wang N, Zhao XM, Ding YZ (1997) Bioconcentration, elimination and metabolism of 2,4-dinitrotoluene in carps (*Cyprinus carpio* L.). Chemosphere 35:1799–1815

159. Wang Y, Wang ZJ, Wang CX, Wang WH (1999) Uptake of weakly hydrophobic nitroaromatics from water by semipermeable membrane devices (SPMDs) and by goldfish (*Carassius auratus*). Chemosphere 38:51–66

160. Belden JB, Ownby DR, Lotufo GR, Lydy MJ (2005) Accumulation of trinitrotoluene (TNT) in aquatic organisms: Part 2—bioconcentration in aquatic invertebrates and potential for trophic transfer to channel catfish (*Ictalurus punctatus*). Chemosphere 58:1161–1168

161. Houston JG, Lotufo GR (2005) Dietary exposure of fathead minnows to the explosives TNT and RDX and to the pesticide DDT using contaminated invertebrates. Int J Environ Res Publ Health 2:286–292

162. Lotufo GR, Blackburn W (2010) Bioaccumulation of TNT and DDT in sheepshead minnows, *Cyprinodon variegatus* L., following feeding of contaminated invertebrates. Bull Environ Contam Toxicol 84:545–549

163. Rosen G, Wild B, George R., Belden JB, Lotufo GR (2017) Optimization and field demonstration of a passive sampling technology for monitoring conventional munitions constituents in aquatic environments. Mar Technol Soc J (in press)

Index